Ultrafast Ion Spectroscopy of Transition Metal Complexes in Gas Phase

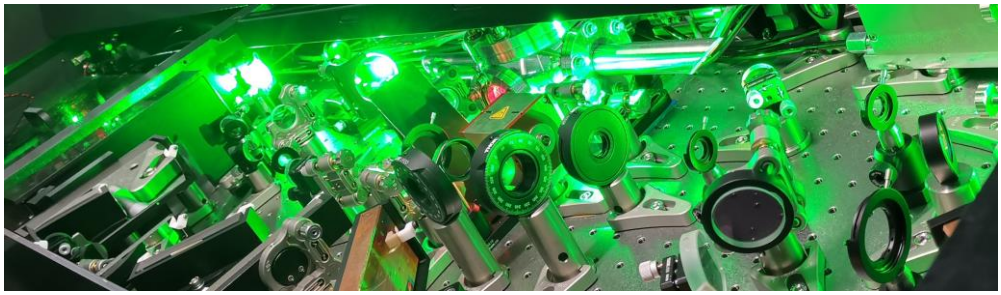

Zur Verleihung des akademischen Grades

'**Doktor der Naturwissenschaften**' (Dr. rer. nat.)

vom Fachbereich Chemie in Kaiserslautern genehmigte Dissertation

vorgelegt von

M. Sc. Roumany G. E. Israil,

geboren in Kairo

Rheinland-Pfälzische Technische Universität Kaiserslautern Landau

Tag der wissenschaftlichen Aussprache: 06.06.2025

Betreuer: PD Dr. Christoph Riehn

DE-386

Die vorliegende Arbeit wurde im Zeitraum von Oktober 2019 bis Mai 2025 im Fachbereich Chemie der Rheinland-Pfälzisch Technischen Universität, Standort Kaiserslautern im Arbeitskreis „Clusterchemie & Dynamik“ angefertigt und durch PD Dr. Christoph Riehn betreut.

Datum des Antrags der Eröffnung des Promotionsverfahrens: 07.02.2025

Promotionskommission:

Vorsitzender:	Prof. Dr. Werner R. Thiel
1. Berichterstatter:	PD Dr. Christoph Riehn
2. Berichterstatter:	Prof. Dr. Dr. Gereon Niedner-Schatteburg

Devoted to my wife Martina Natella and my children

"A scientist is nothing but a curious soul or a child who never stops asking questions."
– inspired by Albert Einstein

"And a scientist takes the mask off nature and stares at the face of God"
– inspired by fictional character Sheldon Cooper

Danksagung

Ein bedeutender Lebensabschnitt geht zu Ende – geprägt von akademischen Herausforderungen, persönlichen Erlebnissen und wertvollen Begegnungen. Diese Gelegenheit möchte ich nutzen, um allen zu danken, die mich auf meinem akademischen Weg während der Promotion auf unterschiedlichste Weise begleitet und unterstützt haben.

Zunächst gilt mein besonderer Dank PD Dr. Christoph Riehn für seine Betreuung und die unbeschwerte Zusammenarbeit. Danke für dein Vertrauen, das mich von meiner Masterarbeit bis zur Promotion begleitet hat. Für die Einführung in die „ultraschnelle Thematik“, die inspirierenden wissenschaftlichen Diskussionen – für die ich manche Züge und Busse gern habe fahren lassen – und für deine unermüdliche Unterstützung. Deine Wertschätzung auf Augenhöhe und die damit verbundene Kollegialität waren für mich eine große Motivation.

Mein Dank geht ebenso an Prof. Dr. Dr. G. Niedner-Schatteburg, der mit seiner inspirierenden und motivierenden Art stets dazu beiträgt, dass wir über uns selbst hinauswachsen. Danke für die Aufnahme in deinen Arbeitskreis und die Übernahme des Zweitgutachtens – das weiß ich sehr zu schätzen und es verleiht dem Abschluss meiner Promotion eine besondere Bedeutung.

Ein herzlicher Dank geht auch an Prof. Dr. W. R. Thiel für die Übernahme des Vorsitzes meiner Promotionskommission und für die Zusammenarbeit bei der Harmonisierung und Veröffentlichung unserer Ergebnisse.

Einen besonderen Dank möchte ich an Dr. Yevgeniy (Eugen) Nosenko richten – den „Drachenzähmer“ aller Lasersysteme. Deine ruhige, analytische, systematische und pragmatische Herangehensweise bei Problemen sowie deine beeindruckende Kompetenz in der Lasertechnik waren für mich eine unschätzbare und unersetzliche Hilfe. Danke für deine Geduld bei meiner Einführung in die Lasersysteme und deren Wartung – ich hoffe, ich konnte etwas von deinen Fähigkeiten übernehmen.

Ein weiterer Dank gilt allen Mitstreitern, Mitautor:innen und Wissenschaftler:innen, die durch ihre Kooperation innerhalb (RPTU) und außerhalb (KIT, UUlm, TU München) unsere Veröffentlichungen ermöglicht haben. Besonders hervorheben möchte ich hier Dr. Lars Schüßler, dessen wissenschaftliche Zusammenarbeit zu einer Freundschaft führte. Mein Dank gilt auch dem Leiter seines Arbeitskreises, Prof. Dr. Rolf Diller, für seine zielorientierte und strukturierte Arbeitsweise, die unseren Arbeitsprozess stets voranbrachte. Danke für die spannenden Diskussionen. Ein Prost auf die „Kaffeemaschine der Zeitkonstanten“!

Ein besonderer Dank an meinen „FemtoLab“-Partner Marcel Schmitt: Danke für die Möglichkeit, mit dir zusammenzuarbeiten, und für das großartige Team, das wir waren. Danke für deinen Einsatz, deine Unterstützung und unseren freundschaftlichen Austausch. Dem frühesten Zuwachs des „FemtoLab“, Philipp Weber, danke ich für deine innovativen Implementierungen, die unsere Auswertungsprozeduren erheblich erleichtert haben. Danke auch, dass ich euch beide in das „FemtoLab“ einführen durfte.

Ebenso danke ich meinen ehemaligen „FemtoLab“-Kollegen Dr. Dimitri Imanbaew und Dr. Sebastian Kruppa, die das „FemtoLab“ vor uns prägten und die Fackel weiterreichten.

Dem gesamten Arbeitskreis GNS danke ich für die freundliche, kollegiale Atmosphäre – insbesondere Mike Lembach, Max Luczak und Christopher Wiehn. Danke an Daniela Fries für die anregenden Gespräche und das Leuchten deiner Laserlampe – genau wie meiner. Eine wunderbare Begleitung in den späten Nächten der Messungen.

Beteiligt an der heiteren Arbeitsatmosphäre danke ich auch der anderen Seite des physikalisch-chemischen Flurs: dem Arbeitskreis von Jun.-Prof. Dr. Jennifer Meyer und dem ehemaligen Arbeitskreis von Prof. Dr. Markus Gerhards. Ich danke euch für die bereichernde Zusammenarbeit und die positive Stimmung. Besonders möchte ich hier Prof. Dr. Markus Gerhards† posthum für seine Begeisterung und Hingabe danken, die den Funken der Spektroskopie durch seine Lehre in vielen Studenten entzündet hat. Gott habe ihn selig.

Mein Dank gilt auch allen Master- und Bachelorpraktikanten, die ich während meiner Promotion betreuen durfte, darunter Marcel Meta, Marcel Schmitt, Xinyue Wang, Ying Chen, Philipp Weber und Syrine Bayrem.

Schließlich möchte ich mich bei meiner Familie bedanken. Mein besonderer Dank gilt meiner Lebenspartnerin und Ehefrau M.A. Martina Natella für ihre unendliche Unterstützung – sei es, das Lächeln in schwierigen Momenten zu finden, oder das Licht am Ende dunkler Tunnel scheinen zu lassen. Danke, dass du mich all die Jahre begleitet hast. Ein herzliches Danke auch an meine Kinder Mariella und Eleonora – ihr inspiriert mich jeden Tag. Ich bin mir sicher, dass das noch nicht Angekommene diese Inspiration ebenfalls fortsetzen wird.

Danke auch an all jene, die nicht namentlich erwähnt wurden. Ein großes Kapitel meines Lebens endet – ohne euch alle wäre dies nicht möglich gewesen. Herzlichen Dank!

Abschließend möchte ich meinen persönlichen Weg reflektieren, der mich zu diesem Meilenstein geführt hat: Mit 8 Jahren bin ich gemeinsam mit meiner Mutter aus unserem Heimatland nach Deutschland emigriert – als koptische Christen, auf der Suche nach besseren Zukunftsperspektiven. Die ersten sechs Jahre unseres Lebens hier waren von Entbehrungen geprägt. Wir lebten in Asylheimen, geteilt auf 15 m², mit langen Schlangen für Essenspakete und Duschen, die 800 Meter entfernt waren. Diese Jahre brachten auch zwei Umzüge mit sich, von Lebach nach Völklingen, was häufige Schulwechsel und wenig Stabilität bedeuteten. Während ich mich an ein völlig neues Leben und eine fremde Kultur gewöhnte, trug ich den Schmerz des Verlusts meiner Großfamilie und meiner Heimat stets mit mir.

Eine der größten Herausforderungen, die mich lange begleitet hat, war die Sprache. Ich hörte Deutsch mit acht Jahren zum ersten Mal und musste es mir im Alltag selbst aneignen – ohne Unterricht, ohne Unterstützung. Oft konnte ich dem Unterricht nicht vollständig folgen und hatte Schwierigkeiten mit Hausaufgaben. Während viele meiner Mitschüler sich ausschließlich auf den Schulstoff konzentrieren konnten, musste ich gleichzeitig eine neue Sprache erlernen. Doch mit der Zeit wurde Deutsch zu meiner zweiten Muttersprache – eine, die ich mir auf meinem eigenen Weg erarbeitet habe, auch wenn sie nie vollkommen fehlerfrei sein wird. Doch in einem Fach hatte ich nie Schwierigkeiten: Mathematik. Während ich mich in anderen Fächern mit der Sprache abmühen musste, war ich in Mathematik oft meinen Mitschülern voraus. Zahlen und Formeln brauchten keine Worte – sie sprachen für sich selbst. Mathematik war meine Konstante, eine universelle Sprache, die mir half, trotz aller Hürden in der Schule zu bestehen.

Später wurde mir bewusst: Mathematik ist die Sprache der Wissenschaft, die Menschen weltweit verbindet – und genau diese Sprache öffnete mir das Interesse an weiteren Naturwissenschaften wie Physik und Chemie.

2006 zogen wir schließlich in eine eigene Wohnung nach Neunkirchen, und ich hatte zum ersten Mal in meinem Leben ein eigenes Zimmer. Dieser Moment markierte für mich das Gefühl, endlich in Deutschland angekommen zu sein. Mein schulischer Weg führte mich von der Realschule, die ich als zweitbester Schüler abschloss, über das Abitur bis hin zu meinem Bachelorstudium in Chemie – ein Fach, das meine Neugier auf die Natur und ihre Gesetze widerspiegelte. Doch der Weg war nicht immer einfach. Wissenschaftliche Bildung spielte in meinem Umfeld kaum eine Rolle – weder in den Asylheimen meiner Kindheit noch später. Ohne akademische Vorbilder oder Unterstützung bei Hausaufgaben und Prüfungen – und das alles in einer Sprache, die mir nicht von Anfang an vertraut war – musste ich mir vieles selbst erarbeiten und konnte oft nicht mit den gleichen Voraussetzungen wie viele meiner Mitschüler konkurrieren. Dies spiegelte sich auch in meinen Noten wider, doch ich habe mich nie von Rückschlägen entmutigen lassen. Meinen Master schloss ich mit für mich zufriedenstellenden Noten ab, was mir die Tür zu tiefergehender Forschung und letztendlich zu diesem Punkt in meiner wissenschaftlichen Laufbahn eröffnete.

Heute bin ich zutiefst dankbar, diesen langen und manchmal steinigen Weg gegangen zu sein. Durch Durchhaltevermögen und die Unterstützung vieler Menschen ist es mir gelungen, den höchsten akademischen Grad zu erreichen. Mittlerweile lebe ich mit meiner Familie im eigenen Haus mit einem großen Garten und einem kleinen Bach. Neben meiner Familie sind meine Leidenschaften für Swing-Tanz und Jazzmusik ein wichtiger Teil meines Lebens – sie verbinden mich mit Leichtigkeit, Eleganz und Improvisation, die mich auch in meinem persönlichen und akademischen Weg begleitet haben.

Ohne die Hilfe und Ermutigung der Menschen, die an mich geglaubt haben, wäre all das nicht möglich gewesen. Euch allen gilt mein tiefster Dank.

List of Publications

The following publications form an integral part of this thesis.

Publication 1:

"Ultrafast Spectroscopy of Ru(II) Polypyridine Complexes in the Gas Phase and the Liquid Phase: $[Ru(2,2'\text{-bipyridine})_2(\text{nicotinamide})_2]^{2+}$"

R. G. E. Israil, L. Schüßler, P. Hütchen, W. R. Thiel, R. Diller, C. Riehn

Physical Chemistry Chemical Physics **2023**, *25* (6), 4899-4914
DOI: 10.1039/d2cp03765c

Publication 2 (submitted on the 18th of February):

"Ultrafast Spectroscopy of a Series of Ru(II) Polypyridine Complexes in Gas Phase and Solution: Control of Electronic State Lifetime and Reactivity by Systematic Ligand Derivatization "

R. G. E. Israil, L. Schüßler, P. Hütchen, W. R. Thiel, R. Diller, C. Riehn

Publication 3:

"Metal-to-Metal Distance Modulated Au (I)/Ru (II) Cyclophanyl Complexes: Cooperative Effects in Photoredox Catalysis"

C. Zippel, R. Israil, L. Schüßler, Z. Hassan, E. K. Schneider, P. Weis, M. Nieger, C. Bizzarri, M. M. Kappes, C. Riehn

Chemistry–A European Journal 2021, 27 (61), 15188-15201
DOI: 10.1002/chem.202102341

Publication 4:

"Time-Resolved Spectroscopy and Electronic Structure of Mono- and Dinuclear Pyridyl-Triazole/DPEPhos-Based Cu (I) Complexes"

M. Grupe, P. Boden, P. Di Martino-Fumo, X. Gui, C. Bruschi, R. Israil, M. Schmitt, M. Nieger, M. Gerhards, W. Klopper

Chemistry–A European Journal **2021**, 27 (61), 15252-15271
DOI: 10.1002/chem.202102760

Contributions on Conferences: Speaking Engagements & Presentations

International Conference on Ultrafast Phenomena, July **2022.**

DPG Spring Meeting “Erlangen22”, March **2022.**

3MET PhD Meeting and Symposium of the Collaborative Research Center of TUK and KIT, October **2021.**

DPG Conference of the Section Atoms, Molecules, Quantum Optics, and Plasmas (SAMOP), September **2021.**

Bunsen Conference, May **2021.**

3rd Workshop on "Light-Controlled Reactivity of Metal Complexes", December **2020.**

22nd Ultrafast Phenomena Conference, November **2020**.

3MET PhD Meeting and Symposium of the Collaborative Research Center of TUK and KIT, September **2020.**

Bunsen Conference, April **2020.**

3MET PhD Meeting and Symposium of the Collaborative Research Center of TUK and KIT, October **2019** and October **2018.**

Conferences Proceedings:

1. “Ultrafast Dynamics of RuII-polypyridyl Complexes – Photoinduced Ligand Dissociation Dynamics in Gas Phase and Solution”, R. Israil, L. Schüßler, M. Schmitt, M. Grupe, P. Hütchen, W. R. Thiel, R. Diller, and C. Riehn, presented at *The International Conference on Ultrafast Phenomena (UP)*, **2022**, Tu4A.4. DOI: 10.1364/UP.2022.Tu4A.4
2. “Gold Rush in Dynamics? Time-resolved Ion Spectroscopy Reveals Ultrafast Processes in Isomorphic, Ligated Ag/Au Coinage Metal Dimers”, S. V. Kruppa, M. Schmitt, R. Israil, F. Bäppler, M. Grupe, L. Schüßler, R. Diller, W. Klopper, and C. Riehn, presented at *The 22nd International Conference on Ultrafast Phenomena*, **2020**, M4B.29. DOI: 10.1364/UP.2020.M4B.29

Table of Contents

1. Introduction 1

2. Experimental Setup and Methods 8

2.1 Electrospray Ionization Quadrupole Ion Trap Mass Spectrometer (ESI-QIT-MS) 8

2.1.1 Electrospray Ionization (ESI) Source 10

2.1.2 Ion Optics 12

2.1.3 Quadrupole Ion Trap (QIT) 15

2.1.4 Scan segments 18

2.1.5 Collision-Induced Dissociation (CID) 19

2.1.6 Negative Chemical Ionization (nCI) Source 23

2.1.7 Gas Inlet Line 27

2.1.8 Detector 29

2.1.9 Space Charge Effect and Ion Charge Control 30

2.2 Femtosecond Laser System 33

2.2.1 Ti:Sa Crystal as Laser Medium 34

2.2.2 Mode-locking and Kerr-lens Effect 35

2.2.3 Ti:Sa Oscillator 36

2.2.4 Chirped-Pulse Amplification (CPA) within the Wyvern 1000™ 39

2.2.5 FROG Scan: Realtime Ultrashort Pulse Measurement 44

2.2.6 Optical Parametric Generator/Amplifier (TOPAS-C) 47

2.3 Nanosecond Laser System 52

2.4 Coupling of the Mass Spectrometer with the Laser Systems 54

2.5 Ion Trap Laser Spectroscopy 56

2.5.1 Static UVPD Spectroscopy in the QIT 59

2.5.2 Transient Photodissociation (τ-PD) 66

2.6 Computational Methods 70

2.6.1 Density Functional Theory (DFT) 70

2.6.2 Time-Dependent Density Functional Theory (TD-DFT) 74

2.7 Measurement Protocols and Data Processing 76

3. Publications and Submissions 83

3.1 Publication 1: Ultrafast Spectroscopy of Ru^{II} Polypyridine Complexes in Gas Phase and Liquid Phase: $[Ru(2,2'\text{-bipyridine})_2(\text{nicotinamide})_2]^{2+}$ 83

3.2 Publication 2: Spectroscopy of a Series of Ru(II) Polypyridine Complexes in Gas Phase and Solution: Control of Electronic State Lifetime and Reactivity by Systematic Ligand Derivatization (submitted manuscript) 103

3.3 Publication 3: Metal-to-Metal Distance Modulated Au(I)/Ru(II) Cyclophanyl Complexes: Cooperative Effects in Photoredox Catalysis 143

3.4 Publication 4: Time-Resolved Spectroscopy and Electronic Structure of Mono- and Dinuclear Pyridyl-Triazole/DPEPhos-Based Cu(I) Complexes 161

4. Additional Research Projects 190

4.1 Ion Trap Spectroscopy on Polyoxovanadates (POV) 190

4.1.1 Introduction 190

4.1.2 Experimental Setup 192

4.1.3 Results and Discussion 193

4.1.4 Conclusion 201

4.2 Ion Trap Spectroscopy on a Ru^{II}-phenazine-Rh^{III} dyad 203

4.2.1 Introduction 203

4.2.2 Experimental Setup 205

4.2.3 Results and Discussion 207

4.2.4 Conclusion 219

5. Summary 220

6. Final Conclusion 227

7. References 228

Eidesstaatliche Erklärung 246

Academic Résumé 247

List of Abbreviations

(TD) DFT	**(time-dependent) density functional theory**
Ac	**acetyl**
ACN	**acetonitrile**
appr.	**approximately**
BBO crystal	**β-barium borate (BaB_2O_4) crystal; NC**
BDE	**bond dissociation energy**
Bpy	**2,2'-bipyridine**
BS	**beam splitter**
CCD	**charge-coupled device**
CEM	**channel electron multiplier**
CID	**collision-induced dissociation**
CM	**curved mirror**
Com	**center-of-mass**
Cp*	**pentamethylcyclopentadienyl**
CPA	**chirped-pulse-amplification**
CRM	**charge residue model**
CT	**charge transfer**
CVM	**convex mirror**
Cw	**continuous wave**
DC	**direct current**
DCM	**dichloromethane**
DeGe	**delay generator**
DF	**dust filter**
DM	**dielectric mirror**
DP	**diode-pumped**
ECP	**effective core potential**
ESI	**electrospray ionization**
ETD	**electron transfer dissociation**
ETnoD	**electron transfer with no dissociation**
ETR	**electron transfer reduction**
FL	**focusing lens**
FR	**Faraday rotator**
Fwhm	**full width at half maximum**
GEA	**gradient-expansion approximation**
GGA	**generalized-gradient approximations**
GVD	**group velocity dispersion**
IC	**internal conversion**
ICC	**ion charge control**
IEM	**ion evaporation model**
ILCT	**inter-ligand charge transfer**

IRMPD	**infrared multiphoton dissociation**
ISC	**intersystem crossing**
ISCID	**in-source collision-induced dissociation**
IVR	**intramolecular vibrational energy redistribution**
KIT	**Karlsruhe Institute of Technology**
KLM	**Kerr lens mode-locking**
L	**lens**
LMCT	**ligand-to-metal charge transfer**
LSDA	**local-spin-density approximation**
m/z	**mass-to-charge ratio**
MC	**metal centered**
Me-	**methyl, CH_3-**
MeH	**methane / CH_4**
ML	**mode-locked**
MLCT	**metal-to-ligand charge transfer**
MS	**mass spectrometer / mass spectrometry**
n.d.	**not determined**
NBA	**n-butylammonium / nBu_4N**
NC	**non-linear crystal**
nCI	**negative chemical ionization**
NIR	**near infrared**
OC	**output coupler**
OD	**optical density**
OPA	**optical parametric amplifier /amplification**
OPG	**optical parametric generator**
P	**prism**
PC	**Pockels cell**
PD	**photodissociation**
PEEK	**polyether ether ketone polymer**
PHD	**photodiode**
PI	**precursor ions**
PM	**plano mirror**
PoA	**pump for power**
POM	**polyoxometalates**
POV	**polyoxovanadates**
Pp	**pulse-pairs**
PrA	**pre-amplification**
PTR	**proton transfer reaction**
QIT	**quadrupole ion trap**
RF	**radio frequency**
RM	**rear mirror**

RPTU	**Rheinland-Pfälzische Technische Universität**
SCE	**Space charge effect**
SF	**sum frequency**
SFP	**spectrometer fiber probe**
S-G	**dispersive stretcher grating**
SH	**second harmonic**
TA	**transient absorption**
TADF	**thermally activated delayed fluorescence**
Tbbpy	**4,4'-di-tert-butyl-2,2'-bipyridine**
TD	**dispersive plate**
TFP	**thin film polarizer**
TFY	**total fragmentation yield**
THF	**tetrahydrofuran**
Ti:Sa	**Titanium (Ti 3+):sapphire (Al_2O_3)**
TM	**transition metal**
TMCs	**transition metal complexes**
TOPAS-C	**traveling-wave optical parametric amplifier of white light continuum**
Tpphz	**tetrapyrido[3,2-a:2',3'-c:3'',2''-h:2''',3'''-j]phenazine**
TU	**Technische Universität**
U	**internal energy**
UEG	**uniform electron gas**
UUlm	**Universität Ulm**
VF	**density filter**
WLC	**white-light continuum**
Ws	**wavelength separator**
YAG	**Yttrium aluminum garnet ($Y_3Al_5O_{12}$)**

1. Introduction

The intricate dance of atoms and electrons during chemical transformations is a fundamental aspect of chemical physics. At the molecular scale, phenomena such as bond formation and cleavage, charge migration and energy distribution occur on ultrafast timescales, typically ranging from femtoseconds (1 fs = 10^{-15} s) to picoseconds (1 ps = 10^{-12} s). Understanding these fleeting phenomena is essential to unraveling the fundamental mechanisms of chemical reactivity and harnessing them in applications such as solar energy conversion[1-2], photocatalysis[3-4], organic light-emitting diodes (OLEDs)[5] and medicine[6-7].

The advent of ultrafast spectroscopy marked a paradigm shift, enabling the study of these rapid molecular dynamics in “real time” and providing tools to investigate phenomena occurring on femtosecond timescales. In the 1980s, Ahmed Zewail pioneered femtochemistry, introducing ultrashort laser pulses that enabled the real-time tracking of molecular events.[8] This groundbreaking innovation allowed researchers to visualize fundamental processes—such as intersystem crossing (ISC), charge transfer (CT), and vibrational relaxation—capturing a "molecular movie" of chemical reactions.[9-11] Zewail's work laid the foundation for understanding reaction mechanisms with unprecedented temporal resolution.[12]

Since then, researchers have developed and advanced methodologies that refine the study of ultrafast processes. Techniques such as transient absorption (TA)[13], femtosecond fluorescence upconversion[14-15] and time-resolved photoelectron spectroscopy[16] are enabling real-time observation of electronic and vibrational state changes. These approaches, combined with advancements in laser technology have expanded the scope of ultrafast spectroscopy to increasingly complex systems enabling the exploration of diverse phenomena ranging from energy redistribution in biomolecules to charge transfer in photovoltaic materials.[17]

The typical approach in time-resolved pump-probe experiments involves ultrashort laser pulses (pump) exciting a molecular ensemble, driving it into specific vibrational or electronic

states or more specific: generating a vibronic wave packet. The subsequent temporal evolution of the excited states is then tracked using a second pulse (probe). For electronically excited states, this often involves monitoring excited-state absorption/emission to higher/lower electronic states. As indicated above, Fourier-transform limited laser pulses enable the coherent excitation of multiple electronic, vibrational and rotational modes, forming wave packets that offer deeper insights into excited-state structures and interactions.[18-19]

Among the many systems studied using ultrafast spectroscopy, transition metal complexes (TMCs)—particularly those containing ruthenium, copper, and gold—have emerged as highly versatile platforms for exploring fundamental photophysical processes and for developing functional light-driven applications.[3-4,20] Their functionality arises from dense manifolds of singlet and triplet states that enable metal-to-ligand charge transfer (MLCT), ligand-to-metal charge transfer (LMCT), and metal-centered (MC) excitations. These transitions often fall in the visible range (400-600 nm), with spectral position and absorption strength determined by the metal oxidation state, ligand field, and π-conjugation.[3,20-21]

Photoexcitation typically populates a Franck-Condon state,[3] which undergoes rapid relaxation via intramolecular vibrational energy redistribution (IVR, 100-500 fs)[22], internal conversion (IC, <1 ps)[23], and intersystem crossing (ISC, ~0.03-30 ps)[20,24-25], the latter driven efficiently by spin-orbit coupling in systems containing heavy atoms such as bromine, iodine, or metal centers[21,26]. As shown in benchmark systems such as $[Ru(bpy)_3]^{2+}$ (bpy = 2,2'-bipyridine),[27-28] these processes determine whether the system evolves into long-lived ^{3}MLCT states (100 ns-1 μs), suitable for energy or electron transfer in photosensitizers[7,27], or into short-lived ^{3}MC states (<1 ns), which often enable ligand dissociation or structural reorganization ideal for photoredox catalysis.[28-29]

The balance between these excited-state pathways is sensitive to molecular design and the external environment. Structural modifications in ligand architecture, such as ligand derivatization or changes in coordination geometry, allow for targeted tuning of the MLCT-MC energy gap, thereby modulating excited-state lifetime, reactivity, and decay channels.[20,30] In

heterobimetallic systems, the intermetallic distance and orbital communication can be adjusted via the linker architecture to influence charge transfer or relaxation dynamics.[31] Similarly, environmental factors—including solvent polarity[32], counterion identity[33-34], pressure and temperature[35-37]—can stabilize or destabilize charge-transfer states and affect the branching between relaxation pathways. These external influences can enhance MLCT state lifetimes, alter vibrational cooling rates, or favor reactive MC population. Understanding these dynamics is essential for the development of TM complexes in applications like photoredox catalysis[29], solar energy conversion[2,4], and light-emitting devices[5].

TMCs are commonly studied in solution, their native environment, but this setting introduces significant challenges. Solvent interactions, counterion effects, and protonation equilibria can obscure intrinsic molecular properties, while solvent reorganization often overlaps with the timescales of molecular dynamics, complicating data interpretation.[32,38-39] These external influences may mask intrinsic deactivation pathways, and the limited resolution of time-resolved spectroscopy can hinder differentiation between competing kinetic models. Benchmarking against quantum chemical calculations is also difficult, as solvent effects alter electronic transitions and require resource-intensive modeling to account for dense electronic states, spin-orbit, and nonadiabatic couplings.[24,40] Similarly, in solid-phase systems, crystal packing and intermolecular interactions add complexity to both experiments and theoretical simulations, demanding explicit inclusion of environmental effects like lattice structures.[41-44]

An effective approach to overcome the limitations and challenges of experimental spectroscopy in liquid and solid phases—while also reducing computational demands—represents gas-phase spectroscopy. In this solvent-free environment, molecular properties can be examined in isolation, enabling the investigation of intrinsic excited-state dynamics, charge-transfer processes, structural changes upon excitation, stability in the gas phase compared to other phases, and fragmentation behavior (whether spontaneous or induced by collisions or light, respectively), without perturbation by surrounding media.

A key challenge in gas-phase studies is the limited particle density, which makes it difficult to observe changes in transmitted light intensity.[45-51] To address this, action spectroscopy, also

called consequence spectroscopy, measures the yield of the reaction products as a result or consequence from photoexcitation. Dynamic experiments extend this approach by tracking the yield as a function of the time delay between pump and probe laser pulses.[52-53] Jouvet *et al.* were among the first to establish the use of pump-probe methods in conjunction with mass spectrometry for gas-phase studies.[54-55] By coupling laser-induced dissociation with mass spectrometric detection, their approach enabled time-resolved investigations of ultrafast dynamics in isolated systems. This method was further extended by Weinkauf *et al.*, who coupled a femtosecond laser system with a commercial quadrupole ion trap mass spectrometer, demonstrating the potential of gas-phase action spectroscopy for dynamic studies.[56-57]

For the experimental work presented in this thesis, a mass spectrometer equipped with an electrospray ionization (ESI) source was used in combination with tunable ultrafast and nanosecond laser systems to investigate photochemical relaxation processes across broad temporal ranges. By enabling time-resolved pump-probe photodissociation action spectroscopy, this setup offers insights into electronically excited-state dynamics, as well as rovibronic dynamics and the associated wave packet motion.

The preparation of the target ionic compounds is achieved via ESI, followed by isolating and storing in a modified quadrupole ion trap. The modification allows for laser beam access to the stored ions, facilitating both static and dynamic laser spectroscopy experiments. In static studies, UV photodissociation (UVPD) is employed to analyze photofragmentation yield as a function of wavelength. In dynamic experiments, time-resolved techniques monitor photofragmentation yields as a function of the time delay between pump and probe laser pulses (τ-PD). Additionally, the inclusion of an electron transfer dissociation (ETD) unit enables reduction of isolated ions in the gas phase, expanding the applicability of the apparatus to a wider range of photochemical relaxation processes.

In this thesis various TMC systems are investigated in the gas phase to gain insights into their photophysical and photochemical properties, focusing on how they differ from those observed in other phases, particularly the liquid phase. Additionally, it explores how structural

modifications influence these properties. Gas-phase studies isolate complexes from solvent interactions, enabling direct characterization of intrinsic relaxation processes. These results can be benchmarked against solution-phase measurements to understand the influence of solvent environments on excited-state properties, including lifetimes, charge-transfer efficiency, and dissociation mechanisms.

The first focus of this thesis lies on the photophysical and photochemical properties of ruthenium polypyridine complexes, particularly $[Ru(bpy)_2(nicotinamide)_2]^{2+}$.[58] Using gas-phase UVPD spectroscopy coupled with femtosecond laser pulses, I investigated their excited-state dynamics and ligand dissociation pathways, supported by (TD-)DFT calculations. Solution-phase transient absorption measurements, which were crucial for benchmarking gas-phase data, were performed by Dr. Lars Schüssler, member of the group of Prof. Dr. Rolf Diller (Department of Physics, RPTU KL-LD).[58] The synthetic efforts for these Ru-polypyridine complexes were conducted by Dr. Patrick Hütchen from the group of Prof. Dr. Werner R. Thiel (Department of Chemistry, Inorganic Chemistry, RPTU KL-LD).[59] By systematically comparing results from gas-phase and solution, these studies revealed the critical role of solvent interactions in electronic relaxation processes and ligand substitution reactions, enabling a deeper understanding of reaction mechanisms and structural dynamics.

Building upon these findings, the second project focuses on elucidating how systematic ligand derivatization influences the photophysical properties of Ru(II) polypyridine complexes. By applying Hammett parameters to quantify the electronic effects of different substituents, the work aims to determine how electron-donating and electron-withdrawing groups impact the energetic landscape and population dynamics of MLCT and metal-centered (MC) states. Central to this investigation is the isolation of intrinsic electronic behavior in the gas phase, with particular attention on how these properties are modulated in solution by solvent-mediated effects on excited-state lifetimes and relaxation pathways.[60-61]

Expanding beyond mononuclear systems, heterobimetallic Au(I)/Ru(II) cyclophanyl complexes were examined with a focus on how variations in spatial metal arrangements influence photophysical behavior and catalytic efficiency.[62] Central to this study is the role of

the rigid [2.2]paracyclophane linker, which allows systematic modulation of the metal-to-metal distance and thus enables exploration of cooperative effects between the two metal centers. Particular attention is given to the consequences of these spatial variations for photoinduced dynamics, charge transfer, and catalytic performance. This work was led by C. Zippel of Prof. Dr. Stefan Bräse's group, who also synthesized the complexes. Crystallographic characterization was provided by Dr. Martin Nieger, computational modeling by Dr. Patrick Weis and Prof. Dr. Manfred M. Kappes, while solution-phase spectroscopy and electrochemical measurements were conducted by Dr. Lars Schüßler, Prof. Dr. Rolf Diller, and the group of Prof. Dr. Claudia Bizzarri.

A related project focuses on mono- and dinuclear copper(I) complexes with pyridyl-triazole ligands, examining the impact of nuclearity on photophysical properties.[63] These heteroleptic Cu(I) complexes, synthesized by Prof. Dr. Bizzarri's group, were spectroscopically characterized in both solution and solid phase by various collaborators at RPTU and KIT.[64] Led by M. Grupe and P. Boden, the study aims to identify structure–function relationships that determine key properties such as excited-state lifetime, geometric relaxation (e.g., flattening distortion), and emission behavior. Of particular interest is the role of nuclearity in modulating non-radiative and radiative decay channels, as well as the extent of cooperative effects in dinuclear systems. My contribution centered on gas-phase time-resolved photodissociation spectroscopy to isolate the intrinsic excited-state dynamics and assess how these properties evolve in the absence of matrix effects.

Another area of focus is the gas-phase investigation of polyoxovanadates (POVs), serving as molecular models for vanadium oxide catalysts. Synthesized by the Streb group and modeled by the Jacob group, these clusters were studied to explore their intrinsic photochemical properties without interference from solvent or counterion effects.[65-66] Using ion trap UV photodissociation and time-resolved spectroscopy, the study characterizes their fragmentation behavior, charge-transfer excitations, and excited-state dynamics. The work highlights the challenges of working with highly fragile or overly stable species and

demonstrates the feasibility of POV characterization in the gas phase—providing a basis for understanding their photoreactivity and guiding future experimental strategies.

The final project of this thesis focuses on the intrinsic properties of the heterobimetallic complex $[(tbbpy)_2Ru(tpphz)Rh(Cp^*)Cl]^{3+}$ across its different redox states. These systems, incorporating a Ru(II) photosensitizer and a catalytically active Rh(III) center bridged by a tpphz ligand, offer an opportunity to probe how stepwise reduction influences electronic structure, bond strengths, and excited-state behavior. Building upon earlier work on Ru–Pd/Pt dyads, this study explores the effects of charge localization and redistribution within the Ru–tpphz–Rh motif using a combination of ion trap mass spectrometry, ETD, CID, and action spectroscopy techniques. The investigation targets redox-induced changes in fragmentation pathways and UV absorption features and evaluates the applicability of time-resolved photodissociation (τ-PD) for capturing early excited-state dynamics in isolated ions.

This thesis compares solvent-free and solution environments, shedding light on the interplay between intrinsic and extrinsic properties. These interactions ultimately determine the system's efficiency and functionality. By integrating gas-phase studies with complementary condensed-phase spectroscopy, this thesis provides a comprehensive perspective on the dynamics of TMCs. The methodology enhances the interpretation of ultrafast spectroscopic data and bridges fundamental research with practical applications, advancing our understanding of TMCs and other molecular systems. Leveraging state-of-the-art ultrafast techniques and fostering interdisciplinary collaborations, the insights gained contribute to the design of next-generation materials for energy conversion, catalysis, and photonics.

2. Experimental Setup and Methods

2.1 Electrospray Ionization Quadrupole Ion Trap Mass Spectrometer (ESI-QIT-MS)

Mass spectrometry, a powerful analytical technique, identifies and characterizes molecules based on their mass-to-charge (m/z) ratio. The ESI technique, particularly pivotal, enables the transfer of compounds of diverse molecular weights from liquid to gas phase, revolutionizing analytical applications in numerous fields including plant metabolomics[67], medicine[68], molecular biology[69-70], as well as areas like food safety[71] and antiterrorism[72].

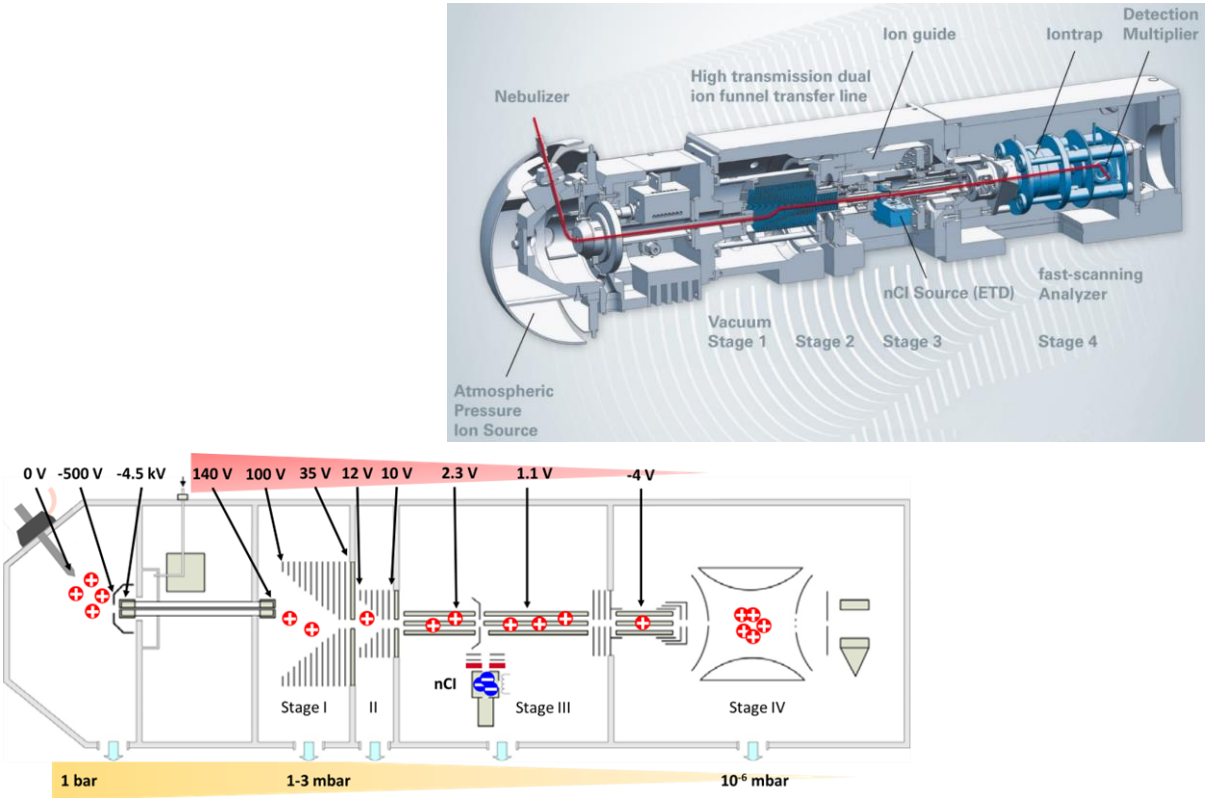

Figure 2.1 TOP: 3D schematic setup of the amaZon series mass spectrometer by Bruker Daltonics. The red highlight indicates the analyte ions' pathway.[73] **BOTTOM**: 2D schematic setup of the amaZon series mass spectrometer, illustrating the ion transfer pathway by cations and showcasing pressure gradient and voltage variations across its distinct segments. The values are derived from measurements using amaZon X, adapted from [73].

In this thesis, mass spectrometric experiments were primarily employed by the amaZonX speed spectrometer (Bruker Daltonics). This instrument, which features an electron transfer dissociation/reduction (ETD/R) unit and a modified quadrupole ion trap (QIT), was specifically adapted to integrate femtosecond laser pulses for spectroscopic analysis. Other spectrometers within our research group, such as the amaZon ETD or amaZon SL, possess slightly different features, often complemented by additional analytical techniques. However, they all share the fundamental setup of an "Apollo II" electrospray ionization (ESI) source and a QIT, as depicted in the schematic in Figure 2.1. A short outline of the fundamental working principles of the amaZonX speed mass spectrometer should be given here, followed by a more detailed description of the specific components.

This setup comprises an ESI source, ion optics for focusing ions, an ion trap, and a detector. Analyte ions are introduced at atmospheric pressure and detected under high vacuum conditions (appr. 10^{-6} mbar). Given the substantial difference in pressure (nine orders of magnitude), the mass spectrometer is equipped with a four-stage differentially pumped vacuum system.

The sample solution enters the ESI source, where ions are transferred from the liquid phase to the gas phase at atmospheric pressure. Subsequently, ions pass through a 200 µm diameter glass capillary, serving as a transfer capillary into the first vacuum stage, maintained at a pressure of a few millibars via a foreline oil pump.

Upon exiting the glass capillary, the ions enter precision ion guides designed to remove neutral particles and adjust the ion path to create a focused beam suitable for analysis. An electric field propels and precisely steers this beam through the ion optics to the quadrupole analyzer. The quadrupole analyzer initially sorts the ions based on their mass-to-charge ratio ("Isolation"). Additionally, a chemical ionization (CI) unit is positioned along the path to the quadrupole, facilitating the use of Electron Transfer Dissociation/Reduction (ETD/R) techniques, thereby expanding the scope of our mass spectrometric capabilities.

After arrival into the ion trap, trapped ions may perform various means of dissociation and gas phase reactions, such as laser radiation at different wavelengths, Collision-Induced Dissociation (CID), ETD/R, etc., or simply pass through to the detector stage. The detector and the ion trap are situated in stage four, where the pressure is lowest (approximately 10^{-6} mbar). However, inside the ion trap a pressure (mainly He) of ca. 10^{-3} mbar is maintained to prevent radiofrequency (RF) heating of the trapped ions and inhibits inelastic collisions between the ions to avoid fragmentation of the molecules of interest. The pressure inside the QIT is estimated by the Helium flow rate and the outside pressure.[74] The stages two to four of the vacuum system are evacuated by a turbo molecular pump.

The mass spectrometer is operated using trapControl – a software provided by Bruker Daltonics. This software facilitates the adjustment of various parameters of the ESI source, the QIT, and the detector to achieve the desired mass resolution, the number of ions stored in the trap or the number of scans for averaging. In the subsequent sections, an overview of the Electrospray Ionization Quadrupole Ion Trap Mass Spectrometer (ESI-QIT-MS) and its main components is provided.

2.1.1 Electrospray Ionization (ESI) Source

The electrospray ionization (ESI) is a widely embraced technique in mass spectrometry, enabling the transfer of ionized molecules from a liquid phase to the gas phase while ensuring a minimal fragmentation of the target molecule. Originating from the groundwork laid by Zeleny *et al.*,[75] the ESI source was initially realized by Dole[76] and further advanced by Fenn *et al*.[55,77-78]. Along with Kōichi Tanaka, Fenn was awarded the Nobel Prize in 2002 for implementing ESI mass spectrometry, a pivotal method in identifying biological macromolecules.[68]

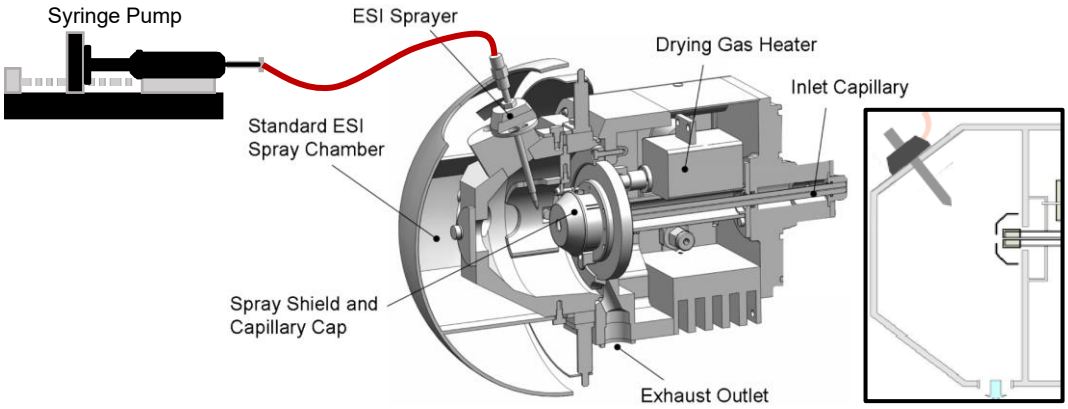

Figure 2.2 Schematic overview of the Apollo II ESI source[73] connected to the syringe pump containing the sample solution. The black-framed region denotes a 2D schematic setup of the ESI source.[79]

The ESI source comprises several integral components, including a spray unit, a spray chamber, a spray shield with a capillary cap, solvent waste outlet, a dry gas heater, and an inlet/transfer capillary, as represented in Figure 2.2.

A continuous introduction of the sample solution into the ESI sprayer occurs through tubing via a syringe pump, typically operating at a standard flow rate of 120 µL/h, if not mentioned otherwise. As the solution traverses the spray needle, it undergoes nebulization at the tip using nitrogen as the nebulizer gas emitted from the surrounding tube, typically regulated at 7 psi (~0.48 bar).

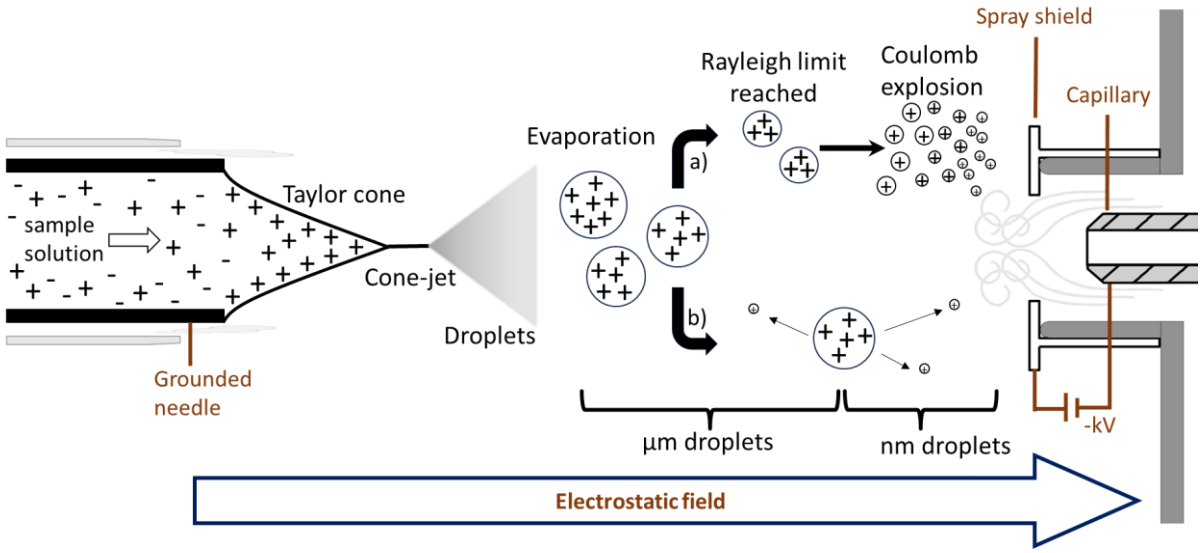

Figure 2.3 Schematic illustration of the ESI process for positive polarity, where two pathways for ion formation are depicted: a) Charge Residue Model and b) Ion Evaporation Model IEM. Adapted from [80].

A central aspect of the ESI process involves a significant potential difference. While the spray needle is grounded, a high voltage (~4.5 kV) is applied to the spray shield and the metal cap of the transfer capillary, creating a robust electrostatic field that eventually propels ions toward the capillary entrance. Depending on polarity of this high electrostatic field, molecules with opposite charges migrate to the surface inducing charge separation within the solution in the spray needle, culminating in the formation of the Taylor cone[81]. The Taylor cone results from deforming the liquid meniscus at the needle's tip into a conical shape that emerges as a fine jet,[82] as depicted in Figure 2.3. Subsequently, microdroplets disperse from this cone-jet due to electrostatic repulsion.[68]

As the solvent in these droplets continuously evaporates due to a countercurrent flow of dry gas at a rate of 4 L/min, maintained at 180°C, droplet size diminishes. The convergence of surface charges amplifies the charge density on the droplet's surface until reaching the Rayleigh limit[83], causing "Coulomb explosion"[84]. This phenomenon disintegrates the microdroplets into nanometer-sized ones, subsequently undergoing additional evaporation due to the drying gas. This iterative process leads to the creation of smaller droplets characterized by a high surface-charge density, ultimately resulting in the production of bare ions. This representation of ion formation is recognized as the Charge Residue Model (CRM).[76,80] An alternative model, proposed for smaller ions, is the Ion Evaporation Model (IEM), elucidating the emission of ions directly from the droplets into the gas phase due to the exceedingly high charge density at the droplet surface, overcoming surface tension.[80,85] Both mechanisms provide insights into ion formation within the ESI process, extensively discussed in literature.[86-89]

2.1.2 Ion Optics

The ion optics of the amaZon mass spectrometers are designed to efficiently transfer ions formed at ambient pressure (10^3 mbar) into the low-pressure (10^{-6} mbar) mass analyzer by manipulating and focusing the ion influx. These ion optics extend from vacuum stage one to three of the mass spectrometer (Figure 2.1) and consist of a double-stage ion funnel, a multipole, and gate and focus lenses (Figure 2.4).

The double-stage ion funnel extends over the first and second vacuum stages of the mass spectrometer (Figure 2.4, Figure 2.1) and consists of two separated ion funnels with closely spaced, thin concentric ring electrodes with subsequently decreasing aperture diameters. The first ion funnel possesses a wide entry aperture, whereas the second ion funnel has a much smaller one.

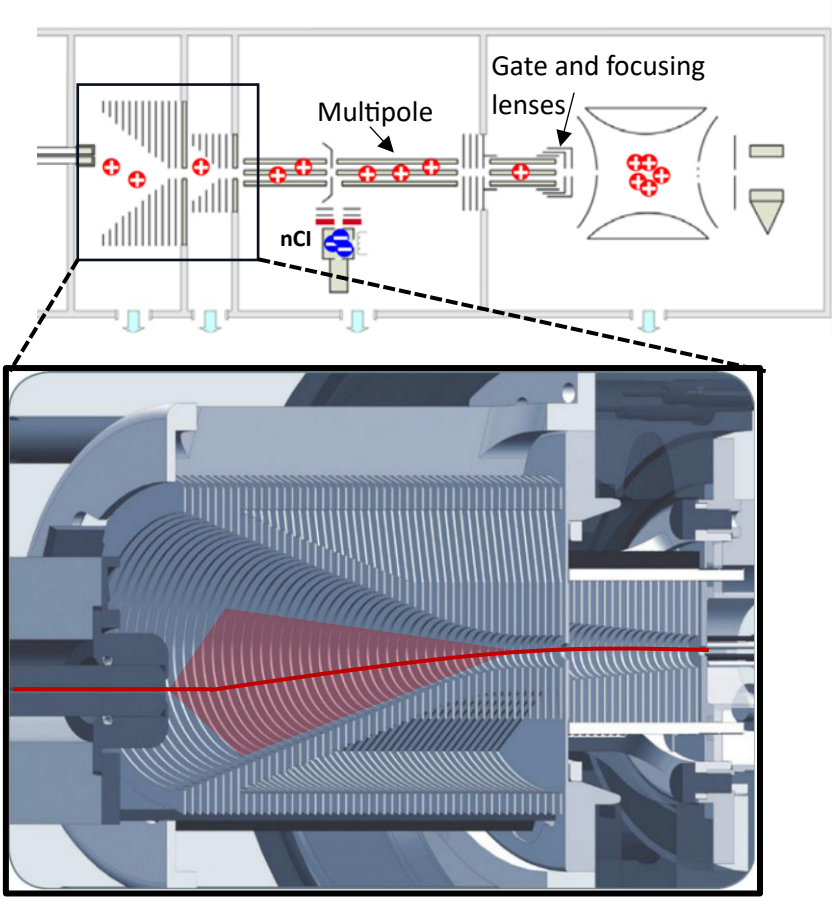

Figure 2.4 3D setup of the double stage ion funnel adapted from [73], illustrating the ion pathway highlighted in red. The conical-shaped red area illustrates the divergence of ions, expanding into a focused beam.

After exiting the capillary carried by the nitrogen carrier gas, the ions experience a strong gas expansion due to the high-pressure gradient from the ambient pressure of the ESI source to the millibar pressure in the first vacuum stage. The ions possess considerable kinetic energy when they enter the wide opening of the first ion funnel and exhibit a finite beam divergence. They are accepted from a wide solid angle without the need for a strong focusing electrostatic field. The kinetic energy of these ions is thermalized by collisional damping through an applied

radiofrequency (RF) voltage on the stacked ring ion guides. This RF voltage generates an effective potential that confines the ions inside the funnel.

The ions then pass through the second ion funnel in stage 2, where they are further confined and guided through a smaller aperture to the next vacuum stage (stage 3). This process not only maintains the integrity of the ion stream but also ensures that it is properly focused and prepared for the subsequent stages of analysis.

The first and second ion funnels share a common axis, which is deliberately positioned off-axis relative to the capillary axis. This configuration does not reduce ion transmission but prevents contamination of the following ion optics from the first ion funnel. Consequently, neutral particles such as solvent molecules or molecules originating from the sample impact the outer funnel and are evacuated from the system, keeping the ion optics clean and efficient.

Both ion funnels are set at different direct current (DC) voltages, creating an axial potential gradient that concentrates the ions without consideration for their mass-to-charge (m/z) ratio. This uniform concentration process ensures that all ions, regardless of their m/z ratio, are directed through the narrow exit aperture to the subsequent pumping stage (stage 3). The higher the DC voltage on the first ion funnel, the faster it reaches the second funnel. This adjustable DC-gradient can be utilized for in-source collision-induced dissociation (ISCID)[90], allowing for selective fragmentation of ions of interest. Even without applying ISCID, the high transmission through the double-stage ion funnel is efficient, even for fragile analyte ions.

Upon exiting the second ion funnel, the focused ion beam enters the third vacuum stage into the multipole mass filter, where ions are selected based on their mass-to-charge (m/z) ratio. The ion beam is focused on the multipole by applying an RF voltage that induces an increasing radial effective potential. This step is crucial in the ion selection process, ensuring that only ions of interest proceed to the next stages of analysis.

Before finally reaching the ion trap module in the fourth vacuum stage, the ion beam passes through the focus lenses and the gate lens. The gate lens plays a vital role in the mass

spectrometry process, as it controls the accumulation time of ions to be scanned within a certain time sequence. This function significantly improves the signal quality by increasing the signal-to-noise ratio and enhancing the sensitivity of the analysis. Additionally, it allows only ions within a certain m/z range to pass through, holding others back and thereby isolating only ions of interest for analysis. In essence, the gate lens serves as a gatekeeper, ensuring that only the relevant ions are admitted for further analysis.

2.1.3 Quadrupole Ion Trap (QIT)

The Quadrupole Ion Trap (QIT) within mass spectrometers is a versatile component, offering a broad spectrum of applications, including mass accumulation, selective mass isolation, excitation for collision-induced dissociation (CID), and enabling potential applications such as electron transfer dissociation (ETD) and laser photodissociation upon modification.[53] Housing in vacuum stage four of the mass spectrometer, the QIT typically operates at an approximate pressure of $5 \cdot 10^{-6}$ mbar. Its functionality hinges on an oscillating RF quadrupole electric field, effectively trapping cations or anions.

Referred to as the Paul trap, the QIT was initially designed by Paul and Steinwedel,[91] for which Paul was honored with the Nobel Prize in 1989.[92] The fundamental elements of the QIT encompass hyperbolic entrance and exit caps, alongside a hyperbolic ring electrode (Figure 2.5), forming an internal surface with an almost three-dimensional hyperbolic profile, essential for generating a 3D quadrupole trapping field (Figure 2.6).

Controlled by the gate lens, ions traverse the QIT by passing through the small central perforations of the entrance and exit caps, where they can either be trapped or continue to the detector. In the trapping mode, referred to as "Isolation," a high-voltage RF potential (Ω = 781 kHz) applied to the ring electrode generates a rapidly oscillating electric field. Simultaneously, a DC voltage applied to the cap electrodes establishes a substantial three-dimensional quadrupolar trapping field, as shown in Figure 2.6.

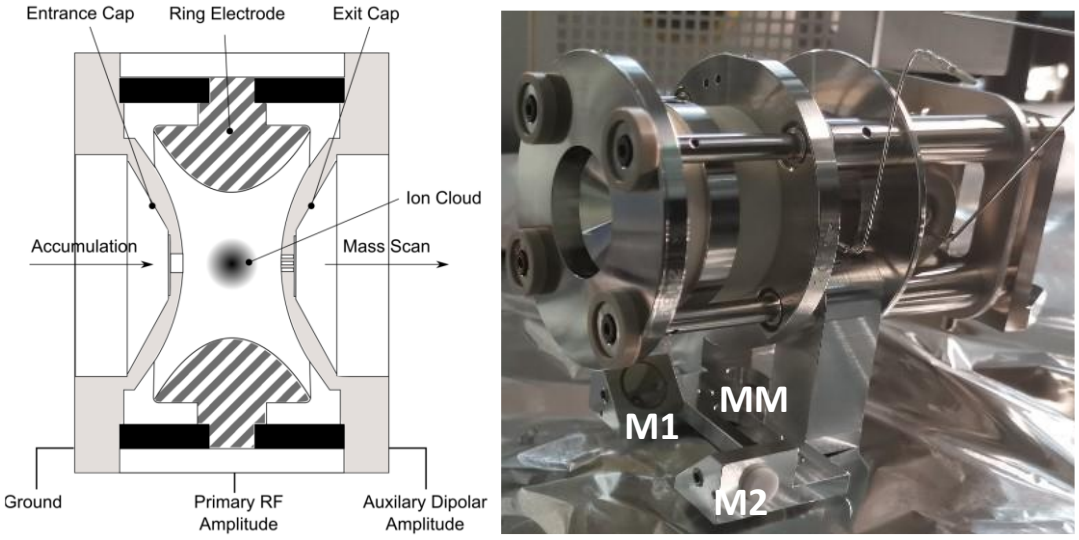

Figure 2.5 LEFT: Schematic illustration of the quadrupole ion trap (QIT).[73] **RIGHT**: A recorded image of the modified ion trap, containing the guiding mirrors (M1-2) on the mirror mount (MM).

The concept of stabilized ions can be likened with a practical example where a ball resting on a saddle-shaped surface, capable of rolling in either direction.[92] However, when the saddle is horizontally rotated at a specific frequency, the ball becomes trapped in the saddle and ceases to roll. It is effectively stabilized in this manner.

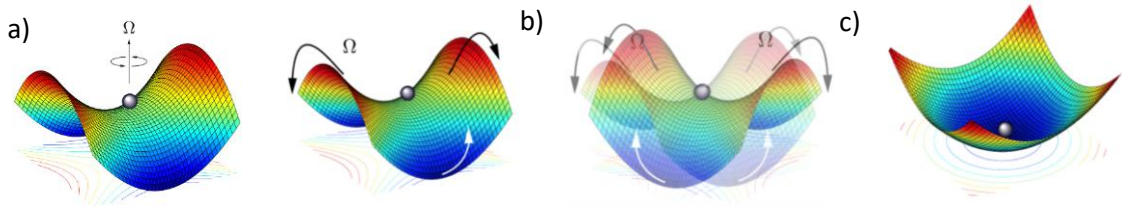

Figure 2.6 Illustration of a confined ion in the QIT. The red and blue coloring areas depict high and low potentials. (a) Time evolution of the rotating saddle potential, (b) Time evolution of the oscillating potential in the RF-electrical QIT, and (c) the effective trapping pseudopotential at stability condition.[93-99]

Trapped ions follow oscillating trajectories determined by the Mathieu equations[100], depending on their mass-to-charge ratio (m/z) values.[100-102] Ions deviating beyond the stable region (green, Figure 2.7) might collide with the trap's walls.

To prevent acceleration in the movement of the ion stream, Helium gas is introduced as a damping agent at a constant partial pressure of approximately $3 \cdot 10^{-6}$ mbar within the trap. Helium, an inert gas with a low sticking probability, serves to extract the kinetic energy of the ion beam and subsequently thermalizes the ion cloud.[98,103]

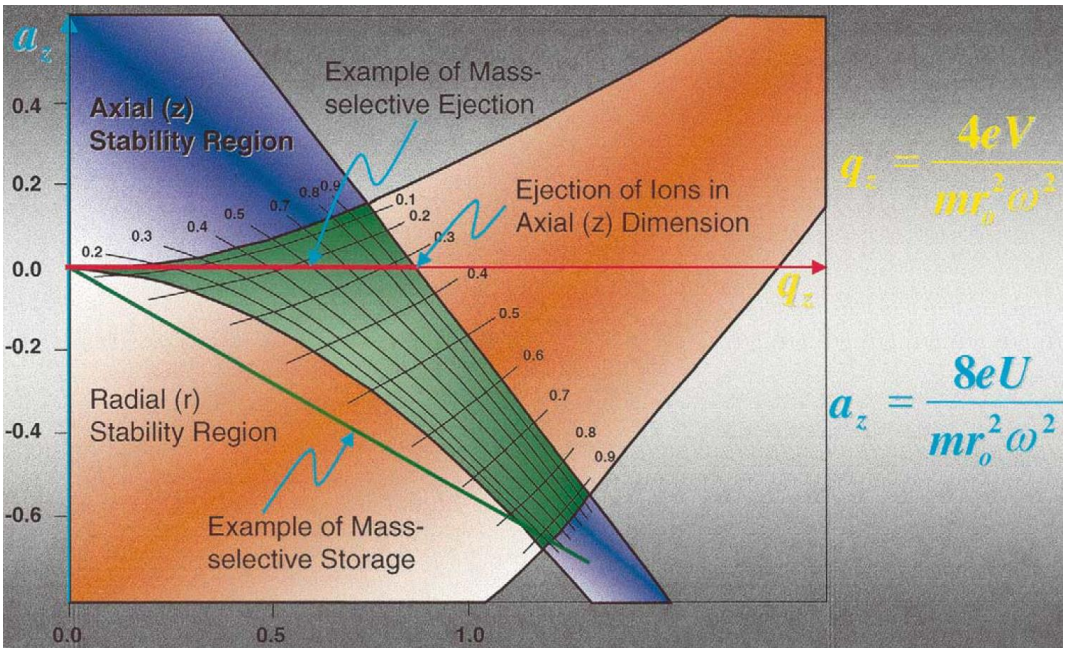

Figure 2.7 "Portion nearest the origin of the quadrupole ion trap stability diagram using a and q parameters for the coordinate axes. V = zero-to-peak amplitude of the radio frequency (RF) voltage applied to the ring electrode; U = amplitude of direct current (DC) voltage applied to the ring electrode; r_0 = hyperbolic radius of the ring electrode; m = mass of the ion; e = electric charge on the ion; $\omega = 2\pi f$ (angular frequency of applied RF voltage); and f being the frequency in hertz. The blue region represents ion motion stability in the axial (z) dimension in the ion trap. The red region represents ion motion stability in the radial (r) dimension in the ion trap. Ions that map onto the a and q coordinates and fall into the green region have stability in both axial and radial trap dimensions." Cited from [104].

2.1.4 Scan segments

The ion pathway through the trap follows a specific sequence: Initially, the ion trap loads by lowering the blocking voltage at the gate lens, enabling the ion beam to enter (segment 2 in Figure 2.8). The Primary RF, applied to the quadrupole ion trap, holds ions in the trap by generating a stable trapping potential. These ions are confined using a low quadrupolar amplitude, often termed the "Trap-Drive mass" in trapControl. Once the specific ion accumulation period concludes, the gate lens switches to blocking mode, halting any further entry of ions. Ensuring the ion cloud at the trap's center, the accumulated ions undergo a "cooling" process through collisions with Helium gas.

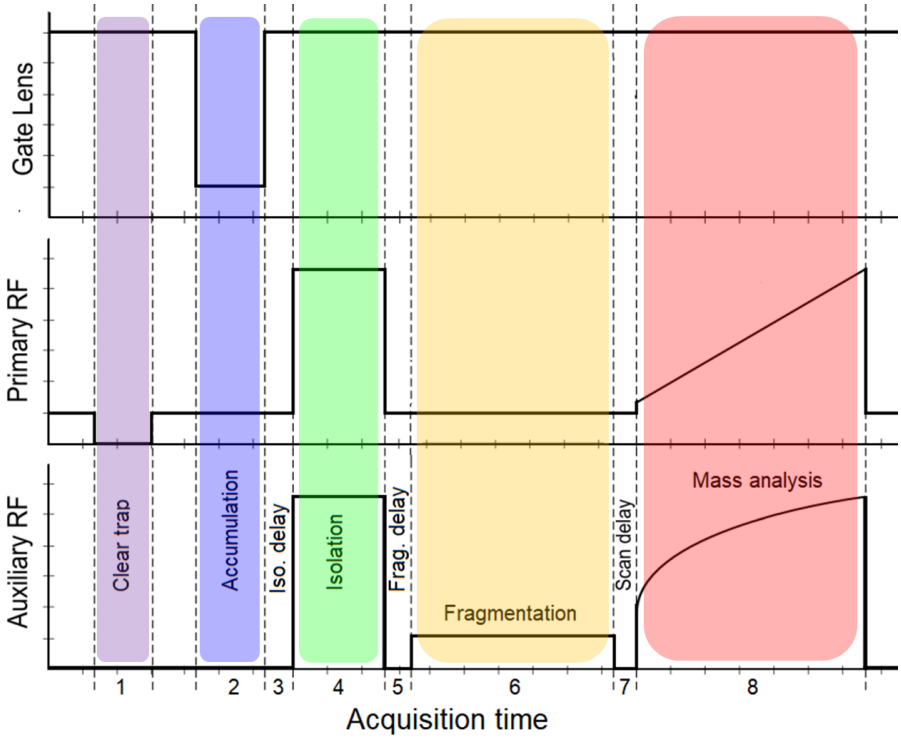

Figure 2.8 The time-segmented scan sequence for MS/MS and MS(n) experiments in a quadrupole ion trap highlights the interaction between the Gate Lens, Primary RF, and Auxiliary RF, which together facilitate the entire process of ion trapping, fragmentation, and mass analysis. 1: Clear trap (5 ms): Residual ions are removed before the new ions are accumulated. 2 Ion accumulation (0.01 – 50 ms): The gate lens lowers its blocking voltage, allowing ions to enter and become trapped by the Primary RF. The Primary RF refers to the radio frequency field that creates a quadrupolar potential, confining ions within the trap. 3: Isolation delay (5 ms): Stabilization before precursor ion isolation. 4: Precursor ion isolation: Primary RF isolates the precursor ion by ejecting all other ions. 5: Fragmentation delay: Stabilization before the application of auxiliary RF. 6: Fragmentation (40 - 120 ms): The Auxiliary RF induces precursor ion fragmentation through resonance excitation. The Auxiliary RF is an additional radio frequency field applied to facilitate fragmentation, allowing precise control over the energy delivered to the ions.

7: Scan delay (5 ms): Stabilization before mass analysis. 8: Mass analysis: Primary RF is ramped to sequentially eject ions based on their m/z ratio, generating a mass spectrum.[73]

Following accumulation, a sequence of isolation and fragmentation steps takes place. During precursor ion isolation (segment 4), the Primary RF is adjusted to eject all ions except the precursor ion of interest, which is trapped for further analysis. Next, during fragmentation (segment 6), the Auxiliary RF is applied, inducing resonance excitation to fragment the precursor ions. The energy applied in this step causes ions to perform inelastic collisions with Helium molecules, resulting in fragmentation for further analysis.

In the final step, during mass analysis (segment 8), the Primary RF is gradually ramped up. This increase in RF amplitude forces ions to sequentially eject from the trap based on their mass-to-charge (m/z) ratio, starting with the lowest mass. The ejected ions are detected, and a mass spectrum is generated. Once the scan is complete, the Primary RF drops to zero, clearing any remaining ions from the trap. This process is repeated to generate consecutive mass spectra.

Throughout this process, the gate lens controls ion entry, the Primary RF determines the trapping and ejection of ions, and the auxiliary RF drives fragmentation.

2.1.5 Collision-Induced Dissociation (CID)

Collision-Induced Dissociation (CID) is a fundamental technique used for ion analysis within the quadrupole ion trap (QIT).[105-106] This method provides valuable insights into the composition and structure of ions, making it a versatile tool with a wide range of applications. CID plays a crucial role in tandem mass spectrometry, enabling the examination of molecular structures and the identification of chemical compounds. It finds extensive use in diverse fields such as proteomics, metabolomics, and small molecule analysis in analytical chemistry.[107-109]

As subjects for fragmentation via CID, ions of interest are initially confined within the QIT based on their mass-to-charge ratio (m/z) and then accelerated by constantly increasing the DC voltage applied to the trap's end caps over time to enhance the number of inelastic

collisions of the ions mainly with Helium molecules but with increasing acceleration also with other molecules and ions. This results in the generation of characteristic fragments that correspond to the analyte ions, which can be subjected to further fragmentation (MSn). The analysis of fragmentation pathways in CID may provide valuable insight into the structure of the analyte molecule, particularly regarding the arrangements and strengths of chemical bonds within these molecules.[110]

When dealing with similar precursor ions, quantitative investigations of their relative dissociation energy can be conducted by measuring CID curves. These CID curves monitor the relative abundance of precursor ions *PI*, specific fragments F_i, and the resulting total fragmentation yield *TFY* as a function of the amplitude of the DC voltage, which corresponds to the average energy transferred by the collisions of the precursor ions with Helium.

$$TFY = \frac{F_i\ (E_{lab})}{\sum F_i(E_{lab}) + PI(E_{lab})} \tag{1}$$

The collisional energy transfer between a precursor and a Helium atom depends on the nominal masses of Helium (m_{He}) and the precursor (m_P). The average collision energies influenced by the amplitude of the applied DC voltage in laboratory frame (E_{lab}) require conversion into the molecular frame through the center of mass (com) transformation, resulting in the center of mass-corrected amplitude E_{com}:

$$E_{com} = \frac{m_{He}}{m_{He} + m_P} \cdot E_{lab} \tag{2}$$

Consequently, E_{com} is employed as a reference value for the qualitative comparison of molecules with similar structures, defining the amplitude at which 50% of the precursor ions undergo fragmentation, referred to as $E_{com}^{50\%}$. This value is determined using a sigmoidal function (4), with A and B serving as fit parameters:

$$TFY^{fit}(E_{com}) = \frac{A}{1 + e^{-B\left(E_{com}^{50\%} - E_{com}\right)}} - TFY_0 \tag{3}$$

Here, TFY_o describes an intrinsic fragmentation (ground fragmentation) of labile precursor ions in the ion trap, occurring without any applied acceleration voltage. This fragmentation arises solely from the interaction of the ions with the helium buffer gas present in the trap. Due to their inherent instability and kinetic motion within the trap, the ions undergo fragmentation through collisions with helium atoms, without the need for external excitation (cf. chapter 4.1).

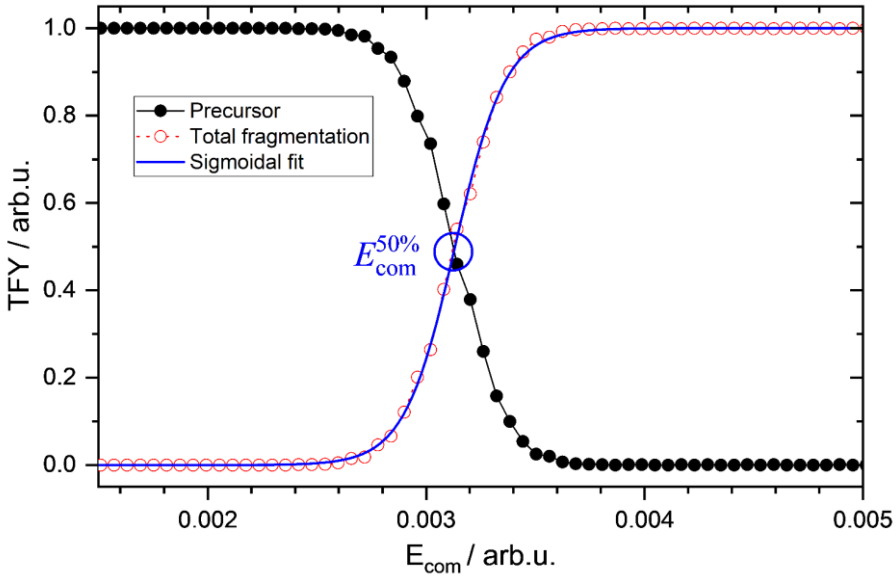

Figure 2.9 CID breakdown curve with the associated appearance curve and the corresponding $\boldsymbol{E_{com}^{50\%}}$ value.

It is worth noting, that the value of $E_{com}^{50\%}$ is inherently linked to the molecular structure and fragmentation behavior of the precursor ions, but is also highly device-specific. Therefore, $E_{com}^{50\%}$ values can only be reliably compared when measured on the same mass spectrometer. An example for a CID-breakdown curve is shown in Figure 2.9.

This collision-induced dissociation (Figure 2.10) can be described as a sequential reaction in the following way,[110-111] where N stands for a neutral compound in this case Helium:

$$P^{\pm} + N \xrightarrow{(1)} (P^{\pm})^{*} + N \xrightarrow{(2)} F_1^{\pm} + F_2^0 + N \quad \text{or} \quad F_1^0 + F_2^{\pm} + N \tag{4}$$

In this sequence, the parent or precursor ion $P^{\pm}$ -positively or negatively charged- is initially accelerated within the QIT. By increasing inelastic collisions with inert Helium molecules

causes the ion to undergo thermal activation, resulting into an excited state $(P^{\pm})^{*}$. These inelastic collisions cause an exchange of kinetic energy between the precursor ions and helium molecules that provides a successive increase in internal energy of the precursor ions. The kinetic energy is converted into internal degrees of freedom, wherefor the internal energy assuming Boltzmann distribution.[111] This transition places the precursor ion into a vibrational state. The intensity of these collision-induced processes is directly proportional to the applied voltage.

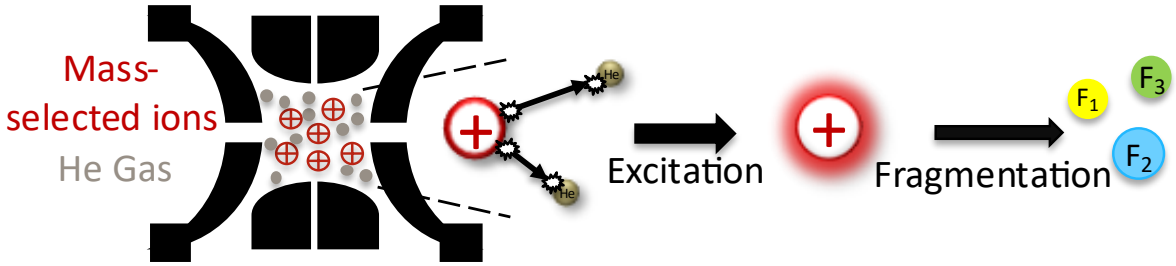

Figure 2.10 Illustration of process of CID fragmentation.

As these collisions continue, the accumulation of internal energy eventually surpasses the dissociation threshold,[110,112] culminating in fragmentation ($F_{1\text{-}3}$, Figure 2.10). This fragmentation can give rise to neutral or charged particles, where only the latter could be directly detected by mass analysis.

The sequential reaction (4) is based on the assumption, that activation and dissociation are separated in time, primarily because the collision time is significantly shorter than the dissociation time for fast-moving ions. Consequently, the collision gas does not disturb the ions energy states during dissociation, even at Boltzmann equilibrium, inferring that the mode of energy transfer does not significantly impact the dissociation process.[111]

Note that a parallel technique is known as Infrared Multiphoton Dissociation (IRMPD),[113-114] where comparable energy accumulation (partially quantifiable) is achieved through successive resonant absorption of infrared (IR) photons in conjunction with fast internal vibrational redistribution (in between absorption events).

2.1.6 Negative Chemical Ionization (nCI) Source

The negative chemical ionization (nCI) source plays a crucial role in enabling electron transfer dissociation/reduction (ETD/R) and proton transfer reaction (PTR) experiments within the QIT.[53,115] This capability significantly enhances the analytical potential of the mass spectrometer. ETD and PTR, which rely on low-energy charge transfer mechanisms, have become widely adopted and are central methods for top-down sequencing of larger peptides and proteins,[116] facilitating the analysis of proteome structural aspects[117] and the identification of post-translational modifications (PTMs)[118-119]. In this thesis, ETD is the primary technique used to reduce multiple positively charged complexes, thus creating new radical species within these complexes. These new species may then be subject to further analysis through CID or exposure to photodissociation experiments.

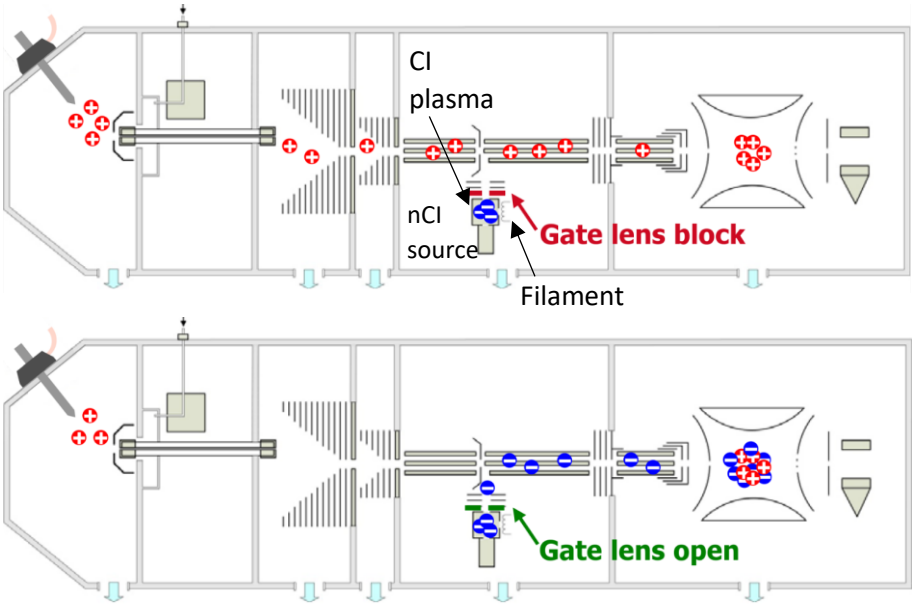

Figure 2.11 Illustration of the CI source operating principle. **TOP**: Gate lens closed, trapping reagent anions within the nCI source; **BOTTOM**: Gate lens open, releasing reagent anions into the octupole, directing them toward the QIT to interact with the trapped ions.[73]

The nCI source module integrates into the standard housing of the mass spectrometer (Figure 2.11), without the need for extensions or additional pumping systems. It is positioned beneath and perpendicular to the RF multipolar transfer optics within the third vacuum stage of the mass spectrometer. The influx of reagent anions into this stage is regulated by the gate lens of the nCI source. Applying a negative voltage effectively blocks the reagent anions, while

applying a positive voltage enables their orthogonal transmission into the octupole and onward to the QIT.

Since electrons cannot be efficiently captured within the ion trap due to the low mass cutoff restrictions of the RF field,[120] Skya *et al.* developed the ETD technique, utilizing anions as electron donors[116]. Reagent anions for ETD and PTR can be produced from a single neutral compound, in this case, fluoranthene. Through its reaction with gaseous ionized reagents, specifically methane. Among compounds like anthracene, azobenzene, and azulene[121], fluoranthene ($C_{16}H_{10}$) stands out due to its favorable electron transfer efficiency of approximately 40% and its low electron affinity (0.757 eV).[122] Additionally, its planar-like structure minimizes steric hindrance, making it a general electron transfer reagent for various analyte cations.[117]

Within the nCI source, neutral fluoranthene evaporates by heating the crucible to 60 °C. Methane gas acts as a mediator for generating thermal electrons, which can bind to fluoranthene forming the anion reagent. Methane is infused at a constant pressure of 0.1 mbar, considered high pressure in this configuration. Primary electrons ionize methane gas by setting the filament at 2 µA and the ionization energy at 70 eV. The collision between primary electrons and neutral methane initiates a cascade of reactions, resulting in the production of various cations and radical cations: $CH_4^{\bullet+}$, CH_3^+, $CH_2^{\bullet+}$, CH^+, und $C^{\bullet+}$,[123] that produces further species: $C_xH_x^+$,[124-128] over secondary and tertiary reaction with e.g., methane, H_2O, O_2, producing even lower energetic electrons and generation of low energy electrons by electron impact ionization:

$$CH_4 + {}^*e^- \text{ ----> } CH_4^{\bullet+} + 2\ e^- \qquad (5)$$

Consequently, a chemical ionization plasma rich in low-energy electrons is generated. These electrons, typically with energies less than 1 eV, can effectively undergo electron attachment reactions.[122] When vaporized fluoranthene is introduced into this environment, it captures one of these low-energy electrons, resulting in the formation of a radical anion.[116] This

radical anion acts as the primary reagent for both electron transfer dissociation (ETD) and proton transfer reaction (PTR) processes[53]:

$$\text{Fluoranthene} + e^- \text{----> Fluoranthene}^{-\bullet} \quad (6)$$

The voltage applied to the chamber determines whether fluoranthene radical anions at m/z 202 ($C_{16}H_{10}^{\bullet-}$) are created (-6 V) or suppressed (-15 V), resulting in anions of composition m/z 201 ($C_{16}H_9^-$) and m/z 203 ($C_{16}H_{11}^-$).[115] However, m/z 201 ($C_{16}H_9^-$) is a minor product and is believed to be generated by hydrogen abstraction from the radical anion m/z 202 ($C_{16}H_{10}^{\bullet-}$). The anion at m/z 203 ($C_{16}H_{11}^-$) is presumably formed by a radical-radical coupling between the radical anion m/z 202 ($C_{16}H_{10}^{\bullet-}$) and a hydrogen atom. Hartmer *et al.* propose a subsequent ring-opening reaction, resulting in an aryl-substituted naphthyl anion.[115] Martens *et al.* have conducted an in-depth investigation into the final structure of these ions,[53] affirming the plausibility of hydrogen attachment occurring in either position 1 or 3 while maintaining the ring-closed structure, supported by the congruence between theoretical predictions and experimental observations. Furthermore, they dismiss the possibility of a ring-opening reaction due to its notably higher energy requirement of 150 kJ/mol.

The radical anions at m/z 202 ($C_{16}H_{10}^{\bullet-}$) serve as an ETD reagent, while the anions at m/z 201 ($C_{16}H_9^-$) and 203 ($C_{16}H_{11}^-$) are used as PTR reagents. It takes approximately 200 ms for the fluoranthene reagents to reach the ion trap. By setting the gate lens potential to positive potential, the generated reagents are released orthogonally into the transmission device, leading to the ion trap, where the precursor ions (P) are already stored.

In the case of PTR,[53] electron reduction occurs through proton abstraction:

$$[PI + nH]^{n+} + C_{16}H_{11}^{-} \text{ -----> } [PI + (n-1)\,H]^{(n-1)+} + C_{16}H_{12} \quad (7)$$

For ETD, a radical anion is transferred to the trap containing the analyte ions,[53] which are often large multi-protonated (multi-cationic) peptides (application for peptide sequencing and structural analysis):

$$[PI + nH]^{n+} + C_{16}H_{10}^{\bullet -} \text{ -----> } [PI + nH]^{(n-1)+\bullet} + C_{16}H_{10} \quad (8)$$

Subsequently, the generated peptide radical cation decays further by cleavage of the N−Cα bond, generating c- and z-type fragment ions, which are characteristic for ETD and provide structural information while preserving labile post-translational modifications.[129] This type of backbone dissociations provides information on amino acid sequence as well as location of post-translational modifications.

In this thesis, ETR has been the primary focus. In this process, an electron is transferred to the analyte ion to reduce its charge, and the so formed radical species is stabilized within the trap through collision with Helium.[130]

$$[PI + nH]^{n+} + C_{16}H_{10}^{\bullet -} \text{ -----> } [PI + nH]^{(n-1)+} + C_{16}H_{10} \quad (9)$$

This process constitutes electron transfer with no dissociation (ETnoD).[130-131]

2.1.7 Gas Inlet Line

A gas inlet line has been integrated into the MS amaZon Speed (Figure 2.12), which is utilized for the experiments in this thesis. This addition enables the easy introduction of various neutral gases and volatile substances into the ion trap. Gases such as methane, O_2, CO_2, or volatile substances like methanol, furan, among others, can form adducts with the precursor ions in the ion trap that could be subject to laser spectroscopic investigations. In this thesis, controlled introduction of furan vapor into the QIT has been employed to assess the temporal resolution for the pump-probe experiment. This assessment can be achieved by observing the ultrafast multiple-photon ionization of furan, providing the cross-correlation function of the ultrashort pump and probe laser pulses.[57,132]

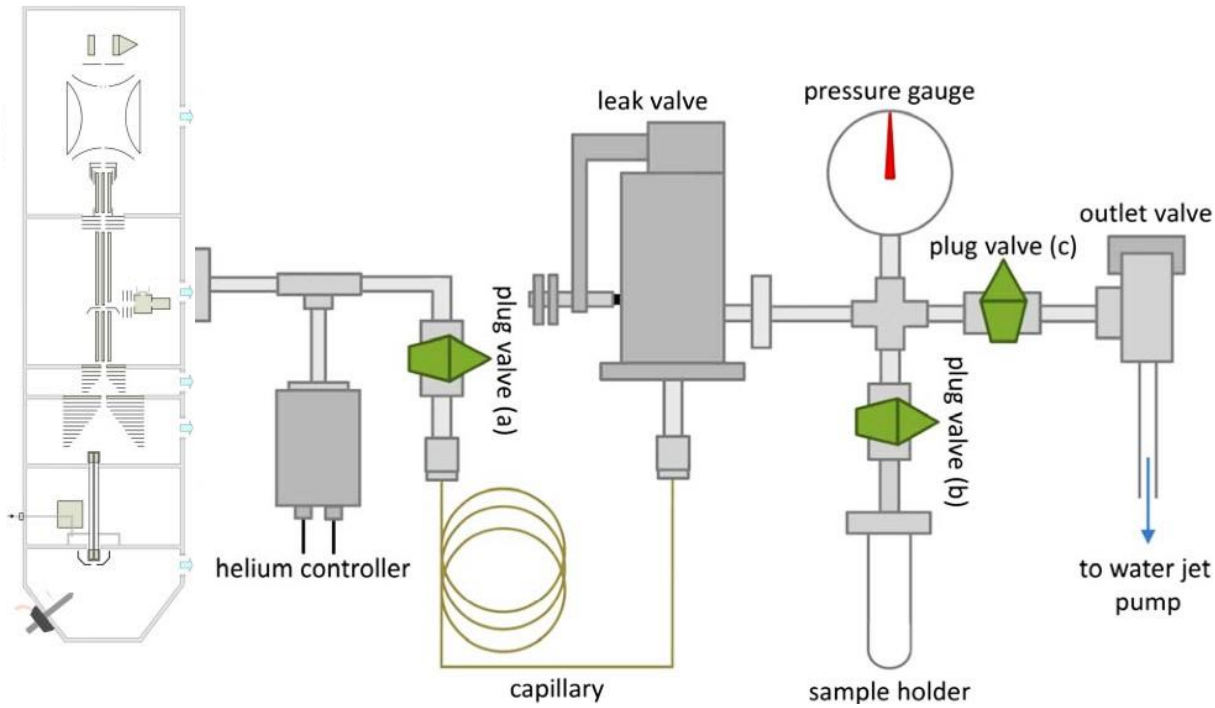

Figure 2.12 Scheme of the gas inlet added to the amaZonX mass spectrometer adapted from [133], where a foreline pump has been used instead of a water jet pump.

As seen in Figure 2.12, the gas inlet is connected to the fourth vacuum stage, where the ion trap is situated. The Helium controller, attached to the QIT, is responsible for regulating the flow of Helium buffer gas to maintain a constant pressure of approx. 10^{-3} mbar within the ion trap.

Initially, liquid furan is placed in a sample holder, which is then immersed in liquid nitrogen. Freezing the sample reduces strongly the vaporization of furan during subsequent evacuation (freeze and thaw procedure). Once the minimal pressure of a few millibars is reached, plug valves (b) and (c), along with the leak valve, are closed, and the liquid nitrogen is removed. As the furan begins to vaporize, valve (b) is opened, allowing furan to evaporate up to a pressure of 300 mbar. To overcome the high-pressure gradient from a few millibars to a pressure of 10^{-3} (5×10^{-6}) mbar within (outside of) the ion trap, a polyether ether ketone (PEEK) capillary with an inner diameter of 180 µm and a length of 1 meter is used in combination with a leak valve (Sapphire poppet). The leak valve is used to pass a controlled amount of furan vapor into the trap. trapControl allows to monitor the sufficient quantity of furan in the trap to yield a satisfactory cross-correlation signal (Cp. 2.7).

In summary, this gas inlet line expands the capabilities of the mass spectrometer, enabling the introduction of various gases and vapors for a range of experiments and analyses.

2.1.8 Detector

The mass spectrometer is equipped with a detector (Figure 2.13) that combines a conversion dynode-based Daly detector[134] and a channel electron multiplier (CEM)[135]. The Daly detector allows for highly sensitive detection of both positive and negative ions while minimizing the typical mass bias associated with electron multipliers.[73]

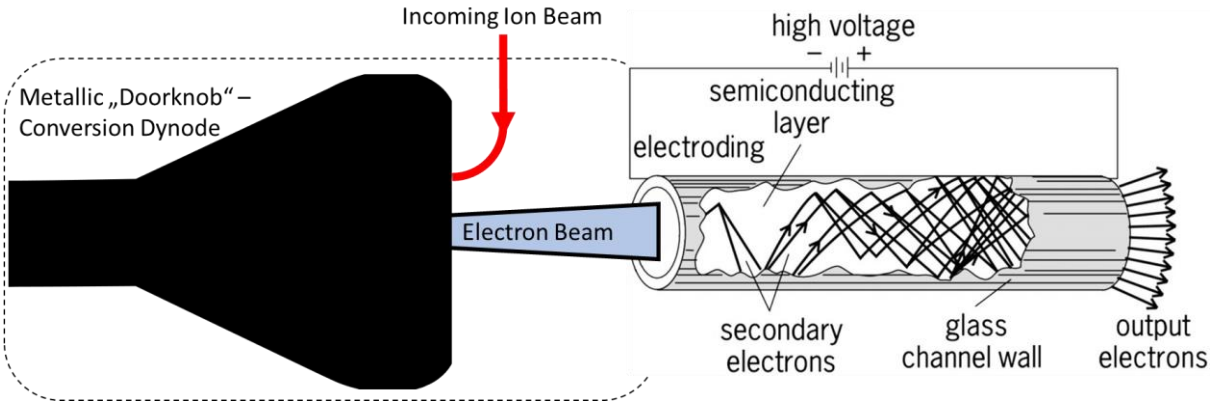

Figure 2.13 Schematic set up of Daly-type detector (dotted frame) combined with a channel electron multiplier (CEM). The schematic illusatrtion of the CEM was adapted from [136].

The detector is positioned after the ion trap and is equipped with a gate lens that controls the flow of ions to the detector. The gate lens plays a crucial role in minimizing the aging of the CEM. Aging refers to the gradual deterioration of the CEM's performance over time, which is strongly influenced by the total amount of detected charges. To mitigate this, the detector is equipped with an ion gate, which prevents the ejection of ions from the trap during isolation or fragmentation steps, thereby reducing unnecessary exposure of the CEM to ions.[73]

Figure 2.13 describes the detection procedure as follows: As the ions are guided from the ion trap or the mass analyzer to the detector, they are accelerated toward the aluminum-coated conversion dynode Figure 2.13. The dynode is held at a high electrical voltage of a few kilovolts, with the polarity of the voltage matching the charges of the ions to be detected. Since ions may exhibit different m/z behaviors, they are accelerated accordingly. The m/z behavior of ions refers to how their mass-to-charge ratios affect their kinetic energies and trajectories within the mass spectrometer.

Upon impact with the dynode, ions emit secondary electrons. In the Daly detector, these electrons are directed toward the CEM, where they undergo a cascade of electron collisions, leading to a substantial multiplication of the electron count. This process, known as electron avalanche, significantly increases the number of electrons generated. The resulting electric current is proportionally converted into an electrical signal by an analog-to-digital converter (ADC)[137]. This enables quantitative analysis and the generation of mass spectra.

The combination of generating secondary electrons and amplifying them within the CEM maximizes the utilization of the signal, greatly enhancing detector sensitivity. Even weak signals resulting from low ion concentrations can be adequately detected, leading to an enhanced signal-to-noise ratio. Amplifying the signal strength also enhances the precision and reliability of the measurements.

2.1.9 Space Charge Effect and Ion Charge Control

In the realm of mass spectrometry, **Space Charge Effect** (SCE) pervades various regions, potentially disrupting the precision and quality of collected data.[138] Based on fundamental principles of electrostatics, SCE arises from the mutual electrostatic repulsion between charged particles confined within limited spatial boundaries. This phenomenon induces deviations in their trajectories, culminating in peak broadening as they reach the detector.

SCE presents a particular challenge when it manifests within the confines of the ion trap. Ions entering the trap experience elevated electric field exposure and restricted spatial allowances in a high vacuum environment. The trap's electric fields serve to retain these ions. However, an abundance of ions leads to electrostatic repulsion among them, perturbing their trajectories and causing variations in their energies and velocities. This heterogeneous ion population, when introduced into the mass analyzer, results in peak broadening, ultimately compromising accuracy and precision.

Ion Charge Control (ICC) serves as a feature within mass spectrometric detection to address the challenges associated with SCE and ensure high data quality. Its primary function is to manage the population of ions within the ion trap, ultimately mitigating the disruptive effects

of SCE. ICC primarily operates by controlling the accumulation time of ions in the ion trap. The accumulation time refers to the duration ions spend within the trap before being released for analysis. The ICC values are in a ratio of 1 to 20 to the actual number of ions.[139] By regulating the accumulation time, ICC indirectly influences the number of ions that enter the trap. This control mechanism allows ICC to fine-tune the population of ions within the trap, making it a vital tool for managing ion density. Also, ICC utilizes the gate lens located at the end of the mass filter. By meticulously managing the accumulation time and controlling the influx of ions, ICC indirectly contributes to improved data quality.

In cases of observed mass signal broadening, ICC values can be adjusted lower, particularly when a high ion density in the trap contributes to SCE. Factors such as elevated sample solution concentrations or increased applied voltages are known to intensify electrostatic repulsion within the limited space. ICC efficiently maintains a consistent ion flux to the detector, preserving high resolution and precision in the acquired data. High-resolution outcomes play a pivotal role for accurately identifying ion molecules through well-resolved isotope patterns.

Conversely, for scenarios involving low-concentration sample solutions, the ICC mode extends the accumulation time to attain the desired ion quantity. However, a lengthier accumulation time exposes ions to prolonged electric fields within the trap, intensifying repulsive interactions among them and resulting in resolution loss.

While SCE primarily affects the ion trap, it can also occur to a lesser extent in other parts of the mass spectrometer under varying conditions. For instance, within the ESI source, injecting a highly concentrated sample while applying voltage gradients can lead to impure ion generation, driven by higher ion density and increased interactions. Consequently, these impure ions result in various oxidation states, unwanted isotopes, and fragmentation products entering the mass spectrometer and potentially overlapping with the signals of interest.

In addition, the application of voltage gradients in the ion optics and mass filter can guide ions along specific paths while simultaneously constraining their spatial domain. In the ion optics, undesired interactions can disrupt the focusing of ions as they exit the capillary, leading to deviations in their trajectory as they enter the mass filter. This effect is particularly exacerbated under conditions of higher concentration and more pronounced voltage gradients. The mass filter uses RF voltage to guide ions in a spiral trajectory, enabling the selection of ions based on their mass-to-charge ratio (m/z). SCE can perturb these RF fields, resulting in improper selection of ions. For example, ions with the same mass but different charges might not be effectively separated or selected. This can lead to a loss of resolution in the mass analysis process, affecting the accuracy and precision of the results.

2.2 Femtosecond Laser System

In this thesis, ultrafast spectroscopy experiments were conducted using the Wyvern 1000TM femtosecond laser system from KMLabs (Boulder, CO, USA). This oscillator/amplifier system generates ~55 fs pulses (FROGScan measurement) at approximately 783 nm, boasting an average power output of approximately 3.3 W and a repetition rate of ~1 kHz (Figure 2.14).

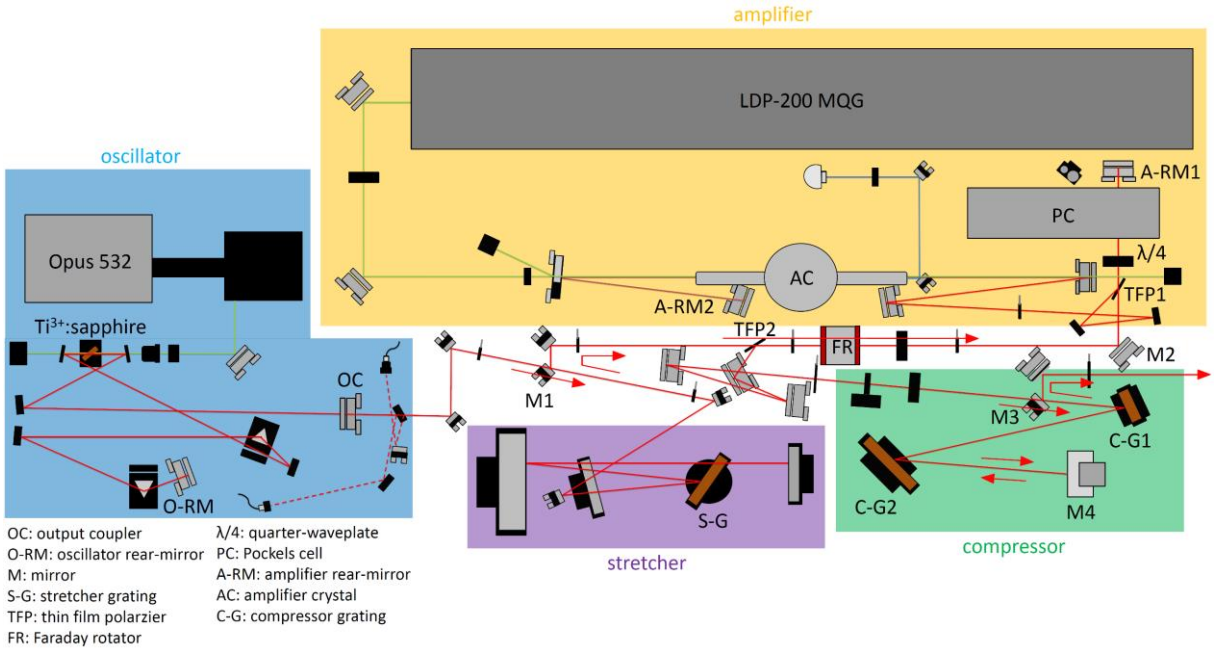

Figure 2.14 Schematic setup of the Wyvern 1000TM femtosecond laser system of KMLabs.[133]

The Wyvern system comprises an oscillator, stretcher, regenerative amplifier, and compressor. The oscillator houses a Ti:Sa crystal, pumped by a diode-pumped Nd:YAG laser (Opus 532, YAG: yttrium-aluminium garnet), generating seed pulses of 120-160 mW at λ = 785 nm with a fwhm of 55-66 nm, operating at ca. 80 MHz using the Kerr

-lens effect for mode-locking. As the pulses enter the stretcher, they undergo temporary stretching via a dispersive medium (grating), before entering the Ti:Sa regenerative amplifier, which is pumped by 532 nm from a ns diode-pumped Nd:YAG laser (Lee Laser, LDP-200 MQG). The amplifier crystal is cooled to -232 °C using a cryogenic He compressor. Within the subsequent compressor, the amplified pulse is recompressed using a grating pair to counteract the resultant positive chirp. This chirped pulse amplification (CPA), a Nobel Prize-

awarded method, mitigates damage to the optical equipment caused by the high peak power (= 7.78 GW/cm^2).

These amplified pulses are subsequently employed to drive two OPG/OPA (optical parametric generator/amplifier) units (TOPAS-C, Light Conversion, Lithuania), enabling the generation of tunable femtosecond laser pulses with wavelengths spanning 230 nm to 2600 nm. The subsequent sections will display and explain the detailed setup of the main components within this complex femtosecond laser system.

2.2.1 Ti:Sa Crystal as Laser Medium

In 1960, Maiman operated the first (solid-state) laser using a synthetic chromium-doped sapphire (Al_2O_3) ruby crystal.[140] In 1982, Moulton demonstrated a broad tunable laser by replacing chromium with titanium.[141] The improved production of higher-quality Ti:Sa (titanium:sapphire) crystals led to their commercial availability, resulting in the emergence of Ti:Sa-based lasers in laboratories around 1988. These lasers have found extensive applications as bases for femtosecond laser systems.[142]

Ti:Sa lasers exhibit exceptional power conversion efficiency, surpassing 70%.[142] They possess the largest fractional tunable range (650 nm-1150 nm) among solid-state lasers,[143] coupled with a broad absorption spectrum (400 nm-600 nm),[144] making them one of the best mediums for generating ultrashort pulses and wavelength tuning[145].

The inclusion of Ti^{3+} as a doping agent enables the broadband characteristics, expanding the high-frequency range, thereby enabling oscillation within a resonator.[141,146-147] The sapphire crystal contributes to high damage thresholds and thermal conductivity.[148] Ti:Sa crystals exhibit strong non-linear susceptibilities giving rise to electrooptical effects. Its strong Kerr effect enables the generation of ultrashort laser pulses, implemented by Kerr lens mode-locking (KLM).[149] Under high-intensity laser light, the electrons undergo significant excitation, resulting in a change in the refractive index known as the Kerr effect. This phenomenon introduces nonlinear effects in the material, enabling the generation of ultrashort pulses.

2.2.2 Mode-locking and Kerr-lens Effect

Mode-locking is a pivotal technique in generating ultrashort laser pulses, operating within the picosecond or femtosecond time regime. A mode-locked laser produces a series of ultrafast light pulses (78 MHz) with durations typically in the range of femtoseconds or picoseconds, resulting in coherent, intense, and periodic patterns of high-power light.[150] Its applications span diverse fields such as materials processing[151], biomedicine[152], medicine[153], surgical procedures[154], communication technology[155], and holds prominence in scientific research.[156-157]

This technique synchronizes the longitudinal modes of a laser to maintain a precise phase relation, leading to constructive interference and the generation of remarkably short pulses (Figure 2.15). Within a laser resonator, only specific longitudinal modes with corresponding frequencies can exist as standing waves resonating between mirrors. Misalignment in their phases results in destructive or partially destructive interference, leading to less efficient mode-locking. Synchronizing these modes causes coherent and in-phase oscillation, optimizing interference and producing amplified and short pulses.

An analogy might be a group of pendulums swinging in perfect synchronization: when all pendulums move in phase, they periodically align to produce a strong, coordinated motion—just as mode-locked laser modes constructively interfere at regular intervals to generate ultrashort pulses. Common mode-locking methods encompass the saturable-absorber mirror (SAM) technique[158] or the Kerr-lens mode-locking technique[159-160]. Within the oscillator, the Kerr-lens effect is harnessed in conjunction with the Ti:Sa crystal to stabilize the pulsed regime of the broad emission spectrum.

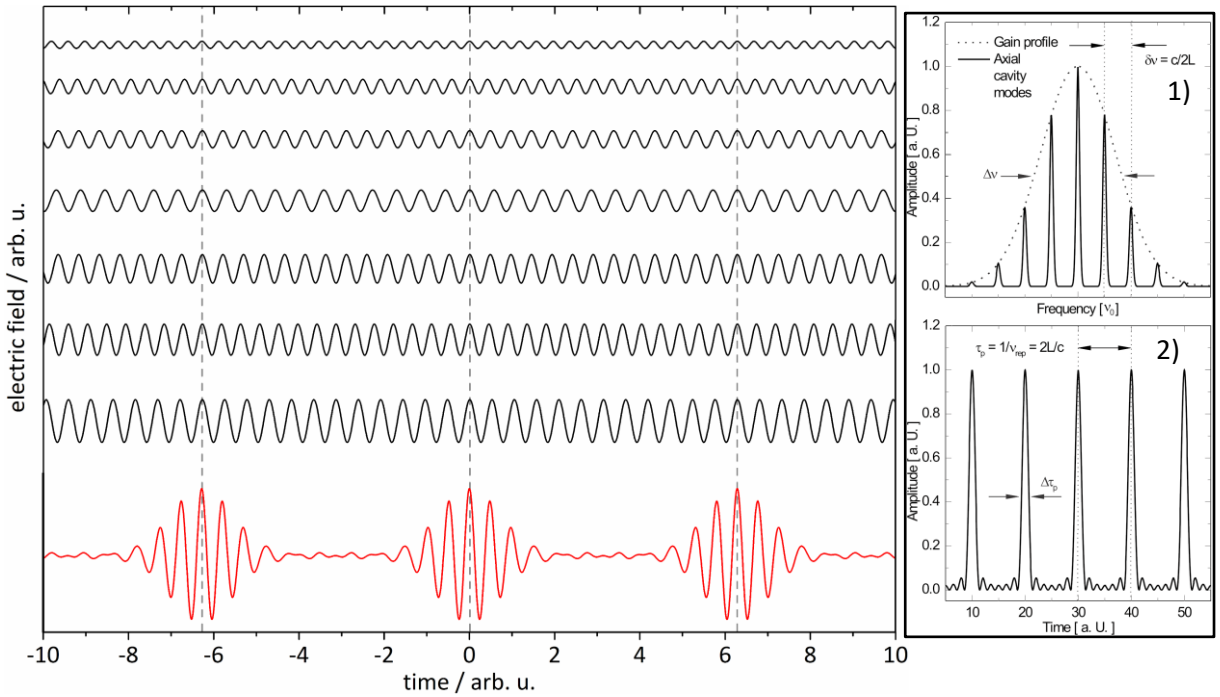

Figure 2.15 LEFT: Constructive interference of multiple longitudinal modes of different frequencies and fixed phase relationships, resulting in the creation of periodic pulses in the time-domain.[133] **RIGHT**: 1) Gain profile situated beneath the axial laser cavity modes, spaced at intervals of δν = c/2L and 2) The temporal development of the combination of seven axial modes with equal intensity and a consistent phase difference.[161]

The Kerr effect, a nonlinear process, causes the refractive index of the Ti:Sa crystal to change nonlinearly depending on the beam's intensity.[162] This change in refractive index leads to self-focusing of the laser beam, amplifying desired modes while suppressing undesired ones.[163] The focused pump laser within the Ti:Sa crystal acts as an aperture, so that only the high intensity (pulsed-mode) of the oscillator experiences a gain (high Q), whereas the low-intensity continuous wave (cw) regime of the oscillator is suppressed and not amplified (low Q). Thus, the pulsed, mode-locked operational regime of the oscillator is preferred and stabilized.

2.2.3 Ti:Sa Oscillator

The Ti:Sa oscillator generates ultrashort pulse (~20 fs) laser radiation in the femtosecond (fs) region with a repetition rate of 78 MHz and a pulse energy of ca. 2 nJ/pulse by KLM with integrated group velocity dispersion (GVD) compensation with a prism pair. The Griffin-W KLM Ti:Sa oscillator system by KMLabs, integrated into the Wyvern 1000^{TM}, serves as the core

apparatus (Figure 2.16). The laser cavity is pumped by a diode-pumped solid-state Nd:YAG laser, specifically the Opus 532 by Laser Quantum, emitting its second harmonic at 532 nm and 2.15 W power. The Opus's beam enters the oscillator area via PM1-2 through an anodized tube, ensuring minimal disturbance by dust particles. It is then focused by the lens FL with a focal length of 10 cm onto a Ti:Sa crystal (3x5x5 mm) placed between the curved dichroic mirrors (CM 1-2) with a 10 cm radius of curvature. A beam dump collects residual radiation, transmitted from CM2.

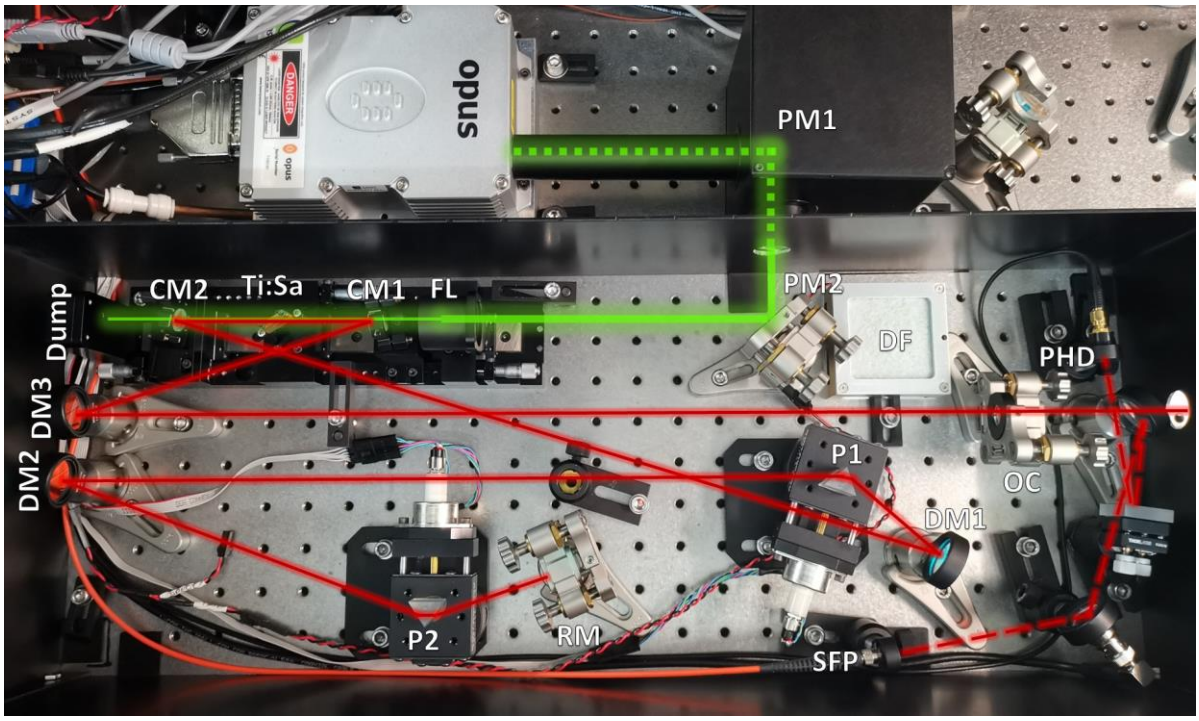

Figure 2.16 Setup of the Griffin-W Ti:Sa oscillator system by KMLabs and the associated beam path. Displaying the different optical components of the oscillator: PM (plano mirror), FL (focusing lens), CM (curved mirror), DM (dielectric mirror), RM (rear mirror), P (prism), OC (output coupler), PHD (photodiode), SFP (spectrometer fiber probe), DF (dust filter). The dotted green beam indicates its path passing through an eloxated tube.

As the beam oscillates between the highly reflective rear mirror (RM) and the output coupler mirror (OC) with a transmission of 10%, a pulse is emitted after each circulation at a repetition rate of approximately 80 MHz, related to the resonator's length. The beam follows this sequence: **CM1** ⇨ CM2 ⇨ DM1 ⇨ P1 ⇨ DM2 ⇨ P2 ⇨ RM ⇨ P2 ⇨ DM2 ⇨ P1 ⇨ DM1 ⇨ CM2 ⇨ CM1 ⇨DM3 ⇨ OC (90%) ⇨DM3 ⇨**CM1…**

The beam's precise path alignment ensures stable operation in continuous wave (cw) and mode-locked (ML) modes. Transitioning from cw mode (λ = 760-780 nm, 90-110 mW) to mode-locked (λ = 785 nm, fwhm = 55-66 nm, 120-160 mW) is realized by slightly adjusting P2, automatically controlled by stepper motors. Both prisms aid in balancing Group Velocity Dispersion (GVD), caused by the gain medium and other optical components, leading to pulse broadening. Stable pulse trains are achieved by suppressing modes with random phases while resonating modes with a fixed phase relation oscillate, achieved through passive mode-locking using the Kerr-lens effect.

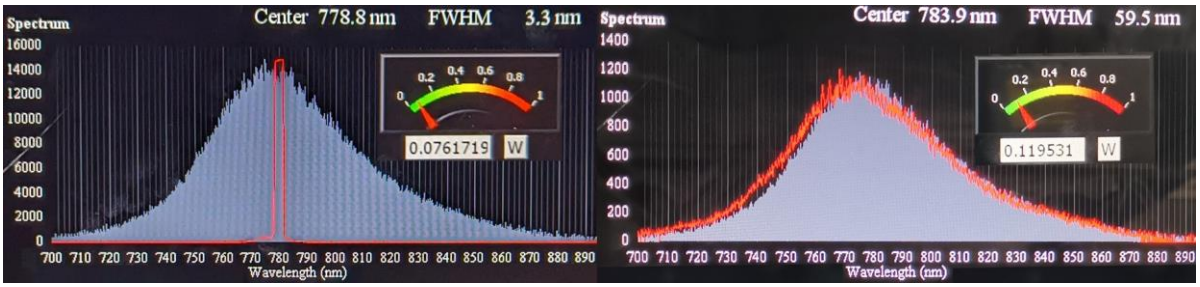

Figure 2.17 LEFT: Cut out of the Wyvern control software's oscillator section, showing the reference mode-locked spectrum (grey area) and the measured spectrum (red) in cw mode and (**RIGHT**) in mode-locked mode (right). In each right corner the power is depicted: 76 mW in cw mode and 120 mW in mode-locked mode, showing a ratio of 2 to 3, which is a requirement to generate a stable pulse train.

As the transmitted beam from OC passes the perforation of the oscillator housing to enter the Stretcher, it produces reflections. Those residual reflections are guided to the spectrometer fiber probe (SFP) and photodiode (PHD) to monitor the emissions spectrum (Figure 2.17) and the pulse train (~25 fs) (Figure 2.18). To maintain optimal conditions, the oscillator area includes an extra cover and a dust filter, reducing airborne contamination.

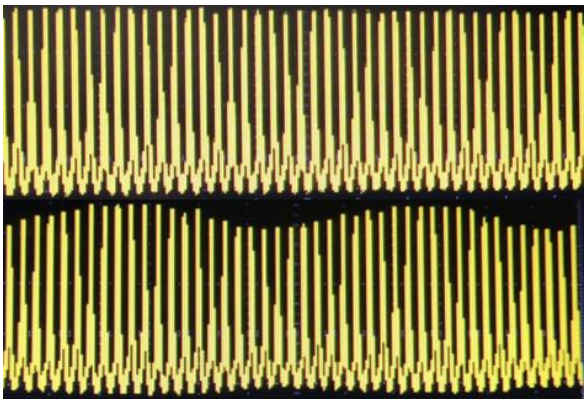

Figure 2.18 Pulse train measured by the digital oscilloscope Rigol D3102CA through the PHD, showing above a stable pulse train below an unstable pulse train (Q-switch overstructure modulation).

2.2.4 Chirped-Pulse Amplification (CPA) within the Wyvern 1000™

The Chirped-Pulse Amplification technique is employed to generate ultrashort laser pulses with high peak power while mitigating the risk of damage to the amplifier medium and other optical components caused by the pulses' high intensity. Strickland and Mourou were honored with the Nobel Prize in physics (2018) for pioneering this technique.[164]

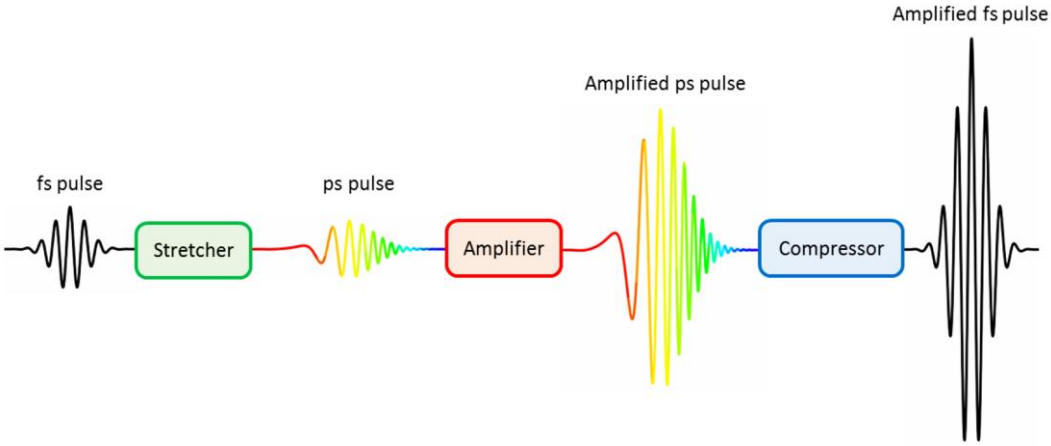

Figure 2.19 Scheme of the chirped-pulse amplification.[165]

The CPA principle (Figure 2.19) involves initial temporally stretching the femtosecond (fs) pulse using a dispersive medium like a pair of gratings. This deliberate elongation of the fs pulse reduces its peak power by four orders of magnitude (from ca. 25 fs to ca. 120 ps), preventing damage during subsequent amplification steps. This controlled elongation creates positive chirp, with lower frequency components leading the pulse (=up-chirp), followed by higher frequency components. This method ensures the preservation of the pulse structure while effectively managing its intensity. The stretched picosecond (ps) pulse undergoes amplification within a regenerative laser amplifier, passing multiple times through the laser medium. Subsequently, the stretched and now amplified ps pulse is recompressed back to its original ultrashort duration by a second dispersive medium within the compressor. This reverses the initial chirping, resulting in the formation of an amplified (by a factor of ca. 10^6) fs pulse.

Within the Wyvern 1000™, the amplification compartment is based on a regenerative amplifier,[166] which selects a single stretched seed pulse out of the input pulse train (reducing

the repetition rate from 80 MHz to 1 kHz) by several polarization-selective optical components.[167] The seed passes multiple times through the gain medium trapped in the cavity until maximum saturation is reached. The regenerative CPA system of the Wyvern 1000^{TM} is depicted in Figure 2.20.

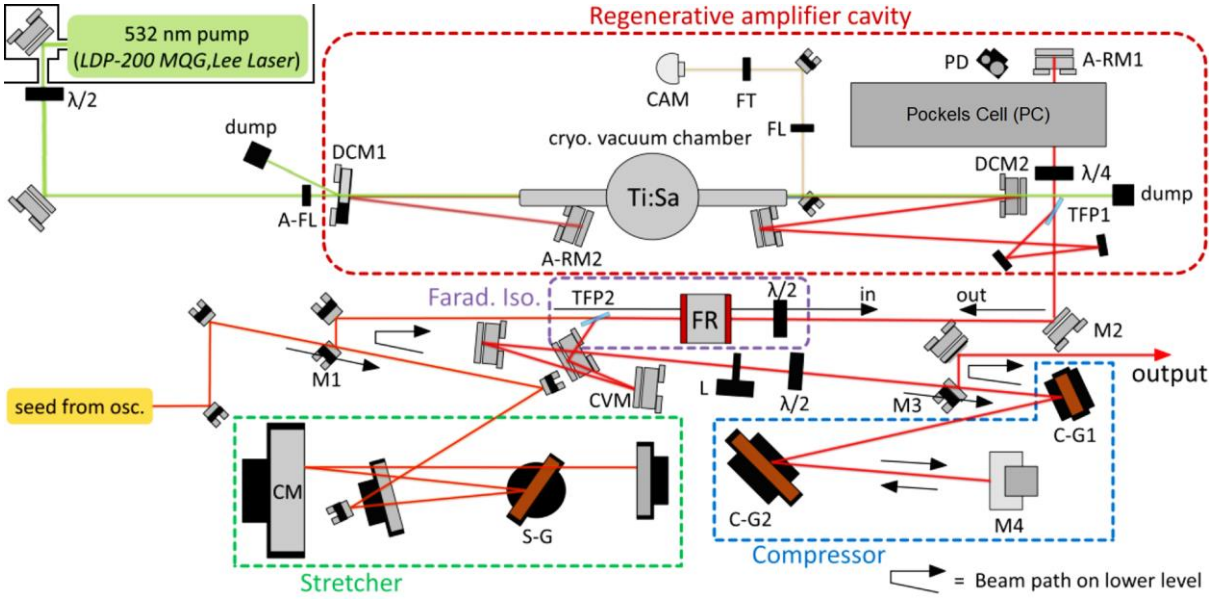

Figure 2.20 Schematic setup of the Wyvern 1000^{TM}, displaying the regenerative CPA system. Abbreviations: λ/2: half-wave plate, λ/4: quarter-wave plate, A-RM1-2: highly reflective rear mirrors, C-G1-2: compressor gratings, CAM: charge-coupled device (CCD) camera, CM: curved mirror, DCM1-2: dichroic mirrors, (A-)FL: focusing lens, FR: Faraday rotator, FT: optical filter, M1-4: mirrors, PD: photodiode, PC: Pockels cell, S-G: stretcher grating, TFP1-2: thin film polarizers. CVM: convex mirror and L: converging lens form a telescope that expands the beam.[165]

As follows, this section provides an in-depth look at the optical path, components, and processes within the Wyvern 1000TM system, including the stretcher, regenerative amplification, and compressor components.

Exiting the oscillator, the seed (784 nm, 120-160 mW, ~25 fs, horizontally polarized) enters the stretcher over M1, where it is temporarily positively chirped to ~120 ps by the dispersive stretcher grating (S-G). Within the **stretcher**, the beam is reflected four times with a complex path on three different height levels and then collimated at the exit and entry by the curved mirror (CM). The distance between S-G and CM determines the GVD as the stretching factor. The GVD can be adjusted by a knob installed externally of the Wyvern housing, controlling the S-G towards the CM.

The stretched ps pulse exits the stretcher in the counter direction of the incoming pulse, however, at a lowered height and is picked up by M1, led into the **Faraday isolator**. The Faraday isolator comprises the Faraday rotator (FR), a thin film polarizer (TFP2), and a half-wave plate (λ/2). The thin film polarizer (TFP1-2) reflects vertically polarized (v-polarized) beam and transmits horizontally polarized (h-polarized) beam. As the beam is h-polarized at this point, it's transmitted through TFP2, vertically rotated by 90° by the Faraday rotator (FR), and then rotated back horizontally by the λ/2 plate. The setting of the Faraday isolator prevents the exiting pulse from the amplifier entering back into the stretcher, as its horizontal polarization is turned to vertical by the λ/2 and is therefore not affected by the Faraday rotator but by the thin film polarizer TFP2, reflecting it into the compressor instead. If the exiting pulse from the amplifier beam were to re-enter the stretcher, it could ultimately reach the oscillator, causing damage.

The Ti:Sa gain medium within the amplifier is powered by a secondary diode-pumped (DP) frequency-doubled Nd:YAG laser (Lee Laser, LDP-200 MQG, 532 nm, 15 W, pulse duration approximately 120 ns). Within the vacuum chamber, the amplifying Ti:Sa crystal is maintained at a cryogenic temperature of -232 °C, facilitated by the PT90 cryostat and the CP950 helium compressor from Cryomech, using adiabatic expansion of helium. This cryogenic cooling process serves to elevate the gain[168] and averts thermal lensing[169]. To preserve the integrity of the pump laser beam as it enters the Wyvern housing, the dielectric mirror redirecting the pump beam is situated within a closed anodized box, extended with anodized tubes connecting the Lee laser and the Wyvern housing. This setup safeguards against dust particles that could considerably diminish the beam's power. Positioned immediately at the Lee laser's entry orifice, a λ/2 plate affixed to an indexing rotation mount adjusts the pump polarization to align with the Brewster windows and the Brewster cut of the Ti:Sa crystal. The pump beam is then directed towards a focusing lens (A-FL), converging the beam onto the Ti:Sa crystal with a focal length of 300 mm. The pump beam is redirected towards a focusing lens, which converges the beam onto the Ti:Sa crystal with a focal length of 300 mm. Given the high power of the beam (15 W), each reflection must be meticulously managed to prevent damage within this delicate optical setup housed within the Wyvern. Upon traversing the vacuum chamber

and DCM2, the pump beam is confined by an optical dump, and reflections emerging from DCM1 are similarly controlled by an additional dump.

The stretched pulse is directed by M2 into the **regenerative amplifier cavity** and, owing to its horizontal polarization, transmitted through the thin-film polarizer TFP1. The regenerative aspect of the amplifier relies on the high-speed PCD8g2 Pockels cell (PC) from BME Bergmann, which traps one stretched seed pulse within the amplifier cavity by applying a high voltage until the amplifier reaches maximum gain and saturation.[164] The trapping occurs as the PC functions as a λ/4 plate. When it's activated, it reverses the effective polarization by λ/4 between TFP1 and A-RM1. Consequently, new incoming pulses that maintain horizontal polarization cannot enter the regenerative amplification setup, and trapped pulses with vertical polarization are captured. However, if turned off, the polarization changes either allows a new pulse to enter or permits an amplified pulse to exit the cavity through its reflective or transmissive character at TFP1, respectively.

The PC enables a new incoming pulse to enter by not applying any voltage. Thus, the horizontally polarized pulse travels twice through the λ/4 plate after bouncing off the highly reflective rear (A-RM1), resulting in a vertically polarized pulse that is reflected by TFP1 towards the Ti:Sa gain medium housing in a vacuum chamber accessible through Brewster-angle windows. Guided by the dichroic mirror (DCM1), the pulse is directed to A-RM2, which reflects it back to TFP1, still vertically polarized.

The dichroic mirrors DCM1-2 are only reflecting the amplified beam, while the (Lee) pump beam is transmitted through. At TFP1, the amplified pulse is reflected towards the PC, passing the λ/4 plate. At this point, the PC is activated, maintaining the polarization as vertical, trapping the amplified beam for further amplification until saturation is reached. In this system, saturation is typically achieved after three iterations of the amplified beam running within A-RM1 and A-RM2 within a few nanoseconds. The saturation in amplification is monitored by an oscilloscope (Figure 2.21).

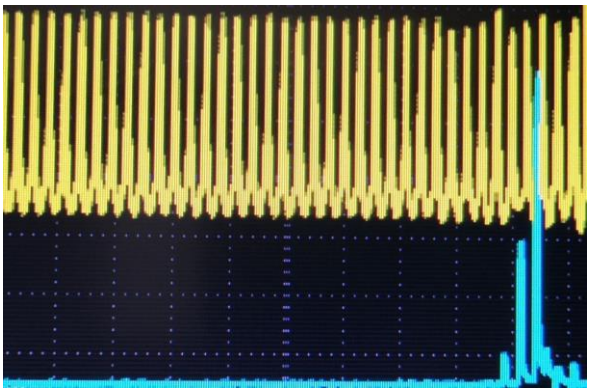

Figure 2.21 Oscillator output pulse train (yellow) and saturated amplification in the amplifier (blue) measured by the digital oscilloscope Rigol D3102CA.

To release the saturated (vertically polarized) pulse, the PC is switched off, allowing the polarization change to horizontal, enabling transmission through TFP1. Concurrently, a new incoming horizontally polarized pulse is effectively rotated twice by the λ/4 plate to vertical polarization, entering the trap as it's reflected at TFP1.

Synchronization of the amplified pulse and pump pulse is achieved through the delay generator card within the Wyvern control software DragonMaster provided by KMLabs. The spatial alignment between the amplified and pump beams can be observed using a CCD camera, facilitated by a lens between two silver-coated mirrors situated at a lower altitude relative to the amplified and pump beam levels. The Brewster window's sufficient size allows for residual radiation to be captured and redirected to the CCD camera. The optical filter is used to block amplifier/Ti:Sa radiation.

The stretched and now amplified pulse exits the amplifier cavity in horizontal polarization and is subsequently transformed to a vertical polarization by the λ/2 plate. This alteration ensures that the pulse remains unaffected by the Faraday rotator but instead gets reflected at TFP2. It proceeds to the telescope, which comprises the convex mirror (CVM) and the converging lens (L), expanding the pulse by approximately a factor of 10, which reduces heating on the compressor optics. The beam is rotated to horizontal by a second λ/2 plate, before passing over M3 to enter the **compressor** compartment, where the stretcher-induced chirp will now be compensated by a grating pair (C-G1-2) in parallel. After passing C-G1 and C-G2, the beam arrives or is retroreflected by the dielectric roof mirror (M4), lowering the altitude of the

beam plane, enabling the pickup by M3 to deflect the final output. The output beam, centered at 780 nm, has a repetition rate of 982 Hz and a pulse duration of ~55 fs.

It is worth noting that the performance of the Wyvern significantly decreased over the years, presumably due to the decreased performance of the pump diodes in the Lee laser (Table 2.1). The Wyvern output yielded 3.8-4 W in 2016, experiencing a noticeable decline to 3-3.5 W, figures predominantly used for all measurements conducted in this thesis. According to documentation throughout these years, the repetition rate varied between 980-985 Hz, and the pulse duration of 50-60 fs. The power of the Wyvern output and its repetition rate have been determined using the VEGA laser power meter, in combination with a thermal energy/power sensor, both sourced from Ophir.

Table 2.1 Performance overview of the Lee laser and the Wyvern final output.

YEAR	LEE PUMP @81% POWER	WYVERN OUTPUT
2016	18.2 W	~3.8 W
2018	18.1 W	~3.7 W
2019	16.7 W	~3.6 W
2020	16.1 W	~3.5 W
2021	15.9 W	~3.4 W
2022	15.6 W	~3.3 W
2023	14.3 W	~3.0 W

2.2.5 FROG Scan: Realtime Ultrashort Pulse Measurement

The pulse width of the final output from the Wyvern laser system was measured using a FROGscan from MesaPhotonics, a commercial implementation of the Frequency-Resolved Optical Gating (FROG) technique. This method enables real-time characterization of ultrashort laser pulses by employing second-harmonic generation (SHG) and spectrally resolved autocorrelation techniques, allowing for a complete temporal and spectral reconstruction of the pulse. The system consists of three main components: the servo stage (SS), the spectrometer, and the SHG (BBO) crystal.

In this setup, the Wyvern output beam enters the FROGscan setup through the first iris and is split by a beam splitter (BS), into two replicas that follow distinct optical paths before

recombining in a nonlinear crystal (Figure 2.22). One pulse, referred to as the servo beam (SB), is transmitted through a servo-controlled delay stage (SS), where its time delay is systematically varied. This controlled delay enables scanning of the temporal overlap between the two pulses, a fundamental requirement for pulse characterization. The SB (dark green) is then focused by a focusing mirror (FM). Simultaneously, the second pulse serving as a reference following a constant optical path, (light green) is reflected toward a fixed delay mirror (FDM). A portion of this beam transmits through an overload mirror (OM) and exits through the second iris, while the remaining portion is directed toward the focusing mirror (FM). This configuration serves for aligning a laser beam into FROGscan.

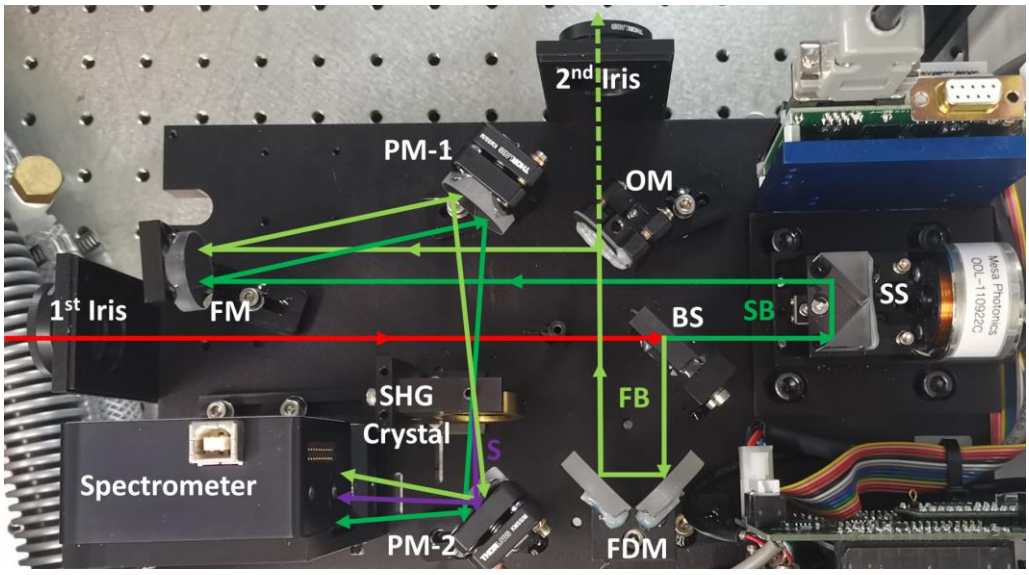

Figure 2.22 Schematic of the beam path[170] in the FROGscan system, highlighting the interaction within the nonlinear crystal and the subsequent spectral detection. Abbreviations: FM (Focusing Mirror), BS (Beam Splitter), SS (Servo Stage), FDM (Fixed Delay Mirror), OM (Overload Mirror), PM-2 (Second Position Mirror), PM-1 (First Position Mirror), SB (Servo Beam), FB (Fixed Beam), S (Signal Beam)

Both beams are then guided by the first position mirror (PM-1) toward the SHG BBO crystal. Within the crystal, the beams interact with the nonlinear medium to generate second-harmonic signals. These signals consist of individual second-harmonic components (SB* and FB*) corresponding to each fundamental beam, as well as a cross-correlation term that forms only when SB and FB overlap temporally and spatially, resulting in the signal beam (S). S carries both the temporal and spectral phase information of the pulse, making it essential for full pulse reconstruction. The generated signal beam (S, purple) is then directed by the second

position mirror (PM-2) into the spectrometer, where it undergoes spectral dispersion and detection.

By systematically varying the delay in the SB path and recording the corresponding SHG signals, a spectrogram is constructed—a two-dimensional plot of intensity versus frequency and delay. This spectrogram encodes the temporal and spectral characteristics of the pulse, enabling phase retrieval algorithms to reconstruct the complete electric field.

The FROGscan software, VideoFROGscan 8, continuously analyzes the measured spectrogram, determining pulse duration, spectral phase, and potential distortions such as chirp or higher-order dispersion effects. Additionally, the software can identify and correct distortions caused by spatial chirp and spectral tilt, which can affect SHG efficiency and spectrogram accuracy. The software also provides real-time feedback (Figure 2.23), allowing for fine adjustments of the delay stage and beam alignment to optimize pulse compression. By iteratively refining these parameters, an accurate pulse measurement is achieved.

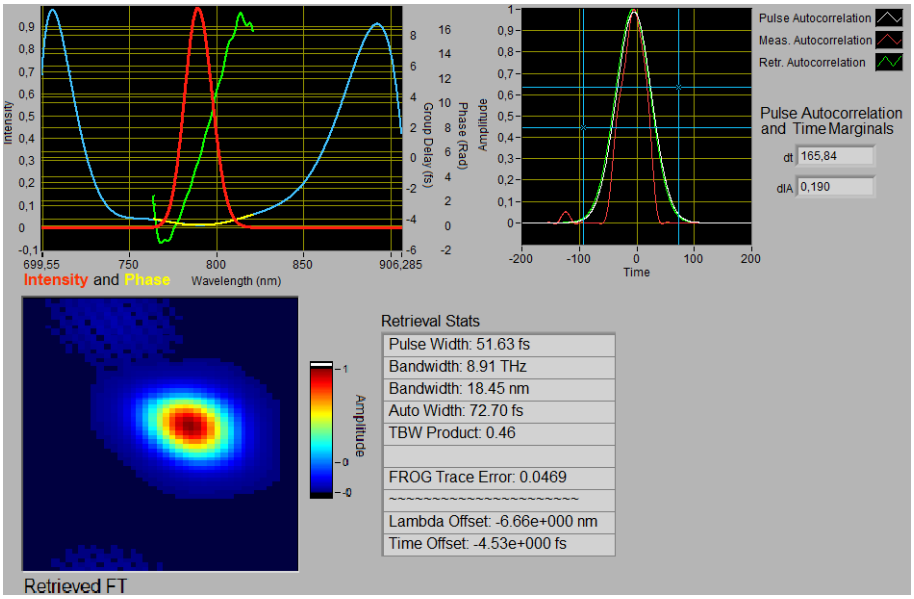

Figure 2.23 Excerpt from the VideoFROGscan 8 software displaying the measured and reconstructed pulse width of the Wyvern laser system.

2.2.6 Optical Parametric Generator/Amplifier (TOPAS-C)

In conjunction with the Wyvern 1000TM, two identical optical parametric generator/amplifier (OPG/OPA) systems, labeled as T6 and T7 in Figure 2.24, are utilized in this study to achieve wavelength-tunable beams ranging from 236 to 2600 nm for both static and transient photodissociation (τ-PD) measurements. Both TOPAS systems (T7 and T6) are driven by the splitted Wyvern's output beam.

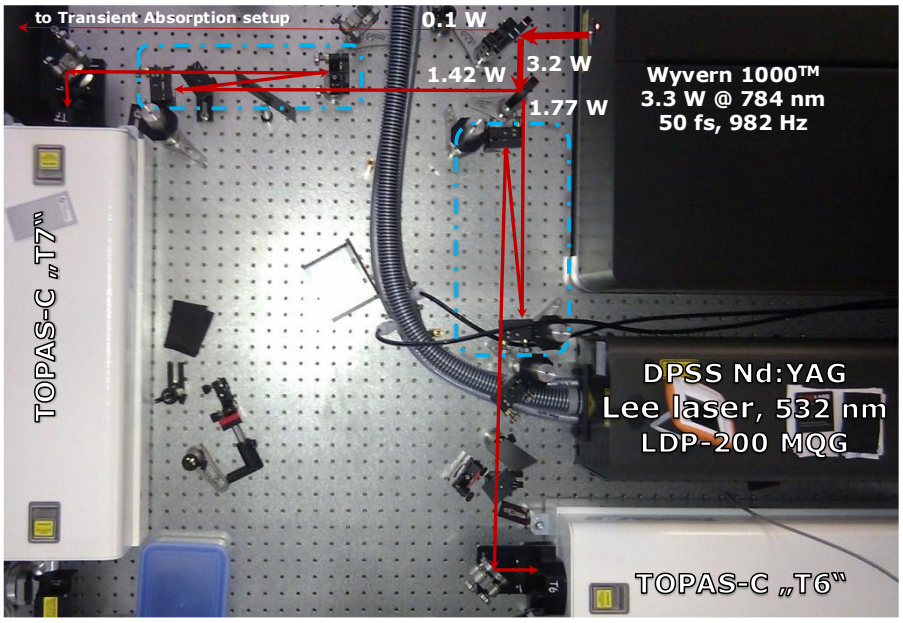

Figure 2.24 Pathway of the Wyvern output directed to both TOPAS-C systems, adapted from [133]. The telescope setup is outlined in blue.

During τ-PD experiment T7 is used as a pump in the UV/Vis region (236-650 nm), while T6 serves as probe beam in near-infrared range (ca. 1200 nm). As depicted in Figure 2.24, the initial beam traverses a series of beam splitters. A smaller fraction (0.1 W) is designated for a transient absorption setup (not utilized in this thesis). The larger portion is further divided, with 45% (1.42 W) directed to T7 and 55% (1.77 W) transmitted to T6 (Figure 2.25).

It is worth mentioning, that the transmitted beam is of lesser quality related to, e.g., pulse duration due to the added dispersion that comes with transmission through diverse optics. Before entering each respective TOPAS system, the splitted beams pass through a telescope, reducing the Wyvern beam's diameter to < 8 mm at the $1/e^2$ intensity level. Upon entry into the TOPAS-C through a mechanical shutter, the Wyvern beam splits into two paths (②,③) using a 96% beam splitter (BS1) (Figure 2.25).

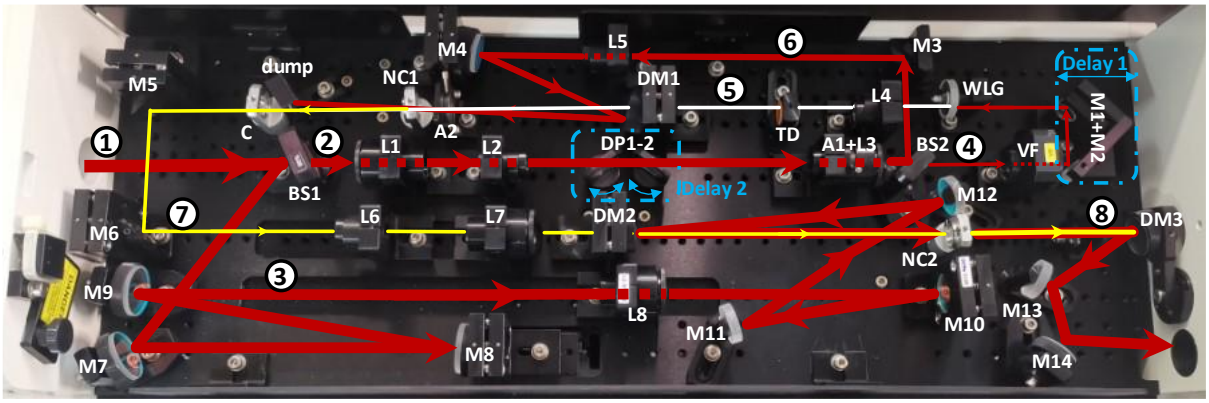

Figure 2.25 Optical layout of the TOPAS-C[171]: 1) Wyvern beam at 780 nm, 1.4/1.7 W, 50 fs pulse width, and a repetition rate of 982 Hz; 2) pump for pre-amplification (PrA) stage; 3) pump for power amplification (PoA) stage; 4) pump for white-light continuum generator; 5) White-light continuum (WLC) beam; 6) pump for pre-amplification of WLC; 7) pre-amplified signal beam; 8) amplified signal+idler beam and residual of ③. **Abbreviations**: A: iris aperture; BS: Beam splitter; C: compressor; DM: dichroic mirror; DP: Brewster angled plates; M: mirror; M1+M2: retro-reflector; L: lens; NC: non-linear crystal; VF: variable density filter; WLG: white-light continuum generator. Delays 1-2 are computer-controlled translations/rotations via the WinTopas 3.3.25 software from Light Conversion.

Depending on the Wyvern's pump energy, 80-98% is reflected into the power amplification (PoA) stage and the rest into the pre-amplification (PrA) stage. The latter is used as a pump for PrA, passing through a two-lens telescope (L1-2) that reduces the beam size to fit into the "delay 2" stage. Delay 2, consisting of Brewster angle plates, is mounted on a rotation stage controllable via the WinTOPAS software. The Brewster plates rotate in opposite directions, altering the path length of the pump for PrA (②, also the seed for PoA) concerning the pump for PoA ③ to optimize their optical temporal delay. ② also passes through an iris aperture (A1) mounted together with the lens (L3) before being split by BS2, transmitting 20% for the generation of the white-light continuum ④. A1, together with A2, used as a point of reference for the WLC beam, aligns the Wyvern beam entry. In combination with the density filter (VF), it balances the intensity of the pump for the white ④ to produce a stable WLC beam. This step is crucial as the pump intensity relies on the pulse width and energy of the Wyvern pump, pulse contrast, and the beam size inside the WLG. A stable WLC beam displays distinct single filaments, while an unstable one exhibits flickering and inhomogeneous filaments. Refer to Figure 2.26 for examples of a stable and a labile WLC beam.

L3 focuses the transmitted beam (④) onto the sapphire plate (WLG) to generate the white-light continuum (WLC). Additionally, it functions as a telescope with L5 for focusing the

reflected beam, which is used to pump the pre-amplification of WLC (⑥). The process for generating WLC (④) involves passing the pump through the density filter (VF) and Delay 1—a retro-reflector mounted on a translative stage controlled via the WinTOPAS software. Delay 1 optimizes the optical delay between the pump for pre-amplification of WLC (⑥) and the WLC itself (⑤). Tuning the wavelength of the signal beam (⑦) is achieved by altering the delay of WLC (⑤) concerning the pump for pre-amplification of WLC (⑥).

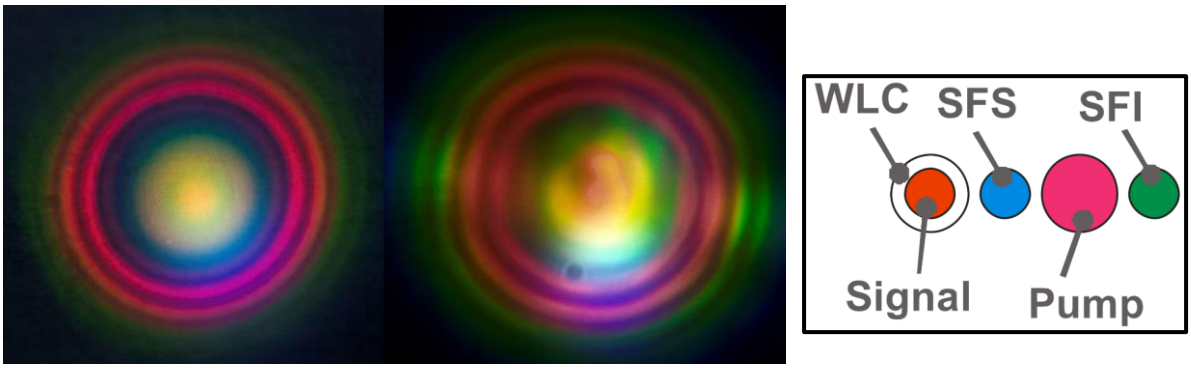

Figure 2.26 WLC seen after WLG. LEFT: Maximum allowable intensity of the pump for the white-light. MIDDLE: too high pump intesity for the white-light.[171] LEFT: Illustration of the different wavelength contained in the resulting pre-amplified signal beam ⑦. **Abbreviation:** SFS: Sum frequency of signal ⑦ and pump ⑥; SFI: Sum frequency idler and pump ⑥.

The WLC beam (⑤), generated by pumping the WLG, is directed onto the nonlinear crystal (NC1) through L4 and temporally stretched by a dispersive plate (TD). Both beams—transmission of ⑤ and reflection of ⑥ via a dichroic mirror (DM1)—intersect non-collinearly within the nonlinear BBO crystal (NC1) for parametric amplification. The non-linear beam layout enables easy separation, capturing the residual pump (⑥) with an optical dump, while the amplified WLC (pre-amplified signal beam, ⑦) proceeds through compensator C. NC1 and C, controlled by WinTOPAS software and mounted on rotational stages running in opposite directions, serve specific functions. NC1 adjusts phase-matching for amplification efficiency based on Delay 1's wavelength settings, while C compensates for any shift in ⑦ due to NC1's rotation. The pre-amplified signal beam (⑦) already encompasses a variety of wavelengths (as illustrated in Figure 2.26) after pre-amplification. To match the pump mode in the PoA stage, the highly divergent beam is redirected by M5-6 into a telescope composed of a negative lens (L6) and a positive lens (L7), collimating the beam and adjusting its size.

Through the dichroic mirror (DM2), the signal (⑦) and the PoA pump (③) combine and pass collinearly through the center of NC2, finally emerging as the TOPAS-C output.

The beam reflected into the PoA stage by BS1 (③) traverses multiple mirrors, culminating at DM2, where it merges with the Signal beam (⑦). M8 was initially used during the installation phase for manually adjusting the delay between ③ and ⑦ at NC2. For achieving optimal amplification, a telescope consisting of L8 and M10 reduces the size of the pump beam (③) to attain the required intensity. The directed pump beam (③) via M11-12 to DM2 results in parametric amplification of the signal beam and the generation of an idler upon passage through NC2. Both beams (signal+idler) exit collinearly as the TOPAS-C output.

DM3, adjustable through a knob located outside the TOPAS housing (Figure 2.27), is utilized to switch in or out, directing the residual pump to an optical dump as required. Similar to NC1, NC2 is also mounted on a rotational stage and controllable via WinTOPAS software.

The resultant signal covers a wavelength range of 1140—1620 nm, while the idler spans 1520—2500 nm in NC2. This is achieved by automatically adjusting Delay 1, Delay 2, NC1 (+C), and NC2. The entire tuning range of 236 – 2600 nm is achieved through various combinations using two external frequency mixer housings located outside the TOPAS-C housing (Table 2.2).

Table 2.2 Overview of the wavelength ranges and the corresponding setting of the frequency mixers and the resulting out waver properties. Abbreviaton: I: idler; S: signal; SH: second harmonic; SF: sum frequency; FH: fourth harmonic.

Wavelength region [nm]	Output Polarization	Wave Type	Crystal of Mixer 1	Crystal of Mixer 2	Use of DM3
1520-2500	Horizontal	I	-	-	Closed
1140-1620	Vertical	S	-	-	Closed
795-1160	Vertical	SHI	2BF	-	Closed
570-810	Horizontal	SHS	2BF	-	Closed
525-580	Vertical	SFI	2BF	-	Opened
472-527	Vertical	SFS	3BF	-	Opened
400-485	Horizontal	FHI	2BF	5BF	Closed
285-400	Vertical	FHS	2BF	5BF	Closed
262.5-287.5	Horizontal	SHSFI	2BF	6BF	Opened
236-263.5	Horizontal	SHSFS	3BF	6BF	Opened

In Mixer 1, crystals 2BF and 3BF are utilized, while Mixer 2 employs crystals BF5 and BF6. These abbreviations refer to part numbers associated with BBO crystals, differing in coatings and cut angles to accommodate specific wavelength ranges. The crystals are mounted on motorized shafts, allowing beam introduction by rotating the shaft through controllable settings in the WinTOPAS software.

The wavelength ranges specified in Table 2.2 represent only a segment of the output beam. Depending on the settings for different wavelength regions, the output beam may include radiation in higher or lower wavelength ranges, or even radiation of opposite polarization. To isolate and obtain the desired wavelength region, two wavelength separators are employed and attached to Mixer 2 (Figure 2.27). Each wavelength separator (WS) comprises two dielectric mirrors equipped with high reflectivity coatings tailored to specific wavelength ranges. These separators can translate the beam either vertically (v) or horizontally (h). Thus, the WS selectively reflects a particular wavelength region based on the coating and polarization, determined by the mounting direction.

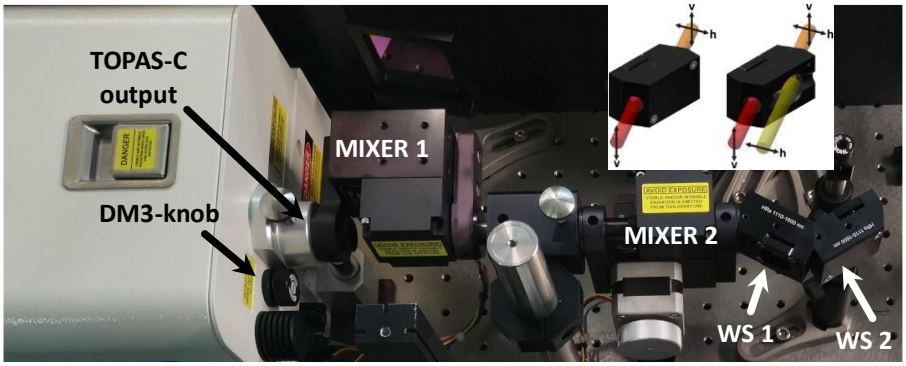

Figure 2.27 External mixer attached to the TOPAS-C output. Filtering residual radiation, wavelength separators are mounted on Mixer 2 exemplary in setting for the output beam in vertical polarization. Insert on the upper right (white background): wavelength separator with and without metal cover, showing the translation of the beam.[172] The DM3-knob is used to block or pass the idler out of the TOPAS-C output.

2.3 Nanosecond Laser System

The EKSPLA NT242-1k-SH/SF is a compact nanosecond laser system (Figure 2.28) offering a wavelength tunability from 210 to 2600 nm. The NT242 comprises two primary components: a laser system housing and a separate unit composes of the power supply, diode laser as pump, cooling interlock, and control mechanisms for internal or external regulation of the laser. Both units are interconnected through cooling tubes carrying double-ionized water, as well as fiber and power umbilicals. The laser system housing incorporates a pump laser (NL210, Master oscillator), a tunable parametric stage (OPO), a second harmonic/sum frequency (SH/SF) generation stage, a fiber output, and harmonics output.

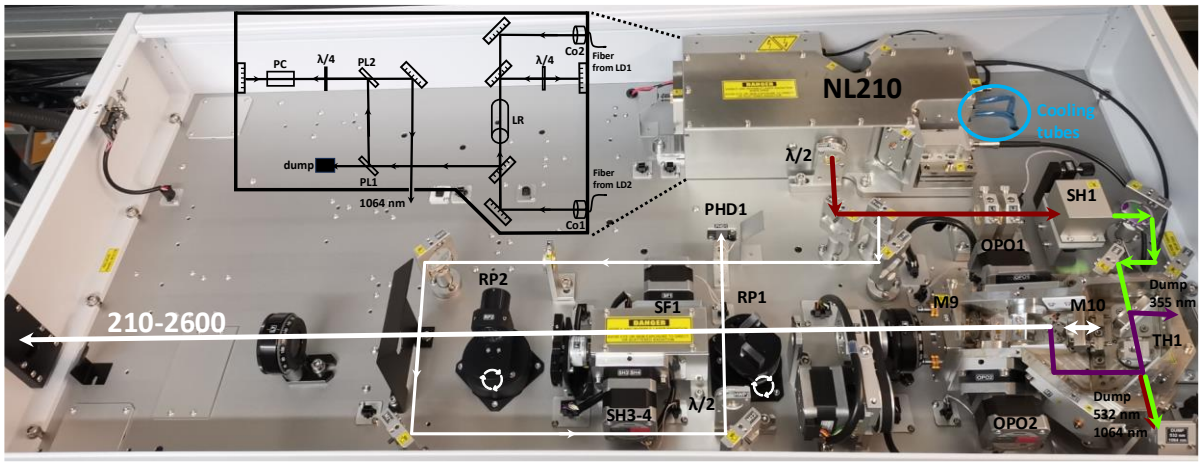

Figure 2.28 Optical layout of the EKSPLA NT242 ns laser system[173]. Abbreviation: Co: collimator; LR: laser rod; PC: Pockels cell; PHD: photodiode; Pl: polarizer; OPO: optical parametric oscillator; RP: Rochon prism; SF: sum frequency generator; SH: second harmonic generator; TH: third harmonic generator.

The NL210 is a Q-switched pump laser producing a 1064 nm wavelength with a pulse duration of 4-6 ns and a repetition rate of 1 kHz. It operates using a Nd:YAG laser rod crystal as the lasing gain medium. Within the NL210 case, components such as the Pockels cell, laser cavity, cavity mirrors, Q-switch thin-film polarizers, and Q-switch electronics are housed. Typically, pulse generation occurs within a cavity equipped with an optical output coupler. However, here, the optical output coupler is replaced by a time-varying output coupler (τ-OC), allowing pulse generation that is independent of gain. At the beginning of pumping, the τ-OC maintains the laser below a specific threshold, and at the end of the pumping cycle, a high voltage is applied to the Pockels cell, closing the cavity. Consequently, the intracavity power rapidly

accumulates with minimal loss. When the maximum intensity is reached, the Pockels cell is switched off, releasing the Q-switched pulse within one cavity round trip. A Beta-Bariumborat (BBO) Pockels cell is utilized due to its high damage threshold and low insertion loss. The rise and fall time for the Pockels cell are within a few nanoseconds.

The fundamental beam passes through a λ/2 plate, splits into two beams after passing through a beam splitter and is directed to a two-lens telescope focusing the beam onto the second harmonic unit (SH1) with a type 1 BBO crystal. The generated second harmonic (532 nm) is then mixed with the residual fundamental in the TH1 unit, producing the third harmonic (355 nm) required for the OPO resonator stage. In the TH1, a type 1 BBO crystal is employed. While the third harmonic is reflected to the OPO resonator, residual of second harmonic and fundamental components are transmitted to a beam dump. The OPO resonator comprises M9-10. Type 2 BBO nonlinear crystals in OPO1-2 are mounted on a controllable rotational stage, enabling wavelength tunability from 405 to 2600 nm with a conversion efficiency of 15%. The Rochon prism RP1 functions as a separator between the signal and idler beams. The returning third harmonic from the OPO is reflected to the second optical dump. The wavelength range of 210 to 404.99 nm is achieved by SH3-4 and sum frequency (SF1) units, housing type 1 BBO crystals. SF generation combines the output of the OPO with the fundamental. A second Rochon prism RP2 separates the signal and idler beams once again. A fraction of the NL210 output is reflected by various optics to a photodiode, monitoring significant parameters of the generated pulses. It is worth noting that this beam is reflected into the SF/SH unit while crossing RP1. The wavelength polarization for the different ranges is given in Table 2.3. Thereby, a second Rochon prism (RP2) separates the signal and idler beams once again.

Table 2.3 Overview of the wavelength ranges of the EKSPLA NT242 ns laser system. Abbreviaton: SH: second harmonic; SF: sum frequency.[173]

Wavelength range [nm]	Polarization	Wave type
710 – 2600	Vertical	Idler
405-709.99	Horizontal	Signal
300-404.99	Vertical	SF
210-299.99	Vertical	SH

2.4 Coupling of the Mass Spectrometer with the Laser Systems

The coupling of the mass spectrometer with the laser systems facilitates optical access to the ion cloud within the ion trap and enables spectroscopic analysis of isolated charged molecules. Hereby, the beam is vertically downward directed into the modified QIT, aiming for the center of the ion cloud (Figure 2.29). As discussed in section 2.1.3, the QIT is an extremely sensitive device capable of storing and isolating ions through the precise application of electrostatic voltage at a controlled pressure by a continuously regulated helium flow. The modification of the ion trap was conducted in collaboration with Bruker Daltonics (support by Dr. Christoph Gebhardt). This development involved creating optical access for a laser beam to traverse through the center of the QIT and extending the QIT using a breadboard to accommodate optical elements that guide the beam into and out of the mass spectrometer (beam path illustrated in Figure 2.29).

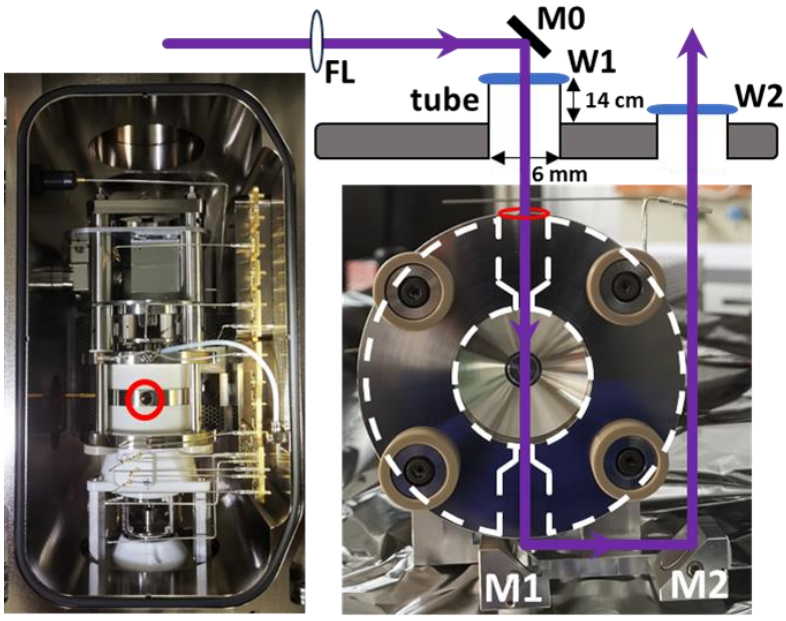

Figure 2.29 LEFT: upside image of the punctured QIT highlighted in red. **RIGHT**: schematic path of the beam (violet) passing through the center of the QIT (white dotted). Abbreviation: FL: focusing lens; M: mirrors; W: windows.

To ensure that the beam illuminates most of the ion cloud, it is directed perpendicular by M0 into a 14 cm tube with a circular opening of 6 mm outer diameter. This opening is sealed with

an uncoated UV fused silica window of 3 mm thickness using a Viton O-ring. Establishing an optical pathway through the ion trap involved two holes at the opposite end of the ring electrode perpendicular to the plane. The orifice within the ring electrode begins with a 6 mm diameter and gradually reduces to a smaller 2 mm diameter within the last 3 mm before entering the trap. The gradual tapering and the tube height complement the focusing lens. This ensures that the beam enters and exits without hitting the tube causing artificial signals due to emitting electrons. As the ion cloud diameter is estimated around 1 mm,[174] the beam is slightly defocused using a plano-convex lens of 50 cm focal length before M0[175]. After passing through the ion cloud as a diverging beam, it is guided to exit the mass spectrometer. For this purpose, the grid beneath the QIT was extended, enabling the installation of two mirrors at a 45° angle. M1-2 directs the beam through the exit opening.

2.5 Ion Trap Laser Spectroscopy

Figure 2.30 illustrates the experimental setup, presenting the optical pathway of the KMLabs Wyvern and EKSPLA laser integrated into the modified QIT for ion trap laser action spectroscopy. This configuration allows for both static UVPD and τ-PD of isolated molecules, utilizing the KMLabs Wyvern or EKSPLA laser, or a combination of both.

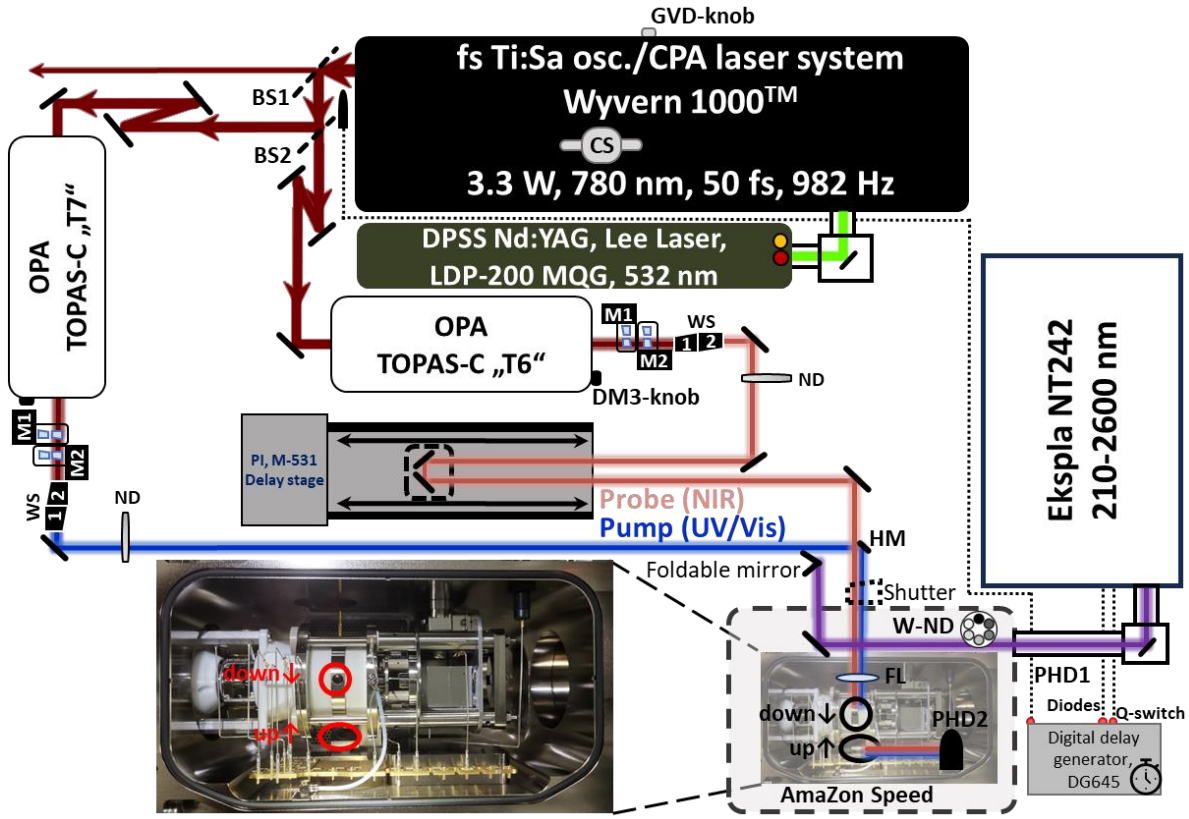

Figure 2.30 Schematic overview of the experimental setup, realizing ion trap spectroscopy by combining the tunable fs Wyvern laser and the ns EKSPLA laser with the modified ion trap of the MS. This setup enables static photodissociation (PD) and transient photodissociation experiments (τ-PD). Abbreviation: BS: beam splitter; CPA: chirped pulse amplification; CS: cryogenic cell; DPSS: double pumped solid state; FL: focusing lens; GVD: group velocity dispersion; HM: half mirror; M: frequency mixer; ND: variable neutral density filter continuous; NIR: near-infrared; PHD: photodiode; OPA: optic parametric amplifier; UV/Vis: ultraviolet/visible; WS: wavelength separator; W-ND: a six-station neutral density filter wheel.

The Wyvern laser beam's wavelength is tuned via TOPAS-C T7 and T6. T7 serves for static UVPD experiments or as a pump beam in τ-PD experiments, while T6 functions as the probe beam in τ-PD experiments in the NIR range. For UVPD experiments, wavelengths were

scanned in 3 nm steps, corresponding to the averaged spectral width of the used ultrashort laser pulses.

The temporal delay between pump and probe beam in τ-PD experiments is realized using a motorized single-axis delay stage (M-531.DD Heavy-Duty micropositioning stage) by PI. Controlled through the PIMikroMove software, its translation is guided by the C-863 Mercury servo controller, facilitating step size and velocity adjustments. This stage, 30 cm in length with a conversion factor of 0.15 mm/ps, provides a time window up to ca. 2 ns. However, time windows beyond 1 ns require substantial laser optimization due to divergence of the laser beams.[165] The resolution, represented by the Q factor, is contingent upon the scan resolutions, where finer time steps lead to better quality of data resolution. The effective temporal resolution is determined by a cross-correlation measurement inside the QIT, estimated to 120-140 fs (Cp. 2.7)[133,165]. The elongation of the 55 fs pulse duration from the Wyvern output is attributed to dispersion and optical non-linear effects incurred during transmission through various optics, including the TOPAS-C until entering the QIT.

As for all PD experiments energy control of the beams is important, therefor neutral density filters with a continuous variability are installed in the beam path. The collinearity of pump and probe beam is achieved by using a half mirror for the T7-beam, leading to a spatially overlap within the QIT after focusing. As the ion cloud diameter is estimated to ca. 1 mm, a plano-convex lens (f = 50 cm) serves to spatially overlap both beams slightly of focus. The EKSPLA beam, after passing through anodized tubes and a neutral density filter (continuously variable or a six-station wheel), is directed by a folding mirror onto the T7-beam path while blocking the T7-beam.

In UVPD measurements, a wavelength-by-wavelength approach with a step of 3 nm is used within the Wyvern setting. However, to enhance control and flexibility, a scan program was developed for the EKSPLA system by M.Sc. Marcel Schmitt utilizing the given controllability of the EKSPLA with LabView. This development, named NEWT (New EKSPLA Wavelength Tuner), enables wavelength-dependent scans with a minimum step width of 0.01 nm and allows the adjustment of illuminating time per wavelength based on desired resolution. This capability

allows for the exploration of vibrational band structures of molecular electronic transitions at room temperature.[176] To ensure synchronization with the mass spectrometer of the Bruker trapControl software, the set wavelength step width and time per wavelength were coordinated with each other. For each wavelength range, a power curve was separately measured (Table 2.3). The maximum power within each wavelength range was adjusted using a neutral density filter to match the dissociation yield of the analytes. Measurement of the power curve was facilitated by the StarLab 2.3 software from Ophir Optronics, monitoring the energy detected from the VEGA laser power/energy meter connected to a pyroelectric energy sensor (PE9-ES-C, Ophir). The implementation of the scan-option for UVPD spectra allows for high-resolution measurements and eliminates the need for manual wavelength adjustments.

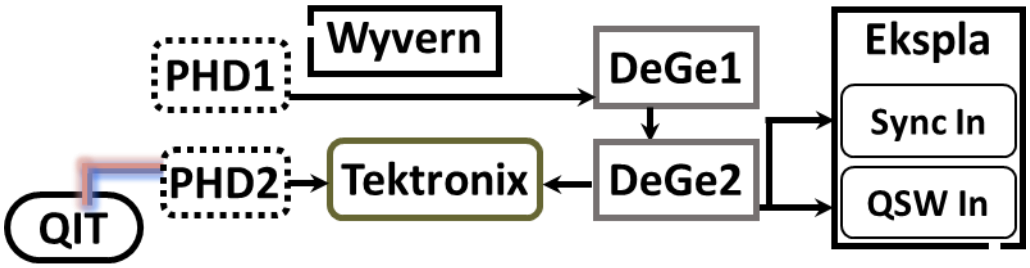

Figure 2.31 Scheme of the temporal synchronisation between the Wyvern and the EKSPLA laser system. Abbreviation: DeGe: Delay Generator, PHD: photodiode, QSW: Q-switch of the EKSPLA laser.

An extension of our analytical methods involved a combination of the ns with the fs laser system to enable τ-PD experiments within the ns to µs time windows. In this setup (Figure 2.31), the EKSPLA operates as the pump, while the Wyvern-T6 beams serve as the probe in the τ-PD setting. A fast photodiode (PHD1, DET10A/M, Thorlabs) monitors the Wyvern output pulses, sending a signal to the first digital delay generator (DeGe1, DG645, Stanford Research Systems). This delay is adjusted to match the EKSPLA pulse generation time. A delayed pulse triggers the second delay generator (DeGe2), which in turn triggers the pump diodes and Q-switch of the EKSPLA oscillator. The set delay between pump and probe laser pulses can now be electronically controlled and be monitored via an oscilloscope by Tektronix (DPO4104B, Digital Phosphor Oscilloscope) using a photodiode (PHD2), placed in the laser beam exiting the QIT. Controlled by a LabView-based program developed by Dr. Aleksej Gaidukov and advanced by M.Sc. Marcel Schmitt, DeGe1 induces successive time delays for τ-PD experiments in the ns-µs time delay range. The maximum time window utilized in this

study is ca. 500 µs. Theoretically, the achievable time resolution falls within the range of a few nanoseconds (≈ pulse width of EKSPLA laser, 4-6 ns). However, due to technical issues of the Wyvern system, particularly instability of the mode-locked seed beam within the oscillator and related “digital” jitter in the regenerative amplifier, only a time resolution of approx. 15 ns was achieved in some instances. To enable irradiation of the ion cloud only during the mass spectrometer set fragmentation time window, all beams pass through a single-blade beam shutter (SH1, Thorlabs) with a Ø1" aperture and closing time (80 to 20%) of 10 ms. Controlled via a Benchtop Optical Shutter Controller (SC10, Thorlabs), the beam shutter operates in synchronization with the QIT. Alternatively, an optical chopper can be installed to reduce the pulse repetition rate.[133]

2.5.1 Static UVPD Spectroscopy in the QIT

UVPD spectroscopy refers to the photoinduced dissociation of molecular (ionic) systems upon electronic excitation by laser irradiation, usually applied in gas phase.[177] The recorded dissociation yield reflects resonance wavelengths passed by during the tuning of the laser radiation. A complementary technique to UVPD spectroscopy is the typical and wide-spread used UV/Vis absorption spectroscopy in solution, where absorption is calculated from the reduced transmission of light through an analyzing medium following the (Bouguer-)Lambert-Beer law [BLB]. Since the analyte molecule's density in the gas phase is usually orders of magnitude smaller than in solution classical absorption spectroscopy is not generally applicable in gas phase, particularly in ion traps.[178] For this reason, "action spectroscopy" or "consequence spectroscopy"[177] provides a viable and reliable alternative. Action spectroscopy revolves around the photoresponse of molecules as a consequence of photoexcitation.[179] Here, the photoresponse manifests as the photodissociation (PD) of the trapped charged molecules in the QIT, and the yield of fragmentation of the analyzing molecule is recorded as a function of the wavelength. UVPD action spectroscopy presents the advantage of spectroscopically analyzing charged, isolated particles, free from interaction with solvent molecules, counter ions and further environmental influences (matrix or crystal effects), allowing a direct comparison to quantum chemical computations by *ab initio* DFT

methods. The ions are stored and mass-selected in the QIT for a set timeframe in the range of 10-100 ms, and interact with passing laser pulses. Dissociation of the trapped ions occurs after photoexcitation, where the MS detects the resulting fragment and parent ion intensities, which are finally converted to specific or total fragment ion yield and plotted against the laser wavelength to give the UVPD spectrum.

While UVPD spectra are often compared directly with UV/Vis absorption spectra in solution, the interpretation is not always straightforward. The dissociation yield in UVPD spectroscopy primarily reflects the absorption characteristics of the molecule, but additional processes, such as energy redistribution and fragmentation dynamics, can influence the spectral shape. One challenge in UVPD action spectroscopy is that in the long-wavelength region, fragmentation often becomes inefficient due to the decreasing photon energy, meaning that single-photon excitation is sometimes insufficient to induce dissociation. As a result, spectral features in this region may be less pronounced or absent, making interpretation more complex. Additionally, helium buffer gas in the ion trap can lead to collisional quenching of the excited state, which may suppress photodissociation to some extent, preventing a 100% yield.[180-182]

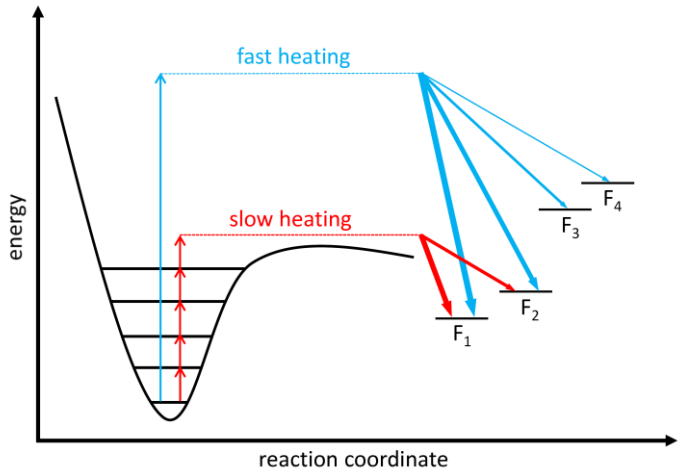

Figure 2.32 Illustration of the molecule excitation processes induced by UV/Vis PD (blue) and CID/IRMPD (red) and resulting fragments upon dissociation. The relative fragment ion intensities are depicted by the boldness of the arrows.[133]

In contrast to CID or IRMPD, where excitation occurs as a slow heating process,[183-184] UV/Vis excitation often leads to a fast heating process, where a large amount of energy (typically 3-6 eV) is instantaneously transferred into the molecule by absorption of a single photon. In the former process via CID or IRMPD, energy is slowly introduced into the molecule through collisions or IR photon absorption, respectively, leaving time for the excited molecules to distribute the energy acquired among the various degrees of freedom and thus rearrange and structurally adopt in order to explore the energetically lowest fragmentation pathways. Therefore, resulting fragmentation may differ between UVPD, CID and IRMPD (Figure 2.32, Figure 2.33). However, it should be noted that also after UV/Vis photoexcitation internal conversion (IC) often accompanied or followed by intramolecular vibrational energy redistribution (IVR) lead to dissociation processes similar to the slow heating scheme of CID and IRMPD.

UV-PD spectroscopy involves electronic transitions coupled with vibrational excitation of chromophores. The strength of these transitions, indicated by the photon absorption cross section (σ_{abs}), varies with photon energy ($E_{h\upsilon}$), i.e., excitation wavelength. To reconstruct the gas phase absorption spectrum from photofragment mass spectra, one assumes a single-photon excitation process and a linear correspondence between photon absorption (σ_{abs}) and the experimentally relevant dissociation cross section (σ_{diss}). This assumption requires several preconditions to be fulfilled.

First, the energy imparted by photon absorption must trigger dissociation within the experiment's timeframe (tens/hundreds of milliseconds = ion storage time). To ensure dissociation occurs efficiently, the photon energy ($E_{h\upsilon}$) must exceed the activation energy (E_A) of the lowest energy fragmentation pathway.[185] Second, the electronic states involved in the dissociation, strongly influence the fragmentation pathways and are closely tied to possible dynamic energy conversion processes (IVR, IC, ISC) (Figure 2.33 a). This leads to the fact that the dissociation yield of individual fragment ions can also provide additional insights beyond the total fragment yield (TFY).[186] While the overall dissociation yield generally correlates with absorption cross-sections, individual fragment channels may exhibit different spectral dependencies. This is particularly relevant in multinuclear transition metal complexes, where

multiple electronic and vibrational states are accessible. For example, at higher photon energies (shorter wavelengths), new fragmentation channels may open, resulting in an increase in specific fragment yields. Conversely, certain fragments may only form when a threshold excitation energy is reached, leading to distinct fragmentation patterns across different spectral regions. Caroline Dessent's work on UVPD fragmentation patterns has shown that such fragment-specific trends can provide insights into electronic state couplings and energy barriers,[187-190] although precise assignments remain challenging due to the unknown dissociation barriers, especially in larger systems.

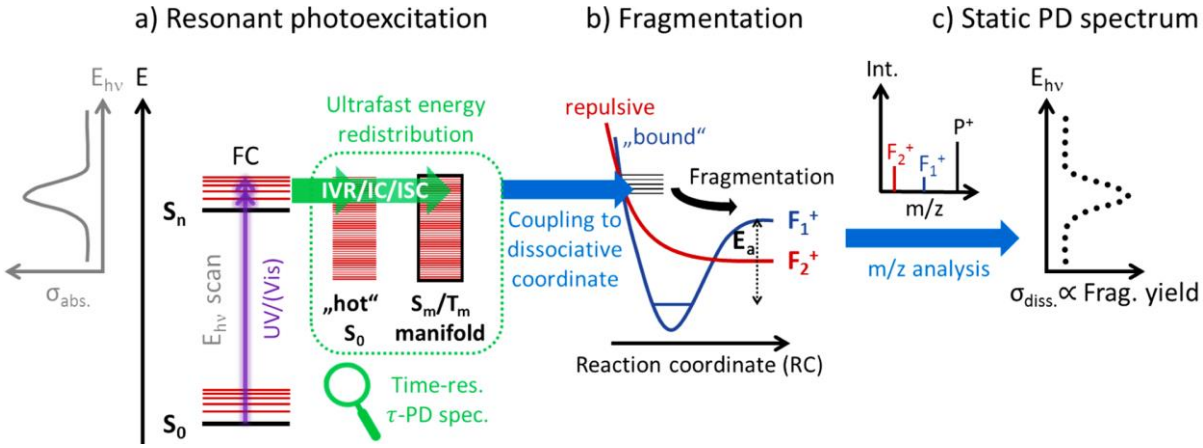

Figure 2.33 "Schematic representation of the correlation between resonant single-photon absorption (gas phase absorption spectrum, grey line) and photodissociation action (PD action spectrum, black dots) as a function of photon energy ($E_{h\nu}$). a) Schematic energy diagram corresponding to UV/(Vis) photoexcitation of gaseous precursor ions from their electronic singlet ground state (S_0) into S_n (n≥1) excited states, and ensuing dynamical processes within the excited-state manifold (FC: Franck-Condon state, S_m/T_m: excited singlet/triplet states, n≥m). b) Exemplified potential curves along a dissociative reaction coordinate (RC), distinguishing between a repulsive and bound character of respective fragmenting states (vibrationally excited S_n, S_0, S_m/T_m states). c) Illustrated PD action spectrum ($E_{h\nu}$ versus dissociation cross section σ_{diss})."[165]

Furthermore, as the excitation wavelength increases (lower photon energy), dissociation via a single-photon process may become less efficient or even impossible if the photon energy falls below the dissociation threshold. This explains why UVPD spectra often show lower signal intensity in the long-wavelength region, where multiphoton processes would be required to induce fragmentation. At shorter wavelengths (higher photon energy), additional fragmentation pathways may become accessible, as electronic excitation to higher-lying states can lead to increased internal energy and subsequent dissociation. Fragment-specific UVPD spectra can help identify such effects, as certain fragments may only appear above

specific excitation thresholds. However, precise assignments remain challenging, as dissociation barriers for larger molecules are often not well-defined.

The primary excited state plays a decisive role for the type of the dissociation process (Figure 2.34). Direct dissociation occurs rapidly on a short time scale (down to femtoseconds), following photoexcitation without energy conversion processes or coupling to internal degrees of freedom (Figure 2.34 a). This mechanism is prevalent when the excited state potential energy surface exhibits a "repulsive" nature, indicating minimal barriers to dissociation.[191] Conversely, dissociation from a bound excited state, known as a "pre-dissociative" state,[192] occurs when the initial vibrational energy along the reaction coordinate surpasses a threshold activation energy (E_A). In this scenario, dissociation proceeds from a bound state with a small dissociation barrier (Figure 2.34 b).

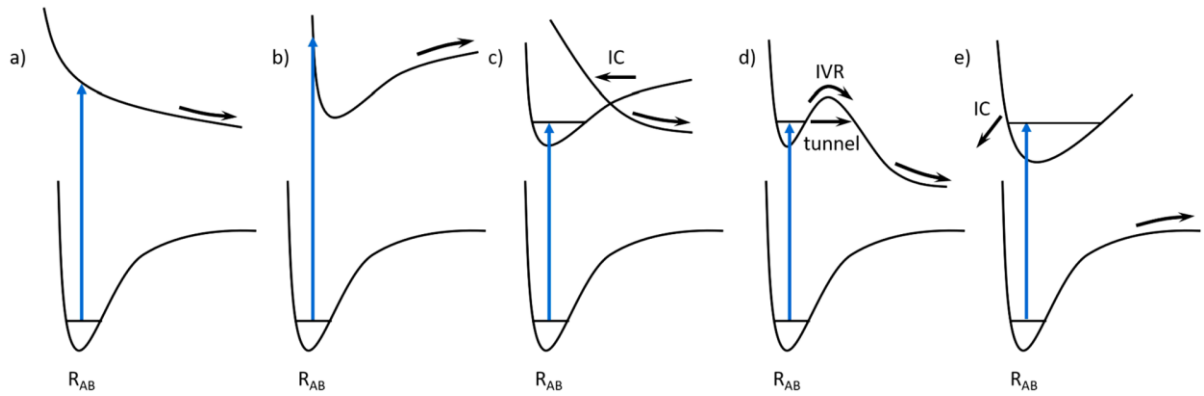

Figure 2.34 Dissociation processes upon UV/Vis photon excitation. Direct dissociation: a) excitation onto a repulsive quantum state, leading to a direct dissociation. b) excitation onto a bond state above dissociation threshold, leading to molecular fragmentation. Indirect dissociation: c) Population of a further electronic state of repulsive character by nonradiative transition (IC), upon photon excitation of a bound state, shows an electronic predissociation. d) Excitation onto a state with a barrier, passable by tunneling or IVR, shows vibrational predissociation. Predissociation: e) Dissociation occurs from a highly vibrationally excited state of the electronic ground state populated by the decay of the initial excited state through IC or fluorescence.[193]

Indirect dissociation is preceded by dynamic processes (IVR, IC, ISC) resulting from overcoming potential barriers or other dynamical constraints (Figure 2.34 c-e). Finally, the fragmentation occurs either from a hot vibrationally excited ground state or a vibronically excited state, causing a delayed fragmentation in reference to the direct dissociation. Consequently, the fragmentation rate for the respective channel, influencing the intensities of occurring fragment ion signals, is determined by the coupling of the excited state to the

ground state, which dictates the internal energy stored in specific internal degrees of freedom. The coupling between states and energy redistribution directly influences the delay in fragmentation (fs-ms)[194] and the extend of this delay is dependent upon the given system. Therefore, e.g., multinuclear transition metal complexes with their different state densities, providing a multitude of electronic states, are targets of high interest and at the same time appropriate candidates for transient photodissociation under such conditions.[195]

Additionally, to the above discussed photodissociation mechanism, the absorption of a second photon may occur. This comes into play if the internal energy after photoexcitation and subsequent IC does not exceed the dissociation barrier[196] and is provoked by high laser pulse energy and/or accidentally large excited state cross sections. However, this scenario is less probable since the cross sections (and in particular Franck-Condon factors) are typically much smaller for non-resonant or two-photon transitions. Within UV/Vis photodissociation, multi-photon processes can be uncovered by measuring the intensity of the fragment ion signals as a function of the laser pulse energy and thus checking for a possible non-linear dependence.

Upon photodissociation, three major fragmentation pathways could be distinguished, depending on the charge state of the precursor ions[197-198]:

a) Electron Detachment (ED) or photodetachment, where an electron is cleaved out of a negatively multi-charged system.[187]

$$PI^{n-} + h\upsilon \longrightarrow F^{(n-1)-} + e^{-} \quad ; n \geq 1 \tag{10}$$

b) Ionic Fragmentation (IF), where photodissociation of a multi-charged system leads to charged fragments and inter alia into lower charged fragments.[199]

$$PI^{n\pm} + h\upsilon \longrightarrow F_1^{m\pm} + F_2^{(n-m)\pm} \quad ; n \geq 2; n > m \tag{11}$$

c) Neutral Loss (NL), where a (multi-)charged system exhibits the loss of an (often small and stable) neutral molecular unit under conservation of charge.

$$PI^{n\pm} + h\upsilon \longrightarrow F^{n\pm} + N \quad ; n \geq 1 \tag{12}$$

The consequence of photodissociation is encapsulated in the total fragment yield (*TFY*) as a function of wavelength:

$$TFY(\lambda) = \frac{\sum F_i}{\sum F_i + PI} \tag{13}$$

where *PI* and F_i are the integrated mass peak intensities of the precursor ion and the ionic fragment species i recorded subsequent to irradiation.

Normalizing *TFY* by the number of photons per laser pulse (N_λ) reconstructs eventually the gas-phase spectra as it accounts for the wavelength-dependent photon energies at constantly held laser pulse energy.

$$N_\lambda = \frac{E_{pulse} \cdot \lambda}{h \cdot c} \tag{14}$$

E_{pulse}: laser pulse energy; h: Planck's quantum of action, c: speed of light; λ: laser wavelength

Hereby, E_{pulse} was generally set at 2 µJ, and adjusted when needed for reducing possible multiphoton absorption processes.

Additionally, when measuring UVPD spectra with the Wyvern system, scaling factors for the *TFY* intensities had to be used in order to compare the TOPAS-C and EKSPLA given wavelength ranges (Table 2.2, Table 2.3).

2.5.2 Transient Photodissociation (τ-PD)

Extending the UVPD method by a pump-probe scheme enables time-resolved detection, i.e., the investigation of the evolution of electronically excited target states. Upon excitation by the pump pulse, molecules tend to energetically relax towards lower energy states, as discussed above. This relaxation process is crucial as it influences the fragmentation pathways and dynamics that we aim to elucidate through our experimental setup. The fragmentation yield is monitored as a function of the time delay between the resonant pump and non-resonant probe pulse by recording fragmentation mass spectra with the QIT.

The way of ultrafast femtosecond spectroscopy was paved by the pioneering work of A. H. Zewail, for which he was granted the Nobel prize in 1999.[200] In the then emerging field of femtochemistry the research started by the photodissociation of neutral compounds such as ICN, which were monitored on a ps-fs scale using, among other schemes, also multiphoton photoionization-based detection.[10] Within the pump-probe scheme, the initial laser pulse, the pump pulse, excites the compound to a higher electronic state. Subsequently, the excited compound is then ionized by absorption of the second laser pulse, the probe pulse. While this photoionization approach is frequently employed in general in gas phase pump-probe spectroscopy, its application to cationic species is generally limited due to the high (second) ionization potentials of cations, which pose significant challenges. Time-resolved detection using a change in fragmentation efficiency for consequence spectroscopy, esp. on larger molecular systems introduced into the gas phase by an electrospray source, effectively overcomes this challenge and represents the method employed in this work. This technique was realized by Jouvet *et al.* on protonated tryptamine and protonated tryptophan.[201-202] Furthermore, this concept was applied for use in commercial ion trap mass spectrometers by Weinkauf *et al*.[57,132]

In this technique the pump pulse excites the respective ions by a resonant excitation wavelength into an electronically excited state, e.g., $S_0 \rightarrow S_1$. By the subsequent probe multi-photon absorption, the target ions are further excited, most probably into higher lying electronic states ($S_1 \rightarrow S_n$), inducing faster and more efficient dissociation, which is observed

by the increase in fragmentation yield at time delay zero. The probe pulse is set at a non-resonant wavelength commonly in the NIR range (ca. 1200 nm), avoiding "probe-pump" or "probe-only" fragmentation signal. Generally, upon increase of the time delay, the signal decreases (multi-)exponentially, indicating that the probe pulse produces fewer additional fragments with increasing delay. This observed decay reflects the ultrafast dynamics of the primary vibronically excited state (Franck-Condon state), e.g., by ISC into the triplet manifold and dynamics of consecutive subsequent processes, like IVR or IC to other electronic states.[203]

In the case of ISC it appears that the probe process for $T_1 \rightarrow T_m$ transitions is often accompanied by lower cross sections and fragmentation efficiencies compared to its counterpart in the singlet moiety (Figure 2.35), which could be rationalized by a combination of the "dilution" of vibrational states by the coupling to an energetically lower electronic state and the vibrational propensity rule (as applied in MATI and R2PI spectroscopy, e.g.,[204-206] and references therein) governing the number and type of higher vibronic states reachable by the probe pulse (see Figure 2.35, fragments F_2, F_3). However, in some rare molecular cases also an increase in ion yield as a function of time delay was observed (see Jouvet "Tryptophan"[202]; S. Kruppa "$Au_2(dcpm)_2$"[207], M. Schmitt "$Cu_2(dcpm)_2$"). In such instances, the fragmentation signal increases rather than decreases, suggesting that the probe pulse interacts with long-lived excited states or promotes transitions to states with higher fragmentation efficiency. This behavior contrasts with the typical decay trend and indicates that alternative relaxation pathways or secondary excitation processes may be at play.

Another relevant process influencing the observed pump-probe signal is the presence of quenching channels due to collisions with helium in the ion trap.[180-182] Excited molecules can be deactivated through these collisions, which does not necessarily occur from an electronically excited state. Instead, this process leads to a general cooling of the excited molecules. This directly competes with the absorption of the second color, as helium induces an energy loss that the two-color signal counteracts. If this quenching process did not exist, one would expect that once a photon is absorbed, fragmentation would inevitably occur.

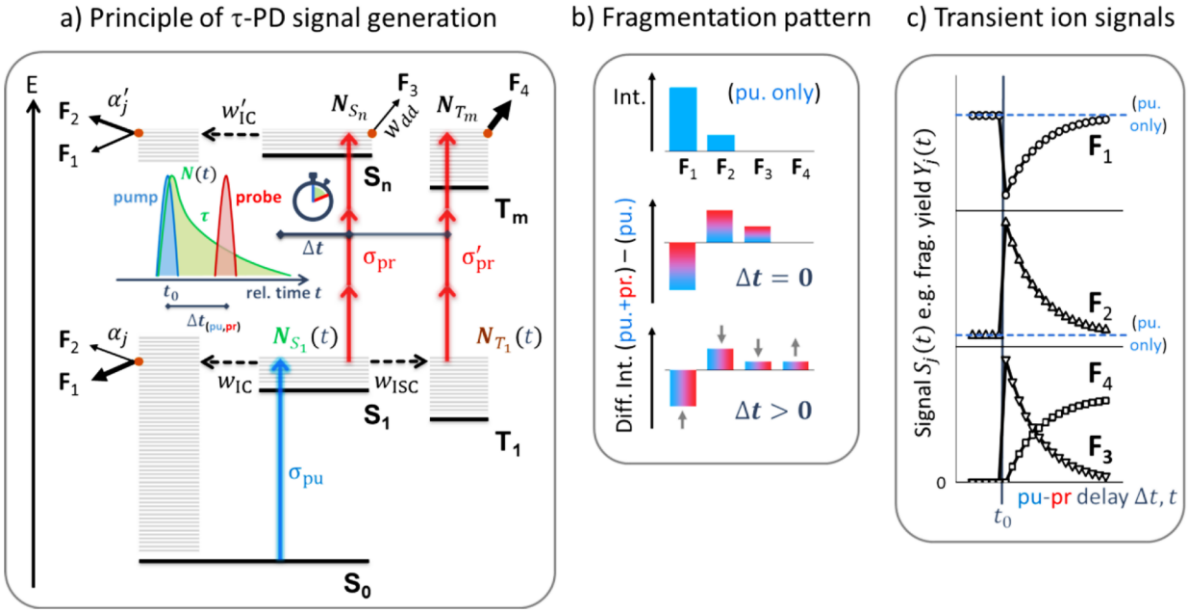

Figure 2.35 "a) Hypothetic τ-PD detection scheme and Jabłoński diagram exemplified for closed-shell coinage metal complex in the gas phase. An ensemble of precursor ions is resonantly excited from electronic ground state ($S_0 \rightarrow S_1$) via pump single-photon absorption with cross section σ_{pu}, generating the transient excited-state population $N_{S1}(t)$. Branching probabilities for nonradiative deactivation processes are denoted by w_x (x= IC, ISC, dd: direct dissociation). Energetically higher singlet/triplet excited states (S_n, T_m; n, m>1) are accessed via excited-state probe (multi)photon absorption (σ_{pr}, $\sigma_{pr'}$), resulting in an increase in the internal energy of the ions. This is accompanied with a change in fragmentation efficiency of photofragments $F_{1\text{-}4}$ through alterations in the population of fragmenting states (orange dots) as well as dissociation rate constants (k_j) and therefore branching ratios ($\alpha_{j=1,2} = k_j/\sum_j k_j$, $\alpha_3 = w_{dd} = k_3/(k_3+k_{IC'})$, $\alpha_4 = 1$) as indicated by thickness of solid black arrows. Inset: pump-probe scheme highlighting the time dependence of excited state population $N(t)$ (t_0: time zero, $\Delta t_{(pu,pr)}$: time delay between pump and probe pulses, sketch of stop clock. b) Top: Schematic fragmentation pattern (intensity distribution of fragment ion signals) obtained following „pump-only" excitation. Bottom: difference plots indicating the respective change in fragment intensity following „pump-probe" absorption at $\Delta t \geq 0$. c) Schematic time evolution of fragment-specific signals (e.g. fragment yield Y_j) as a function of Δt."[165]

However, the existence of a two-color signal demonstrates that molecules can survive despite initial excitation if they do not accumulate sufficient energy for fragmentation or if they dissipate this energy through collisions with helium before fragmenting. The dependence on helium pressure was not specifically investigated in this work, but it is well known that, for example, at Free-Electron Laser for Infrared eXperiments (FELIX) at the Radboud University in Nijmegen[208], fragmentation yield can be intentionally increased by reducing helium pressure. Lower helium pressure results in fewer collisions, leading to the formation of more fragments—an established approach to enhancing PD efficiency. Conversely, increasing helium pressure leads to more effective cooling of the ions, reducing overall fragmentation but improving the signal-to-noise ratio.

The choice of wavelength in the NIR range for the probe pulse is justified by the high density of vibronic states in molecular systems, in particular in transition metal complexes, at the total internal energy after irradiation ($h\nu_{pump}$ + $n \cdot h\nu_{probe}$). To ensure efficient multi-photon absorption, the probe pulse energy must be significantly higher than that of the pump pulse, compensating for the inherently low cross-sections of multiphoton processes.[209-210] Finally, the pump-probe induced dissociation may reveal different or new dissociation pathways compared to the pump-only induced dissociation (see Figure 2.35 , fragment F_4), also based on different energy distribution processes as discussed in chapter 2.5.1. Figure 2.35 gives a detailed illustration of the possibly occurring processes.

The temporal delay between the pump and probe pulses was controlled using a mechanical delay-stage (Physik Instrumente, PI) equipped with a retroreflector. The time delay ranges with typical time steps of µm to 0.4 mm from 2 ps up to 1.6 ns and the velocities were held between 0.5 µm/s to 0.4 mm/s, respectively. To enhance signal fidelity, several scans were averaged, and the resulting data were fitted using OriginLab 2019G with a sum of exponentials (eq. (15), (16)). The inserted error function (erf) resulted from a convolution with the instrument response function (IRF), accounting for the finite laser pulse width.

$$Y(t) = Y_0 + \sum_{i=1}^{n} \left[A_i e^{0.5\left(\frac{w}{\tau_i}\right)^2 - \frac{t-t_0}{\tau_i}} \cdot 0.5 \left(erf\left(\frac{(t-t_0)/w - w/\tau_i}{\sqrt{2}} \right) + 1 \right) \right] \quad (15)$$

t: time, Y_0: offset, A_i: amplitude of component i, τ_i: lifetime of component i, t_0: time zero, w: fwhm/$\left(2\sqrt{2ln2}\right)$ of Gaussian representing the IRF.

In case of the observation of wave packets eq. (16) may be adjusted with an additional damped oscillating term:

$$Y(t) = A_{\mathrm{osc}} \cdot sin^{\frac{2\pi \cdot t}{t_{osc}} + \varphi} \cdot e^{0.5\left(\frac{w}{\tau_d}\right)^2 - \frac{t-t_0}{\tau_d}} \cdot 0.5 \left(erf\left(\frac{(t-t_0)/w - w/\tau_d}{\sqrt{2}} \right) + 1 \right) \quad (16)$$

A_{osc}: oscillation associated amplitude, t_{osc}: oscillation period, φ: oscillation phase, τ_d: decoherence time.

2.6 Computational Methods

In the ever-evolving landscape of scientific research, computational quantum mechanical methods have emerged as indispensable tools for exploring complex phenomena, unraveling fundamental principles, and accelerating innovation across diverse disciplines. From elucidating the behavior of subatomic particles using quantum mechanics to simulating macroscopic systems like ecosystems through classical models,[211-213] computational techniques offer a powerful means to study systems that may be impractical or impossible to analyze solely through experimental methods.

Within this thesis, Density Functional Theory (DFT) and Time-Dependent Density Functional Theory (TD-DFT) have been the methods of choice for supporting and validating the explored experimental data. These methods offer a relatively low computational effort while still providing accurate predictions of electronic properties and molecular structures, making them widely used approaches in theoretical chemistry and physics.[214] All calculations, including geometry optimization and excited state calculations, were performed using the Gaussian 09/16 program package[215].

2.6.1 Density Functional Theory (DFT)

Density functional theory (DFT) stands as a computational quantum mechanics tool extensively employed across physics, chemistry, and materials science for studying the electronic structure of many-body systems. It provides a powerful framework for understanding the electronic structure of molecules and materials and predicting a broad range of properties, from molecular geometries to reaction mechanisms and electronic properties.[216] This method leverages functionals based on the spatially dependent electron density to determine the properties of many-electron systems.[217]

The history of DFT is rooted in the Thomas-Fermi model (1927)[218-219], which treated the atomic shell as a gas of electrons bound by the electrostatic field of the atomic nucleus and assumed the state of lowest possible energy, accounting for the shielding caused by the electron cloud. Consequently, all molecular properties lay within the electronic density, vital

for describing both kinetic and electrostatic energy distributions. : However, a challenge arose when considering the total energy of a molecule, as it often exceeded the sum of the energies of its individual atoms, complicating the accurate representation of chemical bonding within the DFT framework [220]

The total energy functional in the Thomas-Fermi model is defined as:

$$E_{TF} = T(\rho) + V_{ne}(\rho) + J(\rho) \tag{17}$$

$T(\rho)$ the kinetic energy of a free electron gas; ρ being the electronic charge density; $V_{ne}(\rho)$ the interaction energy of the electron gas; $J(\rho)$ coulombic energy resulting from the interaction of the electron gas

In 1930, the model was extended by Dirac, who approximated the exchange energy.[221] It is worth noting that Thomas and Fermi did not introduce the Schrödinger equation (1926)[222] in their theory. Kohn and Hohenberg included the Schrödinger equation in their approach, resulting in major advancements in DFT theory,[223] formulating the following theorems:

1) The electron-density $\rho(r)$ is characteristically defined for a given many-electron system and corresponds to an external potential $\vartheta(r)$,
2) The variational principle can be applied to determine the ground state energy.

Building upon this, Kohn and Sham (1965) introduced a non-interacting reference system, stating that the density of an N-electron interacting system could be computed equivalently to a system of non-interacting fermions.[224] This formulation significantly simplified the energy minimization problem using the variational principle. More crucial than solving the equation explicitly is recognizing that the exchange-correlation term E_{XS} remains unknown.

$$E_{KS} = T(\rho) + \int \rho(\vec{r})[\vartheta_{ext}(\vec{r}) + 0.5\varphi(\vec{r})] + E_{XC}(\rho)\, dr \tag{18}$$

$T(\rho)$: kinetic energy functional of the molecule; $\vartheta_{ext}(\vec{r})$ an external potential; $\varphi(\vec{r})$: Coulomb potential of the nuclei; $E_{XC}(\rho)$: exchange correlation functional

To compute the electron density, DFT requires solving a set of N orthonormal one-electron Schrödinger equations, rather than dealing with the full N-particle system:

$$\left(-\frac{\hbar^2}{2m}\nabla^2 + \vartheta_{eff}(\vec{r})\right)\Phi_i(\vec{r}) = \varepsilon_i\Phi_i(\vec{r}) \tag{19}$$

$\Phi_i(\vec{r})$: Kohn-Sham orbital i; $\vartheta_{eff}(\vec{r})$: effective potential; ε_i: energy eigenvalue of the corresponding orbital Φ_i.

The energy is iteratively minimized to achieve self-consistency, akin to the Hartree-Fock method, whereby the computational effort required for DFT is comparable to that of the HF method. The electron density of the whole many-electron system is obtained by:

$$\rho(\vec{r}) = \sum_{i}^{N}|\Phi_i(\vec{r})|^2 \tag{20}$$

where the effective potential of a single-particle is defined as:

$$\vartheta_{eff}(\vec{r}) = \vartheta_{ext}(\vec{r}) + \int\frac{\rho(\vec{r}')}{|r-r'|}d^3r' + \vartheta_{XC}(\vec{r}) \tag{21}$$

$\vartheta_{XC}(\vec{r})$: exchange-correlation potential

The middle term, known as the Hartree term, characterizes the electron-electron Coulomb repulsion, while $\vartheta_{XC}(\vec{r})$ addresses the interactions among multiple particles. Emphasizing the significance of the Kohn-Sham formalism, $\vartheta_{XC}(\vec{r})$ represents the transition from a many-electronsystem with non-interacting particles to a many-electronsystem with multiple-particle interaction. As for the exchange and correlation, the exact functionals are unknown, and the main objective of DFT in this state is approximating $\vartheta_{XC}(\vec{r})$. Several models have been proposed.[225] Kohn and Sham made the first approximation, namely the local density approximation,[224] treating the exchange-correlation energy density (ε_{XC}) of an inhomogeneous system at a given spatial point as equivalent to that of the uniform electron gas (UEG) with the same density.

Given that the exact form of E_{XC} is unknown, DFT focuses on approximating the exchange-correlation functional. The first and simplest approach was the Local Density Approximation (LDA), where the exchange-correlation energy density ε_{XC} at a given point in space is assumed to be the same as that of a homogeneous electron gas (UEG) with the same density:

$$E_{XC}^{LDA}(\rho) = \int \varepsilon_{XC}^{UEG}(\rho(\vec{r}))dr \tag{22}$$

In the spin-dependent version known as the local-spin-density approximation (LSDA), the exchange-correlation functional incorporates spin densities $\rho_{\uparrow}(\vec{r})$ and $\rho_{\downarrow}(\vec{r})$, representing the spin-up and spin-down components, respectively, of the UEG.[226]

$$E_{XC}^{LSDA}(\rho_{\uparrow}, \rho_{\downarrow}) = \int \varepsilon_{XC}^{UEG}(\rho_{\uparrow}(\vec{r}), \rho_{\downarrow}(\vec{r}))dr \tag{23}$$

For spin-unpolarized systems, the spin-independent LDA is retrieved as a special case of the spin-dependent version. While the L(S)DA model satisfactory results with accuracy for systems with constant electron density, its accuracy diminishes when the electron density varies. Upon LDA, the generalized-gradient approximations (GGA) deliver improvement by incorporating information about the gradients of the electron density, allowing for a more accurate description of systems with varying electron densities. It is derived by expanding the exchange-correlation energy in terms of the gradients of the electron density.

$$E_{XC}^{GGA}(\rho_{\uparrow}, \rho_{\downarrow}) = \int \varepsilon_{XC}^{GGA}(\rho_{\uparrow}(\vec{r}), \rho_{\downarrow}(\vec{r}), \nabla\rho_{\uparrow}(\vec{r}), \nabla\rho_{\downarrow}(\vec{r}))dr \tag{24}$$

The GGA approach was developed to address the deficiencies of its precursor, the gradient-expansion approximation (GEA).[224] A combination of LDA and GGA, released by hybrid functionals[227] such as B3LYP,[228-231] delivers very satisfying results and has become popular[232-233].

2.6.2 Time-Dependent Density Functional Theory (TD-DFT)

Time-Dependent Density Functional Theory (TD-DFT)[234] provides a powerful method for studying electronic excited states in molecules and solids, and as such, it has found broad application in various areas of theoretical and computational chemistry and physics.[235-236] This includes simulations of absorption and emission lines in spectra as well as examining reaction mechanisms and vibrational excitations.[237]

TD-DFT is an extension of DFT that addresses the spatial distribution of electron density as well as its temporal evolution. While standard DFT describes the ground-state electronic structure as a function of electron density, TD-DFT generalizes this to time-dependent electron densities. However, in practical implementations, the explicit time evolution is often circumvented using linear response theory, leading to the widely used Casida equation.[238] This approach allows for the efficient calculation of electronic excitation energies and transition dipole moments, which are essential for predicting spectroscopic properties.

Based on the Runge-Gross theorem, a time dependency of the external potential $\vartheta_{ext}(\vec{r}, t)$ is introduced in relation to the electron density of a system. The theorem states that all observables of an interacting many-body system evolving from an initial state ψ_o can be extracted from the time-dependent electron density $n(\vec{r}, t)$ of a non-interacting (Kohn-Sham) system of fermions starting in an initial state Φ_0.

$$n(\vec{r}, t) \longleftrightarrow \vartheta_{ext}(\vec{r}, t) \tag{25}$$

The formalism of TD-DFT is analogous to DFT and is simply obtained by introducing the time domain in equation (18), whereby the term of the exchange-correlation is additionally treated as a functional of the true initial state ψ_o and the Kohn-Sham initial state Φ_0. However, it should be noted that the exchange-correlation term requires approximation approaches, as the exact forms for parts of the kinetic energy and exchange-correlation functionals are not known, making DFT inherently an approximate method.[239] The Runge-Gross theorem thus provides a formal definition of TD-DFT rather than a specific computational procedure.

The exchange-correlation potential in TD-DFT depends not only on the electron density but also on the system's history, making accurate approximations challenging. In practice, most calculations rely on the adiabatic approximation, which neglects memory effects and assumes an instantaneous functional dependence on the density.

By employing the variational principle within the framework of linear response theory, TD-DFT provides a computationally efficient method for determining excited-state properties while maintaining a cost similar to that of ground-state DFT. Despite its approximate nature, it has become a cornerstone for studying electronic excitations in molecules and materials.

2.7 Measurement Protocols and Data Processing

Throughout this thesis, a wide scope of data acquisition methods has been employed, each requiring specific measurement protocols and data processing techniques. The research employs various data acquisition methods, including:

- General mass spectrometry
- Electron-transfer-dissociation mass spectrometry
- Collision-induced-dissociation mass spectrometry
- UV/Vis photodissociation (point-by-point scan, continuous scan)
- Transient photodissociation spectroscopy (up to 2 ns)
- Transient photodissociation spectroscopy (up to 500 µs)
- Energy-dependent photodissociation spectroscopy
- (TD-)DFT calculations
- UV/Vis absorption spectroscopy in solution

For all the **ESI-MS** investigations, the samples, typically solid compounds, were solved in ESI compatible solvents for preparing stock solutions of 10^{-4} M, which were then diluted to 10^{-6} M solutions. Acetonitrile (ACN) and methanol (MeOH) were the most suited solvents, as they offered good sprayability for the ESI source and good solvation for the investigated samples. To test the disintegration of the analyte molecules in solution, the samples were also solved in additional solvents like dichloromethane (DCM) and tetrahydrofuran (THF), where THF should be used with caution due to THF's potential to swell PEEK material used for the capillary supply lines.

Experimental procedures involve loading the sample solution into a 500 µL Hamilton syringe and precisely infusing it at a controlled flow rate of 120 µL/h using a syringe pump. Optimization of parameters such as nebulizer pressure, nitrogen gas flow, and needle potential are essential to ensure stable ion signals. Typically, the nebulizer pressure is set at 4 psi (~0.28 bar), the nitrogen dry gas flow at 4.5 L/min at 180°C, and the needle potential at 4.5 kV. However, these parameters can be adjusted as needed to achieve stable

and high ion signals. Additionally, a software-controlled parameter known as the "target mass" is set to the m/z value of the analyte ion, optimizing resolution in that specific region of m/z. For mass spectrometric analysis, the instrument is typically set to "enhanced resolution" mode for CID, ETD, or mass spectra, achieving a scan rate of 8100 (m/z)/s with a mass resolution of 0.2 fwhm/(m/z). In photofragmentation experiments, the instrument operates in "ultrascan" mode, achieving a higher scan rate of 32500 (m/z)/s with a mass resolution of 0.4 fwhm/(m/z).

Regarding **ETD** parameters, the "ICC target" can be adjusted within the range of 50k to 500k, with higher values recommended for analytes with higher charge states. The ETD reaction time is determined by parameters such as "CutOff" and "Time," with longer times preferred for analytes with lower charge states. ETD/PTR can only be exposed to trapped ions, while the CID function is excluded.

CID breakdown curves are measurements conducted with the aid of a script in a .csv document that controls various parameters of the MS, including the stepwidth of the accelerating amplitude, the start and end values of amplitude, and the measuring time per sequence. The evaluation of the obtained data, as outlined in Chapter 2.1.4, was facilitated by "CalcCID," a Python-based script developed in-house by Philipp Weber[240]. "CalcCID" distinguishes itself by providing output in both time and lab voltage scales, requiring user input for the starting voltage and step size for the latter. This script manages the conversion of data exported from Bruker software obtained via segmentwise scans with increasing CID voltage, commonly used in acquiring CID spectra.

This method represents an improvement over the LabView-based in-house solution used before within our working group, reducing user input and significantly accelerating data processing, thereby eliminating the need to reprocess data for each segment, which previously led to prolonged evaluation times.

Static UVPD spectra can be acquired using two methods depending on the utilized laser systems. Both methods rely on photofragmentation, resulting in a fragment ion signal obtained from the precursor ions as a function of laser wavelength.

UVPD (fs) The Wyvern fs laser system enables a point-by-point scan, maintaining constant pulse energy at each wavelength. Wavelength switching is controlled by WinTOPAS v3.3.51, compatible with TOPAS, T7, and T6. Output wavelengths from the TOPAS are verified using an AvaSpec USB high-resolution fiber optics spectrometer (ULS3648) from Avantes, and adjusted if needed. Pulse energy variations are monitored using a Vega energy meter equipped with a pyroelectric sensor from Ophir. Pulse energy is adjusted using a circular variable neutral density filter with a diameter of 10 cm and an optical density (OD) of up to 2. Data points are selected with a 3 nm equidistant step size. At each point, mass spectra are recorded for 1 minute, with resolution set to "ultrascan" mode, averaging 7-10 cycles for a single mass spectrum. The ICC mode is set at 100k counts, and the fragmentation time at 100 ms. With a repetition rate of the amplifier at 982 Hz, approximately 100 laser pulses per ion cloud are obtained.

All mass spectrometric parameters are set using Bruker software trapControl 7.0. Parent and fragment ion intensities are exported as chromatograms from the mass spectra within DataAnalysis 4.2, generating a .txt file per wavelength using an in-house developed VisualBasic script,[241] modified by Philipp Weber to accelerate processing. The processed mass spectrometric data are converted into plottable data using the Python-based "calcmeanUVPD",[240] calculating the relative yields of each file corresponding to a wavelength. All acquired mass spectra are averaged, and the relative yield of different mass channels and the total fragment yield (TFY) are calculated according to the specified equations, as well as normalized by the numerical wavelength. Finally, the results are summarized into a single .txt file, importable into OriginLab 2019-2023 for final plotting.

UVPD (ns) Static UVPD spectra obtained through continuous scanning are achieved using the EKSPLA ns laser system in conjunction with the Lab-Talk-based NEWT program developed by M.Sc. Marcel Schmitt, aligned with trapControl to control the .csv file. The spectral resolution

and measurement time are customizable based on preferences. Users can opt for a fast scan over a broad spectral range, resulting in lower resolution, or a slow scan over a narrow spectral range, resulting in higher resolution. This approach marks a significant milestone in attaining high-resolution spectra, with the potential to achieve vibrational state resolution.[176] The step size can be selected as small as 0.01 nm, along with the recording time of mass spectra per point and the averaging.

A power curve of the chosen spectral range is either measured before or after UVPD measurement and is used to correct the obtained ion signal. The power curve is obtained using StarLab 3.40 software, connected with the Vega power meter. The intensities of the ion signals are processed within DataAnalysis using in-house methods like sumoversignals.m and segmentstorettime.m.[240] Subsequently, the data is further processed using the Python-based "calcNEWT" script, analogous to "calcCID," but considering the wavelength instead of the lab voltage.

Ultrafast τ-PD experiments are conducted using the Wyvern fs laser, with the TOPAS “T7” and “T6” generating the pump and probe pulses, respectively, and the mechanical delay stage (M-531.DD Heavy-Duty micropositioning stage) by PI. The time window is determined by input of the corresponding distance, step width, and step velocity of the delay stage, with a conversion factor from distance to time of 0.15 mm/ps. Step width and step velocity are always set equal to ensure smooth movement of the delay stage. These parameters are adjusted to result in a 10-minute scan. When determining the position of the delay for t_0, the start position is selected by taking 10% of the time window distance in the negative direction, introducing an offset in the transient curve form.

Mass spectrometric parameters are configured in “ultrascan mode,” with an averaging of the mass spectra ranging from 7 to 10, and a measurement time of 10 minutes. The initiation of the delay stage run and the start of the mass spectrometric measurement are manually initiated simultaneously. In τ-PD measurement, the ICC option of the MS is turned off, as the accumulation time setting ensures a consistent ion count throughout the measurement. The initial processing of the mass spectrometric data occurs within DataAnalysis using the

advanced VisualBasic script. Subsequently, the "calcdynamic" script[240] is utilized to convert the measured intensities, including the fragmentation channels and absolute time, into relative time delay and relative yield.

Finally, the resulting .txt-file is imported into OriginLab for plotting. To derive the time constant, the equation presented in Chapter 2.5.2 is utilized as the fitting function. In practice, determining the time zero can be challenging due to various factors, including the combination of pump-probe wavelengths, pump-probe cross-section in relation to the given precursor, and calibration of the delay stage. Therefore, achieving overlap of the pump-probe in the QIT and determining the time zero position is facilitated by measuring the multiphoton ionization of neutral furan (cf. Figure 2.36), which is introduced into the QIT through the vacuum line (refer to Chapter 2.1.7).

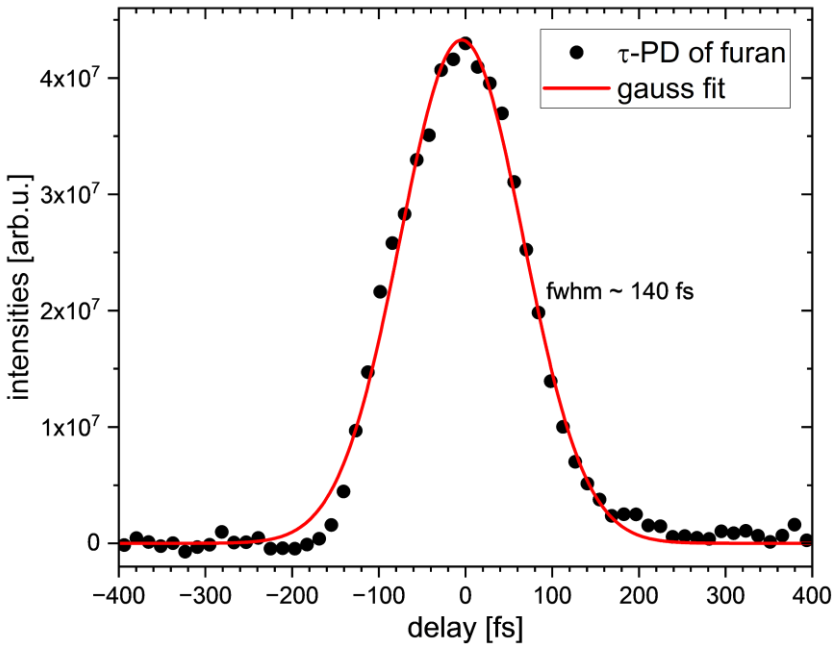

Figure 2.36 τ-PD of furan ionized by λ_{pump}= 350 nm and λ_{probe}= 1200 nm radiation, showing the cross-correlation signal, fitted to a Gaussian.

τ-PD EKSPLA τ-PD measurements for the time window up to 500 µs are performed using the EKSPLA ns laser system in conjunction with the Wyvern fs laser system, generating the pump and probe pulses, respectively. The temporal delay between the pump and the probe pulse is controlled electronically with sub-ns resolution by fast delay generators (DG645, Stanford Research Systems; refer to Chapter 2.5). Activation and control of the delay generators is accomplished through a custom LabView-based program developed by M.Sc. Marcel Schmitt, enabling two methods of time window settings: Either the step width or the duration of the complete measurements is set. By default, the time per delay step, which corresponds to the step velocity of the mechanical delay stage, is set at 1s and can be adjusted if necessary. The evaluation and analysis of the obtained nanosecond τ-PD mass spectra is performed similarly to those of the ultrafast τ-PD measurements, described above.

Laser pulse energy The measurement of the laser pulse energy dependence is conducted to assess an estimate of the number of photons required for fragmentation. Across a desired wavelength range, energy is incrementally increased while measuring the corresponding mass spectrometric fragment ion signal. The evaluation process parallels that of UVPD measurements with the Wyvern fs laser system, utilizing the calcmeanUVPD script, with the dependency on energy rather than wavelength. Subsequently, the resulting .txt file is imported into OriginLab, plotted, and fitted with a polynomial function $TFY = A \cdot E^n$, where 'n' represents an estimation of the number of photons needed for dissociation.[242]

Quantum chemical calculations Regarding theoretical computations, DFT and TD-DFT calculations were performed using the Gaussian program package (versions 09 and 16)[215], predominantly employing the hybrid functional B3LYP[228-229] in combination with cc-PVTZ basis set[243]. Effective core potentials (ECP) were employed for Ru (ECP28MDF)[244] and Au (ECP60MDF)[245] to minimize computational efforts. DFT geometry optimization was carried out to identify the structure of lowest energy, utilizing the sum of electronic and thermal energy corresponding to the internal energy (U) of the molecule at room temperature to determine the bond dissociation energy (BDE). Minimum structures were validated through

frequency calculation. To determine the BDE of compound A-B, the geometry of A, B, and A-B were optimized, yielding the BDE as follows:

$$BDE = U_{A-B} - U_A - U_B \quad (26)$$

On the TD-DFT level of theory, vertically transition energies were computed. GaussSum 3.0 was employed to extract the calculated absorption spectra, generating two text files: I) "UVSpectrum" containing the convoluted line spectra (1500-3000 cm^{-1} fwhm) and the oscillator strengths of the calculated singlet excited state; II) "UVData" containing the contribution of the molecular orbital (MO) corresponding to the transition states. To visualize the related MO, the checkpoint file (.chk) of the population analysis was converted to a formatted checkpoint file (.fchk) and then visualized with GaussView 5.0 utilizing computing clusters.

The calculations were conducted on the computing clusters of TU Kaiserslautern (now: RPTU Kaiserslautern-Landau), managed by Prof. Dr. C. van Wüllen and coworkers.

3. Publications and Submissions

3.1 Publication 1: Ultrafast Spectroscopy of Ru^{II} Polypyridine Complexes in Gas Phase and Liquid Phase: $[Ru(2,2'\text{-bipyridine})_2(\text{nicotinamide})_2]^{2+}$

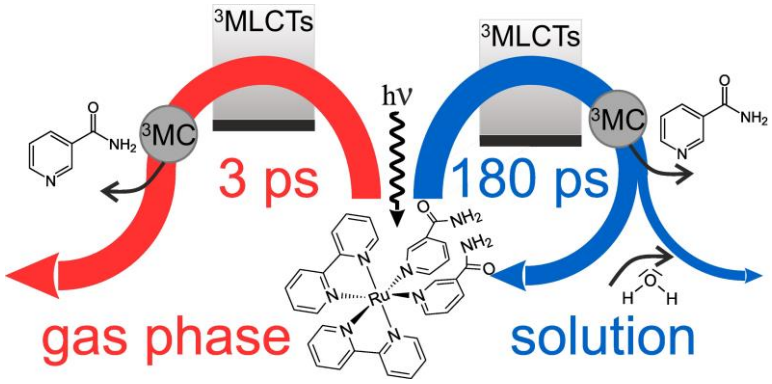

Preamble

R. G. E. Israil, L. Schüßler, P. Hütchen, W. R. Thiel, R. Diller, C. Riehn, *Physical Chemistry Chemical Physics*, **2023**, 25 (6), 4899-4914, https://doi.org/10.1039/D2CP03765C; Copyright © 2023 The Owner Societies, reproduced by permission of the *Physical Chemistry Chemical Physics* Owner Societies.

Contributions I have performed all measurements and data analysis related to gas-phase ion spectroscopy, including UV photodissociation (UVPD), time-resolved photodissociation (τ-PD), collision-induced dissociation (CID), and mass spectrometry (MS^2/MS^3), as well as theoretical calculations. The synthesis of the sample compound was carried out by Dr. Patrick Hütchen, while static and time-resolved spectroscopy experiments in the solution phase were conducted by Dr. Lars Schüssler. I analyzed and evaluated the results obtained from the above-mentioned methods, prepared them for discussion, and contributed them to the discussion section of the manuscript. The initial draft of the manuscript was co-written by Dr. Lars Schüßler and me, and further refined with valuable input from Prof. Dr. Rolf Diller and PD Dr. Christoph Riehn.

Synopsis Ruthenium polypyridine complexes are pivotal in photochemistry due to their broad field of applications, ranging from solar energy harvesting to biophotomedical therapeutics. Their photostability and reactivity depend heavily on the energetics and coupling of metal-to-ligand charge transfer (MLCT) and metal-centered (MC) electronically excited states, as well as their structural relaxation dynamics. This paper investigates the ultrafast photochemical and photophysical processes in ruthenium (Ru^{2+}) polypyridine complexes, specifically $[Ru(bipyridine)_2(nicotinamide)_2]^{2+}$ (**1**) and its monoaqua derivative $[Ru(bipyridine)_2(nicotinamide)(H_2O)]^{2+}$ (**2**). This work is the first to combine static and time-resolved UV photodissociation spectroscopy in the gas phase with transient absorption spectroscopy in solution, enabling a direct comparison of ligand dissociation and ground-state recovery mechanisms under solvent-free and solvated conditions. Quantum chemical methods complement experimental techniques to propose deactivation and reaction pathways and confirm the electronic and structural assignments of intermediate states.

In the gas phase, **1** undergoes ultrafast dissociation (sub-ps to few ps) via nicotinamide loss, forming a penta-coordinated intermediate (PCI), while **2** preferentially dissociates H_2O, as confirmed by mass spectrometry and theoretical calculations. The absence of solvent stabilization in the gas phase leads to an energetic upshift of the ^{3}MLCT states relative to the ^{3}MC states, resulting in faster dissociation dynamics and the absence of long-lived excited states. In solution, slower ground-state recovery (ca. 180 ps for **1** and 83 ps for **2**) and vibrational relaxation dominate, highlighting the critical role of solvent interactions in stabilizing charge-transfer states and modulating photochemical pathways.

The study assigns the spectral region above 550 nm to the ^{3}MC state, providing the first direct evidence of its involvement in the dissociation dynamics of these complexes. A revised kinetic model is proposed, emphasizing the equilibrium between ^{3}MLCT and ^{3}MC states in solution, which enables synchronous ground-state recovery and ligand dissociation. These findings bridge gas-phase and solution-phase studies, offering a comprehensive understanding of the photophysical and photochemical dynamics of Ru(II) polypyridine complexes.

.

Electronic Supporting Information (ESI) Further details on experimental methods and data, that support the findings of this study are available in the ESI accompanying this publication. I contributed to the preparation and analysis of the ESI content, including mass spectra, UVPD spectra, τ-PD data, and theoretical calculations. Below is a summary of the ESI contents:

1. Additional Information on Experimental Methods..... 3

2. Mass Spectra and CID Curves 5

3. UV-PD Spectra, Calculated Absorption Spectra, Comparison with Solution Absorption Spectra 9

4. Ultrafast Transient Photodissociation Spectroscopy..... 15

5. Ultrafast Transient Absorption Spectroscopy..... 17

6. Theoretical Analysis..... 25

7. Purity of the sample $[Ru(bpy)_2(na)_2](PF_6)_2((PF_6)_2)$ 42

8. References 43

Reprint License

Rights and Permission to Include Paper in Doctoral Thesis

Von CONTRACTS-COPYRIGHT (shared) <Contracts-Copyright@rsc.org>
Datum Fr, 22.11.2024 14:33
An 'israil@chemie.uni-kl.de' <israil@chemie.uni-kl.de>

Dear Roumany Israil

The Royal Society of Chemistry (RSC) hereby grants permission for the use of your paper(s) specified below in the printed and microfilm version of your thesis. You may also make available the PDF version of your paper(s) that the RSC sent to the corresponding author(s) of your paper(s) upon publication of the paper(s) in the following ways: in your thesis via any website that your university may have for the deposition of theses, via your university's Intranet or via your own personal website. We are however unable to grant you permission to include the PDF version of the paper(s) on its own in your institutional repository. The Royal Society of Chemistry is a signatory to the STM Guidelines on Permissions (available on request).

Please note that if the material specified below or any part of it appears with credit or acknowledgement to a third party then you must also secure permission from that third party before reproducing that material.

Please ensure that the thesis includes the correct acknowledgement (see http://rsc.li/permissions for details) and a link is included to the paper on the Royal Society of Chemistry's website.

Please also ensure that your co-authors are aware that you are including the paper in your thesis.

Best wishes

Becky

Becky Roberts
Contracts & Copyright Executive, Sales Operations
Royal Society of Chemistry
www.rsc.org

ROYAL SOCIETY OF CHEMISTRY

Material Specification:

R. G. E. Israil; L. Schüßler; P. Hütchen; W. R. Thiel; R. Diller; C. Riehn,
"Ultrafast spectroscopy of Ru^{II} polypyridine complexes in the gas phase and the liquid phase: $[Ru(2,2'\text{-bipyridine})_2(\text{nicotinamide})_2]^{2+}$."
Physical Chemistry Chemical Physics, **2023**, 25, 4899–4914.
DOI: https://doi.org/10.1039/D2CP03765C

PCCP

ROYAL SOCIETY OF CHEMISTRY

PAPER

View Article Online
View Journal

Check for updates

Cite this: DOI: 10.1039/d2cp03765c

Ultrafast spectroscopy of Ru^{II} polypyridine complexes in the gas phase and the liquid phase: $[Ru(2,2'\text{-bipyridine})_2(nicotinamide)_2]^{2+}$†

L. Schüssler,‡[a] R. G. E. Israil,‡[b] P. Hütchen,[c] W. R. Thiel, [c] R. Diller *[a] and C. Riehn *[bd]

$[Ru(bipyridine)_2(nicotinamide)_2]^{2+}$ (**1**) and its monoaqua-complex $[Ru(bipyridine)_2(nicotinamide)(H_2O)]^{2+}$ (**2**) were spectroscopically studied for the first time in the gas phase by static and time resolved UV photodissociation spectroscopy, observing nicotinamide and H_2O ligand dissociation for **1** and **2**, respectively. Both processes and their ultrafast dynamics were investigated in parallel by transient absorption spectroscopy in aqueous solution. The latter data were newly acquired for the long-wavelength MLCT band excitation of **1** and provide novel ultrafast ligand dissociation results for **2**, confirming the gas phase results, *i.e.*, exclusive H_2O cleavage over nicotinamide loss. Similar apparent time constants in the sub-ps and few ps ranges were obtained for **1** in both phases, whereas a larger time constant of *ca.* two hundreds of ps for the ground state recovery was observed exclusively in the solution phase. Our reaction scheme accounts for faster dissociation dynamics in the gas phase by energetical lowering of the ^{3}MC *vs.* the ^{3}MLCT states by lack of solvent stabilization of the latter. Based on the apparent time constants, we favour, for the solution dynamics, a fast bimodal vibrational deactivation in the ^{3}MLCT/^{3}MC manifolds and a slow dissociation obfuscated by the ground state recovery. This is substantiated by a similar reaction scheme proposed for the ultrafast dynamics of **2**, resulting in a new assignment for transient absorption features with $\lambda > 550$ nm to the ^{3}MC manifold, and a common kinetic description for **1** and **2**. Computations at the TD-DFT/cc-PVTZ/MDF28 level support our spectroscopic findings and the suggested deactivation pathways.

Received 16th August 2022,
Accepted 8th January 2023

DOI: 10.1039/d2cp03765c

rsc.li/pccp

Published on 09 January 2023. Downloaded by Universitat Kaiserslautern on 1/26/2023 8:54:05 AM.

Introduction

Ru^{II} polypyridyl coordination compounds are versatile photochemical tools applicable across a broad range of physical processes and chemical transformations. Their usage extends from photocatalysis over solar light harvesting to biomedical and therapeutic purposes, and thus, they have been extensively studied by static and time-resolved spectroscopy for decades.[1] Depending on the scope of application, the polypyridine ligands octahedrally coordinating the d^6-Ru^{II} core are tailored by chemical synthesis in order to provide customized photo properties, *e.g.* (i) strong absorbance in a defined wavelength range, like in the so-called therapeutic window of 650–850 nm, (ii) long excited-state lifetime for efficient sensitizing, or (iii) solvability and stability in the chosen environment for high durability of devices. As a further possible target property, specific complexes (often containing monodentate ligands, like pyridines) are designed to provide (iv) a high photodissociation yield for their usage as caged compounds[2] or photo-prodrugs, with the latter in analogy to *cis*-platinum for crosslinking nucleobases.[3]

The archetypical complex in this field, $[Ru(bpy)_3]^{2+}$ (bpy = 2,2′-bipyridine), provides ^{1}MLCT transitions at *ca.* 450–550 nm, accompanied by a fast and efficient (quantum yield nearly unity[4]) sub-100 fs intersystem crossing (ISC) and a triplet metal-to-ligand charge transfer (^{3}MLCT) state lifetime in the µs region.[5–7] It was one of the first metal complexes studied for its ultrafast excited-state dynamics[8] which brought new impetus to the field of inorganic photochemistry[9] and allowed further on the detailing of relaxation pathways after photoexcitation in

[a] *Department of Physics, Technische Universität Kaiserslautern (TUK), Erwin-Schrödinger-Str. 46, D-67663 Kaiserslautern, Germany. E-mail: diller@physik.uni-kl.de; Tel: +49 631 2052323*
[b] *Department of Chemistry, Technische Universität Kaiserslautern (TUK), Erwin-Schrödinger-Str. 52, D-67663 Kaiserslautern, Germany. E-mail: riehn@chemie.uni-kl.de; Tel: +49 631 2054859*
[c] *Department of Chemistry, Technische Universität Kaiserslautern (TUK), Erwin-Schrödinger-Str. 54, D-67663 Kaiserslautern, Germany*
[d] *Research Center OPTIMAS, Erwin-Schrödinger Str. 46, D-67663 Kaiserslautern, Germany*

† Electronic supplementary information (ESI) available. See DOI: https://doi.org/10.1039/d2cp03765c

‡ Contributed equally to this work.

Published on 09 January 2023. Downloaded by Universitat Kaiserslautern on 1/26/2023 8:54:05 AM.

such systems, *e.g.*, considering the interplay of charge, spin and structural dynamics[10] or comparing the influence of metal centers from different rows of the periodic table, such as Ru^{II} *vs.* Fe^{II} complexes.[11,12]

Early on in research on the photochemistry of Ru^{II} polypyridine complexes, it was established that their ^{3}MLCT lifetimes and related ligand photodissociation depend critically on the type (and functionalization) of the ligands.[13] In particular, temperature-dependent emission studies revealed the thermally activated population of a non-radiatively decaying excited state (denoted as the ligand field state, dd state or ^{3}MC (metal-centered) state), which shortens the observed emission lifetime and moreover represents a major source of photoinstability by leading to photoinduced ligand dissociation or exchange. The dramatic influence of the ^{3}MC state energetics on the photodynamics of Ru^{II} complexes is exemplified for the $[Ru(tpy)_2]^{2+}$ (tpy = 2,2′:6′,2″-terpyridine) system, which is non-emissive and exhibits an overall apparent excited state lifetime of only 124 ps.[14] This is rationalized by the weaker ligand field of the tpy ligands constituting a 'non-optimal' octahedral environment that downshifts the ^{3}MC energy, reinforces the ^{3}MLCT/^{3}MC coupling and finally also the ^{3}MC/ground state (^{1}GS) coupling. It should be further noted that elongation of the Ru–N(py) (py: pyridine) bonds was observed from quantum chemical geometry optimizations leading to a crossing with the ground state surface and, additionally, enabling ligand dissociation.[15,16]

Spectroscopic identification and assignment of the elusive ^{3}MC state by time-resolved methods proved to be difficult and is an ongoing task.[17–19] Even transient IR absorption experiments gave no unique bands that could be attributed to a defined structure.[20,21] By quantum chemical calculations, the ^{3}MC state was geometry optimized and characterized comprehensively, and its dissociation *via* a penta-coordinated intermediate (PCI) was modeled.[16,22,23] Calculations on related systems lead to the characterization of two ^{3}MC geometries on the excited state surface: a 'regular' $^3MC_{hexa}$ state and a $^3MC_{penta}$ state, which shows one particularly long Ru–ligand distance, almost anticipating the PCI configuration.[16,24] However, direct experimental characterization of both the ^{3}MC state and the PCI species are scarce. Thus, new approaches are highly required for providing additional data and characterization of these photochemical gateways.

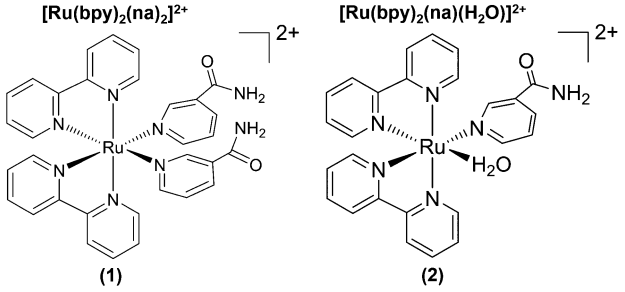

Chart 1 Molecular structures of *cis*-$[Ru(bpy)_2(na)_2]^{2+}$ (**1**) and its photoproduct *cis*-$[Ru(bpy)_2(na)(H_2O)]^{2+}$ (**2**).

In a comprehensive research project, our encompassing goal is to compare the ultrafast dynamics of identical molecular systems (here: Ru^{II} polypyridyl complexes) in the gas phase and solution and particularly to study the influence of ligand functionalization by chemical substitution of both the bpy and py ligands in general complexes of type: $[Ru(bpy\text{-}X)_2(py\text{-}Y)_2]^{2+}$ (X, Y: substituents). Here we combine chemical synthesis, gas phase dynamics and solution dynamics with the objective to study the influence of ligand field strength (tuned by systematic chemical substitution on the bipyridine (X) and pyridine (Y) ligands) *via* relative shifts of the ^{3}MLCT/^{3}MC electronic states onto the excited states lifetimes and dynamics of such complexes. In particular, we apply a mass spectrometry-based gas phase methodology predestined for analysis of ligand dissociation processes, *i.e.*, pump–probe photodissociation, that we have already successfully tested, *e.g.*, on Ru^{II}/Pd^{II} and Ru^{II}/Pt^{II} dinuclear complexes[25] and a Ru^{II} piano-stool complex.[26] This method provides a gas phase approach of time-resolved (τ-PD) and static UV photodissociation (UV PD[27]) action spectroscopy in an ion trap on mass-selected species at room temperature with the samples provided by electrospray ionisation (ESI). The transients of ultrafast electronic dynamics and UV PD spectra are obtained by recording (transient) photofragment yields as a function of pump–probe delay or laser wavelength, respectively. The strength of this approach lies in obtaining intrinsic effects, under solvent-free conditions, ideal for comparison to quantum chemical electronic structure calculations and, above all, to spectroscopy and dynamics in the solution phase for assessing the influence of solvation on photochemical pathways.[28] Cryogenic UV PD spectra on related complexes have been recorded recently using the messenger technique.[29]

In this work, we concentrate on the nicotinamide (na) binding in the complex $[Ru(bpy)_2(na)_2]^{2+}$ (**1**) (Chart 1), *i.e.*, X = H, Y = $CONH_2$ as an introductory example to test the comparison of the gas phase *vs.* solution phase dynamics for such systems. The complex is excellently suited for this purpose since it proved to be experimentally addressable *via* our gas phase photodissociation method, and in addition, a detailed and fundamental kinetic model for its photoinduced primary processes in aqueous solution has been proposed by Greenough *et al.*[30] Thus, together with our own UV/Vis femtosecond transient absorption (UV/Vis fs TA) measurements on **1** and on its mono-aquated form $[Ru(bpy)_2(na)(H_2O)]^{2+}$ (**2**) (Chart 1), this kinetic model now serves as a solid starting point to investigate and discuss the interplay of the excited electronic states in a broader context, *i.e.* in solution and gas phase.

In short, this kinetic model developed by Greenough *et al.*[30] ('model G' from here on) is based on UV/Vis fs TA data on **1**, supported by theoretical calculations. In a 'target analysis' approach, a kinetic model was developed and fit to the data, assuming specific basis spectra for the proposed molecular ground and excited state species. After rapid (sub-100 fs) intersystem crossing (ISC) from the excited ^{1}MLCT to the ^{3}MLCT state, vibrational relaxation (VR) in the latter allows, in a first phase of a barrier imposed process, fast (0.4 ps) internal conversion (IC) to a ^{3}MC state, followed by a rapid loss of one na ligand and the formation of a PCI. Geminate recombination of the dissociated na ligand and its diffusional separation through the solvent shell

 This journal is © the Owner Societies 2023

Published on 09 January 2023. Downloaded by Universitat Kaiserslautern on 1/26/2023 8:54:05 AM.

compete and lead back to the GS of **1** with 155 ps, and to the rapid formation of **2** with a quantum yield of $\phi(_2) = 0.36$, respectively. In a second, lower-energy phase, ^{3}MLCT vibrationally relaxes further with 3.6 ps and replenishes, now decoupled from IC to ^{3}MC, the ground state of **1** with 180 ps.

Note first, that model G predicts apparent time constants, *e.g.* resulting from a branching reaction with two constituting rate constants, which have not been observed experimentally (*cf.* discussion of model G). Second, ligand dissociation is found to occur very fast (0.4 ps). Both results caught our attention.

Here, we present spectroscopic and dynamic gas phase results, which are compared with theoretical calculations as well as with extended data obtained in the solution phase. Crucial for this comparison is the identity of the dicationic chromophore units **1** and **2** in both phases. Isolated in the gas phase of an ion trap, an efficient photodissociation of **1** by loss of one na ligand is observed. The PCI of **1** as a photofragment and **2** could also be isolated in the ion trap, allowing the first spectroscopic analysis of such species in the gas phase. Furthermore, the gas phase dissociation of **2** shows the preference of H_2O over nicotinamide cleavage, as also confirmed by our new results obtained in the solution phase (see below). Density functional theory (DFT) quantum calculations with geometry optimization provide binding energies of these species (H_2O *vs.* na binding) and prepare TD-DFT (time-dependent DFT) calculations in order to characterize the involved singlet and triplet excited states. The photodissociation action spectra in the gas phase obtained by UV PD compare well with the absorption spectra in the solution phase allowing the assignment of the strongest transitions. Transient photodissociation (τ-PD) is used to record the dynamics of **1**, giving time constants for dissociation in the few ps range, which differs from the result of model G. We propose a simplified kinetic scheme, in conjunction with our results for solution dynamics (see below).

For a direct comparison of the gas phase and liquid phase, we studied **1** in H_2O by UV/Vis fs TA spectroscopy *via* long-wavelength MLCT band excitation, and, for the first time, investigated likewise the primary photochemistry of photoproduct **2** in H_2O. Interestingly, the spectro-temporal evolution of the TA data on **2** is, with a few but significant differences, very similar to those on **1**. In contrast to ref. 30, we follow an approach of global and local multiexponential analysis, yielding apparent time constants (as for the gas phase data) and related decay associated spectra (DAS). As our transient absorption data on **1** reproduce well the data in ref. 30, together with our results on **2** our approach allows complementary description and interpretation. We show that some, albeit important, aspects of model G[30] are not compatible with our analysis and that our experimental results on **1** and **2** are consistent with different kinetic schemes.

Methods

Calculations

To support the assignment of the obtained UV PD spectra, the geometry of the complex was optimized, and single-point energy calculations were performed using density functional theory (DFT) and time-dependent (TD-)DFT at the B3LYP/6-31+G*/MWB28 or B3LYP/cc-PVTZ/MDF28 (Stuttgart97) level using the Gaussian program package.[31] The excited states calculations were evaluated using GaussSum 3.0[32] and the orbitals involved in the transitions were visualized using GaussView 6.0.[33]

Gas phase experiments

The gas phase mass spectrometric and laser spectroscopic investigations were performed using an amaZon speed ion trap mass spectrometer (Bruker Daltonik) equipped with an Apollo II electrospray ionization (ESI) source. The Paul-type quadrupole ion trap was modified for the application of laser-induced fragmentation spectroscopy.[26,28,34]

The dicationic $[Ru(bpy)_2(na)_2]^{2+}$ (**1**) complex was transferred into the gas phase by ESI using a *ca.* 10^{-6} M solution in acetonitrile (ACN). Since the complex is photochemically active, the solutions were stored in amber glass bottles to avoid photo-induced decomposition by ambient light. Acetonitrile (ACN) and other solvents were dried over a molecular sieve (4 Å). A syringe pump continuously infused the sample solution into the ESI source at a flow rate of 120 μL min^{-1}. The spray needle was set to 4.5 kV, nitrogen, as a nebulizer and drying gas, was streaming at a flow rate of 4 L min^{-1} at 180 °C and 410 mbar (7 psi).

For static UV photodissociation (UV PD) and transient photofragmentation (τ-PD) measurements, femtosecond pulses were generated in a Wyvern 1000™ cryogenic ultrafast regenerative oscillator/amplifier laser system (KMLabs) and directed into the ion trap. The laser pulse duration was ~50 fs at 780 nm, with an average power ~3.7 W at a repetition rate of 981 Hz (~1 kHz). To produce pump and probe pulses of tuneable wavelengths, the beam was divided to pump two optical parametric amplifier oscillators of a white light continuum (TOPAS-C, Light Conversion).

UV PD was recorded in the range 236–480 nm with 3 nm step size at an energy of *ca.* 2 μJ per pulse by one of the TOPAS-C units. The laser beam was aligned and centered for the highest ion fragment yield of the isolated ion cloud before each measurement. Hereby, the fragmentation time was set to 100 ms, which results in *ca.* 100 pulses of irradiation per ion cloud and was controlled by a laser shutter. On each wavelength ~20 data points were taken, where each data point is averaged by 7 mass spectra. The total fragment yield (TFY) was calculated according to $I_f/(I_f + I_p)$, where I_f and I_p are the sums of the fragments f and parent ion p obtained by integrating over their mass peak intensities. Additionally, the fragment yield was normalized to the number of photons N ($= E_{pulse}\cdot\lambda/(h\cdot c)$).

For the time-resolved measurements (τ-PD), the second TOPAS-C system was used to generate the probe beam at 1200 nm with *ca.* 130 μJ per pulse and overlapped at a small angle with the pump beam in the ion trap. The wavelength of the pump beam was chosen according to an electronic transition obtained from the UV PD measurements and set at low energy (*ca.* 1 μJ) to induce only a one-photon dissociation signal. The time delay of pump and probe pulses was controlled by a mechanical delay-stage (Physik Instrumente, PI) equipped

Published on 09 January 2023. Downloaded by Universitat Kaiserslautern on 1/26/2023 8:54:05 AM.

with a retroreflector. To increase the signal quality, 12 scans were averaged and the result was fitted by a sum of exponentials (eqn (1)) using OriginLab 2019G, where erf (error function) embeds by convolution the instrument response function (IRF) stemming from the finite laser pulse width.

$$Y(t) = Y_0 + \sum_{i=1}^{n}\left[A_i e^{0.5\left(\frac{w}{\tau_i}\right)^2 - \frac{t-t_0}{\tau_i}} \cdot 0.5\left(\mathrm{erf}\left(\frac{(t-t_0)/w - w/\tau_i}{\sqrt{2}}\right) + 1\right)\right] \quad (1)$$

where t is the time, Y_0 is the offset, A_i is the amplitude of component i, τ_i is a lifetime of component i, t_0 is the time zero, and w is the FWHM/$\left(2\sqrt{2\ln 2}\right)$ of Gaussian representing the IRF.

Liquid phase experiments

Static UV/Vis absorption spectra in the solution phase were obtained using a JASCO V-670 spectrophotometer. For femtosecond (fs) transient absorption spectroscopy in the solution phase (UV/Vis fs TA), a Ti:Sa regenerative amplifier laser system (Coherent Libra, 1 kHz repetition rate, 4 mJ per pulse at 800 nm, 100 fs pulse duration (full width at half maximum, FWHM)) was used. All experiments in the solution phase were carried out at room temperature (295 K) and in the dark to avoid photodegradation by ambient light. The pump pulses at 340 and 425 nm were generated by a commercial optical parametric amplifier (Coherent TOPAS-Prime). The single pulse energy was set to ~260 nJ at a focal width of ~100 μm (FWHM) at the sample position. Self-phase modulation in a moving CaF_2-window (5 mm thickness) was used to create a spectral continuum for probe pulses in the spectral range from 350 to 700 nm. The probe beam was focused to a focal width of ~50 μm (FWHM) at the sample position. After the sample, the probe pulses were spectrally dispersed and then detected using a 512-pixel integrated FFT-CCD device (Stresing Camera Control FFTI24 with Hamamatsu FFT S7030-0906). The relative polarization of probe and pump pulses was set to the magic angle (54.7°) at the sample position. A delay stage (Physik Instrumente (PI) M-531.DG) was used to generate time delays t of up to 1.1 ns between the pump and probe pulses. Every second pump pulse was blocked by a chopper to obtain pump induced difference absorbance spectra $\Delta A(\lambda,t)$. A global analysis approach by the global multi-exponential fit function (eqn (2))

$$\Delta A(\lambda, t) = A_0(\lambda) + \sum_{i=1}^{N} A_i(\lambda) \cdot e^{\frac{-t}{\tau_i}} \quad (2)$$

was used to analyse the difference spectra $\Delta A(\lambda,t)$, with the decay associated spectra (DAS) $A_i(\lambda)$ and the corresponding N time constants τ_i, and $A_0(\lambda)$ representing components with infinite lifetime compared to the maximum time delay. The system response time was 230 fs and the fitting routine was started for delay times larger than 0.25 ps.

To prepare **1**, the $[Ru(bpy)_2(na)_2]^{2+}$ $2(PF_6)^-$ (**1**$(PF_6)_2$) salt was dissolved in HPLC-grade H_2O and the $[Ru(bpy)_2(na)(H_2O)]^{2+}$ (**2**) sample was prepared as described below. The fs time-resolved measurements were performed in a rotating CaF_2-cell (1 mm optical path length, 25 mm diameter) or in a flow cell system with *ca.* 100-fold sample volume as compared to the rotating cell, both systems providing fresh-sample condition with respect to the shot-to-shot (1 ms) exchange of excited sample volume. The flow cell setup consisted of a peristaltic pump (Masterflex L/S Economy, Model 7554-95 with the Easy-Load II, Model 77200-50 pump head) and Masterflex L/S 13 Viton tubing, which connected a 30 ml sample reservoir with the flow cell (Harrick Scientific, Model TFC-S13-3, 1 mm optical path length). For the rotating cell measurements, the optical density (OD) of the sample was 0.58 and 0.73 for **1** excited at 425 and 340 nm, respectively, and 0.67 for **2** excited at 340 nm. For the flow cell measurement on **1**, the OD was 0.42 for excitation at 340 nm. The composition of the samples was frequently evaluated by static UV/Vis absorption spectra during ongoing fs TA measurements.

Due to photoinduced mono-aquation (*cf.* Experimental results), formation of **2** is unavoidable during the ongoing measurements on **1**. In the flow cell system with a much higher sample volume, this effect is safely negligible. In contrast, in the rotating cell accumulation of **2** is observed after the first few out of up to 10 measurement cycles (total sweep of delay line). However, it was possible to clearly and quantitatively distinguish between the photoinduced fs-dynamics of **1** and of the accumulation of **2** by a thorough analysis of the data, and by comparison with a flow cell experiment on **1** and a rotating cell experiment on exclusively **2**. This procedure is described in the ESI† and clearly shows that the first measurement cycle (as shown in Fig. 6a) in the rotating cell represents the photoinduced dynamics of **1** without a significant contribution of excited **2**.

The sample for the fs measurements on **2** was prepared by exposing a rotating cell with **1** in H_2O to ambient light sufficiently long to achieve its basically complete photo-transformation into the former but avoiding the formation of $[Ru(bpy)_2(H_2O)_2]^{2+}$. This process was controlled *via* static UV/Vis absorption spectroscopy (Fig. 4 and ESI,† Fig. S28) as described earlier.[30] Besides **2**, the dissociated free na ligands remain in the sample solution. However, as free na does only absorb below 300 nm,[35] it can be neglected for these investigations. Since the sample has not shown further photodegradation during fs TA on **2** (*cf.* Experimental results and ESI,† Fig. S28), it was possible to average the five measured cycles for the analysis.

Synthesis

The synthesis of $[Ru(bpy)_2(na)_2](PF_6)_2$ (**1**$(PF_6)_2$) was performed according to published literature procedures.[30,36,37]

Experimental results

Mass spectrometric analysis of $[Ru(bpy)_2(na)_2]^{2+}$ (1) and $[Ru(bpy)_2(na)(H_2O)]^{2+}$ (2)

The compound salt **1**$(PF_6)_2$ was solved in acetonitrile (ACN, 10^{-6} M), transferred by electrospray ionization (ESI) into the gas phase and the positive ions were stored in an ion trap mass

This journal is © the Owner Societies 2023

Published on 09 January 2023. Downloaded by Universitat Kaiserslautern on 1/26/2023 8:54:05 AM.

spectrometer. The resulting overview mass spectrum is given in Fig. 1 (upper black trace). The main mass peaks are located at *m/z* 329 (**1**, $[Ru(bpy)_2(na)_2]^{2+}$), *m/z* 268 ($[Ru(bpy)_2(na)]^{2+}$) and *m/z* 803 ($[Ru(bpy)_2(na)(PF_6)]^{+}$), with the *m/z* values referring to rounded monoisotopic mass. Magnification of this spectrum by a factor of 10 reveals additional mass peaks (Fig. 1, red trace), with assignments listed in Table 1. Simulations of the isotope patterns were used for identification (Fig. 1, lower trace).

The peaks at *m/z* 207, *m/z* 216 and *m/z* 225 are assigned to $[Ru^{II}(bpy)_2]^{2+}$, $[Ru^{II}(bpy)_2(H_2O)]^{2+}$ and $[Ru^{II}(bpy)_2(H_2O)_2]^{2+}$/$[Ru^{II}(bpy)_2(HCl)]^{2+}$, respectively. The signal at *m/z* 268, resulting from the loss of one na ligand from the molecular ion, appears at a relatively high intensity in the overview spectrum. This indicates a weak coordinative bond between Ru^{II} and na. The ligand loss could occur already in the solution phase but is also likely to be enhanced during the electrospraying process and the ion transfer towards the ion trap. The addition of one H_2O molecule to such an undercoordinated complex is often observed in ion traps and leads here to the broad mass peak centered at *m/z* 277. This signal extends significantly to higher *m/z* values and probably results from the multiple addition/dissociation of an only weakly bound water molecule. Its broadness could also point to its dissociation during the detection process in the ion trap, where collisions with He are important. Note that both, the penta-coordinated intermediate (PCI, $[Ru(bpy)_2(na)]^{2+}$) and the monoaqua species (**2**, $[Ru^{II}(bpy)_2(na)_1(H_2O)]^{2+}$) are observed here in the gas phase.[30]

In order to investigate the fragmentation pathways, we have isolated the main species obtained from the overview MS (Fig. 1) and investigated their fragmentation behaviour by collision-induced dissociation (CID, ESI,† Fig. S5 and S6) and photoinduced dissociation (UV PD, see below). Here, CID of **1** leads to $[Ru(bpy)_2(na)]^{2+}$ (PCI) by loss of one na ligand as the main fragment, with concurrent formation, although at low intensity, of $[Ru(bpy)_2(na)(H_2O)]^{2+}$ (PCI–H_2O, **2**). In turn, the isolation of $[Ru(bpy)_2(na)]^{2+}$ (PCI) also immediately resulted in the formation of its water adduct (PCI–H_2O) and another not assignable broad feature at *m/z* 310 (ESI,† Fig. S8). Very similar fragment patterns have been obtained from UV PD.

Table 1 Assignment of fragments observed in the overview ESI mass spectrum of $[Ru(bpy)_2(na)_2]^{2+}$ (**1**). Molecular ion peak at *m/z* 329 (bold)

Monoisotopic *m/z*	Assignment
(207)	$[Ru^{II}(bpy)_2]^{2+}$
216	$[Ru^{II}(bpy)_2(H_2O)]^{2+}$
225	$[Ru^{II}(bpy)_2(H_2O)_2]^{2+}$ or $[Ru^{II}(bpy)_2(HCl)]^{2+}$
268	$[Ru^{II}(bpy)_2(na)_1]^{2+}$ (PCI)
277	$[Ru^{II}(bpy)_2(na)_1(H_2O)]^{2+}$ (**2**)
285	$[Ru^{II}(bpy)_3]^{2+}$
329	**$[Ru^{II}(bpy)_2(na)_2]^{2+}$** (**1**)
433	$[Ru^{II}(bpy)_2F]^{+}$
477	$[Ru^{II}(bpy)_2(Cl)(CO)]^{+}$
535	$[Ru^{II}(bpy)_2(na)_1]^{+}$-H
555	$[Ru^{II}(bpy)_2(na)_1F]^{+}$
803	$[Ru^{II}(bpy)_2(na)_2(PF_6)]^{+}$

Since monoaqua-complex **2** is an important intermediate in the photoactivation process of **1** in aqueous solution,[30] we tested its direct preparation from solution by starting with a 10^{-4} M aqueous solution of **1**, which was then diluted in ACN to 10^{-6} M and electrosprayed. In this way, a well-structured, sharp peak pattern in the *m/z* range of **2** was obtained. However, close inspection of the isotope pattern (ESI,† Fig. S9) lead us to assign the species' composition to $[Ru^{III}(bpy)_2(na)(OH)]^{2+}$ and $[Ru^{IV}(bpy)_2(na)(O)]^{2+}$, in roughly a 4 : 1 ratio (ESI,† Fig. S9). We assume oxidation of **1** to $Ru^{III/IV}$ in the electrospray process using water as a solvent. The stability and acidity of Ru^{III} hydrates and their water exchange reactions have been described in the literature.[1,38] Additionally in the ESI†, we report on the UV PD

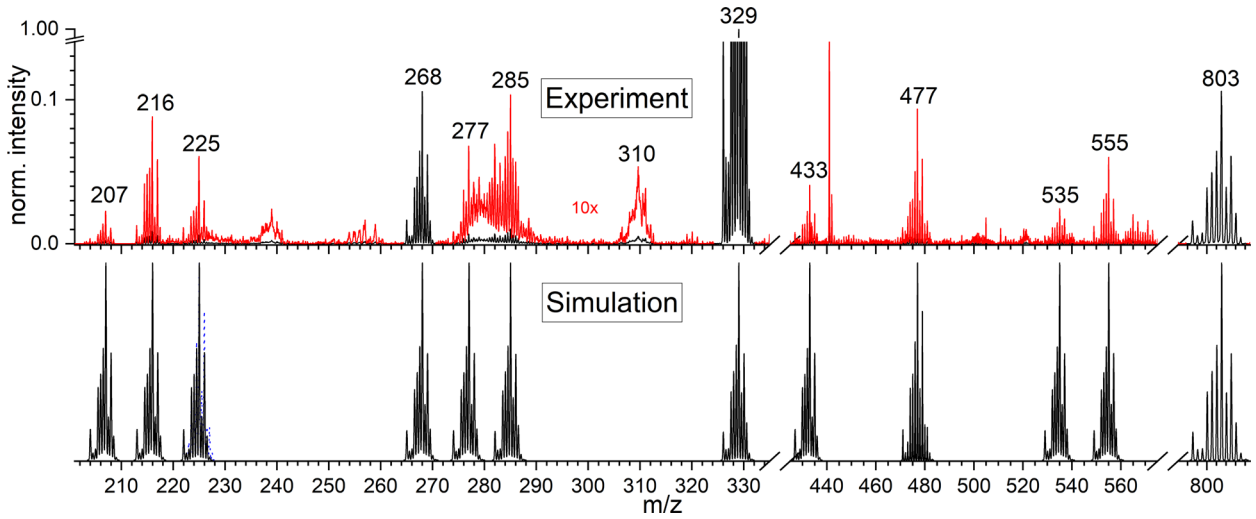

Fig. 1 Top: Overview (ESI) mass spectrum of $[Ru(bpy)_2(na)_2](PF_6)_2$ (**1**$(PF_6)_2$) from acetonitrile solution (black trace). In order to present the characteristic isotope patterns of the observed mass signals and for comparison to the corresponding simulation a magnification by a factor of 10 is displayed (red trace). Note: interrupted intensity scale from 0.14 to 0.95; different *m/z* scaling *m/z* 200–334, 428–572, 788–812. Bottom: Simulations of mass signals with distinct isotope patterns which lead to assignments given in Table 1. Note: the intensity of the simulated peaks is set to an arbitrary, constant value. For a magnified view (simulation, experiment) of the signals at *m/z* 329, 277 and 268, see the ESI,† Fig. S4 and S8.

Published on 09 January 2023. Downloaded by Universitat Kaiserslautern on 1/26/2023 8:54:05 AM.

spectra and associated quantum chemical calculations for the PCI-OH/PCI-O species, which might play a role in water splitting applications as recently reviewed.[39]

UV spectroscopy

UV PD spectra and assignment of electronic transitions. Using an ion-trap mass spectrometer, molecules can be selected and isolated and then exposed in this solvent-free environment to UV radiation of a tuneable laser system, enabling the recording of UV/Vis photodissociation (UV PD) action spectra. These spectra are obtained by scanning the laser wavelength point-by-point at constant pulse energy and detecting the resulting fragment yield. As long as a one-photon excitation process is ensured (see energy dependence, ESI,† Fig. S21), the spectra are representing the UV spectra of the corresponding chromophores in the gas phase. Additionally, the experimental UV PD spectra are here compared to computed spectra obtained from TD-DFT (at the B3LYP/cc-PVTZ level) quantum chemical calculations, whose transitions were analysed orbital-wise and used for assignment of the main bands.

*Molecular complex ion $[Ru(bpy)_2(na)_2]^{2+}$ (**1**).* The overall shape of the UV PD spectrum of **1** resembles its absorption spectrum in the solution phase (Fig. 2). It only differs by a small additional shoulder at 305 nm in the UV PD spectrum and a general blueshift of *ca.* 1200–1500 cm^{-1} in the gas phase, obtained by comparing the bands at 330–340 nm or the peak maxima at 280–290 nm.

For supporting the assignment and characterization of the observed transitions, the involved molecular orbitals (MOs) (ESI,† Table S4) of the corresponding calculated transitions (S_x) were visualized (ESI,† Fig. S31). The transitions S_5 and S_6 show a charge transfer (CT) from Ru^{II} onto the bpy ligands.

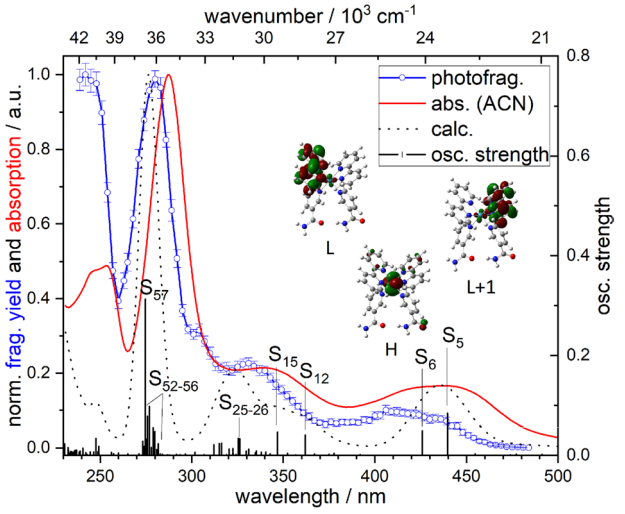

Fig. 2 Gas phase UV PD spectrum (blue) and liquid phase absorption spectrum in ACN (red) of $[Ru(bpy)_2(na)_2]^{2+}$ (**1**). Calculated transitions (stick spectrum) were obtained at the TD-DFT/B3LYP/cc-PVTZ level of theory and convoluted with 1500 cm^{-1} FWHM Gaussian functions (black). The molecular orbitals HOMO, LUMO, and LUMO+1 are depicted, showing the MLCT of S_6 and S_5.

The transitions S_{12-25} at 362, 346, 326 and 325 nm show MLCT character with a weight of 33–82% of CT onto the na ligands. S_{52-57} lead to the strong band at 280 nm and are mainly composed of bpy and na ligand centered (LC) type, *i.e.*, ππ*, transitions within these ligands. With smaller MO weight, the latter states show interligand CT from na towards the bpy ligand or from NH_2 towards the na ligand. The experimentally observed shoulder in the gas phase at 305 nm could not be assigned, since we have obtained from quantum chemical calculations in this wavelength region only a few transitions of very low oscillator strength with the lack of clear, dominating MO contributions.

*Penta-coordinated intermediate (PCI), water adduct (PCI–H_2O, **2**) and $[Ru(bpy)_2(na)_2]^{2+}(PF_6)^-$.* The PCI complex does not show any fragmentation upon UV PD in the region 240–480 nm. This could be due to a high activation barrier for the loss of the second na ligand to produce $[Ru^{II}(bpy)_2]^{2+}$. We calculated the (adiabatic) dissociation energy for: $[Ru^{II}(bpy)_2(na)]^{2+} \rightarrow [Ru^{II}(bpy)_2]^{2+}$ + na to approx. 185 kJ mol^{-1} (ESI,† Fig. S29), which could obviously not explain this behaviour, since the UV absorption (photon energy: 500–250 kJ mol^{-1}) would provide enough energy for this process so that indeed kinetic aspects (high barrier, fast dissipation of excitation energy) have to be invoked.

However, the species at *m*/*z* 277 (PCI–H_2O, **2**) and *m*/*z* 310, obtained after mass-spectrometric isolation of PCI at *m*/*z* 268 (ESI,† Fig. S8), dissociate after UV irradiation, forming again PCI. So, at certain resonant wavelengths, the signal of PCI (*m*/*z* 268) increases, which leads to a 'depletion spectrum', if one plots the fragment yield *vs.* wavelength (ESI,† Fig. S11). For instance, if the laser wavelength is set to 275 nm (a resonance of PCI–H_2O), the intensity of *m*/*z* 277 (broad peak) decreases and the corresponding intensity at *m*/*z* 268 (PCI) increases. For comparison and confirmation of this analysis, a UV PD spectrum of the isolated broad signal at *m*/*z* 277 (PCI–H_2O) is also recorded and plotted in the ESI,† Fig. S11 together with the inverted spectrum for *m*/*z* 268. The similarity of both spectra (based on either the isolation of *m*/*z* 268 or *m*/*z* 277) further supports our conclusion that not the UV PD spectrum of PCI but rather the one of PCI–H_2O was obtained. In Fig. 3, we plot now the inverted trace of the fragment yield of the isolated mass at *m*/*z* 268 (blue trace) as a representation for the UV spectrum of PCI–H_2O (**2**). In comparing this experimental UV PD spectrum to the calculated one for **2** (Fig. 3, black dotted line), particularly at the maxima at 280, 310 and 420 nm (Fig. 3), an acceptable agreement can be observed. From the quantum chemical calculations, we assign the experimentally observed band at 380–460 nm to the transitions S_{5-6} (ESI,† Table S5), which represent MLCTs onto the bpy ligands. The shoulder band at 300–350 nm is represented in the calculations by the transitions S_{11} and S_{23}, which show MLCT character involving a na ligand and bpy ligands, respectively. The strong band at 280 nm is reproduced by the calculated transitions S_{38} and S_{40}, which result mostly from LC states.

In summary, we were able to obtain the UV PD spectrum of PCI–H_2O **2** in the gas phase and compare it to spectra obtained from quantum chemical calculations and the solution phase.

This journal is © the Owner Societies 2023

Published on 09 January 2023. Downloaded by Universitat Kaiserslautern on 1/26/2023 8:54:05 AM.

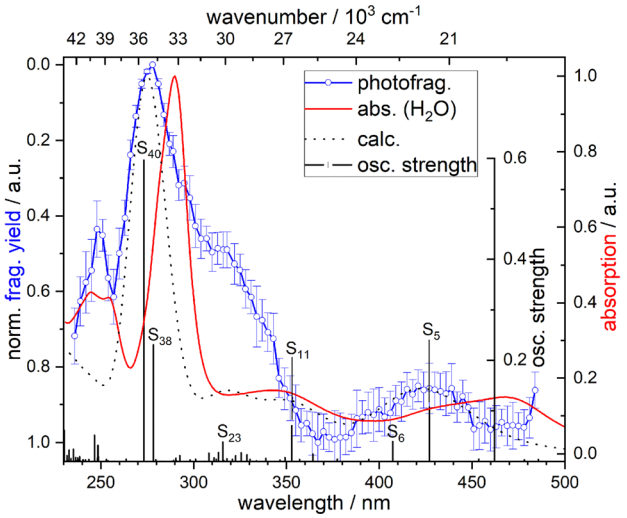

Fig. 3 Gas phase UV PD spectrum (blue) recorded on isolated *m*/*z* 268 (PCI) but assigned to the species PCI–H_2O (**2**) (explanation, see text). Liquid phase absorption spectrum of **2** (red) in ACN/H_2O. Calculated transitions (stick spectrum) were obtained at the TD-DFT/B3LYP/cc-PVTZ level of theory and convoluted with 1500 cm^{-1} FWHM Gaussian functions (black).

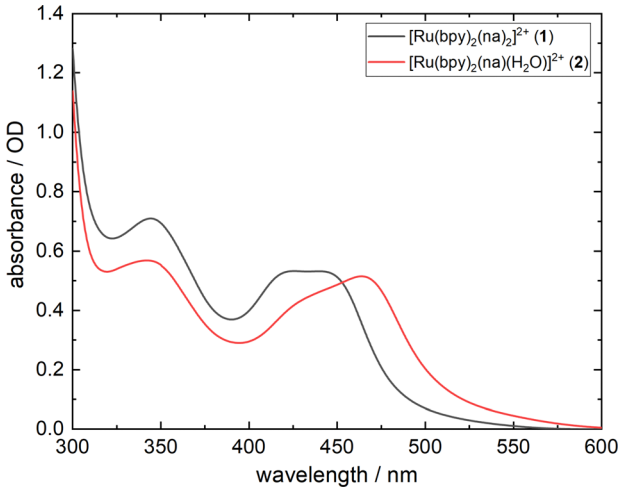

Fig. 4 Static UV/Vis absorption spectrum of $[Ru^{II}(bpy)_2(na)_2]^{2+}$ (**1**) (grey line, *ca.* 1.2 mM) and of $[Ru^{II}(bpy)_2(na)(H_2O)]^{2+}$ (**2**) (red line) in solution (H_2O) – extended view and further information in ESI,† Fig. S28.

In general, for species **2**, again (as for **1**) a blueshift for the gas phase spectrum with respect to the solution spectrum is observed. The main differences to the spectrum of **1** are a slightly red-shifted long-wavelength MLCT region (400–450 nm) and a stronger shoulder band region (300–350 nm). The latter is not observed in the solution spectrum and we suggest that its distinctly higher intensity in the gas phase results from a high dissociation yield owing to the low binding energy of H_2O compared to the na ligand and a better coupling to the dissociation coordinate for the transitions in this region (assigned to the $^1MLCT_{na}$ type). This effect is already indicated in the spectrum of **1** in this region (*cf.* band structure at 305–310 nm, Fig. 2) and also observed for the counterion complex $[Ru(bpy)_2(na)_2]^{2+}(PF_6)^-$ (see ESI,† Fig. S13). The latter's spectrum is interestingly close to the solution spectrum of **1**, which means that the counterion attachment mimics already the solvation induced spectral redshift.

In order to expand the theoretical analyses, we have additionally calculated the gas phase absorption spectra by TD-DFT using B3LYP/cc-PVTZ level of theory of some fragments of **1**, namely: $[Ru(bpy)_2(na)]^{2+}$ (PCI), $[Ru(bpy)_2]^{2+}$ and the na ligand, as well as for the related aqua adducts: $[Ru(bpy)_2(H_2O)_2]^{2+}$ and $[Ru(bpy)_2(H_2O)]^{2+}$ (ESI,† Fig. S14–S16). The characterization of the corresponding orbitals is given in the ESI,† Tables S6, S8–S10 and correspondingly depicted in the ESI,† Fig. S35, S39, S41 and S43.

Furthermore, although not the focus of this work, we have spectroscopically investigated the higher oxidized Ru species $[Ru^{III}(bpy)_2(na)(OH)]^{2+}$ and $[Ru^{IV}(bpy)_2(na)(O)]^{2+}$ as obtained by electrospraying **1** from aqueous solution (see mass spectrometric analysis above). Their experimental UV PD spectrum (ESI,† Fig. S17) is compared to the calculated absorption spectra of PCI-OH and PCI-O and a weighted sum of both calculated spectra of 4 : 1 for PCI-OH/PCI-O, but the agreement is not satisfying. However, we report the results here in order to demonstrate that also elusive oxidation states of metal complexes or intermediates could be generated and spectroscopically interrogated by the used ion trap gas phase methodology.

UV/Vis absorption spectra of $[Ru(bpy)_2(na)_2]^{2+}$ (1) and $[Ru(bpy)_2(na)(H_2O)]^{2+}$ (2) in solution. In Fig. 4, the static UV/Vis absorption spectra of **1** (grey line) and its mono-aquated photoproduct **2** (red line) in H_2O are compared. The maxima of the broad MLCT-dominated features are located at 420–445 nm for **1**. For **2**, a redshift of the maximum to 465 nm is observed and only a shoulder is present around 430 nm. **1** and **2** both show another MLCT band centered around 344 nm.

Ultrafast dynamics of $[Ru(bpy)_2(na)_2]^{2+}$ (1) in the gas phase

Pump–probe photodissociation spectroscopy (τ-PD)[25] is applied in an ion trap on mass-selected isolated complex ions of **1** in order to obtain intrinsic ultrafast dynamics in the gas phase. Hereby, the (total) fragmentation yield (dominated in this case by na ligand dissociation) is recorded as a function of the time delay between the pump and the probe laser pulse. Resonant pump wavelengths of 340, 410 and 430 nm, within the two lowest energetic absorption bands of **1**, were chosen and the non-resonant probe wavelength was fixed to 1200 nm. The probe laser serves to enhance the fragment yield by transferring the pump-excited complex ions by multiphoton excitation into higher electronic states leading to an increase in the fragment yield due to higher internal energy of the ions, and accordingly faster and more efficient dissociation. The probe laser irradiation alone does not generate fragment ions but enhances the fragment ion yield induced by the pump laser by a factor of 3–7 (at time zero). With the assumption that the probe laser absorption cross section depends on the vibronic states in which the molecular system is located, it is expected that the ultrafast dynamics of excited states are reflected in their transient fragmentation yields.

Published on 09 January 2023. Downloaded by Universitat Kaiserslautern on 1/26/2023 8:54:05 AM.

It should be noted that the actual formation of the fragment ions could take place on a different, often μs, time scale and is not directly accessible, since already the MS analysis of the irradiated sample lasts several ms. However, still the fragment yield represents a marker for the ultrafast electronic dynamics supposing that it is proportional to the population of the excited states and to the internal energy of the correspondingly probed ions. In this way, the technique was already successfully applied towards fast IC (back to the electronic ground state) for Ru piano-stool complexes[26] and towards the formation of long-lived ^{3}MLCT states of Ru–Pd/Pt,[25] mono- and dinuclear pyridyl-triazole/DPEPhos-based Cu(I) complexes[40] and Au(I)/Ru(II) cyclophanyl photocatalysts.[41]

The pump and probe laser pulse energies were here set to 1 μJ and 130 μJ, respectively, to achieve the highest pump–probe gain at time zero. In order to further improve the signal quality, 10–15 transient scans were averaged and the transient decay curves, as depicted in Fig. 5, were obtained. These transients were evaluated by a biexponential fit using eqn (1) (see Methods), which resulted in the time constants listed in Table 2.

In summary, the transients could be fitted very well by one sub-picosecond time constant τ_1 (*ca.* 0.6 ps) and one time constant of a few ps τ_2 (*ca.* 3 ps). The total fragment yield decays for all excitation wavelengths to zero within *ca.* 10–12 ps. This obviously means that no long-lived (longer than a few ps) excited states are formed in the gas phase. Thus, this decay to zero is attributed to a fast internal conversion (IC) back to the electronic ground state followed by dissociation or a fast direct dissociation from the excited state. This is supported by the almost exclusive detection of the PCI complex as fragment ion and is also in accordance with the paradigms of Ru-polypyridine dissociation.[13,16–18] Note that we can rule out the exclusive direct fragmentation within the system response time (*ca.* 150 fs), which would result in the cross-correlation signal only. This observation contrasts the reported ultrafast dissociation dynamics of 0.36 ps[30] and emphasizes the shift in dissociation pathways in the gas phase.

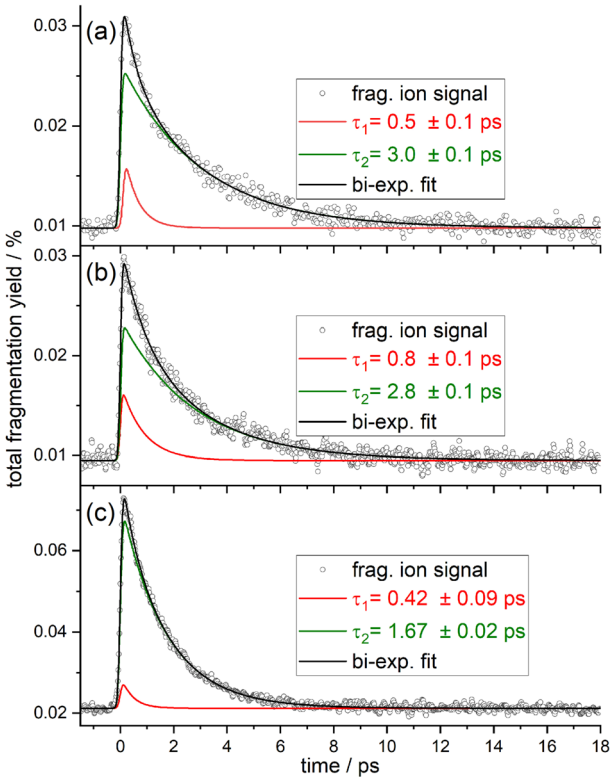

Fig. 5 Normalized transient fragment ion intensity of $[Ru(bpy)_2(na)_2]^{2+}$ (**1**) recorded at λ_{pump} = 430 nm (a), λ_{pump} = 410 nm (b) and λ_{pump} = 340 nm (c); bi-exponential fit (black) is given along the fit decomposition (green and red).

Table 2 Time constants of $[Ru(bpy)_2(na)_2]^{2+}$ (**1**) resulting from fitting the τ-PD transients in Fig. 5 to eqn (1)

	λ_{pump}/nm	A_1/%	τ_1/ps	A_2/%	τ_2/ps
1	**430**	33	0.5 ± 0.1	67	3.0 ± 0.1
1	**410**	36	0.8 ± 0.1	64	2.8 ± 0.1
1	**340**	14	0.42 ± 0.09	86	1.67 ± 0.02

Moreover, the overall excited state dynamics of **1** in the gas phase clearly show an acceleration with decreasing pump wavelength, *i.e.*, with increasing excess energy (*cf.* order a, b, c in Fig. 5). This mainly manifests in the shortening of the dominating time constant τ_2 by nearly a factor of 2 from 430 to 340 nm, whereas the τ_1 values do not show a clear trend.

More details of the mechanism will be discussed below, in conjunction with the results and interpretation obtained for the solution dynamics in this work.

Ultrafast dynamics in solution

UV/Vis fs TA of $[Ru(bpy)_2(na)_2]^{2+}$ (1) in H_2O. Fig. 6a and d show the difference spectra at selected delay times for **1** in H_2O, excited at 425 nm (Fig. 6a) and at 340 nm (Fig. 6d), respectively. Note that all signals, positive and negative, rise instantaneously within our system response of 230 fs, and decay, with few exceptions, on long time scales. Overall, the difference spectra are very similar for excitation at 425 and 340 nm. In both cases, the observed difference spectra are typical for Ru^{II}-polypyridine complexes after ^{1}MLCT-excitation with rapid (sub-100 fs) ISC into a ^{3}MLCT state, represented by the excited state absorption (ESA) band in the region 350 to 390 nm with a maximum at 370 nm.[8,17,20,30,42–45] In the range from 392 to 485 nm, ground state bleach (GSB) is observed, superimposed with ESA on both sides. The spectral shape of the GSB signal resembles the static UV/Vis absorption spectrum in Fig. 4, with a minimum at around 445 nm and a distinct shoulder at around 420 nm. Above 485 nm, a plateau-like behaviour arises instantaneously and comprises two different sections: (i) a part of the ^{3}MLCT-ESA band[17,20,30,42] and (ii) above around 550 nm possibly different additional contributions, depending on the energy-gap between the ^{3}MC- and ^{3}MLCT-excited states. In long-living, luminescence dominated Ru^{II}-polypyridine complexes, the plateau has been observed and assigned to ^{3}MC-ESA.[17,20,42] In photodissociation dominated Ru^{II}-polypyridine complexes, like the investigated **1**, the plateau is also apparent despite the (partially very fast)

This journal is © the Owner Societies 2023

Published on 09 January 2023. Downloaded by Universitat Kaiserslautern on 1/26/2023 8:54:05 AM.

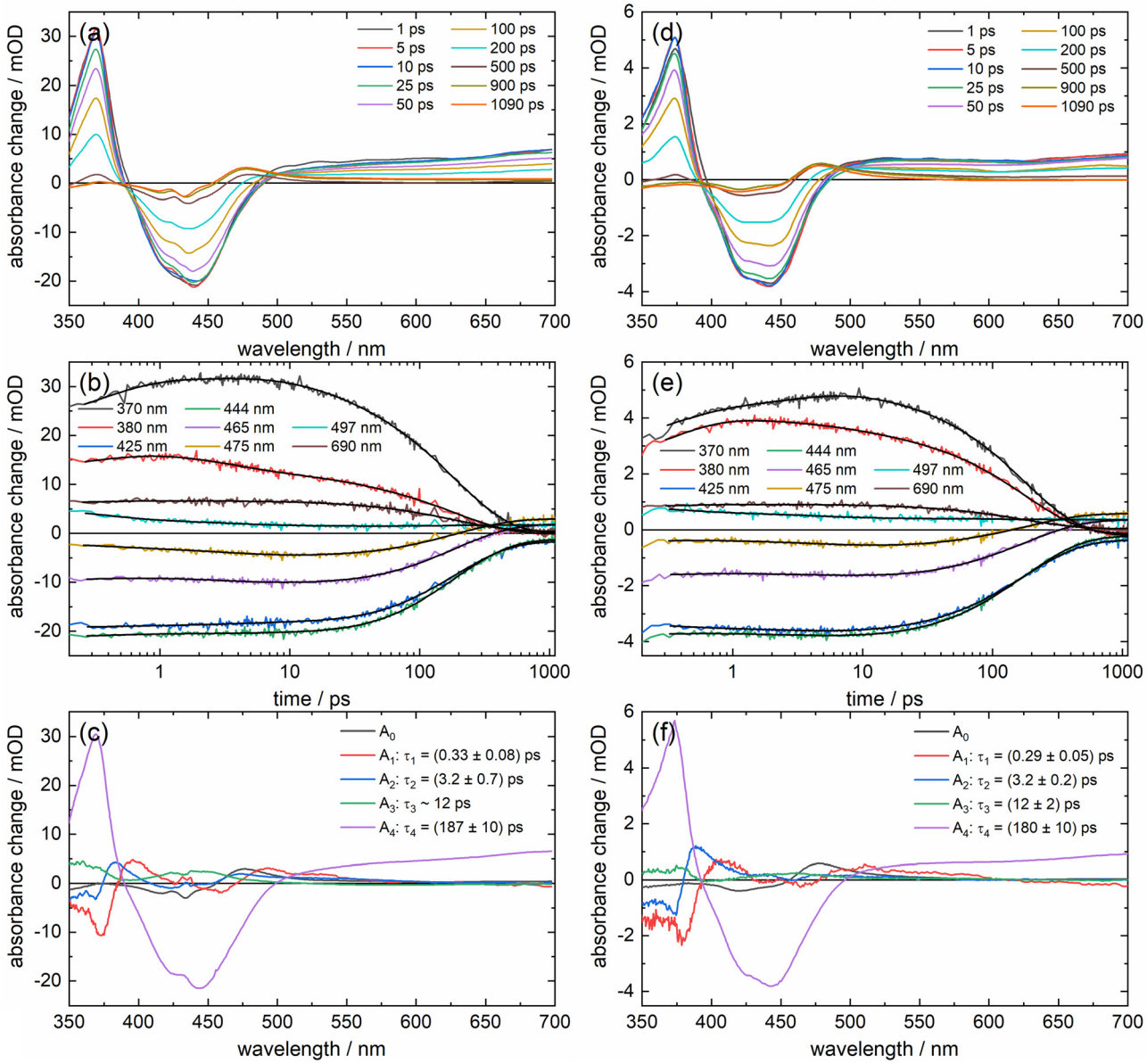

Fig. 6 Difference spectra at selected delay times (a and d), absorbance transients at selected wavelengths (b and e) and decay associated spectra (DAS) (c and f) for $[Ru(bpy)_2(na)_2]^{2+}$ (**1**) in H_2O, excited at 425 nm in a rotating cell (a–c) and at 340 nm in a flow cell (d–f). Solid black line in (b and e) and DAS in (c and f): result of global analysis according to eqn (2).

dissociation of a ligand (*via* a repulsive ^{3}MC-excited state). In consequence, Liu *et al.* suggested for $[Ru(bpy)_2(CH_3CN)_2]^{2+}$, that in the region above 550 nm, the signal can be assigned to the PCI $[Ru(bpy)_2(CH_3CN)]^{2+}$.[22] This suggestion is supported by the investigations on **1** from Greenough *et al.*, where TD-DFT calculations on the PCI, *i.e.* $[Ru(bpy)_2(na)]^{2+}$, revealed absorption of the PCI in this spectral region.[30] Sun *et al.* reported the spectral signature of the ^{3}MLCT state for $[Ru(X\text{-}bpy)_3]^{2+}$ complexes (X = H, 6-methyl), which also shows a plateau-like behaviour above 500 and up to 700 nm.[17,20,42] Therefore, contributions of the ^{3}MLCT-, the ^{3}MC-excited states and the PCI are considered possible above 550 nm. Interestingly, our results on **2** suggest a more accurate assignment (*cf.* discussion of model G).

For long delay times, all signals decay to zero except a residual negative band in the GSB region, and a new, positive band at 475 nm, which is assigned to the formation of the mono-aquated photoproduct **2** *via* coordination of H_2O to the PCI.[30] A simulation of the difference spectrum at the latest delay time (1090 ps) with the static UV/Vis absorption spectra of **1** (as bleach signal) and **2** (as product signal) confirms this assignment (*cf.* ESI,† S5c).

The absorbance transients for selected wavelengths are shown in Fig. 6b and e with fits resulting from global analysis (eqn (2)), which yields the decay associated spectra (DAS) shown in Fig. 6c and f and time constants in Table 3.

As observed for the difference spectra, the global analysis (DAS and time constants) shows that the entire spectro-temporal

Published on 09 January 2023. Downloaded by Universitat Kaiserslautern on 1/26/2023 8:54:05 AM.

evolution for excitation at 425 nm (Fig. 6b and c) and for excitation at 340 nm (Fig. 6e and f) is very similar (Table 3). Thus, it is concluded that in solution excitation at 340 nm leads to similar dynamics as excitation at 425 nm. This is possible *via* ultrafast (within our system response time) internal conversion and ISC to a ^{3}MLCT-excited state after photo-excitation into a higher-lying ^{1}MLCT-excited state, in accordance with the literature.[8,43–45] We thus here confirm by experiment the conjecture by Greenough *et al.*[30] who excited at 340 nm exclusively.

Inspection of the absorbance transients at 370 and 380 nm (Fig. 6b and e) reveals that at least three time constants are required for a sufficient description of the data: a very fast but small increase is followed by a slower decay, which obviously is composed of at least two processes on different timescales (τ_1, τ_2 and τ_4 in Table 3). A fourth-time constant (τ_3 = 12 ps) leads to an improved fit result – especially in the range of the GSB signal around 444 nm. A proper unequivocal fit result with a corresponding fourth time constant could not be obtained for the rotating cell measurements with excitation at 340 nm (see the ESI,† Fig. S1), most likely owed to the small amplitude of A_3 and the smaller signal-to-noise ratio. But it was clearly required in the low-noise flow cell measurements with excitation at 340 nm (Fig. 6e).

A_0 in Fig. 6c and f represents the signal for infinite delay time and is basically identical with the difference spectrum at 1090 ps (*cf.* above).

A_1 and A_2 (Fig. 6c and f) strikingly resemble each other – with A_2 being blue-shifted for $\sim$8 nm compared to A_1 – thus indicating similar processes. Their characteristic difference band-like shape and localization in the red edge of the UV ^{3}MLCT-ESA band suggest vibrational relaxation (VR) of this state, with a signal rise in the higher and simultaneous signal decay in the lower energy region, indicating a VR-typical narrowing of this band (*cf.* difference spectra on this time scale). Note however that the observation of two such features, associated with different time constants τ_1 and τ_2, implies the existence of two kinetically independent processes, *e.g.* consecutive or in parallel (*cf.* discussion below). In addition, a comparison of A_1 (λ_{pump} = 425 nm) (Fig. 6c) with A_1 (λ_{pump} = 340 nm) (Fig. 6f) reveals a redshift of the minima and maxima of $\sim$8 nm for 340 nm excitation, and for A_2 an analogous redshift of $\sim$5 nm. This is in accordance with the assignment to VR, because more excess (vibrational) energy as in the case of 340 nm excitation leads to a larger band broadening and to correspondingly red-shifted features in the DAS. Furthermore, it is noted that for wavelengths above roughly 550 nm, both A_1 and A_2 (as well as A_3) basically are of zero amplitude. This is equally evident in the absorbance transient at 690 nm (Fig. 6b and e), which shows no change for the early timescales. It should be kept in mind that for A_1 and A_2, with the single time constants τ_1 and τ_2, we cannot exclude more complex, underlying processes such as intramolecular vibrational redistribution, structural rearrangements or vibrational cooling. However, they are not analysable with our means here, and thus we apply, pragmatically, single time constants.

A_3 (Fig. 6c and f) is non-zero and of small positive amplitudes only around 365 and 430–460 nm, *i.e.* the region of ground state absorption of **1** and **2** (Fig. 4).

A_4 (Fig. 6c and f) is non-zero in the entire spectral range, *i.e.* ground state recovery (GSR, A_4 neg.) and ESA-decay (A_4 pos.). Assuming that the involved different electronically excited states (^{3}MLCT, ^{3}MC, PCI) and processes might contribute to a different extent in different spectral regions and in preparation for the discussion on the kinetic model(s) below, a more detailed analysis of the TA data was performed, such that local multi-exponential analysis was applied to distinct spectral regions instead of the entire spectral region (*cf.* ESI,† S5a). Interestingly, no deviations (within error limits) were found for the time constants and DAS as compared to the global analysis. It is thus concluded that GSR and decay of ESA, possibly comprising contributions of ^{3}MLCT, ^{3}MC and PCI (*cf.* above), occur simultaneously with solely τ_4. This holds in particular for the region above 550 nm, where A_4 is the only DAS with a significant amplitude, and thus the states contributing to the absorption change in this region are populated within the system response and decay with τ_4.

The formation of **2** is not distinctively assignable to any of the DAS, although it could contribute to A_4, meaning that it would be formed with τ_4. However, our analysis shows as well that the spectral shape of the red edge of the negative GSB (region of photoproduct absorption around 475 nm) in the difference spectrum at 0.3 ps is compatible with a positive contribution of **2** with a quantum yield of up to roughly 35%, suggesting its (possible) formation within the system response time (*cf.* discussion below and ESI,† S5c).

UV/Vis fs TA of $[Ru(bpy)_2(na)(H_2O)]^{2+}$ (2) in H_2O. The photoinduced dynamics of **2** in H_2O was investigated with excitation at 340 nm, the corresponding difference spectra are shown in Fig. 7a. The spectral evolution is very similar to **1** and thus corresponding assignments of the observed signals are obvious: (i) ^{3}MLCT-ESA around 370 nm, (ii) GSB red-shifted with a minimum at 465 nm (in accordance with the static UV/Vis absorption spectra in Fig. 4), (iii) ESA above 540 nm as a possible superposition of ^{3}MLCT-, ^{3}MC-excited states and the PCI. However, no product band is observed for long delay times and all absorbance signals decay completely to zero.

Absorbance transients at selected wavelengths are shown in Fig. 7b and the decay associated spectra (DAS) resulting from global analysis (eqn (2)) are shown in Fig. 7c, with corresponding fit curves in Fig. 7b and time constants in Table 3.

The pattern of A_1 in the ^{3}MLCT-ESA region around 370 nm is basically identical to **1**, with τ_1 roughly twice as large for **2**.

Table 3 Time constants resulting from global analysis (eqn (2)) of femtosecond transient absorption data of $[Ru(bpy)_2(na)_2]^{2+}$ (**1**) (Fig. 6) and $[Ru(bpy)_2(na)(H_2O)]^{2+}$ (**2**) (Fig. 7) in H_2O – corresponding decay associated spectra in Fig. 6c, f and 7c

	λ_{pump}/nm	τ_1/ps	τ_2/ps	τ_3/ps	τ_4/ps
1	**425**	0.3 ± 0.1	3.2 ± 0.7	∼12	187 ± 10
1	**340**	0.3 ± 0.1	3.2 ± 0.2	12 ± 2	180 ± 10
2	**340**	0.6 ± 0.1	3.0 ± 0.3	83 ± 5	

This journal is © the Owner Societies 2023

Published on 09 January 2023. Downloaded by Universitat Kaiserslautern on 1/26/2023 8:54:05 AM.

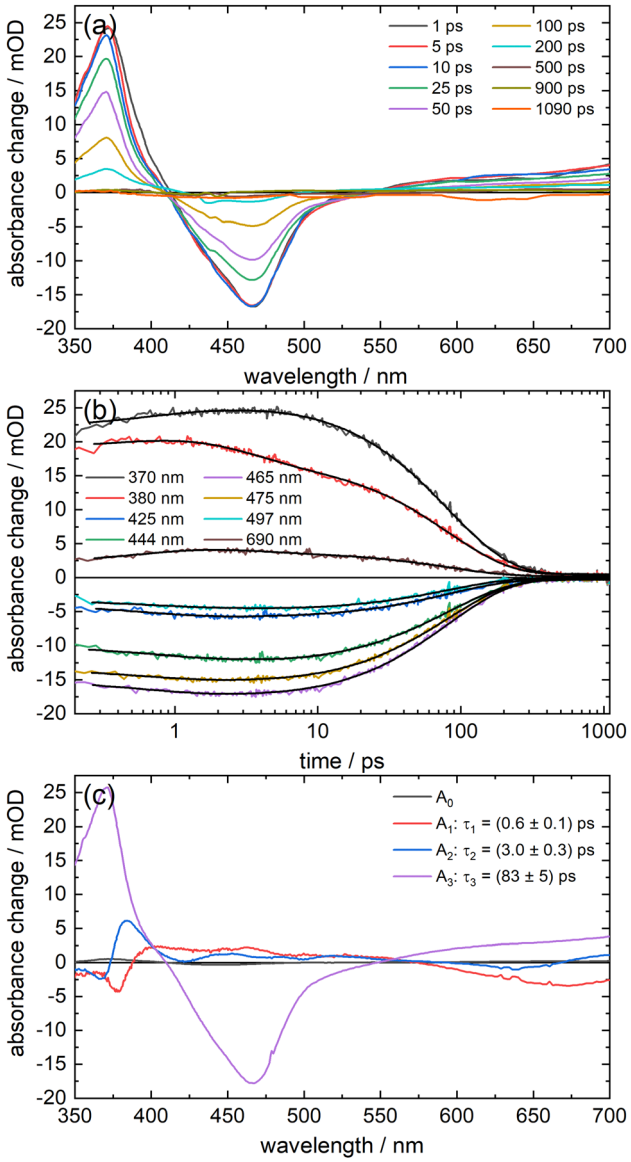

Fig. 7 Difference spectra at selected delay times (a), absorbance transients at selected wavelengths (b), and decay associated spectra (DAS) (c) for $[Ru(bpy)_2(na)(H_2O)]^{2+}$ (**2**) in H_2O excited at 340 nm (rotating cell). Solid black line in (b) and DAS in (c): result of a global analysis according to eqn (2).

However, in contrast to **1**, the ESA above 550 nm increases with τ_1 (negative A_1 in Fig. 7c). It can hardly be associated with ^{3}MLCT ESA since the characteristic band of the latter around 370 nm rises instantaneously.

Note that A_2 and τ_2 are very similar to **1**. A_3 represents GSR (Fig. 7c) and decay of the ESA in the complete spectral range, more than twice as fast as in **1** (*cf.* Table 3). As for **1**, a local analysis yields a single long time constant, *i.e.*, only ~83 ps for the complete spectral range (within error limits). An additional (fourth) time constant, as for **1**, was not clearly identifiable.

It is noted that neither in the difference spectra nor in the DAS indications are found for (transient) photoinduced dissociation of the remaining na ligand of **2**: (i) no significant A_0 amplitude (Fig. 7c) and (ii) no change in the static absorption spectra before and after the measurement occurred, *i.e.* all excited molecules return to the initial electronic ground state and no formation or slow accumulation of a photoproduct is observed, (iii) in particular, no product band arises around 480 nm, *i.e.* the peak of the $[Ru(bpy)_2(H_2O)_2]^{2+}$ absorption spectrum[30] (*cf.* ESI,† Fig. S28). This result is in line with the gas phase data that likewise do not show significant dissociation of the remaining na ligand.

On the other hand, analogous to **1**, excited state deactivation *via* ligand dissociation can be expected for **2** in H_2O, and in fact, in the gas phase UV PD experiments, H_2O-loss was found for **2** (*cf.* above). This is in line with theoretical results on $[Ru(bpy)_2(CH_3CN)(H_2O)]^{2+}$,[46] for which dissociation of the H_2O ligand was found to be preferred to that of the CH_3CN ligand, resulting in the reformation of the monoaqua-complex.

Thus, based on the comparison and great similarities with **1**, we here propose very similar deactivation processes for **2**, with the difference that in the latter, the H_2O- and not the na ligand dissociates. After dissociation of the H_2O ligand, recombination with an H_2O solvent molecule to the PCI leads back to **2**, and no distinguishable photoproduct is formed. These recombination processes are not distinctively observed in our data.

Discussion

Ultrafast dynamics in solution

Based on these observations, in the following, we propose and discuss generalized reaction schemes for **1** and **2**, shown in Fig. 8a and b.

Two possibilities for the formation of the photoproduct **2** from **1** that are compatible with our data are with τ_4, as part of A_4 (model A, slow variant), or within the system response (model B, ultrafast variant). The similarity of the chemical structure of **1** and **2** and their similar observed dynamics strongly suggest analogous deactivation schemes. For both models, we follow the common paradigms, that first, ligand dissociation and exchange are considered to proceed *via* ^{3}MC states[13,16–18] (although exceptions have been proposed, *e.g.* nitrile dissociation from ^{3}MLCT without population of ^{3}MC[47]), and second, the decay of ^{3}MLCT to GS occurs on the μs time-scale,[7] but is strongly accelerated by the coupling with a ^{3}MC state. In consequence, our observation of synchronous GSR and ESA decay at 370 nm (^{3}MLCT) and above 550 nm, requires corresponding strong kinetic coupling of the participating states (*i.e.* boundary conditions for the rate constants involved).

Model A (slow variant). Equally for both **1** (Fig. 8a) and **2** (Fig. 8b):

– Ultrafast ISC from ^{1}MLCT to ^{3}MLCT (within system response).

– VR with τ_1 and τ_2 in two consecutive (or parallel), kinetically separated ^{3}MLCT states.

– Fast equilibria between the ^{3}MLCT states and a $^3MC_{hexa}$ (*cf.* Introduction[16,24]), that, together with VR, constitute the

Published on 09 January 2023. Downloaded by Universitat Kaiserslautern on 1/26/2023 8:54:05 AM.

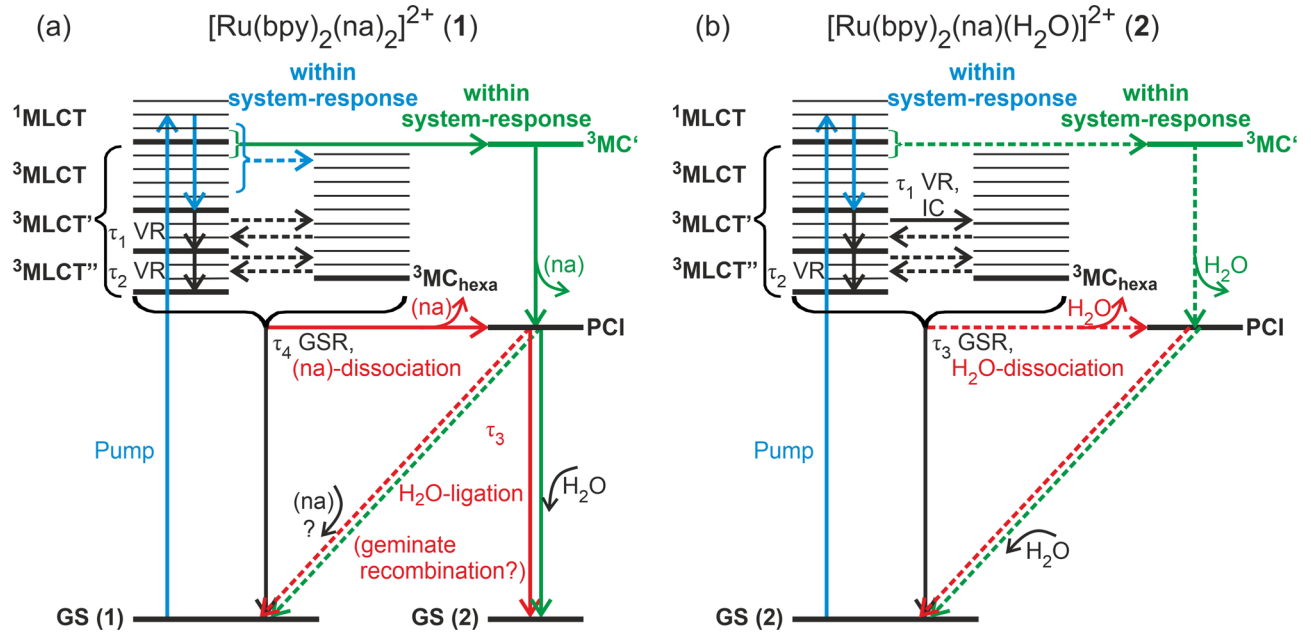

Fig. 8 Reaction schemes for $[Ru(bpy)_2(na)_2]^{2+}$ (**1**) (a), and $[Ru(bpy)_2(na)(H_2O)]^{2+}$ (**2**) (b) in H_2O. Solid: states and pathways as indicated by our observations. Dashed: pathways not directly indicated by our observations. Black: states for both model A and B. Blue: within system response. Red: model A. Green: model B. For a detailed explanation *cf.* main text.

apparent τ_1 and τ_2. This relates to and is justified by the observation of the single slow time constant for the decay of the ESA above 550 nm, assigned to ^{3}MC contributions (*cf.* discussion of model G).

– In particular, the energetically lowest equilibrium is fast with respect to the slowest time constant (τ_4 in **1**, τ_3 in **2**) and thus facilitates the joint decay (as observed) of global ESA *via* distinct channels and the simultaneous GSR with the slowest time constant.

Specifics for **1**:

– Consistent with not observing the build-up of absorption above 550 nm would be an ultrafast (within system response) formation of ^{3}MC *via* branching in ^{3}MLCT or in ^{1}MLCT (blue dashed arrow in Fig. 8a). Branching in the former, in turn, requires three ^{3}MLCT states instead of two, for kinetic decoupling reasons.

– The apparent rate $1/\tau_4$ is the sum of the rates for GSR and for dissociation (formation of PCI).

– From PCI, mono-aquation occurs rapidly with respect to τ_4. This corresponds to the formation of **2** with τ_4 in the slow time regime. Owed to its fast decay, PCI does not build up kinetically and is therefore not directly observed.

– Furthermore, we cannot exclude geminate recombination and thus GSR as another fast decay channel from PCI.

– Indications for the kinetics of mono-aquation and geminate recombination with the common time constant τ_3 emerge from A_3. The shape of A_3 is consistent with the absorption spectrum of **2**, possibly including a contribution from the absorption spectrum of **1**. Note that in this case, the faster kinetic step (τ_3) follows the slower one (τ_4), and A_3 therefore appears with the opposite sign for mathematical reasons (*i.e.*, the apparent positive A_3 indicates the formation and not the decay of a state (*cf.* ESI,† S5e)). The rate τ_3^{-1} is consistent with quantum chemical simulations predicting H_2O-ligation in a range less than 10 ps[48] and the observation of spontaneous attachment of H_2O on PCI in our gas phase experiments.

Specifics for **2**:

– The $^3MC_{hexa}$ is formed with the τ_1 process, as observed for the signal build-up in the long-wavelength region.

– As for **1**, the ^{3}MLCT/$^3MC_{hexa}$ equilibrium decays slowly (with τ_3).

– Subsequent processes such as dissociation, H_2O-coordination and geminate recombination are expected as in **1**, but elude observation (mostly due to degenerate exchange of H_2O/H_2O and thus no distinct photoproduct). If they occur, the kinetic arguments apply as for **1**. However, as stated above, an additional, fourth time constant could not be clearly identified. This is reasonable since here the suspected ligand exchange (H_2O/H_2O) occurs probably faster than for **1** (na/H_2O), where a bulkier na ligand may slow down the H_2O ligation.

Model B (ultrafast variant). Equally for both **1** and **2**:

– Dissociation including subsequent processes (mono-aquation and geminate recombination) occurs in a branching reaction from ^{1}MLCT or ^{3}MLCT *via* ^{3}MC' within the system response, and thus, is kinetically not resolved.

– Kinetically decoupled from this process, VR occurs with τ_1 and τ_2 (*cf.* above).

– As in model A, the ^{3}MLCT/$^3MC_{hexa}$ equilibrium decays with the slowest time constant, however exclusively to the ground state, *i.e.* only *via* one decay channel.

Discussion of model G[30]. In light of the relatively high number of involved states and processes anticipated for the observed ligand exchange reaction, our transient spectra as well as the DAS yield surprisingly little complexity. This may be due

This journal is © the Owner Societies 2023

Published on 09 January 2023. Downloaded by Universitat Kaiserslautern on 1/26/2023 8:54:05 AM.

to extensive spectral similarity of related species or to kinetic reasons. Both aspects are found or required in our models. Interestingly, this is also the case for model G about the primary photoreaction of **1**,[30] which furthermore also includes aspects of both model A and model B:

(i) According to model G, dissociation and formation of a 'caged' PCI-na-complex is indicated by the long-wavelength absorption signal and occurs very fast, with 0.36 ps. However, we do not observe the related signal build-up (*cf.* above).

(ii) In model G, 'caged' PCI-na decays *via* branching with a slow apparent time constant of 155 ps (*cf.* ESI,† S5b) to the GS and, *via* the 'separated' PCI, to the product **2**. Together with the GSR from the relaxed ^{3}MLCT with 180 ps, this generates two feeding processes for GS, that we cannot confirm (*cf.* ESI,† S5b). In particular, following model G, the decay of absorbance $>$ 550 nm should be solely determined by the time constant 155 ps, in contrast to the 180 ps (187 ps), we observe for the complete spectrum investigated. In fact, it is not surprising that in model G, the fit reveals the time constant 155 ps close to the 180 ps found for GSR, since the GSR is clearly dominated by the latter. The similarity of these values of two kinetically independent rates could be accidental. However, our results on **2**, including likewise a single time constant for GSR (τ_3), strongly suggest kinetics very similar to **1**. Thus, if one were to apply the same model of two independent feeding channels for GSR for the photochemistry of **2**, an equivalent 'accident' would be required, now with τ_3 = 83 ps and the hypothetical second time constant. This again makes this aspect of model G unlikely.

(iii) First, (i) and (ii) raise the question of the assignment of the long-wavelength absorption signal ($>$550 nm). Based on the results on **2** and their similarity with **1**, ^{3}MLCT can be excluded, owed to the delayed signal rise (in **2**), as compared to the instantaneous rise around 370 nm. Second, since in **2**, ligand (H_2O) dissociation is expected to occur faster than in **1** (na) (*cf.* gas phase results) and both lead to the same species (PCI), again the delayed signal rise in **2** contradicts its spectral assignment to PCI. Thus, we assign this long wavelength signal to ^{3}MC.

(iv) In order to achieve kinetic decoupling for 'fast' (0.36 ps) and 'slow' (3.6 ps) VR, model G invokes a barrier in ^{3}MLCT. However, this kinetic separation is not included in the set of differential equations that are the quantitative basis for model G.

In summary, model G comes close to our model in that it suggests very fast and very slow processes for dissociation and the GSR, decay of ^{3}MLCT as well as the formation of **2**, respectively, and intermediate time scales for VR. However, it contains aspects that should show with our approach of global analysis in both **1** and **2**, but which we cannot confirm. Note that both target analysis[30] and global analysis have advantages and disadvantages, but global analysis clearly yields, without any model assumptions (as in target analysis), the apparent time constants that are constituted by the underlying rate constants of any kinetic model, including model G.

With regard to model G, our models A and B incorporate several new aspects that have to be introduced on grounds of our experimental results on **1** and **2**. They include the implementation of multiple ^{3}MLCT states to allow kinetically independent processes A_1 and A_2, as well as kinetic equilibria to satisfy the global singular time constant for ^{3}MLCT decay, GSR, mono-aquation and geminate recombination. It is noted that these aspects concerning time scales as well as the participation of several ^{3}MLCT states and their coupling to ^{3}MC states are compatible with and have been broadly discussed in the highly diverse literature on the photochemistry of Ru^{II}-polypyridine complexes. For a more detailed survey and discussion of the literature *cf.* ESI,† S5f.

Ultrafast dynamics in gas phase/ion trap

The scheme for the ultrafast dynamics of $[Ru(bpy)_2(na)_2]^{2+}$ (**1**) in the gas phase is based on the following main experimental observations and results of theoretical calculations: (i) only two time constants in the few ps range (τ_1 = 0.5 ps, τ_2 = 3.0 ps; @430 nm) are necessary to fit the decay curves, (ii) the transient signal decays to zero within a few ps, *i.e.*, no long(er)-lived components are detectable, (iii) the mass spectrometric analysis revealed only one major fragment ion signal, namely $[Ru(bpy)_2(na)]^{2+}$ (PCI), after irradiation in the ion trap, confirming an efficient na ligand photodissociation in the gas phase, (iv) the time constant τ_2 exhibits a monotonic shortening as function of decreasing excitation wavelength (430–340 nm), which suggests an acceleration of the underlying process upon increase of internal energy of the complex, and (v) finally we assume, backed by calculations,[15] that the ^{3}MLCT states are up-shifted in energy (relative to the ^{3}MC states) in the gas phase, due to the lack of solvent stabilization of the charge separation.

These results lead us to propose the following scenario (Fig. 9): after photoexcitation (in the 340–430 nm region), **1** is prepared by metal-to-ligand-charge-transfer in a singlet excited (^{1}MLCT) state, which interconverts by ISC within the experimental system response ($<$100 fs) to the according triplet manifold (^{3}MLCTs). These states could be located on the bpy as well as na ligands (see our calculations/literature) and allow for fast internal vibrational redistribution (IVR) of the excess energy resulting from the IVR process by τ_1. Subsequent to this process, we propose that a strong coupling (IC) to the metal-centered ^{3}MC state takes place, which is often invoked for explaining the photolability of these systems.[13,17] This LF (ligand field) or dd state is characterized by a long Ru–N distance equilibrium value and intersects at elongated Ru–N distances both the ground state as well as a dissociating state. Recently, Göttle *et al.* could locate a hexa as well as a penta coordinated ^{3}MC minimum on the electronically excited state surface.[24] These results further suggest that (in dependence on the type of ligand and thus LF strength) a direct dissociation, *via* the $^3MC_{hexa}$, is feasible, so that we assign this process here to the time constant τ_2 (consistent with the literature, where a clear structure was not attributable to ^{3}MC by spectroscopy). Since we cannot rely on additional structural or spectroscopic information tied to the time constants observed in the gas phase, this scenario cannot be proven beyond doubt and (slightly) different pathways might be possible. For instance

Published on 09 January 2023. Downloaded by Universitat Kaiserslautern on 1/26/2023 8:54:05 AM.

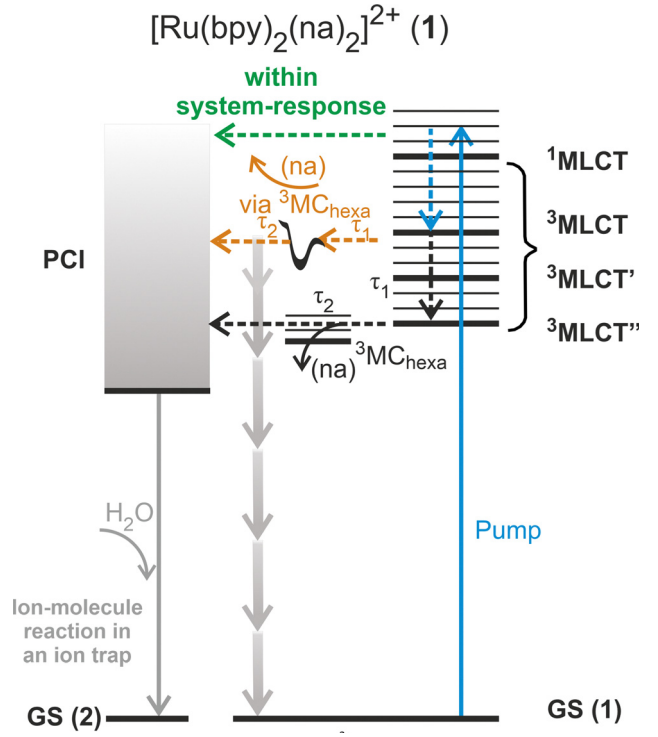

Fig. 9 Reaction scheme for $[Ru(bpy)_2(na)_2]^{2+}$ (**1**) in gas phase. Blue: within system response. Black/yellow/green: pathways consistent with our observations. Dashed: states/pathways not directly indicated by our observations. For a detailed explanation *cf.* main text.

(marked in yellow in the scheme of Fig. 9), one could suggest that the IC to the ^{3}MC proceeds already from energetically higher levels (with τ_1), but is slowed down at the $^3MC_{hexa}$ intermediate due to a barrier (as discussed in ref. 24) towards the $^3MC_{penta}$ (τ_2). This pathway might explain easier the energy dependence of τ_2, since the surmounting of the barrier is facilitated from higher energetic levels. Moreover, we cannot exclude the possibility of a contribution of a direct, very fast (within system response) ligand dissociation (dashed green arrow in Fig. 9), but the gas phase transients do not indicate a significant portion of **1** decaying in this way.

Although an unambiguous classification of the dissociation pathway cannot be given, it is obvious that the time constants obtained from gas phase experiments could be mainly ascribed to the dissociative part of the dynamics and energetic deactivation by VR is not active here. This could be mainly attributed to the lack of solvent acting as a cooling bath and the energetic upshift of the relevant charge-transfer states funnelling population towards the metal-centered state and subsequent dissociation.

Conclusions

In this contribution, we present the comparison of the gas phase and aqueous solution phase ultrafast photodynamics of $[Ru(bipyridine)_2(nicotinamide)_2]^{2+}$ ($[Ru(bpy)_2(na)_2]^{2+}$, (**1**)), which allows assessing molecule–solvent interactions and their consequences for na ligand dissociation and mono-aquation kinetics as well as for according pathways. Additionally, we present the first results on the primary photoinduced dynamics of the photosolvation product ($[Ru(bpy)_2(na)(H_2O)]^{2+}$, (**2**)) in aqueous solution.

The values for the apparent time constants obtained for **1** in the gas phase and solution are similar in the sub-ps and few ps ranges. However, the slower ground state recovery (GSR) on the scale of *ca.* 180 ps was exclusively observed in the solution phase. This is substantiated by the, theoretically predicted,[15] energetical downshift of the ^{3}MC relative to the ^{3}MLCT manifold in the gas phase compared to the solution phase due to the lack of solvent stabilisation of the latter. As a result, no long-lived (>few ps) states were observed and the photoinduced processes are clearly altered in the gas phase. With the high yield of the penta-coordinated intermediate (PCI) as the single photofragment, the processes of the apparent time constants in the gas phase (*ca.* 0.5 ps and *ca.* 3 ps) are strongly connected to the dissociation steps of **1**. In contrast, the observations in the solution phase on these time scales are assigned to vibrational relaxation (VR) in the ^{3}MLCT manifolds. As the dissociation in the gas phase is anticipated to be accelerated in comparison to the solution phase and takes place in the range of a few ps, a substantial part of the dissociation in the solution phase is expected to be slower as the previously reported[30] sub-ps regime. Thus, for the solution phase, we favour our model A, containing the dissociation alongside the GSR with the slow time constant (180 ps for **1** and 83 ps for **2**) in contrast to the previously proposed[30] ultrafast dissociation as featured in our model B.

We investigated **1** in H_2O for the first time under excitation in the lower energy MLCT bands (425 nm) and confirm the often-used assumption that excitation in the higher energy bands (340 nm) does not significantly alter the observed dynamics due to the fast ISC (^{1}MLCT → ^{3}MLCT). Note however that the wavelength-dependency found for the few-ps time constant in the gas phase stands as a warning for a generalization of this assumption.

Even if it is common knowledge from static irradiation experiments and theory, we show, for the first time by direct inspection of the photoinduced primary dynamics of **2** in H_2O, that the biaqua species $[Ru(bpy)_2(H_2O)_2]^{2+}$ is formed *via* a fundamentally different mechanism as the monoaqua species. This is further corroborated by the dissociation behaviour of **2** in the gas phase, where exclusively H_2O- instead of na loss was observed.

In this regard, **2** in aqueous solution furthermore proved as a valuable reference system for **1**. Their similar apparent dynamics suggest an analogous model for both **1** and **2** in solution with na- and H_2O-dissociation and exchange, respectively. This is supported by the gas phase results (H_2O loss for **2** more efficient as na loss for **1**). As an important consequence, our results on **2** yield the assignment of the spectral region > 550 nm to the often elusive ^{3}MC state for **1** and **2**, which is here for the first time reported for this dissociation-prone type of complexes. In addition, this leads to proposing the equilibrium of the ^{3}MLCT/^{3}MC manifolds, which enables the slow dissociation synchronously with GSR and subsequent fast product formation.

This journal is © the Owner Societies 2023

Published on 09 January 2023. Downloaded by Universitat Kaiserslautern on 1/26/2023 8:54:05 AM.

In summary, our strategy of combined investigation of the gas and solution phases clearly shows the impact of solvent interactions on photoinduced ligand dissociation for **1** and **2**. Future studies of chemically substituted ligands of **1** and **2** (as presented in the Introduction section) will allow testing the kinetic model and ligand dissociation pathways presented here.

Conflicts of interest

There are no conflicts to declare.

Acknowledgements

We gratefully acknowledge the support from the German Science Foundation (DFG) by research grants to WT, CR and RD (TH 550/23-1, RI 749/7-1, DI 405/9-1), and Collaborative Research Center CRC/Transregio 88 ''Cooperative effects in homo- and heterometallic complexes (3MET)'', projects B2 (WT) and C4 (CR and RD). CR and RGEI thank the SPP 2102 ''Light-controlled reactivity of metal complexes'' for support. We thank Maximilian Theiss for performing the static irradiation series shown in the ESI,† Fig. S28.

Notes and references

1 *Ruthenium Complexes – Photochemical and Biomedical Applications*, ed. A. A. Holder, L. Lilge, W. R. Browne, M. A. W. Lawrence and J. L. Bullock Jr., Wiley-VCH, Weinheim, 2018 and references within.
2 L. Zayat, O. Filevich, L. M. Baraldo and R. Etchenique, *Philos. Trans. R. Soc., A*, 2013, **371**, 20120330.
3 N. A. Smith and P. J. Sadler, *Philos. Trans. R. Soc., A*, 2013, **371**, 20120519.
4 J. N. Demas and D. G. Taylor, *Inorg. Chem.*, 1979, **18**, 3177–3179.
5 T. J. Meyer, *Pure Appl. Chem.*, 1986, **58**, 1193–1206.
6 D. W. Thompson, A. Ito and T. J. Meyer, *Pure Appl. Chem.*, 2013, **85**, 1257–1305.
7 A. Amini, A. Harriman and A. Mayeux, *Phys. Chem. Chem. Phys.*, 2004, **6**, 1157–1164.
8 N. H. Damrauer, G. Cerullo, A. Yeh, T. R. Boussie, C. V. Shank and J. K. McCusker, *Science*, 1997, **275**, 54–57.
9 A. Vlček, *Coord. Chem. Rev.*, 2000, **200–202**, 933–978.
10 M. Chergui, *Dalton Trans.*, 2012, **41**, 13022–13029.
11 O. S. Wenger, *Chem. – Eur. J.*, 2019, **25**, 6043–6052.
12 C. Cebrián, M. Pastore, A. Monari, X. Assfeld, P. C. Gros and S. Haacke, *ChemPhysChem*, 2022, **23**, e202100659.
13 J. V. Caspar and T. J. Meyer, *Inorg. Chem.*, 1983, **22**, 2444–2453.
14 J. T. Hewitt, P. J. Vallett and N. H. Damrauer, *J. Phys. Chem. A*, 2012, **116**, 11536–11547.
15 A. Soupart, I. M. Dixon, F. Alary and J.-L. Heully, *Theor. Chem. Acc.*, 2018, **137**, 37.
16 A. Soupart, F. Alary, J.-L. Heully, P. I. P. Elliott and I. M. Dixon, *Coord. Chem. Rev.*, 2020, **408**, 213184.
17 Q. Sun, S. Mosquera-Vazquez, L. M. Lawson Daku, L. Guénée, H. A. Goodwin, E. Vauthey and A. Hauser, *J. Am. Chem. Soc.*, 2013, **135**, 13660–13663.
18 P. S. Wagenknecht and P. C. Ford, *Coord. Chem. Rev.*, 2011, **255**, 591–616.
19 A. Cotic, I. Ramírez-Wierzbicki, G. E. Pieslinger, B. M. Aramburu-Trošelj and A. Cadranel, *Inorg. Chim. Acta*, 2021, **518**, 120246.
20 Q. Sun, B. Dereka, E. Vauthey, L. M. Lawson Daku and A. Hauser, *Chem. Sci.*, 2017, **8**, 223–230.
21 T. Mukuta, S. Tanaka, A. Inagaki, S. Koshihara and K. Onda, *ChemistrySelect*, 2016, **1**, 2802–2807.
22 Y. Liu, D. B. Turner, T. N. Singh, A. M. Angeles-Boza, A. Chouai, K. R. Dunbar and C. Turro, *J. Am. Chem. Soc.*, 2009, **131**, 26–27.
23 B. Durham, J. L. Walsh, C. L. Carter and T. J. Meyer, *Inorg. Chem.*, 1980, **19**, 860–865.
24 A. J. Göttle, F. Alary, M. Boggio-Pasqua, I. M. Dixon, J.-L. Heully, A. Bahreman, S. H. C. Askes and S. Bonnet, *Inorg. Chem.*, 2016, **55**, 4448–4456.
25 D. Imanbaew, J. Lang, M. F. Gelin, S. Kaufhold, M. G. Pfeffer, S. Rau and C. Riehn, *Angew. Chem., Int. Ed.*, 2017, **56**, 5471–5474.
26 D. Imanbaew, Y. Nosenko, C. Kerner, K. Chevalier, F. Rupp, C. Riehn, W. R. Thiel and R. Diller, *Chem. Phys.*, 2014, **442**, 53–61.
27 F. Tureček, *Mass Spectrom. Rev.*, 2021, 1–21.
28 S. V. Kruppa, F. Bäppler, W. Klopper, S. P. Walg, W. R. Thiel, R. Diller and C. Riehn, *Phys. Chem. Chem. Phys.*, 2017, **19**, 22785–22800.
29 S. Xu, J. E. T. Smith and J. M. Weber, *J. Chem. Phys.*, 2016, **145**, 024304.
30 S. E. Greenough, G. M. Roberts, N. A. Smith, M. D. Horbury, R. G. McKinlay, J. M. Żurek, M. J. Paterson, P. J. Sadler and V. G. Stavros, *Phys. Chem. Chem. Phys.*, 2014, **16**, 19141–19155.
31 M. J. Frisch, *et al.*, *Gaussian 16, Revision C.01*, Gaussian, Inc., Wallingford CT, 2016, (full ref. in ESI†).
32 N. M. O'Boyle, A. L. Tenderholt and K. M. Langner, *J. Comput. Chem.*, 2008, **29**, 839–845.
33 R. Dennington, T. A. Keith and J. M. Millam, *GaussView, Version 6.0*, Semichem Inc., Shawnee Mission, KS, 2016.
34 J. Martens, G. Berden, C. R. Gebhardt and J. Oomens, *Rev. Sci. Instrum.*, 2016, **87**, 103108.
35 H. H. G. Jellinek and M. G. Wayne, *J. Phys. Chem.*, 1951, **55**, 173–180.
36 B. P. Sullivan, D. J. Salmon and T. J. Meyer, *Inorg. Chem.*, 1978, **17**, 3334–3341.
37 P. Hütchen, PhD thesis, TU Kaiserslautern, 2021.
38 L. Helm and A. E. Merbach, *Chem. Rev.*, 2005, **105**, 1923–1960.
39 R. Matheu, M. Z. Ertem, C. Gimbert-Suriñach, X. Sala and A. Llobet, *Chem. Rev.*, 2019, **119**, 3453–3471.
40 M. Grupe, P. Boden, P. Di Martino-Fumo, X. Gui, C. Bruschi, R. Israil, M. Schmitt, M. Nieger, M. Gerhards, W. Klopper, C. Riehn, C. Bizzarri and R. Diller, *Chem. – Eur. J.*, 2021, **27**, 15252–15271.

Published on 09 January 2023. Downloaded by Universitat Kaiserslautern on 1/26/2023 8:54:05 AM.

41 C. Zippel, R. Israil, L. Schüssler, Z. Hassan, E. K. Schneider, P. Weis, M. Nieger, C. Bizzarri, M. M. Kappes, C. Riehn, R. Diller and S. Bräse, *Chem. – Eur. J.*, 2021, **27**, 15188–15201.
42 Q. Sun, S. Mosquera-Vazquez, Y. Suffren, J. Hankache, N. Amstutz, L. M. Lawson Daku, E. Vauthey and A. Hauser, *Coord. Chem. Rev.*, 2015, **282–283**, 87–99.
43 J. K. McCusker, *Acc. Chem. Res.*, 2003, **36**, 876–887.
44 A. C. Bhasikuttan, M. Suzuki, S. Nakashima and T. Okada, *J. Am. Chem. Soc.*, 2002, **124**, 8398–8405.
45 A. Cannizzo, F. van Mourik, W. Gawelda, G. Zgrablic, C. Bressler and M. Chergui, *Angew. Chem., Int. Ed.*, 2006, **45**, 3174–3176.
46 M. Kayanuma, M. Shoji and Y. Shigeta, *J. Phys. Chem. A*, 2019, **123**, 2497–2502.
47 L. M. Loftus, J. J. Rack and C. Turro, *Chem. Commun.*, 2020, **56**, 4070–4073.
48 I. M. Dixon, S. Bonnet, F. Alary and J. Cuny, *J. Phys. Chem. Lett.*, 2021, **12**, 7278–7284.

 This journal is © the Owner Societies 2023

3.2 Publication 2: Spectroscopy of a Series of Ru(II) Polypyridine Complexes in Gas Phase and Solution: Control of Electronic State Lifetime and Reactivity by Systematic Ligand Derivatization (submitted manuscript)

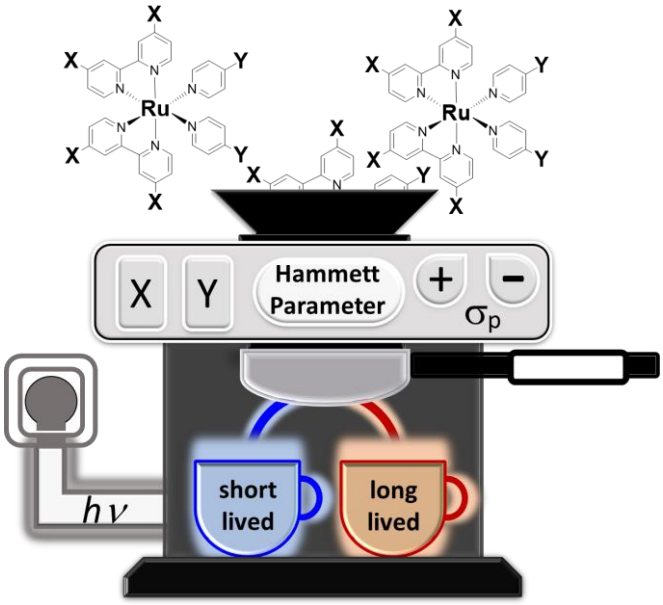

Preamble

R. G. E. Israil, L. Schüßler, P. Hütchen, W. R. Thiel, R. Diller, C. Riehn. The manuscript of this study has been submitted to *Chemistry - A European Journal* on the 18th of February **2025** with the number "chem.202500614" and is currently under review.

Contribution I was responsible for all measurements and data analysis related to gas-phase ion spectroscopy for 15 different compounds, encompassing UV photodissociation (UVPD), time-resolved photodissociation (τ-PD), collision-induced dissociation (CID), and mass spectrometry (MS^2/MS^3), along with theoretical calculations. I examined and interpreted the results from the methods outlined above, organized them for discussion, and incorporated them into the discussion section of the manuscript. The synthesis of the sample compounds and their characterization by NMR was carried out by Dr. Patrick Hütchen. Experiments involving static and time-resolved spectroscopy in the solution phase for four selected compounds were conducted by Dr. Lars Schüßler. The initial draft of the manuscript was

co-written by Dr. Schüssler and me, and further refined with valuable input from Prof. Dr. Rolf Diller and PD Dr. Christoph Riehn.

Synopsis The study investigates the ultrafast spectroscopy of Ru(II) polypyridyl complexes, focusing on how ligand modifications by chemical substitution influence their photophysical and photochemical properties in both gas-phase and solution environments. These complexes are critical for applications in solar energy conversion, luminescent imaging, and photocatalysis, where controlling the excited-state lifetimes and reactivity is essential. The research explores the effects of electron-donating and electron-withdrawing substituents on bipyridine (X-series) and pyridine (Y-series) ligands, using Hammett parameters to correlate these modifications with changes in the complexes' photochemical behavior, such as absorption wavelengths, excited state lifetimes, and computed ligand dissociation energies.

Ru(II) polypyridyl complexes typically exhibit metal-to-ligand charge transfer (MLCT) states, which play a key role in energy transfer and subsequent reactivity. The study differentiates between long-lived ^{3}MLCT states, crucial for luminescence and energy transfer, and metal-centered (^{3}MC) states, which promote ligand dissociation and other reactive processes such as ligand exchange, electron transfer, and the formation of reactive intermediates. Ligand substituents influence these electronic states in different ways: in the X-series, electron-withdrawing groups stabilize the MLCT state, increasing its lifetime and reducing dissociation, while in the Y-series, electron-withdrawing groups destabilize the MLCT state, facilitating ^{3}MC coupling, shortening lifetimes, and enhancing dissociation.

Gas-phase experiments, combined with ultrafast spectroscopy and quantum chemical calculations (TD-DFT), provided intrinsic insights into the electronic dynamics without solvent interference, confirming the trends observed in solution. The study demonstrates that Hammett parameters can be used to predict and control the photophysical behavior of Ru(II) complexes, offering a strategy for designing complexes with tailored excited-state properties for applications in photocatalysis, photodynamic therapy, and solar energy conversion. These findings lay the groundwork for further exploration of other Ru(II) complexes to refine control over their photochemical behavior.

Electronic Supporting Information (ESI) Further details on experimental methods and data, that support the findings of this study are available in the ESI, which I was in charge of creating. I contributed to the preparation and analysis of the ESI content, including mass spectra, UVPD spectra, τ-PD data, and theoretical calculations. Below is a summary of the ESI contents:

1. Synthesis and Sample Characterization..... 3

2. NMR Analysis and Correlation of Chemical Shift with Hammett Parameters..... 17

3. Mass Spectra and CID Breakdown/Appearance Curves..... 23

4. UV-PD Spectra, Calculated Absorption Spectra, Photoinduced Ligand Exchange..... 38

5. Transient Photodissociation Spectroscopy (τ-PD)..... 74

6. Ultrafast Transient Absorption Spectroscopy..... 172

7. X-Ray Structure Analysis and Refinement of the Complex Y6: CCDC 2418660..... 175

8. References 176

ESI Excerpts

The complete Electronic Supplementary Information (ESI) will be available upon acceptance of this manuscript. The following excerpts are provided to illustrate representative examples of the data included. Figure and table numbering corresponds to that in the original ESI document and has not been altered.

"3.2 Mass spectrometric analysis of the Y complexes"

f) Y6: $[Ru(bpy)_2(py\text{-}Y)_2]^{2+}$ with Y = (Me)

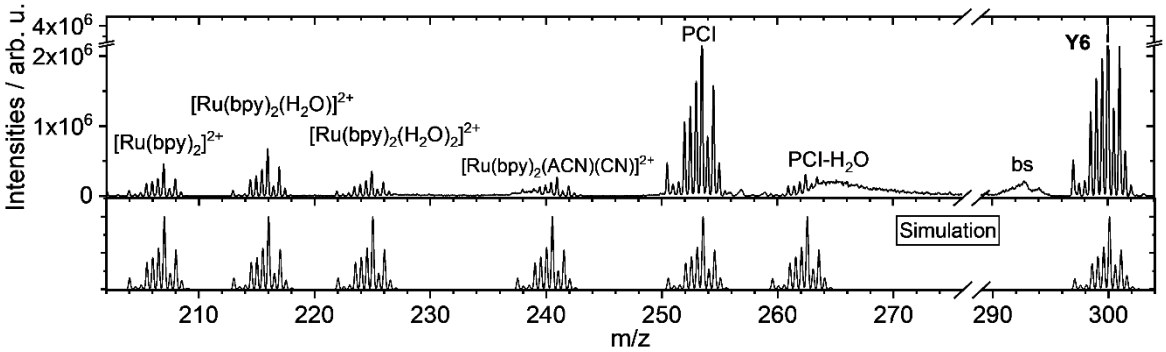

Figure 28 Photodissociation mass spectrometry of the **Y6** complex ($[Ru(bpy)_2(py\text{-}Me)_2]^{2+}$), isolated at m/z 300 and dissociated upon irradiation at 270 nm with a pulse energy of 1.8 µJ. The simulated isotope patterns are shown in the lower trace for comparison. The X- and Y-axes are truncated to focus on the isotope distribution, as no additional signals were observed. PCI = pentacoordinated intermediate; bs = broad signal.

Table 13 Assignment of the main fragments of **Y6** upon photodissociation, derived from Figure 28.

nominal m/z	assignment
207	$[Ru^{II}(bpy)_2]^{2+}$
216	$[Ru^{II}(bpy)_2(H_2O)]^{2+}$
225	$[Ru^{II}(bpy)_2(H2O)_2]^{2+}$
240	$[Ru^{II}(bpy)_2(ACN)(CN)]^{2+}$
253	$[Ru^{II}(bpy)_2(py\text{-}Me)]^{2+}$ (PCI)
262	$[Ru^{II}(bpy)_2(py\text{-}Me)(H_2O)]^{2+}$ (PCI-H_2O)
292	broad signal
300	**$[Ru^{II}(bpy)_2(py\text{-}Me)_2]^{2+}$**

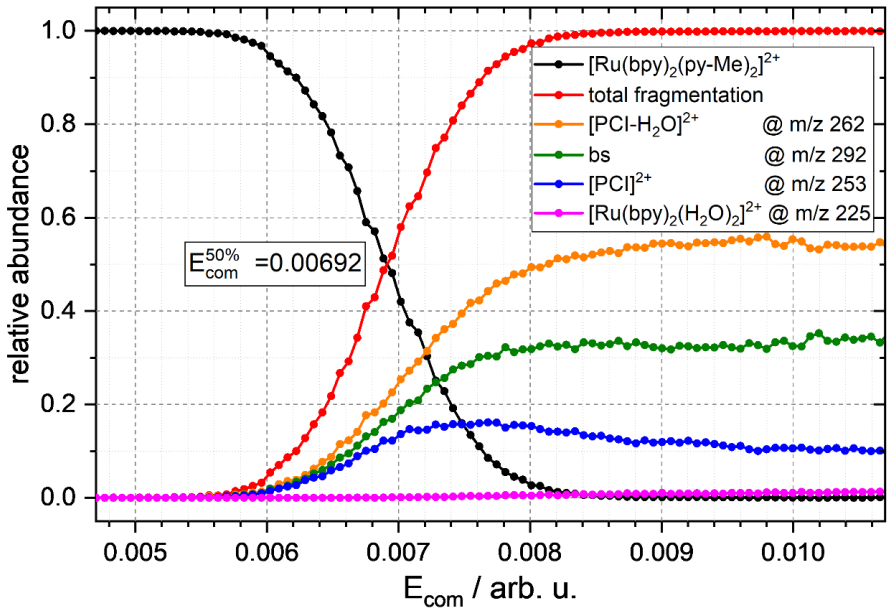

Figure 1 CID breakdown/appearance curves of **Y6**. $E_{com}^{50\%}$ value determined through sigmoidal fitting of the total fragment yield appearance curve.

"4. UV-PD Spectra, Calculated Absorption Spectra, Photoinduced Ligand Exchange":

"4.1 Approaches to determine electronic transition states"

The UVPD spectra of X and Y complexes were acquired using the Wyvern laser system, with a step size of 3 nm and a pulse energy of 2 µJ. In order to characterize the electronic transitions, geometry optimizations were performed as a first step using density functional theory (DFT). In a second step, time-dependent DFT (TD-DFT) single-point calculations were performed to compute the excited states, following the ground-state geometry optimizations. Both calculations were conducted at the B3LYP/cc-PVTZ/MDF28 level of theory within the Gaussian Software package. The most significant singlet transitions were selected based on their oscillator strengths, and the major molecular orbital (MO) contributions to each state were correlated with the structural elements of the complexes (Figure 35) to determine the character of each electronic transition based on the electron distribution in the MOs. To visualize the MOs, cubegen files were generated from the Gaussian checkpoint files, which were then processed using VMD v1.9.4, along with a custom script.

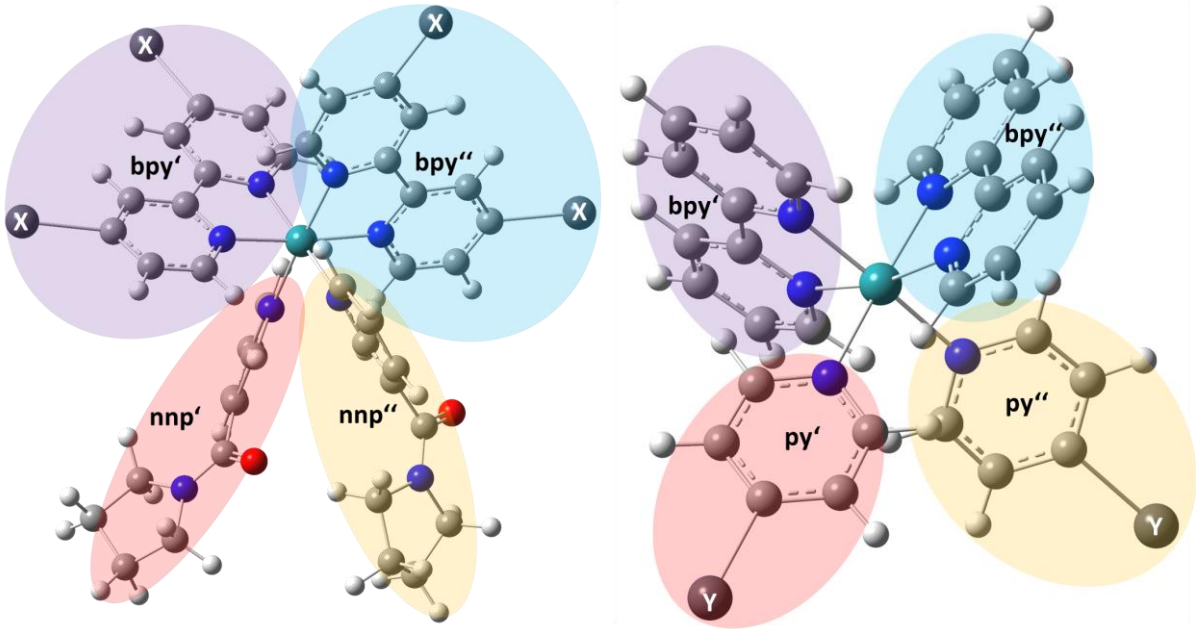

Figure 35 Schematic structure of the X (left) and Y (right) complexes. Each complex includes four main structural components: the 2,2'-bipyridine ligands (bpy' and bpy''), auxiliary ligands (nnp' and nnp'' for X complexes, referring to N-nicotinyl-pyrrolidine, and py' and py'' for Y complexes, referring to pyridine), and para-substituents specific to each series (X and Y groups, respectively). In the following tables, ligands of the same type are summarized using ''' notation (e.g., bpy''' for bpy' and bpy''). The colored ovals highlight these structural elements, used in assigning molecular orbitals (MOs) to help characterize excited states based on the electron distribution between the ruthenium center and the ligands.

"4.3 UVPD spectra of the X complexes and the characterization of their states"

f) Y6: $[Ru(bpy)_2(py\text{-}Y)_2]^{2+}$ with Y = (Me)

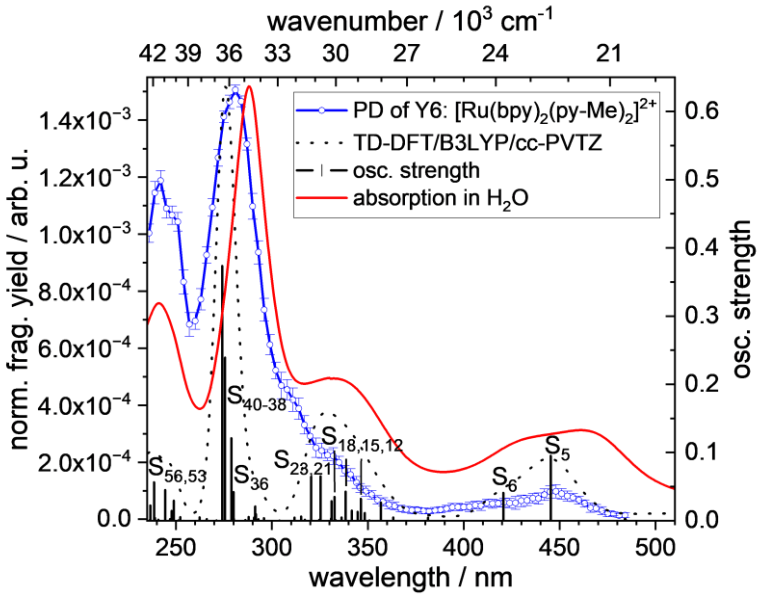

Figure 58 UVPD spectrum of the **Y6** complex (blue point-line). The dotted black line represents the TD-DFT calculated absorption spectrum, convoluted with a Gaussian function at 1500 cm^{-1} fwhm. The stick spectrum shows the vertical electronic transitions. S_n labels transitions with an oscillator strength of > 0.03. The red line is the absorption in H_2O.

Table 28 Calculated transitions of **Y6** at the ground state geometry (TD-DFT/B3LYP/cc-PVTZ). The singlet transitions with an oscillator strength of f > 0.03 are displayed and major contributions to electronic transitions with a weight of ≥ 10%.

State	λ_{cal} [nm]	E_v [eV]	f	Transitions	Weight [%]	Involved ligands/metal	Transition type
S_5	445.3	2.79	0.095	H-2 → L H-1 → L+1	85 13	Ru → bpy''' Ru → bpy'''	MLCT
S_6	420.6	2.95	0.041	H-2 → L+1	79	Ru → bpy'''	MLCT
S_{12}	346.4	3.58	0.032	H → L+4	81	Ru → bpy'''	MLCT
S_{15}	338.4	3.66	0.043	H → L+5	80	Ru → bpy'''	MLCT
S_{18}	332.6	3.74	0.035	H-1 → L+4	60	Ru → bpy'''	MLCT
S_{21}	325.4	3.81	0.065	H-2 → L+11 H-1 → L+7	11 65	Ru → Ru Ru → py''',bpy'''	MLCT
S_{23}	320.5	3.87	0.065	H-2 → L+4 H-1 → L+6	29 59	Ru → bpy''' Ru → py'''	MLCT
S_{36}	280.0	4.43	0.042	H-5 → L H-4 → L+1	50 25	py''' → bpy''' bpy''' → bpy'''	ILCT
S_{38}	278.9	4.46	0.121	H-5 → L H-4 → L+1	28 45	py''' → bpy''' bpy''' → bpy'''	ILCT, LC
S_{39}	275.6	4.50	0.239	H-5 → L+1 H-3 → L+1	49 35	py''' → bpy''' bpy''' → bpy'''	ILCT, LC
S_{40}	274.1	4.53	0.374	H-5 → L+1 H-3 → L+1	39 43	py''' → bpy''' bpy''' → bpy'''	ILCT, LC
S_{53}	244.4	5.06	0.045	H-4 → L+2 H-1 → L+10	48 28	bpy''' → bpy''' Ru → bpy'''	LC, MLCT
S_{56}	238.6	5.20	0.057	H-3 → L+3	72	bpy''' → py''',bpy'''	ILCT

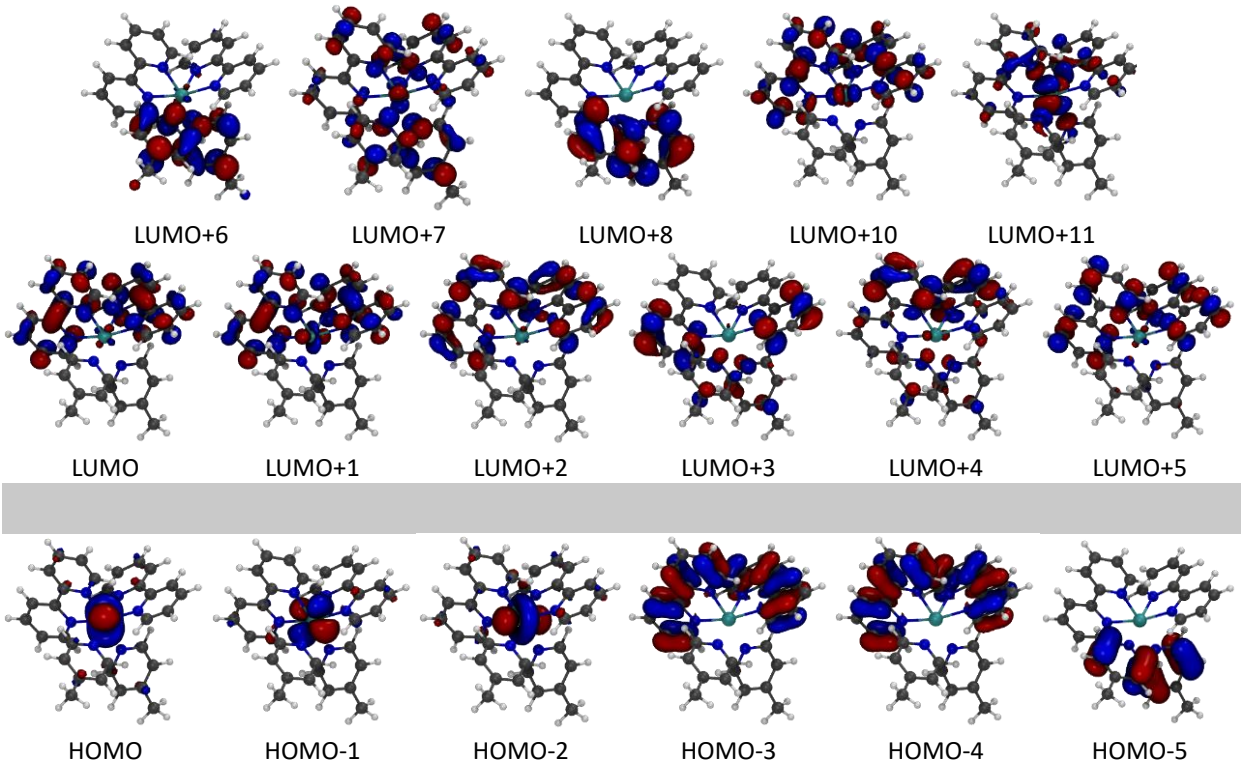

Figure 59 Molecular orbital isosurfaces of **Y6**, contributed to electronic transition with a weight of < 10%.

"4.4 Comparison of the UVPD spectra of the complexes of the X and Y series"

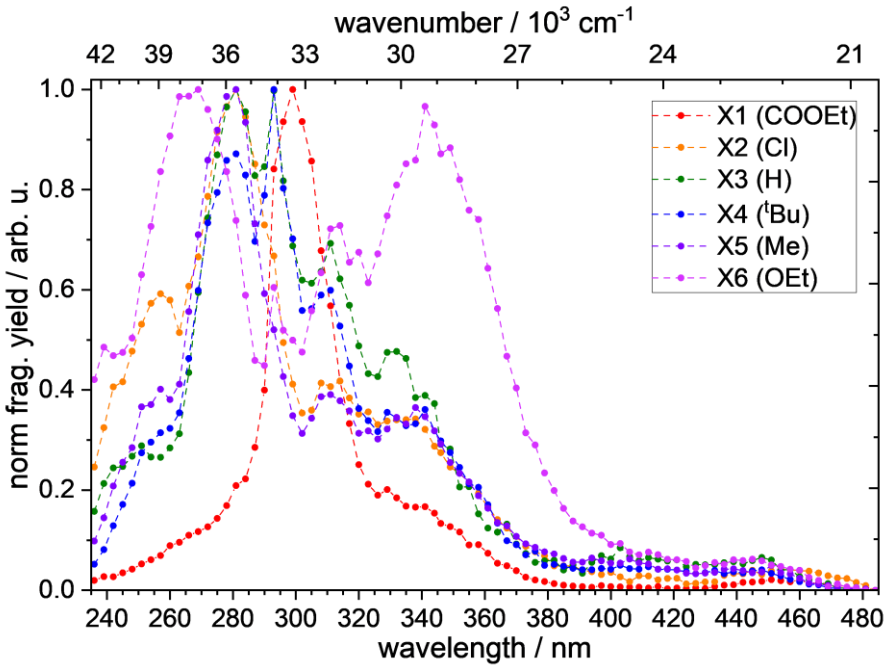

Figure 66 UVPD spectra of complexes of X series, measured by the Wyvern laser system at a 3 nm step size.

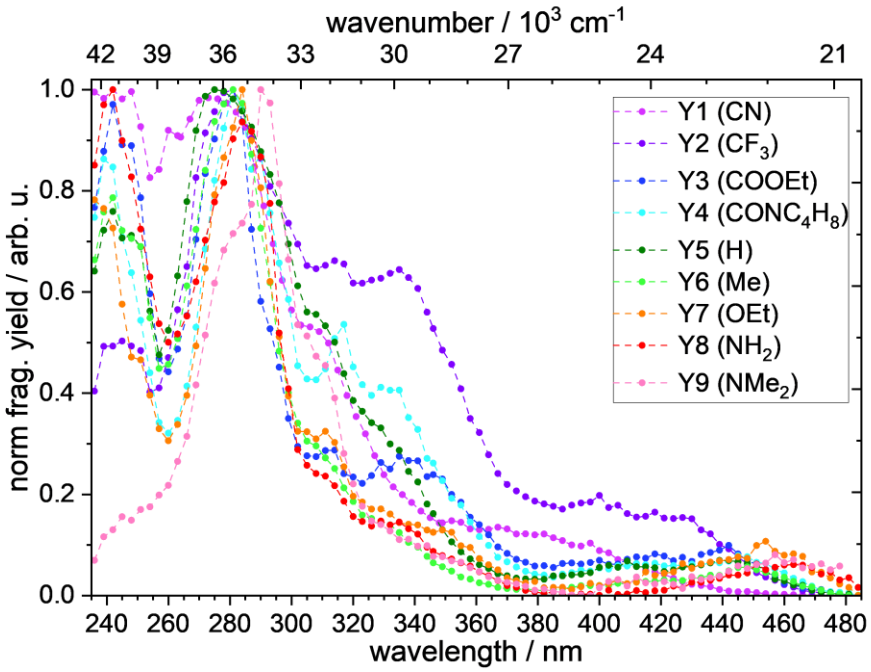

Figure 67 UVPD spectra of complexes of Y series, measured by the Wyvern laser system at a 3 nm step size.

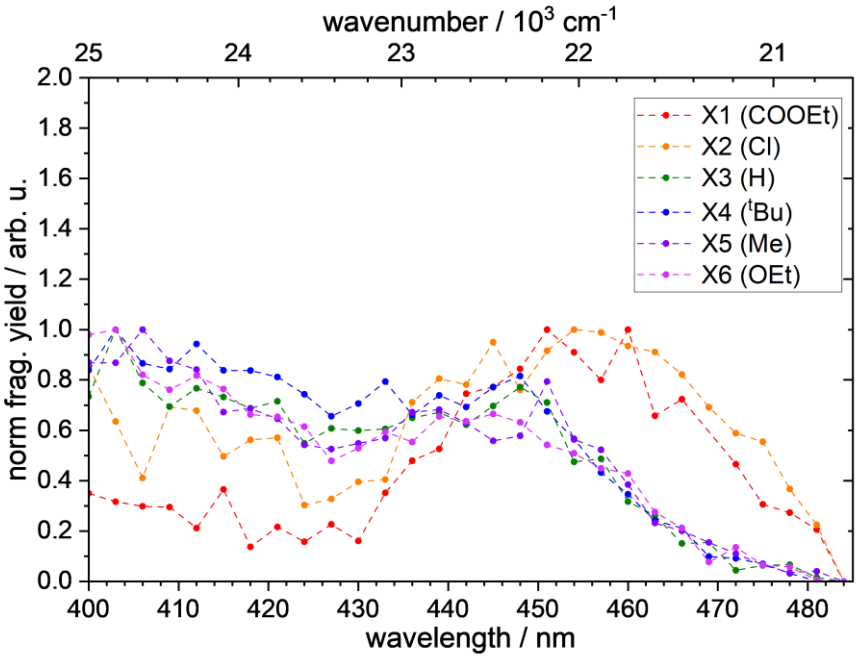

Figure 68 UVPD spectra of the complexes of the X series, zoomed in on the range of 400–485 nm, measured using the Wyvern laser system.

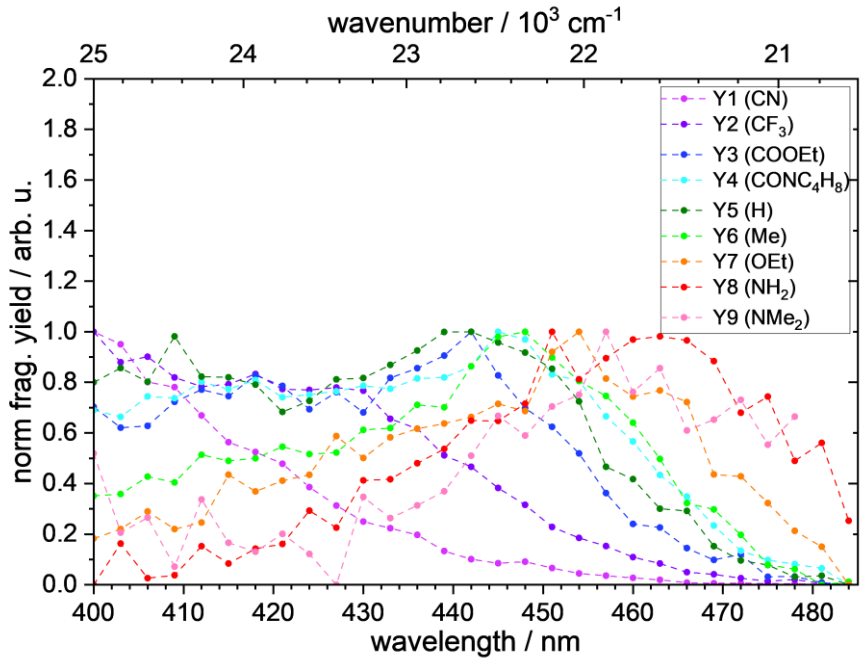

Figure 69 UVPD spectra of the complexes of the Y series, zoomed in on the range of 400–485 nm, measured using the Wyvern laser system.

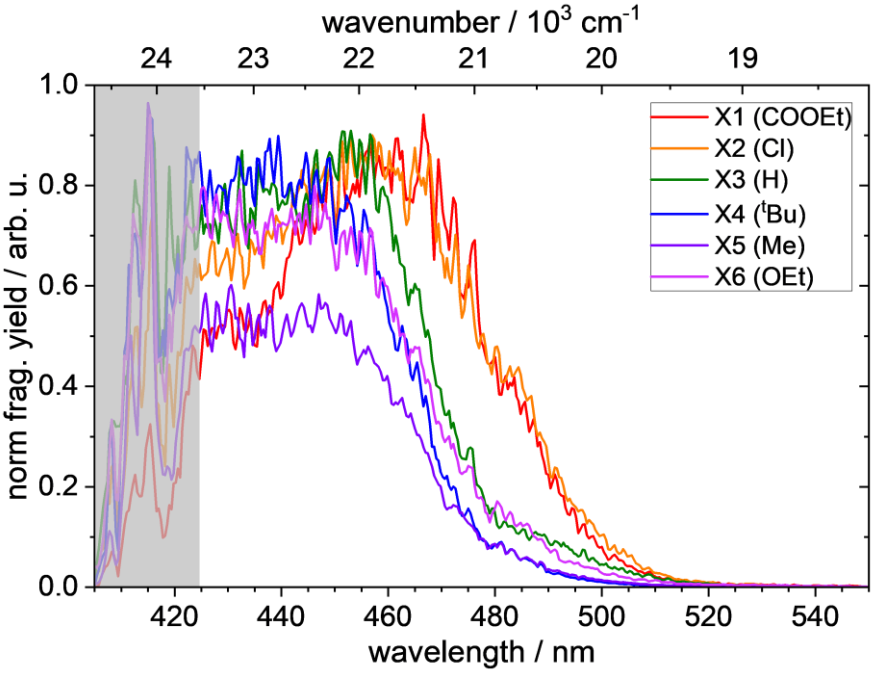

Figure 70 UVPD spectra of the complexes of the X series, measured using the EKSPLA laser system at a 0.4 nm step size, in the range of 400–550 nm.

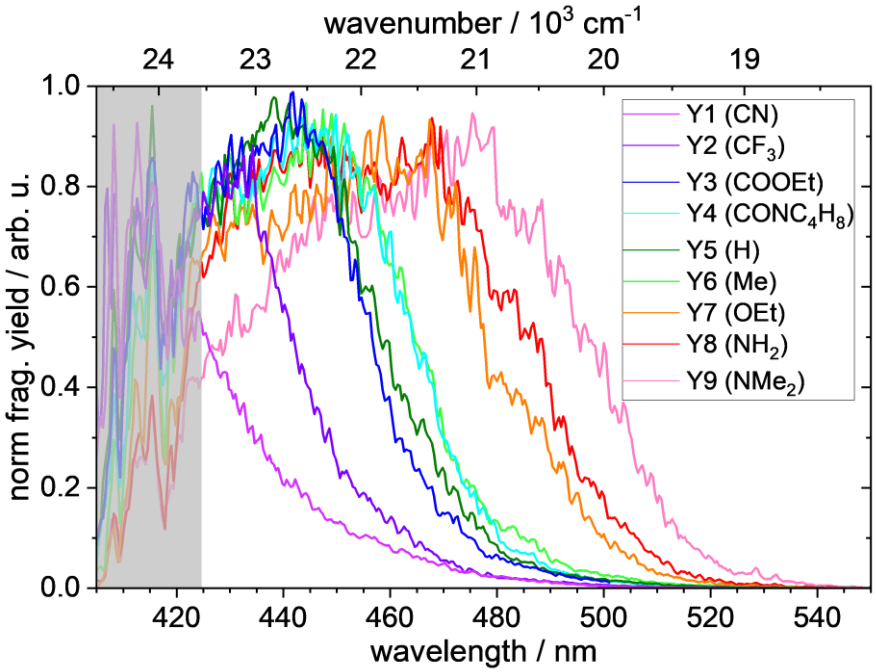

Figure 71 UVPD spectra of the complexes of the Y series, measured using the EKSPLA laser system at a 0.4 nm step size, in the range of 400–550 nm.

"4.5 Comparison of the calculated absorption spectra for the complexes of the X and Y series"

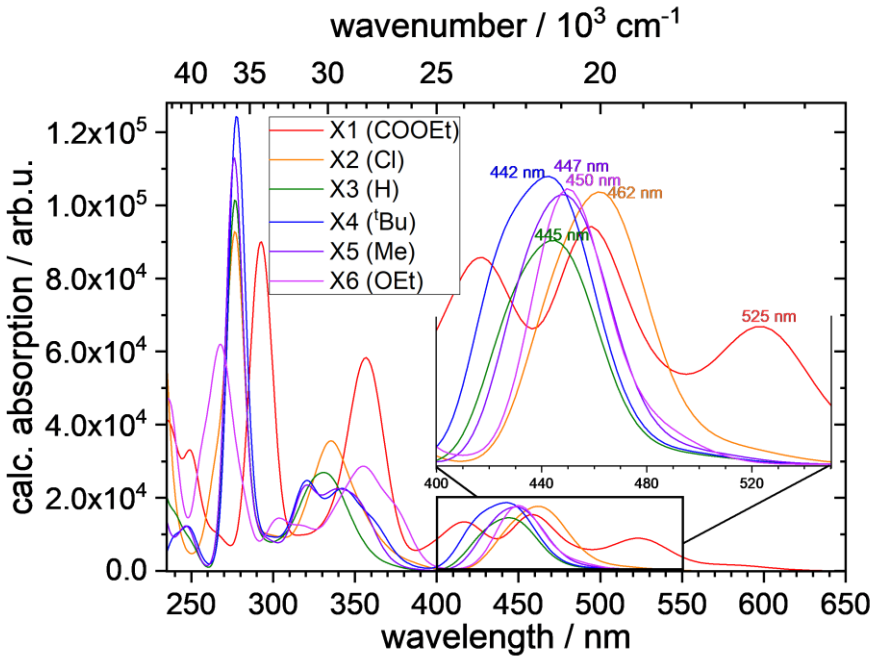

Figure 722 Calculated absorption spectra of the X complexes, using TD-DFT at the B3LYP/cc-pVTZ/MDF28 (Stuttgart97) level of theory at the ground-state geometry. The spectra are convoluted with a 1500 cm^{-1} fwhm Gaussian to simulate experimental broadening. The plotted wavelength values correspond to the according band maxima.

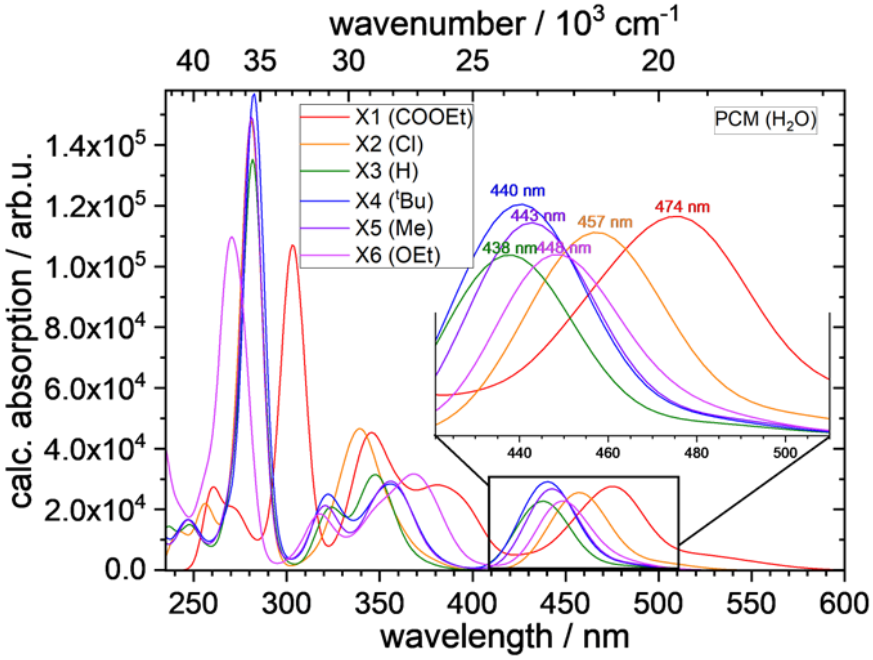

Figure 73 Calculated absorption spectra of the X complexes, using TD-DFT at the B3LYP/cc-pVTZ/MDF28 (Stuttgart97) level of theory at the ground-state geometry. The spectra are convoluted with a 1500 cm^{-1} fwhm Gaussian to simulate experimental broadening. Polarizable continuum model (PCM) for H_2O was applied. The plotted wavelength values correspond to the according band maxima.

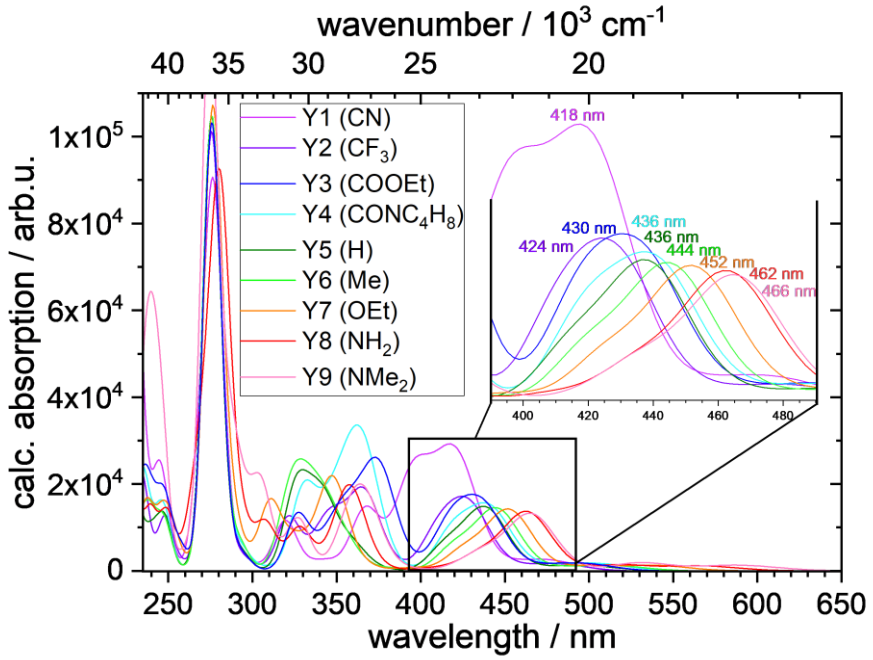

Figure 74 Calculated absorption spectra of the Y complexes, using TD-DFT at the B3LYP/cc-pVTZ/MDF28 (Stuttgart97) level of theory at the ground-state geometry. The spectra are convoluted with a 1500 cm^{-1} fwhm Gaussian to simulate experimental broadening. The plotted wavelength values correspond to the according band maxima.

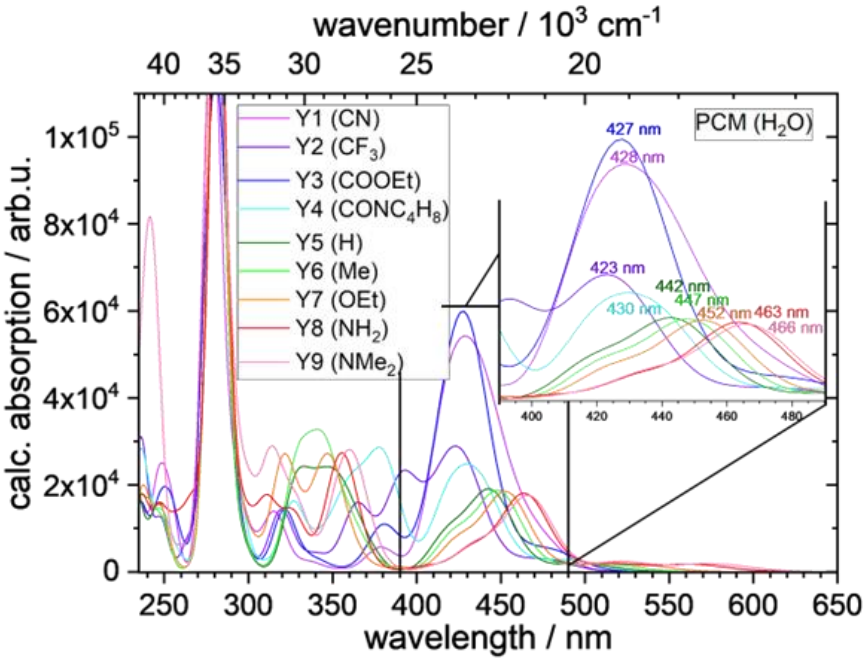

Figure 75 Calculated absorption spectra of the Y complexes, using TD-DFT at the B3LYP/cc-pVTZ/MDF28 (Stuttgart97) level of theory at the ground-state geometry. The spectra are convoluted with a 1500 cm^{-1} fwhm Gaussian to simulate experimental broadening. Polarizable continuum model (PCM) for H_2O was applied. The plotted wavelength values correspond to the according band maxima.

"5. Transient Photodissociation Spectroscopy (τ-PD)"

"5.1. Overview of time constants of the X and Y complexes"

The lifetimes of the X and Y complexes in the ion trap (gas phase) range from 700 fs to 2 ns. Due to technical limitations, the measurement time duration in the laboratory for a τ-PD scan is fixed to 10 minutes. Since the complexes have time constants that vary significantly, capturing these distinct lifetimes with optimal resolution required performing scans in multiple time frames. For example, to accurately resolve a 50 ps time constant, a time window of at least 200 ps is needed. However, using a 200 ps time window alone would lead to poor resolution for smaller time constants.

To address this, τ-PD was performed in time frames tailored to each lifetime. Consequently, the shorter the time frame, the higher the resolution, as smaller step sizes are feasible within the fixed 10-minute scan period. Table 32-33provide a selected summary of these values (see Table 34-41 for the comprehensive data set), reflecting the most accurate representation of the time constants across different time windows. Signal enhancement involved averaging 12 scans and fitting using OriginLab 2019G with a sum of exponentials equation (eq. 4), incorporating the instrument response function (IRF) convolution through an error function (erf).

$$Y(t) = Y_0 + \sum_{i=1}^{n}\left[A_i e^{0.5\left(\frac{w}{\tau_i}\right)^2 - \frac{t-t_0}{\tau_i}} \cdot 0.5\left(\mathrm{erf}\left(\frac{(t-t_0)/w - w/\tau_i}{\sqrt{2}}\right) + 1\right)\right] \quad (4)$$

t: time, Y_0: offset, A_i: amplitude of component i, τ_i : lifetime of component i, t_0: time zero, w: FWHM/$\left(2\sqrt{2\ln 2}\right)$ of Gaussian representing the IRF.

Table 32 Representative time constants (τ_1 and τ_2) in picoseconds for X complexes measured by τ-PD at excitation wavelengths of 340 nm, 410 nm, 430 nm, and 450 nm. The values are selected based on accuracy relative to the time window and are rounded to one decimal place for clarity. For a comprehensive dataset, including exact values and amplitude contributions, see Table 33-41. Signal enhancement involved averaging 12 scans and fitting using a sum of exponentials equation (eq. 4), incorporating the instrument response function (IRF) convolution via an error function (erf).

Complexes	σ_p^+	340 nm		410 nm		430 nm		450 nm	
		τ_1	τ_2	τ_1	τ_2	τ_1	τ_2	τ_1	τ_2
X1 (COOEt)	0.48	2.0 ± 0.2	8.9 ± 0.4	1.6 ± 0.0	14.3 ± 0.3	1.7 ± 0.0	13.4 ± 0.2	1.4 ± 0.0	16.5 ± 0.4
X2 (Cl)	0.11	2.5 ± 0.2	6.5 ± 0.4	1.1 ± 0.0	9.1 ± 0.2	1.3 ± 0.0	9.3 ± 0.1	1.3 ± 0.0	13.2 ± 0.2
X3 (H)	0	0.8 ± 0.1	3.3 ± 0.1	1.1 ± 0.1	5.9 ± 0.1	0.9 ± 0.0	6.5 ± 0.1	0.7 ± 0.0	8.2 ± 0.1
X4 (tBu)	-0.26	0.7 ± 0.1	3.5 ± 0.0	0.8 ± 0.0	5.3 ± 0.1	1.0 ± 0.0	6.2 ± 0.1	1.0 ± 0.0	6.7 ± 0.1
X5 (Me)	-0.31	0.5 ± 0.0	3.5 ± 0.0	0.8 ± 0.0	4.9 ± 0.1	0.8 ± 0.0	6.6 ± 0.1	0.7 ± 0.0	6.5 ± 0.1
X6 (OEt)	-0.81	0.8 ± 0.1	4.0 ± 0.1	1.1 ± 0.0	6.5 ± 0.1	1.1 ± 0.0	8.1 ± 0.2	1.3 ± 0.0	9.7 ± 0.2

Table 33 Representative time constants (τ_1 and τ_2) in picoseconds for Y complexes measured by τ-PD at excitation wavelengths of 340 nm, 410 nm, 430 nm, and 450 nm. The values are selected based on accuracy relative to the time window and are rounded to one decimal place for clarity. For a comprehensive dataset, including exact values and amplitude contributions, see Table 33-41. Signal enhancement involved averaging 12 scans and fitting using a sum of exponentials equation (eq. 4), incorporating the instrument response function (IRF) convolution via an error function (erf). The asterisks (*) indicate measurements performed with excitation at 370 nm.

Complexes	σ_p^+	340 nm		410 nm		430 nm		450 nm	
		τ_1	τ_2	τ_1	τ_2	τ_1	τ_2	τ_1	τ_2
Y1 (CN)	0.66	0.5 ± 0.0*	2.0 ± 0.1*	0.7 ± 0.1	2.5 ± 0.8	0.8 ± 0.1	3.2 ± 0.9	0.8 ± 0.0	2.1 ± 0.1
Y2 (CF3)	0.54	-	-	1.2 ± 0.1	3.5 ± 0.4	1.2 ± 0.1	4.1 ± 0.6	0.7 ± 0.2	3.7 ± 0.2
Y3 (COOEt)	0.45	1.4 ± 0.1	4.0 ± 0.4	1.2 ± 0.1	4.0 ± 0.1	1.8 ± 0.1	6.0 ± 0.2	1.5 ± 0.1	5.4 ± 0.2
Y4 (CONC4H8)	0.10	0.4 ± 0.1	3.6 ± 0.2	1.4 ± 0.1	9.8 ± 0.7	1.2 ± 0.1	6.9 ± 1.0	1.3 ± 0.0	6.3 ± 0.1
Y5 (H)	0	1.8 ± 0.1	9.9 ± 2.6	1.7 ± 0.0	13.7 ± 1.8	1.8 ± 0.0	16.5 ± 1.1	2.0 ± 0.1	19.4 ± 0.9
Y6 (Me)	-0.31	2.3 ± 0.1	16.2 ± 1.3	2.8 ± 0.1	27.6 ± 3.3	3.3 ± 0.1	31.0 ± 1.3	3.3 ± 0.1	42.7 ± 2.0
Y7 (OEt)	-0.81	3.6 ± 0.1	19.3 ± 0.9	3.3 ± 0.3	41.4 ± 3.4	3.0 ± 0.2	53.8 ± 3.9	4.3 ± 0.1	50.2 ± 2.3
Y8 (NH2)	-1.30	3.9 ± 0.2	22.5 ± 1.2	6.2 ± 0.4	55.5 ± 1.5	5.0 ± 0.7	79.0 ± 2.2	7.8 ± 0.2	87.4 ± 3.8
Y9 (NMe2)	-1.70	6.4 ± 0.4	> 800	9.7 ± 0.5	> 800	8.0 ± 0.3	> 800	8.8 ± 0.2	> 800

Table 34 Biexponential decay analysis of transient photodissociation (τ-PD) measurements for the X complexes at an excitation wavelength of 340 nm. Shown are decay time constants (τ_1 and τ_2) in picoseconds (ps), alongside amplitude contributions (A_1 and A_2) and coefficient of determination (R^2) values. Each complex was measured within distinct time windows (e.g., 20 ps, 40 ps, 100 ps, etc.) to capture dynamic processes over short to intermediate timescales, providing insight into decay behaviors across a range of time windows for each complex. Complex labels include their substituent groups in parentheses for reference.

Complex	Time window	τ_1 / ps	τ_2 / ps	A_1	A_2	R^2
X1 (COOEt)	20 ps	2.0 ± 0.2	8.9 ± 0.4	44	56	0.972
	100 ps	4.2 ± 0.2	18 ± 2	80	20	0.965
	200 ps	3.2 ± 0.3	9.6 ± 0.6	54	47	0.980
X2 (Cl)	20 ps	2.5 ± 0.2	6.4 ± 0.4	53	47	0.991
	40 ps	2.6 ± 0.2	8 ± 1	72	28	0.980
	200 ps	3.3 ± 0.1	8.1 ± 0.4	84	16	0.963
X3 (H)	20 ps	0.83 ± 0.06	3.31 ± 0.06	33	67	0.994
	40 ps	0.44 ± 0.05	2.86 ± 0.04	29	71	0.991
X4 (^{t}Bu)	20 ps	0.70 ± 0.05	3.45 ± 0.04	26	74	0.996
	40 ps	0.59 ± 0.06	3.06 ± 0.04	23	77	0.994
X5 (Me)	20 ps	0.51 ± 0.02	3.53 ± 0.03	33	67	0.997
	40 ps	0.62 ± 0.04	3.57 ± 0.05	39	61	0.992
X6 (OEt)	20 ps	0.75 ± 0.05	3.98 ± 0.05	37	63	0.991
	40 ps	1.2 ± 0.4	4.2 ± 0.4	87	13	0.888

Table 35 Biexponential decay analysis of transient photodissociation (τ-PD) measurements for the X complexes at an excitation wavelength of 410 nm. Shown are decay time constants (τ_1 and τ_2) in picoseconds (ps), alongside amplitude contributions (A_1 and A_2) and coefficient of determination (R^2) values. Each complex was measured within distinct time windows (e.g., 20 ps, 40 ps, 100 ps, etc.) to capture dynamic processes over short to intermediate timescales, providing insight into decay behaviors across a range of time windows for each complex. Complex labels include their substituent groups in parentheses for reference.

Complex	Time window	τ_1 / ps	τ_2 / ps	A_1	A_2	R^2
X1 (COOEt)	20 ps	1.58 ± 0.04	11.6 ± 0.2	47	53	0.993
	100 ps	2.14 ± 0.06	14.3 ± 0.3	62	38	0.991
	200 ps	2.0 ± 0.1	12.9 ± 0.6	68	32	0.948
	400 ps	4.3 ± 0.2	19.1 ± 0.5	58	42	0.989
X2 (Cl)	20 ps	1.08 ± 0.03	8.1 ± 0.1	53	47	0.996
	40 ps	1.79 ± 0.09	9.1 ± 0.2	45	55	0.989
	100 ps	1.96 ± 0.09	9.2 ± 0.2	47	53	0.992
X3 (H)	20 ps	1.10 ± 0.07	5.6 ± 0.3	53	47	0.986
	100 ps	1.50 ± 0.11	5.9 ± 0.1	40	60	0.990
X4 (^{t}Bu)	20 ps	0.82 ± 0.03	5.8 ± 0.1	49	51	0.993
	60 ps	0.66 ± 0.03	4.9 ± 0.1	62	38	0.984
X5 (Me)	20 ps	0.79 ± 0.04	5.3 ± 0.1	31	69	0.995
	100 ps	1.7 ± 0.1	6.4 ± 0.2	46	54	0.989
X6 (OEt)	20 ps	1.08 ± 0.03	6.5 ± 0.1	50	50	0.994
	100 ps	1.16 ± 0.06	6.8 ± 0.2	60	40	0.981

Table 36 Biexponential decay analysis of transient photodissociation (τ-PD) measurements for the X complexes at an excitation wavelength of 430 nm. Shown are decay time constants (τ_1 and τ_2) in picoseconds (ps), alongside amplitude contributions (A_1 and A_2) and coefficient of determination (R^2) values. Each complex was measured within distinct time windows (e.g., 20 ps, 40 ps, 100 ps, etc.) to capture dynamic processes over short to intermediate timescales, providing insight into decay behaviors across a range of time windows for each complex. Complex labels include their substituent groups in parentheses for reference.

Complex	Time window	τ_1 / ps	τ_2 / ps	A_1	A_2	R^2
X1 (COOEt)	20 ps	1.72 ± 0.03	13.4 ± 0.2	52	48	0.996
	100 ps	1.82 ± 0.05	13.8 ± 0.4	73	27	0.984
X2 (Cl)	20 ps	1.26 ± 0.03	9.3 ± 0.1	44	56	0.997
	100 ps	1.53 ± 0.06	9.6 ± 0.1	49	51	0.992
X3 (H)	20 ps	0.90 ± 0.03	5.7 ± 0.1	49	52	0.991
	100 ps	1.01 ± 0.04	6.5 ± 0.1	49	51	0.995
X4 (^{t}Bu)	20 ps	1.03 ± 0.03	6.9 ± 0.1	39	61	0.995
	40 ps	0.81 ± 0.07	6.1 ± 0.1	40	60	0.979
	100 ps	0.63 ± 0.04	6.2 ± 0.1	38	62	0.992
X5 (Me)	20 ps	0.77 ± 0.02	6.6 ± 0.1	55	45	0.994
	100 ps	0.98 ± 0.02	6.6 ± 0.1	60	40	0.996
X6 (OEt)	20 ps	1.05 ± 0.03	7.1 ± 0.1	50	50	0.995
	100 ps	1.21 ± 0.05	8.1 ± 0.2	62	38	0.983

Table 37 Biexponential decay analysis of transient photodissociation (τ-PD) measurements for the X complexes at an excitation wavelength of 450 nm. Shown are decay time constants (τ_1 and τ_2) in picoseconds (ps), alongside amplitude contributions (A_1 and A_2) and coefficient of determination (R^2) values. Each complex was measured within distinct time windows (e.g., 20 ps, 40 ps, 100 ps, etc.) to capture dynamic processes over short to intermediate timescales, providing insight into decay behaviors across a range of time windows for each complex. Complex labels include their substituent groups in parentheses for reference.

Complex	Time window	τ_1 / ps	τ_2 / ps	A_1	A_2	R^2
X1 (COOEt)	40 ps	1.40 ± 0.03	11.4 ± 0.4	74	26	0.988
	100 ps	1.39 ± 0.04	13.2 ± 0.4	75	25	0.978
	200 ps	2.21 ± 0.06	19.7 ± 0.3	62	38	0.989
X2 (Cl)	40 ps	1.27 ± 0.03	10.1 ± 0.2	54	46	0.994
	200 ps	1.90 ± 0.07	13.1 ± 0.2	54	46	0.992
	400 ps	3.8 ± 0.6	14 ± 1	50	50	0.943
X3 (H)	40 ps	0.65 ± 0.02	6.6 ± 0.1	42	58	0.996
	200 ps	1.03 ± 0.05	8.2 ± 0.1	55	45	0.989
X4 (^{t}Bu)	20 ps	0.95 ± 0.02	7.2 ± 0.1	41	59	0.997
	40 ps	0.53 ± 0.03	6.9 ± 0.1	37	63	0.991
	100 ps	1.44 ± 0.07	8.3 ± 0.1	41	59	0.994
X5 (Me)	40 ps	0.72 ± 0.02	6.5 ± 0.1	60	40	0.994
	100 ps	0.96 ± 0.02	7.4 ± 0.1	63	37	0.993
X6 (OEt)	40 ps	1.26 ± 0.03	8.5 ± 0.1	56	44	0.995
	100 ps	1.51 ± 0.05	9.7 ± 0.2	61	39	0.989

Table 38 Biexponential decay analysis of transient photodissociation (τ-PD) measurements for the Y complexes at an excitation wavelength of 340 nm. Shown are decay time constants (τ_1 and τ_2) in picoseconds (ps), alongside amplitude contributions (A_1 and A_2) and coefficient of determination (R^2) values. Each complex was measured within distinct time windows (e.g., 20 ps, 40 ps, 100 ps, etc.) to capture dynamic processes over short to intermediate timescales, providing insight into decay behaviors across a range of time windows for each complex. Complex labels include their substituent groups in parentheses for reference. *Y1 was excited at 370 nm.

Complex	Time Window	τ_1 / ps	τ_2 / ps	A_1	A_2	R^2
Y1 (CN)*	10 ps	0.48 ± 0.01	2.04 ± 0.09	82	18	0.995
Y2 (CF_3)	-	-	-	-	-	-
Y3 (COOEt)	20 ps	1.43 ± 0.09	4.0 ± 0.4	66	34	0.988
	40 ps	1.82 ± 0.09	15 ± 4	92	8	0.890
	60 ps	1.73 ± 0.04	10 ± 2	94	6	0.983
Y4 ($CONC_4H_8$)	20 ps	0.44 ± 0.05	2.47 ± 0.5	27	73	0.995
	40 ps	1.33 ± 0.08	3.6 ± 0.2	54	46	0.993
Y5 (H)	20 ps	1.79 ± 0.06	10 ± 3	92	8	0.971
	40 ps	1.66 ± 0.05	21 ± 7	96	4	0.935
	60 ps	1.78 ± 0.03	25 ± 4	95	5	0.964
	100 ps	1.5 ± 0.2	6 ± 3	88	12	0.801
Y6 (Me)	20 ps	2.34 ± 0.05	18 ± 4	92	8	0.988
	100 ps	2.11 ± 0.06	16 ± 1	87	13	0.971
	200 ps	2.4 ± 0.1	17 ± 2	89	11	0.915
Y7 (OEt)	20 ps	3.60 ± 0.08	46 ± 18	89	11	0.992
	100 ps	4.0 ± 0.2	32 ± 5	86	14	0.917
	200 ps	3.15 ± 0.07	19.3 ± 0.9	83	17	0.986
Y8 (NH_2)	20 ps	3.9 ± 0.2	37 ± 13	78	22	0.977
	100 ps	3.2 ± 0.2	20 ± 2	75	25	0.922
	200 ps	3.7 ± 0.1	23 ± 1	78	22	0.972
Y9 (NMe_2)	20 ps	8 ± 1	N/A*	72	23	0.978
	100 ps	6.4 ± 0.4	N/A*	54	46	0.963
	400 ps	5.8 ± 0.6	> 1 ns	51	49	0.944

Table 39 Biexponential decay analysis of transient photodissociation (τ-PD) measurements for the Y complexes at an excitation wavelength of 410 nm. Shown are decay time constants (τ_1 and τ_2) in picoseconds (ps), alongside amplitude contributions (A_1 and A_2) and coefficient of determination (R^2) values. Each complex was measured within distinct time windows (e.g., 20 ps, 40 ps, 100 ps, etc.) to capture dynamic processes over short to intermediate timescales, providing insight into decay behaviors across a range of time windows for each complex. Complex labels include their substituent groups in parentheses for reference.

Complex	Time Window	τ_1 / ps	τ_2 / ps	A_1	A_2	R^2
Y1 (CN)	20 ps	0.69 ± 0.09	2.5 ± 0.8	81	19	0.925
	40 ps	0.69 ± 0.01	4.7 ± 0.3	91	9	0.989
Y2 (CF_3)	20 ps	1.16 ± 0.06	3.4 ± 0.4	75	25	0.988
	40 ps	0.9 ± 0.1	2.7 ± 0.2	57	43	0.973
Y3 (COOEt)	20 ps	1.21 ± 0.06	4.0 ± 0.1	46	54	0.996
	40 ps	1.8 ± 0.1	5.3 ± 0.4	67	33	0.989
Y4 ($CONC_4H_8$)	20 ps	1.4 ± 0.1	5.1 ± 0.4	54	46	0.985
	100 ps	2.36 ± 0.07	9.8 ± 0.7	83	17	0.986
Y5 (H)	20 ps	1.68 ± 0.04	5.6 ± 0.3	74	26	0.997
	40 ps	1.95 ± 0.05	13 ± 2	89	11	0.968
	60 ps	2.45 ± 0.03	23 ± 2	93	7	0.989
	100 ps	2.68 ± 0.03	23 ± 1	92	8	0.995
Y6 (Me)	20 ps	2.8 ± 0.1	11.1 ± 0.9	73	27	0.991
	100 ps	3.18 ± 0.06	22 ± 2	88	12	0.985
	200 ps	3.0 ± 0.1	28 ± 3	90	10	0.928
Y7 (OEt)	20 ps	3.3 ± 0.3	14 ± 1	47	53	0.981
	100 ps	5.19 ± 0.07	54 ± 2	83	17	0.989
	200 ps	5.0 ± 0.3	41 ± 3	82	18	0.948
Y8 (NH_2)	20 ps	6.2 ± 0.4	N/A*	83	17	0.990
	200 ps	6.1 ± 0.1	56 ± 2	72	28	0.989
	400 ps	6.4 ± 0.2	49 ± 2	70	30	0.973
	800 ps	4.8 ± 0.5	37 ± 2	66	34	0.927
Y9 (NMe_2)	20 ps	10 ± 3	N/A*	55	46	0.981
	200 ps	9.7 ± 0.5	N/A*	44	56	0.965
	800 ps	69 ± 3	> 1 ns	82	18	0.813

Table 40 Biexponential decay analysis of transient photodissociation (τ-PD) measurements for the Y complexes at an excitation wavelength of 430 nm. Shown are decay time constants (τ_1 and τ_2) in picoseconds (ps), alongside amplitude contributions (A_1 and A_2) and coefficient of determination (R^2) values. Each complex was measured within distinct time windows (e.g., 20 ps, 40 ps, 100 ps, etc.) to capture dynamic processes over short to intermediate timescales, providing insight into decay behaviors across a range of time windows for each complex. Complex labels include their substituent groups in parentheses for reference.

Complex	Time Window	τ_1 / ps	τ_2 / ps	A_1	A_2	R^2
Y1 (CN)	20 ps	0.80 ± 0.08	3.2 ± 0.9	83	17	0.935
	40 ps	0.80 ± 0.05	3.5 ± 0.5	85	15	0.950
Y2 (CF_3)	20 ps	1.21 ± 0.08	4.1 ± 0.6	76	24	0.971
	40 ps	1.01 ± 0.05	3.5 ± 0.2	67	33	0.986
Y3 (COOEt)	20 ps	1.75 ± 0.05	6.0 ± 0.2	64	36	0.996
	40 ps	1.97 ± 0.09	6.3 ± 0.5	70	30	0.987
	100 ps	1.83 ± 0.07	7.2 ± 0.4	73	27	0.987
Y4 ($CONC_4H_8$)	20 ps	1.2 ± 0.1	5.1 ± 0.3	48	52	0.989
	40 ps	1.5 ± 0.2	7 ± 1	66	34	0.956
Y5 (H)	20 ps	1.80 ± 0.04	6.7 ± 0.3	74	26	0.995
	40 ps	1.0 ± 0.1	4.4 ± 0.3	50	50	0.940
	60 ps	2.90 ± 0.04	17 ± 1	88	12	0.993
	100 ps	2.44 ± 0.07	15 ± 2	91	9	0.971
	200 ps	2.0 ± 0.2	11 ± 2	87	13	0.891
Y6 (Me)	20 ps	3.27 ± 0.9	14 ± 1	75	25	0.995
	100 ps	3.61 ± 0.06	29 ± 2	87	13	0.988
	200 ps	3.88 ± 0.05	31 ± 1	88	12	0.991
Y7 (OEt)	20 ps	3.0 ± 0.2	12.4 ± 0.6	38	62	0.988
	100 ps	5.2 ± 0.1	40 ± 2	47	53	0.979
	200 ps	6.3 ± 0.1	67 ± 4	83	17	0.971
	300 ps	5.7 ± 0.2	54 ± 4	86	14	0.958
	400 ps	3.6 ± 0.3	33 ± 2	75	25	0.904
Y8 (NH_2)	20 ps	5.0 ± 0.7	28 ± 9	60	40	0.971
	200 ps	7.9 ± 0.1	83 ± 2	72	28	0.988
	400 ps	8.7 ± 0.2	79 ± 2	72	28	0.983
	800 ps	8.5 ± 0.5	62 ± 2	65	35	0.963
Y9 (NMe_2)	20 ps	2.5 ± 0.5	N/A*	17	83	0.967
	200 ps	8.0 ± 0.3	N/A*	54	46	0.960
	600 ps	11.4 ± 0.7	> 1 ns	52	48	0.948

Table 41 Biexponential decay analysis of transient photodissociation (τ-PD) measurements for the Y complexes at an excitation wavelength of 450 nm. Shown are decay time constants (τ_1 and τ_2) in picoseconds (ps), alongside amplitude contributions (A_1 and A_2) and coefficient of determination (R^2) values. Each complex was measured within distinct time windows (e.g., 20 ps, 40 ps, 100 ps, etc.) to capture dynamic processes over short to intermediate timescales, providing insight into decay behaviors across a range of time windows for each complex. Complex labels include their substituent groups in parentheses for reference.

Complex	Time Window	τ_1 / ps	τ_2 / ps	A_1	A_2	R^2
Y1 (CN)	20 ps	0.83 ± 0.03	3.6 ± 0.3	81	19	0.981
	40 ps	0.45 ± 0.05	2.06 ± 0.09	53	47	0.963
Y2 (CF_3)	20 ps	0.7 ± 0.2	2.4 ± 0.1	29	71	0.970
	40 ps	1.23 ± 0.06	3.7 ± 0.2	67	33	0.991
Y3 (COOEt)	20 ps	1.52 ± 0.08	5.8 ± 0.2	53	47	0.989
	40 ps	1.7 ± 0.1	5.4 ± 0.2	52	48	0.989
	100 ps	2.37 ± 0.07	8.3 ± 0.4	75	25	0.993
Y4 ($CONC_4H_8$)	20 ps	1.31 ± 0.05	6.7 ± 0.2	54	46	0.995
	40 ps	0.98 ± 0.05	6.0 ± 0.1	44	56	0.995
	100 ps	0.92 ± 0.05	6.3 ± 0.1	46	54	0.990
	200 ps	0.51 ± 0.08	6.2 ± 0.1	57	43	0.962
Y5 (H)	20 ps	2.02 ± 0.07	8.3 ± 0.6	76	24	0.988
	40 ps	2.37 ± 0.05	19 ± 2	90	10	0.971
	60 ps	3.25 ± 0.04	19 ± 1	88	12	0.995
	100 ps	1.4 ± 0.2	4.9 ± 0.3	74	26	0.958
Y6 (Me)	20 ps	3.34 ± 0.09	15.0 ± 0.9	68	32	0.996
	40 ps	4.15 ± 0.09	35 ± 4	86	14	0.983
	100 ps	4.32 ± 0.09	37 ± 4	89	11	0.973
	200 ps	5.02 ± 0.09	43 ± 2	89	11	0.992
Y7 (OEt)	40 ps	4.3 ± 0.12	27 ± 2	66	33	0.955
	200 ps	6.0 ± 0.2	51 ± 4	80	20	0.953
	400 ps	6.1 ± 0.2	50 ± 2	81	19	0.972
	800 ps	6.8 ± 0.1	55 ± 2	79	21	0.987
Y8 (NH_2)	40 ps	7.8 ± 0.2	75 ± 6	65	35	0.994
	200 ps	8.9 ± 0.2	99 ± 3	72	28	0.987
	400 ps	9.3 ± 0.3	97 ± 3	73	27	0.977
	800 ps	11.5 ± 0.6	87 ± 4	69	31	0.955
Y9 (NMe_2)	20 ps	5.0 ± 0.6	N/A*	31	69	0.989
	200 ps	8.8 ± 0.2	N/A*	46	54	0.987
	800 ps	12.6 ± 0.7	> 1 ns	48	52	0.964
	1600 ps	N/A*	> 1.9 ns	67	33	0.960

"5.3. τ-PD of Y complexes"

f) Y6: $[Ru(bpy)_2(py\text{-}Y)_2]^{2+}$ with Y = (Me)

Table 53 Biexponential decay analysis of τ-PD measurements for **Y6**, recorded at pump wavelengths (λ) of 340, 410, 430, and 450 nm, with various time windows. Columns list the decay constants (τ_1 and τ_2) with associated uncertainties, amplitude coefficients (A_1 and A_2), and R^2 values.

λ_{pump}	Time window	τ_1 / ps	τ_2 / ps	A_1	A_2	R^2
340 nm	20 ps	2.34 ± 0.05	18 ± 4	92	8	0.988
	100 ps	2.11 ± 0.06	16 ± 1	87	13	0.971
	200 ps	2.4 ± 0.1	17 ± 2	89	11	0.915
410 nm	20 ps	2.8 ± 0.1	11.1 ± 0.9	73	27	0.991
	100 ps	3.18 ± 0.06	22 ± 2	88	12	0.985
	200 ps	3.0 ± 0.1	28 ± 3	90	10	0.928
430 nm	20 ps	3.27 ± 0.9	14 ± 1	75	25	0.995
	100 ps	3.61 ± 0.06	29 ± 2	87	13	0.988
	200 ps	3.88 ± 0.05	31 ± 1	88	12	0.991
450 nm	20 ps	3.34 ± 0.09	15.0 ± 0.9	68	32	0.996
	40 ps	4.15 ± 0.09	35 ± 4	86	14	0.983
	100 ps	4.32 ± 0.09	37 ± 4	89	11	0.973
	200 ps	5.02 ± 0.09	43 ± 2	89	11	0.992

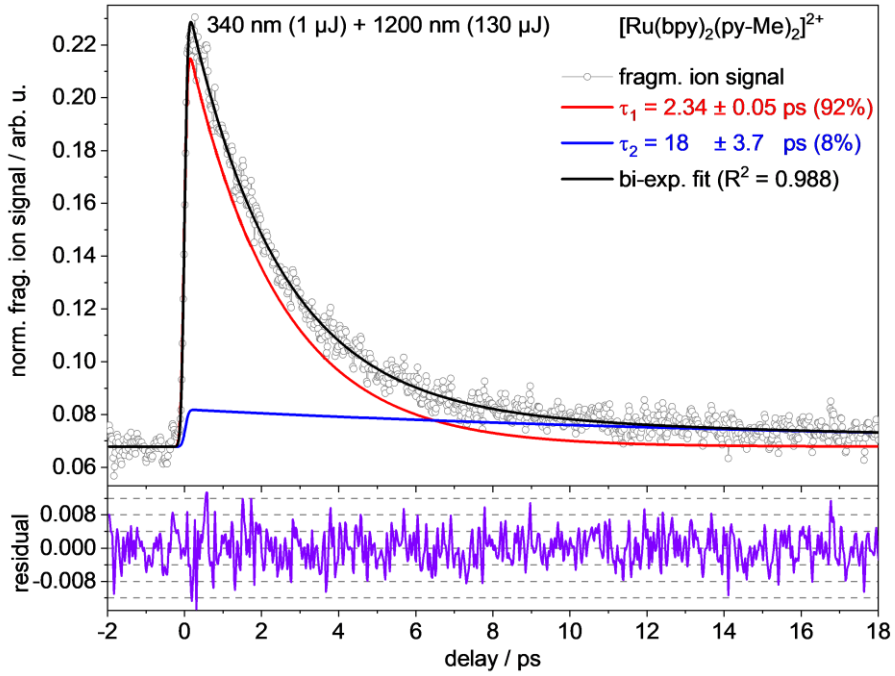

Figure 189 τ-PD of **Y6** recorded at a pump wavelength of 340 nm and probed at 1200 nm within a 20 ps time frame. The bi-exponential fit is shown in black, with the individual fit components represented in red and blue. The fit residuals are displayed below in purple.

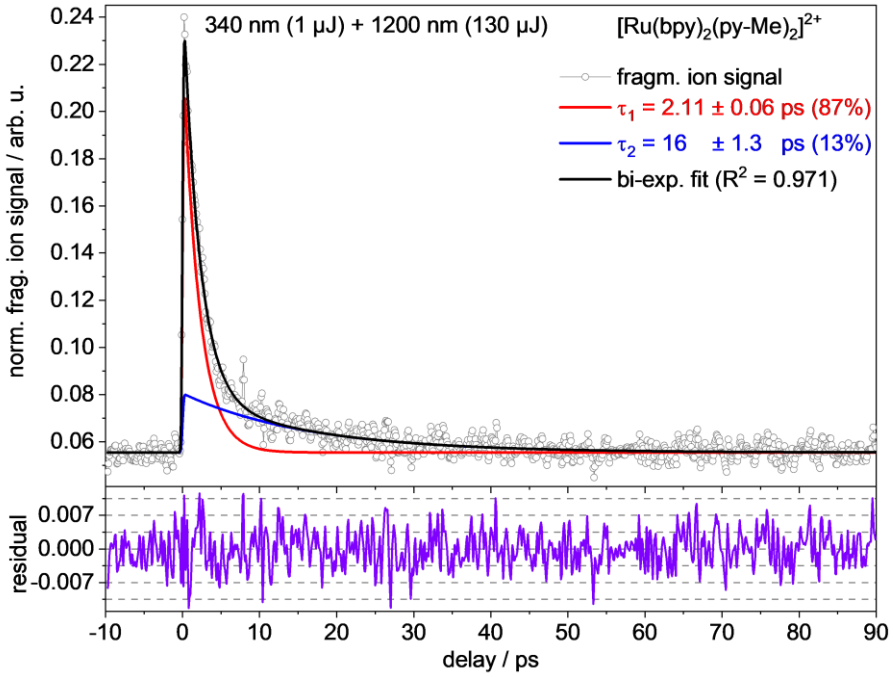

Figure 190 τ-PD of **Y6** recorded at a pump wavelength of 340 nm and probed at 1200 nm within a 100 ps time frame. The bi-exponential fit is shown in black, with the individual fit components represented in red and blue. The fit residuals are displayed below in purple.

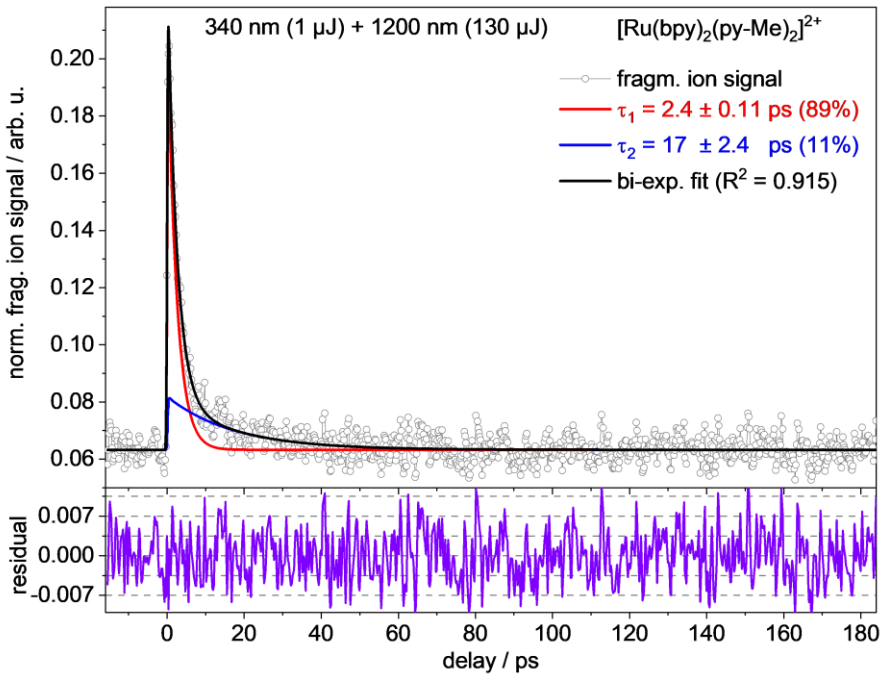

Figure 191 τ-PD of **Y6** recorded at a pump wavelength of 340 nm and probed at 1200 nm within a 200 ps time frame. The bi-exponential fit is shown in black, with the individual fit components represented in red and blue. The fit residuals are displayed below in purple.

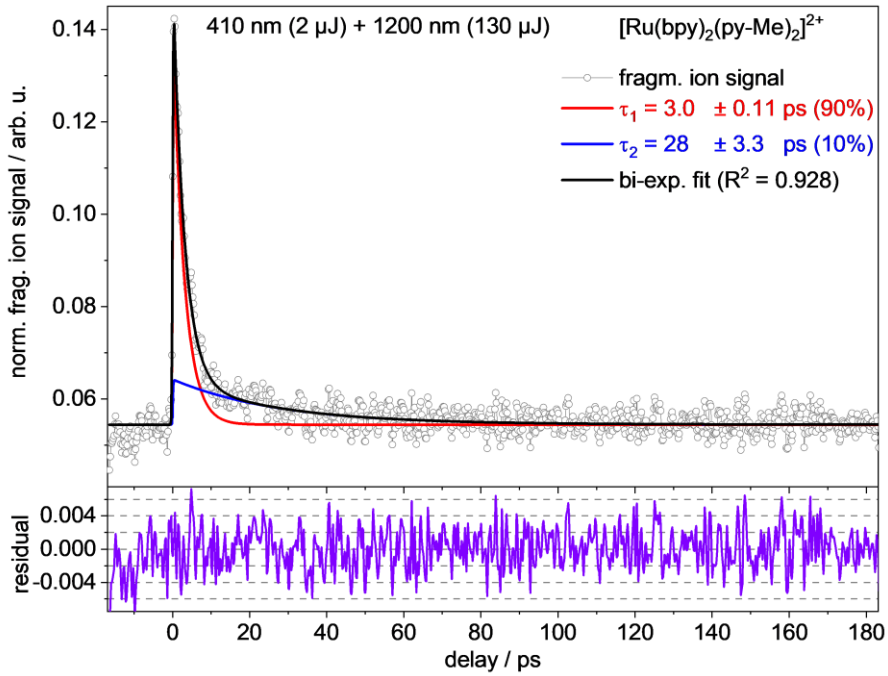

Figure 194 τ-PD of **Y6** recorded at a pump wavelength of 410 nm and probed at 1200 nm within a 200 ps time frame. The bi-exponential fit is shown in black, with the individual fit components represented in red and blue. The fit residuals are displayed below in purple.

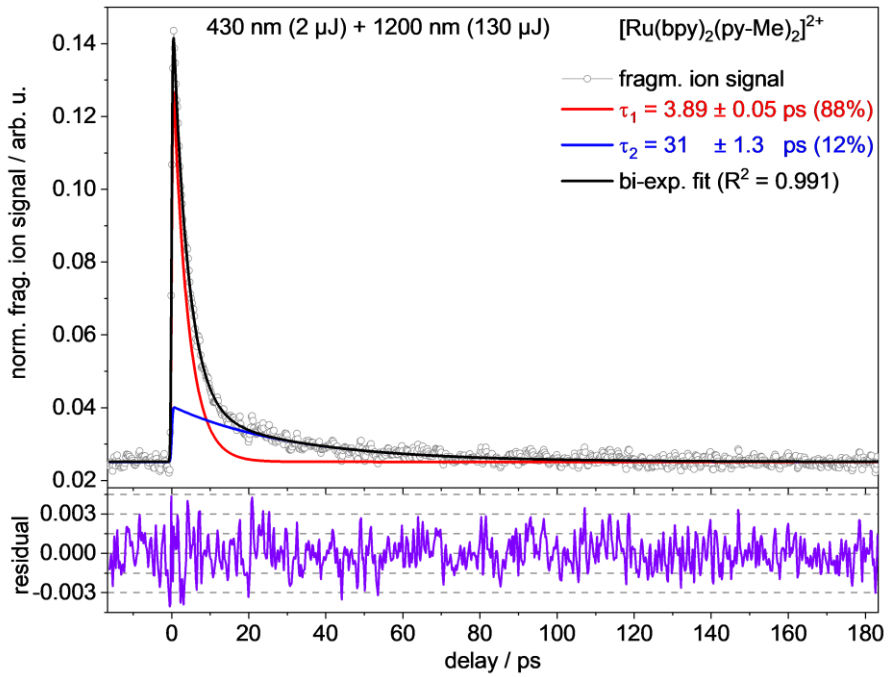

Figure 197 τ-PD of **Y6** recorded at a pump wavelength of 430 nm and probed at 1200 nm within a 200 ps time frame. The bi-exponential fit is shown in black, with the individual fit components represented in red and blue. The fit residuals are displayed below in purple.

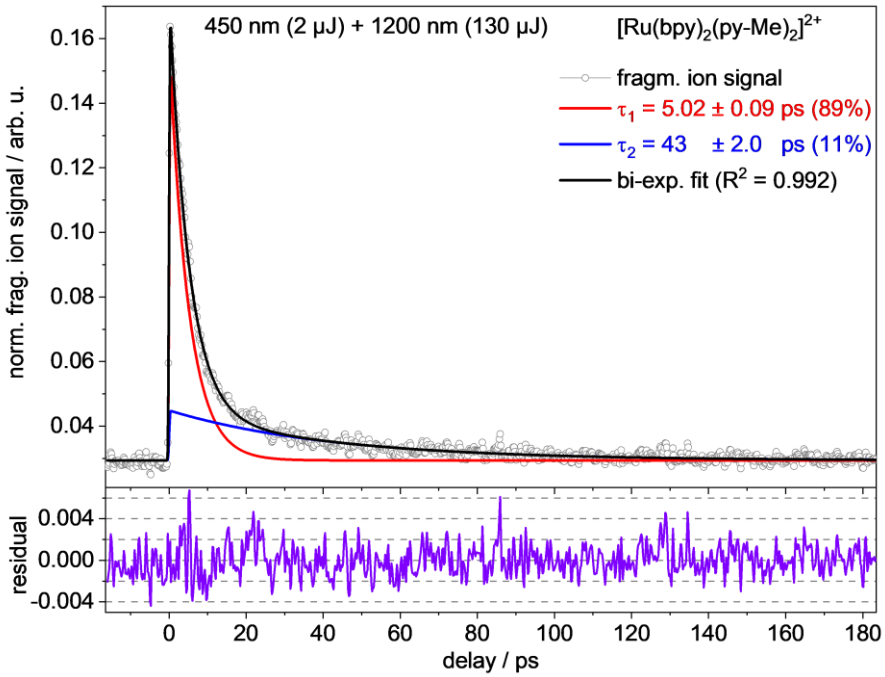

Figure 201 τ-PD of **Y6** recorded at a pump wavelength of 450 nm and probed at 1200 nm within a 200 ps time frame. The bi-exponential fit is shown in black, with the individual fit components represented in red and blue. The fit residuals are displayed below in purple.

"5.4 Correlation time constant τ_1, BDE and Hammett parameters"

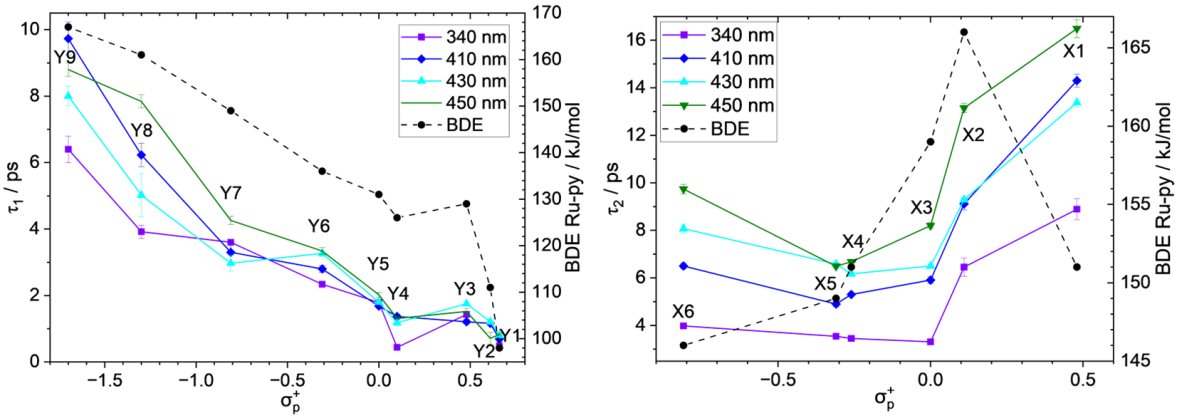

Figure 245 Correlation of time constant τ_1 (gas phase, τ-PD; λ_{ex}: 340-450 nm) and bond dissociation energy BDE (DFT calculation, pyridine ligand loss) for the X- and Y-series of complexes with the values of the Hammett parameter σ_p^+ of the substituents. Experimental points are connected to guide the eye.

Material Specification:

R. G. E. Israil, L. Schüßler; P. Hütchen; W. R. Thiel; R. Diller; C. Riehn,
"Spectroscopy of a Series of Ru(II) Polypyridine Complexes in Gas Phase and Solution: Control of Electronic State Lifetime and Reactivity by Systematic Ligand Derivatization."

Submitted to *Chemistry - A European Journal* on the 18th of February **2025**
Manuscript Number: chem.202500614

Manuscript includes TOC

WILEY VCH

FULL PAPER

Ultrafast Spectroscopy of a Series of Ru(II) Polypyridine Complexes in Gas Phase and Solution: Control of Electronic State Lifetime and Reactivity by Systematic Ligand Derivatization

Roumany G. E. Israil,*[a] Lars Schüssler,[b] Patrick Hütchen,[c] Werner R. Thiel,[c] Rolf Diller[b] and Christoph Riehn[a,d]

[a] R. G. E. Israil, PD Dr. C. Riehn
Department of Chemistry
Rheinland-Pfälzische Technische Universität Kaiserslautern-Landau (RPTU)
Erwin-Schrödinger-Str. 52, D-67663 Kaiserslautern, Germany
E-Mail: riehn@chemie.uni-kl.de; Tel: +49 631 205 4859

[b] Dr. L. Schüssler, Prof. Dr. R. Diller
Department of Physics
Rheinland-Pfälzische Technische Universität Kaiserslautern-Landau (RPTU)
Erwin-Schrödinger-Straße 46, D-67663 Kaiserslautern (Germany)

[c] Dr. P. Hütchen, Prof. Dr. W. R. Thiel
Department of Chemistry
Rheinland-Pfälzische Technische Universität Kaiserslautern-Landau (RPTU)
Erwin-Schrödinger-Straße 54, D-67663 Kaiserslautern (Germany)

[d] PD Dr. C. Riehn
Research Center OPTIMAS
Erwin-Schrödinger-Straße 46, D-67663 Kaiserslautern (Germany)

Supporting information for this article is given via a link at the end of the document.

Abstract: The importance of Ru(II) polypyridine complexes for photochemical applications hinges on the ability to specifically control their photoreactivity via appropriate substituents. Here, a series of complexes of type $[Ru(X_2\text{-bpy})_2(py\text{-}Y)_2]^{2+}$ is studied, where substituents of either the 2,2'-bipyridine (*bpy*) ligand or the pyridine (*py*) ligand with systematically varying values of Hammett parameter σ_p^+ are employed. A combined approach is used for in-depth characterization: UV spectroscopy and dynamics in gas phase, (TD-)DFT calculations, and static and transient absorption spectroscopy in solution. Corresponding to the electron-donating or -withdrawing character of X and Y, given by σ_p^+, clear trends for the complex properties are observed: While increasing σ_p^+ for the X-series leads to energetically lowered ^{1}MLCT states, increasing ^{3}MLCT lifetime and decreasing ligand dissociation quantum yield, the opposite effects occur for the Y-series due to energetically lowered ^{3}MC states. Thus, the Hammett parameter renders as an effective predictive tool for electronic tuning of Ru(II) polypyridine complexes. The applied concept is perfectly suited to analyze such series of complexes, where the gas phase experiments enable an efficient screening to evaluate possible trends and to pre-select suitable complexes for the application-relevant, but technically more demanding solution phase experiments with characterization of ligand to solvent exchange.

Introduction

A detailed understanding of the photophysics and photochemistry of Ru(II) polypyridine complexes based on their electronically excited state lifetimes is crucial for their application in technology and medicine.[1] These complexes are employed as photosensitizers and light-harvesting complexes in solar energy conversion,[2] luminescent materials for imaging,[3] and photosensitive agents for targeted control of biomolecular processes,[4] ranging from neurobiology to photodynamic therapy as cytostatics.[5] They also represent key compounds in photocatalysis, e.g., in water splitting applications.[6] Depending on the application, different properties of these complexes are desired. For some applications, the formation of a long-lived electronically excited state, specifically the metal-to-ligand charge transfer triplet state (^{3}MLCT), is required as a prerequisite for subsequent energy or charge transfer.[2b] Conversely, for other applications, the fast formation of dissociative reaction products with the highest possible quantum yield is required,[4b] necessitating short-lived electronically excited states, such as the metal-centered triplet (^{3}MC) state, coupled to a reactive coordinate. The efficiency of these two contrasting scenarios hinges on the coupling of the various electronic states in the octahedrally coordinated Ru(II) polypyridine complex, including MLCT, MC, ligand-to-metal charge transfer (LMCT), ligand-centered (LC) states, etc. According to the current research,[7] this coupling depends on several parameters, particularly the multiplicity, energy and equilibrium geometry of the according electronic states. In general, these parameters can be modulated by the type and redox properties of the central ion (here Ru(II)), the ligands, their bite angle, substituents, solvation shell (solvent), temperature, pressure, and the state of aggregation (gas phase, solution, solid).

Typical for octahedral Ru(II)-(N,N') complexes (N,N': 2,2'-bipyridine (*bpy*) or related ligands), with Ru(II) as a d^6 system in a singlet ground state (t_{2g}^6), are relatively low-lying (singlet) ^{1}MLCT transitions into the $\pi\pi^*$ states of the ligands.[8] From these Franck-Condon states, a very rapid (sub-ps[9]) intersystem crossing (ISC) with a high quantum yield ($\Phi(^3\text{MLCT}) \approx 1$[8]) occurs into a manifold of vibrationally excited ^{3}MLCT states, which relax in solution into their vibrational ground states within the ps time range. In many Ru(II) polypyridine systems, luminescence originating from this state is observed, with long triplet lifetimes of hundreds of nanoseconds.[9]

In contrast, it has been observed that systems in which the ^{3}MC state lies energetically below the ligand-centered ^{3}MLCT state or is thermally accessible from the latter, exhibit thermally induced luminescence quenching and increased reactivity (such as ligand dissociation, formation of mono-aqua or di-aqua complexes in aqueous solution, or in general ligand exchange).[10] The occupation of this ^{3}MC (also referred to as: ^{3}dd, $t_{2g}^5e_g^1$ or ligand field LF) state requires a shift of a metal-centered t_{2g} electron into an e_g orbital, which leads to an increase in the Ru-ligand, i.e., Ru-N, distance and, depending on its redox properties, a destabilization of this bond, resulting in dissociation, either directly or by coupling back into highly vibrationally excited ground state levels.

However, the experimental detection and characterization of the ^{3}MC state in Ru(II) polypyridines remains challenging[11] and important aspects of its structure and dynamics, leading to the so-called penta-coordinated intermediate (PCI) with one coordinative bond cleaved, were disclosed solely by comprehensive quantum chemical calculations for homoleptic tris-bidentate complexes.[7a, b, 11c, 12] As a result of these theoretical efforts two minimum structures could be located on the excited state surface: a $^3MC_{hexa}$ state followed along the reaction coordinate by a $^3MC_{penta}$ state, where the former exhibits entrance and exit barrier and the latter is characterized by an elongated Ru–ligand distance pointing towards the PCI configuration. This model was further refined by consideration of $^3MC_{cis}$ and $^3MC_{trans}$ states[13] and very recently applied in a new way to explore the non-radiative decay of homoleptic complexes based on a series of 4,4'-substituted 2,2'-bipyridine ligands (*X$_2$-bpy*).[7f]

The complexity of this electronic surface makes it necessary to develop and explore further experimental methods to provide additional data for its characterization and photochemical pathways. Thus, here we follow an alternative experimental approach to investigate this difficult-to-grasp electronic state. We apply chemical derivatization to control the relevant electronic state energies by systematic substitution on the ligands, modifying their σ donor/π acceptor function, all within a rigid, well-defined complex framework. The resulting variation of the Ru-pyridine (Ru-py) bond and electronic states of the complexes should be correlated with values given by the empirical σ-Hammett parameter of substituents on the according *bpy* or *py* ligands.[14] These Hammett substituent constants (σ_p, σ_p^+) provide in terms of a linear free energy relationship a quantitative measure of the electron-donating (negative values) or electron-withdrawing (positive values) effects of substituents on the ligands and therefore should be critical in predicting and understanding the photophysical and photochemical behavior of Ru(II) polypyridine complexes. Thus, by varying the substituents on the ligands, it should be possible to control the overall electronic spectroscopic properties of the complexes, thereby influencing their excited state lifetimes and resulting reactivity.

Previous studies along these lines can be categorized according to the type of substituted ligands, their involvement in the photoexcitation (as chromophore) and/or subsequent dissociation (as leaving group), extent of variation in the substituents and documented impact on the complex properties. In this context, Ford and coworkers early-on demonstrated the electronic influence on complexes by ligand derivatization using compounds of type $[Ru(NH_3)_5(py\text{-}X)]^{2+}$ (with *py-X*: substituted *py*).[15] They observed that electron-withdrawing groups lead to a red-shift in absorption/emission and elongation in excited state lifetime whereas electron-donating groups provoked a blue-shift and shortening of lifetime. Similar trends of spectroscopic shifts and non-radiative decay times were reported by Ciana et al.[16] for substituted bipyridine, although for Os(II) complexes. Though, in both reported studies[15-16] the derivatized ligand acts as the MLCT chromophore and also as leaving group[15] or trigger of non-radiative decay.[16] Furthermore, other approaches to monitor photoinduced dynamics make use of ancillary ligands not exclusively involved in the electronic absorption process;[17] a procedure that we will also elaborate on (see below, X-series). Note that counter-intuitive effects on the photochemical properties with respect to ligand derivatization have been observed in some of these systems.[17c]

Despite the importance of the electronic character of the ligands, one should not neglect the influence of their steric demand which determines the ligand field splitting as well as the resulting shifts of MC levels in energy. Along these reflections one would expect electron-withdrawing (-donating) substituents on the ligands to lower (rise) the MC energies and thus shorten (elongate) the excited state lifetimes, after all counteracting the effects as reported for the MLCT states.[15-16] An illustrative example for this behavior was reported by Sun et al.[11a, d] Using sterically active substituents (e.g., $[Ru(m\text{-}bpy)_3]^{2+}$, *m-bpy* = 6-methyl-2,2'-bipyridine) the authors argued that their results from femtosecond transient absorption (fs-TA) and time-dependent density functional theory (TD-DFT) are consistent with the lowering of the ^{3}MC state induced by the low ligand field strength of the non-optimal octahedral N_6 arrangement and consequentially a rapid depopulation of the ^{3}MLCT state, whereas spectroscopic shifts seem to be negligible.[10] This emphasizes the need for systematic investigations of such phenomena as a function of ligand substitution patterns, the major theme of this work.

Moreover, Ershov and Meyer published a study[18] on the band position of bipyridine MLCT transitions and the rate of radiative and non-radiative decay in compounds of the type $[(bpy)_2Ru(L)NO_2]^+$ (L = pyridine derivative). Their spectroscopic data showed excellent correlation with the values of the Hammett parameter σ_p of the L ligand series, supported by TD-DFT calculations,[19] with electron-donating substituents causing a spectroscopic red shift and electron-withdrawing substituents causing a spectroscopic blue shift. However, the role of the MC states and consequences for the ligand dissociation process were

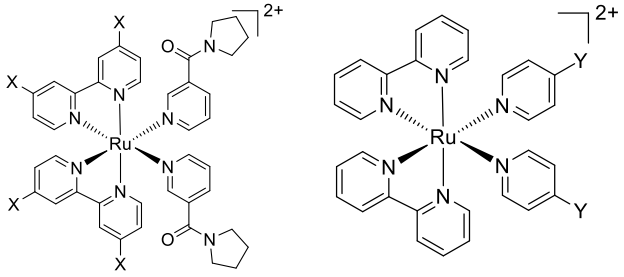

Figure 1. Structure of the $[Ru(X_2\text{-}2,2'\text{-bipyridine})_2(\text{pyridine-Y})_2]^{2+}$ of the X- and Y-series. The X-series involves substituents on positions 4,4' of the 2,2'-bipyridine (left) and *nnp* (N-nicotinoylpyrrolidine). The Y-series involves substituents in para position of the pyridine (right).

not elucidated as the experiments were performed at 77 K. Similar approaches of photochemical ligand tuning (mostly by bipyridine derivatization) with a limited set of variations[20] also directed and supported by quantum chemical calculations[21] have been reported, driven by the many applications for such compounds as mentioned above.

In order to give a comprehensive classification on the influence of ligand substitution patterns on the spectroscopy, energetics and dissociation dynamics of Ru(II) polypyridines including the effect of environment (gas phase vs. solution), we are now presenting the systematic investigation at room temperature of complexes of the types $[Ru(X_2\text{-bpy})_2(\text{py-Y})_2]^{2+}$ (Figure 1), which provide both types of chemical substitutions, covering the Hammett parameter scale as discussed above, on the chromophoric *bpy* ligands as well as on the non-chromophoric (or less chromophoric) *py* ligands. In addition to electronic absorption spectra, we also record the electronic dynamics, *py* ligand dissociation and substitution in aqueous solution and supplement the data by TD-DFT calculations.

In this study, we follow up on a unique approach,[22] which includes the synthesis of novel complexes, their quantum chemical characterizations, and UV/Vis spectroscopy in solution as well as in gas phase and additionally applies fs-photofragmentation spectroscopy in the gas phase. For selected complexes, we also utilize fs-UV/Vis transient absorption spectroscopy in solution. The methods we employ for transient spectroscopy in the gas phase and in solution, along with fragment yield measurements in the gas phase, provide an accurate picture of the ultrafast electronic dynamics, and photodissociation (PD) and demonstrate clearly the influence of solvation or, in general, the environment on such dynamics,[23] as provided by our recent pilot study on $[Ru(II)(bpy)_2(\text{nicotinamide})_2]^{2+}$.[22b]

In the latter we have provided a detailed kinetic scheme for both gas phase and solution ligand dissociation pathways after photoexcitation, which we expand and refine here. Specifically, we have investigated a series of Ru(II) complexes $[Ru(X_2\text{-bpy})_2(nnp)_2]^{2+}$ (Figure 1, **X1-6**) and $[Ru(bpy)_2(\text{py-Y})_2]^{2+}$ (Figure 1, **1-9**), where X is a substituent at 4,4'-position of bipyridine and Y is a substituent in the para-position of *py* (Table 1). The selection of substituents was based on covering a broad range of σ_p^+ values (X-series: -0.81 to +0.48, Y-series: -1.70 to +0.66), systematically varying electron-donating and -withdrawing substituents to affect the coupling of the ^{3}MLCT and ^{3}MC states as discussed above.

Results and Discussion

Mass Spectrometric Analysis and Gas Phase Photodissociation

All compounds in this study, i.e., $[Ru(X_2\text{-bpy})_2(nnp)_2](PF_6)_2$ (**X1-6**) and $[Ru(bpy)_2(\text{py-Y})_2](PF_6)_2$ (**Y1-9**), were investigated in gas phase using ion trap laser PD spectroscopy. First of all, the samples were characterized using electrospray ionization mass spectrometry (ESI-MS) from 10^{-6} M acetonitrile solutions. The resulting overview mass spectra prominently displayed the intact dicationic complexes of types $[Ru(X_2\text{-bpy})_2(nnp)_2]^{2+}$ (**X1-6**) and $[Ru(bpy)_2(\text{py-Y})_2]^{2+}$ (**Y1-9**) as the most intense parent ion signals, verified by their isotopic patterns (SI-Figs. 9-34). These species were isolated in the ion trap and fed to multistage mass spectrometric (MS^n) methods applied subsequently. The second prominent signal in the overview mass spectrum is usually identified as the PCI: $[Ru(X_2\text{-bpy})_2(nnp)]^{2+}$ or $[Ru(bpy)_2(\text{py-Y})]^{2+}$, formed by a loss of an *nnp* or a *py-Y* ligand, which could stem from a dissociative equilibrium in solution or, more likely, was generated by the ESI process. The PCI represents a very important, but difficult-to-grasp intermediate,[7a, b, 11b-d] and was previously identified in related complex systems upon photosubstitution reactions in aqueous solution (see also below).[22b, 24] Following the isolation of the parent ions in the ion trap, fragmentation was induced by collision-induced dissociation (CID) with the He buffer gas and decisively by laser PD, resulting in a similar series of fragment ions (SI-Tabs. 2-16), again with the major fragment ions corresponding to the PCI species. Thus, we were able to show that the same or a very similar process, namely the PD of a *py* ligand, can be effectively scrutinized both in gas phase and in solution (see below[22b]), forming a crucial foundation for this study.

More specifically, all the $[Ru(X_2\text{-bpy})_2(nnp)_2]^{2+}$ species disassembled upon PD (and also CID) solely into the PCI by loss of an *nnp* ligand, whereas the series of $[Ru(bpy)_2(\text{py-Y})_2]^{2+}$ species exhibited more complex fragmentation and ion-molecule reaction pathways, which are detailed below. For instructive comparison, the photofragment mass spectra of **Y4** and **X3** are exemplified in Figure 2. It is noteworthy that these complexes differ structurally only in the chemical configuration of the N-carbonyl-pyrrolidine substituent on the pyridinyl-type ligand, i.e., para- substitution at the *py* ring (**Y4**, N-*iso*-nicotinoyl-pyrrolidine, *iso-nnp*) vs. meta-substitution at the pyridine ring (**X3**, *nnp*). For **Y4** (Figure 2, upper trace), the ion signal at m/z 207, assigned to $[Ru(bpy)_2]^{2+}$, arose from the double loss of the *py-Y* ligands. Signals at m/z 216 and 225 were attributed to water association, forming $[Ru(bpy)_2(H_2O)]^{2+}$ and $[Ru(bpy)_2(H_2O)_2]^{2+}$, resp., with residual water in the ion trap, which is a common observation for undercoordinated metal complexes in the ion trap environment. Even more importantly, the mono-aqua complex (PCI-H_2O, $[Ru(bpy)_2(\text{py-Y})(H_2O)]^{2+}$, nominally at m/z 304) was observed as a broad, unstructured mass peak, likely due to a gas phase equilibrium formed by the addition and dissociation of the

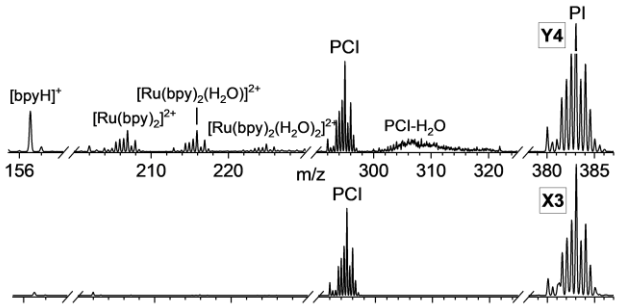

Figure 2. Photodissociation mass spectra of the X- and Y-series complexes subsequent to mass isolation of the parent species, exemplified for **X3** ($[Ru(bpy)_2(nnp)_2]^{2+}$) and **Y4** ($[Ru(bpy)_2(iso\text{-}nnp)_2]^{2+}$ (λ_{exc} = 270 nm, 3.6 µJ/pulse). PCI at m/z 295. PI: parent/precursor ion.

weakly bound water molecule. Its width may also result from dissociation during the detection process, where strong collisions with He are present. Alongside the PCI, the PCI-H_2O adduct is a critical intermediate for modelling photoreactions of Ru(II) polypyridine complexes in aqueous solution, ultimately leading to the di-aqua species ($[Ru(bpy)_2(H_2O)_2]^{2+}$), which in turn is recognized as a key player in the bioactivity of Ru(II)-based photodrugs.[4a, 5, 22b, 24] Note that the formation of PCI-H_2O was exclusively observed for the Y-series of complexes.

This behavior (as exemplified for **Y4** and **X3**; Figure 2) is attributed to the steric properties of the ligands: the *nnp* ligand used in the X-series is significantly more sterically demanding compared to the *iso-nnp* ligand used in the Y-series. Moreover, the pyridinyl ring of the *nnp* ligand used in the X-series enables intramolecular hydrogen bonding (C=O…H-$C_{pyrrolidin}$[25]), resulting in higher binding energies of the *nnp* ligands. Consequently, in the X series the formation of H_2O adducts is hindered. The latter might also indicate the tendency towards a bidentate coordination, although our DFT calculations do not reveal a stable structure of this type, opposite to ortho-substituted carboxamides, which are known to form N- and O-chelates with Ru(II).[26] However, the meta-positioned N-carbonyl-pyrrolidine group of the X-series may obstruct the addition of H_2O to the PCI structure by hindering its transport to the metal center by weak H-bond interaction, which appears insufficiently stable for MS detection. In addition to steric effects, we have thoroughly investigated the electronic influence of the various substituents on ligand binding energy, spectroscopy and dynamics which will be further elaborated upon in the following subsections.

Characterization of the Ru(II) Ligand Binding

To analyze the ligand-binding characteristics, particularly of the "designed-to-be-released" pyridinyl-type ligands, in the complexes of this study, we carried out quantum chemical geometry and energy optimizations using density functional theory (DFT) at the B3LYP[27]/cc-pVTZ/MDF28[28] level of theory. Based on this approach, the bond dissociation energy (BDE) of the Ru-pyridine bond for each complex was determined by comparing the calculated energies of the intact complexes, the corresponding PCI structures, and the free *py* ligands as follows: $BDE = E_{complex} - E_{PCI} - E_{py\ ligand}$ (Table 1).

To examine the correlation between the ligand substitution and the calculated BDEs, the complexes of the X- and Y-series in Table 1 were arranged in descending order of the σ_p^+ Hammett substituent constants, from the electron-withdrawing groups (positive values) at the top to electron-donating groups (negative values) at the bottom. For the Y-series, a clear correlation was observed: a more negative value of σ_p^+ (indicating stronger electron-donating character of substituent at the pyridine) goes hand in hand with an increasing *py* ligand BDE, which we would rationalize by the in parallel increasing σ donor strength of the ligands towards the Ru(II) center and hence elevated ligand binding. In contrast, the trend in the X-series, which contains more remote substituents on the *bpy* ligands, is less straightforward. First, the in general higher BDEs could be attributed to the intramolecular H-bonds between the *nnp* ligands as discussed in the section above. Second, we believe that a weak but systematic opposite trend in the BDEs is recognizable, i.e., a decrease in BDE with electron-donating strength. A rough explanation for this trend could be a kind of staggered influence of the electron density from the *bpy* ligands via the Ru(II) center onto the Ru(II)-*nnp* bond, i.e., a decrease of charge on the metal center leads to an according decrease in the Ru(II)-*nnp* BDE. The weakness of this trend is attributed to the only indirect influence and thus weak coupling of the *bpy* substituents to this bond. Additionally, steric crowding by the two substituents on each bipyridine could also influence the ligand field as discussed in the introduction of this work and reported by other groups.[11]

The correlations of the BDEs with the σ_p^+ Hammett constants of the Y- and the X-series are also visualized in Figure 6 below. Figure 6 (and Table 1) also highlights a notable deviation for complexes containing ligands with COOEt substituents (**X1**, **Y3**), which do not conform to the observed trends. These discrepancies likely arise from difficulties in accurately calculating the BDEs for flexible substituents like COOEt, where locating the global structural minimum is challenging.

To complement the trends observed in the calculated BDEs, we have measured collisional-induced dissociation (CID) breakdown curves from 0 to 3 V excitation amplitude in the ion trap mass spectrometer with the goal to determine the according breakdown/appearance potentials and approximate activation energies for dissociation (SI-Figs. 10-33). The decreasing relative ion signals of the corresponding parent ions and increasing fragment ion signals were fitted to a sigmoidal function. Ions of different mass experience different acceleration in the electric field so that the applied excitation voltage was further transformed into a center-of-mass value (E_{COM}). The $E_{com}^{50\%}$ values, which relate to a voltage where 50% of the precursor ions are fragmented, serve as a measure for relative stability in the gas phase, i.e., here as a measure of pyridine BDE (Table 1). Within the Y-series, the $E_{com}^{50\%}$ values increase for the more electron-donating substituents in correlation with the increasing calculated BDEs. However, the value for **Y3** does not fit into this trend.

In the X-series, the $E_{com}^{50\%}$ values show a slight increase for **X6** to **X4**, consistent with the observed trend in BDEs. However, the values

Table 1. The complexes of the X-series (**X1-X6**) and the Y-series (**Y1-Y9**) with their substituents listed in parentheses, along with their corresponding Hammett parameters σ_p^+: positive value: electron-withdrawing, negative value: electron-donating.[14d, e] *Hammett parameter for the N-carbonyl-pyrrolidine substituent of **Y4** is assumed to be similar to that of $CONMe_2$ due to structural similarity. The $E_{com}^{50\%}$ values (arb. units) represent appearance potentials from collision-induced dissociation (CID) breakdown curves obtained in the ion trap. Bond dissociation energies (BDE, kJ/mol) of pyridine ligands were calculated using DFT (B3LYP/cc-pVTZ/MDF28). ^{1}MLCT band maxima (nm), predicted via TD-DFT (SI-Figs. 72-75) within 400–550 nm, are listed; values in parentheses indicate calculations in H_2O using the polarizable continuum model (PCM).

Complex	σ_p^+	$E_{com}^{50\%}$*10^{-3}	BDE	^{1}MLCT
		$[Ru(X_2\text{-bpy})_2(nnp)_2]^{2+}$		
X1 (COOEt)	0.48	1.57	151	525 (474)
X2 (Cl)	0.11	1.96	166	462 (457)
X3 (H)	0	-	159	445 (438)
X4 (^{t}Bu)	-0.26	2.04	151	442 (440)
X5 (Me)	-0.31	2.00	149	449 (443)
X6 (OEt)	-0.81	1.97	146	447 (448)
		$[Ru(bpy)_2(py\text{-}Y)_2]^{2+}$		
Y1 (CN)	0.66	-	98	418 (428)
Y2 (CF_3)	0.61	3.05	111	424 (423)
Y3 (COOEt)	0.48	2.05	129	430 (427)
Y4 ($CONC_4H_8$)	0.10*	-	126	436 (430)
Y5 (H)	0	3.40	131	436 (442)
Y6 (Me)	-0.31	3.47	136	444 (447)
Y7 (OEt)	-0.81	3.55	149	452 (452)
Y8 (NH_2)	-1.30	3.60	161	462 (463)
Y9 (NMe_2)	-1.70	-	167	466 (466)

for **X1** and **X2** deviate from this pattern, and overall, the variation in these values is very small. Note that absolute $E_{com}^{50\%}$ values depend strongly on the type and also conditioning of the applied mass spectrometer. Thus, the values of the X- and Y-series cannot be directly compared, especially since they have been obtained in separate experimental sessions.

Finally, we would like to point out that the obtained NMR spectra and thereof derived chemical shifts of protons in the according ligands of the synthesized compounds of the X- and Y-series correlate very well with the values of the σ_p^+ Hammett substituent constants (SI-Figs. 1-8). Additionally, since the underlying shielding is linked to the electron density in the ligands, this data further substantiates our earlier analysis and the trends summarized in Table 1.

Static Spectroscopy: UV Photodissociation (UVPD) in Gas Phase

After isolation in the ion trap gas phase, all complex species of the X- and Y- series were subjected to laser photodissociation, whereby so-called UVPD[29] spectra, comparable to UV absorption spectra but without influence of a solvent, were recorded accordingly by employing stepwise tunable laser radiation (Figure 3). These experimental spectra were subsequently compared to quantum-chemically simulated absorption spectra obtained from TD-DFT calculations, for which the underlying multitude of electronic transitions were characterized by visualizing the involved molecular orbitals (MOs) (SI-Figs. 36-75). A close inspection of this computational data reveals that metal-to-ligand charge transfer (MLCT) onto the *bpy* ligands occurs primarily within the range of 400 nm to 550 nm leading to broad but still slightly structured bands. Additionally, MLCT towards the *py* ligands forms bands around 350 nm. Moreover, in the range of 300 nm and below, intra-ligand charge transfer (ILCT) and ligand-centered (LC) transitions are often assignable from the calculations. However, due to their broadness we refrain from discussing evaluated *experimental band positions*, but rather use the *quantum-chemically calculated values* for comparison, in particular since they follow by and large the experimental ones (see Table 1 and discussion below). These theoretical values have been obtained as the long-wavelength maxima resulting from the quantum-chemical stick spectra upon superposition and convolution (Gaussian, fwhm of 1500 cm^{-1}).

At first glance, the UVPD spectra as given in Figure 3 for the main MLCT bands of the X- and Y-series, resp., appear to be more pronouncedly shifted for the Y-series than for the X-series. However, this observation correlates with the range of Hammett parameter values (0.66 to -1.70 for the Y-series and 0.48 to -0.81 for the X-series), indicating that indeed the spectroscopic shifts in both series follow the σ_p^+ values in same measure.

In detail, the bands in the UVPD spectra for the X-series (**X6** to **X1**) (Figure 3, top) reveal a gradual red shift that correlates with the increasing electron-withdrawing character of the ligand substituents. This observed trend aligns with theoretical predictions and reported results from literature,[15-16] as referred to in the introduction. It posits a direct relationship between the electron-withdrawing nature of substituents and the lowering of the energy of the lowest energy MLCT state by increase in delocalization. Notably, **X6** (substituent: OEt) deviates from this trend, exhibiting an unusual red-shift. We hypothesize that the presence of the oxygen atom close to the *bpy* ring possibly enhances its electron-withdrawing, i.e., σ acceptor character (- I effect), thereby stabilizing the MLCT state and resulting in a more pronounced red shift than anticipated. The TD-DFT analysis (Table 1) indicates that the trend in spectroscopic red-shift is not so clear-cut, e.g., the calculated wavelengths for **X6** to **X3** all lie within a region of only 7 nm; similarly when the solvent is computationally taken into account using the simple polarizable continuum model (PCM) model (Table 1, values in parentheses). Nevertheless, an overall trend of spectroscopic red-shift with increasing electron-withdrawing character can be stated.

For the Y-series, a very clear pattern of opposite trend emerges (Figure 3, bottom). The successive increase in electron-withdrawing character of the substituents on the *py* ligands leads to a successive blue-shift in the UVPD spectra, in parallel with the positively increasing values of the Hammett parameter σ_p^+. This trend is strongly supported by the computational results (Table 1), which predict a blue-shift along the Y-series of ca. -50 nm in gas-phase (ca. -40 nm in the PCM modelled solution). We rationalize this trend by the successive lowering of the σ donor character of the substituted *py* ligands, which increases the positive charge on the Ru(II) center and, on the other side, reduces the ability of charge transfer onto the *bpy* ligands.

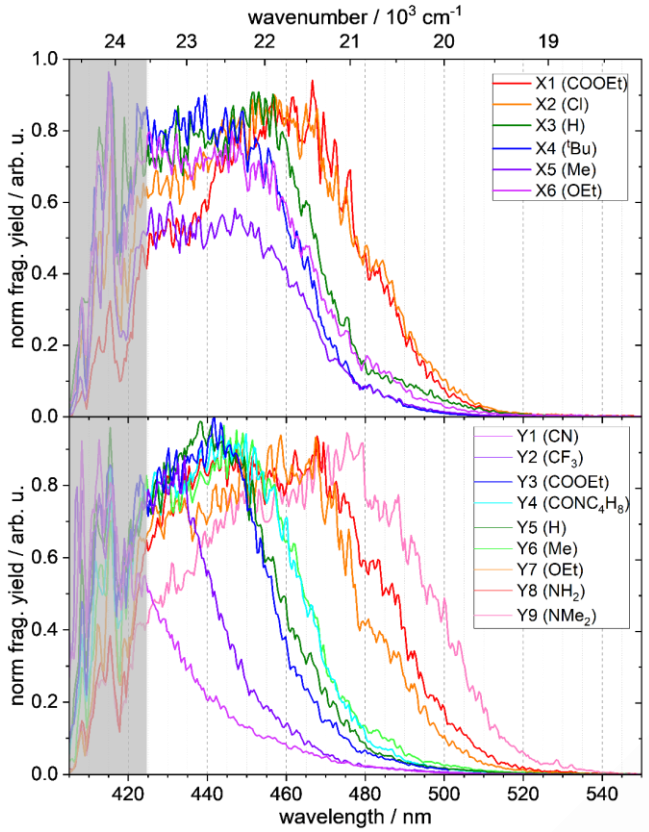

Figure 3. Nanosecond-UVPD (see Experimental Section) spectra of the X- (top) and Y- (bottom) series in the MLCT region, recorded in 0.4 nm steps by the EKSPLA laser system. The curves were smoothed over 5 data points. The grey area (400-425 nm) cannot be analyzed due to the strong modulation of the laser pulse energy.

The latter destabilizes the $MLCT_{bpy}$ electronic states resulting in an energetic upshift, which in turn leads to the observed spectroscopic blue-shift in absorption.

Notably, **Y4** (py-$CONC_4H_8$) exhibits experimentally an unexpected red shift, which might be associated at first glance with steric effects given the bulkiness of the *iso-nnp* ligand. Moreover, inspection of the isomeric **X3** complex, containing the even bulkier *nnp* ligand (a configuration isomer of *iso-nnp*; see discussion above) shows a calculated and experimentally observed even larger red-shift in its absorption (see SI-Figs. 78-79 for spectral comparison). However, it remains incomprehensible how steric repulsion within the *py* ligand moiety could lead to a stabilization of the MLCT states on the bipyridines. Additionally, the probable deficiency in the TD-DFT description of **Y4**, where its MLCT absorption is predicted close to that of **Y5**, rather than to **Y6** as experimentally observed, remains unexplained, leaving the exceptional behavior of **Y4** elusive.

In summary, we have observed a clear and overall understandable correlation of the spectroscopic positions of the main (longest-wavelength) MLCT absorption bands with the values of the Hammett parameter σ_p^+ for the *py* ligand substitution (Y-series) and a weaker but opposite correlation for the *bpy* ligand substitution of the X-series. Both trends agree quite well with the TD-DFT calculations for the absorption bands, so that the quantum-chemical description allows for an adequate representation of the energetics and spectroscopy of all the complexes of the X- and Y-series under study.

Static Spectroscopy: UV/Vis Absorption Spectra of Y2, Y3, Y6 and Y9 in Aqueous Solution

Selected complexes of the Y-series were as well investigated in solution (H_2O) to obtain a direct comparison between the gas phase and the (application relevant) solution and to elucidate the influence of the solvent on the primary photoinduced dynamics, in particular ligand exchange leading to mono- and di-aquation.

A comparison of the static UV/Vis absorption spectra of **Y2**, **Y3**, **Y6** and **Y9** in H_2O in Figure 4 reveals minor changes in the LC and ILCT bands around 290 nm. However, distinct differences are observed in the region of the ^{1}MLCT bands above ≈ 315 nm. As expected from the gas phase results above, the lower-energy ^{1}MLCT bands are red-shifted from **Y2** to **Y9** (**Y2** and **Y3**: ~ 425 nm, **Y6**: ~ 450 nm, **Y9**: ~ 480 nm). Additionally, the corresponding molar absorption coefficients decrease from **Y2** to **Y9**, with the exception of **Y3** (higher molar absorption coefficient). In compliance with the differences of σ_p^+ from **Y2** to **Y3**, **Y3** to **Y6** and **Y6** to **Y9** (0.13, 0.79 and 1.39), the according positions of the ^{1}MLCT bands increase qualitatively from **Y2** resp. **Y3** to **Y9**, even though **Y3** presents an outlier (no pronounced shift and a high molar absorption coefficient).

In contrast to the red-shift of the lower-energy bands, the higher-energy ^{1}MLCT bands around ≈ 330 nm (as assigned to ^{1}MLCT on the *py* ligands, see above) are blue-shifted from **Y2** to **Y9** (**Y2**, **Y3**: ~ 355 nm, **Y6**: ~ 332 nm, **Y9**: ~ 325 nm). Due to the opposing shifts of the higher- and the lower-energy ^{1}MLCT bands, the distance of the (higher- and lower-energy) ^{1}MLCT bands increases from **Y2** resp. **Y3** to **Y9**. Note that due to the superposition of multiple bands leading to the apparent features, an unambiguous determination of band positions is obscured. However, the observed trends are in line with the results of TD-DFT calculations including the PCM (H_2O) solvent model and the resulting simulated UV/Vis spectra (SI-Figs. 77): while a red-shift of the lowest-energy features is observed from **Y2** to **Y9**, the

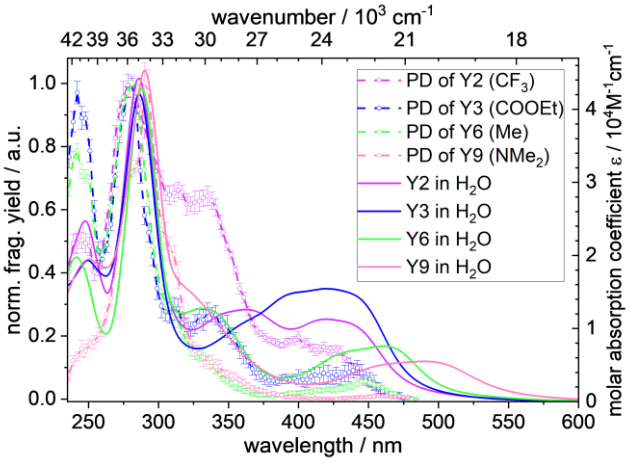

Figure 4. Static UV/Vis absorption spectra of **Y2**, **Y3**, **Y6** and **Y9** in H_2O (solid line) in comparison to the corresponding fs-UVPD (see Experimental Section) spectra in gas phase (data points and dashed lines).

pattern of the resulting simulated bands varies more strongly in the higher-energy (^{1}MLCT-dominated) range. Especially, the calculations for **Y9** show an overall broad distribution of different ^{1}MLCT-bands. Note that the calculated results for **Y3**, similar to the experimental results, give only a small shift of the lower-energy ^{1}MLCT-feature compared to **Y2**, and it shows (again similar to the experiments) the largest simulated absorbance compared to the other complexes.

For comparison with gas phase, Figure 4 depicts additionally the corresponding fs-UVPD spectra of **Y2**, **Y3**, **Y6** and **Y9**. Albeit the expected redshift of the solution spectra compared to the gas phase spectra, the trend over the Y-series is found similarly in both phases (see also Figure 3). Note the differences for $\lambda > \approx$ 420 nm of the fs-UVPD spectra to the ns-UVPD spectra in the previous section (Figure 3), which we attribute to a technical issue (see Experimental Section). We consider the recorded fs-UVPD spectra reliable in the range below 420 nm, whereas the ns-UVPD method succeeds for larger wavelengths.

Irradiation of the samples of **Y2**, **Y3**, **Y6** and **Y9** in H_2O with light from an LED (λ = 340 nm, P ≈ 4 mW) leads to a photo-induced and irreversible formation of photoproducts in analogy to $[Ru(bpy)_2(nicotinamide)_2]^{2+}$ as reported earlier.[22b, 24] This photoreaction is reflected by a red-shift in the lower-energy ^{1}MLCT region of the static UV/Vis absorption spectra (SI-Fig. 80). For **Y2**, **Y3** and **Y6** this redshift occurs in two pronounced temporal phases. Analogous to $[Ru(bpy)_2(nicotinamide)_2]^{2+}$ this most probably represents the fast formation of the mono-aquated photoproducts of **Y2**, **Y3** and **Y6** ($[Ru(bpy)_2(py\text{-}Y)(H_2O)]^{2+}$), followed by the slower formation of further photoproducts, e. g., $[Ru(bpy)_2(H_2O)_2]^{2+}$. In contrast, the changes for **Y9** are not as pronounced as for **Y2**, **Y3** and **Y6** and occur on a longer time scale (without a clear distinction of two temporal phases).

Ultrafast Dynamics: Transient Photodissociation (τ-PD) in Gas Phase

Transient photodissociation (τ-PD, see Experimental Section) measurements were conducted in the ion trap for all species of the X- and Y- series. In order to achieve both a high time resolution and appropriate coverage of time scales, different maximum delay time windows with accordingly optimized time resolution were applied. The resulting comprehensive data sets are given in the SI (SI-Figs. 81-244 and SI-Tabs. 34-41). On this basis, the most accurate representation of fitted time constants across different time windows is compiled in the SI-Tabs. 32-33 and also given in Table 2. In Figure 5, the τ-PD data for **Y2**, **Y3**, **Y6** and **Y9** are depicted as representative examples, especially since the dynamics of these complexes were analyzed in parallel in solution (see below). The according transient decay curves were best analyzed by a two-parameter (time constant) fit (eq. 1 in Experimental Section) listed as τ_1 and τ_2 in Table 2.

For the X-series, a notable increase in the time constant τ_2 was observed from **X5** to **X1**, i.e., from electron-donating to electron-withdrawing substituents, while τ_1 remained relatively unchanged (Table 2). Since the increase of electron-withdrawing character of the substituents (increase of the σ_p^+ values) stabilizes the ^{1}MLCT state reached by photoabsorption and in parallel lowers the energy of the close-by ^{3}MLCT states, reached by the complexes on a sub-ps time scale, the subsequent coupling towards the ^{3}MC states is reduced.

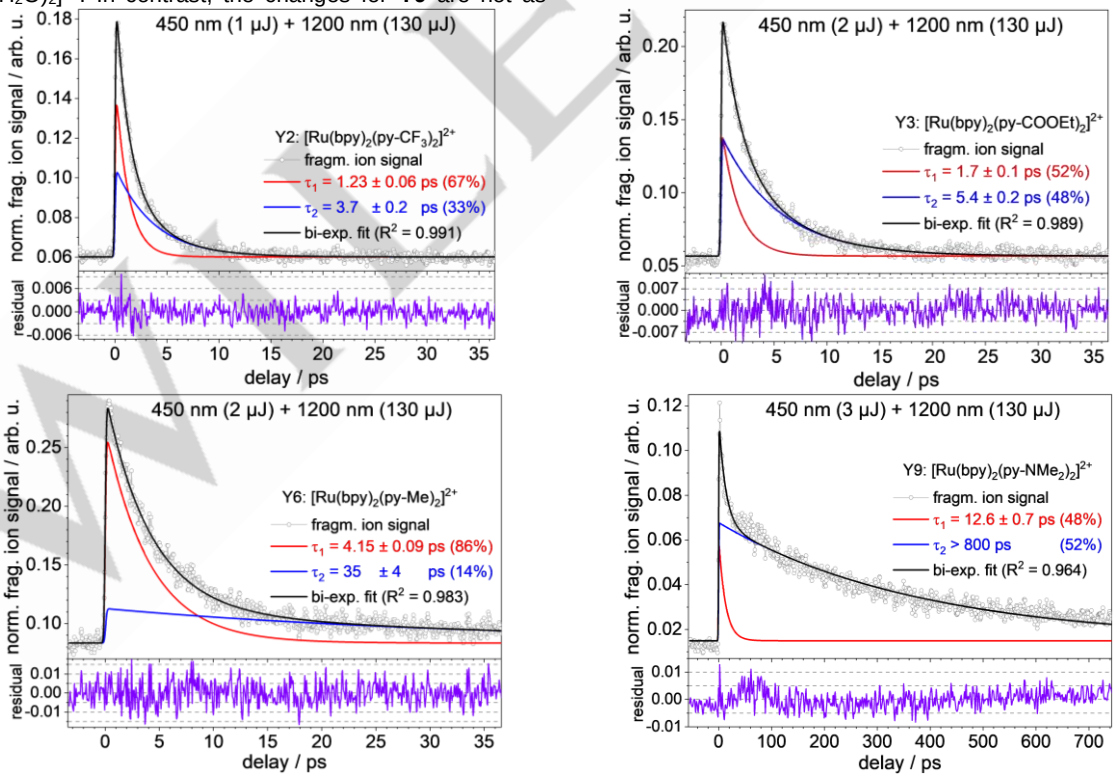

Figure 5. *τ-PD transients of **Y2**, **Y3**, **Y6** and **Y9**. Experimental conditions, fitting results and residua given in the graphs.*

The underlying energetic shift for the ^{1}MLCT states was previously deduced from the static UVPD and absorption spectra, as discussed above. We propose that the reduced field strength of the ligands has relatively minimal influence on the ^{3}MC states energy and argue that the resulting increase of the gap E(^{3}MC) - E(^{3}MLCT) contributes to the deceleration of the deactivation dynamics. Moreover, since the internal conversion towards the ^{3}MC leads to an increase in the Ru-N equilibrium distance, it further (probably via a $^3MC_{hexa}$[7a, b, 12-13, 22b]) proceeds to ligand dissociation forming the PCI directly or by coupling to vibrationally highly excited ground state levels, so that this dissociation is accordingly slowed down upon increase in σ_p^+. This trend in time constant (τ_2) values for the X-series is visualized in Figure 6 (top), where the exception of **X6** is obvious. Notably, its longer-than-expected lifetime aligns with stronger-than-anticipated red-shift in absorption, as described earlier. Further, the 2-3 fold acceleration of the ultrafast dynamics encoded in τ_2 by increase of photon energy (λ_{ex} = 450 nm → 340 nm) seen in Figure 6 (top) supports the model of an activated dissociation process.[22b]

For the Y-series (**Y9** to **Y1**), an even more well-defined correlation between *both* time constants (τ_1, τ_2) and σ_p^+ is observed (Table 2): however, now as σ_p^+ increases both time constants are systematically and strongly decreased, i.e., we observe the opposite behavior, as emphasized by the graph in Figure 6 (bottom; value for **Y9** not to scale) for τ_2. In this case, i.e., the *py* ligand substitution (Y-series), the increase of electron-withdrawing character lowers the ^{1}MC and in parallel the ^{3}MC states due to the reduced ligand field strength and according smaller ligand field splitting. As discussed above, the consequences of this down-shift of the dissociative ^{3}MC states are enhanced by the up-shift (destabilization) of the ^{1}MLCT/^{3}MLCT states resulting from the less compensated charge on the metal center for lower σ donating ligands, as clearly demonstrated by the according spectroscopic blue-shift (see above). In summary, the low energy ^{3}MC states dominate now the ultrafast dynamics, leading to rapid deactivation of the triplet states and ligand dissociation, as previously attributed to τ_2.[22b] Additionally, a similar and strong trend is observed for the τ_1 value (Table 2; SI-Fig. 245) decreasing continuously along **Y9** to **Y1**, in total by a factor of ~10. This time constant has been previously assigned[22b] to internal vibrational relaxation (IVR) within the ^{3}MLCT manifold and/or coupling towards the ^{3}MC, more specific: formation of the $^3MC_{hexa}$ intermediate, which proceeds further towards the $^3MC_{penta}$ and PCI.[12] Now this work demonstrates by the proven ligand dependence that the obvious σ_p^+ correlation clearly put the electronic coupling aspect (^{3}MLCT→$^3MC_{hexa}$) of τ_1 into the foreground. Thus, the results of this study lead to a support and refinement of our kinetic model for the Ru(II) polypyridine gas phase dynamics,[22b] with a more explicit assignment of τ_1.

Table 2. Fitted time constants from the τ-PD transients for the X and Y complexes (λ_{exc} = 450 nm) in gas phase. Listed time constants are derived from measurements of different delay time windows (SI-Tabs. 34-41). Marked in grey data from transient absorption (TA) spectroscopy in aqueous solution (**Y2**, **Y3**: λ_{exc} = 350 nm, **Y6**, **Y9**: λ_{exc} = 332 nm). TA of **Y2** for λ_{exc} = 430 nm yields time constants τ_1 = 0.4 ± 0.2, τ_2 = 2.8 ± 0.3, τ_3 = 23 ± 4 and τ_4 = 144 ± 4 ps (cf. main text).

Complex	τ_1 / ps	τ_2 / ps	τ_3 / ps	τ_4 / ps
		$[Ru(X_2\text{-bpy})_2(nnp)_2]^{2+}$		
X1 (COOEt)	1.4 ± 0.1	16.5 ± 0.4		
X2 (Cl)	1.3 ± 0.1	13.2 ± 0.2		
X3 (H)	0.7 ± 0.1	8.2 ± 0.1		
X4 (^{t}Bu)	1.0 ± 0.1	6.7 ± 0.1		
X5 (Me)	0.7 ± 0.1	6.5 ± 0.1		
X6 (OEt)	1.3 ± 0.1	9.7 ± 0.2		
		$[Ru(bpy)_2(py\text{-}Y)_2]^{2+}$		
Y1 (CN)	0.8 ± 0.1	2.1 ± 0.1		
Y2 (CF_3)	0.7 ± 0.2	3.7 ± 0.2		
in solution	0.3 ± 0.2	3.4 ± 0.2	14 ± 1	(138 ± 3)
Y3 (COOEt)	1.5 ± 0.1	5.4 ± 0.2		
in solution	0.4 ± 0.2	3.0 ± 0.2	19 ± 1	(263 ± 4)
Y4 ($CONC_4H_8$)	1.3 ± 0.1	6.3 ± 0.1		
Y5 (H)	2.0 ± 0.1	19.4 ± 0.9		
Y6 (Me)	3.3 ± 0.1	42.7 ± 0.1		
in solution	0.7 ± 0.2	3.4 ± 0.2	36 ± 7	≈ (2 - 3) ns
Y7 (OEt)	4.3 ± 0.1	50 ± 2.0		
Y8 (NH_2)	7.8 ± 0.2	87 ± 3.0		
Y9 (NMe_2)	8.8 ± 0.2	> 800		≈ (2 - 3) ns
in solution	0.5 ± 0.2	2.8 ± 0.2	36 ± 5	≈ (4 - 5.5) ns

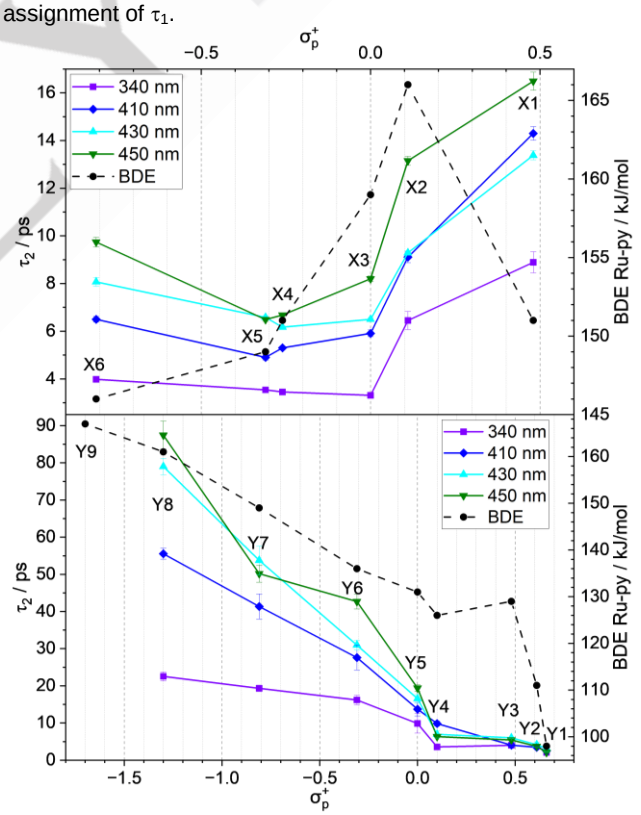

Figure 6. Correlation of time constant τ_2 (gas phase, *τ-PD; λex:* 340-450 nm) and bond dissociation energy BDE (DFT calculation, *py* ligand loss) for the X-series (top) and Y-series (bottom) of complexes with the values of the Hammett parameter σ_p^+ of the substituents. Experimental points are connected to guide the eye. (Time constant value for **Y9** not to scale)

Moreover, the wavelength dependence of both time constants with a distinct increase upon shortening of the pump wavelengths (resulting in larger excess energy) points towards activated processes for the underlying elementary steps (SI-Fig. 245 for τ_1; Figure 6 (bottom) for τ_2), which is consistent with mechanistic considerations from the literature.[7a, 12, 22b] Here, it is noticeable, that this energy dependence is less pronounced for **Y1-Y4**, which could be interpreted in a way that the ^{3}MLCT/^{3}MC$_{hexa}$/^{3}MC$_{penta}$ barriers are already quite low for **Y4**, and thus, further increase in photon energy (excess energy) does not lead to additional strong acceleration of the dynamics.

Overall, the time constants of both the X- and Y-series (Table 1), exhibit clear and unequivocal correlations with the σ_p^+ values. These values reflect the substituent-dependent ligand electron density distributions, which not only govern the complexes' UV spectroscopy but also influence their electronic state energies. Consequently, these factors control both the excited state lifetimes and their associated dissociative reactivity.

Ultrafast Dynamics: Transient Absorption in Aqueous Solution

UV/Vis fs TA in H_2O was performed on **Y2** and **Y3** excited at 350 nm and on **Y6** and **Y9** excited at 332 nm. The resulting difference spectra are shown in Figure 7 and selected transients are compared in Figure 8. The collected data were analyzed via global analysis (eq. 2, Experimental Section), which yields the DAS and time constants shown in Figure 9 and Table 2 (further transients and their corresponding fit curves are shown in SI-Fig. 246). Note that excitation at 430 nm yields the same results for **Y2** as excitation at 332 nm, and the difference spectra of **Y9** excited at 450 nm show no change compared to an excitation at 350 nm (cf. SI-Figs. 247-248). Thus, analogous to $[Ru(bpy)_2(nicotinamide)_2]^{2+}$,[22b] a higher-energy ^{1}MLCT-excitation of **Y2**, **Y3**, **Y6** and **Y9** results in similar dynamics as a lower-energy ^{1}MLCT-excitation due to rapid conversion processes during the system response time of 230 fs, including the typical sub-100 fs ISC from the ^{1}MLCT to the ^{3}MLCT-manifold.[30]

All difference spectra in Figure 7 exhibit typical features of Ru(II)-polypyridine complexes: (i) ^{3}MLCT-excited state absorption (ESA) roughly around 370 nm,[11a, c, d, 24, 30a, c, 31] (ii) ground state bleach (GSB) roughly around 430 nm for **Y2**, **Y3**, around 466 nm for **Y6** and around 496 nm for **Y9** (with a red-shift consistent with the static UV/Vis absorption spectra in Figure 4), and (iii) ESA above roughly 500 nm (depending on the GSB). Contributions from ^{3}MLCT-ESA are evident above 500 nm,[11a, c, d, 24, 30a, c, 31] while the ESA above 550 nm is primarily associated with the ^{3}MC state for **Y2**, **Y3**, **Y6** and **Y9**, consistent with assignments for $[Ru(bpy)_2(nicotinamide)_2]^{2+}$ and other Ru(II)-polypyridine complexes.[11a, c, d, 22b] Notably, for **Y9** (Figure 7d) the signal in the longer wavelength region is significantly stronger than for the other investigated complexes. This can partially be explained by a red-shift of the ^{3}MLCT-ESA and thus a larger resulting superposition of the ^{3}MLCT- and ^{3}MC-ESA in this region.

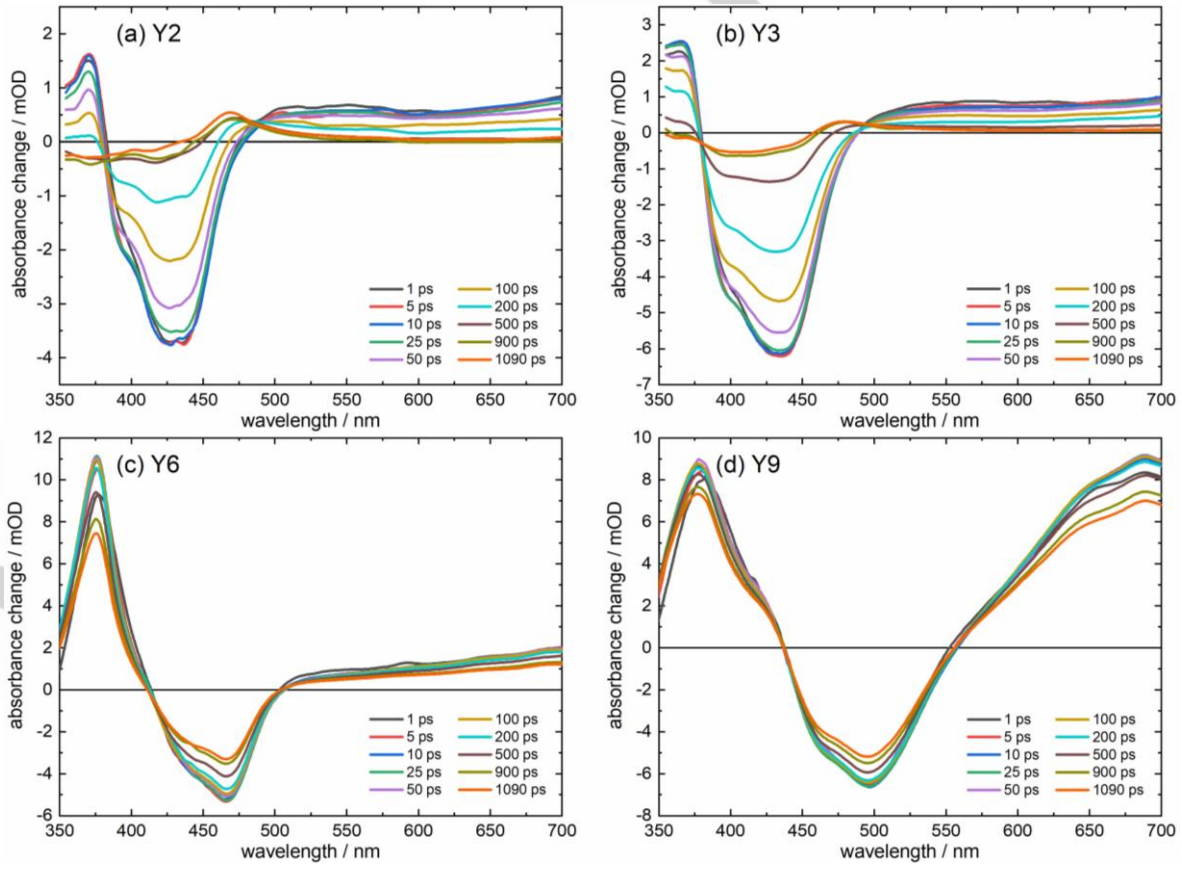

Figure 7. Difference spectra at selected delay times for **Y2** (a), **Y3** (b), **Y6** (c) and **Y9** (d) in H_2O after ^{1}MLCT-excitation (**Y2** and **Y3** excited at 350 nm, **Y6** and **Y9** excited at 332 nm).

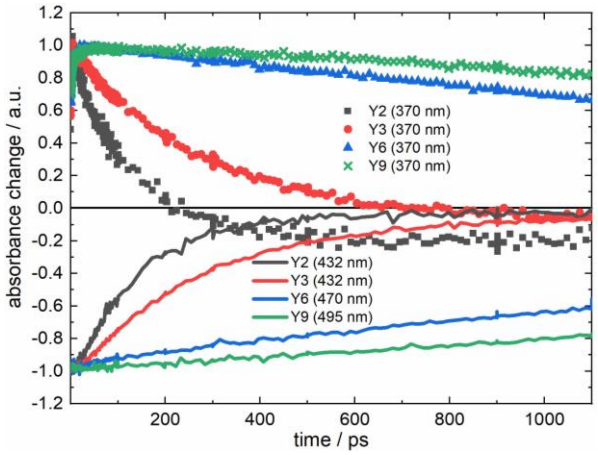

Figure 8. Normalized absorbance transients for **Y2**, **Y3**, **Y6** and **Y9** in H_2O after ^{1}MLCT-excitation at a selected wavelength of 370 nm (ESA, symbols) and 432, 432, 470 and 495 nm, resp. (GSB, lines). **Y2** and **Y3** were excited at 350 nm, **Y6** and **Y9** at 332 nm.

However, further investigation is required to unravel this behavior. Taking the static UV/Vis absorption spectra into account (relative molar absorption coefficients, Figure 4), the contribution of the GSB to the superimposed ^{3}MLCT-ESA around 370 nm in Figure 7 is larger for **Y2** and **Y3** as for **Y6** and **Y9**. This results in smaller apparent ESA signals in this region for **Y2** and **Y3**. In addition, a shoulder around 415 nm occurs solely for **Y9**, probably indicating a larger separation of ^{3}MLCT states in the manifold.

The temporal evolution of the difference spectra clearly shows an increase of the excited state lifetimes from **Y2** to **Y9**. Whereas a large residual signal remains for **Y6** and **Y9** at 1090 ps, only a small signal in the GSB region remains for **Y2** and **Y3** at 1090 ps and an additional positive band roughly around 475 nm arises. This residual signal for **Y2** and **Y3** at 1090 ps represents the photo-induced formation of the irreversible mono-aquated photoproduct in analogy to $[Ru(bpy)_2(nicotinamide)_2]^{2+}$.[22b, 24] The global analysis (DAS in Figure 9) yields four components for all complexes **Y2**, **Y3**, **Y6** and **Y9**. The most important result is the increase of τ_4 from **Y2** to **Y9** with $\tau_4 \approx 140$ ps (**Y2**), 263 ps (**Y3**), 2-3 ns (**Y6**) and > 4 ns (**Y9**). A_4 covers signal decay in the complete investigated spectral range (350-700 nm) and thus the ground state recovery (GSR) simultaneous with the decay of the ESA around 370 nm and above ≈ 500 nm. Thus, A_4/τ_4 clearly shows an increase of the ^{3}MLCT lifetime (ESA around 370 nm) from **Y2** to **Y9** in accordance with the corresponding Hammett parameter values. This increase is clearly visualized by the slowdown of absorbance decay in Figure 8. In contrast, there is no trend regarding $\tau_1 \approx 0.3$-0.7 ps, $\tau_2 \approx 2.8$-3.4 ps and $\tau_3 \approx 14$-36 ps over the series, albeit τ_3 is larger for **Y6** and **Y9**. However, all results on **Y2**, **Y3**, **Y6** and **Y9** in H_2O are in line with, and further corroborate, a model analogous to the already published model for $[Ru(bpy)_2(nicotinamide)_2]^{2+}$ in H_2O ("slow" model "A"[22b]). Based on this model the component with A_3/τ_3 represents H_2O-ligation to the PCI along with geminate recombination of the previously (with τ_4) dissociated *py-Y* ligand. Thus, this component (A_3/τ_3) is probably not directly related to the Hammett parameter σ_p^+, but rather determined by solvent cage dynamics, which are beyond the scope of this work.

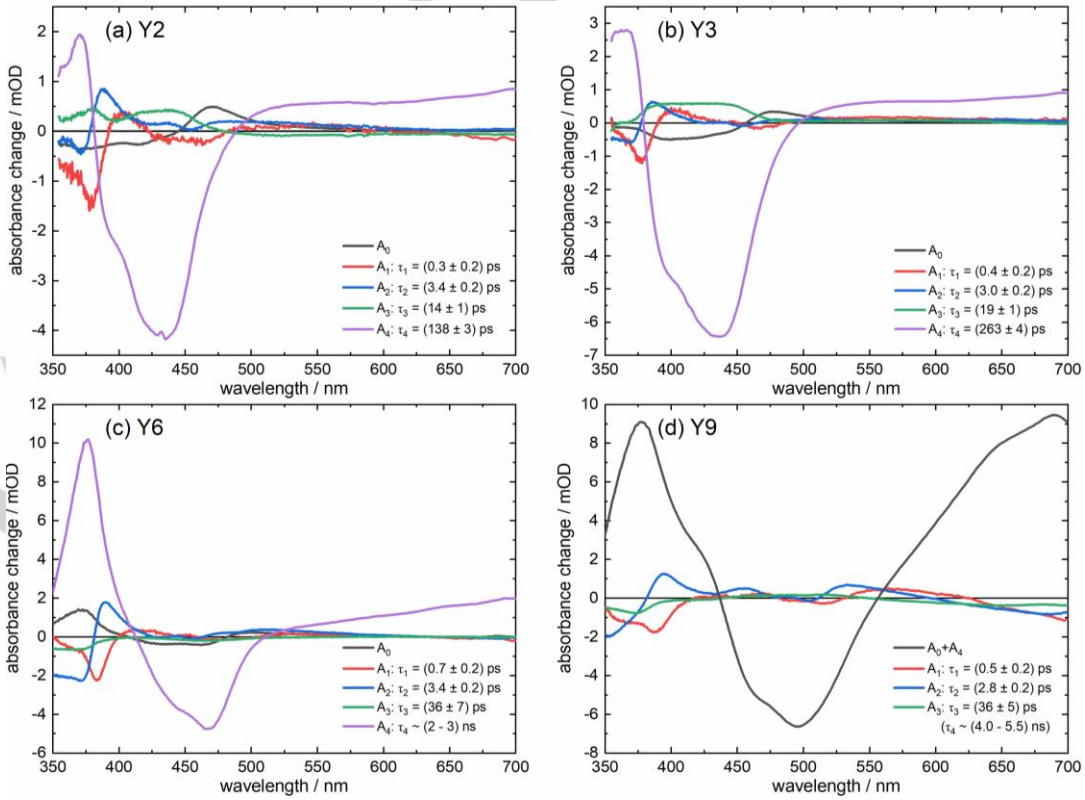

Figure 9. Decay associated spectra (DAS) for **Y2** (a), **Y3** (b), **Y6** (c) and **Y9** (d) in H_2O after ^{1}MLCT-excitation (**Y2** and **Y3** excited at 350 nm, **Y6** and **Y9** excited at 332 nm) as a result of a global analysis according to eq. 2 (Experimental Section).

A_0 represents the extent of the mono-aquated photoproduct for **Y2**, **Y3** and **Y6.**[22b] In the case of **Y9**, the longest lifetime exceeds 4 ns (τ_4 > 4 ns), much longer than the investigated time window (1.1 ns). Thus, an unambiguous distinction between A_4 and A_0 was not possible, and in consequence A_4 was added to A_0 in order to account for the longest-lived states.

Conclusion

From the presented experimental and theoretical data it is obvious, that the observed trends in excited state lifetimes, bond dissociation energies, reaction yields and spectroscopic properties correlate well with the values of the Hammett parameter σ_p^+ for the substituents on both X- and Y-series ligands.

The significance of this central result is further strengthened by the fact that the kinetic data confirm and strongly support our photochemical pathway model developed previously for the deactivation of the structurally related $[Ru(bpy)_2(nicotinamide)_2]^{2+}$ after photoexcitation.[22b] Besides ultrafast intersystem crossing to the ^{3}MLCT manifold, the model comprises - in solution phase - picosecond time constants, τ_1 and τ_2, corresponding to vibrational relaxation, while a third, τ_3, captures water ligation to the PCI and geminate recombination of the nicotinamide ligand. The same model applies to the here investigated Y-series, where similar time constants τ_1, τ_2 and τ_3 were determined and show no trend related to the Hammett parameter values, in line with the expectation for relaxation processes independent of the ^{3}MLCT lifetime.

In contrast, the fourth, slower time scale constant τ_4, equally observed for ^{3}MLCT decay and ground state recovery in solution, is assigned to concomitant ligand dissociation and clearly shows an increase from **Y2** to **Y9**, indicating an increased ^{3}MLCT lifetime and reduced ligand dissociation quantum yield, in correlation to the respective Hammett parameter values. Analogous results are obtained for the X- and Y-series in gas phase, where ligand dissociation is expected to occur faster, with strongly changed degrees of freedom for intra- and intermolecular energy dissipation pathways and dynamics.

Our data reveal distinct trends in the properties of the X- and Y-series, reflecting the impact of substituent electronic effects on both ligand moieties (*X_2-bpy*, *py-Y*) of the $[Ru(X_2\text{-bpy})_2(nnp)_2]^{2+}$ (**X1-X6**) and $[Ru(bpy)_2(py\text{-}Y)_2]^{2+}$ (**Y1**-**Y9**) complexes under study. Thus, our parallel gas phase/solution approach and the selected X- and Y-series are perfectly suited to systematically elucidate the contrary effects on the electronic properties while going from electron-donating to electron-withdrawing substituents (i.e. increasing Hammett parameter σ_p^+). The following trends were identified: While for the X-series increasing σ_p^+ values lead to energetically lowered ^{1}MLCT states, increased ^{3}MLCT lifetime and bond dissociation energy (BDE), as well as a lowered dissociation yield, the opposite effect occurs for the Y-series, where increasing σ_p^+ values enhance the ^{3}MLCT/^{3}MC coupling to the reactive coordinate and the ground state, shortening the ^{3}MLCT lifetime, decreasing the BDE and increasing the dissociation yield. The X-series shows comparatively small variations in properties, which is consistent with its narrower range of σ_p^+ values. This is strongly supported by the TD-DFT results, that suggest more subtle electronic influences on the complex's MLCT states in the X-series relative to the Y-series. Overall, both series display contrasting spectroscopic and kinetic variations, albeit in line with the expected electronic trends. Outliers indicate that additional factors - such as further -I/+I and -M/+M effects, substituent configurations, and steric influences - contribute to these properties. This suggests that the Hammett parameter values of ligand substituents offer predictive utility for electronic tuning of Ru(II) polypyridine complexes, but the full substitution effects must be experimentally evaluated (if possible in both gas phase and solution) for precise control and optimization of excited state dynamics.

In conclusion, the combined approach of gas phase and solution experiments with quantum chemical calculations has proven effective for capturing the intricate dynamics of Ru(II) polypyridine complexes. The gas phase measurements efficiently delineate overall trends across substituent series and are perfectly suited to screen and pre-select complexes for the more challenging and time-consuming solution phase experiments that translate these insights to practical, application-relevant conditions. This approach allows a nuanced understanding of how substituents impact photophysical properties, providing a framework for designing Ru(II) complexes with tailored excited state characteristics.

Our results emphasize that Hammett parameter-guided ligand substitution is a valuable strategy for controlling the lifetimes and reactivity of electronic states in Ru(II) polypyridine complexes, advancing their potential for fine-tuned design in photosensibilisation applications ranging from photocatalysis, photomedical therapy to solar energy conversion. Future work should extend this methodology to additional Ru(II) complexes with diverse ligand structures to deepen the understanding and refine the control over their photophysical and photochemical properties.

Experimental Section

Gas Phase/Ion Trap

Ion trap mass spectrometry and photodissociation spectroscopy: The experimental setup for gas-phase mass spectrometric and laser spectroscopic investigations utilized an amaZon speed ion trap mass spectrometer (Bruker Daltonik) equipped with an Apollo II electrospray ionization (ESI) source. Modifications were made to the Paul-type quadrupole ion trap to facilitate laser-induced fragmentation spectroscopy.[22a, 32]

To introduce the dicationic complexes of the X- and Y-series ($[Ru(X_2\text{-bpy})_2(nnp)_2]^{2+}$ (**X1-6**) and $[Ru(bpy)_2(py\text{-}Y)_2]^{2+}$ (**Y1-9**)) into the gas phase, a solution of approximately 10^{-6} M in acetonitrile (ACN) was employed. To prevent photoinduced decomposition by ambient light, solutions were stored in amber glass bottles. ACN and other solvents were pre-treated with molecular sieve (4 Å). A syringe pump continuously delivered the sample solution to the ESI source at a flow rate of 120 µL/min. The spray needle operated at 4.5 kV, with nitrogen serving as the nebulizer and

drying gas flowing at 4 L/min, maintained at 180°C and 410 mbar (7 psi).

Femtosecond-UVPD and τ-PD: For both static femtosecond UV photodissociation (fs-UVPD) and transient photofragmentation τ-PD) measurements, appropriate laser pulses were generated based on a Wyvern 1000 TM cryogenic ultrafast regenerative oscillator/amplifier laser system (KMLabs). These amplifier laser pulses had a duration of ca. 50 fs at 780 nm at an average power of ca. 3.5 W and a repetition rate of 981 Hz (≈ 1 kHz). The laser beam was split to pump two optical parametric amplifier systems (Light Conversion, TOPAS-C) generating pump and probe pulses, both with variable wavelengths.

Femtosecond-UVPD spectra were recorded from 236 to 480 nm with a 3 nm step size, each pulse providing ca. 2 μJ energy using one of the TOPAS-C units. The laser beam alignment ensured optimal ion fragment yield from the isolated ion cloud for each measurement. Fragmentation time was set at 100 ms, corresponding to about 100 pulses of irradiation per ion cloud, controlled by a laser shutter. Each wavelength was sampled with ca. 20 data points, and each data point represented an average of 7 mass spectra. Total fragment yield (TFY) was calculated as $I_f/(I_f + I_p)$, where I_f and I_p represent the sums of fragment (f) and parent ion (p) mass peak intensities, resp. Additionally, the fragment yield was normalized to the number of photons N (= $E_{pulse} \cdot \lambda / (h \cdot c)$).

For time-resolved measurements (τ-PD), the second TOPAS-C system produced a probe beam at 1200 nm with ca. 130 μJ/pulse, overlapping with the pump beam in the ion trap. The pump beam wavelength was selected based on electronic transitions identified from UVPD measurements, set at low energy (≈ 1 μJ) to induce single-photon excitation. Pump and probe pulse timing was controlled using a mechanical delay-stage (Physik Instrumente, PI) equipped with a retroreflector. Signal collection and analyses involved averaging 12 scans and fitting using OriginLab 2019G to a sum of exponentials (eq. (1)), incorporating the instrument response function (IRF) convolution through an error function (erf).

$$Y(t) = Y_0 + \sum_{i=1}^{n} \left[A_i e^{0.5\left(\frac{w}{\tau_i}\right)^2 - \frac{t-t_0}{\tau_i}} \cdot 0.5 \left(erf\left(\frac{(t-t_0)/w - w/\tau_i}{\sqrt{2}} \right) + 1 \right) \right]$$

eq. (1)

t: delay time, Y_0: offset, A_i: amplitude of component i, τ_i: lifetime constant of component i, t_0: time zero, w: fwhm/$(2\sqrt{2ln2})$ of Gaussian representing the IRF.

Nanosecond-UVPD: Given the significance of the main MLCT region (420 nm – 550 nm) for elucidating the influence of X- and Y-ligand substituents on the photochemistry of the investigated complexes of this study, we applied a complementary laser method for recording the UVPD spectra using an EKSPLA NT242-1k-SH/SF nanosecond optical parametric oscillator (OPO) laser system, which offers wavelength tunability from 210 nm to 2600 nm at high pulse energy (> 60 μJ) and small linewidth (<5 cm^{-1}). The NL210 pump laser, a Q-switched Nd-YAG laser, emits 1064 nm pulses with durations of 4-6 ns at a repetition rate of 1 kHz. The fundamental output is frequency-doubled and tripled to generate the third harmonic at 355 nm, which feeds into the OPO stage, providing precise wavelength tunability for the experiments. A home-written control software (NEWT, New Ekspla Wave Tuner) based on LabTalk facilitates precise, automatic wavelength tuning at fixed wavelength intervals and thus enables high-resolution ns-UVPD experiments. The wavelength adjustments were synchronized with the ion trap mass spectrometer software (Bruker TrapControl), ensuring that fragmentation data was recorded at each selected wavelength. Scans were typically carried out in 0.4 nm steps, and separate power curve measurements were performed for each scan to match the maximum pulse energy with the specific experimental conditions. Power adjustments, controlled by the Ophir Starlab software, accounted for the varying pulse energies across different wavelength ranges, ensuring accurate and efficient dissociation within the 210-650 nm range.

The experimental approaches for recording UVPD spectra differ significantly depending on the laser system employed, with the Wyvern and EKSPLA OPO systems offering distinct advantages and challenges, particularly in terms of wavelength resolution and experimental practicality. The Wyvern laser system allows for measurements at each wavelength with constant low pulse energy (3-6 μJ), ensuring consistent experimental conditions and representative photodissociation behavior, particularly in resonant regions. However, this method is relatively time-consuming, as each wavelength must be measured individually. Additionally, the pulse energy of the Wyvern system is sometimes insufficient for dissociation above 400 nm. In contrast, the EKSPLA OPO system enables rapid measurements across a tunable wavelength range. Wavelength steps can be adjusted according to the experimental needs – from coarse intervals for quick measurements to very fine steps (e.g., 0.01 nm) for high resolution. This flexibility allows for either fast acquisition of UVPD spectra or detailed, high-resolution studies. However, the EKSPLA system cannot maintain constant pulse energy across the scanned range. For example, in the 400–425 nm region, the strong modulation in laser pulse energy could lead for weakly absorbing and fragmenting molecular systems to artificial modulations in fragment ion yield (artifacts in the UVPD spectra). We consider the recorded fs-UVPD spectra reliable in the range below 420 nm, whereas the ns-UVPD method succeeds for larger wavelengths (λ > 420nm).

Quantum Chemical Calculations

To validate UVPD spectra assignment, complex geometry optimization and single-point energy calculations utilized density functional theory (DFT) and time-dependent (TD-)DFT at the B3LYP[27]/cc-pVTZ/MDF28[28] levels within the Gaussian software package. Calculations in solvent were executed exploiting the polarizable continuum model (PCM). Excited state calculations were evaluated with GaussSum 3.0,[33] and a customed script on VMD v1.9.4[34] was used for visualization of the involved orbitals.

Solution Experiments

Static UV/Vis absorption spectroscopy in aqueous solution was performed with a JASCO V-670 spectrophotometer. The setup for femtosecond (fs) transient absorption spectroscopy in solution (UV/Vis fs TA) has been described in detail elsewhere.[22b] A

Coherent Libra regenerative amplifier laser system (1 kHz repetition rate, 4 mJ/pulse at 800 nm, 100 fs pulse duration) was used to generate the probe pulses with a spectral range from 350 to 700 nm (via self-phase modulation in a moving 5 mm CaF_2-window) and the pump pulses at 450, 430, 350 or 332 nm (via Coherent TOPAS-Prime). The focal width of the probe beam at sample position was ≈ 50 µm (FWHM: Full width at half maximum), and that of the pump beam ≈ 100 µm (FWHM). The single pulse energy of the pump pulses was 260 nJ. The relative polarization of pump and probe beam was 54.7° at sample position (magic angle condition). A chopper blocked every second pump pulse to obtain pump induced difference absorbance spectra $\Delta A(\lambda, t)$ of the detected probe pulses, where the delay time t between the pump and probe pulses was generated by a delay stage. The difference spectra $\Delta A(\lambda, t)$ were analyzed by a global analysis approach with the global multi-exponential fit function

$$\mathbf{\Delta A}(\boldsymbol{\lambda}, \boldsymbol{t}) = \mathbf{A_0}(\boldsymbol{\lambda}) + \sum_{i=1}^{N} \mathbf{A_i}(\boldsymbol{\lambda}) \cdot \boldsymbol{e}^{-t/\tau_i} \qquad \text{eq. (2)}$$

with $A_i(\lambda)$ the decay associated spectra (DAS), τ_i the time constants, and $A_0(\lambda)$ the residual signal for long delay times (components with “infinite” lifetime compared to the maximum delay time). The global fit was started for delay times > 0.3 ps as the system response time was 230 fs.

Y2, **Y3**, **Y6** and **Y9** were prepared by dissolving the corresponding salt $[Ru(bpy)_2(py\text{-}Y)_2](PF_6)_2$ in HPLC-grade H_2O. The concentration for the UV/Vis fs TA measurements was 0.23, 0.33, 0.20 and 0.20 mmol/l for **Y2** (λ_{ex} = 350 nm), **Y3** (λ_{ex} = 350 nm), **Y6** (λ_{ex} = 332 nm) and **Y9** (λ_{ex} = 332 nm), resp., and 0.23 and 0.31 mmol/l for **Y2** (λ_{ex} = 430 nm) and **Y9** (λ_{ex} = 450 nm), resp.

In order to compensate for the (irreversible) photo-induced formation of mono-aquated photoproducts $[Ru(bpy)_2(py\text{-}Y)(H_2O)]^{2+}$ during the ongoing UV/Vis fs TA measurements a flow cell[22b] with large sample volume (ca. 30 ml) was used. All experiments were performed in the dark to avoid photo-degradation by ambient light and at ambient temperature of 295 K.

Sample Preparation

The synthesis and full characterization of the compounds used in this study are detailed in the Supplementary Information (SI), including the X-ray structure analysis of the complex Y6 ($[Ru(bpy)_2(py\text{-}NMe_2)_2](PF_6)_2$).These supplementary crystallographic data are provided free of charge by the Cambridge Crystallographic Data Centre number 2418660.

Supporting Information

The authors have cited additional references within the Supporting Information.

Acknowledgements

We gratefully acknowledge the support from the German Science Foundation (DFG) by research grants to WT, CR and RD (TH 550/23-1, RI 749/7-1, DI 405/9-1), and Collaborative Research Center CRC/Transregio 88 ‘‘Cooperative effects in homo- and heterometallic complexes (3MET)’’. CR and RGEI thank the SPP 2102 ’’ Light-controlled reactivity of metal complexes’’ for support. We thank Xinyue Wang for performing the CID measurements and Marko Leist for the synthesis of precursor complexes.

Keywords: photochemistry • ruthenium • Hammett parameter • ligand-controlled dynamics • excited state lifetimes

[1] a) W. R. Browne, A. A. Holder, M. A. Lawrence, J. L. Bullock Jr and L. Lilge, *Ruthenium Complexes*, **2018**, p; b) D. W. Thompson, A. Ito and T. J. Meyer, *Pure and Applied Chemistry* **2013**, *85*, 1257-1305.

[2] a) Y. Qin and Q. Peng, *International Journal of Photoenergy* **2012**, *2012*, 1-21; b) A. Breivogel, S. Wooh, J. Dietrich, T. Y. Kim, Y. S. Kang, K. Char and K. Heinze, *European Journal of Inorganic Chemistry* **2014**, *2014*, 2720-2734.

[3] E. S. Villani, K.; Einaga, Y.; Inagi, S.; Fiorani, *Journal of Electroanalytical Chemistry* **2022**, *921*.

[4] a) T. L. Rapp and C. A. DeForest, *Adv Drug Deliv Rev* **2021**, *171*, 94-107; b) L. Zayat, C. Calero, P. Albores, L. Baraldo and R. Etchenique, *J Am Chem Soc* **2003**, *125*, 882-883.

[5] S. Bonnet, *J Am Chem Soc* **2023**, *145*, 23397-23415.

[6] J. J. Concepcion, J. W. Jurss, M. K. Brennaman, P. G. Hoertz, A. O. Patrocinio, N. Y. Murakami Iha, J. L. Templeton and T. J. Meyer, *Acc Chem Res* **2009**, *42*, 1954-1965.

[7] a) A. Soupart, F. Alary, J.-L. Heully, P. I. P. Elliott and I. M. Dixon, *Coordination Chemistry Reviews* **2020**, *408*, 213184; b) A. Soupart, I. M. Dixon, F. Alary and J.-L. Heully, *Theoretical Chemistry Accounts* **2018**, *137*; c) J. Moll, C. Wang, A. Papcke, C. Forster, U. Resch-Genger, S. Lochbrunner and K. Heinze, *Chemistry* **2020**, *26*, 6820-6832; d) G. E. Shillito, S. Rau and S. Kupfer, *ChemCatChem* **2023**, *15*; e) D. Hernandez-Castillo, R. E. P. Nau, M. A. Schmid, S. Tschierlei, S. Rau and L. Gonzalez, *Angew Chem Int Ed Engl* **2023**, *62*, e202308803; f) D. Hernández-Castillo, I. Eder and L. González, *Coordination Chemistry Reviews* **2024**, *510*.

[8] V. Balzani and S. Campagna, *Photochemistry and Photophysics of Coordination Compounds I*, **2007**, p.

[9] W. Henry, C. G. Coates, C. Brady, K. L. Ronayne, P. Matousek, M. Towrie, S. W. Botchway, A. W. Parker, J. G. Vos, W. R. Browne and J. J. McGarvey, *J Phys Chem A* **2008**, *112*, 4537-4544.

[10] P. S. Wagenknecht and P. C. Ford, *Coordination Chemistry Reviews* **2011**, *255*, 591-616.

[11] a) Q. Sun, S. Mosquera-Vazquez, Y. Suffren, J. Hankache, N. Amstutz, L. M. Lawson Daku, E. Vauthey and A. Hauser, *Coordination Chemistry Reviews* **2015**, *282-283*, 87-99; b) T. Mukuta, S. i. Tanaka, A. Inagaki, S.-y. Koshihara and K. Onda *ChemistrySelect* **2016**, *1*, 2802-2807; c) Q. Sun, B. Dereka, E. Vauthey, L. M. Lawson Daku and A. Hauser, *Chem Sci* **2017**, *8*, 223-230; d) Q. Sun, S. Mosquera-Vazquez, L. M. Daku, L. Guenee, H. A. Goodwin, E. Vauthey and A. Hauser, *J Am Chem Soc* **2013**, *135*, 13660-13663.

[12] A. J. Gottle, F. Alary, M. Boggio-Pasqua, I. M. Dixon, J. L. Heully, A. Bahreman, S. H. Askes and S. Bonnet, *Inorg Chem* **2016**, *55*, 4448-4456.

[13] K. Eastham, P. A. Scattergood, D. Chu, R. Z. Boota, A. Soupart, F. Alary, I. M. Dixon, C. R. Rice, S. J. O. Hardman and P. I. P. Elliott, *Inorg Chem* **2022**, *61*, 19907-19924.

[14] a) L. P. Hammett, *Chemical Reviews* **1935**, *17*, 125-136; b) L. P. Hammett, *Journal of the American Chemical Society* **1937**, *59*, 96-103;

c) D. H. McDaniel and H. C. Brown, *The Journal of Organic Chemistry* **1958**, *23*, 420-427; d) C. Hansch, A. Leo and R. W. Taft, *Chemical Reviews* **1991**, *91*, 165-195; e) R. S. Sengar, V. N. Nemykin and P. Basu, *New Journal of Chemistry* **2003**, *27*.

[15] P. C. Ford, *Reviews of Chemical Intermediates* **1979**, *2*, 267-296.

[16] L. Della Ciana, W. J. Dressick, D. Sandrini, M. Maestri and M. Ciano, *Inorganic Chemistry* **1990**, *29*, 2792-2798.

[17] a) Y. Liu, D. B. Turner, T. N. Singh, A. M. Angeles-Boza, A. Chouai, K. R. Dunbar and C. Turro, *J Am Chem Soc* **2009**, *131*, 26-27; b) J. D. Knoll, B. A. Albani, C. B. Durr and C. Turro, *J Phys Chem A* **2014**, *118*, 10603-10610; c) H. J. Jang, S. L. Hopkins, M. A. Siegler and S. Bonnet, *Dalton Trans* **2017**, *46*, 9969-9980.

[18] S. V. Litke, A. Y. Ershov and T. J. Meyer, *J Phys Chem A* **2014**, *118*, 6216-6222.

[19] K. I. Reshetova, I. V. Krauklis, S. V. Litke, A. Y. Ershov and Y. V. Chizhov, *Optics and Spectroscopy* **2016**, *120*, 566-574.

[20] D. A. Santos, A. T. Vu, W. W. Brennessel, C. R. Reed and R. N. Garner, *Journal of Coordination Chemistry* **2022**, *75*, 752-763.

[21] M. Jäger, L. Freitag and L. González, *Coordination Chemistry Reviews* **2015**, *304-305*, 146-165.

[22] a) S. V. Kruppa, F. Bäppler, W. Klopper, S. P. Walg, W. R. Thiel, R. Diller and C. Riehn, *Phys Chem Chem Phys* **2017**, *19*, 22785-22800; b) L. Schüßler, R. G. E. Israil, P. Hutchen, W. R. Thiel, R. Diller and C. Riehn, *Phys Chem Chem Phys* **2023**, *25*, 4899-4914.

[23] M. Semwal, N. Vashistha, S. Rau and B. Dietzek-Ivansic, *J Phys Chem A* **2024**.

[24] S. E. Greenough, G. M. Roberts, N. A. Smith, M. D. Horbury, R. G. McKinlay, J. M. Zurek, M. J. Paterson, P. J. Sadler and V. G. Stavros, *Phys Chem Chem Phys* **2014**, *16*, 19141-19155.

[25] R. G. E. Israil,. Master Thesis, TU Kaiserslautern, **2019**.

[26] S. Yadav, P. Vijayan and R. Gupta, *Journal of Organometallic Chemistry* **2021**, *954-955*.

[27] a) A. D. Becke, *Journal of Chemical Physics* **1993**, *98*, 5648-5652; b) C. Lee, W. Yang and R. G. Parr, *Phys Rev B Condens Matter* **1988**, *37*, 785-789.

[28] K. A. Peterson, D. Figgen, M. Dolg and H. Stoll, *J Chem Phys* **2007**, *126*, 124101.

[29] a) S. Xu, J. E. Smith and J. M. Weber, *J Chem Phys* **2016**, *145*, 024304; b) S. Xu, J. E. Smith and J. M. Weber, *Inorg Chem* **2016**, *55*, 11937-11943; c) F. Turecek, *Mass Spectrom Rev* **2023**, *42*, 206-226.

[30] a) N. H. Damrauer, G. Cerullo, A. Yeh, T. R. Boussie, C. V. Shank and J. K. McCusker, *Science* **1997**, *275*, 54-57; b) A. C. Bhasikuttan, M. Suzuki, S. Nakashima and T. Okada, *J Am Chem Soc* **2002**, *124*, 8398-8405; c) J. K. McCusker, *Acc Chem Res* **2003**, *36*, 876-887; d) A. Cannizzo, F. van Mourik, W. Gawelda, G. Zgrablic, C. Bressler and M. Chergui, *Angew Chem Int Ed Engl* **2006**, *45*, 3174-3176.

[31] a) G. A. Heath, L. J. Yellowlees and P. S. Braterman, *Journal of the Chemical Society, Chemical Communications* **1981**; b) N. H. Damrauer and J. K. McCusker, *The Journal of Physical Chemistry A* **1999**, *103*, 8440-8446.

[32] a) D. Imanbaew, Y. Nosenko, C. Kerner, K. Chevalier, F. Rupp, C. Riehn, W. R. Thiel and R. Diller, *Chemical Physics* **2014**, *442*, 53-61; b) J. Martens, G. Berden, C. R. Gebhardt and J. Oomens, *Rev Sci Instrum* **2016**, *87*, 103108.

[33] N. M. O'Boyle, A. L. Tenderholt and K. M. Langner, *J Comput Chem* **2008**, *29*, 839-845.

[34] W. Humphrey, A. Dalke and K. Schulten, *J Mol Graph* **1996**, *14*, 33-38, 27-38.

Entry for the Table of Contents

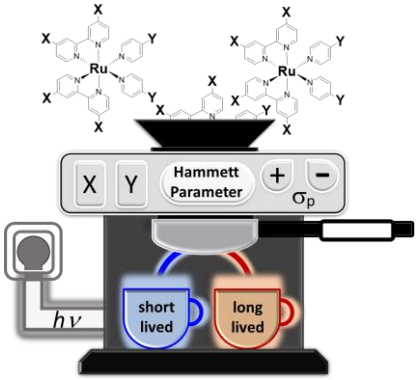

The photochemistry of a series of Ru(II) polypyridine complexes is analyzed by advanced spectroscopy and quantum chemical calculations, both in solution and ion trap gas phase. Clear correlations between Hammett parameter values of ligand substituents and bond dissociation energy, absorption wavelength and excited state lifetime are revealed. For specific applications the choice of substituents allows to select customized optochemical complexes.

Key words:

- Programmable optochemical properties
- Tailored substituent selection based on Hammett parameters
- Correlation between Hammett parameters and photophysical properties
- Ruthenium(II) polypyridine complexes: spectroscopy & quantum chemistry
- Gas-phase and solution-phase spectroscopy
- Customizable ligand effects on bond dissociation energy and excited-state lifetime
- Optochemical tuning for targeted applications
- Structure–property relationship in Ru(II) complexes

WILEY VCH

3.3 Publication 3: Metal-to-Metal Distance Modulated Au(I)/Ru(II) Cyclophanyl Complexes: Cooperative Effects in Photoredox Catalysis

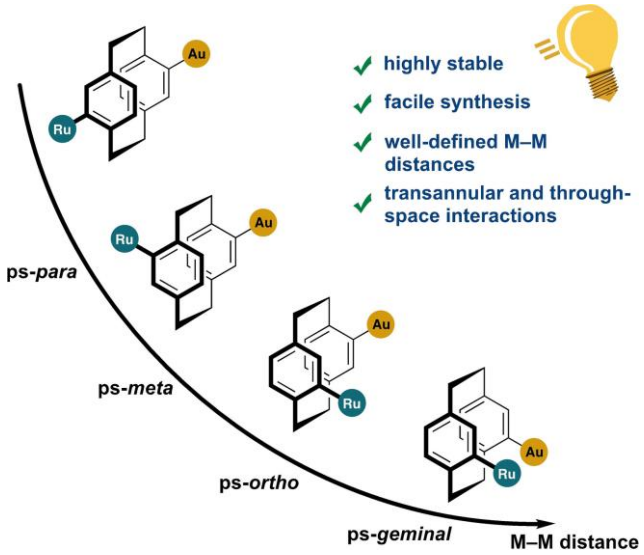

Preamble

Christoph Zippel, Roumany Israil, Lars Schüßler, Zahid Hassan, Erik K. Schneider, Patrick Weis, Martin Nieger, Claudia Bizzarri, Manfred M. Kappes, Christoph Riehn, Rolf Diller, Stefan Bräse, *Chemistry - A European Journal*, **2021**, 27, 15188-15201, https://doi.org/10.1002/chem.202102341; Copyright © 2021 Wiley-VCH GmbH, reproduced with permission from *Chemistry - A European Journal*.

Contribution My contribution to this publication focuses on experimental ion spectroscopy and mass spectrometry, including static and ultrafast transient photodissociation experiments, as well as mass spectrometric analysis and theoretical computations characterizing the relevant electronic transitions. These investigations, conducted under the guidance of Dr. Christoph Riehn, were crucial in probing the excited-state dynamics and metal interactions in a solvent-free environment. I assessed and processed the data obtained using the aforementioned techniques, structured them for the discussion, and contributed them to the manuscript's discussion section. Dr. Martin Nieger contributed crystallographic analyses, while Dr. Christoph Zippel supervised by Prof. Dr. Stefan Bräse synthesized the Au(I)/Ru(II)

heterobimetallic complexes. Structural insights were complemented by calculations of metal-to-metal distances for global minima and Boltzmann-averaged rotamers using DFT geometry optimizations, performed by Dr. Patrick Weis and Prof. Dr. Manfred Kappes. Ion mobility spectrometry validated these structural calculations, alongside absorption and emission spectroscopy experiments. Lars Schüßler and Prof. Dr. Rolf Diller conducted static and time-resolved spectroscopy experiments in the solution phase, while Prof. Dr. Claudia Bizzarri performed electrochemical analyses and Stern-Volmer quenching experiments. The manuscript was written collaboratively with significant contributions from all coauthors, led by Christoph Zippel.

Synopsis This work explores the modulation of metal-to-metal distances in heterobimetallic Au(I)/Ru(II) complexes using [2.2]paracyclophane (PCP) as a rigid bridging ligand. By systematically varying the substitution patterns—pseudo-geminal, -ortho, -meta, and -para—we achieved precise spatial organization of the metal centers, enabling a detailed investigation of their photophysical and catalytic properties. The complexes exhibited promising catalytic activity in a visible-light-mediated arylative Meyer-Schuster rearrangement, with performance strongly influenced by steric effects, electronic parameters, and metal-to-metal distances. Notably, the pseudo-para isomer (pAuRu) demonstrated the highest catalytic efficiency (63% yield), highlighting the importance of spatial organization in photocatalysis. Using ultrafast transient absorption spectroscopy, we observed non-additive interactions between the Au(I) and Ru(II) centers, particularly when excited at 312 nm. This suggests that the presence of the Au(I) moiety significantly influences the excited-state dynamics of the Ru(II) center, a phenomenon not observed in monometallic Ru(II) complexes. Gas-phase photodissociation experiments confirmed the intrinsic nature of long-lived electronically excited states, revealing solvent-free insights into the complexes' photophysical properties. These results emphasize the role of cooperative interactions between metal centers and how fine-tuning their spatial arrangement influences catalytic performance. A clear structure–activity relationship emerged: decreasing the metal-to-metal distance (from pseudo-para to pseudo-geminal) reduced catalytic efficiency, indicating that effective electronic communication is essential for the reaction mechanism.

Electronic Supporting Information (ESI) Further details on experimental methods and data that support the findings of this study are available in the ESI accompanying this publication. I contributed to the preparation and analysis of the ESI content, including mass spectra, UVPD spectra, τ-PD data, and theoretical calculations. Below is a summary of the ESI contents:

1. Material and Methods..... 3

2. Synthetic Protocols..... 12

3. NMR Spectra..... 50

4. Absorption and Emission Spectra..... 88

5. Cyclic Voltametry..... 89

6. Ultrafast Transient Absorption Spectroscopy..... 92

7. X-Ray Diffractometry..... 95

8. Mass Spectrometric Analysis..... 98

9. Laser Pulse Energy Dependency of Fragmentation Yield..... 101

10. UV-PD and Calculated Absorption Spectra, Comparison with Liquid Phase Absorption Spectra..... 103

11. Theoretical Analysis of the Electronic Transitions..... 106

12. Ultra Fast Dynamic in Gas Phase..... 117

13. DFT-calculations of the conformational space of o-, m-, p- and gem-AuRu..... 119

14. References..... 124

Reprint License

© 2021 The Authors. Chemistry - A European Journal published by Wiley-VCH GmbH

This is an open access article under the terms of the http://creativecommons.org/licenses/by-nc-nd/4.0/ License, which permits use and distribution in any medium, provided the original work is properly cited, the use is non-commercial and no modifications or adaptations are made.

PMC Copyright notice

PMCID: PMC8596992 PMID: 34655123

Material Specification:

Christoph Zippel, Roumany Israil, Lars Schüßler, Zahid Hassan, Erik K. Schneider, Patrick Weis, Martin Nieger, Claudia Bizzarri, Manfred M. Kappes, Christoph Riehn, Rolf Diller, Stefan Bräse, "Metal-to-Metal Distance Modulated Au(I)/Ru(II) Cyclophanyl Complexes: Cooperative Effects in Photoredox Catalysis."
Chemistry - A European Journal, **2021**, 27, 15188-15201.
DOI: https://doi.org/10.1002/chem.202102341

Check for updates

Chemistry–A European Journal
Full Paper
doi.org/10.1002/chem.202102341
Chemistry Europe
European Chemical Societies Publishing

Special Issue

Metal-to-Metal Distance Modulated Au(I)/Ru(II) Cyclophanyl Complexes: Cooperative Effects in Photoredox Catalysis

Christoph Zippel,[a] Roumany Israil,[b] Lars Schüssler,[c] Zahid Hassan,[a] Erik K. Schneider,[d] Patrick Weis,[d] Martin Nieger,[e] Claudia Bizzarri,[a] Manfred M. Kappes,[d, f] Christoph Riehn,[b, g] Rolf Diller,[c] and Stefan Bräse*[a, h]

Abstract: The modular synthesis of Au(I)/Ru(II) decorated mono- and heterobimetallic complexes with π-conjugated [2.2]paracyclophane is described. [2.2]Paracyclophane serves as a rigid spacer which holds the metal centers in precise spatial orientations and allows metal-to-metal distance modulation. A broad set of architectural arrangements of pseudo *-geminal*, *-ortho*, *-meta*, and *-para* substitution patterns were employed. Metal-to-metal distance modulation of Au(I)/Ru(II) heterobimetallic complexes and the innate transannular π-communication of the cyclophanyl scaffold provides a promising platform for the investigations of structure-activity relationship and cooperative effects. The Au(I)/Ru(II) heterobimetallic cyclophanyl complexes are stable, easily accessible, and exhibit promising catalytic activity in the visible-light promoted arylative Meyer-Schuster rearrangement.

Introduction

Heterometallic complexes have received considerable attention due to their distinctive magnetic and optical properties and further their emerging synthetic applications in catalysis.[1] Installation of heterometallic moieties in one framework – each intended to serve a particular, independent purpose, can execute precise sequences of multiple reactions in a one-pot fashion. The activity of one metal is enhanced by the other and in combination, may reduce the activation barrier by cooperative effects.[2] Incorporating a second metal center into mononuclear organometallic complexes can lead to novel reactivity and enhanced selectivity compared to the reaction performed with a mixture of related monometallic complexes.[3] However, it remains a synthetic challenge to position heteronuclear metal centers with a well-defined electronic environment in a predefined orientation to one another to achieve cooperative effects. Among various contributing factors based on the nature of the metal, oxidation state, and coordination number, metal-to-metal (M–M) distance modulation has been a promising approach to identify and fine-tune cooperative effects in (hetero)bimetallic systems.[4] Especially the bridging ligand design is decisive to incorporate multiple metal centers in defined orientations and stands in the center from a perspective of application.[5] The choice of the coordination environment, ligand effects like flexibility, sterics, electronic parameters, and an appropriate spacer that allows for systematic variation of M–M distances are crucial contributing factors.[6] The presence of two or more metal centers with defined M–M distances can be achieved either by a conjugated or non-

[a] C. Zippel, Dr. Z. Hassan, Dr. C. Bizzarri, Prof. Dr. S. Bräse
Institute of Organic Chemistry (IOC)
Karlsruhe Institute of Technology (KIT)
Fritz-Haber-Weg 6, 76131 Karlsruhe (Germany)
E-mail: braese@kit.edu
Homepage: http://www.ioc.kit.edu/braese

[b] R. Israil, Dr. C. Riehn
Department of Chemistry, Technische Universität Kaiserslautern (TUK)
Erwin-Schrödinger-Str. 52, 67663 Kaiserslautern (Germany)

[c] L. Schüssler, Prof. Dr. R. Diller
Department of Physics, Technische Universität Kaiserslautern (TUK)
Erwin-Schrödinger-Str. 46, 67663 Kaiserslautern (Germany)

[d] E. K. Schneider, Dr. P. Weis, Prof. Dr. M. M. Kappes
Institute of Physical Chemistry, Karlsruhe Institute of Technology (KIT)
Fritz-Haber Weg 2, 76131 Karlsruhe (Germany)

[e] Dr. M. Nieger
Department of Chemistry
University of Helsinki
P. O. Box 55, Helsinki, 00014 (Finland)

[f] Prof. Dr. M. M. Kappes
Institute of Nanotechnology, Karlsruhe Institute of Technology
Herman-von Helmholtz-Platz 1, 76344 Eggenstein-Leopoldshafen (Germany)

[g] Dr. C. Riehn
Research Center OPTIMAS
Erwin-Schrödinger-Str. 46, 67663 Kaiserslautern (Germany)

[h] Prof. Dr. S. Bräse
Institute of Biological and Chemical Systems
Functional Molecular Systems (IBCS-FMS) Karlsruhe Institute of Technology (KIT)
Hermann-von-Helmholtz-Platz 1, 76344 Eggenstein-Leopoldshafen (Germany)

Supporting information for this article is available on the WWW under https://doi.org/10.1002/chem.202102341

Special Issue This manuscript is part of a Special Issue "Cooperative effects in heterometallic complexes".

© 2021 The Authors. Chemistry - A European Journal published by Wiley-VCH GmbH. This is an open access article under the terms of the Creative Commons Attribution Non-Commercial License, which permits use, distribution and reproduction in any medium, provided the original work is properly cited and is not used for commercial purposes.

conjugated tether. Both types of tethers have been reported for bimetallic ruthenium complexes,[7] whereas a conjugated tether allows an electronic communication between the metal centers and thus an alteration of the electronic properties of one or both metal centers.

Our research group has a long-standing interest in the chemistry of [2.2]paracyclophane (PCP) scaffolds for a diverse range of applications, including developing versatile PCP-derived planar chiral ligands and catalysts – employed most notably for various enantioselective transformations.[8] PCP is a co-facially stacked prochiral scaffold that displays unusual characteristics caused by transannular π-π electronic interactions of the benzene rings fixed in close proximity and exhibits unique stereochemical features on selective functionalization.[9] When employing carefully chosen transformations, different substituents can be positioned selectively either at only one or both benzene rings, i.e., mono-, and differently functionalized disubstituted PCP regioisomers including pseudo-*para*, -*ortho*, -*meta*, and -*geminal*, derivatives can be synthesized (Figure 1). The prefix pseudo refers to substituents positioned on different decks of the PCP scaffold. From a geometric point of view, the two moieties on PCP can be held parallel to each other, i.e., pseudo-*geminal*, anti-parallel in pseudo-*para* and variants of V-shaped geometries are obtained in pseudo-*ortho* and pseudo-*meta* position. The substitution pattern on PCP heavily influences the nature of the respective compound and even minor changes can alter its properties significantly.[10]

The application of PCP derivatives as chiral ligands or catalysts for stereoselective syntheses have been extensively investigated.[8b,11] Installation of (hetero)bimetallic centers using PCP as a bridging ligand can bring the metals in a well-defined and spatially-oriented relation to one another where M–M distance modulation and the extent of through-space electronic communication can be studied with regard to a structure-activity relationship and cooperative effects. Recent examples

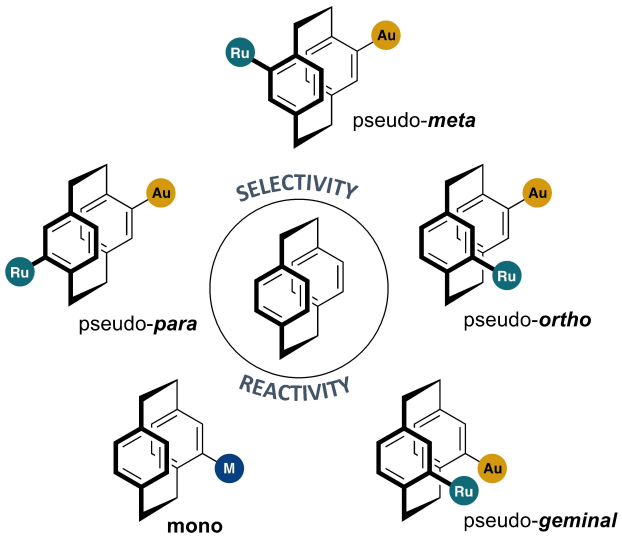

Figure 1. Substitution pattern of [2.2]paracyclophane based monometallic complexes and bimetallic Au(I)/Ru(II) complexes.

of PCP as a bridging ligand include distance-modulated cycloruthenated complexes holding two ruthenium metal centers selectively either at only one or both decks with varying M–M distances.[12] PCP porphyrin conjugates allow convenient access to modular fixed-distance bimetallic Cu/Zn complexes.[13] In the context of π-electronic communication, "through-space" (i.e., π-stacking) via the co-facially stacked benzenes, various constitutional isomers of bis(ferrocenylvinyl)-substituted PCPs and diruthenium cyclophanyl complexes have been investigated and compared to their non-PCP analogues, where electron delocalization is a prominent contributing factor.[14] The regioselective substitution pattern of PCP can be used for M–M distance modulation. PCP-derived homobimetallic gold(I) complexes with varying intramolecular Au–Au distances based on the diphosphine ligands Ph_2-GemPhos and PhanePhos have previously been reported. By single crystal X-ray diffraction, the Au–Au distance in pseudo-*geminal* (2.98 Å) and pseudo-*ortho* (5.23 Å) position, as well as the respective P–P distances of 4.068 Å and 5.014 Å, in case of the corresponding ligands were found.[15] In this work, we report the modular synthesis of a series of cyclophanyl-derived mono- and M–M distance modulated (hetero)bimetallic complexes by combining Au(I) with $Ru(bpy)_2ppy$ as a photosensitizer to explore the structure-activity relation and their synthetic applicability. Merging transition metal and photocatalysis to enable chemical synthesis with naturally abundant, visible light will significantly impact the emerging field of photocatalysis.[16]

Results and Discussion

Synthesis: The Au(I) was to be incorporated by coordination with a triarylphosphine ligand while a cyclometallated phenylpyridine substituent would allow installation of the Ru(II).

Starting from 4,16-dibromo[2.2]paracyclophane (**1**),[17] selective mono-lithiation and reaction with chlorodiphenylphosphine gave 4-bromo-16-diphenylphosphoryl[2.2]paracyclophane (**2**, Scheme 1). The phosphine is prone to oxidation in air and is rapidly converted to the phosphine oxide, making its isolation by column chromatography impractical. Therefore, before purification, the phosphine was oxidized with hydrogen peroxide to the corresponding phosphine oxide **2**, which simplified its isolation. Under optimized Suzuki-Miyaura reaction conditions, a new C–C bond to 2-phenylpyridine was formed. After two steps, compound **3** was obtained in 92% yield and bears both the phosphine oxide as a precursor for the selective binding of Au(I) and 2-phenylpyridine for the incorporation of Ru(II).[18]

Reduction of phosphine oxide **3** with trichlorosilane/triethylamine[11a] and reaction of the phosphine, which was obtained after rapid aqueous workup, with [(tht)AuCl],[19] gave compound **4** in 36% yield (Scheme 2).

Initial attempts to incorporate the $Ru(II)(bpy)_2$-structure into compound **4** were made by using $[Ru(bpy)_2Cl_2]$ and silver(I) tetrafluoroborate as dechlorination agent to aid the cyclometallation reaction.[20] This method was unsuccessful, presumably due to the chlorine-abstracting properties of the silver salt,

© 2021 The Authors. Chemistry - A European Journal published by Wiley-VCH GmbH

15213765, 2021, 61, Downloaded from https://chemistry-europe.onlinelibrary.wiley.com/doi/10.1002/chem.202102341, Wiley Online Library on [03/02/2025]. See the Terms and Conditions (https://onlinelibrary.wiley.com/terms-and-conditions) on Wiley Online Library for rules of use; OA articles are governed by the applicable Creative Commons License

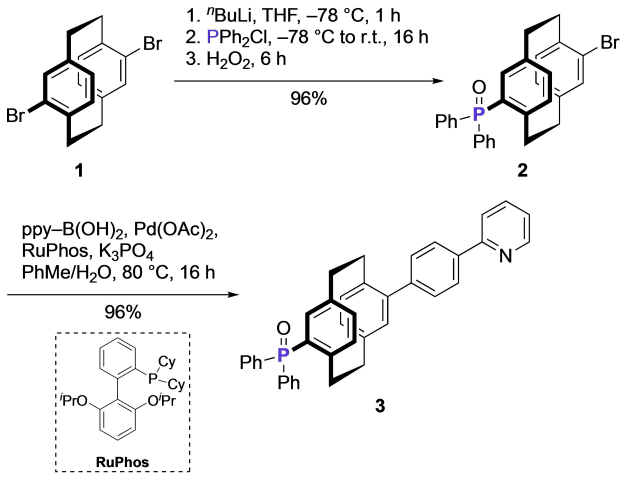

Scheme 1. Selective mono lithiation followed by Suzuki-Miyaura reaction to obtain the intermediate ligand structure **3**. ppy = 2-phenylpyridine.

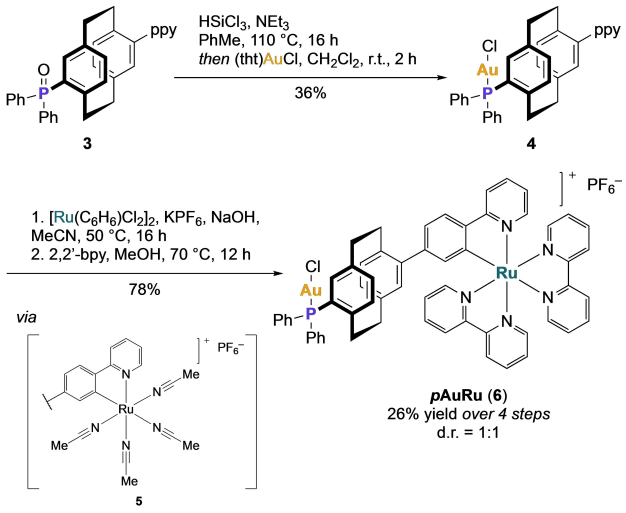

Scheme 2. Incorporation of the gold(I) chloride and ruthenium(II) moiety to obtain ***p*AuRu** (**6**) as a 1:1 mixture of diastereomers. tht = tetrahydrothiophene, 2,2′-bpy = 2,2′-bipyridine.

which led to the decomposition of the gold moiety. The alternative approach that forgoes any dechlorination agent involves the formation of a cyclometallated tetraacetonitrile Ru(II) complex.[21] Complex **5** is formed by the reaction of ligand **4** with benzeneruthenium(II) chloride dimer in acetonitrile and sodium hydroxide as a base. Displacement of the labile acetonitrile ligands with 2,2′-bipyridine gave the final ***p*AuRu** complex **6** in 26% yield over four steps. The final complex **6** was obtained as a mixture of diastereomers with a planar chiral and a chiral-at-metal stereocenter.The molecular structure of the ***p*AuRu** precursors **3** was confirmed by single-crystal X-ray diffraction (Figure 2).

The selective bromination of 4-diphenylphosphonyl [2.2] paracyclophane (**7**), in pseudo-*geminal* position, gave compound **8** in 94% yield.[15c] Thermal isomerization of **8**, which involves the homolytic cleavage of one ethylene bridge (under

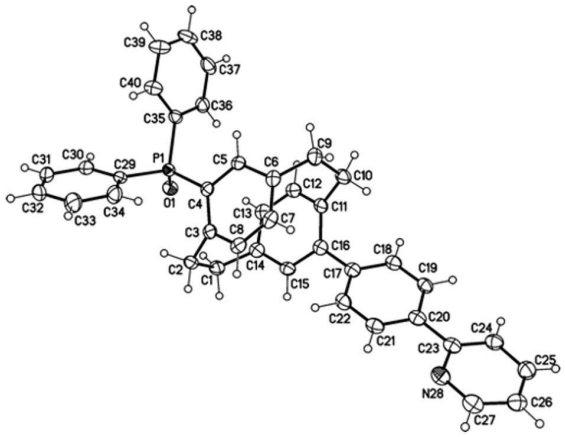

Figure 2. Crystal structures of ***p*AuRu** precursor 3. Displacement parameters are drawn at a 50% probability level.

the formation of a diradical, rotation, and subsequent ring closure), gave the pseudo-*meta* derivative **9** in 85% yield (Scheme 3, A).[17b,c,22] Similarly, pseudo-*ortho* derivative **10** was obtained by isomerization of **1** at 215 °C, in 85% yield. Followed by monolithiation and reaction with diphenylphosphine chloride gave 4-bromo[2.2]paracyclophane-12-diphenylphosphine oxide (**11**) in 61% yield (Scheme 3, B).[23]

The general synthesis route established for the preparation of ***p*AuRu** was also applied in the synthesis of the pseudo-*meta*, -*ortho*, and -*geminal* regioisomers, with slight variations. The Suzuki-Miyaura reaction conditions for both pseudo-*ortho* and -*geminal* derivatives **11** and **8** were modified since the standard protocol employing RuPhos as ligand only led to the isolation

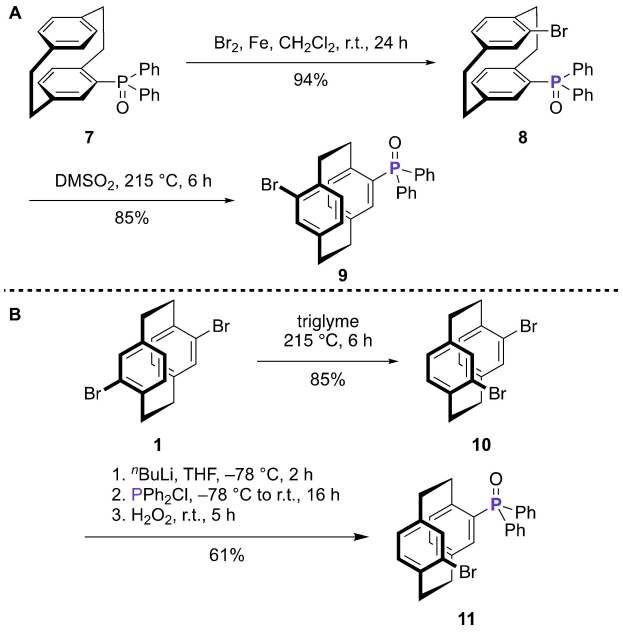

Scheme 3. Synthesis of compounds **8** and **9** towards ***gem*AuRu** and ***m*AuRu** (A). Synthesis of compound **11** via thermal isomerization of **1** towards ***o*AuRu** (B).

© 2021 The Authors. Chemistry - A European Journal published by Wiley-VCH GmbH

15213765, 2021, 61, Downloaded from https://chemistry-europe.onlinelibrary.wiley.com/doi/10.1002/chem.202102341, Wiley Online Library on [03/02/2025]. See the Terms and Conditions (https://onlinelibrary.wiley.com/terms-and-conditions) on Wiley Online Library for rules of use; OA articles are governed by the applicable Creative Commons License

of starting material. The use of (*rac*)-AntPhos, which is more adapted for the cross-coupling of sterically demanding substrates, gave the corresponding products **12** and **13** in 59% and 60% yield, respectively (Scheme 4).

Successive incorporation of the gold(I) chloride and ruthenium(II) bipyridyl moiety into the pseudo-*geminal* **13**, pseudo-*ortho* **12**, and pseudo-*meta* isomers **14** enabled to prepare a complete set of differently functionalized Au(I)/Ru(II) heterobimetallic complexes, ***gem*AuRu** (**18**), ***o*AuRu** (**19**), and ***m*AuRu** (**20**), with overall yields ranging from 10% to 28% (Figure 3). All **AuRu** isomers were obtained as diastereomeric mixtures with a d.r. = 1:1. For the detailed synthesis of the mono-metallic precursors **15**, **16**, and **17**, as well as ***gem*AuRu** (**18**), ***o*AuRu** (**19**), and ***m*AuRu** (**20**), see the Supporting Information. The respective mono-metallic **PCP-Au** (**21**) and **PCP-Ru** (**22**) were also prepared for their comparison with literature known complexes (Figure 4).

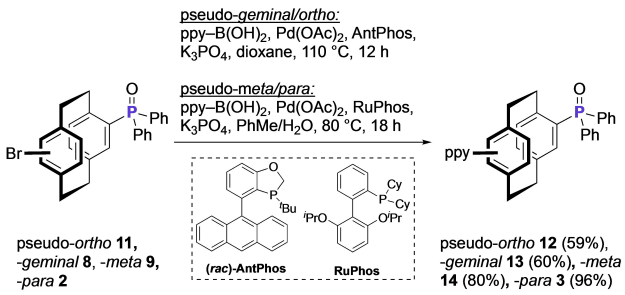

Scheme 4. Suzuki cross-coupling conditions for incorporating the 2-phenylpyridine (ppy) moiety into pseudo-*geminal*/*ortho*- and pseudo-*meta*-/*para*-isomers.

The molecular structure of the ***m*AuRu** precursor **14**, the ***o*AuRu** precursor **11** and monometallic **PCP-Au** (**21**) were confirmed by single-crystal X-ray diffraction (Figure 5). Single crystals of the final heterobimetallic **AuRu** complexes suitable for X-ray diffraction were not obtained.

Mass Spectrometric Analysis: The metal complexes **AuRu** (**6**, **18**–**20**), **PCP-Ru** (**22**) and **Ru(bpy)$_2$(ppy)** were analyzed by ESI-MS in their monocationic form, without counterions. In a second step, those were isolated in the ion trap and exposed to collision induced dissociation (CID) and photodissociation (PD). A qualitative examination of the **AuRu** complexes is exemplarily performed for the pseudo-*para* isomer ***p*AuRu** (**6**). All complexes were dissolved in acetonitrile and then injected by electrospray ionization into the mass spectrometer.

The molecular peaks for **[*p*AuRu]$^+$**, **[PCP-Ru]$^+$** and **[Ru(bpy)$_2$ppy]$^+$** are found at m/z 1190, 774 and 568, respectively, and identified by their isotope patterns. CID of **[*p*AuRu]$^+$** (Supporting Information-Figure S89) takes place by two fragmentation pathways. The first pathway starts with the neutral loss of one bpy ligands forming the fragment with the highest intensity at m/z 1034. Subsequently [AuCl(PPh$_2$)-PCP-(ppy)Ru(bpy)]$^+$, either splits off a second bpy ligand giving m/z 878 or is subject to the loss of an HCl molecule at the ClAu(PPh$_2$)-PCP reactive site of the complex forming m/z 998. Since the latter peak appears only at a lower intensity, the loss of the second bpy seems to be favored. However, the loss of HCl takes place even after the loss of the second bpy ligand resulting in a peak at m/z 842. In each case, the proton (or H-atom) for the HCl loss probably stems from the spatially close phenyl group of the PPh$_2$ ligand or from the PCP ligand. Such cleavages are often observed in MS fragmentation.[24] Eventually, the loss of

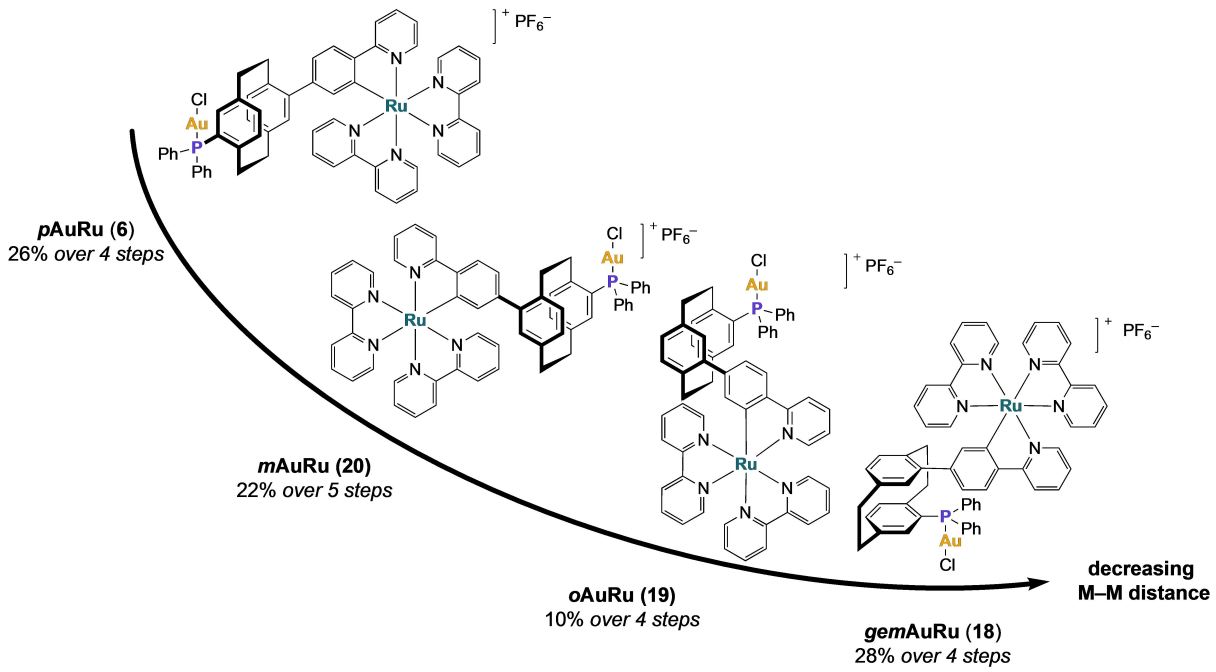

Figure 3. [2.2]Paracyclophane-based Au(I)/Ru(II) isomer set ***p*AuRu** (**6**), ***m*AuRu** (**20**), ***o*AuRu** (**19**), and ***gem*AuRu** (**18**) in order of decreasing M–M distance, based on the results obtained from IMS measurements (see Table 1).

© 2021 The Authors. Chemistry - A European Journal published by Wiley-VCH GmbH

15213765, 2021, 61, Downloaded from https://chemistry-europe.onlinelibrary.wiley.com/doi/10.1002/chem.202102341, Wiley Online Library on [03/02/2025]. See the Terms and Conditions (https://onlinelibrary.wiley.com/terms-and-conditions) on Wiley Online Library for rules of use; OA articles are governed by the applicable Creative Commons License

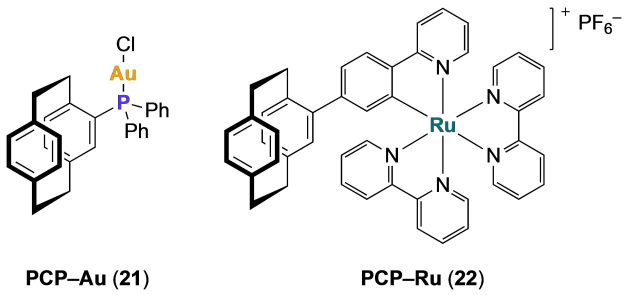

Figure 4. Monometallic complexes **PCP-Au** (**21**) and **PCP-Ru** (**22**).

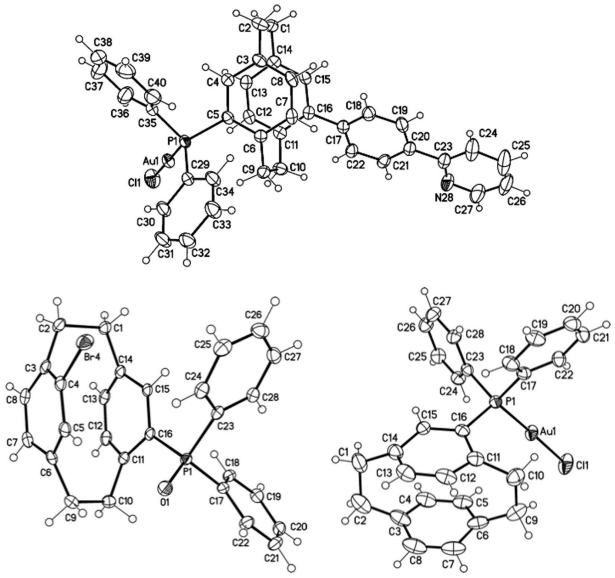

Figure 5. Crystal structures of ***m*AuRu** precursor **17** (top), ***o*AuRu** precursor **11** (bottom left) and **PCP-Au** (**21**, bottom right). Displacement parameters are drawn at a 50% probability level in case of **17** and **11**, and at a 30% probability level in case of **21**.

the Au atom and a Ph substituent leads to the species [[(PPh)-PCP-ppy)Ru]-H]$^+$ appearing with low intensity at m/z 568.

The second pathway, marked by the peak at m/z 670, is assigned to [C_8H_7-(ppy)Ru(bpy)$_2$]$^+$, which is formed by the cleavage of the aliphatic group of PCP. The further loss of the bpy ligand leads to [C_8H_7-(ppy)Ru(bpy)]$^+$ at m/z 514 and in combination with the decomposition of the PCP residual (C_8H_7) to the fragment at m/z 412. All fragment assignments are summarized in Supporting Information-Table 1.

The photofragmentation of [***p*AuRu**]$^+$ again leads to two fragmentation channels: either the cleavage of a bpy ligand or the -C_8H_7-(PPh_2)-AuCl unit. Judging by the intensity differences, the disintegration to [AuCl(PPh_2)-PCP-(ppy)Ru(bpy)]$^+$ (m/z 1034) is preferred over [C_8H_7-(ppy)Ru(bpy)$_2$]$^+$ (m/z 670). In comparison to CID, both species match the above discussed fragmentation pathways, whereby the peak at m/z 1034 only appears with very low intensity by CID. The isolation and fragmentation of **[PCP-Ru]**$^+$ (Supporting Information-Figure S91) leads to only one fragment at m/z 670, which is assigned to [C_8H_7-(ppy)Ru(bpy)$_2$]$^+$ and formed as discussed before. To confirm the assignment, the ions related to m/z 670 were isolated in a MS^2 step and subjected to fragmentation. The resulting fragments at m/z 514 and 412 match the previously discussed fragmentation pathway. However, the photoinduced dissociation only leads to the fragment at m/z 670. The CID fragmentation of **[Ru(bpy)$_2$ppy]**$^+$ (Supporting Information-Figure S93), results in the loss of one bpy ligand leading to the species [Ru(bpy)ppy]$^+$ at m/z 412 and the subsequent attachment of one H_2O molecule forms [Ru(bpy)ppy(H_2O)]$^+$ at m/z 430, which is a common ion-molecule reaction for undercoordinated Ru^{II} complexes in ion traps. The photodissociation approach shows barely any fragmentation yield, probably since the necessary dissociation energy for the bidentate ligands cannot be achieved by one-photon absorption processes.

Table 1. M-to-M distances of the global minima and the Boltzmann average of the possible rotamers.

entry	compound	Calculated CCS [Å^2][a,b]	Au–Ru distance [au][a]	Boltzmann Average [au][c]
1	***p*AuRu (6)**	325	22.36	22.2
2	***m*AuRu (20)**	311	15.49	18.5
3	***o*AuRu (19)**	298	11.98	14.4
4	***gem*AuRu (18)**	305	11.70	12.3

[a] Global minimal structure; [b] all calculated CCS are scaled by 0.89; [c] Boltzmann average of local minimum structures, 1.5 eV internal energy was assumed. 1 au = 0.529 Å.

Ion Mobility Spectrometry: A combination of quantum chemical calculations and ion mobility spectrometry (IMS) was used to obtain structural parameters and estimate the M–M distances of the AuRu complexes (Table 1).

Trapped ion mobility spectrometry coupled with a time of flight mass spectrometer (timsTOF) was performed to determine the collision-cross sections (CCS) of the **AuRu** ions in the gas-phase (Figure 6).

The obtained CCS follow the order ***p*AuRu** > ***m*AuRu** > ***o*AuRu** ≈ ***gem*AuRu** and are qualitatively consistent with calculated CCS of the complexes (Figure 7, obtained by trajectory calculations with the IMoS package).[25]

Additionally, IMS allows the differentiation of isomers and conformers that differ by less than 0.5% in CCS. The diastereomeric nature of the **AuRu** complexes indicated by a double signal set in NMR spectroscopy was also confirmed by the two peaks present in each mobilogram.

Ground State Studies: Electronically excited states, which are essential in photoredox chemistry, are generated by the light absorption of a molecule in the ground state. Selective and efficient irradiation and the evaluation of redox properties are essential for understanding and ultimately, applying new photoredox catalysts. For this purpose, absorption and emission spectroscopy and cyclic voltammetry were performed.

© 2021 The Authors. Chemistry - A European Journal published by Wiley-VCH GmbH

15213765, 2021, 61, Downloaded from https://chemistry-europe.onlinelibrary.wiley.com/doi/10.1002/chem.202102341, Wiley Online Library on [03/02/2025]. See the Terms and Conditions (https://onlinelibrary.wiley.com/terms-and-conditions) on Wiley Online Library for rules of use; OA articles are governed by the applicable Creative Commons License

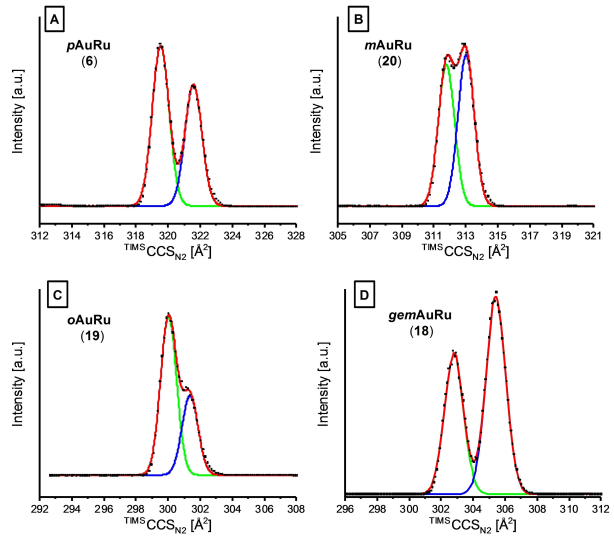

Figure 6. Mobilograms of the **AuRu** isomers obtained from IMS.

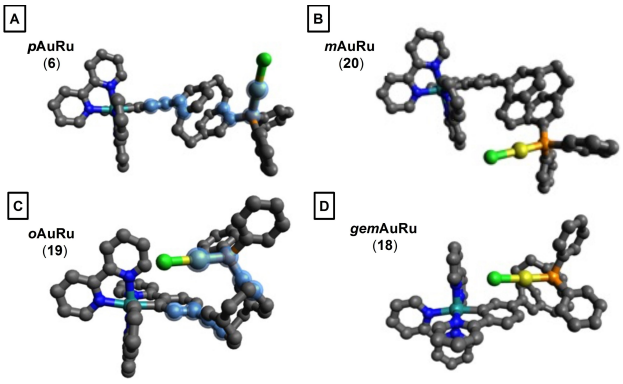

Figure 7. Global minimal structures obtained from DFT-geometry optimizations by varying all degrees of freedom (see Supporting Information).

Absorption/Emission Spectroscopy

The room temperature absorption spectra of monometallic and heterobimetallic Au(I)/Ru(II) PCP complexes are shown in Figure 8. The UV region below 310 nm is dominated by spin allowed ligand centered (LC) transitions and additional interligand (ppy – bpy) transitions. Additionally, the monometallic **PCP-Ru** (**22**) and the heterobimetallic **AuRu** isomers **6** and **18**–**20** show an additional band at 320 nm, where the PCP backbone is likely to contribute.[26] Examining the lower energy absorption bands reveals a large spectral envelope that arises from the cyclometalated 2-phenylpyridine ligand. The two absorption bands in the region between 350–450 nm and 450–600 nm result from metal-to-ligand charge transfer (MLCT) transitions.[20b] The MLCT bands show similarly high molar extinction coefficients for all heterobimetallic **AuRu** isomers while being substantially more prominent than the monometallic **PCP-Ru** (Table 2). The first band can be assigned to an MLCT from the ruthenium center to the cyclometalating 2-phenylpyridyl ligand, whereas the band at higher wavelengths is primarily localized on the bipyridyl ligands, indicating a delocalization of the LUMO mostly on the bipyridyl ligand, whereas the HOMO is most likely localized on the cyclometalating phenylpyridyl.[20b,27]

The emission spectra were recorded under argon atmosphere at 20 °C under excitation at wavelengths defined by the absorption maximum at 495 nm (Figure 8, right). This produces an emission band with a substantial Stokes shift at 795 nm. The excited-state energy of the first singlet excited state $E_{0,0}$ was estimated from the crossing point between absorption and emission profile.[28] This energy refers to the transition between the lowest energy vibrational state ($\nu = 0$) of S_1 to $\nu = 0$ of S_0. Alternative methods to approximate this value use the earliest onset (highest energy) of fluorescence, the midpoint between emission and absorption maxima (one-half Stoke-shift), or the

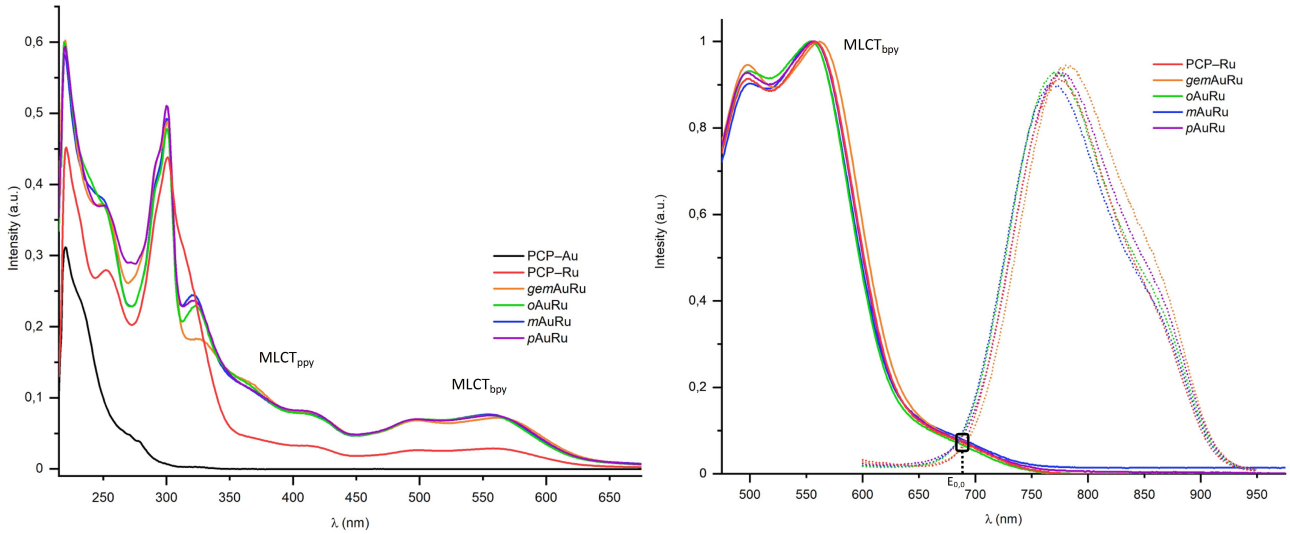

Figure 8. Normalized absorption (solid lines) and emission (dotted lines) spectra of **PCP-Au** (**21**), **PCP-Ru** (**22**), and **AuRu** isomers **6** and **18**–**20**. ($\lambda_{ex} = 495$ nm, 100 μM in CH_2Cl_2, 20 °C).

© 2021 The Authors. Chemistry - A European Journal published by Wiley-VCH GmbH

15213765, 2021, 61, Downloaded from https://chemistry-europe.onlinelibrary.wiley.com/doi/10.1002/chem.202102341, Wiley Online Library on [03/02/2025]. See the Terms and Conditions (https://onlinelibrary.wiley.com/terms-and-conditions) on Wiley Online Library for rules of use; OA articles are governed by the applicable Creative Commons License

fluorescence maximum. Each method is an approximation and is likely to over- or underestimate the value for $E_{0,0}$. In combination with the ground state reduction and oxidation potentials, which are obtained from cyclic voltammetry (see below), it is used to estimate the excited state potentials E*.

Action Spectroscopy in Gas-phase and TD-DFT Calculations

Ion trap UV photodissociation (UV-PD) spectroscopy in gas phase is an established technique, even though its application was realized with different experimental setups and primarily used for the investigation of biomolecular systems.[29] It has recently been applied to study metal complexes or aggregates.[24,30] However, studies for multimetallic, especially heterometallic, molecular systems are still scarce in this field.[24,31] In order to determine the intrinsic UV spectra devoid of counterions and solvent effects, UV photodissociation (UV-PD) spectra of the pseudo-*para* complex **6**, the monometallic complex **22** and **[Ru(bpy)$_2$ppy]$^+$** were recorded. After electrospray ionization and mass-selective ion-trap isolation at room temperature the corresponding cations **[*p*AuRu]$^+$**, **[PCP-Ru]$^+$** (**22**) and **[Ru(bpy)$_2$ppy]$^+$** were examined at m/z 1190, 774 and 568.

UV-PD spectra represent gas phase *action spectra* recorded by UV laser irradiation of the mass-selected and stored species in an ion trap by monitoring their relative photofragment yield (since photoexcitation usually leads to dissociation if the photon energy exceeds possible fragmentation barriers) as a function of laser wavelength. Here, **[*p*AuRu]$^+$** shows two bands in the CT region ($>$400 nm) and more intense bands at 350 nm, 295 nm, and 260 nm. The UV-PD spectrum of **[PCP-Ru]$^+$** exhibits similar band positions as **[*p*AuRu]$^+$** below 400 nm, however, the bands at 350 nm and 260 nm appear with lower intensity (Supporting Information-Figure S97). The UV-PD spectrum of **[Ru(bpy)$_2$ppy]$^+$** only shows a band at 295 nm with low intensity. For **[PCP-Ru]$^+$** and **[Ru(bpy)$_2$ppy]$^+$** above 400 nm the fragment yield was too low for analysis, possibly due to the relatively high activation barriers for dissociation, so that the UV-PD spectra could not be obtained in those CT regions.

A comparison of the gas phase to the solution phase spectra reveals similarity for all studied species with the strongest band close to 300 nm. Remarkably, for **[*p*AuRu]$^+$** a second peak (red-shifted to 350 nm) appears in the gas phase spectrum resembling the double-peak structure observed in other Ru^{II} complexes in the gas phase.[32] It could originate from the shoulder or a small peak observed at 320 nm in solution. However, this feature does not appear in the spectrum of the **[Ru(bpy)$_2$ppy]$^+$** species and is related to the PCP and/or the PPh_2AuCl unit and constitutes an interesting target wavelength for ultrafast pump-probe studies (see below).

Quantum-chemical calculations based on time-dependent density functional theory (TD-DFT) using the hybrid functional (CAM-)B3LYP with the cc-PVT(D)Z basis set (ECP for Ru and Au, Stuttgart97) were employed to get insight into the underlying electronic transitions. The B3LYP functional delivers satisfying results for Ru(II) polypyridyl complexes,[33] while CAM-B3LYP corrects for the long/short range correlation issue of larger molecules.[34] From these calculations, theoretical absorption spectra were obtained for all conformational isomers of both diastereomers of **[*p*AuRu]$^+$** (**6**) and plotted in Figure 9 and Supporting Information-Figure S101. The spectra are remarkably similar to each other and display only a slight variability in the shoulder at 320 nm. Moreover, the spectra mimic the experimental solution spectra in the short wavelength region quite nicely, although the CT region, especially above 500 nm is not well reproduced. However, the calculated spectrum using the B3LYP functional shows more similarity to the UV-PD gas phase spectrum and reproduces its strong band at 350 nm (Supporting Information-Figure S99).

The type of transition is identified by visualizing the involved molecular orbitals (MOs, Supporting Information-Figure S104). The absorption and UV-PD spectrum of **[*p*AuRu]$^+$** and the calculated transitions in form of vertical sticks are shown in Figure 10. The broad bands in the experimental data, their intensity, and shape depend critically on the calculated "density", position and oscillator strength of these electronic transitions. The percentages of the coupled ground and excited state MOs for each transition is shown in Supporting Information-Table S7. Based on the contribution of the involved MOs the type of transition can be estimated. For **[*p*AuRu]$^+$** only transitions possessing an oscillator strength of $\geq$0.03 and MOs with a weight $\geq$10% were considered. The bands in the CT region (370 nm–560 nm) are assigned to the states S5, S6, S22, and S29 and characterized as MLCT transition, where the electron density from Ru is moved partially to the ligands bpy and bpy' (Supporting Information-Figure S103, structural breakdown).

The transitions for the band around 360 nm cannot be clearly and uniformly assigned due to the low contribution of the involved MOs. However, S38, S39 and S40 suggest a MLCT transition partially from **AuRu** onto the ligands coordinated at Ru (ppy, bpy, bpy'). The transition S45 at 345 nm shows ILCT (interligand charge transfer) character, where the electron

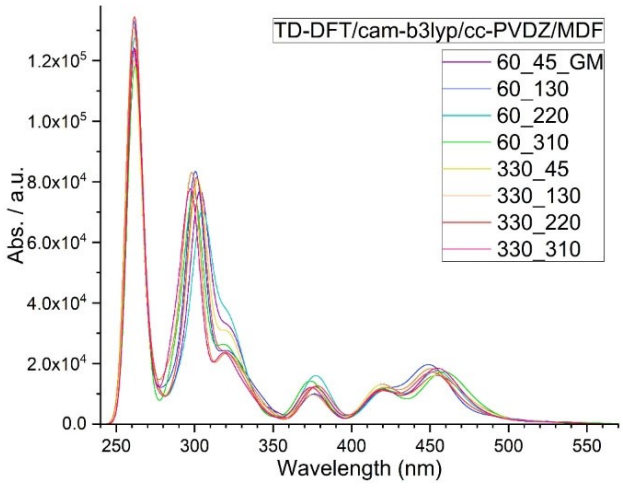

Figure 9. Calculated absorption spectra of the eight conformers of one diastereomer of **[*p*AuRu]$^+$**.

© 2021 The Authors. Chemistry - A European Journal published by Wiley-VCH GmbH

15213765, 2021, 61, Downloaded from https://chemistry-europe.onlinelibrary.wiley.com/doi/10.1002/chem.202102341, Wiley Online Library on [03/02/2025]. See the Terms and Conditions (https://onlinelibrary.wiley.com/terms-and-conditions) on Wiley Online Library for rules of use; OA articles are governed by the applicable Creative Commons License

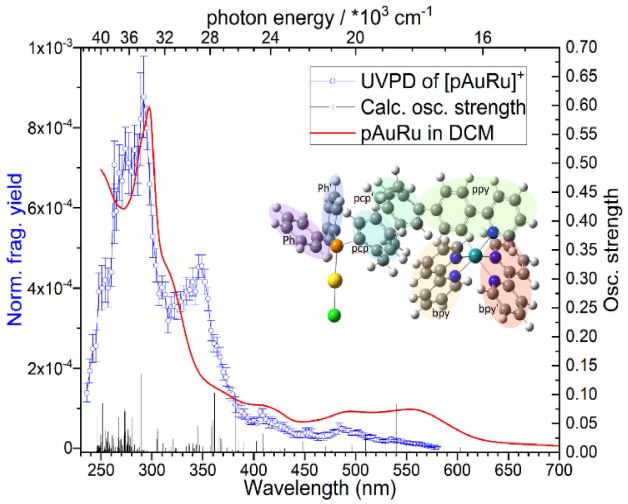

Figure 10. Gas phase UV-PD spectrum (blue) and calculated transitions (stick) of [***p*AuRu**]$^+$ calculated with B3LYP, as well as the liquid phase absorption spectrum in CH_2Cl_2 (red) of ***p*AuRu** (**6**). The different ligands of the complex are marked with their abbreviations.

density moves from a ligand coordinated at Au to the ppy ligand. In the UV-PD gas phase spectrum of ***p*AuRu** (**6**), a weak shoulder appears around 310 nm. This is assigned to the transitions S79 and S80, characterized as MLCT involving Au and the ligands ppy, bpy and bpy′. This wavelength region was also used for transient absorption spectroscopy in this work (see below). The calculation for S98 did not result in a clear type of this transition. However, an LC transition is assigned to S111. The remaining states do not possess MOs with a significant contribution, so that the characterization of those transitions is unclear. However, the states under 300 nm strongly suggest ILCT and LC transitions. The calculations with the CAM-B3LYP functional (Figure 9, Supporting Information-Figure S107–111, Supporting Information-Table S10–S12) deliver a better description of the MOs and the according transitions. By and large, their assignment follows those obtained with the B3LYP functional. However, the calculated spectrum using CAM-B3LYP is blue shifted in comparison to the results presented in Figure 10. The MLCT transitions involving Au appear at 254 nm, the ILCT transitions involving PCP at 280 nm and the MLCT transitions involving Ru at >300 nm. In summary, the theoretical analysis by TD-DFT agrees only partially with the experimental results but allows for adequate and generic assignment of the transitions in order to characterize the observed bands in Figures 8, and .

Cyclic Voltammetry

The redox behavior of **PCP-Ru** (**22**) and all **AuRu** isomers **6** and **18**–**20** consists of a reversible metal-based oxidation process in the range of +0.26–+0.51 V, which is assigned to the $Ru^{II/III}$ redox couple (Figure 11, left). An irreversible ligand-based reduction process at −1.67–−2.24 V is observed and can be ascribed to reducing the bipyridyl ligands. The anionic and electron-rich character of the 2-phenylpyridyl ligands makes its reduction more complicated such that it occurs at lower reduction potentials.

CV measurements of **PCP-Ru** (**22**) and ***m*AuRu** (**20**) were conducted at different scan rates (see Supporting Information-Figure S77 and S78). The peak current was plotted against the square root of the scan rate to obtain the Randles-Sevcik plots (see Supporting Information-Figure S79 and S80).[35] The linear relationship between peak current and the square root of the scan rate indicates that the oxidation process is diffusion controlled. The measurements were only conducted for the monometallic **PCP-Ru** (**22**) and heterobimetallic complex ***m*AuRu** (**20**). Similar behavior is assumed for all other **AuRu** isomers.

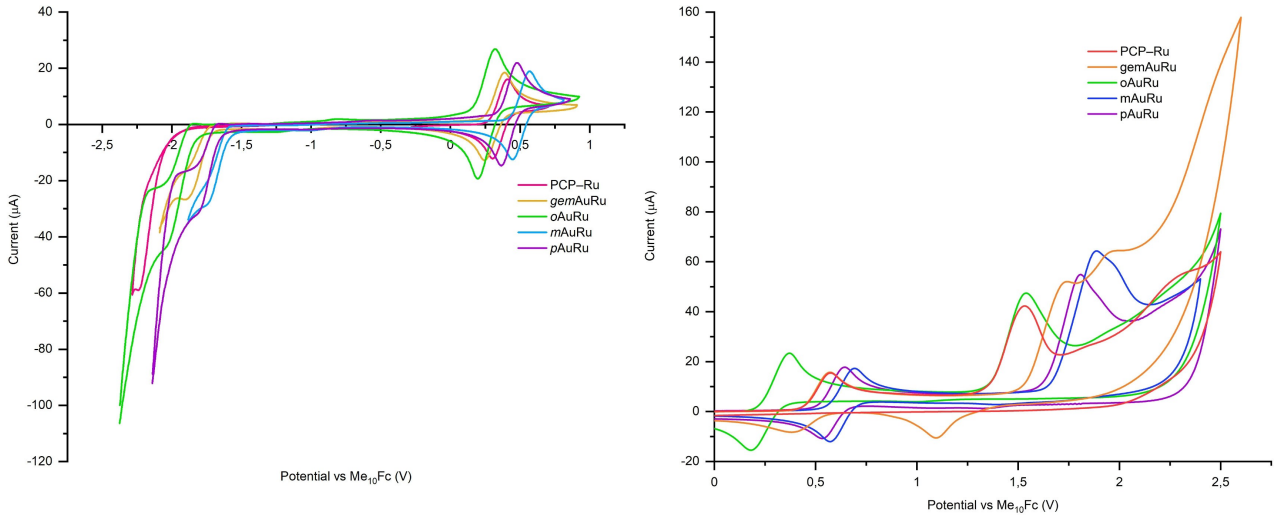

Figure 11. Cyclic voltammograms of **PCP-Ru** (**22**) and **AuRu** isomers **6** and **18**–**20** (left) and CV spectra of the second oxidation process (right) (0.1 M $^nBu_4NPF_6$, CH_2Cl_2, 100 mV/s).

© 2021 The Authors. Chemistry - A European Journal published by Wiley-VCH GmbH

15213765, 2021, 61, Downloaded from https://chemistry-europe.onlinelibrary.wiley.com/doi/10.1002/chem.202102341, Wiley Online Library on [03/02/2025]. See the Terms and Conditions (https://onlinelibrary.wiley.com/terms-and-conditions) on Wiley Online Library for rules of use; OA articles are governed by the applicable Creative Commons License

A second and third oxidation process takes place in the range of 1.45–1.90 V (Figure 11, right) and are irreversible. Upon repeated cycles, an insulating layer forms on the electrode surface, which causes a decrease in current intensity from cycle to cycle. These oxidation processes can either be attributed to a $Ru^{II/IV}$ oxidation or ligand decomposition, displayed by cyclometallated complexes.[36] Additionally, the (electro)chemical oxidation of [2.2]paracyclophane and some of its derivatives is well established and leads to the formation of benzyl radical/benzyl cation intermediates under C–C bond scission of the ethano bridges. The highly reactive intermediate readily reacts either with itself or other molecules to form an insulating polymeric species.[9d,37] The combined data obtained from absorption/emission spectroscopy and cyclic voltammetry measurements are summarized in Table 2. Most ground state parameters such as absorption maxima (λ_{max}^{abs}), molar extinction coefficient (ε_{495nm}), HOMO-LUMO gap ($\Delta E_{HOMO\text{-}LUMO}$), and $E_{0,0}$ show only slight deviations among the **AuRu** isomers **6** and **18**–**20**. The oxidation and reduction potentials $E_{1/2}^{ox}$ and $E_{1/2}^{red}$ indicated a significant M–M interaction.

The first oxidation potential describes the oxidation of Ru^{II} to Ru^{III}, whereas the reduction takes place on the 2-phenylpyridine moiety of the **AuRu** isomers. The order for oxidation and reduction potential is mirrored, where the most substantial oxidation potential and therefore the weakest reduction potential are found for ***m*AuRu** (**20**, **Equation (1)**).

$$E_{ox}^{mAuRu} > E_{ox}^{pAuRu} > E_{ox}^{gemAuRu} > E_{ox}^{oAuRu}$$

$$E_{red}^{oAuRu} < E_{red}^{gemAuRu} < E_{red}^{pAuRu} < E_{red}^{mAuRu}$$

Equation 1 Order of oxidation (top) and reduction potentials (bottom) of **AuRu** isomers **6** and **18**–**20** from strongest to weakest (left to right).

These results can be rationalized by transannular and through-space interactions between the gold and ruthenium centers. In pseudo-*para* position, electron-donation of the gold moiety onto the ruthenium center is possible by trans-annular communication and leads to an increase of $E_{1/2}^{ox}$ by 0.09 V. This type of communication is most pronounced in pseudo-*ortho* position, which leads to an oxidation potential which is 0.10 V less than the monometallic **PCP-Ru** (**22**). It is least pronounced in the pseudo-*meta* position, which accounts for a difference of 0.15 V compared to **PCP-Ru** (**22**), such that the value of E_{ox}^{oAuRu} is 0.25 V less than for ***m*AuRu** (**20**). The oxidation potential of ***gem*AuRu** (**18**) indicates a very weak interaction between the gold and ruthenium centers, which is a deviation of 0.04 V compared to the monometallic **PCP-Ru** (**22**).

From the obtained oxidation and reduction potentials combined with $E_{0,0}$, an approximate value for the excited state potentials E* can be obtained and summarized in Table 2.

The excited state reduction potential E_{ox}* shows that both monometallic catalyst **PCP-Ru** (**22**) and the **AuRu** isomers **6** and **18**–**20** are considerably stronger reducing agents in their excited than in their ground state. The order of redox potentials is consistent with the corresponding ground state values, where ***o*AuRu** (**19**) is the most potent reducing agent and ***m*AuRu** (**20**) the weakest. Photoinduced reduction with either **PCP-Ru** (**22**) or any of the **AuRu** isomers is unfavorable since E_{red}* is either negative or has small positive values. This is in agreement with the proposed mechanisms presented in the literature where it is shown that the excited state of Ru undergoes oxidative quenching by the aryldiazonium salt.[38]

Ultrafast Transient Absorption Spectroscopy: As a first step to further unravel the M–M interactions via femtosecond (fs) transient absorption spectroscopy, the photo-induced dynamics of ***p*AuRu** (**6**) was compared to the monometallic **PCP-Ru** (**22**) and **Ru(bpy)$_2$ppy**.[20b] For ***p*AuRu** (**6**) in CH_2Cl_2 no significant difference was observed for the photoinduced dynamics when excited at 405 nm or 495 nm (Figure 12A, Supporting Information-Figure S81A). Comparison to **Ru(bpy)$_2$ppy** in CH_2Cl_2, excited at 405 nm and 312 nm (Supporting Information-Figure S81B, C), also shows no change in dynamics. Thus, under excitation in the MLCT-bands around 405 nm and 495 nm no significant influence of the PCP-Au-moiety on the photoinduced dynamics of ***p*AuRu** (**6**), but only the dynamics of the Ru-moiety was observed. However, when ***p*AuRu** (**6**) is excited at 312 nm, an impact on the difference spectra is obvious (Figure 12A and B). Even more striking, the difference spectra of **PCP-Ru** (**22**) in CH_2Cl_2 excited at 312 nm (Figure 12C) clearly differ from those of ***p*AuRu** (**6**) as well as **Ru(bpy)$_2$ppy**. Thus, in contrast to excitation at 405 and 495 nm, excitation at 312 nm dramatically changes the kinetics in ***p*AuRu** (**6**) and **PCP-Ru** (**22**), although in a different manner. In other words, the addition of the Au-moiety (which does not exhibit an absorption band at 312 nm) to **PCP-Ru** (**22**) (which does exhibit an absorption band at 312 nm, Figure 8),[18b] leads to a significant and non-additive change of the excited state dynamics.

Table 2. Summary of ground-state and excited-state properties of **PCP-Ru** and **AuRu** isomers.

entry	compound	λ_{max}^{abs} [nm]	ε_{495nm} [10^5 $M^{-1}cm^{-1}$]	$E_{1/2}^{ox}$ [V]	$E_{1/2}^{red}$ [V]	$\Delta E_{HOMO\text{-}LUMO}$ [eV]	λ_{max}^{em} [nm]	$E_{0,0}$ [eV]	E_{ox}* [V]	E_{red}* [V]
1	**PCP-Ru (22)**	558	3.49	0.36; 1.45	−2.24	2.60	774	1.81	−1.45	−0.43
2	***gem*AuRu (18)**	562	9.07	0.32; 1.53	−1.80	2.10	781	1.79	−1.47	−0.01
3	***o*AuRu (19)**	554	9.30	0.26; 1.60	−1.95	2.20	774	1.82	−1.56	−0.13
4	***m*AuRu (20)**	554	9.18	0.51; 1.79	−1.67	2.20	769	1.81	−1.30	0.14
5	***p*AuRu (6)**	557	9.31	0.42; 1.86	−1.75	2.20	777	1.81	−1.39	0.06

λ_{max}^{abs} = absorption maximum of $ML_{bpy}CT$, ε_{495nm} = molar extinction coefficient, $E_{1/2}^{ox}/E_{1/2}^{red}$, = ground state oxidation/reduction potential, E_{ox}*/E_{red}* = excited state oxidation/reduction potential, $\Delta E_{HOMO\text{-}LUMO}$ = HOMO-LUMO gap energy, λ_{max}^{em} = emission maximum, $E_{0,0}$ = excited state energy of the first singlet excited state S_1 (zero-zero transition energy).

 © 2021 The Authors. Chemistry - A European Journal published by Wiley-VCH GmbH

15213765, 2021, 61, Downloaded from https://chemistry-europe.onlinelibrary.wiley.com/doi/10.1002/chem.202102341, Wiley Online Library on [03/02/2025]. See the Terms and Conditions (https://onlinelibrary.wiley.com/terms-and-conditions) on Wiley Online Library for rules of use; OA articles are governed by the applicable Creative Commons License

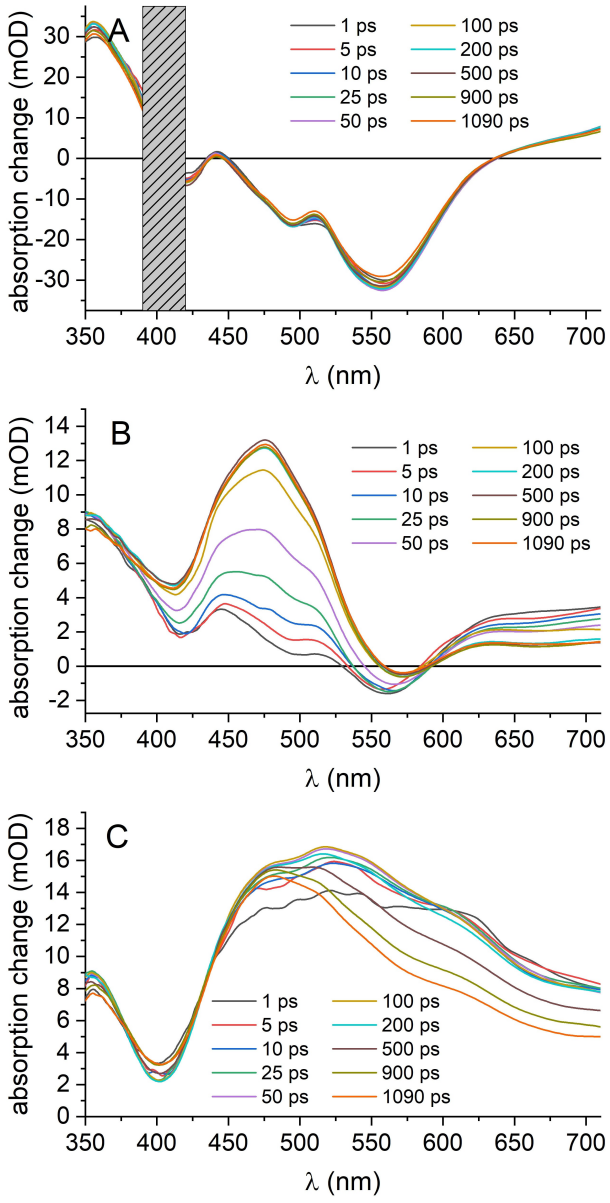

Figure 12. Difference spectra at selected delay times for ***p*AuRu** (**6**) in CH_2Cl_2 excited at 405 nm (A), ***p*AuRu** (**6**) in CH_2Cl_2 excited at 312 nm (B) and **PCP-Ru** (**22**) in CH_2Cl_2 excited at 312 nm (C). The grey area in A from 390 nm to 420 nm is excluded from data analysis due to pump scattering.

Independent of excitation wavelength (312, 405, 495 nm), all measured complexes in Figure 12 and Supporting Information-Figure S81 show the excited state absorption (ESA) band at around 355 nm which is typical for the ^{3}MLCT excited states of Ru(II)-bipyridyl complexes.[33,39] After a strong instantaneous rise the signal shows only small amplitude changes.

***p*AuRu** (**6**) excited at 405 nm and 495 nm as well as **Ru(bpy)$_2$ppy** excited at 405 nm and 312 nm (Figure 12A, Supporting Information-Figure S81A, B, C) show the typical instantaneous ground state bleach (GSB) of Ru(II)-bipyridyl complexes (around 400–625 nm), paralleled by superimposed (^{3}MLCT-) ESA bands on both sides of the spectrum.[27b,33] For wavelengths above about 600 nm, ESA contributions from ^{3}MLCT[33] and a ^{3}MC excited state[39] are expected. After instantaneous rise the signals in this region show only small amplitude changes over the entire time range of 1.1 ns.

For ***p*AuRu (6)** excited at 312 nm (Figure 12B) instead of the GSB a strong ESA band with maximum at 475 nm is observed. This ESA band is distinctively separated from the ^{3}MLCT-ESA band around 355 nm by a local minimum at 410 nm and exhibits a completely different temporal evolution for wavelengths above 390 nm: After a decent rise within ca. 1 ps the signal strongly increases to maximum with $t_3 = 68$ ps (according to global analysis, see Table 3 and Supporting Information) and remains basically constant up to 1 ns. Between 528 and 592 nm a small residual GSB signal is present with kinetics dominated by the overlapping ESA. The ESA band for wavelengths above 592 nm is probably caused by the ^{3}MLCT and ^{3}MC-excited states, in analogy to Ru(II)-polypyridine complexes.[33,39] This band partially decays as well with τ_3. Thus, τ_3 seems to represent the depopulation of the ^{3}MC-excited states and the simultaneous population of a state X (which is not yet specified in more detail) around 475 nm (see A_3 in Supporting Information-Figure S83D). Therefore, we propose an intersystem crossing (ISC) or internal conversion (IC) process from the ^{3}MC excited states to an unknown state X with τ_3. This process is not observed for ***p*AuRu (6)** excited at 405 nm and 495 nm or **Ru(bpy)$_2$ppy**, excited at 405 and 312 nm.

The monometallic **PCP-Ru** (**22**) excited at 312 nm (Figure 12C) only shows a broad ESA band besides the ^{3}MLCT-ESA-band at 355 nm and no bleach band in the examined spectral window. Inspection of Figure 12B and C (and decay associated spectra in Supporting Information-Figure S83D and E) reveal that the spectro-temporal evolution is significantly different from that in ***p*AuRu** (**6**), but bears also characteristic similarities: (i) In **PCP-Ru** (**22**) the same band (at 475 nm) as in ***p*AuRu** (**6**) is formed, but much faster, i.e. with a strong instantaneous component (ca. 70%, see Supporting Information-Figure S83E) and two weak components ($\tau_1 = 1.1$ and $\tau_3 = 42$ ps), and a lifetime much larger than 1 ns. However, signal decay in the region of ^{3}MC absorption in synchrony with the ultrafast rise of the band at 475 nm is not observed, possibly due to non-sufficient time resolution. (ii) In contrast to ***p*AuRu** (**6**) in **PCP-Ru** (**22**) an additional strong band at around 565 nm is formed concomitantly with the band at 475 nm but lifetime of about 2 ns.

The process of the proposed ISC or IC with τ_3 in ***p*AuRu** (**6**) is not distinctively observed in **PCP-Ru** (**22**), where the same state X seems to be populated much faster, and a strong ESA absorption around 565 nm indicates the formation of another

Table 3. Time constants resulting from a global analysis of femtosecond transient absorption data in CH_2Cl_2 (see Supporting Information).

entry	compound	λ_{ex} [nm]	τ_1 [ps]	τ_2 [ps]	τ_3 [ps]	τ_4 [ns]
1	**Ru(bpy)$_2$(ppy)**	405	0.7 ± 0.2	17 ± 3	/	/
2	***p*AuRu (6)**	405	1.0 ± 0.3	14 ± 3	/	/
3	***p*AuRu (6)**	495	1.2 ± 0.2	14 ± 1	/	/
4	***p*AuRu (6)**	312	0.3 ± 0.1	5.5 ± 1.0	68 ± 3	/
5	**PCP-Ru (22)**	312	1.1 ± 0.2	8 ± 2	42 ± 6	(~2)

© 2021 The Authors. Chemistry - A European Journal published by Wiley-VCH GmbH

15213765, 2021, 61, Downloaded from https://chemistry-europe.onlinelibrary.wiley.com/doi/10.1002/chem.202102341, Wiley Online Library on [03/02/2025]. See the Terms and Conditions (https://onlinelibrary.wiley.com/terms-and-conditions) on Wiley Online Library for rules of use; OA articles are governed by the applicable Creative Commons License

state, possibly quenched in ***p*AuRu** (**6**). This highlights the influence of the Au-moiety when ***p*AuRu** (**6**) is excited at 312 nm. Analogous investigations are in progress to analyze the underlying processes in the isomers **6** and **18**–**20**, in particular with respect to the varying M–M-distance.

Ultrafast Transient Photodissociation Spectroscopy: In order to obtain intrinsic ultrafast dynamics we have applied our technique of *pump-probe photodissociation spectroscopy* (τ-PD) to the isolated ions **[*p*AuRu]$^+$** (**6**, m/z 1190) and **[PCP-Ru]$^+$** (**22**, m/z 774) in an ion trap at room temperature, with the aim to discern the influence of the PPh_2AuCl moiety on the **[PCP-Ru]$^+$** unit.[32] We have restricted ourselves to the investigation of the pseudo-*para* isomer, since its observed photocatalytic efficiency was the highest (Table 4) and hence dynamic effects of energy or excitation transfer from the Ru antenna unit to the reactive Au center are expected. Using τ-PD we record ultrafast dynamics of species produced by electrospray-ionization with subsequent mass-selection in an ion trap mass spectrometer after resonant photoexcitation in gas phase by monitoring their photofragment yield as a function of resonant *pump* (UV)-non-resonant-*probe* (NIR) time delay.

Here, the pump wavelength for excitation for both, **[*p*AuRu]$^+$** (**6**) and **[PCP-Ru]$^+$** (**22**) was set to 350 nm, which stems from the assignment of this peak in the gas phase spectrum (Supporting Information-Figure S100) to a band containing "cyclophane and phenyl-pyridine ($\pi\rightarrow\pi^*$) transitions" (see above). Note, that we assume that in the solution spectra a similar transition is observed at 312 nm (as a shoulder) and subsequently explored by ultrafast transient absorption as described above. However, the transients obtained for the gas phase by τ-PD (Supporting Information-Figure S110–S114) give a relatively limited picture and exhibit for both species a fast sub-picosecond relaxation, possibly internal vibrational redistribution (IVR, with $\tau_1 \sim 0.5$ ps +/− 0.05 and 0.4 ps +/− 0.04, for **[*p*AuRu]$^+$** (**6**) and **[PCP-Ru]$^+$** (**22**), respectively; Figure 13 and Supporting Information-Table S8) followed by stabilization of a long-lived state with a lifetime $\tau_2 > 1$ ns, likely a ^{3}MLCT state. Unfortunately, we cannot conclude on any influence or electronic coupling originating in the PPh_2AuCl substituent. Remarkably though, the comparison to the solution data above reveals that time constants in the intermediate range of a few ps to a few tens of ps (cf. τ_2 and τ_3 of Table 3) seem to be completely missing for the gas phase dynamics. A technical possibility, which we cannot completely exclude, is that these intermediate time constants might belong to states with a low probe amplitude and elude our τ-PD analysis technique. However, related complexes containing Ru-polypyridyl units have been successfully analyzed using τ-PD.[32,40]

To sum up, the τ-PD method was successfully applied to the isolated complexes **[*p*AuRu]$^+$** (**6**) and **[PCP-Ru]$^+$** (**22**) resulting in intrinsic sub-ps formation of a long-lived electronically excited state. However, an influence of the PPh_2AuCl reactive center on the ultrafast dynamics was not detectable in the gas phase. In contrast, in solution, vibrational cooling or energy transfer to the solvent might be responsible for the richer dynamics and concomitant opening of different relaxation pathways.

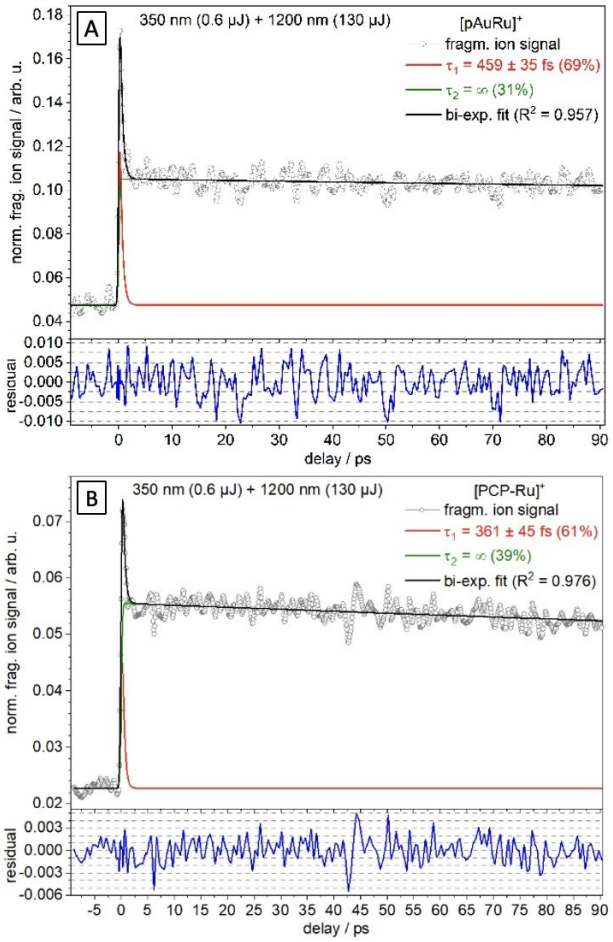

Figure 13. Normalized transient fragment ion intensity of **[*p*AuRu]$^+$** (**A**) and **[PCP-Ru]$^+$** (**B**) recorded at $\lambda_{pump} = 350$ nm on a 100 ps time window; bi-exponential fit (black) is given along the fit decomposition (green and red). Fit residual is shown below (blue).

Table 4. Catalytic application of the Au(I)/Ru(II) model complexes in a Meyer-Schuster rearrangement reaction.

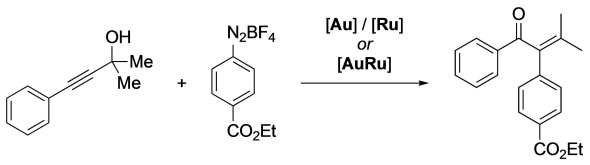

23 **24** **25**

entry	catalyst	yield [%][a]
1	$PPh_3AuCl/Ru(bpy)_3Cl_2$	73[b], 76[c]
2	$PPh_3AuCl/Ru(bpy)_2(ppy)PF_6$	73
3	**PCP-Au** (**21**)/**PCP-Ru** (**22**)	70
4	***p*AuRu** (**6**)	63
5	***m*AuRu** (**20**)	30
6	***o*AuRu** (**19**)	26
7	***gem*AuRu** (**18**)	13

23 (0.10 M, 156 µmol), **24** (624 µmol), **Au**/**Ru** or **AuRu** (3.90 µmol, 2.5 mol%), CH_3OH/CH_3CN (3:1), r.t., green LEDs (524 nm, 30 W), 12 h; [a] determined via ^{1}H NMR with 1,3,5-trimethoxybenzene as an internal standard; [b] isolated yield; [c] CH_3OH was used as a solvent.

© 2021 The Authors. Chemistry - A European Journal published by Wiley-VCH GmbH

15213765, 2021, 61, Downloaded from https://chemistry-europe.onlinelibrary.wiley.com/doi/10.1002/chem.202102341, Wiley Online Library on [03/02/2025]. See the Terms and Conditions (https://onlinelibrary.wiley.com/terms-and-conditions) on Wiley Online Library for rules of use; OA articles are governed by the applicable Creative Commons License

AuRu Heterobimetallic Cyclophanyl-Complexes in Meyer-Schuster Rearrangement: The Meyer-Schuster rearrangement (MSR) is a useful transformation of bifunctional, readily accessible propargyl alcohols into α,β-unsaturated carbonyl products.[41] Advancing the catalysis concept, Glorius,[38,42] Luna,[43] Shin,[44] and others have reported visible-light promoted arylative MSR as testing ground to explore dual catalytic pathways under Au(I) and Ru(II) catalysis. The mechanism for the arylative MSR was proposed by Glorius et al. and is based on previous reports on dual gold photoredox catalysis.[38] The catalytic cycle of the gold species is responsible for the formation of the arylated product. The ruthenium-based photoredox cycle oxidizes the intermediary Au(II) to Au(III) by single electron transfer. The MSR reaction was also reported by Shin and co-workers employing a 1:1 ratio of Au(I)/Ru(II) and were most fit for comparison with the heterobimetallic **AuRu** complexes. The diazonium salt **24** in combination with the propargylic alcohol **23** as test substrates afforded the arylated enone **25** in 76% yield (Table 4, entry 1) under the conditions reported by Shin and co-workers. To exclude possible electronic effects induced by the different coordination spheres that arise from the 2-phenylpyridine unit within the **AuRu** isomers, control experiments were also conducted following the literature procedure reported by Shin and co-workers using $Ru(bpy)_2(ppy)PF_6$ as photocatalyst (Table 4, entry 2).

Furthermore, the impact of the PCP backbone on the overall reaction was investigated by applying the monometallic PCP derivatives **PCP-Au** (**21**) and **PCP-Ru** (**22**) (Table 4, entry 3). Demonstrating its potential as photoredox catalyst, ***p*AuRu** (**6**) performed the arylative MSR under irradiation with green LEDs (524 nm, 30 W) and afforded enone **25** in 63% yield (Table 4, entry 4). Employing the isomeric **AuRu** complexes **18**–**20** under similar reaction conditions led to a drop in yield. Reducing the M–M distance from ***p*AuRu** (**6**) to ***m*AuRu** (**20**) (entry 5) led to a reduction in yield, which decreased even further in case of ***o*AuRu** (**19**) and ***gem*AuRu** (**18**) (Table 4, entry 6 and 7). This reflects a structure-activity correlation and the observed reduction in yield by reducing the M–M distance supports electronic communication between the Au(I) and Ru(II) moiety which is likely to play a crucial role.

The oxidation potential ***m*AuRu** is the highest of the **AuRu** complexes, followed by ***p*AuRu**. In particular, the oxidation of the Ru(II) metal core to Ru(III) is more difficult for ***m*AuRu** and ***p*AuRu** by 0.15 V and 0.09 V, respectively when compared to the mononuclear **PCP-Ru** (**22**). That means that the oxidized form Ru(III) is less stable in ***m*AuRu** than in **PCP-Ru** (**22**). On the contrary, ***gem*AuRu** has almost the same oxidation potential as **PCP-Ru** (**22**), while ***o*AuRu** oxidation occurs 0.1 V earlier than in **PCP-Ru** (**22**). The presence of the electron-donating gold moiety stabilizes the Ru(III) core not only *via* a transannular effect, but also thanks to the close proximity of the two metal centers in ***o*AuRu**. Thanks to the position of the gold moiety, ***o*AuRu** and ***gem*AuRu** are more easily oxidized.

If we compare these results to the proposed mechanisms presented in the literature,[38] we can see that the first step, that is the oxidative quenching of Ru(II) by the aryl diazonium salt, should be easier for the ***o*AuRu**, followed by ***gem*AuRu**, ***p*AuRu** and ***m*AuRu**. On the other hand, the second step, which is the reduction of Ru(III) by Au(II), is less favored for ***m*AuRu**. As the photocatalytic results for ***o*AuRu** and ***m*AuRu** are very similar to each other (26% and 30%, respectively), we can say that the redox potentials play an important role in the catalytic activity of these complexes but are not the only effect to be considered.

Conclusion

In summary, the formation of a series of cyclophanyl-derived Au(I)/Ru(II) decorated mono- and tunable heterobimetallic systems is described. Tailoring the cyclophanyl ligand by employing pseudo *-geminal*, *-ortho*, *-meta*, and *-para* substitution patterns, allow to precisely organize the **AuRu** metal centers in spatial orientation, and enable M–M distance modulation. The photophysical and electronic ground-state properties of the **AuRu** isomers were investigated and suggest M–M interactions. Exemplified for ***p*AuRu** (**6**), ultrafast transient absorption spectroscopy indicates dynamic and non-additive M–M interactions. Gas phase ultrafast photodissociation dynamics on isolated $[$***p*AuRu**$]^+$ (**6**) confirms the intrinsic nature for the ultrafast formation of a long-lived electronically excited and reactive state.

At this point, a comprehensive interpretation of the ultrafast photo-induced dynamics is not yet possible – with ***p*AuRu** (**6**) being the only isomer investigated with fs time-resolved methods, so far. Hence, the impact of the current results of ultrafast transient spectroscopy on the photocatalytic mechanism is not clear, yet. The ongoing investigations of the other isomers including ***m*AuRu** (**20**), ***o*AuRu** (**19**) and ***gem*AuRu** (**18**) is necessary to get profound insights into the M–M interaction. The data of ***p*AuRu** (**6**) has shown a clear influence of the Au-moiety on the dynamics of ***p*AuRu** (**6**), when excited at 312 nm. In contrast, the excitation of ***p*AuRu** (**6**) at lower energy bands (405 or 495 nm) leads only to dynamics analogues to **Ru(bpy)$_2$(ppy)**. The wavelength-dependency of the photo-induced dynamics might as well affect the performance in photocatalysis. Thus, the preliminary results of the time resolved data are pointing at the benefits of further investigations on the system in catalysis, for example, considering photoreactivity under irradiation with different wavelengths.

As an initial study, the performance of the **AuRu** complexes proved viable in visible-light mediated arylative Meyer-Schuster rearrangement and emphasizes the viability of this approach. In this particular setup, the chemical reactivity is influenced by steric effects, electronic parameters, and a reduction in M–M distance between the Au(I) and Ru(II) moieties, which is likely to play a crucial role.

Developing catalysts by combining multiple metal centers is an emerging field of interest. The underlying mechanisms and influences that govern activity and selectivity in catalysts that combine multiple metal centers in a single molecule are scarcely understood. This is especially the case in light-driven reactions, where the different timescales for light absorption, generation of the excited state, and the actual chemical

© 2021 The Authors. Chemistry - A European Journal published by Wiley-VCH GmbH

15213765, 2021, 61, Downloaded from https://chemistry-europe.onlinelibrary.wiley.com/doi/10.1002/chem.202102341, Wiley Online Library on [03/02/2025]. See the Terms and Conditions (https://onlinelibrary.wiley.com/terms-and-conditions) on Wiley Online Library for rules of use; OA articles are governed by the applicable Creative Commons License

reaction are crucial parameters. Concerning the net effects of changing metal to metal distance in complexes, more research represents an important step forward for its practical applications. With this work we hope to spark further investigations which will help in the design of enhanced catalysts.

Experimental Section

Deposition Numbers 2080313 (**3**), 2080314 (**11**), 2080315 (**21**), and 2080316 (**17**) contain the supplementary crystallographic data for this paper. These data are provided free of charge by the joint Cambridge Crystallographic Data Centre and Fachinformationszentrum Karlsruhe Access Structures service.

Experimental procedures and spectral data for all these new compounds are available in the Supporting Information.

Acknowledgments

This work is supported by the DFG-funded Collaborative Research Centre (SFB) TRR 88/3MET "Cooperative Effects in Homo- and Heterometallic Complexes" at Karlsruhe Institute of Technology (KIT) and TU Kaiserslautern. ZH and SB acknowledge Deutsche Forschungsgemeinschaft (DFG) under Germany's Excellence Strategy 3DMM2O-EXC-2082/1-390761711 for financial contributions. CR and RI are thankful for financial support by the DFG Priority Program SPP 2102 "Light-controlled reactivity of metal complexes". Open Access funding enabled and organized by Projekt DEAL.

Conflict of Interest

The authors declare no conflict of interest.

Keywords: metal-to-metal distance modulation · heterometallic complexes · cooperative effects · photoredox catalysis · [2.2] paracyclophane · gold · ruthenium

[1] a) J. Campos, *Nat. Chem. Rev.* **2020**, *4*, 696–702; b) J. A. Mata, F. E. Hahn, E. Peris, *Chem. Sci.* **2014**, *5*, 1723–1732; c) J. Park, S. Hong, *Chem. Soc. Rev.* **2012**, *41*, 6931–6943.
[2] a) S. Martínez, L. Veth, B. Lainer, P. Dydio, *ACS Catal.* **2021**, *11*, 3891–3915; b) I. Bratko, M. Gomez, *Dalton Trans.* **2013**, *42*, 10664–10681.
[3] a) R. Maity, B. S. Birenheide, F. Breher, B. Sarkar, *ChemCatChem* **2021**, *13*, 2337–237; b) K. L. Skubi, T. R. Blum, T. P. Yoon, *Chem. Rev.* **2016**, *116*, 10035–10074.
[4] I. G. Powers, C. Uyeda, *ACS Catal.* **2017**, *7*, 936–958.
[5] a) R. H. Duncan Lyngdoh, H. F. Schaefer, 3rd, R. B. King, *Chem. Rev.* **2018**, *118*, 11626–11706; b) P. C. Kamer, P. W. van Leeuwen, J. N. Reek, *Acc. Chem. Res.* **2001**, *34*, 895–904.
[6] Z. Hassan, S. Bräse, *Chem. Eur. J.* **2021**, https://doi.org/10.1002/chem.202102336.
[7] a) X. Lang, J. Zhao, X. Chen, *Chem. Soc. Rev.* **2016**, *45*, 3026–3038; b) M. Natali, S. Campagna, F. Scandola, *Chem. Soc. Rev.* **2014**, *43*, 4005–4018.
[8] a) Z. Hassan, E. Spuling, D. M. Knoll, J. Lahann, S. Bräse, *Chem. Soc. Rev.* **2018**, *47*, 6947–6963; b) G. J. Rowlands, *Isr. J. Chem.* **2012**, *52*, 60–75; c) S. E. Gibson, J. D. Knight, *Org. Biomol. Chem.* **2003**, *1*, 1256–1269; d) J. Paradies, *Synthesis* **2011**, 3749–3766; e) S. Bräse, M. Christmann, *Asymmetric Synthesis – The Essentials*, Wiley-VCH, Weinheim, **2006**.
[9] a) Z. Hassan, E. Spuling, D. M. Knoll, S. Bräse, *Angew. Chem. Int. Ed.* **2020**, *59*, 2156–2170; *Angew. Chem.* **2020**, *132*, 2176–2190; b) A. de Meijere, B. Stulgies, K. Albrecht, K. Rauch, H. A. Wegner, H. Hopf, L. T. Scott, L. Eshdat, I. Aprahamian, M. Rabinovitz, *Pure Appl. Chem.* **2006**, *78*, 813–830; c) O. R. P. David, *Tetrahedron* **2012**, *68*, 8977–8993; d) R. Gleiter, H. Hopf, *Modern Cyclophane Chemistry*, Wiley-VCH, Weinheim, **2004**; e) H. Hopf, *Isr. J. Chem.* **2012**, *52*, 18–19.
[10] S. F. Nelsen, A. E. Konradsson, J. P. Telo, *J. Am. Chem. Soc.* **2005**, *127*, 920–925.
[11] a) P. J. Pye, K. Rossen, R. A. Reamer, N. N. Tsou, R. P. Volante, P. J. Reider, *J. Am. Chem. Soc.* **1997**, *119*, 6207–6208; b) V. Rozenberg, T. Danilova, E. Sergeeva, E. Vorontsov, Z. Starikova, K. Lysenko, Y. Belokon, *Eur. J. Org. Chem.* **2000**, 3295–3303; c) J. F. Schneider, R. Fröhlich, J. Paradies, *Isr. J. Chem.* **2012**, *52*, 76–91; d) S. Ay, R. E. Ziegert, H. Zhang, M. Nieger, K. Rissanen, K. Fink, A. Kubas, R. M. Gschwind, S. Bräse, *J. Am. Chem. Soc.* **2010**, *132*, 12899–12905; e) S. Bräse, S. Dahmen, S. Hofener, F. Lauterwasser, M. Kreis, R. E. Ziegert, *Synlett* **2004**, *14*, 2647–2669, https://doi.org/10.1055/s-2004-836029; f) N. Hermanns, S. Dahmen, C. Bolm, S. Bräse, *Angew. Chem. Int. Ed.* **2002**, *41*, 3692–3694; *Angew. Chem.* **2002**, *114*, 3844–3846.
[12] C. Braun, M. Nieger, W. R. Thiel, S. Bräse, *Chem. Eur. J.* **2017**, *23*, 15474–15483.
[13] a) D. M. Knoll, T. B. Wiesner, S. M. Marschner, Z. Hassan, P. Weis, M. Kappes, M. Nieger, S. Bräse, *RSC Adv.* **2019**, *9*, 30541–30544; b) C. Schissler, E. K. Schneider, B. Felker, P. Weis, M. Nieger, M. M. Kappes, S. Bräse, *Chem. Eur. J.* **2021**, *27*, 3047–3054.
[14] a) P. Mücke, R. F. Winter, K. Kowalski, *J. Organomet. Chem.* **2013**, *735*, 10–14; b) P. Mücke, R. F. Winter, I. Novak, K. Kowalski, *J. Organomet. Chem.* **2012**, *717*, 14–22; c) P. Mücke, M. Zabel, R. Edge, D. Collison, S. Clément, S. Záliš, R. F. Winter, *J. Organomet. Chem.* **2011**, *696*, 3186–3197; d) S. Clement, T. Goudreault, D. Bellows, D. Fortin, L. Guyard, M. Knorr, P. D. Harvey, *Chem. Commun.* **2012**, *48*, 8640–8642; e) J.-L. Xia, W. Y. Man, X. Zhu, C. Zhang, G.-J. Jin, P. A. Schauer, M. A. Fox, J. Yin, G.-A. Yu, P. J. Low, S. H. Liu, *Organometallics* **2012**, *31*, 5321–5333.
[15] a) R. J. Felix, D. Weber, O. Gutierrez, D. J. Tantillo, M. R. Gagne, *Nat. Chem.* **2012**, *4*, 405–409; b) C. Sarcher, A. Lühl, F. C. Falk, S. Lebedkin, M. Kühn, C. Wang, J. Paradies, M. M. Kappes, W. Klopper, P. W. Roesky, *Eur. J. Inorg. Chem.* **2012**, *2012*, 5033–5042; c) F. C. Falk, R. Fröhlich, J. Paradies, *Chem. Commun.* **2011**, *47*, 11095–11097.
[16] a) C. Stephenson, T. Yoon, *Acc. Chem. Res.* **2016**, *49*, 2059–2060; b) M. Kozlowski, T. Yoon, *J. Org. Chem.* **2016**, *81*, 6895–6897; c) M. H. Shaw, J. Twilton, D. W. MacMillan, *J. Org. Chem.* **2016**, *81*, 6898–6926; d) A. B. Beeler, *Chem. Rev.* **2016**, *116*, 9629–9630; e) L. Marzo, S. K. Pagire, O. Reiser, B. Konig, *Angew. Chem. Int. Ed.* **2018**, *57*, 10034–10072; *Angew. Chem.* **2018**, *130*, 10188–10228; f) S. E. Braslavsky, *Pure Appl. Chem.* **2007**, *79*, 293–465; g) J. Busch, D. M. Knoll, C. Zippel, S. Bräse, C. Bizzarri, *Dalton Trans.* **2019**, *48*, 15338–15357.
[17] a) C. Bolm, K. Wenz, G. Raabe, *J. Organomet. Chem.* **2002**, *662*, 23–33; b) D. C. Braddock, I. D. MacGilp, B. G. Perry, *J. Org. Chem.* **2002**, *67*, 8679–8681; c) H. Hopf, L. Bondarenko, I. Dix, H. Hinrichs, *Synthesis* **2004**, *16*, 2751–2759, https://doi.org/10.1055/s-2004-834872; d) C. Braun, M. Nieger, W. R. Thiel, S. Bräse, *Chem. Eur. J.* **2017**, *23*, 15474–15483.
[18] a) D. M. Knoll, H. Šimek, Z. Hassan, S. Bräse, *Eur. J. Org. Chem.* **2019**, *36*, 6198–6202, https://doi.org/10.1002/ejoc.201901171; b) D. M. Knoll, C. Zippel, Z. Hassan, M. Nieger, P. Weis, M. M. Kappes, S. Bräse, *Dalton Trans.* **2019**, *48*, 17704–17708.
[19] J. Malberg, M. Bodensteiner, D. Paul, T. Wiegand, H. Eckert, R. Wolf, *Angew. Chem. Int. Ed.* **2014**, *53*, 2771–2775; *Angew. Chem.* **2014**, *126*, 2812–2816.
[20] a) B. Matt, C. Coudret, C. Viala, D. Jouvenot, F. Loiseau, G. Izzet, A. Proust, *Inorg. Chem.* **2011**, *50*, 7761–7768; b) P. G. Bomben, K. C. Robson, P. A. Sedach, C. P. Berlinguette, *Inorg. Chem.* **2009**, *48*, 9631–9643.
[21] S. Fernandez, M. Pfeffer, V. Ritleng, C. Sirlin, *Organometallics* **1999**, *18*, 2390–2394.
[22] a) N. V. Vorontsova, V. I. Rozenberg, E. V. Sergeeva, E. V. Vorontsov, Z. A. Starikova, K. A. Lyssenko, H. Hopf, *Chem. Eur. J.* **2008**, *14*, 4600–4617; b) D. C. Braddock, S. M. Ahmad, G. T. Douglas, *Tetrahedron Lett.* **2004**, *45*, 6583–6585; c) H. J. Reich, D. J. Cram, *J. Am. Chem. Soc.* **1969**, *91*, 3517–3526.
[23] C. Bolm, T. Focken, J. Rudolph, *Synthesis* **2005**, *3*, 429–436, https://doi.org/10.1055/s-2005-861800.
[24] S. V. Kruppa, F. Bäppler, C. Holzer, W. Klopper, R. Diller, C. Riehn, *J. Phys. Chem. Lett.* **2018**, *9*, 804–810.
[25] a) C. Larriba, C. J. Hogan, Jr., *J. Phys. Chem. A* **2013**, *117*, 3887–3901; b) C. Larriba, C. J. Hogan, *J. Comput. Phys.* **2013**, *251*, 344–363.

 © 2021 The Authors. Chemistry - A European Journal published by Wiley-VCH GmbH

15213765, 2021, 61, Downloaded from https://chemistry-europe.onlinelibrary.wiley.com/doi/10.1002/chem.202102341, Wiley Online Library on [03/02/2025]. See the Terms and Conditions (https://onlinelibrary.wiley.com/terms-and-conditions) on Wiley Online Library for rules of use; OA articles are governed by the applicable Creative Commons License

[26] V. Boekelheide, in *Cyclophanes I*, **1983**, 87–143.
[27] a) Y. Ohsawa, K. W. Hanck, M. K. DeArmond, *J. Electroanal. Chem. Interfacial Electrochem.* **1984**, *175*, 229–240; b) W. T. Kender, C. Turro, *J. Phys. Chem. A.* **2019**, *123*, 2650–2660.
[28] L. Buzzetti, G. E. M. Crisenza, P. Melchiorre, *Angew. Chem. Int. Ed.* **2019**, *58*, 3730–3747; *Angew. Chem.* **2019**, *131*, 3768–3786.
[29] R. Antoine, P. Dugourd, *Phys. Chem. Chem. Phys.* **2011**, *13*, 16494–16509.
[30] a) S. Xu, J. E. Smith, J. M. Weber, *Inorg. Chem.* **2016**, *55*, 11937–11943; b) M. Förstel, W. Schewe, O. Dopfer, *Angew. Chem. Int. Ed.* **2019**, *58*, 3356–3360; *Angew. Chem.* **2019**, *131*, 3394–3398; c) C. van der Linde, S. Hemmann, R. F. Hockendorf, O. P. Balaj, M. K. Beyer, *J. Phys. Chem. A* **2013**, *117*, 1011–1020; d) M. Srnec, R. Navratil, E. Andris, J. Jasik, J. Roithova, *Angew. Chem. Int. Ed.* **2018**, *57*, 17053–17057; *Angew. Chem.* **2018**, *130*, 17299–17303.
[31] F. Liedy, F. Bäppler, E. Waldt, Y. Nosenko, D. Imanbaew, A. Bhunia, M. Yadav, R. Diller, M. M. Kappes, P. W. Roesky, D. Schooss, C. Riehn, *ChemPhysChem* **2018**, *19*, 3050–3060.
[32] D. Imanbaew, J. Lang, M. F. Gelin, S. Kaufhold, M. G. Pfeffer, S. Rau, C. Riehn, *Angew. Chem. Int. Ed.* **2017**, *56*, 5471–5474; *Angew. Chem.* **2017**, *129*, 5563–5566.
[33] S. E. Greenough, G. M. Roberts, N. A. Smith, M. D. Horbury, R. G. McKinlay, J. M. Zurek, M. J. Paterson, P. J. Sadler, V. G. Stavros, *Phys. Chem. Chem. Phys.* **2014**, *16*, 19141–19155.
[34] T. Yanai, D. P. Tew, N. C. Handy, *Chem. Phys. Lett.* **2004**, *393*, 51–57.
[35] A. J. Bard, L. R. Faulkner, *Electrochemical methods: fundamentals and applications*, 2 ed., Wiley, New York, **2001**.
[36] a) S. H. Wadman, M. Lutz, D. M. Tooke, A. L. Spek, F. Hartl, R. W. Havenith, G. P. van Klink, G. van Koten, *Inorg. Chem.* **2009**, *48*, 1887–1900; b) W. W. Yang, Y. W. Zhong, S. Yoshikawa, J. Y. Shao, S. Masaoka, K. Sakai, J. Yao, M. A. Haga, *Inorg. Chem.* **2012**, *51*, 890–899; c) B. D. Koivisto, K. C. Robson, C. P. Berlinguette, *Inorg. Chem.* **2009**, *48*, 9644–9652; d) W.-W. Yang, L. Wang, Y.-W. Zhong, J. Yao, *Organometallics* **2011**, *30*, 2236–2240.
[37] a) T. Sato, K. Torizuka, R. Komaki, H. Atobe, *J. Chem. Soc. Perkin Trans. 2* **1980**, *4*, 561–568, https://doi.org/10.1039/P29800000561; b) T. Sato, K. Torizuka, *J. Chem. Soc. Perkin Trans. 2* **1978**, *11*, 1199–1204, https://doi.org/10.1039/P29780001199; c) S. Sankararaman, H. Hopf, I. Dix, Peter G. Jones, *Eur. J. Org. Chem.* **2000**, *15*, 2711–2716.
[38] A. Tlahuext-Aca, M. N. Hopkinson, R. A. Garza-Sanchez, F. Glorius, *Chem. Eur. J.* **2016**, *22*, 5909–5913.
[39] a) Q. Sun, B. Dereka, E. Vauthey, L. M. Lawson Daku, A. Hauser, *Chem. Sci.* **2017**, *8*, 223–230; b) Q. Sun, S. Mosquera-Vazquez, Y. Suffren, J. Hankache, N. Amstutz, L. M. Lawson Daku, E. Vauthey, A. Hauser, *Coord. Chem. Rev.* **2015**, *282–283*, 87–99; c) Q. Sun, S. Mosquera-Vazquez, L. M. Daku, L. Guenee, H. A. Goodwin, E. Vauthey, A. Hauser, *J. Am. Chem. Soc.* **2013**, *135*, 13660–13663.
[40] a) D. Imanbaew, Y. Nosenko, C. Kerner, K. Chevalier, F. Rupp, C. Riehn, W. R. Thiel, R. Diller, *Chem. Phys.* **2014**, *442*, 53–61.
[41] a) F. Justaud, A. Hachem, R. Grée, *Eur. J. Org. Chem.* **2021**, *4*, 514–542, https://doi.org/10.1002/ejoc.202001494; b) V. Cadierno, P. Crochet, S. E. Garcia-Garrido, J. Gimeno, *Dalton Trans.* **2010**, *39*, 4015–4031; c) D. A. Engel, G. B. Dudley, *Org. Biomol. Chem.* **2009**, *7*, 4149–4158; d) K. H. Meyer, K. Schuster, *Berichte der deutschen chemischen Gesellschaft (A and B Series)* **1922**, *55*, 815–819.
[42] M. N. Hopkinson, A. Tlahuext-Aca, F. Glorius, *Acc. Chem. Res.* **2016**, *49*, 2261–2272.
[43] B. Alcaide, P. Almendros, E. Busto, A. Luna, *Adv. Synth. Catal.* **2016**, *358*, 1526–1533.
[44] J. Um, H. Yun, S. Shin, *Org. Lett.* **2016**, *18*, 484–487.

Manuscript received: June 30, 2021
Accepted manuscript online: October 16, 2021
Version of record online: October 28, 2021

 © 2021 The Authors. Chemistry - A European Journal published by Wiley-VCH GmbH

15213765, 2021, 61, Downloaded from https://chemistry-europe.onlinelibrary.wiley.com/doi/10.1002/chem.202102341, Wiley Online Library on [03/02/2025]. See the Terms and Conditions (https://onlinelibrary.wiley.com/terms-and-conditions) on Wiley Online Library for rules of use; OA articles are governed by the applicable Creative Commons License

3.4 Publication 4: Time-Resolved Spectroscopy and Electronic Structure of Mono- and Dinuclear Pyridyl-Triazole/DPEPhos-Based Cu(I) Complexes

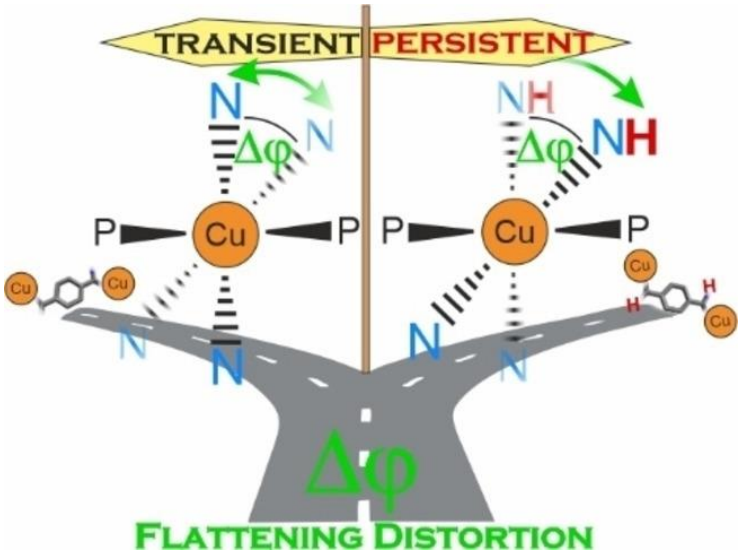

Preamble

Merten Grupe, Pit Boden, Patrick Di Martino-Fumo, Xin Gui, Cecilia Bruschi, Roumany Israil, Marcel Schmitt, Martin Nieger, Markus Gerhards, Wim Klopper, Christoph Riehn, Claudia Bizzarri, Rolf Diller, *Chemistry - A European Journal*, **2021**, 27, 15252-15271, https://doi.org/10.1002/chem.202102760; Copyright © 2021 Wiley-VCH GmbH, reproduced with permission from *Chemistry - A European Journal*. This article is dedicated to the memory of Prof. Dr. Markus Gerhards, a distinguished contributor to the field.

Contribution My contribution to this publication focuses on conducting mass spectrometry (MS^2/MS^3) and gas-phase ion spectroscopy, which included both static and ultrafast time-resolved photofragmentation experiments on the complexes in the ion trap. Marcel Schmitt was responsible for developing and setting up the experimental system and coupling the EKSPLA laser with the mass spectrometer, enabling for the first time pump-probe experiments in an ion trap with a time delay of up to 500 μs. Both Marcel and I worked under the supervision of PD Dr. Christoph Riehn on these essential measurements for exploring the photochemistry and dynamics of the title complexes in a solvent-free environment at room temperature. I reviewed and analyzed the outcomes from the methods described earlier,

prepared them for the discussion, and integrated them into the discussion section of the manuscript. Pit Boden conducted step-scan FTIR and luminescence spectroscopy in the solid state at various temperatures. Dr. Patrick Di Martino-Fumo contributed Density Functional Theory (DFT) calculations, which were crucial in modeling the electronic properties of the compounds. Both Pit and Patrick worked under the supervision of Prof. Dr. Markus Gerhards. Dr. Merten Grupe performed static and femtosecond transient UV/VIS absorption spectroscopy in the condensed phase, under the supervision of Prof. Dr. Rolf Diller, providing valuable insights into the complex's dynamics. Dr. Xin Gui performed Bethe-Salpeter and additional DFT calculations under the supervision of Prof. Dr. Willem Klopper, further strengthening the study's theoretical framework. Cecilia Bruschi and Prof. Dr. Claudia Bizzarri played key roles in synthesizing the complexes and conducting electrochemical and Stern-Volmer quenching experiments, with Cecilia working under Claudia's supervision. The overall research concept was designed by Prof. Dr. Rolf Diller and Prof. Dr. Claudia Bizzarri. The manuscript was written collaboratively, with substantial contributions from all coauthors.

Synopsis This study explores the photophysical properties of copper(I) complexes with pyridyl-triazole ligands, focusing on both mononuclear and dinuclear systems. By combining experimental techniques and high-level quantum chemical calculations, we investigated how charge and nuclearity influence the electronic structures and excited-state dynamics of these complexes.

One of the key findings is the role of protonation in structural relaxation. For the neutral mononuclear complex [(DPEPhos)Cu(I)(MPyrT)] (**CuL**), flattening distortion (FD) occurs in the singlet excited state (S_1) but is reversed in the triplet state (T_1). In contrast, the protonated mononuclear complex $[(DPEPhos)Cu(I)(MPyrT)]^+$ (**CuLH**) shows persistent FD in both S_1 and T_1 states, demonstrating how charge affects structural dynamics. The luminescence lifetimes of the complexes were found to be in the microsecond range, with dinuclear systems exhibiting longer lifetimes compared to their mononuclear counterparts. Temperature-dependent luminescence studies revealed TADF in the mononuclear and protonated

dinuclear systems, while the neutral dinuclear complex [(DPEPhos)$_2$Cu(I)$_2$(MPyrT)$_2$Ph] (**Cu$_2$L'**) displayed efficient phosphorescence with minimal TADF contribution.

The dinuclear complexes [(DPEPhos)$_2$Cu(I)$_2$(MPyrT)$_2$Ph]$^{0/2+}$ (**Cu$_2$L'** and **Cu$_2$L'H$_2$**) exhibited non-additive photophysical properties, suggesting cooperative interactions between the two **CuL** units. Theoretical calculations predicted symmetry breaking in the excited states of the dinuclear systems. The protonated dinuclear complex **Cu$_2$L'H$_2$** showed localized triplet states on one Cu unit, while the neutral dinuclear complex **Cu$_2$L'** exhibited a more symmetric triplet state. Time-resolved photodissociation experiments in the gas phase provided data on the intrinsic lifetimes of the excited states, confirming the formation of long-lived triplet states. These experiments also revealed that ISC rates are faster in the gas phase than in the condensed phase, highlighting the influence of solvent interactions on photophysical processes. This work impacts the importance of molecular structure, charge, and nuclearity in shaping the photophysical properties of Cu(I) complexes. The findings contribute to the design of efficient photosensitizers and luminescent materials, with potential applications in OLEDs and photocatalysis.

Electronic Supporting Information (ESI) Further details on experimental methods and data, that support the findings of this study are available in the ESI accompanying this publication. I contributed to the preparation and analysis of the ESI content, including mass spectra, UVPD spectra, τ-PD data, and theoretical calculations. Below is a summary of the ESI contents:

1. General methods and procedure.....2

2. Synthetic procedures and analyses 2

3. NMR spectroscopy 3

4. Mass spectrometric measurements.....7

5. UV/Vis fs transient absorption of CuL, CuLH and Cu_2L' as transparent film 8

6. UV/Vis fs transient photodissociation of $[CuLH]^+$, $[Cu_2L'H]^+$ and $[Cu_2L'H_2]^{2+}(PF_6)^-$ in gas phase 9

7. µs transient photodissociation of $[CuLH]^+$ in gas phase.....12

8. Absorption spectra in gas/liquid phase and the comparison to the calculations **.....13**

9. Luminescence spectroscopy.....16

10. Static and step-scan FTIR spectroscopy 23

11. Stern-Volmer plots.....42

12. Cyclic voltammetry.....42

13. Quantum chemical calculations performed in Karlsruhe.....43

14. Quantum chemical calculations performed in Kaiserslautern 51

Additional investigations (related to **Publication 4**)

Subsequent and parallel to the work presented in **Publication 4**, further investigations were conducted regarding the microsecond electronic state lifetime (given by time constants τ_1 and τ_2) of the Cu(I) complexes **[CuLH]$^+$** ([(DPEPhos)Cu^I(MPyrT)]$^+$) and **[Cu$_2$L'H]$^+$** ([(DPEPhos)$_2$Cu$^I_2${((MPyrT)$_2$Ph)-H}]$^+$) in the gas phase, leveraging the ns EKSPLA laser system. By extending the time delay range from 90 µs to 500 µs, additional insights were obtained. It should be noted that the µs excited state decay of the monomeric complex **[CuLH]$^+$** was already reported in **Publication 4**, whereas for the dimeric species **[Cu$_2$L'H]$^+$** and **[Cu$_2$L'H$_2$]$^{2+}$**(PF$_6$)$^-$ only ps dynamics (up to 800 ps) could be obtained, owing to challengingly small signal intensities for the according µs pump-probe experimental setup (cf. chapter 2.5). As a reminder (see discussion in **Publication 4**): the "original" dicationic dimer, as present in the compound salt, namely **[Cu$_2$L'H$_2$]$^{2+}$**, was unfortunately not observed after electrospray ionization in the gas phase of the ion trap, instead the deprotonated species **[Cu$_2$L'H]$^+$** and its counter ion aggregate **[Cu$_2$L'H$_2$]$^{2+}$**(PF$_6$)$^-$ could be detected and isolated. For **[CuLH]$^+$**, additional and extended measurements within a 120 µs time window yielded τ_1=2.8 µs and τ_2=22 µs (Figure 3.1), consistent with the reported values in **Publication 4** (τ_1=2 µs, τ_2=18 µs) with only minor baseline differences. Importantly, the extended time range allowed for a clear observation of relaxation to the baseline, whereas in the earlier study, this relaxation was only partially captured and therefore the presence of possibly longer-lived low-amplitude components in the decay curve could not be excluded.

For the deprotonated complex dimer **[Cu$_2$L'H]$^+$**, data collected within a 500 µs window revealed after multiexponential fitting also two, but clearly larger, time constants: τ_1=37 µs and τ_2 > 270 µs (Figure 3.2), indicating that the long time decay component extends beyond the technical measurement limit. The value of τ_1 reflects a decay process, likely tied to an electronical and/or structural relaxation within the triplet manifold. When compared to the mononuclear system, the extended τ_1 in the dimer suggests that cooperative effects or enhanced electronic delocalization between the two copper centers slow down the early decay dynamics.

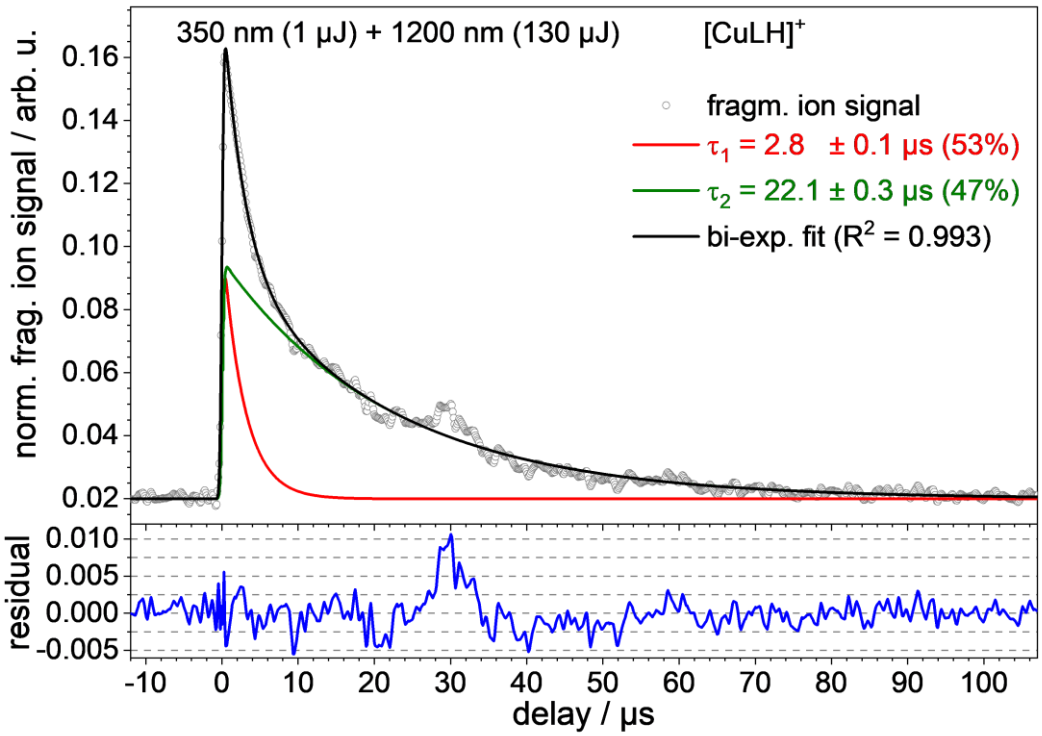

Figure 3.1 Normalized transient fragmentation ion intensity of **[CuLH]**$^{+}$ for a 120 µs time delay window; ns pump (350 nm, 1 µJ) and fs probe (1200 nm, 130 µJ) experiment.

The observed value for τ_2 is astonishingly large (in particuar in comparison to the condensed phase results at room temperature; see Table 3 in **Publication 4**) and a final rationalization of this observation cannot be given at the current status of research. The mentioned mismatch of species, **[Cu$_2$L'H$_2$]$^{2+}$** vs. **[Cu$_2$L'H]$^{+}$**, as stated above, might be of relevance here. However, this result underscores for the dimeric species the possibly enhanced stabilization of a fully developed triplet state or could maybe relate to the observation of thermally activated delayed fluorescence (TADF) for this compound as inferred from temperature-dependent luminescence measurements discussed in **Publication 4**. In general, in gas phase the absence of solvent interactions reduces nonradiative decay pathways and leads to an increase of the excited state lifetimes (e.g., compare the luminescence lifetimes as reported in Tab. 3 of **Publication 4**).

Note, that the variation in amplitude along the decay curve in Figure 3.2 (and less in Figure 3.1) is not due to signal-to-noise ratio (with the noise level being rather on the order of the size of the data point symbols), but represents "genuine" signal. This oscillatory

modulation observed in the lifetime decay curves (Figure 3.1, Figure 3.2), especially pronounced for the dimer in the gas phase, is very intriguing. Given the timescale of microseconds, these oscillations are unlikely to arise from vibrational coherent wavepacket motion, which typically oscillates in the femtosecond regime and decays within picoseconds to nanoseconds due to dephasing and coupling to other internal modes. Instead, the modulation could be attributed to a technical aspect of ion trap spectroscopy in general.

Regarding the spectrum of **[CuLH]**$^+$ in Figure 3.1, there is a notable difference compared to the transient shown in Publication 4 (Figure 8). In the earlier measurement, the ion cloud oscillations had a period of approximately 15 μs, whereas in Figure 3.1, the oscillations appear at around 30 μs, as clearly seen in the residuals of the exponential fit. This discrepancy suggests that the amplitude and appearance of these oscillations are highly dependent on the experimental setup and tuning of the ion trap parameters (e.g., RF field, low mass cut-off, and laser alignment). This observation further supports the interpretation the oscillations are primarily a technical or instrumental effect rather than a molecular or intrinsic property of the complexes.

Since the ions are confined in the Paul trap by a quadrupolar RF electrical field (781 kHz) they move under stable trapping conditions on quasi-periodic trajectories.[95] The time scale of this secular periodic motion of the ions depends in detail on the ion's m/z ratio and the ion trap's operating parameters (voltage, RF frequency, trap dimensions), and it could be estimated for standard trapping parameters to lie in the tens of μs region.[95,246] It seems now that, in the pump-probe experiment, the (inside the pump laser focus) photoexcited ions move within μs in and out of the more-or-less overlapping probe laser focus, leading to the accordingly oscillating fragmentation yield signal. The operating software for our commercial ion trap mass spectrometer (Bruker amaZon speed) does not allow to directly control all electrical trap parameters individually. Rather we have to refrain to the so-called relative “low mass cut-off” value (LMCO, by default set to 27%). From this value it is possible to calculate the relevant secular ion frequency to approx. 68 kHz, associated with a period of 14.7 μs, corresponding well to the oscillations in the traces of Figure 3.1 and Figure 3.2.[247] Obviously,

upon inspection of the residua of the corresponding exponential fits, the modulation for the monomer (Figure 3.1) appears much less pronounced than for the dimer (Figure 3.2). However, at the current status of research a full rationalization and elaboration of these observations is not feasible. A further detailed investigation of molecular ion's secular motion with respect to signal amplitude, frequencies and decay as well as its dependence and control by different ion trap parameters is underway and part of the PhD theses of Philipp Weber and partially Marcel Schmitt.

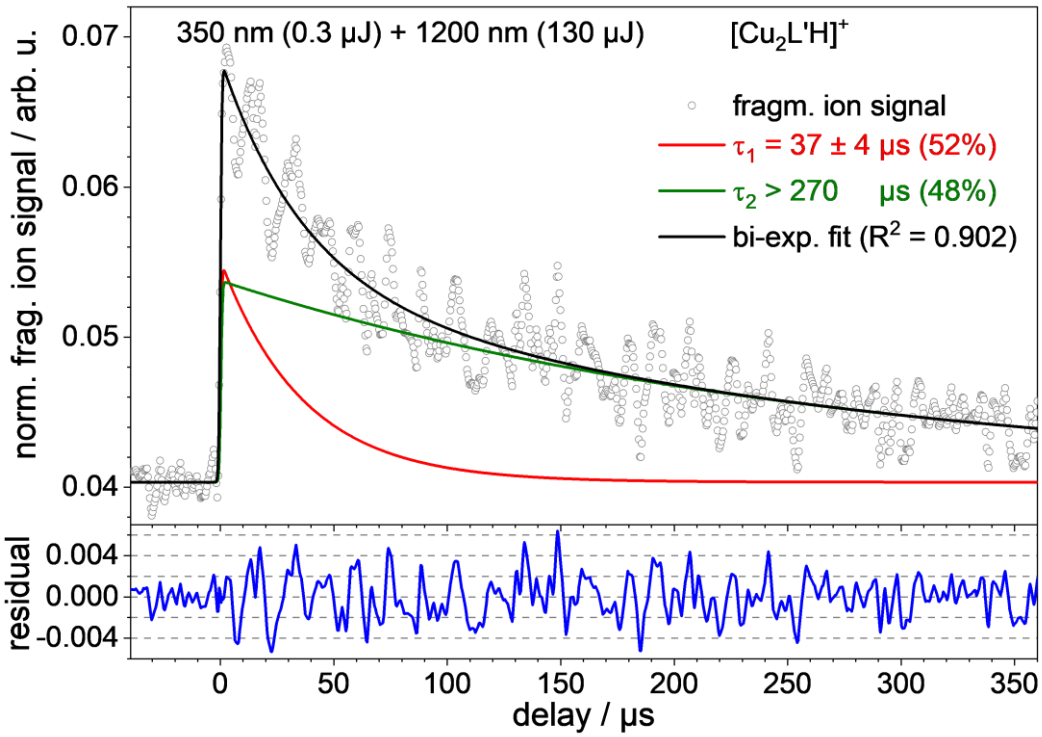

Figure 3.2 Normalized transient fragmentation ion intensity of **$[Cu_2L'H]^+$** for a 400 µs time delay window; ns pump (350 nm, 0.3 µJ) and fs probe (1200 nm, 130 µJ) experiment.

Reprint License

© 2021 The Authors. Chemistry - A European Journal published by Wiley-VCH GmbH

This is an open access article under the terms of the http://creativecommons.org/licenses/by-nc-nd/4.0/ License, which permits use and distribution in any medium, provided the original work is properly cited, the use is non-commercial and no modifications or adaptations are made.

PMC Copyright notice

PMCID: PMC8597052 PMID: 34550622

Material Specification:

Merten Grupe, Pit Boden, Patrick Di Martino-Fumo, Xin Gui, Cecilia Bruschi, Roumany Israil, Marcel Schmitt, Martin Nieger, Markus Gerhards, Wim Klopper, Christoph Riehn, Claudia Bizzarri, Rolf Diller,

"Time-Resolved Spectroscopy and Electronic Structure of Mono- and Dinuclear Pyridyl-Triazole/DPEPhos-Based Cu(I) Complexes."

Chemistry - A European Journal, **2021**, 27, 15252-15271.

DOI: https://doi.org/10.1002/chem.202102760

Check for updates

Chemistry–A European Journal
Full Paper
doi.org/10.1002/chem.202102760
Chemistry Europe
European Chemical Societies Publishing

Special Issue

Time-Resolved Spectroscopy and Electronic Structure of Mono-and Dinuclear Pyridyl-Triazole/DPEPhos-Based Cu(I) Complexes

Merten Grupe[+],[a] Pit Boden[+],[b] Patrick Di Martino-Fumo,[b] Xin Gui,[c] Cecilia Bruschi,[d] Roumany Israil,[e] Marcel Schmitt,[e] Martin Nieger,[f] Markus Gerhards[#],[b, g] Wim Klopper,[c] Christoph Riehn,[e, g] Claudia Bizzarri,*[d] and Rolf Diller*[a]

This article is dedicated to the memory of our esteemed colleague Markus Gerhards.

Abstract: Chemical and spectroscopic characterization of the mononuclear photosensitizers [(DPEPhos)Cu(I)(MPyrT)]$^{0/+}$ (**CuL**, **CuLH**) and their dinuclear analogues (**Cu_2L'**, **$Cu_2L'H_2$**), backed by (TD)DFT and high-level G*W*-Bethe-Salpeter equation calculations, exemplifies the complex influence of charge, nuclearity and structural flexibility on UV-induced photophysical pathways. Ultrafast transient absorption and step-scan FTIR spectroscopy reveal flattening distortion in the triplet state of **CuLH** as controlled by charge, which also appears to have a large impact on the symmetry of the long-lived triplet states in **Cu_2L'** and **$Cu_2L'H_2$**. Time-resolved luminescence spectroscopy (solid state), supported by transient photodissociation spectroscopy (gas phase), confirm a lifetime of some tens of μs for the respective triplet states, as well as the energetics of thermally activated delayed luminescence, both being essential parameters for application of these materials based on earth-abundant copper in photocatalysis and luminescent devices.

Introduction

Coordination complexes employing earth-abundant metals, like copper, have a multitude of applications from solar energy conversion over efficient emitters for new organic light-emitting diode (OLED) materials[1] to photocatalysis[2] for small-molecule, for example CO_2, activation.[3] The increasing demand for sustainable materials and processes motivates researchers to exploit earth-abundant resources. In particular, coordination metal complexes based on copper in its oxidation state +1 have been addressed as promising alternatives in respect of other complexes based on expensive and rare metals such as ruthenium, iridium or platinum.[4] Tetracoordinated copper(I) complexes have a pseudo-tetrahedral geometry in the ground

[a] Dr. M. Grupe,[+] Prof. Dr. R. Diller
Department of Physics
TU Kaiserslautern
Erwin-Schrödinger-Straße 46
67663 Kaiserslautern (Germany)
E-mail: diller@physik.uni-kl.de

[b] P. Boden,[+] P. Di Martino-Fumo, Prof. Dr. M. Gerhards[#]
Department of Chemistry
TU Kaiserslautern
Erwin-Schrödinger-Straße 52
67663 Kaiserslautern (Germany)

[c] Dr. X. Gui, Prof. Dr. W. Klopper
Institute of Physical Chemistry
Karlsruhe Institute of Technology (KIT)
Fritz-Haber-Weg 2, 76131 Karlsruhe (Germany)

[d] C. Bruschi, Dr. C. Bizzarri
Institute of Organic Chemistry (IOC)
Karlsruhe Institute of Technology (KIT)
Fritz-Haber-Weg 6, 76131 Karlsruhe (Germany)
E-mail: claudia.bizzarri@kit.edu

[e] R. Israil, M. Schmitt, Dr. C. Riehn
Department of Chemistry
TU Kaiserslautern
Erwin-Schrödinger-Straße 52
67663 Kaiserslautern (Germany)

[f] Dr. M. Nieger
Department of Chemistry
University of Helsinki
A.I. Virtasen aukio 1, 00014 Helsinki (Finland)

[g] Prof. Dr. M. Gerhards,[#] Dr. C. Riehn
Research Center OPTIMAS
Erwin-Schrödinger-Straße 46
67663 Kaiserslautern (Germany)

[+] These authors contributed equally to this work.

[#] Deceased December 28th 2020

Supporting information for this article is available on the WWW under https://doi.org/10.1002/chem.202102760

Special Issue This manuscript is part of a Special Issue "Cooperative effects in heterometallic complexes".

© 2021 The Authors. Chemistry - A European Journal published by Wiley-VCH GmbH. This is an open access article under the terms of the Creative Commons Attribution Non-Commercial NoDerivs License, which permits use and distribution in any medium, provided the original work is properly cited, the use is non-commercial and no modifications or adaptations are made.

state. When excited, the complex populates a metal-to-ligand charge-transfer (MLCT) state since the low-lying metal-centered states are prevented in Cu(I) due to its completely filled d-orbitals (d^{10} metal). In this MLCT state, the copper center is formally oxidized and therefore, the complex undergoes a flattening distortion to arrange in a square planar geometry, which is usual for tetracoordinated Cu(II) complexes. To use Cu(I) complexes as photosensitizers, they should possess a good chemical stability in solution, and an excited state lifetime in the microsecond scale. In order to have an emissive and long-lived excited state, the strategy is to reduce this flattening distortion to a minimum level, which can be afforded by using rigid ligands with bulky substituents. This is the reason why heteroleptic Cu(I) complexes of type (NN)Cu(PP) are gaining attention, as reviewed recently.[5] Here, (PP) is a chelating diphosphine, such as (9,9-dimethyl-9H-xanthene-4,5-diyl)bis (diphenylphosphane) (Xantphos) or bis(2-(diphenylphosphanyl) phenyl)ether (DPEPhos), and (NN) is the diimine ligand, where usually the LUMO of the complex is localized. In particular, the diimine ligand is often based on 1,10-phenanthroline and derivatives and, with the right substituents, the excited state lifetimes of heteroleptic Cu(I) complexes of this structure can reach up to 20 μs.[4a,6] Heteroleptic Cu(I) complexes with pyridyl-triazole as diimine are less investigated. However, they do not only show long-lived excited state lifetimes, but they are usually highly stable in solution, without forming the homoleptic $Cu(NN)_2$ complex upon time, as it is often the case with 1,10-phenanthroline derivatives.[7] Since they often present efficient solid-state emission in the light-blue/cyan region, Cu(I) complexes with pyridyl-triazole (or tetrazole) ligands find usually applications in OLEDs,[8] while their usage as photosensitizers or photoredox catalysts is rather limited,[3h,9] in contrast to the cuprous complexes based on 1,10-phenanthroline.[2a,b, 10]

Key to the understanding of the related photochemistry is to find correlations between molecular structure and optical properties, i.e. establish a structure-function relationship.[5] Therefore, the determination of important experimental and theoretical spectroscopic and structural data is central to investigation of such photoactive compounds and fuels the discussion of their application by delivering, for example absorption spectra and assignment of transitions and electronic states, lifetimes of electronically excited states, for example luminescent triplet states, and non-radiative relaxation pathways, quantum yields (if possible), (photo-)stability and reactivity in different environments. It should be emphasized, that the exploration of (ultrafast) time scales and the connections or sequences of elementary photochemical pathways after excitation are essential for gaining fundamental insights into their "functionality" and in parallel supports the rational design of such metal complexes, displaying a highly active field of research.

Specific to Cu(I) complexes is the question of the occurrence and ultrafast time scale of structural relaxation (Jahn-Teller flattening distortion (FD)) in the excited state.[8b,11] Since FD, within its own temporal evolution, is likely to change rates for internal conversion (IC) and intramolecular vibrational relaxation (IVR), it poses a challenge for the disentanglement of photoinduced primary processes. This concerns in particular excited electronic state deactivation and lifetime shortening, as well as its involvement in the formation of a long-lived electronically excited state via intersystem crossing (ISC).[12] The related putative involvement of several low-lying singlet and triplet states has been discussed recently.[13] Here we report a study on a series of heteroleptic Cu(I) complexes, based on chelating diimine unit 6′-methyl-pyrid-2′-yl-*1H*-1,2,3-triazole (MPyrT), i.e. the two mononuclear complexes [(DPEPhos) Cu(I)(MPyrT)]$^{0/+}$ (neutral **CuL** and cationic **CuLH**), and the two dinuclear complexes, where the diimine units are linked together by a phenyl ring $(MPyrT)_2Ph$, i.e. $[(DPEPhos)_2Cu(I)_2(MPyrT)_2Ph]^{0/2+}$ (neutral **Cu_2L'** and dicationic **$Cu_2L'H_2$**). For the reported mass spectrometric and gas phase investigations within this text we abbreviate the cationic complexes explicitly with their charge. These complexes are designed as photosensitizers, envisaging their use in the photoactivated CO_2 reduction in combination with an appropriate (earth-abundant metal-based) catalyst.[14] We reveal here the new structures of the compounds **CuL** and **Cu_2L'** as received by X-ray diffraction analysis. The molecular structures of all complexes, here under investigation, are based on the same and formative heteroleptic unit **CuL**, and thus allow the comparative study of their chemical and in particular their photophysical properties with regard to charge and nuclearity. To this end we have applied a broad variety of experimental and theoretical methods. Our study also focuses on cooperative effects[15] apparent as non-additive contributions of dimerization and/or protonation. Most photophysical and electrochemical properties observed, for example for the dinuclear charged system cannot be derived from the characteristics of the protonated monomer and the neutral dimer, which is discussed qualitatively as a kind of cooperative effect. Furthermore, a quantification of cooperativity is presented for the luminescence energies.

Electrochemical analysis and Stern-Volmer quenching experiments were performed to obtain redox and photocatalytic properties, respectively, in particular for the new (neutral) complexes **CuL** and **Cu_2L'**. Time-resolved spectroscopic methods were used to explore photoinduced dynamics. (i) Femtosecond UV/Vis transient absorption (fs-TA) reveals ultrafast processes, such as Franck-Condon-state relaxation, FD and intersystem crossing. Both solution and solid phase (neat film) preparations were addressed to study, in general, the influence of the environment and in particular exploit the extent of environment rigidity on the photodynamics. (ii) Step-scan FTIR spectroscopy was applied to KBr pellets for structural characterization of long-lived excited (triplet) states, the lifetimes of which were determined as function of temperature via (iii) time-correlated single photon counting (TCSPC). The latter yields valuable information on the S_1-T_1 energy gap, crucial for the luminescence efficiency, determined by thermally activated delayed fluorescence (TADF)[1d,16] via reverse intersystem crossing (RISC). As photophysical properties are prone to matrix effects, (iv) femtosecond and, as a novel variant, microsecond transient photodissociation (τ-PD) in gas phase were applied, allowing direct comparison with the condensed phase measurements. Our experimental results are compared with the results

© 2021 The Authors. Chemistry - A European Journal published by Wiley-VCH GmbH

15213765, 2021, 61, Downloaded from https://chemistry-europe.onlinelibrary.wiley.com/doi/10.1002/chem.202102760, Wiley Online Library on [03/02/2025]. See the Terms and Conditions (https://onlinelibrary.wiley.com/terms-and-conditions) on Wiley Online Library for rules of use; OA articles are governed by the applicable Creative Commons License

of high-level quantum chemical computations on the electronic absorption spectra in gas and condensed phase, the IR-vibrational spectra of the long-lived excited triplet states, and the magnitude of FD.

Results and Discussion

Synthesis and structural properties

The heteroleptic copper complexes investigated in this paper were prepared using a commercially available chelating phosphine, the so-called DPEPhos (from bis[(2-diphenylphosphino)phenyl] ether), and diimine ligands based on 6'-methylpyridyl-*1H*-1,2,3-triazole (MPyrT). Pyridyl-triazoles are well known chelating ligands for a variety of coordination metal complexes,[17] as well for Cu(I), as it is demonstrated by various publications.[8c,14, 18] As stated in the introduction, despite their high stability in solution, heteroleptic Cu(I) complexes based on pyridyl-triazole have been less investigated. Moreover, beyond the increased stability, our motivation is enforced by the straightforward preparation of such ligands. In this work we followed the two-steps synthesis reported by Bizzarri et al.,[14] consisting of a Sonogashira cross-coupling reaction between one or two equivalents (for the dichelating diimine) of 2-bromo-6-methyl-pyridine and one equivalent of phenylacetylene or 1,4-diethynylbenzene, respectively, followed by a Huisgen cycloaddition with an excess of NaN_3 at high temperature. The charged Cu(I) complexes **CuLH** and $\mathbf{Cu_2L'H_2}$ were prepared in dichloromethane (DCM) at room temperature under argon (Ar) atmosphere, by dissolving DPEPhos and $Cu(NCCH_3)_4BF_4$ together with the corresponding ligand. The neutral complexes **CuL** and $\mathbf{Cu_2L'}$ were obtained via deprotonation by washing the DCM solution of the respective charged complexes with a saturated aqueous solution of K_2CO_3. In Figure 1, next to the chemical structures of the four complexes, the crystal of the charged dinuclear Cu(I) complex is shown. Suitable crystals for X-ray diffractometry were obtained only for the charged species, by slow evaporation of solvent ($CDCl_3$). The colorless crystals of $\mathbf{Cu_2L'H_2}$ have a monoclinic system with a C2/c space group, whilst the mononuclear **CuLH** crystals are tetragonal with $P4_32_12$ space group, as reported earlier.[14] In both cases, the geometry around the Cu(I) nuclei is pseudotetrahedral. While the N–Cu-N angles are very similar in the mononuclear and in the dinuclear complexes, (circa 79.9° for both), the P–Cu–P angles are smaller in $\mathbf{Cu_2L'H_2}$ (111.2° compared to 114.6° for **CuLH**). Dihedral angles between the N–Cu–N plane and the P–Cu–P plane are 92.8° for **CuLH** and 91.3° for $\mathbf{Cu_2L'H_2}$. Those values are similar to those calculated for the S_0 ground state (see below). Selected bond lengths and angles are reported in Table SI–1. The complete crystallographic set can be found in the Crystallographic Cambridge Database Center.

Mass spectrometric analysis and fragmentation of ionic complexes

The ionic complexes **CuLH** and $\mathbf{Cu_2L'H_2}$ were analyzed by electrospray ionization mass spectrometry (ESI-MS) from different solvents (DCM, acetonitrile, methanol) and isolated in an ion trap for interrogation by collision-induced (CID) and UV laser photodissociation (UV PD).

The mononuclear compound $\mathbf{[CuLH](BF_4)}$ is detected from a methanolic solution as intact molecular ion: $\mathbf{[CuLH]^+}$ at m/z 836 (nominal mass). The dinuclear compound $\mathbf{[Cu_2L'H_2](BF_4)_2}$, however, is observed as the *deprotonated* monocationic species $\mathbf{[Cu_2L'H]^+}$ at m/z 1595 and upon ESI from the precursor $\mathbf{[Cu_2L'H_2](PF_6)_2}$ observed both as a $\mathbf{[Cu_2L'H]^+}$ and the counter ion complex $\mathbf{[Cu_2L'H_2]^{2+}(PF_6)^-}$ (m/z 1741). Identification of all species was achieved by comparison of the according isotope patterns (see Figure SI-9). CID and UV PD of $\mathbf{[CuLH]^+}$ both lead mainly to the loss of the neutral ligand LH, so that $[Cu(DPEPhos)]^+$ (m/z 601) is detected as ionic fragment. UV PD of

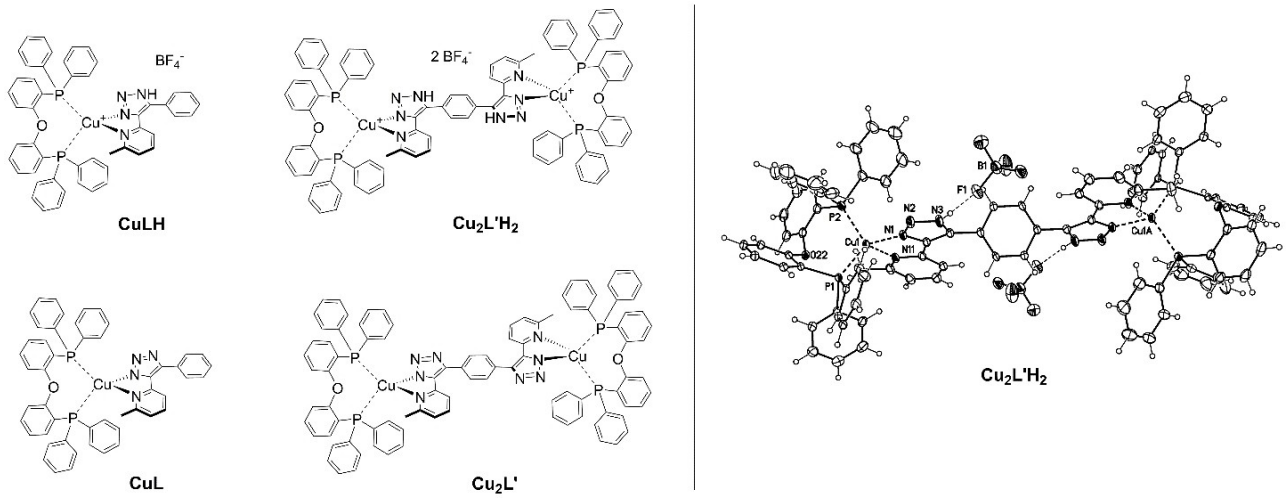

Figure 1. Chemical structures of the Cu(I) complexes investigated in this work (left). Molecular structure of $\mathbf{Cu_2L'H_2}$ (right).

 © 2021 The Authors. Chemistry - A European Journal published by Wiley-VCH GmbH

15213765, 2021, 61, Downloaded from https://chemistry-europe.onlinelibrary.wiley.com/doi/10.1002/chem.202102760, Wiley Online Library on [03/02/2025]. See the Terms and Conditions (https://onlinelibrary.wiley.com/terms-and-conditions) on Wiley Online Library for rules of use; OA articles are governed by the applicable Creative Commons License

$[Cu_2L'H]^+$ leads mainly to the loss of N_2, while CID favours the cleavage of DPEPhos, giving the fragment [Cu(L'H) Cu(DPEPhos)]$^+$ (m/z 1057), and to a lower amount again to the formation of [Cu(DPEPhos)]$^+$. UV PD and CID of $[Cu_2L'H_2]^{2+}(PF_6)^-$ results in $[Cu_2L'H]^+$ as the main fragment, whereas the cleavage of [Cu(DPEPhos)]$^+$ and of LH is also observed. UV PD of $[Cu_2L'H_2]^{2+}(PF_6)^-$ leads additionally to the loss of N_2 and DPEPhos. In summary, the compound cations have been identified mass spectrometrically and their ion trap isolation proved possible which is a prerequisite for further gas phase laser spectroscopy (see below). **CuLH** gave intense molecular signals, whereas $[Cu_2L'H_2]^{2+}$ deprotonates easily to form the probably quite stable $[Cu_2L'H]^+$. Overall, the dissociation pathways following thermal (CID) or photoexcitation (UV PD) are similar and limited in variety.

Electrochemical properties and Stern-Volmer quenching

The redox properties of the mononuclear and dinuclear complexes were investigated by cyclic voltammetry (CV) in acetonitrile for the charged species[14] and in *N,N*-dimethylformamide for the neutral compounds. Tetrabutylammonium hexafluorophosphate ($TBAPF_6$) was used in all cases as supporting electrolyte. The redox potentials are reported versus ferrocene oxidation, as recommended by IUPAC[19] and the voltammograms are shown in the Supporting Information (see Figure SI–76). In oxidation, we can identify a one-electron process assigned to the oxidation of the copper metal Cu(I)/Cu(II). This process is irreversible for all four complexes. Moreover, there is a light difference when comparing the oxidation potentials of the charged with the neutral species, taking into account that slight discrepancies might also be due to the different solvent used. In particular the neutral compounds **CuL** and **Cu_2L'** oxidize almost 1000 mV earlier than the corresponding charged species (see Table 1). This is in agreement with the fact that in the neutral species **CuL** and **Cu_2L'**, the Cu(I) nuclei are coordinated by a negatively-charged diimine, which can stabilize the oxidized form of copper more than the neutral ligand in complexes **CuLH** and **$Cu_2L'H_2$**. In the reduction, one irreversible process is present for all complexes around −2.6 V for the neutral species and −2.7 V for the charged complexes. This redox process is localized on the diimine ligand and the 100 mV difference has to be ascribed to the diverse influence of the solvent used. As the first oxidation can be associated to the HOMO level in solution of the corresponding sample, the redox process correlates well with the theoretical calculation, as it is mainly localized on the metal core Cu(I). On the other side, the reduction processes are associated to the LUMO levels, and the localization on the diimine is also in agreement with quantum chemical calculation (see below). These assignments are confirmed also by the emission profiles of the four complexes. In fact, the observed emission is broad and unstructured, which is typical for metal-to-ligand charge transfer states.

Table 1. Electrochemical potentials of the ground and excited state vs. Fc/Fc$^+$ and quenching constants.[a]

Sample	E_{ox}/V	E_{red} /V	K_{SV}[c]/ M^{-1}	k_q[d]/s^{-1} M^{-1}
CuLH	1.30	−2.65	1900	$3.5\ 10^{10}$
$Cu_2L'H_2$	1.93	−2.65	3270	$1.7\ 10^{10}$
CuL	0.49[b]	−2.54[b]	630	$1.5\ 10^{10}$
Cu_2L'	0.37 [b]	−2.56[b]	1190	$1.4\ 10^{10}$

[a] In acetonitrile (0.1 M $TBAPF_6$). [b] in *N,N*-dimethylformamide (0.1 M $TBAPF_6$). [c] K_{SV} is the slope of the linear fit $I_0/I = 1 + [Q]$. [d] $k_q = K_{SV}/\tau$.

As we have previously shown for the charged complexes,[14] the investigated Cu(I) complexes undergo an oxidative quenching with a nickel(II) 1,4,8,11-tetraazacyclotetradecane (cyclam) complex: Ni(cyclam)Cl_2, known to reduce CO_2 to CO.[20] This is demonstrated by Stern-Volmer analysis, which was done in air-equilibrated solutions of the Cu complexes by addition of known aliquots of the nickel(II) complex (Figure SI-75). According to the Stern-Volmer equation, we can extract the apparent quenching constant k_q from the Stern-Volmer constant K_{SV} (see Table 1). The quenching rate is diffusion limited for each Cu(I) complex, having a k_q of the order of magnitude of 10^{10} $s^{-1}M^{-1}$. When comparing the values between the mononuclear complexes **CuLH** and **CuL**, the quenching is twice faster for the protonated compound. This is true also if we compare the quenching rate of the charged mononuclear and dinuclear complexes (**CuLH** and **$Cu_2L'H_2$**). Nevertheless, we observe almost no difference between the quenching rates of the charged and neutral dinuclear complexes, as well as the neutral mononuclear and dinuclear complexes. With this, we have demonstrated how these Cu(I) complexes undergo an oxidative quenching and can potentially act as photosensitizers. Nevertheless, a photoactivated catalysis for CO_2 reduction involves many components and the reaction parameters have to be chosen accurately. Thus, although preliminary photocatalytic tests were done, their results are still not satisfying. Optimizations of the conditions are ongoing and are out of the target of the present work.

Quantum chemical calculations

Quantum chemical computations were performed in order to serve three purposes. Firstly, we have simulated the ground state absorption (GSA) spectra of **CuL**, **CuLH**, **Cu_2L'**, and **$Cu_2L'H_2$** in order to compare these with the experimental GSA spectra measured in CH_2Cl_2, measured as neat film, and as obtained from gas phase UV laser photodissociation action spectroscopy. Secondly, we have determined the equilibrium structures of the long-lived excited triplet states of **CuL**, **CuLH**, **Cu_2L'**, and **$Cu_2L'H_2$** in order to compare the corresponding computed excited state harmonic vibrational frequencies with the experimental structural characterization by step-scan FTIR spectroscopy (in KBr pellets). Thirdly, we have optimized the equilibrium structures of low-lying singlet and triplet excited states of the mononuclear complexes in order to obtain insight into the flattening distortion (FD) that may occur in the excited states.[8b,11,21]

We have performed quantum chemical computations at the density functional theory (DFT) and time-dependent DFT (TDDFT) levels using the functionals B3LYP[22] and PBE0[23] in

 © 2021 The Authors. Chemistry - A European Journal published by Wiley-VCH GmbH

15213765, 2021, 61, Downloaded from https://chemistry-europe.onlinelibrary.wiley.com/doi/10.1002/chem.202102760, Wiley Online Library on [03/02/2025]. See the Terms and Conditions (https://onlinelibrary.wiley.com/terms-and-conditions) on Wiley Online Library for rules of use; OA articles are governed by the applicable Creative Commons License

Kaiserslautern and in Karlsruhe, respectively. Using these two functionals, the TDDFT optimized equilibrium structures of the low-lying singlet and triplet excited states of the mononuclear systems (**CuL** and **CuLH**) mutually agree very well, giving confidence to having found meaningful structures. States of ligand-centered $\pi\pi^*$ and MLCT character are found as a function of the geometry, making these computations very challenging for TDDFT. For the dinuclear systems, the structural flexibility is even more difficult to handle at the TDDFT level because of the possible mutual orientations of the two fragments and the occurrence of localized (on one fragment) and delocalized (on both fragments) excited states. Therefore, for the systems **Cu_2L'**, and **$Cu_2L'H_2$**, we focus in the following on the geometry optimization of the first triplet excited states and the computation of their harmonic vibrational frequencies at the level of *spin-unrestricted DFT theory* (UDFT). We suspect that the dinuclear systems can be excited locally at both mononuclear fragments of the dinuclear complex, leading to two nearly degenerate localized excited states and an asymmetric complex. Alternatively, two delocalized states (symmetric and antisymmetric) may be found. Not surprisingly, the coordination of the Cu ion in the locally excited state of the dinuclear complex was found to be very similar to the coordination of the Cu ion in the mononuclear complex.

For the computation of the GSA spectra, we have employed the *GW*/Bethe-Salpeter equation (*GW*/BSE) approach.[24] We have chosen the *GW*/BSE method because we expected to be dealing with charge-transfer states and since TDDFT is known to fail for long-range charge-transfer excited states.[25] The *GW*/BSE calculations were based on ground-state DFT calculations with the PBE0 functional,[23] which is common in *GW*/BSE computations.[24b,c]

For the computation of the equilibrium structures and harmonic vibrational frequencies of the first excited triplet states of the four systems, we have optimized the Kohn-Sham determinant in terms of a UDFT calculation with two unpaired electrons (spin quantum number $M_S = 1$). Since this is a ground-state type optimization, charge-transfer issues are much less severe than at the TDDFT level. Here, we employed the B3LYP-D3(BJ) level of DFT,[22,26] as done already with great success in many of our earlier works. See, for example Goswami et al. and references therein.[27]

We have optimized the geometries of the S_0, S_1, and T_1 states of **CuL** and **CuLH** at the TDDFT and UDFT (for T_1) levels using the functionals PBE0 and B3LYP. The results obtained with these two functionals mutually agree very well and so do the TDDFT and UDFT results for the T_1 states. The main finding is that FD is observed for all of the excited states except for the T_1 state of **CuL**. For the latter state, the dihedral angle between the P–Cu–P and N–Cu–N planes is nearly 90°, whereas this angle is reduced by ca. 10° in the other three excited states (S_1 and T_1 of **CuLH** and S_1 of **CuL**). We furthermore note that the metal-to-ligand charge-transfer (MLCT) character is significant for the S_1 and T_1 excited states of **CuLH** and for the S_1 state of **CuL**, whereas it is basically absent in the T_1 state of **CuL**. A natural population analysis of the hole and particle unrelaxed difference densities of the T_1 state of **CuL** (in its own T_1-optimized geometry) shows that the 3d orbitals of Cu contribute only 1–3% to the unrelaxed hole density (values highlighted with red color in Tables SI-12–SI-14). This contribution is significantly larger (10-40%) for the states that show FD.

Static absorption in condensed and gas phase

The static electronic ground state absorption (GSA) spectra (Figure 2) of the four complexes in DCM as well as neat film are quite similar (besides different overall extinction coefficients), with increasing absorption only below 400 nm. **CuLH** and **$Cu_2L'H_2$** in DCM show a pronounced shoulder around 350 nm, assigned to a MLCT transition from the Cu atom to the MPyrT- respectively the $(MPyrT)_2Ph$-ligand.[14] This shoulder is not as good observable in the neutral systems, possibly due to stronger overlap with ligand-centered (LC) ππ* transitions below 350 nm[14] and less pronounced MLCT character (see Comparison of condensed phase absorption spectra with the theoretical prediction).

In gas phase, i.e. in a room temperature ion trap, we have recorded UV PD action spectra of the ionic complexes which should represent UV absorption spectra (Figures 3, SI-23 and SI-26).[28] The species **$[CuLH]^+$** (Figure 3, blue trace) shows two bands at 270 nm and 305 nm and a less intense feature at ca. 350 nm. The UV PD spectrum of **$[Cu_2L'H]^+$** also reveals two bands (270 nm, 315 nm; Figure 3, green trace), however with reversed intensities and a broad shoulder (centered at ca. 330 nm) on the long wavelength side extending up to 400 nm. Additionally, a weak feature could be located at ca. 370 nm. The UV PD spectrum of **$[Cu_2L'H_2]^{2+}(PF_6)^-$** (Figure 3, red trace) is similar to the one of **$[Cu_2L'H]^+$**. However, the broad shoulder at 330 nm is no longer observed, but a weaker band plateau at ca. 350 nm. The absorption spectrum of **$[CuLH](BF_4)$** (Figures 2 and 3) in DCM overlaps well with the gas phase spectrum, but exhibits less pronounced structures. Instead, it shows a plateau-like shoulder at 290 nm and a shoulder at 350–370 nm. In solution (MeOH, DCM) the spectra of the dinuclear **$[Cu_2L'H_2](BF_4)_2$** and **$[Cu_2L'H_2](PF_6)_2$** complexes are both red-

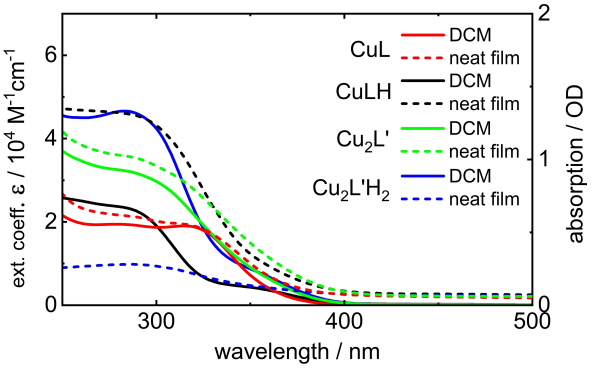

Figure 2. Static UV/Vis absorption spectra of **CuL**, **CuLH**, **Cu_2L'** and **$Cu_2L'H_2$** in DCM (solid) as decadic ext.-coeff. (solvent contributions subtracted), and as transparent neat film (dotted) in OD units (offset above 400 nm due to scattering), at room temperature. Excitation for UV/Vis fs-TA at 350 nm.

© 2021 The Authors. Chemistry - A European Journal published by Wiley-VCH GmbH

15213765, 2021, 61, Downloaded from https://chemistry-europe.onlinelibrary.wiley.com/doi/10.1002/chem.202102760, Wiley Online Library on [03/02/2025]. See the Terms and Conditions (https://onlinelibrary.wiley.com/terms-and-conditions) on Wiley Online Library for rules of use; OA articles are governed by the applicable Creative Commons License

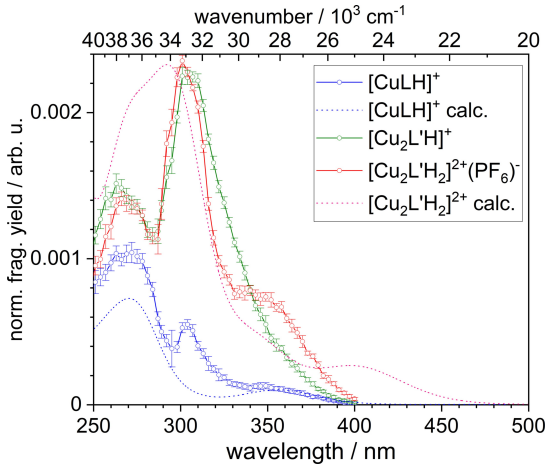

Figure 3. UV PD spectra of **[CuLH]**$^+$, **[Cu$_2$L'H]**$^+$ and **[Cu$_2$L'H$_2$]**$^{2+}$**(PF$_6$)**$^-$ and the calculated absorption spectra of **[CuLH]**$^+$ and **[Cu$_2$L'H$_2$]**$^{2+}$ obtained at PBE0 ev*GW*-BSE/def2-TZVP level and convoluted with 1500 cm^{-1} full width at half maximum (FWHM).

shifted with respect to the spectra of the mononuclear ones (Figure SI-24). They display a similar behavior with more distinct band structure in gas phase (Figure SI-25). In addition, the absorption spectra obtained in methanol reveal a slight blue-shift by ca. 15 nm with respect to DCM (Figure SI-24), but nearly no change in spectral shape.

In summary, the gas phase spectra exhibit two pronounced band structures in the region of the plateau feature found in solution. The solution spectra are slightly red-shifted with respect to the gas phase spectra which we ascribe to stabilization by solvation, however the onsets on the red side of all spectra (at ca. 400 nm) are very similar.

Comparison of condensed phase absorption spectra with the theoretical prediction

The comparison of the recorded spectra in solution with the calculated spectra (PBE0/ev*GW*-BSE/def2-TZVP, Figure 4) shows a good agreement. Since solvent effects have not been included, there is better agreement with the obtained UV PD spectra in gas phase (Figure 3). The calculations show that in the excitation range of 340–355 nm, MLCT transitions or ππ* transitions localized on the pyridyl-triazole residue with some MLCT character are excited (Figure 4). For energetically higher excitations, transitions of different nature are expected, where the corresponding molecular orbitals are localized on the nitrogen-containing ligand as well as on the phenyl groups of the phosphine ligand. Those energetically higher lying transitions show ππ* as well as MLCT character (for a more detailed discussion, see Supporting Information chapter 13 and 14). Of interest to note is the theory-predicted but absent red-shifted band at about 400 nm of the **Cu$_2$L'H$_2$** species. This may indicate that the calculated structure found is not the structure present in the experiment and therefore shows slightly different electronic properties. The electronic excitations of the optimized structures (gas phase) were also calculated with TDDFT, but showed a poorer agreement with the experimentally recorded spectra. (Even after the application of COSMO, a better match could be achieved, but the intrinsic problem of underestimating the energy of MLCT transitions could not be compensated (see Supporting Information chapter 14). In general, the TDDFT calculations show the same electronic transitions as the ev*GW*-BSE calculations, but significantly red-shifted.)

Excited state dynamics on ultrafast time scale

Ultrafast pump-probe experiments were applied to study the primary processes after photoexcitation, such as FC-state relaxation, FD, IVR and ISC. Their entanglement is crucial for the formation of long-lived, functionally important states, which are then further characterized by step-scan FTIR, TCSPC and microsecond transient photodissociation (see below). In order to distinguish between matrix-related and intrinsic effects we used femtosecond UV/Vis transient absorption (fs-TA) for solution and solid phase, as well as femtosecond transient photodissociation (τ-PD) for gas phase conditions.

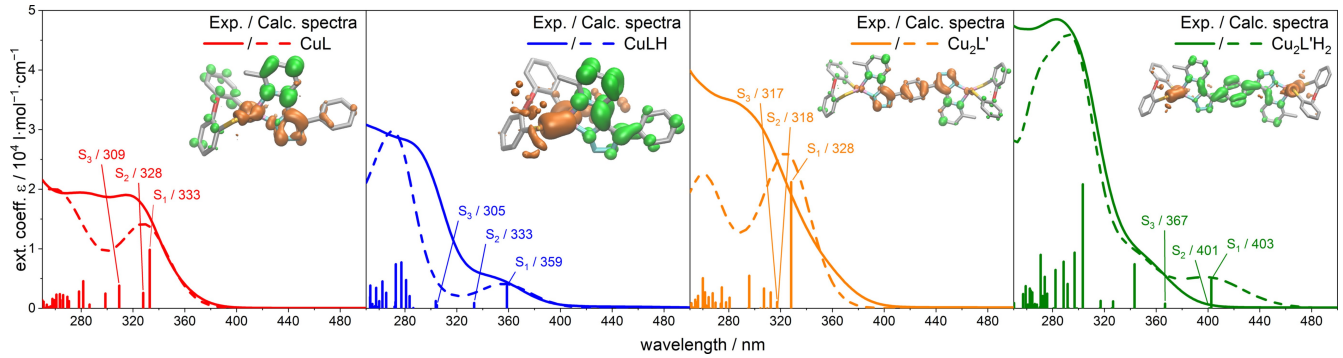

Figure 4. Comparison of static UV/Vis absorption spectra of **CuL**, **CuLH**, **Cu$_2$L'** and **Cu$_2$L'H$_2$** in DCM (solid lines) and calculated vertical transitions (dashed lines, PBE0/ev*GW*-BSE/def2-TZVP, Gaussian convolution with FWHM = 1500 cm^{-1}). The transition densities of the respective S_1 states are plotted with the isovalue of $\pm 0.0015 a_0^{-3}$, where green represents a gain and orange a loss of electron density. Corresponding natural transition orbitals are depicted in Figure SI-78.

© 2021 The Authors. Chemistry - A European Journal published by Wiley-VCH GmbH

15213765, 2021, 61, Downloaded from https://chemistry-europe.onlinelibrary.wiley.com/doi/10.1002/chem.202102760, Wiley Online Library on [03/02/2025]. See the Terms and Conditions (https://onlinelibrary.wiley.com/terms-and-conditions) on Wiley Online Library for rules of use; OA articles are governed by the applicable Creative Commons License

Femtosecond UV/Vis transient absorption (fs-TA) in solution and solid phase

UV/Vis fs-TA experiments were performed with excitation at 350 nm. The results are shown in Figure 5 for DCM and in Figure SI-13 for solid neat film as early (a) and late (b) difference spectra, decay associated spectra (DAS) from global analysis according to Equation (3) (c), and absorbance transients with fit (d). In all samples a global, positive excited state absorption (ESA) appears within system-response, evolves on the ps-timescale and merges into a long-lived-state (with lifetime $\gg$1ns) absorption (A_0), identified as triplet state (T_1), which is further characterized by step-scan FTIR, TCSPC and τ-PD in the following chapters. The very similar A_4, with $\tau_4 \approx 1$–2 ns, is only shown for completeness and not assigned to a specific photophysical relaxation process. Inspection of the DAS and related time constants (see Table 2) shows that - besides specific differences discussed below - in all samples the overall spectro-temporal evolution is quite similar and well described by (similar) three processes. For the reasoning of their assignment we resort in the following to the very much resembling results on the chemically akin neutral mononuclear system [(DPEPhos)Cu(PyrTet)],[8b] featuring a tetrazole- instead of phenyltriazol-unit and a pyridyl- instead of a sterically demanding methylpyridyl-substituent. This chemical similarity is given accordingly for the mononuclear subunits of the dinuclear **Cu_2L'** and **$Cu_2L'H_2$**.

(i) For the sub-ps dynamics (A_1) neither phase-state (solution vs. film) nor charge effects are observed. This strongly suggests

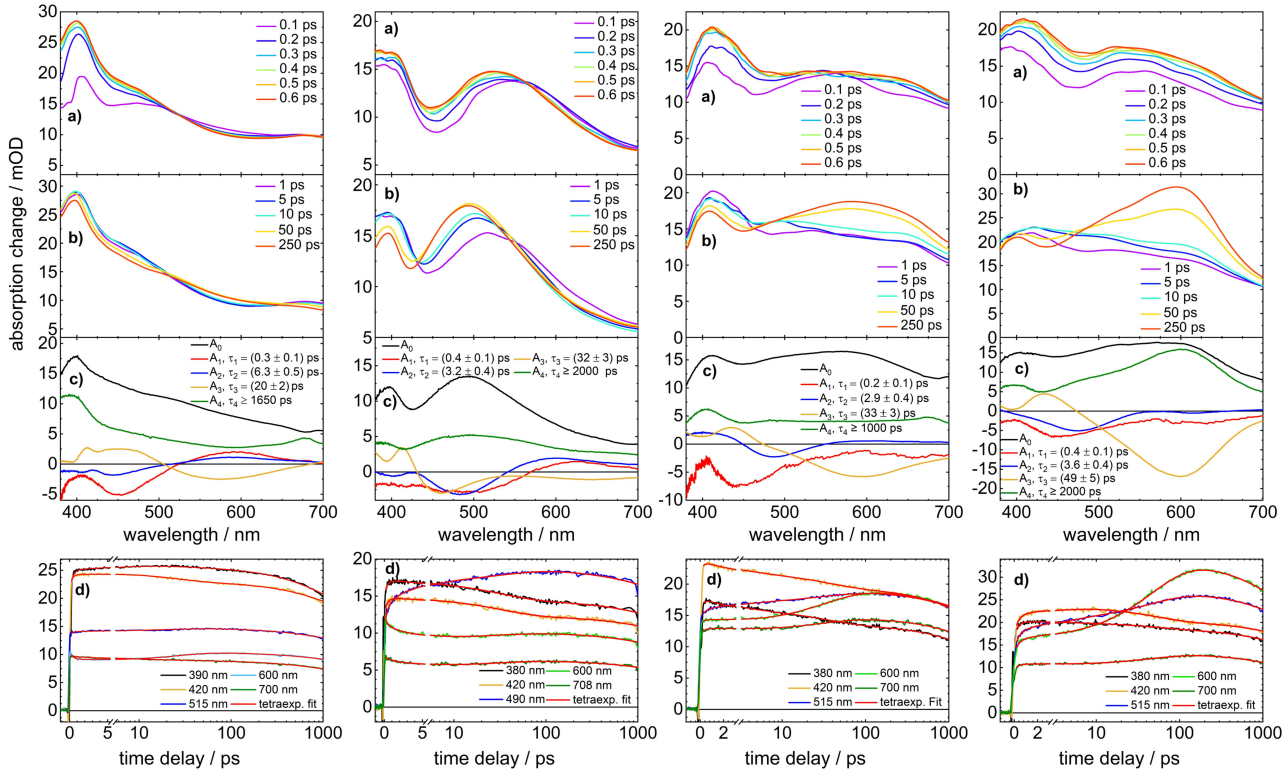

Figure 5. UV/Vis fs transient absorption of **CuL** (far left), **CuLH** (left), **Cu_2L'** (right) and **$Cu_2L'H_2$** (far right) in DCM. Excitation at 350 nm. (a) Sub-ps difference spectra; (b) 1–250 ps difference spectra; (c) DAS; (d) Absorbance transients at specific wavelengths with tetraexponential fit. Data in (a) and (b) are smoothed via 10-point FFT-filter.

Table 2. Static absorption properties and excited state dynamics, obtained by ultrafast spectroscopy of **CuL**, **CuLH**, **Cu_2L'** and **$Cu_2L'H_2$** in solution and film, and of **$[CuLH]^+$**, **$[Cu_2L'H]^+$** and **$[Cu_2L'H_2]^{2+}(PF_6)^-$** in gas phase, at $\lambda_{pump} = 350$ nm.

Complex	ext. coeff. in CH_2Cl_2 at 350 nm/10^3 $M^{-1}cm^{-1}$	CH_2Cl_2 solution/ps gas phase/ps				neat film/ps			
		τ_1	τ_2	τ_3	τ_4	τ_1	τ_2	τ_3	τ_4
CuL	6.9 ± 0.3	0.3 ± 0.1	6.3 ± 0.5	20 ± 2	≥1650	0.10 ± 0.06	3.2 ± 0.5	20 ± 3	≥300
CuLH	4.3 ± 0.8	0.4 ± 0.1	3.2 ± 0.4	32 ± 3	≥2000	0.2 ± 0.1	6.5 ± 0.7	48 ± 5	≥650
$[CuLH]^+$	–	0.7 ± 0.1	–	–	>800	–	–	–	–
Cu_2L'	10.5 ± 0.7	0.2 ± 0.1	2.9 ± 0.4	33 ± 3	≥1000	0.2 ± 0.1	4 ± 1	25 ± 4	≥600
$Cu_2L'H_2$	9.1 ± 1.4[a]	0.4 ± 0.1	3.6 ± 0.4	49 ± 5	≥2000	–	–	–	–
$[Cu_2L'H]^+$[b]	–	<0.1	7.2 ± 0.7	–	>800	–	–	–	–
$[Cu_2L'H_2]^{2+}$ $(PF_6)^-$	–	0.26 ± 0.03	6.0 ± 0.4	–	>800	–	–	–	–

[a] refinement with respect to Bizzarri et al.[14] [b] species observed as deprotonation product in gas phase from **$[Cu_2L'H_2]^{2+}$**.

© 2021 The Authors. Chemistry - A European Journal published by Wiley-VCH GmbH

15213765, 2021, 61, Downloaded from https://chemistry-europe.onlinelibrary.wiley.com/doi/10.1002/chem.202102760, Wiley Online Library on [03/02/2025]. See the Terms and Conditions (https://onlinelibrary.wiley.com/terms-and-conditions) on Wiley Online Library for rules of use; OA articles are governed by the applicable Creative Commons License

Table 3. Photophysical properties of the long-lived excited states of **CuL**, **Cu_2L'**, **CuLH** and **$Cu_2L'H_2$**.

Complex	λ_{em} / nm			τ_{em} / µs			τ/ µs (amplitude)	Φ/%
	CH_2Cl_2/Ar	KBr, 290 K	KBr, 10 K	CH_2Cl_2/Ar	KBr, 290 K[a]	KBr, 5 K[a]	gas phase	CH_2Cl_2/Ar
CuL	555	520	516	1.8	12	203	–	7
CuLH	554[14]	500	507	0.9[14]	20	234	2 (55%) 18 (45%)	5[14]
Cu_2L'	564	519	511	2.9	44	64	–	10
$Cu_2L'H_2$	556[14]	519	536	2.8[14]	9.4	225	–	14[14]

[a] Given values are average lifetimes τ_{av}.

a relaxation process, which is not significantly influenced by the molecular environment. Thus, A_1 ($\tau_1 \approx 0.3$ ps) is assigned to Franck-Condon (FC) state dynamics via intramolecular vibrational relaxation or internal conversion.

(ii) For [(DPEPhos)Cu(PyrTet)],[8b] A_2 (τ_2) has been associated with flattening distortion (FD of ca. 40°), accompanied by vibrational relaxation respectively cooling on the same, early ps-timescale. This was based on mid-IR fs-TA and UV/Vis anisotropy experiments (directly measuring the viscosity dependent angular evolution of the corresponding transition dipole moments), a pronounced spectral difference between solution and solid film (significantly hindered FD in the latter), as well as TDDFT calculations.

In fact, our TDDFT calculations predict for both mononuclear complexes FD in the relaxed S_1 state (Tables 4 and SI-9), the small magnitude of which can be related to the sterically demanding methyl group.[29] Note that for [(DPEPhos)Cu(PyrTet)] in solution, FD has been associated with a spectral blue-shift of the ESA on the early ps-timescale.[8b] We do not observe such a blue-shift for the four complexes, possibly due to their small FD as compared to [(DPEPhos)Cu(PyrTet)]).

Further, mid-IR investigations on [(DPEPhos)Cu(PyrTet)] revealed characteristics of vibrational cooling (VC) on the same time scale, suggesting the same process for the four complexes. Thus, based on phase state characteristics (see below) of **CuL**, **CuLH** and **Cu_2L'**, as well as TDDFT calculations on the monomers and the reports on [(DPEPhos)Cu(PyrTet)] we assign A_2 ($\tau_2 \approx 3$–6 ps) to FD in solution in combination with VC.

Table 4. Calculated dihedral angles [°] between the planes defined by P–Cu–P and N–Cu–N (DFT/B3LYP-D3(BJ)/def2-TZVP). Flattening angles compared to the S_0 state are given in brackets, with the angles of both Cu moieties for **Cu_2L'** and **$Cu_2L'H_2$**. For the T_1 states of these dinuclear systems both the symmetric and the asymmetric structures are listed, including the relative energies.

Complex	S_0 (B3LYP)	T_1 (TDDFT/B3LYP)	T_1 (UDFT/B3LYP)	S_1 (TDDFT/B3LYP)
CuL	90.6	89.9 (-0.7)	89.9 (−0.7)	73.7 (−16.9)
CuLH	92.8	84.2 (-8.6)	81.0 (−11.8)	80.3 (−12.5)
Cu_2L'	89.6	–	91.7/91.7 (2.1/2.1) (sym., 0 kJ/mol) 78.3/90.2 (−11.3/0.6) (asym., 30.9 kJ/mol)	–
$Cu_2L'H_2$	91.3	–	92.5/81.5 (1.2/−9.8) (asym., 0 kJ/mol) 89.9/89.9 (−0.4/−0.4) (sym., 19.7 kJ/mol)	–

Considering the similarity of all four A_2, this assignment holds equally for both monomers and dimers.

The rigidity of the solid state counteracts large amplitude distortions[30] and changes VC characteristics, reflected by the altered A_2. Due to the comparatively small FD amplitude predicted for **CuL** and **CuLH** in S_1, FD (or its onset) may occur in solid state as well, however, in different extent compared to solution.

(iii) A_3 ($\tau_3 \approx 20$–50 ps) describes the formation of a long-lived excited state, which is reasonable for triplet states. Experimental[8a] and theoretical[31] studies on [(DPEPhos)Cu(PyrTet)] made an unambiguous assignment of ISC to this time scale. Furthermore, the similarity of A_3 in the dynamics of the neutral [(DPEPhos)Cu(PyrTet)][8b] with those of the four complexes (in particular of the neutral **CuL**) is obvious. Thus, based on the formation of a long-lived state with τ_3 and literature reports on the very similar complex [(DPEPhos)Cu(PyrTet)], A_3 (τ_3) is assigned to ISC for the four complexes. However, ultrafast ISC on the sub-ps timescale as suggested by a theoretical investigation cannot be excluded.[32] Influences of charge and nuclearity are discussed below.

Although charge, nuclearity and phase are not observed to alter the spectro-temporal evolution (and thus the described processes) dramatically, they do lead to variations that are discussed in context with the respective processes in the following.

(i) The only (small) differences of A_1 in all samples concern negative or positive sign above ca. 550 nm. Among the solution samples, the dinuclear systems show negative, the mononuclear systems positive sign. All solid samples show positive sign, irrespective of being mono- or dinuclear, charged or neutral. Thus, FC-relaxation appears basically unchanged with respect to charge, nuclearity and phase, with phase possibly having the strongest impact.

(ii) The TDDFT calculations predict the strongest (but small) FD for **CuL** in the relaxed S_1 (−16.9°, Table 4) and, interestingly, its complete reversal in the relaxed T_1 (−0.7°). At first sight, the results of *GW*/BSE calculations of the ground state, predicting predominantly $\pi\pi^*$ character for S_1 excitation (Figure 4, Table SI-13), appear contradictory to the occurrence of FD (requiring MLCT). However, one can expect that small structural fluctuations may alter the electronic transitions significantly (see S_0 and S_1 geometries in Table SI-13), thereby changing the

 © 2021 The Authors. Chemistry - A European Journal published by Wiley-VCH GmbH

15213765, 2021, 61, Downloaded from https://chemistry-europe.onlinelibrary.wiley.com/doi/10.1002/chem.202102760, Wiley Online Library on [03/02/2025]. See the Terms and Conditions (https://onlinelibrary.wiley.com/terms-and-conditions) on Wiley Online Library for rules of use; OA articles are governed by the applicable Creative Commons License

character from predominantly ππ* to predominantly MLCT,[33] enabling FD and its reversal with ISC. For **CuL** the strong influence of the molecular structure on the electronic states is also exemplified by TDDFT calculations on the triplet manifold, where small alterations of the FD angle converge to three energetically close-lying structures (within 16 kJ/mol, Table SI-19), with either ππ* or MLCT character (Figure SI-89 and SI-91). In contrast, for **CuLH** only one structural minimum (with clear MLCT character, see Figure SI-93, Table SI-13) was identified.

The result of the TDDFT calculations on **CuL** (FD and its reversal, Table 4) correlates well with the nearly mirror-image of A_2 and A_3, solely observed for **CuL** among all solution samples. For the neutral system the reversal of FD could reflect a formally (partial) reduction from Cu(II) to Cu(I) in the excited MLCT state (charge backdonation). In contrast, the protonated ligands of **CuLH** and **$Cu_2L'H_2$** are more electronegative and thus they are less prone to backdonate (stabilizing MLCT character). In agreement, the CV data show a lower oxidation potential for the neutral complexes, since the negatively charged ligand stabilizes the oxidized Cu atom (Cu(II)) by a charge donation (see Electrochemical properties) - already without a MLCT-induced additional ligand-centered negative charge. This is the case for **CuL**.

For the dinuclear **Cu_2L'**, a comparable process is not suggested by fs-TA data. Due to the difficulties with optimizing S_1 structures of the dinuclear complexes at the TDDFT level (see Quantum chemical calculations), theoretical predictions must be taken with care. For the dinuclear complexes, LC (**Cu_2L'**) or MLCT (**$Cu_2L'H_2$**) vertical transitions are predicted (*GW*/BSE level, see Supporting Information chapter 13) and thus a clear effect on occurrence of FD is expected, in addition to altered relaxations pathways in general. Interestingly, despite the different predicted transitions, the fs-TA measurements revealed nearly identical spectra (Figure 5) in solution. This astonishingly high similarity strongly suggests that the same electronic relaxation processes take place in both dimers (neutral and charged) in solution, independent of the predicted LC (**Cu_2L'**) and MLCT (**$Cu_2L'H_2$**) excitation. Hence, due to the very floppy character of the dimers and the high similarity of the fs-TA data we assume that different structures are present in equilibrium in solution in a quite similar ratio for both dimers. The general structural flexibility of the dimers seems to be reflected by the phase dependencies observed for **Cu_2L'**.

(iii) ISC (τ_3) appears to be slower in the dinuclear systems (when systems with same charge are compared) for both solution and solid phase, possibly owed to conjugation expansion[34] in the dinuclear systems. In addition, the charged systems show a slightly slower ISC (when systems with same nuclearity are compared), for both solution and solid phase. The reason is possibly a reduced influence of spin-orbit coupling on ISC, due to a more efficient separation of the electron from the copper atom, which seems conceivable when taking solely the electrostatic properties of the nitrogen-ligand into account. Further support for the significant participation of the copper atom on ISC is given by TDDFT calculations (on the monomers). In the S_1-state both monomers reveal FD which persists in the triplet state solely for the charged monomer and not for the neutral one (reversal FD). This implies an effective reduction of Cu(II) to Cu(I) in the neutral system. Consequently, the stronger influence of the copper atom on ISC seems evident for the neutral systems.

Femtosecond transient photodissociation (τ-PD) in gas phase

UV pump-NIR probe τ-PD spectroscopy[35] was conducted on the isolated ionic complexes **$[CuLH]^+$**, **$[Cu_2L'H]^+$** and **$[Cu_2L'H_2]^{2+}(PF_6)^-$** in an ion trap mass spectrometer (with time delays up to 800 ps and the pump wavelength set to 350 nm), whereas the probe wavelength was fixed at 1200 nm for multiphoton excitation and fragmentation. An important prerequisite for obtaining transients by this method, however, is that the interrogation by the probe pulse should lead to different fragmentation efficiencies (or different fragment species) for the primary electronically excited state in comparison to the subsequently reached states, which are produced by (electronic) relaxation processes, for example IC or ISC.[35b,36] Characteristic transients of the three species for a maximum time delay of 180 ps are displayed in Figure 6, kinetic fit results are given in Table 2. Additionally, transients for different maximum time delays are presented in Figures SI-14–SI-21.

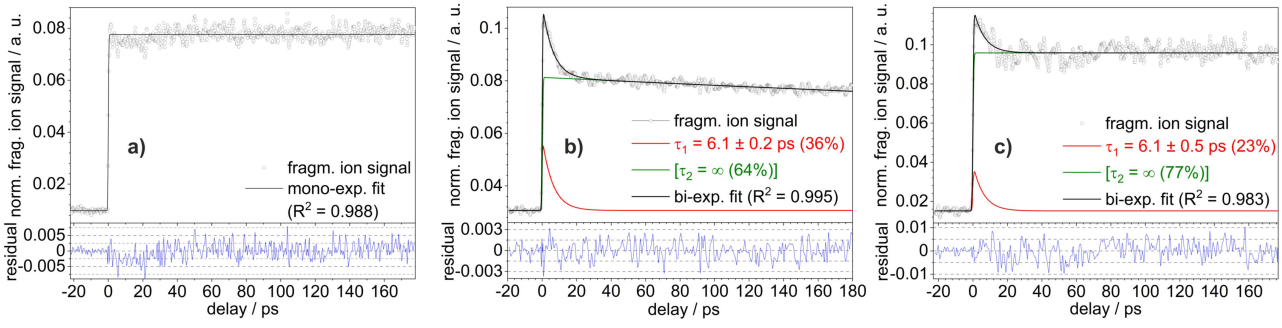

Figure 6. Normalized transient fragmentation ion intensity of a) **$[CuLH]^+$**, b) **$[Cu_2L'H]^+$** and c) **$[Cu_2L'H_2]^{2+}(PF_6)^-$** for a 200 ps time delay window with λ_{pump} = 350 nm at 0.3 μJ and λ_{probe} = 1200 nm at 130 μJ.

© 2021 The Authors. Chemistry - A European Journal published by Wiley-VCH GmbH

15213765, 2021, 61, Downloaded from https://chemistry-europe.onlinelibrary.wiley.com/doi/10.1002/chem.202102760, Wiley Online Library on [03/02/2025]. See the Terms and Conditions (https://onlinelibrary.wiley.com/terms-and-conditions) on Wiley Online Library for rules of use; OA articles are governed by the applicable Creative Commons License

The τ-PD data on $[CuLH]^+$ (Figure 6, a) show after photoexcitation mainly the fast population of a long-living excited state (>800 ps). A closer look in the 10 ps and 2 ps time delay windows (Figure SI-14) reveals possibly low-frequency wave packet modulations (with an oscillation period of ca. 1 ps, associated with a frequency of ca. 30 cm^{-1}). The τ-PD trace was fitted so that the amplitude of the chosen function was adjusted with a damped sine curve in order to fit the oscillatory behavior. The resulting damping time constant (0.7 ± 0.1 ps), which, however, can only be estimated with large uncertainty, correlates with the fast time constants found in solution (0.4 ps) and in film (0.2 ps; Table 2). The according wavepacket motion could relate to some low-frequency large amplitude relaxation, for example flattening distortion (FD), which was recently observed by optical and X-ray spectroscopy in solution for copper phenanthroline complexes to dephase in the sub-ps regime, but showing higher vibrational frequencies than observed here.[21a,37] For the related [(DPEPhos)Cu(PyrTet)] complex FD was found on a longer time scale of a few ps.[8b] However, no additional time constants were found here in gas phase in longer 1–50 ps time delay windows. A possibility, which we cannot completely exclude, is that intermediate time constants (as observed in TA solution dynamics, see above) relate to states with low contrast in probe amplitude and elude our τ-PD analysis technique (see discussion above). However, since we have no further indications for such an assumption, we conclude that in gas phase a very fast decay of the primary excited state (presumably by FD/IVR/ISC) is followed up by population of a long-living state (possibly of triplet character), which points, upon comparison of the related solution dynamics by TA, towards a strong acceleration of ISC rate in gas phase. A similar behavior was recently observed for the photodynamics of the dinuclear platinum metal complex $[Pt_2(pop)_4H_2]^{2-}$ ($pop = P_2H_5O_2^{2-}$) in gas phase[38] and discussed in terms of closing the "dissipation-to-solvent" channel and the increase of ligand backbone flexibility, both of which should increase the ISC rate in gas phase.

The transient photodissociation data of $[Cu_2L'H]^+$ (Figure 6b) exhibit a very short time constant (<0.1 ps) and an intermediate time constant (~6 ps) leading again towards a long-living state. These data agree acceptably with time constants from transient absorption (TA) measurements for $[Cu_2L'H_2]^{2+}$ obtained in solution (DCM) (0.4 ps and 3.6 ps), where additionally a third time constant of ~49 ps was found and assigned to ISC in comparison to former results on structurally similar copper complexes (see above).[8b] In gas phase we would assign tentatively the sub-ps time constant to IVR (possibly also FD) and the ~6 ps time constant to ISC, clearly slower than in the monomeric complex $[CuLH]^+$, which could also result from increased conjugation of the dimer.[34] Moreover, the τ-PD measurements implicate (also in agreement with the TA results from condensed phase dynamics) that a longer-living excited state (>800 ps) exists. Its long intrinsic lifetime was obtained by a new ns pump/fs probe setup and gave a decay in the μs regime (see Microsecond transient photodissociation (τ-PD) in gas phase).

Finally, the transient photodissociation data of $[Cu_2L'H_2]^{2+}(PF_6)^-$ (Figure 6c) reveal a very similar dynamical behavior as the just presented deprotonated $[Cu_2L'H]^+$ species. From the fitting analysis of the τ-PD transients we obtain again a fast sub-ps time constant (0.26 ps) and an intermediate constant (6.0 ps). Eventually a long-living state is formed which decays only in the μs regime. Thus, here also agreement with the first two time constants from solution dynamics is observed. However, also here we would assign a clear acceleration of ISC, although it is slower than for the monomeric complex $[CuLH]^+$.

In summary, all three ionic species show in gas phase the fast population of a long-living state, presumably a triplet state, consistent with the overall observations of dynamics in condensed phase. The intermediate dynamics (in the few ps and few tens of ps regime) obtained in solution are hardly observed in the gas phase. Only a time constant of ~6–7 ps was revealed for the dinuclear species. So, we conclude that i) solvent relaxation (and energy transfer to solvent) is involved in these ps processes and ii) ISC dynamics are strongly accelerated in gas phase for all species, where the ISC rate seems to be slower for the dinuclear ($[Cu_2L'H]^+$, $[Cu_2L'H_2]^{2+}(PF_6)^-$) vs. the mononuclear ($[CuLH]^+$) complexes. The same qualitative dependence on nuclearity was found for the condensed phase ultrafast dynamics.

Excited state dynamics on the nano- and microsecond time scale

Luminescence in solution and solid phase

As ultrafast spectroscopy evidenced long-lived excited states with lifetimes of nanoseconds or longer, static and time-resolved luminescence spectroscopy was applied to analyze potential emissions. Indeed, all four complexes show luminescence in the solid state (KBr matrix, neat film) and in solution (CH_2Cl_2) after UV excitation. Broad emission bands centered at 555–500 nm are observed, depending on the complex and the medium (Table 3), which are common values for Cu(I) complexes with emissive MLCT states.[1c,5,14,16b] The emission maxima in CH_2Cl_2 (Figure SI-28, Table 3) are red-shifted by up to 64 nm compared to the solid state (KBr matrix) luminescence (Figure SI-29, Table 3), which may be explained by a more efficient structural relaxation in the electronically excited state in the liquid phase (see also respective discussion on FD in solution vs. solid media in the fs-TA section).[12a,30] At the same time, the emission maxima in solution are almost unaffected by the charge and the nuclearity of the complexes. However, the impact is much larger in the solid state (KBr matrix) with, for example the emission maximum of **CuLH** being blue-shifted by 19 nm and 29 nm as compared to $Cu_2L'H_2$ at 290 K and 10 K, respectively (see below and Table 3). Similar results were obtained in the solid phase by probing neat films (Figure SI-30), so that the influence of KBr is insignificant here.

The effects of charge and nuclearity on the luminescence energy (via the respective emission maxima) can be considered

© 2021 The Authors. Chemistry - A European Journal published by Wiley-VCH GmbH

15213765, 2021, 61, Downloaded from https://chemistry-europe.onlinelibrary.wiley.com/doi/10.1002/chem.202102760, Wiley Online Library on [03/02/2025]. See the Terms and Conditions (https://onlinelibrary.wiley.com/terms-and-conditions) on Wiley Online Library for rules of use; OA articles are governed by the applicable Creative Commons License

in the sense of two body cooperativity[39] by applying the following Equation (1):

$$\Delta E_{coop} = E(Cu_2L'H_2) - E(Cu_2L') - 2\,(E(CuLH) - E(CuL)) \quad (1)$$

Interestingly, the values for ΔE_{coop} are not equal to zero in all the studied media and amount to absolute values of up to 1600 cm^{-1} in the solid state at 10 K (see below), which is a contribution of 8% (Table SI-4). The ΔE_{coop} values in the solid phase are throughout negative, while positive numbers are obtained in CH_2Cl_2. This means that the effects of charge and nuclearity on the emission properties are not additive, indicating negative (solid state) and positive (CH_2Cl_2) cooperative effects, respectively. The magnitude of the observed luminescence shifts is of the order or even larger than the effects obtained, for example experimentally for dinuclear iridium, palladium and platinum containing transition metal complexes with (2-dimethylamino)-4-(2-pyrimidinyl)pyrimidine ligands.[39b]

The photoluminescence quantum yield amounts to 5–14% in deaerated CH_2Cl_2 with a luminescence decaying monoexponentially with a lifetime of $\tau = 0.9$–2.9 µs (Table 3). In general, these values are quite high compared to related Cu(I) complexes,[5,8c,40] which directly correlates with the throughout small flattening angles in the excited state (Tables 4 and SI-9, see also fs-TA and step-scan FTIR spectroscopy). It is important to mention that in CH_2Cl_2 the lifetimes of the dinuclear systems are longer than those of the mononuclear analogues, paralleled by higher photoluminescence quantum yields. In the solid state, the emission shows a bi- or triexponential decay with an increased average lifetime of $\tau_{av} = 9.4$–44 µs (290 K) compared to the monoexponential decay constants in solution (Table 3). This increase from the liquid to the solid phase may be explained by the absence of non-radiative deactivation channels via solvent molecules in the KBr matrix and the smaller excited state distortions in the more rigid medium further slowing down non-radiative deactivations.[12a,30] The average decay constant τ_{av} was calculated by considering the time constants τ_1, τ_2 (and τ_3) with their relative contributions (Eq. (4)), where one should be aware that τ_{av} is appropriate to discuss relative trends, but cannot be directly assigned to one specific excited state. In detail, the emission decay in the solid state is composed of two dominating (≥80% in total) long-lived components of several microseconds (up to 94 µs in KBr at 290 K, Table SI-5). The bi- or triexponential decay in the solid state might result from contributions of energetically higher substates or different microenvironments (e.g. distance to counter ions, packing effects, solvent molecules in the crystal lattice) in the solid sample. Considering the literature reports on related Cu(I) complexes, two separate long-lived triplet states are less likely due to a fast spin-lattice relaxation between the triplet sublevels at 290 K[16a,41] and at the same time a potential thermally activated delayed fluorescence mechanism (see below) does rather not involve two distinct excited triplet states, at least in the solid state.[13] This means that two different excited states in one molecule are improbable with respect to the literature. However, the biexponential decays on the microsecond time scale observed in the gas phase by transient photofragmentation rather indicate two different electronically excited (micro)states (see Femtosecond transient photodissociation in gas phase), so that this point can unfortunately not be fully answered by the applied time-resolved methods.

The above mentioned average emission lifetime of $\tau_{av} = 9.4$–44 µs at 290 K could be assigned either to phosphorescence or delayed fluorescence. In the literature many reports on Cu(I) complexes describe thermally activated delayed fluorescence (TADF) at room temperature by an efficient reverse intersystem crossing from the lowest excited triplet state to the lowest excited singlet level and subsequent delayed fluorescence to the electronic ground state.[5,16, 42] To achieve a deeper understanding for potential thermally activated deactivation processes, temperature-dependent static and time-resolved luminescence investigations were performed on KBr pellets. Cooling of KBr samples of the four complexes to 170 K/130 K red-shifts the static emission spectrum by 250–780 cm^{-1}, which is characteristic for the inhibition of a TADF mechanism at lower thermal energy and phosphorescence from the triplet state T_1 (Figures 7 and SI-31–SI-33). Surprisingly, this initial red-shift turns into a blue-shift of 210–720 cm^{-1} when the sample is

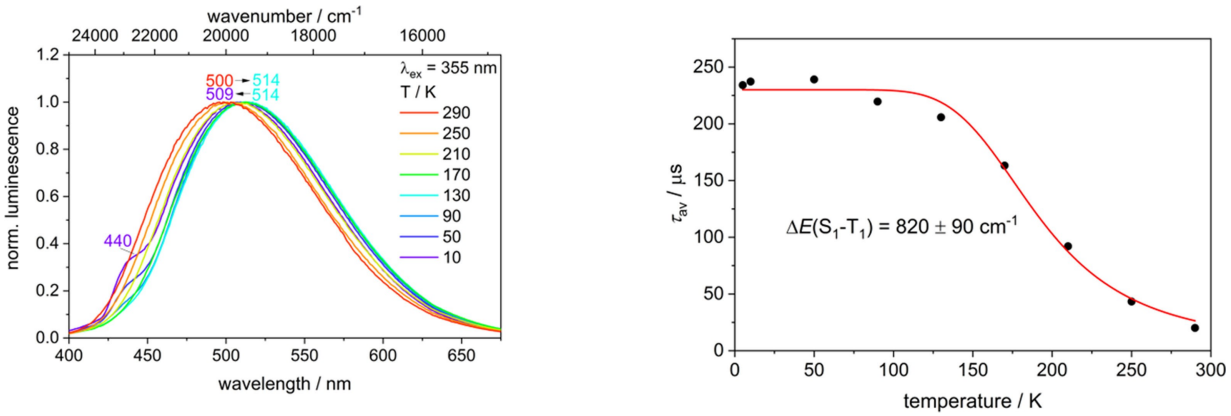

Figure 7. Static emission spectra of **CuLH** in a KBr matrix at 10–290 K (left). Average lifetime τ_{av} of **CuLH** at temperatures of 5–290 K (right).

© 2021 The Authors. Chemistry - A European Journal published by Wiley-VCH GmbH

15213765, 2021, 61, Downloaded from https://chemistry-europe.onlinelibrary.wiley.com/doi/10.1002/chem.202102760, Wiley Online Library on [03/02/2025]. See the Terms and Conditions (https://onlinelibrary.wiley.com/terms-and-conditions) on Wiley Online Library for rules of use; OA articles are governed by the applicable Creative Commons License

15213765, 2021, 61, Downloaded from https://chemistry-europe.onlinelibrary.wiley.com/doi/10.1002/chem.202102760, Wiley Online Library on [03/02/2025]. See the Terms and Conditions (https://onlinelibrary.wiley.com/terms-and-conditions) on Wiley Online Library for rules of use; OA articles are governed by the applicable Creative Commons License

further cooled down to 10 K. Hence, this indicates two opposite effects at low temperature. The blue-shift may result from an inhibited excited state relaxation at low temperature, which is termed as "rigidochromism" in the literature.[43] Indeed, this effect is typical for ^{3}MLCT states and is definitely conceivable for the emissive triplet states (see following section on temperature dependent luminescence lifetimes) of the four complexes.

The blue-shift may be smaller for **CuLH**/**$Cu_2L'H_2$** as a result of their higher intrinsic flexibility (see fs-TA in the condensed phase, step-scan FTIR spectroscopy and DFT calculations). Beside the described spectral shifts, pronounced shoulders appear at temperatures of $\leq$50 K, particularly for **CuL** (Figure SI-31). These shoulders are separated by approx. 1000 cm^{-1} and are assigned to a vibrational progression. Indeed, the measured FTIR ground state spectrum reveals several vibrations around 1000 cm^{-1} (Figure SI-43).

For a deeper elucidation of the radiative deactivation mechanisms, time-resolved luminescence studies were performed at temperatures down to 5 K. Interestingly, the average luminescence lifetime τ_{av} increases sharply between approximately 250–130 K by a factor of approx. 7–9 to values of τ_{av}= 203–234 μs (5 K) for **CuL**, **CuLH** and **$Cu_2L'H_2$** (Figures 7, SI-35 and SI-37). This should result from a significant contribution of thermally activated delayed fluorescence at room temperature and a steadily growing contribution of long-lived phosphorescence from the T_1 state at low temperature. Assuming that the S_1 and T_1 states are in thermal equilibrium, the following equation[16a] can be considered to get an estimation of the energy separation $\triangle E$ between the T_1 and S_1 states:

$$\tau(T) = \frac{3 + \exp(-\frac{\Delta E}{kT})}{\frac{3}{\tau(T_1)} + \frac{1}{\tau(S_1)}\exp(-\frac{\Delta E}{kT})} \quad (2)$$

where kT is the thermal energy, $\tau(S_1)$ and $\tau(T_1)$ are the intrinsic fluorescence and phosphorescence lifetimes and the factor 3 is introduced to consider three triplet substates. The experimental temperature-dependent trend of τ_{av} can be very well fitted with Equation (2) with energy barriers of 800–960 cm^{-1} for **CuL**, **CuLH** and **$Cu_2L'H_2$**. The observations for the temperature dependent evolution of the luminescence lifetimes and the deduced energy gaps ΔE (800–960 cm^{-1} according to Equation (2)) correlate with the spectral red-shifts (550–780 cm^{-1}) observed upon cooling from 290 K to 170/130 K (Table SI-6). The slightly lower values obtained from the static spectra should result from the blue-shift at low temperature. Overall, the experimental ΔE values are similar to the S_1–T_1 gaps of related complexes reported in the literature.[5] However, the experimental values are lower than those obtained by the DFT/PBE0 and DFT/B3LYP calculations for the mononuclear systems (Tables SI-11 and SI-18). Furthermore, the fit based on Equation (2) gives an approximation of the intrinsic S_1 and T_1 lifetimes $\tau(S_1)$ and $\tau(T_1)$ amounting to 40–170 ns and 180–230 μs, respectively (Table SI-5). Interestingly, $\tau(T_1)$ is slightly higher for the dinuclear system **$Cu_2L'H_2$** compared to the mononuclear analogue **CuLH**, in analogy to the lifetimes observed in CH_2Cl_2 solution (Table 3). This correlation might indicate pure phosphorescence in solution, which may result from increased S_1–T_1 energy gaps.

In contrast to the three systems **CuL**, **CuLH** and **$Cu_2L'H_2$** with strongly temperature dependent luminescence lifetimes, the average time constant of **Cu_2L'** only increases by approx. a factor of 1.5 with a high value of τ_{av} = 44 μs at 290 K (Table 3, Figure SI-36), so that Equation (2) is not applicable. This indicates efficient phosphorescence also at 290 K in the solid state and at most a small contribution of TADF. Hence, the photoluminescence behavior of **Cu_2L'** strongly differs from the emission properties of the other three complexes, which can also be understood as a kind of cooperative effect. The absence of (efficient) TADF also explains the very small spectral red-shift of only 250 cm^{-1} upon cooling, which does not necessarily result from a suppression of a TADF process.

Considering the full picture of the luminescence properties in the condensed phase, charge and nuclearity do not have a systematic influence on emission maxima and lifetimes (including intrinsic time constants). At the same time, it was observed that the effects are clearly not additive with respect to charge and nuclearity, so that they could be evaluated in the sense of two-body cooperativity. The most surprising point is that the temperature-dependent behavior is significantly different for **Cu_2L'**, which may be explained by an efficient phosphorescence combined with a very moderate reverse intersystem crossing at room temperature. In the next step, we move to the analysis of the long-lived electronically excited states in the gas phase to achieve further information on their intrinsic properties.

Microsecond transient photodissociation (τ-PD) in gas phase

In order to complement the luminescence lifetime data of the preceding paragraph, we evaluate now the intrinsic electronic lifetimes, i.e. lifetimes of the isolated chromophore units without interaction with solvent molecules, counter ions or matrix environment, on the microsecond time scale. This investigation serves to verify the assignment of electronic states, assess environmental influences and excludes processes like excimer or exciplex formation and can, naturally, only be achieved under gas phase conditions. Therefore we utilized an upgraded laser setup (see Experimental Section), where an additional ns kHz OPO laser was synchronized with the existing femtosecond laser system, it is now possible to perform excited state lifetime measurements by transient pump-probe photodissociation (τ-PD) for long-living states, for example triplets, employing (electronically scanned) time delays in the ns-ms regime.[44] This novel approach is of special interest for non-luminescent, isolated systems which can hardly be interrogated otherwise for their intrinsic lifetimes.

The complex cation **$[CuLH]^+$** was thus investigated by ns pump (350 nm)/fs probe (1200 nm) with a time resolution of ca. 50 ns and a time delay of up to 200 μs. The τ-PD result (Table 3) shows a biexponential decay for **$[CuLH]^+$** (~2 μs, ~18 μs) as displayed in Figure 8. Unfortunately, we could not study the **$[Cu_2L'H]^+$** and **$[Cu_2L'H_2]^{2+}(PF_6)^-$** complex using this technique due to too small ns pump/fs probe contrast signal. The lifetimes

 © 2021 The Authors. Chemistry - A European Journal published by Wiley-VCH GmbH

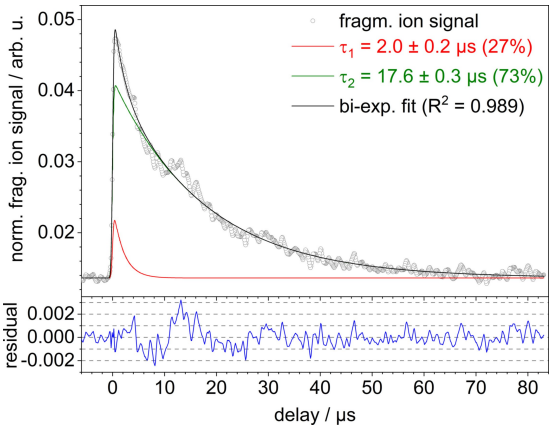

Figure 8. Normalized transient fragmentation ion intensity of **[CuLH]$^+$** for a 90 µs time delay window; ns pump (350 nm, 1 µJ) and fs probe (1200 nm, 130 µJ) experiment.

for **[CuLH]$^+$** are clearly longer than the results from DCM solution and correspond well to results obtained by TCSPC luminescence (**[CuLH](BF$_4$)**, 290 K, KBr matrix; Table 3) of 20 µs as recorded at the slightly longer excitation wavelength of 390 nm.

In summary, using a new ns/fs pump-probe τ-PD setup we were able to obtain the intrinsic µs lifetime of a photocatalytically active ionic species under isolated conditions in an ion trap mass spectrometer. The results give strong support for a long-lived excited state (triplet state), point towards significant quenching in DCM solution and relate relatively well to luminescence lifetimes in KBr matrix for **[CuLH]$^+$**.

Structural characterization of the long-lived excited states in solid phase by step-scan FTIR

Subsequent to the clear evidence of long-lived (microseconds) excited states in the time-resolved luminescence and photofragmentation (gas phase) studies, which are populated after UV excitation and femtosecond deactivation processes (see fs-TA spectroscopy in the condensed and gas phase), we conducted step-scan FTIR experiments to analyze the structures of the long-lived electronically excited states. The step-scan technique has previously been successfully applied to transition metal complexes,[45] including the structural characterization of di- and tetranuclear Cu(I) complexes.[46]

Prior to the step-scan FTIR investigations, ground state FTIR spectra of solid samples (KBr pellets) were recorded at 20 K and 290 K. The ground state FTIR spectra of the four compounds are very similar (Figure SI-42), as the differences mostly result from the absorption of the BF_4^- counterion at 1250–950 cm^{-1} (see IR spectrum of $NaBF_4$ in KBr as a reference for the anion, Figure SI-51) in case of the charged systems **CuLH** and **Cu$_2$L'H$_2$** (Figure SI-42). Furthermore, the ground state IR absorption is hardly influenced by temperature (Figures SI-43–SI-46). The experimental ground state spectra are in very good agreement with the calculated IR spectra (B3LYP-D3(BJ)/def2-TZVP), where one should be aware that the counter ions were not considered in the calculations for the protonated species (Figures 9, SI-47–SI-50). The theoretical spectra enabled the assignment of the different absorption bands to specific vibrations, which are for the most part delocalized (Tables SI-7 and SI-8).

The samples were then excited with a 355 nm UV laser pulse at 20 K and 290 K to measure step-scan difference spectra (Figures SI-52–SI-59) and thus analyze small but nevertheless significant vibrational changes in the solid medium. In these difference spectra, averaged over the first microsecond after laser excitation, the peaks pointing in negative direction are almost identical to the corresponding vibrations in the electronic ground state and result from the depopulation of the electronic ground state. At the same time, the peaks pointing in positive direction are assigned to the populated long-lived electronically excited states. It should be mentioned here that the difference spectra show a compound specific positive offset of unclear origin, so that also the Δabsorbance values of the negative peaks are mostly positive. For this reason, no reliable excited state lifetimes could be extracted from the step-scan data in this particular case. Nevertheless, it is obvious from the transient FTIR data that the complexes show lifetimes of at least several microseconds at 290 K and 20 K in the solid state, in full agreement with the time-resolved luminescence experiments in solid phase (see also microsecond τ-PD). This underlines that the lowest excited triplet state is probed in the step-scan FTIR experiments. Note that also at 290 K with occurrence of a TADF mechanism mainly the lowest triplet state T_1 should contribute

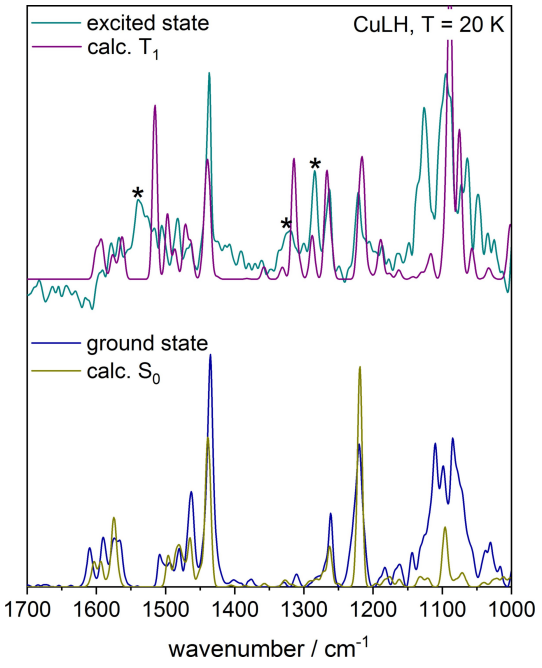

Figure 9. Excited state IR spectrum (1.0% of the ground state spectrum added to the step-scan difference spectrum) and calculated T_1 spectrum of **CuLH** (top). Static FTIR ground state spectrum (KBr pellet, 20 K) and calculated S_0 spectrum of **CuLH** (bottom). Calculations: (TD-)DFT/B3LYP-D3(BJ)/def2-TZVP, scaled by 0.975, FWHM = 8 cm^{-1}, Gaussian profile. The bands marked with asterisks are discussed in the text.

© 2021 The Authors. Chemistry - A European Journal published by Wiley-VCH GmbH

15213765, 2021, 61, Downloaded from https://chemistry-europe.onlinelibrary.wiley.com/doi/10.1002/chem.202102760, Wiley Online Library on [03/02/2025]. See the Terms and Conditions (https://onlinelibrary.wiley.com/terms-and-conditions) on Wiley Online Library for rules of use; OA articles are governed by the applicable Creative Commons License

to the step-scan spectrum, as the intrinsic lifetime of the S_1 state is much shorter (see luminescence spectroscopy).

For a better direct comparison between the IR absorption in the electronic ground state and in the electronically excited state the pure excited state IR absorption spectra were generated by addition of 0.5–2.0% (depending on the sample and temperature) of the ground state spectrum to the step-scan difference spectrum to compensate the negative bands (Figures SI-60–SI-63). The low ground state contribution results from the small number of molecules in the pellet excited by each laser pulse. The obtained excited state IR spectra can then be directly compared to the corresponding ground state spectra, where it is observed that strong excited state specific peaks are observed for **CuLH** (Figure SI-60) and **$Cu_2L'H_2$** (Figure SI-63). The mentioned peaks are observed at wavenumbers where the IR absorption in the electronic ground state is much weaker or even completely absent. For instance, these bands are localized at 1539, 1320 and 1285 cm^{-1} for **CuLH** (see asterisks in Figure 9). Excited state specific features of similar intensity were obtained for **$Cu_2L'H_2$** (see asterisks in Figure SI-63), whereas the effects were weaker for **CuL** (Figure SI-61). This is a first indication for smaller geometrical distortions in the excited triplet state for **CuL** (see below). Beside the investigations in the KBr matrix, **$Cu_2L'H_2$** was measured as neat film with spectra very similar to those obtained in KBr, so that matrix effects are not relevant here (Figure SI-64).

Comparing the excited state IR spectra at 20 K with those recorded analogously at 290 K, it is observed that the effects are principally the same (Figures SI-60–SI-63). However, the excited state specific features are weaker at 290 K compared to 20 K, which may result from the coupling of vibrational modes in the region of approx. 1700–1000 cm^{-1} with thermally populated low frequency vibrations. These couplings induce vibrational broadening, so that the transient IR absorption features are then hard to probe experimentally.

For a more profound structural characterization of the excited triplet states of the mononuclear complexes **CuL** and **CuLH**, the experimental excited state IR spectra were directly compared to the theoretical T_1 spectra. Generally, the experimental spectra are in good agreement with the corresponding calculated spectra obtained by TDDFT and UDFT (B3LYP-D3(BJ)/def2-TZVP). Interestingly, the intense excited state specific features of **CuLH** observed experimentally are very well reproduced by theory (TDDFT). Hereby, it should be mentioned that all the TDDFT optimizations with different starting structures (e.g. with different dihedral angles) converged into the same minimum structure. Analogous results were obtained by calculating the triplet state as ground state (UDFT) (Figure SI-66). Similar statements hold for **CuL** with the main difference that there are no pronounced excited state specific features, as described above (Figures SI-61 and SI-65). Furthermore, an important point is that TDDFT yielded three energetically close-lying triplet states (within 16 kJ/mol, Table SI-19), so that corresponding harmonic frequency calculations could give an even better agreement between experiment and theory, which is however beyond the focus of this work.

The good agreement between the experimental and theoretical excited state IR spectra allowed a deeper analysis of the excited triplet geometries and the underlying electronic characters, especially with respect to the flattening distortion (FD) under consideration of the change of the calculated dihedral angle between the planes defined by P–Cu–P and N–Cu–N in the excited triplet state (Tables 4 and SI-9). In the case of **CuL**, the dihedral angle is almost identical in the ground state and in the T_1 state with values of 90.6° and 89.9°, respectively (considering (TD-)DFT/B3LYP, see also UDFT in Tables 4 and SI-9). This is confirmed by the large similarities between the ground and excited state spectra observed experimentally as well as the good correlation between the experimental and calculated T_1 spectra. A different situation is observed in the case of **CuLH**, with a significant FD of 8.6° from the ground state to the triplet state. This was confirmed experimentally by the strong changes in the excited state IR spectrum compared to the ground state, in accordance with the simulated S_0 and T_1 IR spectra. Hence, the protonation of the triazole ring leads to an increased flexibility and persistent FD of the complex (**CuLH** vs. **CuL**, see also fs-TA in the condensed phase), which is explained by the efficient oxidation of Cu(I) to Cu(II) (inducing FD) and transfer of electron density to the electronegative triazole ligand. The electronegative character of the protonated systems correlates with the higher redox potentials of **CuLH** and **$Cu_2L'H_2$** compared to their neutral analogues (Table 1). However, the observed FDs are throughout small compared to the much larger flattening angle of 40° for the related complex [(DPEPhos)Cu(PyrTet)][8b] and other mononuclear Cu(I) complexes.[5,47] For both mononuclear complexes, **CuLH** and **CuL**, the populated long-lived triplet state shows a significant MLCT contribution according to the differential electron and spin densities calculated by TDDFT and UDFT, respectively (Figures SI-88 and SI-89 for **CuL**; Figures SI-92 and SI-93 for **CuLH**, see also natural population analysis in Tables SI-12–SI-14). However, a ligand-centered $\pi\pi^*$ contribution dominates over the MLCT character for **CuL**, which should arise from the intrinsically negatively charged triazole ligand making a shift of electron density from the Cu center to the ligand less advantageous.

With respect to the dinuclear complexes, the experimental excited triplet IR spectra of **Cu_2L'** and in particular **$Cu_2L'H_2$** show significant differences compared to the ground state spectra indicating structural changes (Figures SI-62 and SI-63). At the same time, the excited state spectra of both complexes resemble each other, but are clearly not identical, which may result from distinct geometries even though their ultrafast dynamics are very similar (Figures SI-71 and SI-74) (see fs-TA in the condensed phase).

For the dinuclear complexes **$Cu_2L'H_2$** and **Cu_2L'** two different triplet minimum structures were obtained by UDFT with a symmetric and an asymmetric structure for each complex. In the symmetric triplet the FD is identical on each Cu subunit with very small changes compared to the electronic ground state of −0.4° and 2.1° for **$Cu_2L'H_2$** and **Cu_2L'**, respectively (Tables 4 and SI-9). The asymmetric triplets, for their part, show a much larger FD on one Cu subunit of −11.3° for **Cu_2L'** and

© 2021 The Authors. Chemistry - A European Journal published by Wiley-VCH GmbH

15213765, 2021, 61, Downloaded from https://chemistry-europe.onlinelibrary.wiley.com/doi/10.1002/chem.202102760, Wiley Online Library on [03/02/2025]. See the Terms and Conditions (https://onlinelibrary.wiley.com/terms-and-conditions) on Wiley Online Library for rules of use; OA articles are governed by the applicable Creative Commons License

15213765, 2021, 61, Downloaded from https://chemistry-europe.onlinelibrary.wiley.com/doi/10.1002/chem.202102760, Wiley Online Library on [03/02/2025]. See the Terms and Conditions (https://onlinelibrary.wiley.com/terms-and-conditions) on Wiley Online Library for rules of use; OA articles are governed by the applicable Creative Commons License

−9.8° for $Cu_2L'H_2$, whereas the other Cu center is mostly unaffected (Tables 4 and SI-9). Interestingly, the asymmetric triplet is energetically lower by 19.7 kJ/mol compared to the symmetric one for $Cu_2L'H_2$, while it is the other way around for **Cu_2L'** (+30.9 kJ/mol for the asymmetric triplet) (Table 4).

Comparing the corresponding calculated IR spectra of the described triplet states with the experimental IR spectra, it is observed that the spectrum of the asymmetric triplet state of $Cu_2L'H_2$ gives a good description of the excited state specific features observed by step-scan FTIR (Figure SI-68). The theoretical spectrum of the symmetric triplet state, however, shows three intense bands in the region of 1350–1420 cm^{-1}, which were not found experimentally. Nevertheless, as described in the introductory part on quantum chemical calculations, one should be aware of the very large conformational flexibility of the mononuclear systems, so that other triplet conformers may give an even better agreement with the experiment. Considering the currently available data set, the found asymmetric and energetically most stable triplet state with a local FD on one Cu unit is assigned to the experiment. As the spin density is mainly localized on one copper core, the pyridyl-triazole ligand and the phenyl bridge, the triplet state is of localized ^{3}MLCT character (Figure SI-103).

This discussion is less evident for the deprotonated complex **Cu_2L'**, where the calculated IR spectra of both triplet states (symmetric and asymmetric) are both in reasonable agreement with the experiment (Figure SI-67). For the symmetric and energetically lowest triplet state the strong calculated band at 1360 cm^{-1} is not obviously present in the measured excited state spectrum, but might contribute via a broad absorption to the particularly large offset in this region. Furthermore, it cannot be excluded that the very high calculated intensity of the band results partially from a methodical artefact. Finally, no unambiguous assignment of a calculated triplet state to the experiment is possible for **Cu_2L'** by considering solely the measured and calculated IR spectra. However, the symmetric triplet state being 30.9 kJ/mol lower in energy, it is conceivable that this one is finally populated. The spin density of this triplet state is mainly localized on the pyridyl-triazole ligand and the phenyl bridge, indicating a ππ* transition on the bridging ligand (Figure SI-98). The absence of a significant oxidation of a Cu center thus explains the small FD.

According to the experimental results at both 20 K (Figures SI-69–SI-70) and 290 K (Figures SI-72–SI-73), the excited state spectra of the dinuclear systems do not correspond to the sum of the spectra of the underlying mononuclear subunits, which can be attributed to a cooperative effect.

Summarizing the step-scan FTIR analysis, it should be said that the protonated mononuclear system clearly has a higher flexibility compared to the neutral one (consider FD angles, Tables 4 and SI-9) according to step-scan FTIR spectroscopy in combination with theory. Considering the dinuclear systems, it is concluded that the different triplet characters (^{3}MLCT for $Cu_2L'H_2$ and ππ* for **Cu_2L'**) and the resulting differing geometries (asymmetric for $Cu_2L'H_2$ and symmetric for **Cu_2L'**) would explain the discrepancies in the experimental excited state spectra.

Conclusion

Applying a broad range of physicochemical methods together with high-level quantum chemical calculations we here present a comprehensive photochemical and photophysical characterization of a set of closely related complexes, that build on the **CuL** unit with a methylpyridyl-triazole (MPyrT)/DPEPhos ligand system and differ in charge and nuclearity. Including condensed phase (solution and solid state, i.e. neat films and KBr matrix) as well as gas phase conditions, this concerted approach allows to explore - in a synoptic manner - the impact of a large variety of physical parameters on the molecular structure in the ground and electronically excited states, and their ultrafast and long-term dynamics by non-radiative and radiative, i.e. luminescent, deactivation.

In particular, our investigations demonstrate that a small variation (protonation/deprotonation) in the ligand sphere, going from the negatively charged MPyrT (in **CuL**) to the neutral one (in **CuLH**), leads to profound changes in the photochemistry and dynamics of the complexes. The mononuclear neutral **CuL** and cationic **CuLH** complexes exhibit (in part) strikingly different behavior with respect to **1)** their electrochemical reactivity (strong shift to lower oxidation potential for **CuL**), **2)** oxidative quenching, **3)** electronic absorption (red-shift of **CuL**), **4)** ultrafast dynamics (time constants and excited state spectra support flattening distortion (FD) relaxation in S_1 for **CuL** and **CuLH** but reversal of FD in T_1 for **CuL**) and **5)** long-lived electronically excited state vibrational and structural properties (small changes for **CuL** but strong changes for **CuLH** with respect to the IR spectra of S_0 and T_1 state). However, the condensed phase luminescence spectra and lifetimes are very similar for both mononuclear complexes supporting the formation of a long-lived triplet state, with further proof for its intrinsic nature by the gas phase dynamics results, and temperature characteristics of a TADF process.

This behavior is well supported and rationalized by electronic structure calculations at TDDFT, UDFT and G*W*-BSE (Bethe-Salpeter equation) level for ground (S_0) and excited states (S_1, T_1). Additionally, theory served to provide simulations for the absorption spectra of the investigated species in agreement with experimental results in gas and condensed phases and allowed for assignment of the relevant electronic transitions and vibrational modes.

It should be emphasized that the exploration and rationalization of such sensitivity on ligand-sphere modifications is highly important for applications, for example as OLEDs or photosensitizers, and should ultimately guide efficient compound optimization.

The interpretation of the results for the dimers **Cu_2L'** and $Cu_2L'H_2$, with the latter structure revealed here for the first time, turned out to be more challenging both from an experimental and a theoretical perspective. A difference in electrochemical reactivity is observed as for the mononuclear complexes, but their absorption spectra are very similar. Moreover, the ultrafast dynamics of the dinuclear **Cu_2L'** resemble very much those of $Cu_2L'H_2$, despite their different charge. Also, their luminescence spectra and lifetimes in solid state and solution are similar, but

 © 2021 The Authors. Chemistry - A European Journal published by Wiley-VCH GmbH

from the lifetimes-temperature dependence we assigned a TADF process to $Cu_2L'H_2$, whereas only a very moderate effect of thermal energy was observed for the deactivation in Cu_2L'. The latter shows lower RISC efficiency than the monomer **CuL**, where a more effective restriction of specific vibrations via intermolecular interactions in the solid state sample may take place, as discussed by Li et al. for closely related complexes.[48]

However, the dimers T_1 vibrational spectra show significant and distinct differences compared to the respective S_0 vibrational spectra, suggesting structural changes such as FD, yet with subtle structural differences comparing the two dimers. It is noted, that also significant differences are observed between the T_1 vibrational spectra of the mono- and the dinuclear systems. This implies that the coupling between the monomer-like units in the respective neutral or charged dinuclear system efficiently alters the (structural) dynamics observed in Cu_2L' and $Cu_2L'H_2$ in a non-additive manner to a certain extent. Interestingly, from the theoretical analysis the UDFT geometry optimizations of the T_1 states of the dinuclear complexes let us expect that they would rather behave in the same manner as their mononuclear counterparts. The calculated dihedral angles in the T_1 state show no FD for Cu_2L' but decent FD (ca. 10°) for $Cu_2L'H_2$ for the respective lowest energy structures. Thus, with respect to charge, FD is predicted by theory for the dinuclear systems in the same qualitative way as for the mononuclear ones. This was confirmed for $Cu_2L'H_2$ by considering the experimental and calculated T_1 spectra with the assignment of the asymmetric triplet structure (excitation on one monomeric unit) to the experiment. However, the same considerations for Cu_2L' do not allow an unambiguous conclusion on this issue with the current set of calculations. Thus, it is concluded that, at the present state, the calculations do not fully support the experimental results for the dinuclear systems. Reasons for this might be found in the coexistence of conformers of the dinuclear systems in solution, respectively neat film or KBr matrix, which might alter significantly kinetic relaxation rates and pathways (e.g. branching reactions to various T states), as well as excited electronic state energies. These factors are not taken into account by the current calculations.

To sum up, there is a limited and not so clear-cut influence of charge for the dimeric complexes and we have experimentally observed some results that point towards non-additive interaction between the **CuL** moieties. However, a cooperative interaction is difficult to ascertain at the current level of research. On the contrary, our theoretical analysis predicts symmetry and symmetry breaking for the electronically excited states of Cu_2L' and $Cu_2L'H_2$, respectively, where the former might point to some degree of cooperative interaction but reveals no structural change compared with the related monomer **CuL**.

Finally, we have presented here a class of four copper diimine complexes that allow for a unique study to investigate the interdependence of a great variety of photophysical and photochemical processes over nine orders of magnitude in time (scales) on both charge and nuclearity with a connection to application. We believe that the opportunities to explore the photochemistry of this compound class are not exhausted but rather offer possibilities to tackle important questions of current (inorganic) photochemistry, like symmetry breaking in the excited state,[49] design of efficient earth-abundant photosensitizers[50] and cooperative interactions in multimetallic complexes[15] in the future.

Experimental Section

Synthesis

Syntheses were performed according the literature.[14] Experimental details are given in the Supporting Information.

Crystal structure determinations

The single-crystal X-ray diffraction of $Cu_2L'H_2$ study was carried out on a *Bruker* D8 Venture diffractometer with PhotonII detector at 123(2) K using Cu–Kα radiation (λ = 1.54178 Å) or Mo–Kα radiation (λ = 0.71073 Å). Dual space methods (SHELXT)[51] were used for structure solution and refinement was carried out using SHELXL-2014 (full-matrix least-squares on F^2).[52] Hydrogen atoms were refined using a riding model. A semi-empirical absorption correction was applied. The central phenyl moiety and solvent molecules $CDCl_3$ were disordered (see cif-files for details). $Cu_2L'H_2$: colorless crystals, $C_{94}H_{74}CuN_8O_2P_4 \cdot 2\ BF_4 \cdot 8\ CDCl_3$, $M_r = 2735.18$, crystal size $0.22 \times 0.18 \times 0.14$ mm, monoclinic, space group *C*2/c (No. 15), $a = 44.0823(10)$ Å, $b = 10.6559(2)$ Å, $c = 31.5479(8)$ Å, $\beta = 125.145(1)°$, $V = 12117.6(5)$ Å^3, $Z = 4$, $\rho = 1.499$ Mg/m^{-3}, μ(Cu-K$_\alpha$) = 6.32 mm^{-1}, $F(000) = 5496$, $T = 123$ K, $2\theta_{max} = 144.6°$, 88283 reflections, of which 11937 were independent ($R_{int} = 0.036$), 740 parameters, 892 restraints (see cif-file for details), $R_1 = 0.092$ (for 10461 $I > 2\sigma(I)$), wR_2 = 0.272 (all data), $S = 1.03$, largest diff. peak / hole = 2.10 (in solvent $CDCl_3$) / −1.11 e Å^{-3}. Deposition Number 2084996 ($Cu_2L'H_2$) contains the supplementary crystallographic data for this paper. These data are provided free of charge by the joint Cambridge Crystallographic Data Centre and Fachinformationszentrum Karlsruhe Access Structures service.

Computational details

All quantum-chemical calculations in Karlsruhe were performed with the TURBOMOLE program package.[53] The resolution-of-the-identity (RI) approximation was used for all two-electron integrals. The equilibrium geometries were optimized at the PBE0-D3(BJ) level of theory,[26,54] and the electronic excitations were calculated at the CD-*evGW*(10)/BSE level of theory (eigenvalue-only self-consistent GW (*evGW*)[55] employing contour deformation (CD)[24c] for highest 10 occupied and lowest 10 unoccupied orbitals followed by the Bethe-Salpeter equation (BSE)[24a,b] approach). For further computational details see Supporting Information. The quantum-chemical calculations performed in Kaiserslautern were done as follows: the crystal structures were used as input structures. Geometry optimizations were performed with the Berny algorithm of Gaussian 09[56] by using energies and gradients computed by TURBOMOLE.[53a] All calculations were performed with the functional B3LYP with dispersion correction (no three-body interaction) (D3(BJ)).[26,54a]

Static spectroscopy

Static UV/Vis absorption spectra were recorded on *Jasco*-V670 and *Perkin Elmer* Lambda 900 spectrophotometers. Solutions were prepared in cuvettes of 1 or 10 mm optical path length. The spectra

 © 2021 The Authors. Chemistry - A European Journal published by Wiley-VCH GmbH

15213765, 2021, 61, Downloaded from https://chemistry-europe.onlinelibrary.wiley.com/doi/10.1002/chem.202102760, Wiley Online Library on [03/02/2025]. See the Terms and Conditions (https://onlinelibrary.wiley.com/terms-and-conditions) on Wiley Online Library for rules of use; OA articles are governed by the applicable Creative Commons License

of solid samples were recorded on single thin transparent films on CaF_2 substrate. Decadic extinction coefficients in DCM were determined via ground state absorption spectra at given concentration and optical path length. The presented extinction coefficients are averaged over the results achieved at both instruments, error bars corresponding to the absolute deviations.

Femtosecond transient absorption in solution and solid phase

The UV/Vis fs-TA pump-probe measurements were performed based on a Ti:Sa chirped pulse regenerative amplifier system (*Coherent* Libra, 120 fs pulse duration FWHM, 4 mJ/pulse at 800 nm, 1 kHz repetition rate). The excitation pulses with 240–380 nJ per pulse at 350 nm were generated by an optical parametric amplifier (*Light Conversion* TOPAS-Prime)) with focal width of ≈100 μm FWHM at sample position. The probe pulses (broad spectral continuum) were generated from weak pulses at 800 nm via self-phase-modulation in a moving CaF_2 window, with focal width of ≈40 μm at sample position. The probe pulses were spectrally dispersed and detected with an integrated 512-pixel PDA camera device (*Stresing*). For time delay (up to 1 ns) between pump and probe pulse, a delay stage (*Physik Instrumente, PI*) was used and each second pump pulse was blocked by a chopper to obtain pump-induced absorbance differences. Pump- and probe-pulse were superimposed in the sample with polarization in magic angle (54.7°) configuration. Time-zero at each probe-wavelength and system response time (260 fs) were obtained by pump-probe experiments in oxazin-4 or coumarine-152 dyes. For the solution experiments the complexes were dissolved in DCM (UVASOL grade), with an optical path length of 1 mm and optical density of 1 at the excitation wavelength (350 nm). Thin films of pure **CuL**, **CuLH** and **Cu_2L'** (not for **Cu_2L'H_2**, due to poor solubility) were obtained via spin-coating (*Ossila*, Spin Coater 3.0) from DCM-solutions with optical density of 0.35–0.47 at 350 nm and effectively doubling the OD by matching two films of each kind face-to-face. During measurements samples were rotated and moved perpendicular to the laser beam to provide fresh sample conditions. Static absorption spectra were taken before and after the fs-experiments to ensure sample integrity. All experiments were performed at room temperature. The pump-induced absorption difference data $\Delta A(t,\lambda)$ of the transient UV/VIS experiments were analyzed using the multiexponential global fit function

$$\Delta A(t,\lambda) = A_0(\lambda) + \sum_{i=1}^{N} A_i(\lambda)\cdot e^{-t/\tau_i} \quad (3)$$

with the decay-associated spectra (DAS) $A_i(\lambda)$, and the corresponding time constants τ_i, beginning at time delay of 200 fs.

Luminescence spectroscopy

Emission and excitation spectra in solution were recorded with a Fluoromax 4 from *Horiba Jobin.* All the solutions were air-free by letting Ar bubbling inside for 10 minutes at least. Lifetime experiments were performed by time-correlated single-photon counting method (TCSPC) with a DeltaTime kit for DeltaDiode source on FluoroMax systems, including DeltaHub and DeltaDiode controller. NanoLED 370 was used as the excitation source (λ = 366 nm). Static temperature dependent (20–290 K at the sample) emission spectra were recorded in the solid state with a FluoroMax-2 (Horiba Jobin-Yvon) spectrometer using a closed cycle helium cryostat (ARS Model DE-202 A). The cryo cooler was equipped with a copper pellet holder and CaF_2 windows. KBr pellets of the four complexes were prepared by mixing (1.5 mg for **CuL** and **CuLH**; 2.2 mg for **CuL'** and **CuL'H**) with dry KBr (ca. 200 mg, stored in a compartment dryer at 80 °C, purchased from Merck) and grinding to a homogeneous mixture. Neat films were prepared by spraying a solution of the compound in CH_2Cl_2 on a CaF_2 substrate (13 mm diameter, 1 mm thick), followed by evaporation of the solvent. The luminescence lifetimes were determined with the time-correlated single photon counting technique (TCSPC) at temperatures of 5–290 K with an analogous cryostat (*ColdEdge*, 101 J cryocooler). Data were recorded with a DeltaFlex (*Horiba Scientific*) spectrometer. The sample was excited with short light pulses of a SpectraLED (390 nm) and the emission monochromator was set to the corresponding emission maximum (λ_{max} = 500–541 nm). The emitted light was detected with a picosecond photon counting (PPT) detection module. In all the time-resolved luminescence experiments a long pass filter (475 nm or 500 nm) was mounted between the sample and the emission monochromator to prevent scattered excitation light from reaching the detector. Average lifetimes were calculated using the amplitude average lifetime, which is defined by

$$\tau_{av} = \sum_i a_i\tau_i \quad (4)$$

Step-scan FTIR spectroscopy

Step-scan FTIR experiments were performed with a *Bruker* Vertex 80v FTIR spectrometer, operated in the step-scan mode. Temperature dependent measurements were performed at 290 K and 20 K by the use of KBr pellets and neat films. The samples were prepared as described for the solid state luminescence spectroscopy and cooled using the cryostat *ARS* Model DE-202 A. A liquid-nitrogen-cooled mercury cadmium telluride (MCT) detector (*Kolmar Tech.*, Model KV100-1-B-7/190) with a rise time of 25 ns, connected to a fast preamplifier and a 14-bit transient recorder board (*Spectrum Germany*, M3I4142, 400 MS s^{-1}), was used for signal detection and processing. The laser setup includes the Q-switched Nd:YAG lasers *Innolas* SpitLight 1000.2 and *Innolas* SpitLight Evo I generating pulses with a band-width of 6 ns at repetition rates of 10 Hz and 100 Hz, respectively. Apart from the measurements on KBr pellets of the neutral systems **CuL** and **Cu_2L'** at 20 K (10 Hz), all the experiments were performed at 100 Hz. The third harmonic (355 nm) of the Nd:YAG laser was used for sample excitation. The UV pump beam was attenuated to 2.0 mJ and 0.2 mJ per shot at a diameter of 9 mm for measurements on KBr pellets and neat films, respectively. The beam was directed onto the sample and adjusted to have a maximal overlap with the IR beam of the spectrometer. The sample chamber was equipped with anti-reflection-coated germanium filters to prevent the entrance of laser radiation into the detector and interferometer compartments. The time delay between the start of the experiment and the UV laser pulse was controlled with a *Stanford Research Systems* DG535 delay generator and the time where the laser pulse reached the sample was set as zero point in all spectra. The temporal resolution was set to 20 ns or 100 ns. The spectral region was limited by undersampling to 0–1975 cm^{-1} or 988–1975 cm^{-1} with a spectral resolution of 4 cm^{-1} resulting in 1110 and 555 interferogram points, respectively. An IR broad band filter (850–1750 cm^{-1}) and the CaF_2 windows (no IR transmission $< 1000\ cm^{-1}$) of the cryostat prevented problems when performing a Fourier transformation (i.e. no IR intensity outside the measured region should be observed). FTIR ground state spectra were recorded systematically to check for sample degradation. A more detailed description of the step-scan setup is given elsewhere.[46a,b,57]

 © 2021 The Authors. Chemistry - A European Journal published by Wiley-VCH GmbH

15213765, 2021, 61, Downloaded from https://chemistry-europe.onlinelibrary.wiley.com/doi/10.1002/chem.202102760, Wiley Online Library on [03/02/2025]. See the Terms and Conditions (https://onlinelibrary.wiley.com/terms-and-conditions) on Wiley Online Library for rules of use; OA articles are governed by the applicable Creative Commons License

15213765, 2021, 61, Downloaded from https://chemistry-europe.onlinelibrary.wiley.com/doi/10.1002/chem.202102760, Wiley Online Library on [03/02/2025]. See the Terms and Conditions (https://onlinelibrary.wiley.com/terms-and-conditions) on Wiley Online Library for rules of use; OA articles are governed by the applicable Creative Commons License

Ion-trap mass spectrometry (ESI-MS)

Ion-trap mass spectrometric analyses were performed using a Paul-type 3D quadrupole ion trap mass spectrometer (*Bruker Daltonics*, amaZon speed) which was modified for laser irradiation experiments.[35a,58] For examination of trapped ions in positive ion mode, solutions of **[CuLH]BF_4**, **[$Cu_2L'H_2$](BF_4)$_2$** and **[$Cu_2L'H_2$](PF_6)$_2$** in methanol ($c = 10^{-6}$ M) were electrosprayed (ESI needle at 4.5 kV) at a continuous infusion rate of 120 μl h^{-1} with coaxial flow of nitrogen sheath gas (7 psi, 483 mbar) as support. Also, nitrogen was used as drying gas (4 l min^{-1}, 180 °C) to assist the desolvation process. The mass-spectra were recorded in enhanced resolution scan mode (8100 amu s^{-1}, ca. 0.25 FWHM) with a mass isolation window of $\triangle m/z = 9$. The instrument was controlled using the trapControl 7.4 software (*Bruker Daltonics*) and spectra were analyzed using the dataanalysis 4.4 software (*Bruker Daltonics*).

Gas phase UV-photodissociation (UV PD, τ-PD)

The experimental setup for photodissociative action spectroscopy was described elsewhere in detail.[35b,59] Shortly, a femto- or nanosecond, respectively, UV-pump (λ_{pump}: 350–370 nm, 0.3 μJ) beam is focused ($f = 50$ cm) and quasi-collinearly combined with a femtosecond NIR-probe (λ_{probe}: 1200 nm, 130 μJ) beam in a Paul-type ion trap (~1 mm diameter) through fused silica window (3 mm thickness) of the modified mass spectrometer. For static photodissociation spectra only the pump beam (femto- or nanosecond pulses, respectively) is used and manually scanned in 3–5 nm steps in the range of 240–400 nm with a constant pulse energy (2 μJ) controlled by neutral density filters and an irradiation time of 100 ms, so that each ion packet was irradiated with ~100 UV pulses followed by mass spectrometric analysis. The individual (Y_i) and total fragment yields (TFY) were calculated from the resulting mass spectra using

$$Y_i = F_i/(\sum F_i + P) \tag{5}$$

$$\mathrm{TFY} = \sum F_i/(\sum F_i + P) \tag{6}$$

where F_i and P were the integrated mass peak intensities of the fragments and precursor ions and $\sum F_i$ represents the sum of all fragment product intensities. For static PD spectra the resulting fragment yields were normalized to photon number using

$$N = E_{\mathrm{pulse}} \cdot \lambda/(h \cdot c) \tag{7}$$

For τ-PD experiments an average of 12 scans for each time window was used. A convolution of a Gaussian system response function with a multiexponential decay function in accordance with

$$S(t) = \sum_i A_i(\exp\left(-\frac{t}{\tau_i}\right) \times g(t, t_0, t_p) \tag{8}$$

was used to fit the transient data using *Origin* 2021 software (τ_i decay time constants, t_0 time zero, t_p FWHM of Gaussian, A_i amplitude of τ_i).

Femto- and nanosecond time-resolved transient photodissociation (τ-PD)

The femtosecond pump-probe experiments were performed using a Ti:Sa chirped pulse cryogenic regenerative amplifier system (*KMLabs*, Wyvern 1000™) with an output pulse of ~ 780 nm (982 Hz, 3.1 W, FWHM ~50 fs). This pump beam was split in order to pump two nonlinear frequency converters (*Light Conversion*, TOPAS-C) to generate tunable wavelength output (tuning range: 240–2600 nm). A delay stage (*Physik Instrumente*, *PI*) was used to generate time delay between pump and probe pulses for femtosecond transient photodissociation measurements. For the ns pump/fs probe experimental setup with two pulsed laser systems, the femtosecond amplified laser output (at ca. 1 kHz) is used as the master clock and a ns kHz laser system (see below) is synchronized with electronically variable time delay between the ns pulse and the following (next) fs pulse. The femtosecond seed laser pulse is picked up by a fast photodiode (*Thorlabs*, DET10 A/M) to start a delay generator (*Stanford Research Systems*, Model DG645) which then triggers at appropriate delay a second, the main, delay generator. This configuration is used because of the necessity of a negative pump-probe delay $\triangle t < 0$ which functionality is not offered in the used delay generators.[44] The first delay generator creates a variable pre-delay which is variably controlled by the data acquisition PC using a *LabView*2018 program. The main delay generator is triggered by the first one and generates two trigger output pulses for the *EKSPLA* NT242: first a pump trigger signal and, at appropriate delay, second a Q-switch trigger signal which eventually releases the ns laser pulse. For an *in operando* check of the time overlap of the two pulses another fast photodiode (Soliton EOT ET-2000) at the optical output of the ion trap was used and the signal monitored on an oscilloscope (*Tektronix* DPO4101B). The resulting time delay has a time window of up to 200 μs. The time resolution is currently limited by a jitter in the regenerative amplifier switchout of the Wyvern system to ca. 50 ns, but it should be possible to reduce it to < 1 ns.

Nanosecond kHz OPO laser system

Nanosecond laser pulses were generated using a tunable diode-pumped OPO Laser System (*EKPSLA*, NT242). The 1064 nm fundamental pulse generated by a Q-switched diode-pumped Nd:YAG pump laser NL210 with a pulse duration of 4–6 ns and a repetition rate of 1 kHz was split and frequency doubled to 532 nm. Lastly, the third harmonic beam was generated to pump the nonlinear type-II BBO crystals for the OPO processes to obtain wavelengths in the range of 405–2600 nm. To achieve shorter wavelengths, a second harmonic and a sum frequency generator were used combining with the remaining fundamental Nd:YAG beam. The resulting wavelengths could be easily adjusted in the range of 210–2600 nm.

Acknowledgements

This work is supported by the DFG-funded Collaborative Research Centre (SFB) TRR 88 on Cooperative Effects in Homo- and Heterometallic Complexes "3MET" (Projects B9, C1, C2 and C4). The opportunity to use the cluster ELWE of Allianz für Hochleistungsrechnen Rheinland-Pfalz (AHRP) for calculations presented in this work is greatly acknowledged. C.R. and R.D. are thankful to the Laboratory for Advanced Spin Engineering (LASE, TUK) for laser support. We would like to appreciate the enduring and inspiring partnership in "3MET" and thank Gereon Niedner-Schatteburg (TUK) and (CB^2) Stefan Bräse (KIT) for continuous support. Open Access funding enabled and organized by Projekt DEAL.

 © 2021 The Authors. Chemistry - A European Journal published by Wiley-VCH GmbH

Conflict of Interest

The authors declare no conflict of interest.

Keywords: copper(I) complexes · cooperative effects · flattening distortion · photosensitizers · time-resolved spectroscopy

[1] a) L. P. Ravaro, K. P. Zanoni, A. S. de Camargo, *Energy Reports* **2020**, *6*, 37–45; b) C. Bizzarri, E. Spuling, D. M. Knoll, D. Volz, S. Bräse, *Coord. Chem. Rev.* **2018**, *373*, 49–82; c) R. Hamze, J. L. Peltier, D. Sylvinson, M. Jung, J. Cardenas, R. Haiges, M. Soleilhavoup, R. Jazzar, P. I. Djurovich, G. Bertrand, *Science* **2019**, *363*, 601–606; d) H. Yersin, *Highly efficient OLEDs: Materials based on thermally activated delayed fluorescence*, John Wiley & Sons, **2019**.

[2] a) C. Sandoval-Pauker, G. Molina-Aguirre, B. Pinter, *Polyhedron* **2021**, 115105; b) A. Hossain, A. Bhattacharyya, O. Reiser, *Science* **2019**, *364*; c) J. Kim, D. R. Whang, S. Y. Park, *ChemSusChem* **2017**, *10*, 1883–1886.

[3] a) K. E. Dalle, J. Warnan, J. J. Leung, B. Reuillard, I. S. Karmel, E. Reisner, *Chem. Rev.* **2019**, *119*, 2752–2875; b) A. Rosas-Hernández, C. Steinlechner, H. Junge, M. Beller, *Green Chem.* **2017**, *19*, 2356–2360; c) H. Takeda, H. Kamiyama, K. Okamoto, M. Irimajiri, T. Mizutani, K. Koike, A. Sekine, O. Ishitani, *J. Am. Chem. Soc.* **2018**, *140*, 17241–17254; d) H. Takeda, K. Ohashi, A. Sekine, O. Ishitani, *J. Am. Chem. Soc.* **2016**, *138*, 4354–4357; e) W. J. Ong, L. K. Putri, A. R. Mohamed, *Chemistry–A European Journal* **2020**, *26*, 9710–9748; f) H. Rao, J. Bonin, M. Robert, *ChemSusChem* **2017**, *10*, 4447–4450; g) Y. Sakaguchi, A. Call, M. Cibian, K. Yamauchi, K. Sakai, *Chem. Commun.* **2019**, *55*, 8552–8555; h) L. L. Gracia, L. Luci, C. Bruschi, L. Sambri, P. Weis, O. Fuhr, C. Bizzarri, *Chemistry (Weinheim an der Bergstrasse, Germany)* **2020**, *26*, 9929; i) J. Schneider, H. Jia, J. T. Muckerman, E. Fujita, *Chem. Soc. Rev.* **2012**, *41*, 2036–2051.

[4] a) N. Armaroli, G. Accorsi, F. Cardinali, A. Listorti, *Photochemistry and Photophysics of Coordination Compounds I* **2007**, 69–115; b) A. C. Hernandez-Perez, S. K. Collins, *Acc. Chem. Res.* **2016**, *49*, 1557–1565; c) M. Wallesch, D. Volz, D. M. Zink, U. Schepers, M. Nieger, T. Baumann, S. Bräse, *Chemistry–A European Journal* **2014**, *20*, 6578–6590.

[5] Y. Zhang, M. Schulz, M. Waechtler, M. Karnahl, B. Dietzek, *Coord. Chem. Rev.* **2018**, *356*, 127–146.

[6] a) Y. Zhang, L. Zedler, M. Karnahl, B. Dietzek, *Phys. Chem. Chem. Phys.* **2019**, *21*, 10716–10725; b) Y. Zhang, P. Traber, L. Zedler, S. Kupfer, S. Gräfe, M. Schulz, W. Frey, M. Karnahl, B. Dietzek, *Phys. Chem. Chem. Phys.* **2018**, *20*, 24843–24857.

[7] A. Kaeser, M. Mohankumar, J. Mohanraj, F. Monti, M. Holler, J.-J. Cid, O. Moudam, I. Nierengarten, L. Karmazin-Brelot, C. Duhayon, *Inorg. Chem.* **2013**, *52*, 12140–12151.

[8] a) L. Bergmann, G. J. Hedley, T. Baumann, S. Bräse, I. D. Samuel, *Sci. Adv.* **2016**, *2*, e1500889; b) M. Grupe, F. Bäppler, M. Theiß, J. M. Busch, F. Dietrich, D. Volz, M. Gerhards, S. Bräse, R. Diller, *Phys. Chem. Chem. Phys.* **2020**, *22*, 14187–14200; c) C. Bizzarri, C. Fléchon, O. Fenwick, F. Cacialli, F. Polo, M. D. Gálvez-López, C.-H. Yang, S. Scintilla, Y. Sun, R. Fröhlich, *ECS Journal of Solid State Science and Technology* **2016**, *5*, R83; d) J.-L. Chen, X.-F. Cao, J.-Y. Wang, L.-H. He, Z.-Y. Liu, H.-R. Wen, Z.-N. Chen, *Inorg. Chem.* **2013**, *52*, 9727–9740; e) F. Ferrari, J. Braun, C. E. Anson, B. D. Wilts, D. Moatsou, C. Bizzarri, *Molecules* **2021**, *26*, 2567; f) Q. Zhang, X.-L. Chen, J. Chen, X.-Y. Wu, R. Yu, C.-Z. Lu, *Dalton Trans.* **2015**, *44*, 10022–10029; g) L. Lin, D.-H. Chen, R. Yu, X.-L. Chen, W.-J. Zhu, D. Liang, J.-F. Chang, Q. Zhang, C.-Z. Lu, *J. Mater. Chem. C* **2017**, *5*, 4495–4504.

[9] C. Bruschi, X. Gui, N. Salaeh-arae, T. Barchi, O. Fuhr, S. Lebedkin, W. Klopper, C. Bizzarri, *Eur. J. Inorg. Chem.* doi.org/10.1002/ejic.202100653.

[10] a) P. A. F. Cortés, M. Marx, M. Trose, M. Beller, *Chem Catalysis* **2021**; b) G. Noirbent, F. Dumur, *Catalysts* **2020**, *10*, 953; c) Y. Yamazaki, T. Onoda, J. Ishikawa, S. Furukawa, C. Tanaka, T. Utsugi, T. Tsubomura, *Front. Chem.* **2019**, *7*, 288.

[11] a) G. B. Shaw, C. D. Grant, H. Shirota, E. W. Castner, G. J. Meyer, L. X. Chen, *J. Am. Chem. Soc.* **2007**, *129*, 2147–2160; b) M. Iwamura, S. Takeuchi, T. Tahara, *Acc. Chem. Res.* **2015**, *48*, 782–791.

[12] a) H. Yersin, R. Czerwieniec, M. Z. Shafikov, A. F. Suleymanova, *ChemPhysChem* **2017**, *18*, 3508–3535; b) S. Garakyaraghi, C. E. McCusker, S. Khan, P. Koutnik, A. T. Bui, F. N. Castellano, *Inorg. Chem.* **2018**, *57*, 2296–2307; c) P. A. Papanikolaou, N. V. Tkachenko, *Phys. Chem. Chem. Phys.* **2013**, *15*, 13128–13136.

[13] A. Stoïanov, C. Gourlaouen, S. Vela, C. Daniel, *J. Phys. Chem. A* **2018**, *122*, 1413–1421.

[14] C. Bizzarri, A. P. Arndt, S. Kohaut, K. Fink, M. Nieger, *J. Organomet. Chem.* **2018**, *871*, 140–149.

[15] a) G. Niedner-Schatteburg, *Clusters–Contemporary Insight in Structure and Bonding* **2016**, 1–40; b) G. Niedner-Schatteburg, in *Clusters–Contemporary Insight in Structure and Bonding*, Springer, **2017**, pp. 375–376.

[16] a) M. J. Leitl, F.-R. Küchle, H. A. Mayer, L. Wesemann, H. Yersin, *J. Phys. Chem. A* **2013**, *117*, 11823–11836 b) R. Czerwieniec, M. J. Leitl, H. H. Homeier, H. Yersin, *Coord. Chem. Rev.* **2016**, *325*, 2–28.

[17] P. A. Scattergood, P. I. Elliott, *Dalton Trans.* **2017**, *46*, 16343–16356.

[18] J. I. Mapley, D. A. Ross, C. J. McAdam, K. C. Gordon, J. D. Crowley, *J. Coord. Chem.* **2019**, *72*, 1378–1394.

[19] G. Gritzner, J. Kuta, *Pure Appl. Chem.* **1984**, *56*, 461–466.

[20] a) E. Kimura, X. Bu, M. Shionoya, S. Wada, S. Maruyama, *Inorg. Chem.* **1992**, *31*, 4542–4546; b) E. Kimura, S. Wada, M. Shionoya, Y. Okazaki, *Inorg. Chem.* **1994**, *33*, 770–778; c) C. A. Craig, L. O. Spreer, J. W. Otvos, M. Calvin, *J. Phys. Chem.* **1990**, *94*, 7957–7960; d) J. L. Grant, K. Goswami, L. O. Spreer, J. W. Otvos, M. Calvin, *J. Chem. Soc. Dalton Trans.* **1987**, 2105–2109; e) C. Herrero, A. Quaranta, S. El Ghachtouli, B. Vauzeilles, W. Leibl, A. Aukauloo, *Phys. Chem. Chem. Phys.* **2014**, *16*, 12067–12072; f) M. F. Kuehnel, C. D. Sahm, G. Neri, J. R. Lee, K. L. Orchard, A. J. Cowan, E. Reisner, *Chem. Sci.* **2018**, *9*, 2501–2509; g) M. A. Méndez, P. Voyame, H. H. Girault, *Angew. Chem.* **2011**, *123*, 7529–7532; *Angew. Chem. Int. Ed.* **2011**, *50*, 7391–7394; h) K. Mochizuki, S. Manaka, I. Takeda, T. Kondo, *Inorg. Chem.* **1996**, *35*, 5132–5136; i) C. R. Schneider, H. S. Shafaat, *Chem. Commun.* **2016**, *52*, 9889–9892.

[21] a) M. Iwamura, H. Watanabe, K. Ishii, S. Takeuchi, T. Tahara, *J. Am. Chem. Soc.* **2011**, *133*, 7728–7736; b) M. W. Mara, N. E. Jackson, J. Huang, A. B. Stickrath, X. Zhang, N. A. Gothard, M. A. Ratner, L. X. Chen, *J. Phys. Chem. B* **2013**, *117*, 1921–1931; c) M. T. Miller, P. K. Gantzel, T. B. Karpishin, *J. Am. Chem. Soc.* **1999**, *121*, 4292–4293.

[22] a) A. D. Becke, *J. Chem. Phys.* **1993**, *98*, 1372–1377; b) P. J. Stephens, F. J. Devlin, C. F. Chabalowski, M. J. Frisch, *J. Phys. Chem.* **1994**, *98*, 11623–11627.

[23] J. P. Perdew, M. Ernzerhof, K. Burke, *J. Chem. Phys.* **1996**, *105*, 9982–9985.

[24] a) K. Krause, W. Klopper, Wiley Online Library, **2017**; b) X. Gui, C. Holzer, W. Klopper, *J. Chem. Theory Comput.* **2018**, *14*, 2127–2136; c) C. Holzer, W. Klopper, *J. Chem. Phys.* **2019**, *150*, 204116.

[25] A. Dreuw, M. Head-Gordon, *J. Am. Chem. Soc.* **2004**, *126*, 4007–4016.

[26] S. Grimme, J. Antony, S. Ehrlich, H. Krieg, *J. Chem. Phys.* **2010**, *132*, 154104.

[27] B. Goswami, T. J. Feuerstein, R. Yadav, S. Lebedkin, P. J. Boden, S. T. Steiger, G. Niedner-Schatteburg, M. Gerhards, M. M. Kappes, P. W. Roesky, *Chemistry–A European Journal* **2021**.

[28] a) S. V. Kruppa, C. Groß, X. Gui, F. Bäppler, B. Kwasigroch, Y. Sun, R. Diller, W. Klopper, G. Niedner-Schatteburg, C. Riehn, *Chemistry–A European Journal* **2019**, *25*, 11176–11176; b) N. C. Polfer, P. Dugourd, *Laser photodissociation and spectroscopy of mass-separated biomolecular ions*, Springer, **2013**; c) J. S. Brodbelt, *Chem. Soc. Rev.* **2014**, *43*, 2757–2783.

[29] C. L. Linfoot, M. J. Leitl, P. Richardson, A. F. Rausch, O. Chepelin, F. J. White, H. Yersin, N. Robertson, *Inorg. Chem.* **2014**, *53*, 10854–10861.

[30] a) H. Yersin, A. F. Rausch, R. Czerwieniec, T. Hofbeck, T. Fischer, *Coord. Chem. Rev.* **2011**, *255*, 2622–2652; b) R. Czerwieniec, K. Kowalski, H. Yersin, *Dalton Trans.* **2013**, *42*, 9826–9830.

[31] N. Lüdtke, J. Föller, C. M. Marian, *Phys. Chem. Chem. Phys.* **2020**, *22*, 23530–23544.

[32] G. Capano, M. Chergui, U. Rothlisberger, I. Tavernelli, T. J. Penfold, *J. Phys. Chem. A* **2014**, *118*, 9861–9869.

[33] C. Müller, M. Schulz, M. Obst, L. Zedler, S. Gräfe, S. Kupfer, B. Dietzek, *J. Phys. Chem. A* **2020**, *124*, 6607–6616.

[34] C. Ma, C. T.-L. Chan, W.-M. Kwok, C.-M. Che, *Chem. Sci.* **2012**, *3*, 1883–1892.

[35] a) D. Imanbaew, Y. Nosenko, C. Kerner, K. Chevalier, F. Rupp, C. Riehn, W. Thiel, R. Diller, *Chem. Phys.* **2014**, *442*, 53–61; b) D. Imanbaew, J. Lang, M. F. Gelin, S. Kaufhold, M. G. Pfeffer, S. Rau, C. Riehn, *Angew. Chem.* **2017**, *129*, 5563–5566; *Angew. Chem. Int. Ed.* **2017**, *56*, 5471–5474.

[36] a) D. Nolting, T. Schultz, I. Hertel, R. Weinkauf, *Phys. Chem. Chem. Phys.* **2006**, *8*, 5247–5254; b) H. Kang, C. Jouvet, C. Dedonder-Lardeux, S. Martrenchard, C. Charriere, G. Gregoire, C. Desfrancois, J. Schermann, M. Barat, J. Fayeton, *J. Chem. Phys.* **2005**, *122*, 084307; c) G. Grégoire, B.

 © 2021 The Authors. Chemistry - A European Journal published by Wiley-VCH GmbH

15213765, 2021, 61, Downloaded from https://chemistry-europe.onlinelibrary.wiley.com/doi/10.1002/chem.202102760, Wiley Online Library on [03/02/2025]. See the Terms and Conditions (https://onlinelibrary.wiley.com/terms-and-conditions) on Wiley Online Library for rules of use; OA articles are governed by the applicable Creative Commons License

Lucas, M. Barat, J. Fayeton, C. Dedonder-Lardeux, C. Jouvet, *The European Physical Journal D* **2009**, *51*, 109–116.
[37] T. Katayama, T. Northey, W. Gawelda, C. J. Milne, G. Vankó, F. A. Lima, Z. Németh, S. Nozawa, T. Sato, D. Khakhulin, *Nat. Commun.* **2019**, *10*, 1–8.
[38] a) R. Monni, G. Capano, G. Auböck, H. B. Gray, A. Vlček, I. Tavernelli, M. Chergui, *Proc. Natl. Acad. Sci. USA* **2018**, *115*, E6396-E6403; b) M.-O. Winghart, J.-P. Yang, M. Vonderach, A.-N. Unterreiner, D.-L. Huang, L.-S. Wang, S. Kruppa, C. Riehn, M. M. Kappes, *J. Chem. Phys.* **2016**, *144*, 054305.
[39] a) C. Mueck-Lichtenfeld, S. Grimme, *Dalton Trans.* **2012**, *41*, 9111–9118; b) T. Wall, M. Leist, F. Dietrich, W. R. Thiel, M. Gerhards, *ChemPlusChem* **2021**, *86*, 622–628.
[40] Y. Sun, V. Lemaur, J. I. Beltran, J. Cornil, J. Huang, J. Zhu, Y. Wang, R. Fröhlich, H. Wang, L. Jiang, *Inorg. Chem.* **2016**, *55*, 5845–5852.
[41] R. Czerwieniec, J. Yu, H. Yersin, *Inorg. Chem.* **2011**, *50*, 8293–8301.
[42] R. Czerwieniec, H. Yersin, *Inorg. Chem.* **2015**, *54*, 4322–4327.
[43] a) M. Mohankumar, M. Holler, E. Meichsner, J.-F. o. Nierengarten, F. D. R. Niess, J.-P. Sauvage, B. A. Delavaux-Nicot, E. Leoni, F. Monti, J. M. Malicka, *J. Am. Chem. Soc.* **2018**, *140*, 2336–2347; b) D. Felder, J.-F. Nierengarten, F. Barigelletti, B. Ventura, N. Armaroli, *J. Am. Chem. Soc.* **2001**, *123*, 6291–6299; c) A. J. Lees, *Comments Inorg. Chem.* **1995**, *17*, 319–346.
[44] E. Riedle, M. Wenniger, Chapter 16 in: B. König, *Chemical photocatalysis*, Walter de Gruyter GmbH & Company KG, **2013**.
[45] a) J. R. Schoonover, G. F. Strouse, *Chem. Rev.* **1998**, *98*, 1335–1356; b) G. D. Smith, M. S. Hutson, Y. Lu, M. T. Tierney, M. W. Grinstaff, R. A. Palmer, *Appl. Spectrosc.* **2001**, *55*, 637–642; c) J. Torres-Alacan, P. Vöhringer, *Chemistry–A European Journal* **2017**, *23*, 6746–6751; d) P. Boden, P. Di Martino-Fumo, G. Niedner-Schatteburg, W. W. Seidel, K. Heinze, M. Gerhards, *Phys. Chem. Chem. Phys.* **2021**.
[46] a) F. Bäppler, M. Zimmer, F. Dietrich, M. Grupe, M. Wallesch, D. Volz, S. Bräse, M. Gerhards, R. Diller, *Phys. Chem. Chem. Phys.* **2017**, *19*, 29438–29448; b) M. Zimmer, F. Dietrich, D. Volz, S. Bräse, M. Gerhards, *ChemPhysChem* **2017**, *18*, 3023–3029; c) P. Boden, P. Di Martino-Fumo, J. M. Busch, F. R. Rehak, S. Steiger, O. Fuhr, M. Nieger, D. Volz, W. Klopper, S. Bräse, *Chemistry (Weinheim an der Bergstrasse, Germany)* **2021**, *27*, 5439.
[47] S. Tschierlei, M. Karnahl, N. Rockstroh, H. Junge, M. Beller, S. Lochbrunner, *ChemPhysChem* **2014**, *15*, 3709–3713.
[48] G. Li, R. S. Nobuyasu, B. Zhang, Y. Geng, B. Yao, Z. Xie, D. Zhu, G. Shan, W. Che, L. Yan, *Eur. J. Chem.* **2017**, *23*, 11761.
[49] B. Dereka, A. Rosspeintner, Z. Li, R. Liska, E. Vauthey, *J. Am. Chem. Soc.* **2016**, *138*, 4643–4649.
[50] a) C. Förster, K. Heinze, *Chem. Soc. Rev.* **2020**, *49*, 1057–1070; b) O. S. Wenger, *J. Am. Chem. Soc.* **2018**, *140*, 13522–13533.
[51] G. M. Sheldrick, *Acta Crystallographica Section A: Foundations and Advances* **2015**, *71*, 3–8.
[52] G. M. Sheldrick, *Acta Crystallographica Section C: Structural Chemistry* **2015**, *71*, 3–8.
[53] a) F. Furche, R. Ahlrichs, C. Hättig, W. Klopper, M. Sierka, F. Weigend, *WIREs Comput. Mol. Sci.* **2014**, *4*, 91–100; b) *TURBOMOLE V7.4, 2019, a development of University of Karlsruhe and Forschungszentrum Karlsruhe GmbH, 1989–2007,TURBOMOLE GmbH, since 2007; available from* http://www.turbomole.com.
[54] a) S. Grimme, S. Ehrlich, L. Goerigk, *Journal of computational chemistry* **2011**, *32*, 1456–1465; b) J. P. Perdew, K. Burke, M. Ernzerhof, *Rev. Lett* **1997**, *78*, 1396; c) J. P. Perdew, K. Burke, M. Ernzerhof, *Physical review letters* **1996**, *77*, 3865.
[55] X. Blase, C. Attaccalite, V. Olevano, *Physical Review B* **2011**, *83*, 115103.
[56] M. Frisch, G. Trucks, H. Schlegel, G. Scuseria, M. Robb, J. Cheeseman, G. Scalmani, V. Barone, G. Petersson, H. Nakatsuji et al., *Gaussian, Inc., Wallingford CT* **2016**.
[57] M. Zimmer, F. Rupp, P. Singer, F. Walz, F. Breher, W. Klopper, R. Diller, M. Gerhards, *Physical Chemistry Chemical Physics* **2015**, *17*, 14138–14144.
[58] a) Y. Nosenko, F. Menges, C. Riehn, G. Niedner-Schatteburg, *Physical Chemistry Chemical Physics* **2013**, *15*, 8171–8178; b) S. Kruppa, F. Bäppler, Y. Nosenko, S. Walg, R. Diller, C. Riehn, in *International Conference on Ultrafast Phenomena*, Optical Society of America, **2016**, p. UW4 A. 33; c) J. Martens, G. Berden, C. R. Gebhardt, J. Oomens, *Review of Scientific Instruments* **2016**, *87*, 103108.
[59] a) Y. Nosenko, C. Riehn, W. Klopper, *Chemical Physics Letters* **2016**, *659*, 55–60; b) S. V. Kruppa, Y. Nosenko, M.-O. Winghart, S. P. Walg, M. M. Kappes, C. Riehn, *International Journal of Mass Spectrometry* **2016**, *395*, 7–19.

Manuscript received: July 29, 2021
Accepted manuscript online: September 22, 2021
Version of record online: October 14, 2021

 © 2021 The Authors. Chemistry - A European Journal published by Wiley-VCH GmbH

15213765, 2021, 61, Downloaded from https://chemistry-europe.onlinelibrary.wiley.com/doi/10.1002/chem.202102760, Wiley Online Library on [03/02/2025]. See the Terms and Conditions (https://onlinelibrary.wiley.com/terms-and-conditions) on Wiley Online Library for rules of use; OA articles are governed by the applicable Creative Commons License

4. Additional Research Projects

The following chapters describe two research projects that I started and advanced. Thus, these projects have not been published, the chapters are structured as paper drafts and basis for future publications (introduction, experimental setup, results and discussion, conclusion).

4.1 Ion Trap Spectroscopy on Polyoxovanadates (POV)

4.1.1 Introduction

Polyoxovanadates (POVs), a highly studied subset of polyoxometalates (POMs), represents a cornerstone of molecular inorganic chemistry due to their remarkable structural diversity, redox activity, and photochemical functionality. These vanadium-oxide-based clusters have garnered significant attention as molecular catalysts for photoredox transformations and as models for heterogeneous vanadium oxide catalysts. With applications ranging from solar-driven energy conversion and catalytic organic transformations to advanced material synthesis, POVs stand at the interface of fundamental research and technological innovation.[248-249]

At the molecular level, POVs exhibit tunable electronic properties, primarily dictated by their vanadium oxidation states, ligand environment, and overall topology. This tunability facilitates systematic investigations into the factors governing photoredox processes such as photoexcitation, charge transfer, and substrate oxidation. Crucially, these molecular catalysts can mimic the complex behavior of solid-state vanadium oxides, allowing insights into their heterogeneous counterparts under well-defined conditions.[250]

Despite their promise, the mechanistic understanding of photophysical processes in POV systems remains incomplete. Current gaps include the precise dynamics subsequent to light absorption, the role of electronic and structural modifications in photoactivation, and the mechanisms of catalyst regeneration following turnover.[251] Moreover, while solution-phase studies have advanced our understanding of solvent-catalyst interactions and substrate pre-association, gas-phase studies offer a complementary perspective by isolating the intrinsic

properties of the clusters. This isolation provides a unique opportunity to probe their behavior devoid of extraneous effects such as solvent polarity, hydrogen bonding, or counterion interactions.[252]

Ion trap spectroscopy is a highly effective method for studying the intrinsic properties of molecular systems[203] and should therefore also be applicable to POV. This technique involves the electrospray ionization (ESI) of dissolved molecular or cluster ions, followed by their isolation and interrogation within a controlled gas-phase environment. By coupling this setup with advanced laser-based methodologies, including ultraviolet photodissociation (UVPD) spectroscopy and femtosecond pump-probe techniques, it should be possible to directly observe the primary photophysical events that govern POV photoactivity. Specifically, this approach enables the resolution of electronic transitions, photoinduced fragmentation pathways, and transient excited-state dynamics on ultrafast timescales.

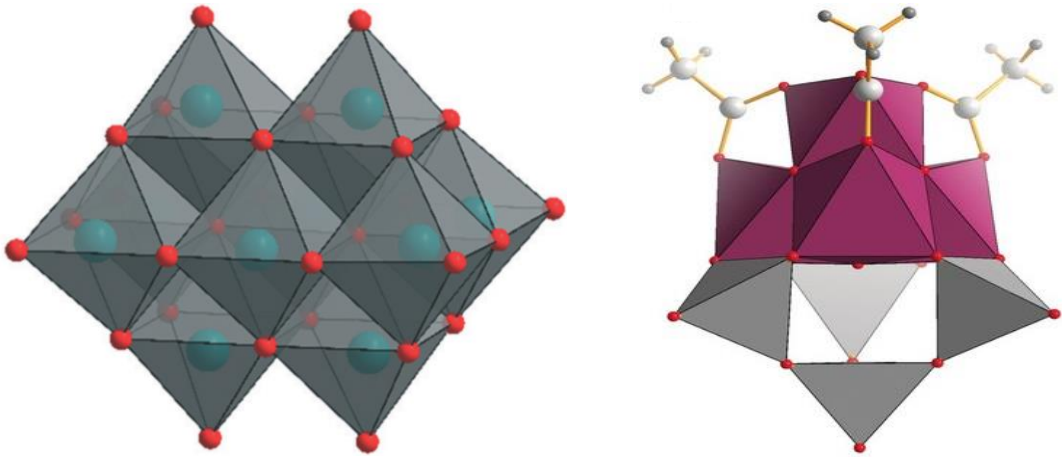

Figure 4.1 LEFT: Structural representation of $\{V_{10}\}$ = $[V_{10}O_{28}]$ out of the $(^{n}Bu_4N)_3H_3\{V_{10}\}$ complex and (**RIGHT**) $[Mn_4V_4O_{17}(OAc)_3]$ out of the $(^{n}Bu_4N)_3[Mn_4V_4O_{17}(OAc)_3]\cdot 3H_2O$ complex (right).[253-254]

This research project is based on the collaboration of expertise across multiple fields of chemistry. The synthesis of POV complexes was conducted by the Streb group at Johannes Gutenberg University Mainz (before: Ulm University), while theoretical modelling and computational studies were led by the Jacob group at Ulm University. Solution-phase photooxidation studies were also performed in the Streb group. The gas-phase photodissociation and time-resolved spectroscopy experiments were conducted by myself, in continuation and strong extension of the preliminary mass spectrometric and

photodissociation investigations by Dr. Dimitri Imanbaew, under the supervision of PD Dr. Riehn at RPTU Kaiserslautern, utilizing a customized ion trap spectrometer. The studies presented within this thesis includes the complexes shown in Figure 4.1.

4.1.2 Experimental Setup

The spectrometric analysis of $(^{n}Bu_4N)_3H_3$ $\{V_{10}\}$, ($\{V_{10}\}$ = $[V_{10}O_{28}]$) was performed using an amaZon speed spectrometer of Bruker Daltonic, whose Paul-type quadrupole ion trap was modified to allow laser-induced fragmentation for spectroscopic investigations. The complex was transferred into gas phase using electrospray ionization (ESI), where a syringe pump continuously infused a sample solution with a concentration of 10^{-6} mol/L into the source at a flow rate of 120 µL/min. Hereby, nitrogen gas functioned as a nebulizer and drying gas under 7 psi (~410 mbar) and at a flow rate of 4 L/min and 180° C.

Mass-selected ions were trapped within a modified radio-frequency (RF) Paul ion trap, equipped with optical ports for laser irradiation experiments. This setup allows for the controlled interaction of trapped ions with set laser pulses, enabling the study of photophysical processes under well-defined conditions void of solvent and counterion influences.

Ions stemming from $\{V_{10}\}$ were isolated in the ion trap and then exposed to laser radiation for photodissociation (PD) reactions and UVPD spectroscopy. The static UV/Vis photofragmentation (UVPD) was conducted with a tunable ns laser system (EKSPLA NT242 ns-OPO) operating in the ultraviolet (UV) to near-infrared (NIR) range (210–2400 nm) and the fs laser system (Wyvern; (236 nm-650 nm). Both systems operated at a 3 nm step size and a pulse energy of 2 µJ per pulse. The EKSPLA laser system – a only recently implemented system in the ion trap spectroscopy apparatus- offered automated tunability, significantly reducing manual workload compared to the Wyvern system, which required manual adjustments of pulse energy at each wavelength. The UVPD spectra of $\{V_{10}\}$ were measured with both laser systems to compare their results.

The laser beams were directed into the ion trap, resulting in photofragmentation after resonant absorption of the photons. The arising fragment yield was monitored as a function of laser wavelength so that action spectra were obtained, which serve as proxies for the electronic absorption spectra of the isolated ions. Within the ion trap, the fragmentation time was set at 100 ms, corresponding to 100 laser pulse pairs. The fragmentation yield was calculated by $I_f/(I_f+I_p)$, where I_f and I_p are the sums of the fragment and parent ion signal. Additionally, the fragment yield was then normalized to photon flux by the according numeric wavelength value. For comparison, solution-phase absorption spectra of the complexes were measured using a Lambda 25 UV-Vis spectrometer from PerkinElmer. This allowed for direct comparison between gas phase and solution phase photophysical properties, highlighting, e.g., shifts attributable to solvent or counterion effects.

Time-resolved pump-probe spectroscopy was conducted to investigate the dynamics of electronically excited states in the POV clusters. The femtosecond laser system (Wyvern1000, KMLabs) was used to generate the pump and probe pulses. The pump pulse excited the trapped ions resonantly to their according electronic excited states, while the probe pulse monitored the evolution of these states over time by inducing photodissociation. The delay between the pump and probe pulses was systematically varied using an optical delay line, allowing the capture of transient decay profiles. The fragment ion intensities were recorded as a function of pump-probe delay times, providing insights into the lifetimes and relaxation pathways of the excited states.

4.1.3 Results and Discussion

The mass spectrometric analysis of polyoxovanadates (POVs) served as a fundamental step for subsequent spectroscopic experiments. However, the inherent fragility of these clusters presented challenges, as evidenced by the observation of extensive fragmentation in the overview mass spectrum (Figure 4.2). Similar fragmentation behavior has been reported previously.[255-256] The parent ion of interest, $[V_{10}O_{28}]^{6-}$ (denoted as $\{V_{10}\}$), was accompanied by a series of smaller fragments resulting from the loss of oxygen atoms or hydroxide groups

during electrospray ionization and ion transport into the trap. The fragments and according pathways are consistent with known fragmentation mechanisms of vanadium oxides.[65]

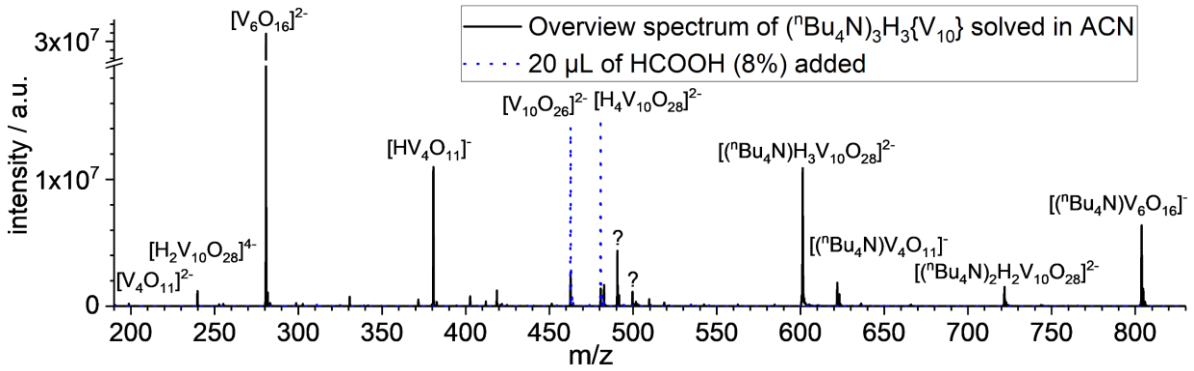

Figure 4.2 Overview mass spectrum of (^{n}Bu$_4$N)$_3$H$_3${V$_{10}$} solved in ACN (black) and mass spectrum of the protonated solution (blue dotted).

Despite fragmentation, isotopic distribution analysis confirmed the integrity of the vanadium-oxygen framework. However, the identification and disentangling of individual charge states and compositions remain challenging. The nearly monoisotopic nature of vanadium posed challenges in resolving overlapping charge states, particularly for multiply protonated or reduced species. This limitation was partially mitigated using high-resolution mass spectrometry simulations, which helped distinguish closely spaced isobaric peaks. Despite this, only a limited number of signals in Figure 4.1 could be clearly identified through isotope pattern simulations (Table 4.1). The vanadium oxide isotope patterns combined with the measurement accuracy limited to 0.02 m/z, restrict the certainty of these assignments. Nevertheless, they serve as a starting point for further investigation.

Table 4.1 Assignment of fragments of the measured overview mass spectrum of (^{n}Bu$_4$N)$_3$H$_3${V$_{10}$}.

Found m/z	Simulated m/z	Δ (|m/z$_{found}$- m/z$_{sim}$|)	Assignment
189.774	189.860	0.086	[V$_4$O$_{11}$]$^{2-}$
239.752	239.829	0.077	[H$_2$V$_{10}$O$_{28}$]$^{4-}$
280.708	280.792	0.084	[V$_6$O$_{16}$]$^{2-}$
380.674	380.728	0.054	[HV$_4$O$_{11}$]$^-$
462.638	462.654	0.016	[V$_{10}$O$_{26}$]$^{2-}$
480.633	480.665	0.062	[H$_4$V$_{10}$O$_{28}$]$^{2-}$
562.599	562.591	0.008	[HV$_6$O$_{16}$]$^-$
601.285	601.303	0.018	[(^{n}Bu$_4$N)H$_3$V$_{10}$O$_{28}$]$^{2-}$
621.949	621.005	0.944	[(^{n}Bu$_4$N)V$_4$O$_{11}$]$^-$
721.841	721.942	0.101	[(^{n}Bu$_4$N)$_2$H$_2$V$_{10}$O$_{28}$]$^{2-}$
803.728	803.868	0.140	[(^{n}Bu$_4$N)V$_6$O$_{16}$]$^-$

Further analysis of each signal with secondary mass spectrometric steps was prevented due to strong decrease of signal intensity upon isolation. To stabilize the $\{V_{10}\}$ composition and to reduce the versatile number of fragments while increasing the relative abundance, formic acid was added to solution prior to ESI. This adjustment shifted the solution conditions to an acidic pH range, promoting thermodynamically stabilization.[257-258] So, to a 1 mL acetonitrilic sample solution (10^{-6} M) 20 µL of formic acid (8%) were added. The mass spectrum (Figure 4.3) exhibited two prominent signals at m/z 462 and 480, potentially representing overlapping species ($[V_5O_{13}]^-/[V_{10}O_{26}]^{2-}$ and $[H_4V_5O_{14}]^-/[H_4\ V_{10}O_{28}]^{2-}$, respectively). For an unequivocal assignment of those closely spaced peaks, the resolution of the mass spectrometer (2000–3000 m/Δm) is insufficient. Mass spectrometers of Q-TOF or ICR type might offer a much higher resolution for a separation of here overlapping signals.[259]

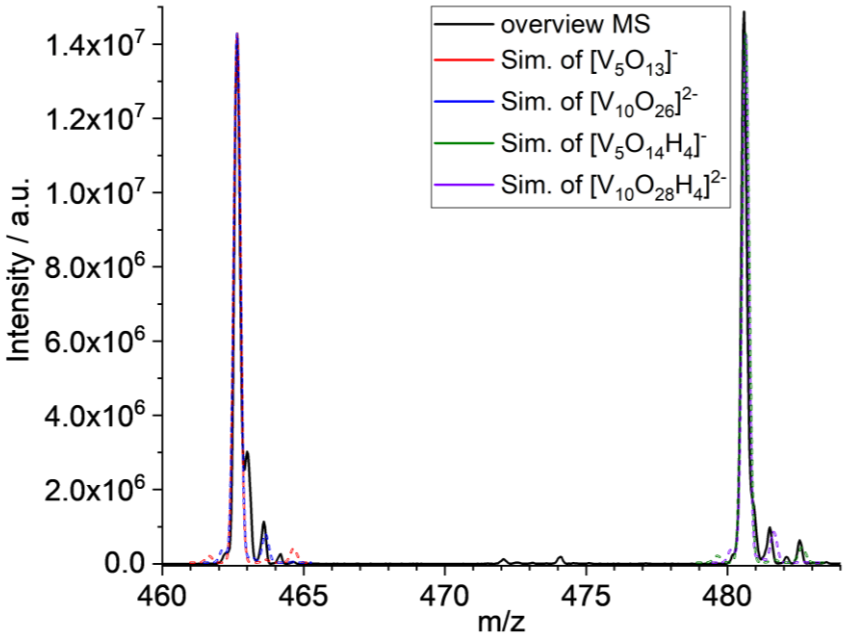

Figure 4.3 Mass spectrum of $(^nBu_4N)_3H_3\{V_{10}\}$ with formic acid addition and the simulations of selected ions.

Alternative approaches for the preparation of overview mass spectra with a low amount of fragments and decent ion intensity from ESI of $(^nBu_4N)_3H_3\{V_{10}\}$ have been previously explored extensively by Dr. Dimitri Imanbaew, where spray parameters as capillary end voltage, dry gas temperature/flow rate, syringe flow rate, etc. were varied, however with very limited success. Application of a nano-ESI source was tested by me, unfortunately also without success.

Therefore, for future applications the employment of a cold spray ionization source seems essential for overcoming these major obstacles.[260-261]

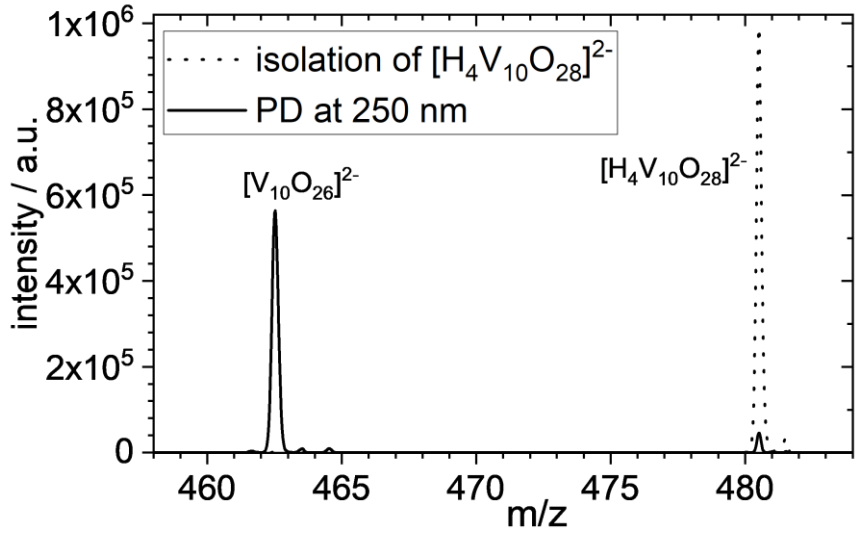

Figure 4.4 Mass spectrum of the isolated $[HV_{10}O_{28}]^{2-}$ at m/z 481 and its fragment upon photodissociation at 250 nm.

For the preparation of photodissociation experiments we have identified $[(^nBu_4N)H_3V_{10}O_{28}]^{2-}$ and $[H_4V_{10}O_{28}]^{2-}$ as promising candidates. Photodissociation at 250 nm (Figure 4.4) revealed that while $[H_4V_{10}O_{28}]^{2-}$ (photo-)dissociates primarily forming the $[V_{10}O_{26}]^{2-}$ species (m/z 462) by a loss of 2 H_2O molecules. $[V_{10}O_{26}]^{2-}$ is a very stable structure exposing a high electron affinity; well known for POVs[262] in general, and subsequently poses no subject for further UVPD as it is not prone to other fragmentation or electron detachment.

Conversely, $[(^nBu_4N)H_3V_{10}O_{28}]^{2-}$ dissociates into a series of fragments (Figure 4.5). Though assignment is aggravated by vanadium's isotopic simplicity, a preliminary assignment is given in Table 4.2.

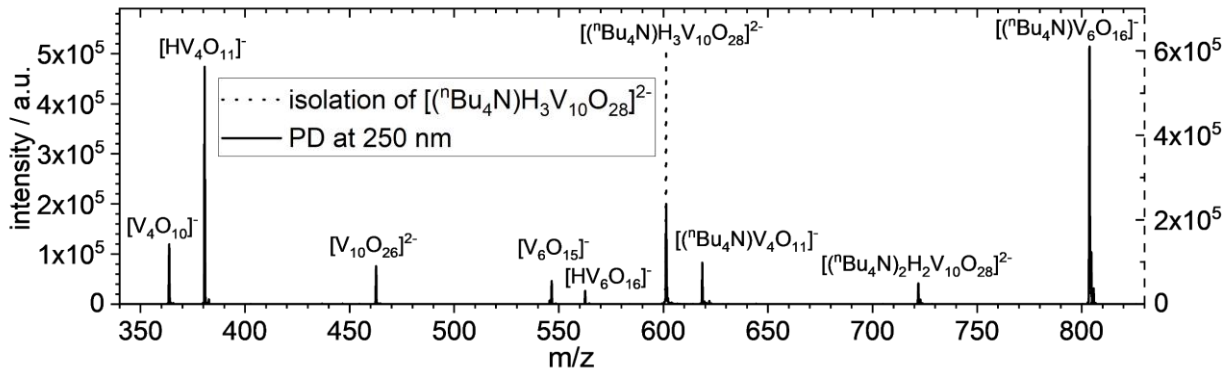

Figure 4.5 Mass spectrum of the isolated $[(^nBu_4N)H_3V_{10}O_{28}]^{2-}$ at m/z 601 and its fragments upon photodissociation at 250 nm.

The species $[(^nBu_4N)H_3V_{10}O_{28}]^{2-}$ and $[H_4V_{10}O_{28}]^{2-}$ do not meet the "regular" requirements for ionic species to be studied by UVPD spectroscopy, since they exhibit a strong intensity loss upon mass isolation within the ion trap. Their lability posed a major challenge for their ion trap spectroscopic characterization. For instance, for $[H_4V_{10}O_{28}]^{2-}$, while it appeared in MS^1 with intensity in the 10^7 (arbitrary units; proprietary Bruker ion count rate) range (Figure 4.3), it decreased to 10^5 upon isolation in the ion trap (Figure 4.4). However, by tuning the MS settings for storing ions in the trap and averaging over an extended irradiation exposure time, the UVPD in (Figure 4.6, LEFT) were successfully recorded with a ns OPO laser (EKSPLA, NT242) and for comparison with a fs (KMLabs, Wyvern 1000) laser system, showing similar curve shapes and thus indicating that the pulse characteristics (e.g., pulse duration, spectral width and intensity) do not influence the spectral shape for these POV systems.

Table 4.2 Assignment of fragments resulting upon photodissociation of species $[(^nBu_4N)H_3V_{10}O_{28}]^{2-}$ at m/z 601.

Found m/z	Simulated m/z	Δ ($\lvert m/z_{found} - m/z_{sim} \rvert$)	Assignment
363.688	363.725	0.037	$[V_4O_{11}]^{2-}$
380.674	380.728	0.054	$[HV_4O_{11}]^{-}$
462.638	462.654	0.016	$[V_{10}O_{26}]^{2-}$
546.563	545.587	0.024	$[V_6O_{15}]^{2-}$
562.599	562.591	0.008	$[HV_6O_{16}]^{-}$
601.285	601.303	0.018	$[(^nBu_4N)H_3V_{10}O_{28}]^{2-}$
621.949	621.005	0.944	$[(^nBu_4N)V_4O_{11}]^{-}$
721.841	721.942	0.101	$[(^nBu_4N)_2H_2V_{10}O_{28}]^{2-}$
803.728	803.868	0.140	$[(^nBu_4N)V_6O_{16}]^{-}$

UVPD spectra of $[(^{n}Bu_4N)H_3V_{10}O_{28}]^{2-}$ and $[H_4V_{10}O_{28}]^{2-}$ (Figure 4.6, RIGHT) revealed broad absorption features slowly rising towards short wavelengths extending from 500 to 250 nm, consistent with charge-transfer transitions involving the vanadium-oxide framework as known from UV/Vis spectroscopy in solution. $[(^{n}Bu_4N)H_3V_{10}O_{28}]^{2-}$ differs from $[H_4V_{10}O_{28}]^{2-}$ by the replacement of one proton by the counter cation $(^{n}Bu_4N)^{+}$; however, it shows only minimal spectroscopic deviation, suggesting that the core electronic transitions are largely independent of external ionic interactions. Comparing these gas phase spectra with the UV/Vis absorption spectrum of $(^{n}Bu_4N)_3H_3[V_{10}O_{28}]$ in acetonitrile, mainly minor differences in the shape were observed, especially for the rising band region from 450 nm to 315 nm, which is less pronounced in the solution spectrum.

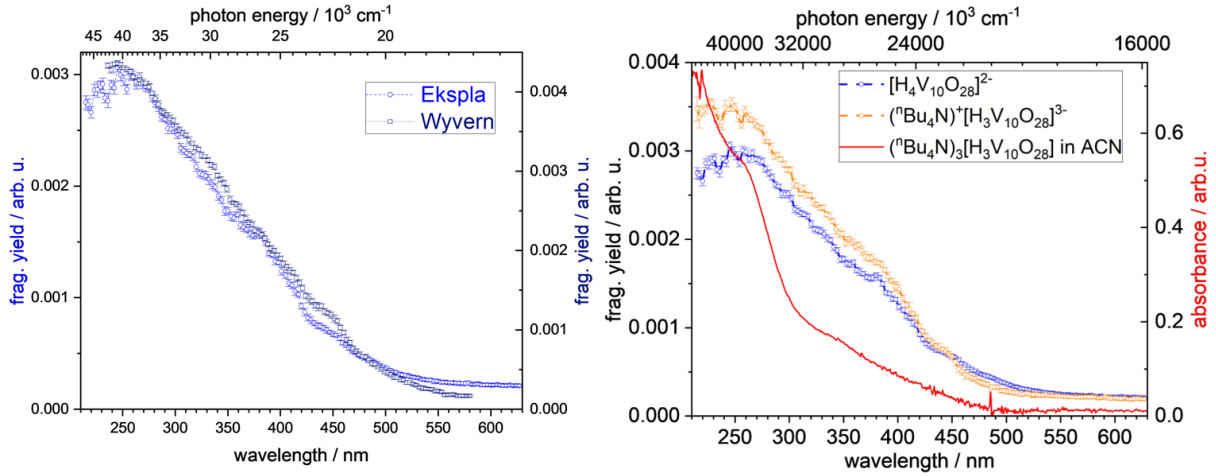

Figure 4.6 LEFT: UVPD spectra of $[H_4V_{10}O_{28}]^{2-}$ measured by ns laser system (EKSPLA, NT242) and the fs laser system (KMLabs, Wyvern 1000) at 3 nm step size and a constant pulse energy of 2 µJ. **RIGHT**: UVPD spectra of $[H_4V_{10}O_{28}]^{2-}$ and $[(^{n}Bu_4N)H_3V_{10}O_{28}]^{2-}$ measured with ns laser system (EKSPLA, NT242) at 3 nm step size and a constant pulse energy of 2 µJ, as well as the absorption spectrum of $(^{n}Bu_4N)_3H_3[V_{10}O_{28}]$ in ACN.

In same approach, UVPD investigations were conducted on the species $[Mn_4V_4O_{17}(OAc)_3]^{2-}$ and $[(^{n}Bu_4N)Mn_4V_4O_{17}(OAc)_3]^{-}$ and $(^{n}Bu_4N)_3[Mn_4V_4O_{17}(OAc)_3]*3H_2O$, with the latter studied by UV/Vis absorption spectroscopy in ACN (Figure 4.7). Similar conclusions as for the former species (Figure 4.6) could be drawn: $[Mn_4V_4O_{17}(OAc)_3]^{2-}$ and $[(^{n}Bu_4N)Mn_4V_4O_{17}(OAc)_3]^{-}$ show no drastic influence of the counter cation on the photochemical properties, though the corresponding spectrum in solution differs slightly; however it extends now further to the red compared to the gas phase spectra. In general, for both tapes of POVs (Figure 4.6 and

Figure 4.7), the general trend (= more or less structureless, slow rise towards the UV region) for the UV spectra in gas phase and solution is similar.

Note that the UVPD spectra for $[Mn_4V_4O_{17}(OAc)_3]^{2-}$ were measured by M.Sc. Marcel Schmitt, serving merely as a comparison to the $\{V_{10}\}$ and are here not discussed in further detail.

Probing the stable $[V_{10}O_{26}]^{2-}$ for photofragmentation, it turned out that only high laser pulse energies (≈150 µJ) produced minimal fragmentation yield. This indicates that multiple UV photons are required to dissociate $[V_{10}O_{26}]^{2-}$, likely via short-lived electronic states that equilibrate into vibrationally excited states. The large size and high heat capacity of the V-O framework allow it to accommodate several high-energy UV photons (ca. 4-5 eV) before dissociation occurs, reminiscent of the electronic excitation-to-heat conversion mechanism in sunscreen compounds,[263] which leads to a strongly nonlinear laser pulse energy dependence.

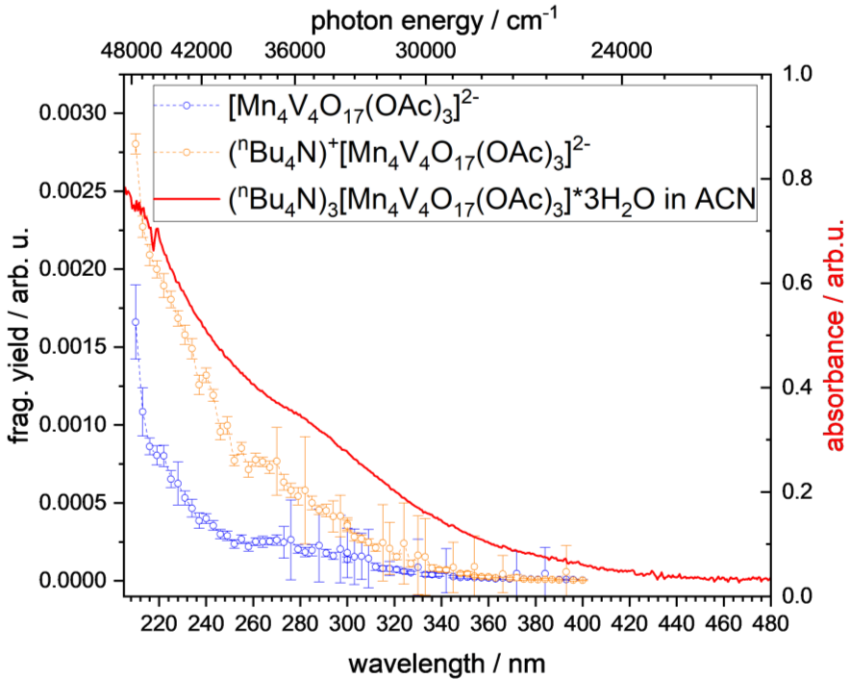

Figure 4.7 UVPD spectra of $[Mn_4V_4O_{17}(OAc)_3]^{2-}$ and $[(^nBu_4N)\ [Mn_4V_4O_{17}(OAc)_3]^-$ measured with ns laser system (EKSPLA, NT242) at 3 nm step size and a constant pulse energy of 2 µJ, as well as the absorption spectrum of $(^nBu_4N)_3[Mn_4V_4O_{17}(OAc)_3]*3H_2O$ in ACN.

On the other hand, for transient photodissociation, initial attempts to perform τ-PD experiments on $[(^nBu_4N)H_3V_{10}O_{28}]^{2-}$ and $[H_4V_{10}O_{28}]^{2-}$ were hindered by their instability in the

ion trap, resulting in an insufficient two-color enhancement upon pump-probe irradiation. In contrast, the $[V_{10}O_{26}]^{2-}$ species, owing to its greater stability, enabled τ-PD measurements, albeit only under high energy laser pulse conditions.

Transient photodissociation experiments on $[V_{10}O_{26}]^{2-}$ revealed ultrafast decay dynamics, as shown in Figure 4.8. Pump-probe measurements were conducted at two excitation wavelengths, 320 nm and 360 nm, which highlighted distinct ultrafast decay components.

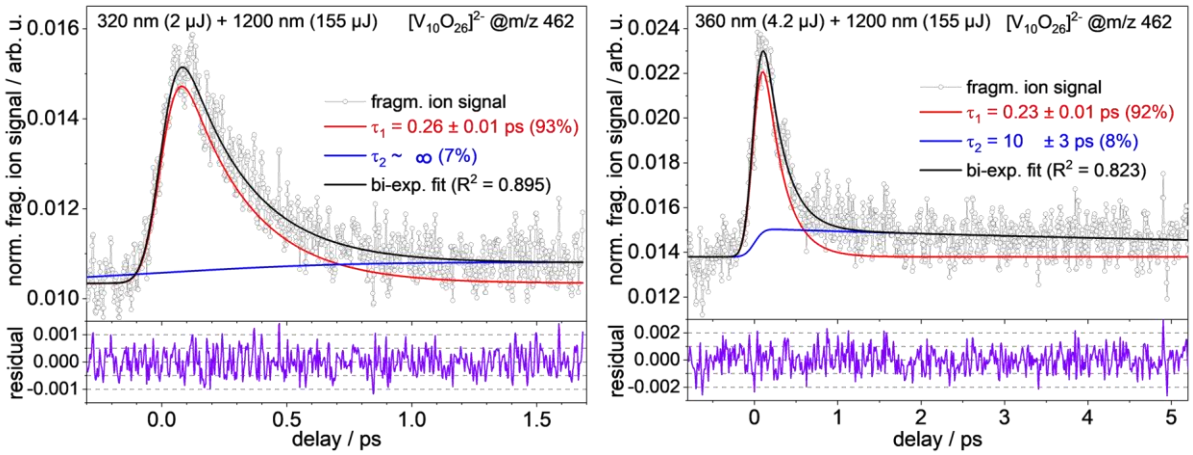

Figure 4.8 Transient photodissociation of $[V_{10}O_{26}]^{2-}$. **LEFT**: λ_{ex} =320 nm within a 2 ps time window. **RIGHT**: λ_{ex} =360 nm within a 6 ps time window. Decay fitted to a sum of two exponentials.

The primary decay component (~250 fs) could probably be attributed to nonradiative relaxation via internal conversion (IC), wherein the molecule crosses non-radiatively from an excited electronic state to a lower-lying state. A longer-lived secondary decay component (τ_2 > 10 ps), probably corresponding to vibrational relaxation or intersystem crossing (ISC), was also observed. This process dissipates energy through vibrational modes or transitions between spin states. However, the low amplitude of this secondary component and limitations in the experimental setup made its precise determination not possible. As a result, the given interpretation is considered speculative, moreover since also the static spectroscopic data is insufficient for a definitive assignment of electronic states.

The minimal spectroscopic data obtained underscores the inherent stability of $[V_{10}O_{26}]^{2-}$ which remained largely unaffected except under near damage-threshold (with respect to optical elements in the beam path) laser conditions. A common workaround in such cases

within action spectroscopy is "mass-tagging".[264] However here, attempts were made to form adducts at room temperature with cationic compounds such as silver salts or longer-lived complexes, like $[Ru(bpy)_3]^{2+}$ and not with an inert gas under cryogenic conditions which "mass-tagging" actually refers to. Unfortunately, these efforts were not successful, as no stable adducts could be identified or isolated in the ion trap.

4.1.4 Conclusion

This study represents the first steps toward exploring the photochemical properties of polyoxovanadates (POVs) using ion trap spectroscopy, i.e., in gas phase without influence of solvents. The mass spectrometric analysis, performed using electrospray ionization (ESI), revealed extensive fragmentation of the POV complexes in the gas phase at room temperature, highlighting their inherent fragility. Despite the isotopic simplicity of vanadium several fragmentation pathways could be assigned. The addition of formic acid helped to reduce the number of species (probably already in solution) and enhance the amount of stable species in the gas phase to some degree. Static UVPD spectra successfully revealed charge-transfer transitions within the vanadium-oxygen framework very similar to solution spectra, with the counterion (e.g., tetrabutylammonium) having no significant impact on the electronic states in the gas phase, moreover suggesting that these electronic transitions are largely intrinsic to the POV core. Transient photodissociation (τ-PD) experiments were hindered by the extreme fragility of certain species, such as $[(^nBu_4N)H_3V_{10}O_{28}]^{2-}$ and $[H_4V_{10}O_{28}]^{2-}$, which resulted in no significant ion signal under experimental conditions. However, the more stable $[V_{10}O_{26}]^{2-}$ species showed more promising results, revealing ultrafast decay dynamics (~250 fs and >10 ps). These results, though preliminary, provide a basis for future investigations into the excited-state dynamics of POVs. Note that here the first data of ion trap spectroscopy on $\{V_{10}\}$ are reported.

While these experiments have provided some insights into how the photochemistry of POVs might be studied in gas phase in the future, they also highlighted the strong challenges posed by the intrinsic properties of the complexes themselves and the limitations of the experimental setup. On the one hand, the fragility of the POVs led to significant fragmentation

during ionization, preventing the isolation of intact parent ions at sufficient to high count rates. In contrast, certain species, such as $[V_{10}O_{26}]^{2-}$, proved too stable under the experimental conditions, resisting photodissociation and requiring near damage-threshold laser conditions. This inherent instability of some complexes and the over-stability of others suggest that more robust and flexible complexes or adducts must be developed for future studies—complexes that are stable under normal conditions but can dissociate upon irradiation or two-color laser excitation. On the other hand, the experimental setup also presented limitations that hindered further progress. Despite testing various parameters of the existing system, including electrospray ionization (ESI) conditions, no significant improvement in ion stability was achieved. The resolution of the mass spectrometer was insufficient to resolve overlapping peaks, and the laser energy could not be increased beyond a certain threshold without risking damage to the optics. This clearly indicates the need for significant upgrades to the experimental approach, such as, e.g., employing cold-spray ESI to enhance ion stability or using mass spectrometers with higher resolution units like Q-TOF or ICR to better identify the compositions and charge states of the POVs under study and capture complex fragmentation patterns.

In conclusion, although the study faced significant obstacles, it has established some fundamental aspects for perspective research on POVs and similar molecular systems. The interdisciplinary collaboration between the Streb, Jacob, and Riehn groups was indispensable, as their contributions in the synthesis, computational modeling, and experimental design provided critical context for the findings. Moving forward, the focus should be on optimizing ionization techniques, improving mass resolution, and exploring alternative molecular systems with adapted fragmentation stability that could be more amenable to photodissociation studies. The lessons learned from the limitations encountered here will guide future efforts to understand the dynamics and reactivity of POVs and related systems. Ultimately, overcoming these challenges might allow for a better understanding of POVs elementary photophysical processes and thereon based for a better justified design and optimization of their application properties in areas such as energy conversion, photocatalysis, and other advanced technologies.

4.2 Ion Trap Spectroscopy on a Ru^{II}-phenazine-Rh^{III} dyad

4.2.1 Introduction

Transition metal-based complexes have long been at the forefront of photocatalytic research due to their remarkable ability to drive light-induced reactions, particularly in the quest for sustainable hydrogen production.[265] Among these, Ru^{II}-polypyridine complexes stand out as archetypal photosensitizers, capable of efficient energy transfer and charge separation.[266] These complexes are widely used in catalysis due to their tunable photophysical properties, including strong absorption in the visible range and efficient electron transfer capabilities, making them central to efforts in artificial photosynthesis and hydrogen generation.[267-268] Building on this framework, bimetallic complexes such as **Ru^{II}-tpphz-TM** have garnered significant attention for their catalytic potential, incorporating a Ru(II)-polypyridine antenna unit linked to a catalytically active transition metal (**TM = Rh^{III}, Pt^{II}, Pd^{II}**) center via a tetrapyrido[3,2-a:2',3'-c:3'',2''-h:2''',3'''-j]phenazine (tpphz) bridging ligand. This π-conjugated bridging ligand facilitates directed electron transfer, stabilizing charge-separated states, and enhancing catalytic efficiency.[269-270]

The design of such supramolecular assemblies offers several advantages over intermolecular systems, including reduced diffusion limitations, better stability under catalytic conditions, and easier optimization of structure-function relationships via chemical modifications. These features make **Ru^{II}-tpphz-TM** complexes ideal for investigating light-induced processes relevant to photocatalysis.[271]

Ion trap spectroscopy enables the exploration of the intrinsic photochemical properties of these systems in a solvent-free environment. The pioneering work of Dimitri Imanbaew on this topic utilized ion spectroscopy with pump-probe photodissociation to unravel ultrafast dynamics in molecular photocatalysts.[272] His study on the related **Ru^{II}-Pt^{II}** and **Ru^{II}-Pd^{II}** dyads revealed significant differences in photostability and charge transfer dynamics. Notably, the **Ru^{II}-Pt^{II}** complex exhibited after photoexcitation three primary decay time constants in the gas phase: 0.6 ps, 6.5 ps, and a longtime constant of ≫ 800 ps, whereas the latter was

attributed to a ligand-to-metal charge transfer (LMCT) process from the tpphz bridging ligand onto the catalytic center. The lifetimes aligned with those measured in solution but revealed slower LMCT dynamics in the gas phase, likely due to reduced stabilization of charge-separated states. Comparable trends were observed for **Ru^{II}-Pd^{II}** with time constants of 0.9 ps, 6.9 ps, and ≫800 ps, emphasizing again comparable initial dynamics but an increased time scale for the generation of the charge-separated state in gas phase compared to the obtained time constants in solution. These insights underscore the utility of gas-phase techniques for isolating intrinsic photochemical properties, highlighting the influence of solvation on the formation timescales of charge-separated states and therefore allow for enhanced resolution of these ultrafast processes.[203,271,273-274]

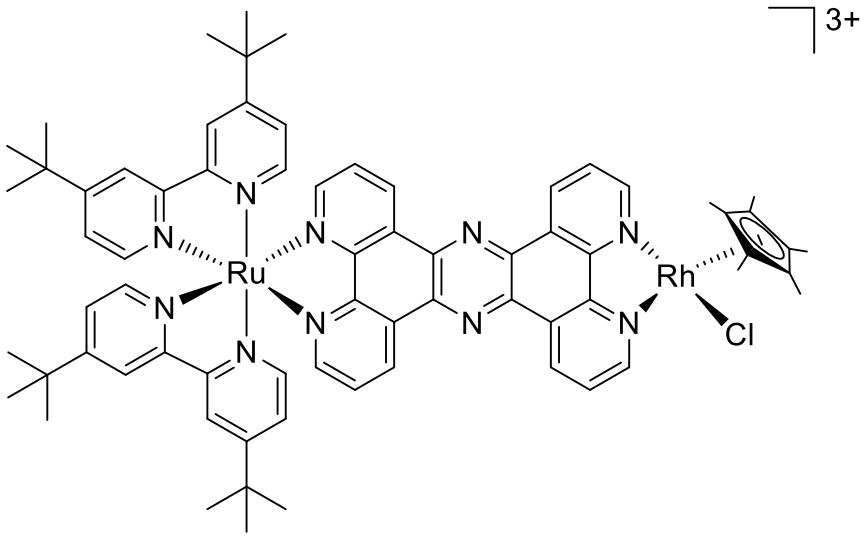

Figure 4.9 Structural representation of $[(tbbpy)_2Ru(tpphz)Rh(Cp^*)Cl]^{3+}$ complex cation.

Building upon these pioneering studies, my research focuses on the complex $[(tbbpy)_2Ru^{II}(tpphz)Rh^{III}(Cp^*)Cl]Cl(PF_6)_2$ (abbreviated: **RutpphzRh** for the triply charged cation in the following) (Figure 4.9), where tbbpy denotes 4,4'-di-tert-butyl-2,2'-bipyridine, and Cp* represents pentamethylcyclopentadienyl. The Cp* ligand, being highly electron-rich, acts as a robust electron donor, stabilizing the metal-ligand bond and enhancing thermal resilience. Its steric bulk mitigates intermolecular interactions, enabling the stabilization of complexes with fragile ligands.[275] The complex is distinct from the platinum(II) and palladium(II) centers explored by Dimitri Imanbaew due to the substitution with rhodium(III) as the catalytic center. In combination with electrochemical reduction in solution or electron transfer

dissociation/reduction (ETD/R) in the gas phase of an ion trap it provides an opportunity to investigate the influence of different oxidation states of Rh (possibly: III, II and I) on the electronic, structural and reactive properties of the complex (Figure 4.9).[271,276]

A recent experimental upgrade of the previously used ESI mass spectrometer system with an ETD/R capability has enabled the generation and spectroscopic investigation of such reduced species in the gas phase. This advancement opens new avenues for the examination of ground-state structures and excited-state dynamics of $[(tbbpy)_2Ru(tpphz)Rh(Cp^*)Cl]^{3+}$ and its reduced species via CID, ETD, UV photodissociation (UVPD) and transient photodissiciation (τ-PD) in a solvent free environment.[117,277] The complex $[(tbbpy)_2Ru^{II}(tpphz)Rh^{III}(Cp^*)Cl]Cl(PF_6)_2$ was synthesized by Prof. Dr. Sven Rau's group (Ulm University) and provided for the here reported ion trap investigations.

This conceptional study was pursued in more detail by B. Sc. Philipp Weber in his master's thesis, where additionally the variation of the bridging ligand was explored and highlighted.[240]

4.2.2 Experimental Setup

The mass spectrometric experiments were performed using a Bruker amaZon speed quadrupole ion trap spectrometer modified to enable laser-induced fragmentation. The complex salt $[(tbbpy)_2Ru^{II}(tpphz)Rh^{III}(Cp^*)Cl]Cl(PF_6)_2$ was dissolved in acetonitrile (10^{-6} M solution) and introduced into the gas phase via electrospray ionization (ESI). A syringe pump infused the sample at a flow rate of 120 µL/min, while nitrogen served as both nebulizing and drying gas, applied at 7 psi (~410 mbar) and 4 L/min at 180 °C.

The resulting cations were mass-selected and trapped within the radio-frequency Paul ion trap, which was equipped with optical ports for laser irradiation experiments. Therefore, three different experimental approaches for the investigation of this complex were performed: CID, UVPD, τ-PD. Collision-Induced Dissociation (CID) methods with custom scripts were used to monitor the fragmentation behavior and structural stabilities, i.e., appearance potentials for fragmentations, by varying the fragmentation amplitude and/or the

scan time. For the investigation of the photophysical properties of this complex UV photodissociation (UVPD) experiments were conducted. To achieve a photofragmentation spectrum, the total fragment yield as a function of wavelength (normalized to the photon flux) of a femtosecond laser system (Wyvern1000, KMLabs) was used to irradiate ions across wavelengths ranging from 236 nm to 650 nm in 3 nm steps, with a pulse energy of ca. 2 µJ. For the third experimental approach in this study transient photodissociation (τ-PD) experiments were performed. Therefore, pump-probe experiments were conducted using the same fs laser system. The pump pulse excited the trapped ions resonantly by UV radiation, while the probe pulse induced fragmentation non-resonantly at a NIR wavelength after varying time delay, revealing relaxation dynamics of electronically excited states. The relative polarization of the pump and probe beams was adjusted to the so-called magic angle. Additionally, parallel or perpendicular polarization configurations were adjusted using a Berek compensator functioning as a λ/2 plate for each laser beam.

Fragmentation yields were calculated as the ratio of fragment ion intensities to the sum of fragment and parent ion signal intensities. Fragmentation times were set to 100 ms, corresponding to ca. 100 laser pulse pairs per ion trap cycle.

4.2.3 Results and Discussion

The overview mass spectrum after ESI of **RutpphzRh** in Figure 4.10 shows mainly one prominent signal at m/z 431, assigned to $[RutpphzRh]^{3+}$ by comparison to simulated isotopic patterns.

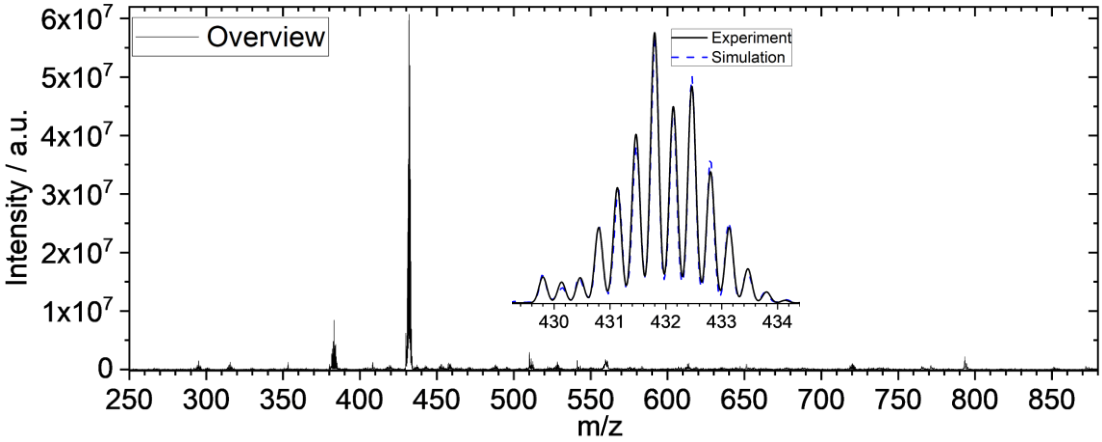

Figure 4.10 Overview mass spectrum of $[RutpphzRh]^{3+}$ showing a dominant signal at m/z 431, which is displayed with its isotopic pattern simulation in the inlet graphic.

After isolation of $[RutpphzRh]^{3+}$ in the ion trap ETD, CID and UVPD experiments were performed. ETD allows for the reduction of the tricationic complex into dicationic (647 m/z) and finally monocationic (1195 m/z) congeners (Figure 2.11).

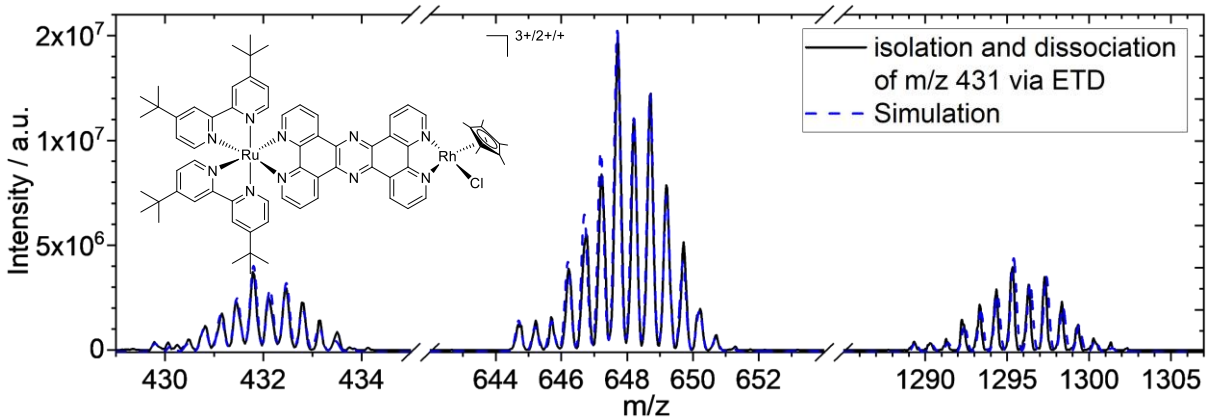

Figure 4.11 The isolation and ETD of $[RutpphzRh]^{3+}$ at m/z 431. The reduced species appears at m/z 647 ($[RutpphzRh]^{2+}$) and at m/z 1295 ($[RutpphzRh]^{+}$).

For identification of the observed species, CID and photodissociation (PD) experiments were performed. For $[RutpphzRh]^{3+}$ CID and PD result in the same type of fragments at m/z 419 and 511 (Figure 4.12).

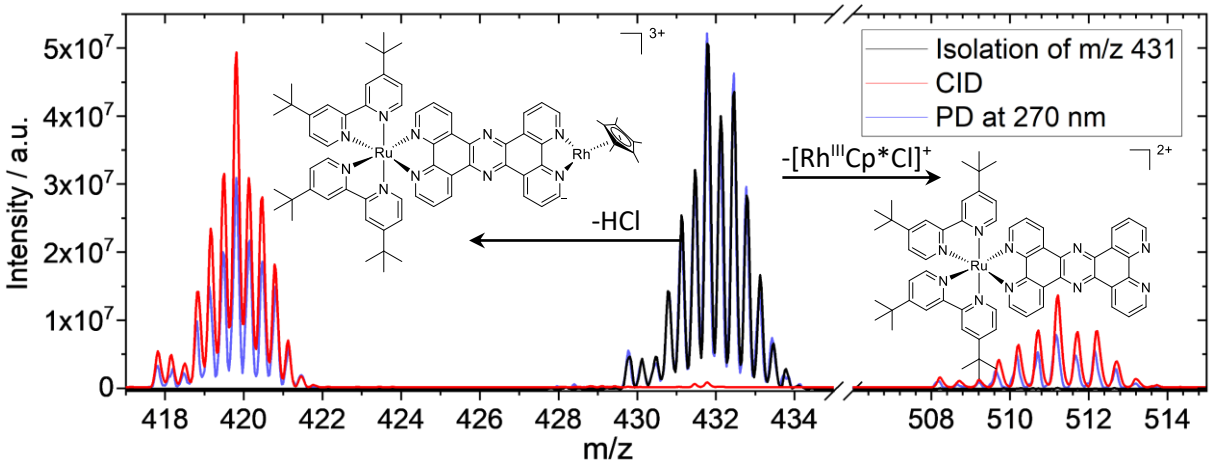

Figure 4.12 The isolation and ETD of $[RutpphzRh]^{3+}$ at m/z 431 and its fragmentation via CID and PD.

The fragment at m/z 419 stems from the (neutral) loss of HCl, which is a "good leaving group", often encountered in chlorine containing (organic) species. The proton most likely originates from the Cp* unit, as supported by previous studies on Cp* deprotonation leading to fulvene-like structures with metal stabilization (see [278], particularly Fig. 1). Further evidence is provided by collision-induced dissociation (CID) spectra (cf. Master's thesis of B. Sc. Philipp Weber, p. 41), where the intensity of the $[M–HCl]^+$ fragment decreases over time, while the fragment at m/z 510 becomes dominant.[240] In the competing fragmentation channel, the loss of the monocationic $[Rh(III)Cp^*Cl]^+$-group (m/z 272, experimentally observed[240]) reduces the total charge by one unit, yielding the dicationic species of $[Rutpphz]^{2+}$ at m/z 511. This charge-separation mechanism is consistent with established fragmentation behavior, as the diminished overall charge enhances the stability of the residual complex. Notably, the detected $[Rh(III)Cp^*Cl]^+$ fragment (m/z 272) corroborates the assignment of Rh(III) as the oxidation state upon elimination.

As observed for $[RutpphzRh]^{3+}$, the ETD reduced $[RutpphzRh]^{2+}$ species fragments under CID and PD conditions (Figure 4.13) via two pathways: (i) neutral HCl loss (m/z 629) and (ii) loss of a [RhCp*Cl] group (m/z 511). The absence of a signal at m/z 272[240] corresponding to

[Rh(III)Cp*Cl]$^+$ suggests the leaving group may be neutral [Rh(II)Cp*Cl], potentially indicating reduction of Rh(III) to Rh(II). However, this interpretation requires further validation, as Rh(II) has not been observed in analogous solution-phase electrochemical studies.

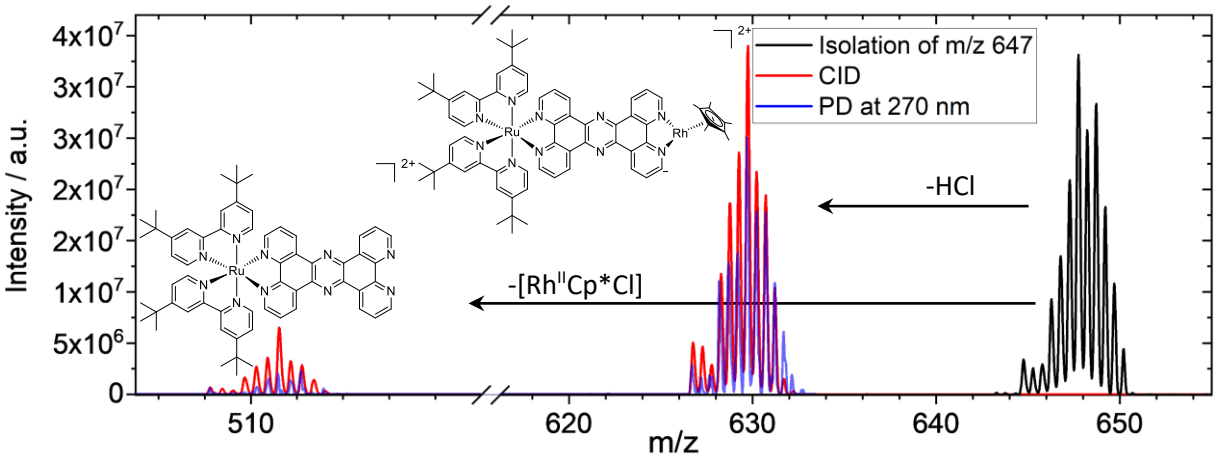

Figure 4.13 The isolation of [RutpphzRh]$^{2+}$ at m/z 647 and its fragmentation via CID and PD.

Finally, for the monocation [RutpphzRh]$^+$ (Figure 4.14) a fragment at m/z 1260, again by a loss of a neutral HCl is formed, while another fragment at m/z 1022 is formed again by the loss of a neutral [Rh^{II}Cp*Cl], forming the fragment ion [Rutpphz]$^+$. Note that minor fragment ions are observed but not further discussed.

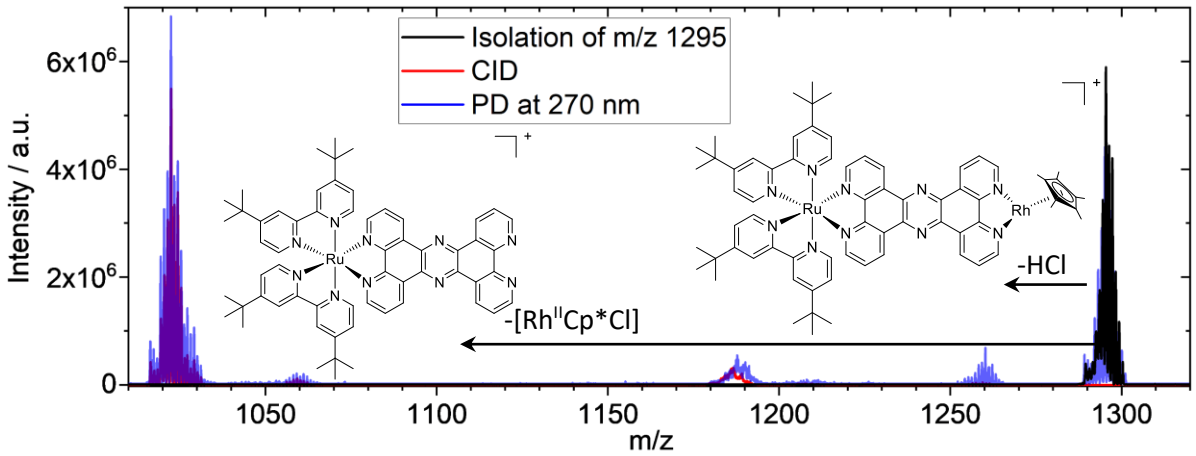

Figure 4.14 The isolation of [RutpphzRh]$^+$ at m/z 1295 and its fragmentation via CID and PD.

In summary, the fragmentation behavior of [RutpphzRh]$^{2+}$ and [RutpphzRh]$^+$ demonstrates that probably first the reduction of Rh^{III} to Rh^{II} occurs and in the second reduction step either the Ru center (Ru^{II} → Ru^{I}) or a ligand, probably phenazine (tpphz →tpphz$^-$), is reduced upon

ETD.[130,279-281] Note however, that from the mass spectrometric data alone it cannot be completely excluded that the first reduction step is not also leading to a ligand reduction since both bipyridine and tetrapyrido-phenazine could afford the reduction with up to two electrons. Note further, that in the latter case the apparent loss of the neutral [Rh^{II}Cp*Cl] unit would have to be explained by a preceding charge transfer before fragmentation. In Table 4.3 the major fragments of the different species [RutpphzRh]$^{3+/2+/+}$ are listed.

Table 4.3 Assignment of fragments occurring during the fragmentation of [RutpphzRh]$^{3+/2+/+}$ and $\boldsymbol{E_{com}^{50\%}}$ values of the complex in each cationic form. The assignment of the metal oxidation states is preliminary and based on the present results, as discussed in the text. Note that for the monocation a charge reduction in ligand sphere is assumed. Abbreviation: tbbpy= $C_8H_{18}N_2C_{10}H_6$, tpphz= $N_6C_{24}H_{12}$, Cp*= $C_5(CH_3)_5$.

Monoisotopic m/z	Loss	Assignment	$E_{com}^{50\%}$ * 10^{-3}
419	-HCl	$[(tbbpy)_2Ru^{II}(N_6C_{24}H_{11})Rh^{III}Cp^*]^{3+}$	
431	**Isolated**	**$[(tbbpy)_2Ru^{II}(N_6C_{24}H_{12})Rh^{III}Cp^*Cl]^{3+}$**	**262**
511	-$[Rh^{III}Cp^*Cl]^+$	$[(tbbpy)_2Ru^{II}(N_6C_{24}H_{12})]^{2+}$	
647	**Isolated**	**$[(tbbpy)_2Ru^{II}(N_6C_{24}H_{12})Rh^{II}Cp^*Cl]^{2+}$**	**232**
629	-HCl	$[(tbbpy)_2Ru^{II}(N_6C_{24}H_{11})Rh^{II}Cp^*]^{2+}$	
512	-$[Rh^{II}Cp^*Cl]$	$[(tbbpy)_2Ru^{II}(N_6C_{24}H_{12})]^{2+}$	
1022	-$[Rh^{II}Cp^*Cl]$	$[(tbbpy)_2Ru^{I}(N_6C_{24}H_{12})]^+$	
1260	-HCl	$[(tbbpy)_2Ru^{I}(N_6C_{24}H_{11})Rh^{II}Cp^*]^+$	
1295	**Isolated**	**$[(tbbpy)_2Ru^{I}(N_6C_{24}H_{12})Rh^{II}Cp^*Cl]^+$**	**343**

To gain insights into the energetics of the different fragmentation channels, particularly in dependence of the charge state of the dyadic complex, CID breakdown/appearance curves have been recorded for the according species.

The CID breakdown/appearance curves in Figure 4.15 were obtained under same ESI conditions for all investigated species. The derived $E_{com}^{50\%}$ values—0.00262 (trication), 0.00232 (dication), and 0.00343 (monocation)—reveal a stability trend: [RutpphzRh]$^+$ > [RutpphzRh]$^{3+}$ > [RutpphzRh]$^{2+}$. Since CID fragmentation follows the lowest-activation-energy pathway, the observed patterns suggest that ETD-induced changes in oxidation state (Ru/Rh) modify the weakest bond: (i) for [RutpphzRh]$^{3+}$/$^{2+}$, Rh–Cl cleavage (with possible Cp* deprotonation[278]) dominates, yielding HCl loss; (ii) for [RutpphzRh]$^+$, Rh–N,N(tpphz) cleavage prevails, producing [Rh^{II}Cp*Cl] loss, while HCl loss becomes negligible.

The dominant fragmentation channel of the trication and the dication is the HCl loss. Therefor a comparison can be made regarding the Rh-Cl bond strength. the observed $E_{com}^{50\%}$ values (0.00262 for the trication vs. 0.00232 for the dication) suggest that the Rh^{III}-Cl bond may be slightly more stable than the Rh^{II}-Cl bond in these systems.

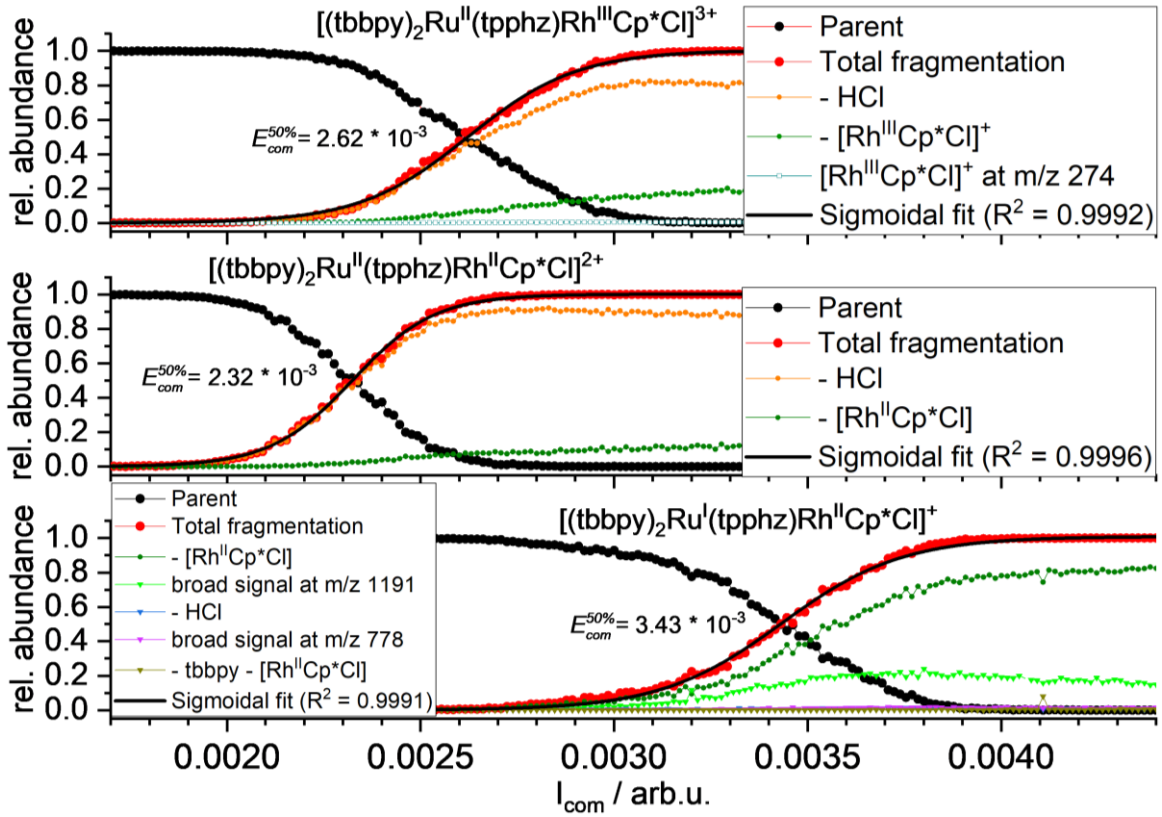

Figure 4.15 CID breakdown curves of m/z 431 ($[Ru^{II}tpphzRh^{III}]^{3+}$), m/z 647 ($[Ru^{II}tpphzRh^{II}]^{2+}$) and m/z 1295 ($[Ru^{I}tpphzRh^{II}]^{+}$). The assignment of the metal oxidation states is preliminary and based on the present results, as discussed in the text.

With higher charge reduction via ETD the main fragmentation channel appears to change, as for the monocation the Rh–N,N(tpphz) cleavage prevails. This shift in fragmentation channels with increasing reduction (from HCl loss to [RhCp*Cl] loss) suggests that the dominant fragmentation pathway changes as the system is reduced. Initially, HCl loss dominates; this channel appears to become even more favorable upon the first reduction (trication → dication). However, upon further reduction (monocation), HCl loss is no longer observed, and instead, neutral loss of $[Rh^{II}Cp^*Cl]$ occurs, albeit at higher energies. This indicates that the

Rh-N,N bond (of tpphz) becomes the preferred cleavage site in the monocation, though the exact reasons for this switch remain unclear.

Furthermore, the role of reduction in these changes is still speculative. While it is clear that the first charge reduction occurs on the Rh center ($Rh^{III} \rightarrow Rh^{II}$) evident by the disappearing signal of the [Rh^{II}Cp*Cl] group, the exact nature of the second reduction (e.g., metal-centered vs. ligand-centered) is uncertain. For the monocation, a ligand-centered reduction mechanism may be more plausible than the formation of Ru(I). For simplicity, the formula $[Ru^{I}tpphzRh^{II}]^{+}$ may also refer to $[Ru^{II}tpphzRh^{II}]^{+}$ where instead of the reduction $Ru^{II} \rightarrow Ru^{I}$ the additional electron is localized within the ligand environment.

In summary, the CID data document a clear shift in fragmentation behavior with charge state, but a straightforward interpretation of bond strengths or oxidation states is currently not possible. The observed trends likely reflect a combination of electronic and structural changes upon reduction, warranting further investigation. Moreover, it is evident that the successive reduction of the Ru-tpphz-Rh complex influences the electronic distribution across its whole structure, with the tpphz bridging ligand playing a key role in this process. This shift in electronic distribution, e.g., after photoexcitation, extends towards the Rh-Cl/Cp* bonds. By reducing the complex from the tricationic via the dicationic to the monocationic state, the positive electronic charge is successively decreased on the Rh center. Upon this process additional negative charge is accumulated in the Rh center vicinity probably stabilized by and/or located on the tetrapyrido-phenazine bridging ligand. Thus, reduction of the complex activates the Rh center as a first step for the catalytic hydrogen production.

An important aspect of this preliminary study on **Ru-tpphz-Rh** is to explore the applicability of combined mass spectrometric/spectroscopic techniques on the isolated different charge states of the complexes. Among these techniques UVPD spectroscopy allows for the recording of action absorption spectra and, further on by combination with quantum chemical calculations, for characterization of the relevant electronic states devoid of influence of solvation. Here I report the first results along these lines. The UVPD spectra of $[(tbbpy)_2Ru^{II}(tpphz)Rh^{III}(Cp^*)Cl]Cl(PF_6)_2$ in its tricationic ($[Ru^{II}tpphzRh^{III}]^{3+}$), dicationic

([Ru^{II}tpphzRh^{II}]$^{2+}$), and monocationic ([Ru^{I}tpphzRh^{II}]$^{+}$) charge states reveal distinct absorption bands categorized in four spectral regions (I-IV): 265–285 nm, 295–325 nm, 345–400 nm, and 415–525 nm (Figure 4.16), each highlighting unique photophysical properties.

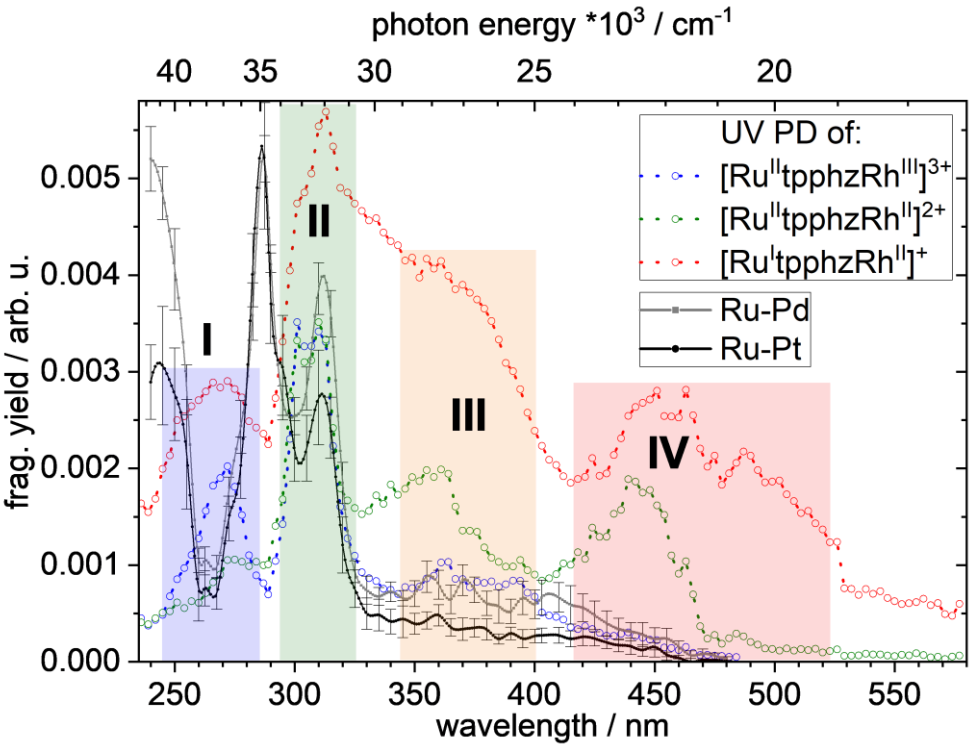

Figure 4.16 UVPD spectra of [Ru^{II}tpphzRh^{III}]$^{3+}$, [Ru^{II}tpphzRh^{II}]$^{2+}$ and [Ru^{I}tpphzRh^{II}]$^{+}$ via Wyvern laser system. For comparison, the UVPD spectra of Ru-Pd and Ru-Pt from [203] are plotted with independent scalability on the Y-axis, measured by Dr. D. Imanbaew. Four band ranges are marked I-IV: 265-285 nm, 295-325nm, 345-400 nm, 415-525 nm

The preliminary assignment and interpretation of these bands is mainly based on comparison with literature-known spectroscopic data of similar molecular systems, mostly from absorption measurements in solution, but also from the groundbreaking research of Dr. Dimitri Imanbaew on the similar systems Ru-Pd and Ru-Pt.[203]

The first spectral region, spanning 265–285 nm, is associated with π–π* transitions localized on the tbbpy ligand. Such transitions are well-documented in Ru-polypyridine complexes, where tbbpy or bpy (2,2'-bipyridine) ligands serves as a primary chromophore in this range. Similar behavior has been reported in UV-visible studies of [Ru(tbbpy)$_3$]$^{2+}$ systems in solution.[282] The band position in this range varies very subtly across the charge states, reflecting minor electronic perturbations caused by reduction.[283-285] However, the band

intensities clearly increase with degree of reduction. A note of caution upon comparison of the band intensities is here mandatory, since strictly speaking the *absolute intensities* should not be compared due to the arbitrary units used for the fragment yield. However, under the very similar experimental conditions used for data collections, at least a tendency (towards higher or lower fragment yield) could be established.

The second spectral region, 295–325 nm, corresponds mainly to π–π* transitions on the phen/tpphz ligand, as observed in Ru-Pd and Ru-Pt systems,[197] but might also contain π–π* transitions on the tbbpy and Cp* ligand. These transitions are particularly strong and display consistent intensity across the tricationic, dicationic, and monocationic species. Observations in this region align with earlier studies of $Ru(tbbpy)_2(tpphz)PtCl_2$ (including an indicated band splitting), where the tpphz ligand showed similar absorptions, which were also partially assigned before to contain $MLCT_{Pt}$ character. The invariance in band intensity across charge states indicates that the phen/tpphz-centered π–π* transitions remain largely unaffected by the reductions.[283,285]

In the 345-400 nm range, the observed bands are primarily attributed to π-π* transitions localized on the tpphz ligand. Computational studies have suggested potential inter-ligand charge transfer character in this spectral region.[274] Band positions shift between charge states, consistent with perturbation of the π-system upon reduction. Similar redox-dependent spectral changes have been documented for Ru-tpphz complexes.[203]

The final spectral region, 415–525 nm, is dominated by metal-to-ligand charge transfer (MLCT) transitions involving both Ru and Rh centers. The progressive red shift observed from the tricationic to monocationic species highlights the stabilization of charge-separated states as the system becomes increasingly reduced. Such shifts are characteristic of Ru-polypyridine complexes and have been corroborated by TDDFT calculations.[283,285] This region is analogous to the weak CT band observed in Ru-Pd and Ru-Pt systems, which was attributed to collisional quenching effects in the gas phase.[203]

For the tricationic species $[Ru^{II}tpphzRh^{III}]^{3+}$, the UVPD spectrum features a strong absorption at 310 nm, attributed to tpphz- and tbbpy-centered π–π* transitions, along with a sharp band at 380 nm indicative of Ru(II) MLCT. The latter transition suggests localized interactions between Ru(II) and the tpphz ligand, consistent with studies of Ru-polypyridine systems that exhibit well-defined MLCT bands in similar regions.[203,286] The dicationic species $[Ru^{II}tpphzRh^{II}]^{2+}$ displays additional absorptions, with prominent bands at 310 nm (π–π*), 360 nm (π–π*), and 440 nm (MLCT involving Rh and tpphz). The emergence of the 440 nm band might result from a contribution of a reduced Rh center.[287]

The monocationic species $[Ru^{I}tpphzRh^{II}]^{+}$ exhibits absorptions at 445 nm and 500 nm, consistent with MLCT transitions involving the Ru center and the tpphz bridging ligand, as observed in analogous Ru(II)-Rh(III) dyads with HAT bridges.[288] The pronounced red shift and stabilization of charge-separated states align with their assignment of low-energy CT bands to Ru→HAT or Rh→HAT transitions. Notably, their electrochemical data suggest that reduction preferentially localizes on the bridging ligand, supporting our ETD/CID observations of Rh–Cl bond weakening upon reduction.

The electronic transitions observed in the UVPD spectra are corroborated by theoretical studies on analogous systems. TDDFT calculations on Ru(II)-tpphz complexes confirm that bands in the 265–325 nm region arise from π→π* excitations localized on the tpphz and tbbpy ligands.[287] For the 345–400 nm region, computational studies suggest mixed character transitions with partial interligand charge transfer (ILCT) contribution, though experimental comparisons indicate π→π* transitions remain dominant.[289-290] The progressive red shift of MLCT bands (415–525 nm) in the monocationic state reflects enhanced electron delocalization across the tpphz bridge upon reduction[288], as suggested in TDDFT studies of similar systems.[269,287]

These spectra represent the first promising approaches for a detailed investigation of the intrinsic spectroscopic properties of the different charge states of the Ru-tpphz-Rh complexes and should finally lead, in combination with quantum chemical calculations and/or further experimental data (e.g. gas-phase vibrational spectra), to unequivocal assignment of the

oxidation states of the metal centers and ligands. Similar behaviors have been reported in Philip Weber's studies on RuRh complexes, such as RuRhPhen and RuRhAlk, where reductions led to red shifts in the MLCT region and band splitting, similar to the trends observed here.[240]

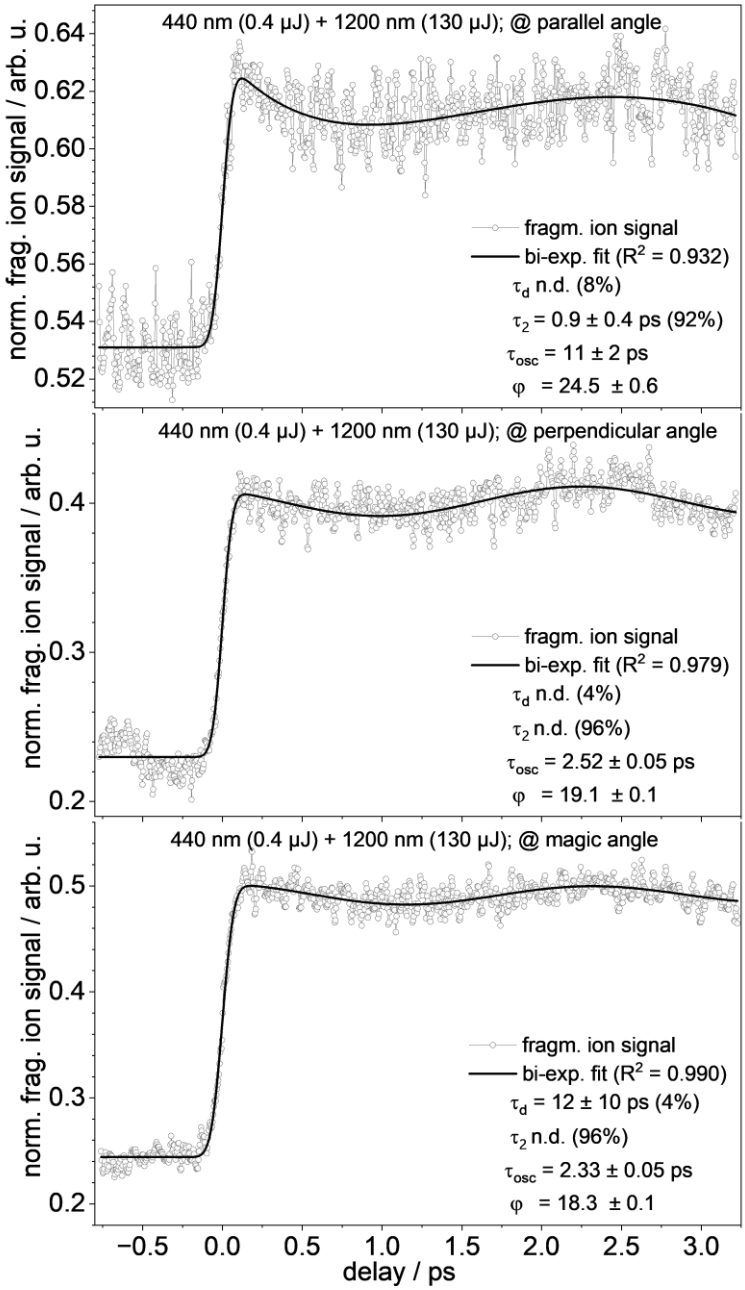

Figure 4.17 Transient photodissociation of $[Ru^{II}tpphzRh^{III}]^{3+}$ within a 4 ps time window showing wave packet dynamics. The time windows were recorded with pump and probe beam polarizations set relative to each other as parallel, perpendicular, and at the magic angle. Note that some time constants were not determinable (n.d.).

A further important aspect of this preliminary study on **Ru-tpphz-Rh** is to explore the applicability of ion trap-based time-resolved spectroscopic techniques on the isolated different charge states of the complexes. Here I report the first results using τ-PD transient pump-probe spectroscopy in order to characterize the electronically excited state lifetimes and possible ultrafast relaxation dynamics. Provisional transient photodissociation experiments were conducted based on the pioneering work of Dimitri Imanbaew on the **Ru-tpphz-Pt/Pd** complexes. Following these precedents, the pump wavelength was set to 440 nm with a pulse energy of 0.4 μJ and the probe at 1200 nm set at a pulse energy of 60 μJ. This choice of pulse energy was determined to minimize probe-only fragmentation, which was a significant issue at higher energies. The selected values provided a balanced trade-off, ensuring sufficient signal intensity for pump-probe measurements while maintaining acceptable pump-only to pump-probe fragment yield ratios.

The anisotropic absorption behavior of the **RutpphzRh** complex presented an additional challenge, necessitating careful control of the relative linear light polarization between the pump and probe laser beams. To address this, the polarization configurations were systematically varied between parallel, perpendicular, and magic angle (54.7°) the latter achieved using a Berek compensator. At the magic angle, the anisotropy is theoretically minimized to near zero, facilitating a more isotropic signal and providing a robust baseline for analyzing the dynamic behavior of the complex, as illustrated in Figure 4.17. However, the very moderate signal/background ratio of 1:1 constrained the determination of the molecular system's ultrafast dynamics. Despite these challenges the data in Figure 4.17 was fitted to a “step function” with an oscillatory component (eq. 16, Cp. 2.5.2), but its value of ca. 2.5 ps could only match very low-frequency (≈13.3 cm^{-1}) molecular modes and a more precise long delay-time investigation failed due to the poor obtained signal/noise.

In order to characterize the longer time dynamics, measurements were attempted over extended time windows ranging from 40 ps to 1600 ps (Figure 4.18). However, the underlying longer time constants could not be adequately resolved, necessitating the use of pump-probe measurements in conjunction with an electronically delayed nanosecond laser (NT242, EKSPLA). Such experiments were conducted by Philipp Weber and described in his master's thesis.[240]

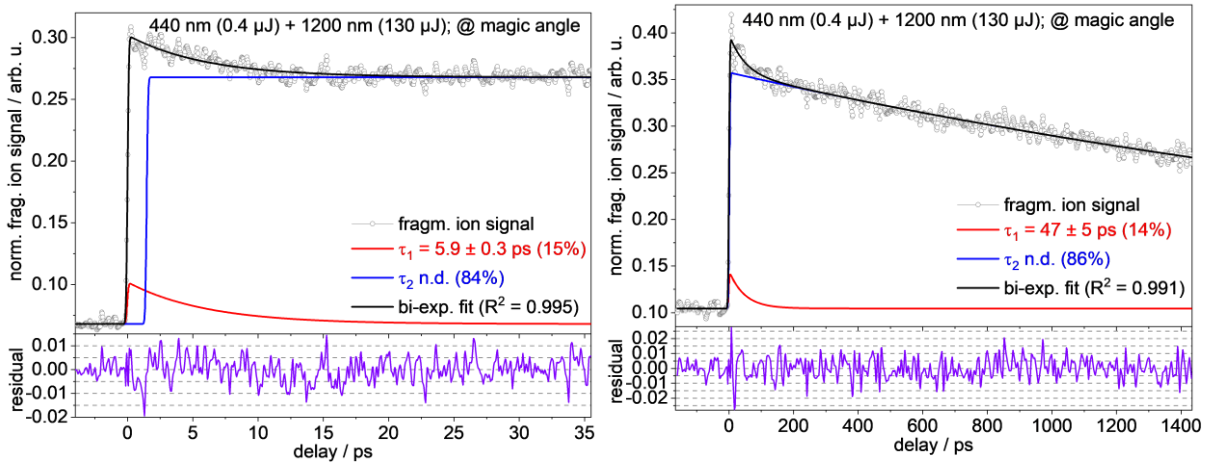

Figure 4.18 Transient photodissociation of $[Ru^{II}tpphzRh^{III}]^{3+}$ within a 40 ps (**LEFT**) and 1600 ps (**RIGHT**) time window. The pump and probe beam polarizations set relative to each other in magic angle condition. Note that the longer time constant was not determinable (n.d.).

4.2.4 Conclusion

The study of the $[RutpphzRh]^{3+}$ complex and its reduced congeners $[RutpphzRh]^{2+}$ and $[RutpphzRh]^{+}$ via ion trap mass spectrometric, CID, ETD, and UVPD analyses provided preliminary results on the energetics, spectroscopy and dynamics as a function of charge state for dyadic complexes. These outcomes could be categorized as a proof-of-concept study motivating further, more detailed investigations in the future in order to explore the actual metal and ligand oxidation states of such systems. The probable stepwise reduction from Rh(III) to Rh(II) and of the tpphz ligand significantly impacts the electronic distribution, bond strengths, and fragmentation pathways of the complex. CID experiments revealed a clear switch-over in fragmentation channel upon successive reduction. UVPD spectroscopic results demonstrated distinct MLCT and intraligand transitions with red-shifting absorption bands as the complex becomes increasingly reduced.

The interplay of electronic effects between the Ru and Rh centers, mediated by the tpphz bridging ligand, highlights its critical role in determining the photophysical and chemical behavior of the complex. These findings contribute to a deeper understanding of the electronic and photophysical properties of RuRh systems, with implications for their application in catalysis and optoelectronic devices. Further studies utilizing advanced pump-probe techniques are necessary to resolve dynamic processes on extended timescales.

These studies could open new avenues for optimizing the design and application of RuRh-based complexes.

5. Summary

This thesis explores the ultrafast photophysical and photochemical dynamics of TM complexes using gas-phase action spectroscopy. A combination of steady-state UVPD spectroscopy and τ-PD experiments was employed to investigate electronic structures, excited-state relaxation pathways, and ligand dissociation dynamics. Mass spectrometry was used to prepare and isolate ion ensembles, ensuring the study of intrinsic molecular properties free from solvent and counterion effects. Additional mass spectrometric techniques, including CID and ETD, were applied to probe molecular fragmentation patterns and charge-transfer processes. In parallel, computational studies, including DFT-based geometry optimizations, BDE and TD-DFT calculation were used to complement experimental findings. This work examines a range of TM systems, including ruthenium polypyridine complexes, heterobimetallic Au(I)/Ru(II) cyclophanyl complexes, Cu(I) coordination compounds, and polyoxovanadates, offering a comprehensive understanding of how molecular structure and electronic interactions govern photochemical behavior. By benchmarking gas-phase results against solution-phase data, this research establishes a framework for understanding solvent-mediated effects in TM photophysics. In the following the salient results of this thesis organized in relation to the underlying publications 1-4 and the additional projects are summarized.

Publication 1 The photodynamics and fragmentation behavior of the Ru(II) polypyridine complex $[Ru(bpy)_2(nicotinamide)_2]^{2+}$ (**1**) and its monoaqua derivative $[Ru(bpy)_2(nicotinamide)(H_2O)]^{2+}$ (**2**) were explored using both gas-phase and solution-phase spectroscopy. By combining mass spectrometry, UVPD, and τ-PD in the gas phase, along with TA spectroscopy in solution, we separated the intrinsic excited-state dynamics of these complexes from solvent-induced effects. Gas-phase UVPD spectra provided the first direct absorption data for these complexes in the absence of solvation, revealing spectral shifts between gas phase and solution absorption spectra as well as distinct spectral shifts between **1** and **2**. Photodissociation studies demonstrated that ligand loss pathways were highly dependent on the coordination environment: **1** preferentially lost nicotinamide,

while **2** exhibited selective dissociation of the aqua ligand. These observations emphasize that coordination geometry significantly influences relaxation and dissociation processes.

Time-resolved photodissociation experiments in the gas phase revealed two distinct time constants (0.5 ps and 3.0 ps), which closely matched early relaxation lifetimes observed in solution-phase TA spectroscopy, erroneously suggesting that initial excited-state relaxation is largely independent of solvation. However, a third, longer-lived component (~180 ps) was observed in solution experiments, highlighting the role of solvent-induced stabilization (solvent cage effect) in suppressing rapid ligand loss. The further study established that in the gas phase, ligand dissociation occurred in the few ps time range with an increased yield due to the energetic up-shift of the ^{3}MLCT state in the absence of its solvent stabilization. Conversely, in solution, solvent stabilization favors longer-lived ^{3}MLCT-^{3}MC-equilibria, shifting relaxation pathways towards electronic relaxation, significantly slowing down the dissociation and reducing the dissociation quantum yield. While the two short time constants in the gas phase are closely connected to dissociation, in solution they are linked to vibrational relaxation. These findings demonstrate how solvent interactions fundamentally alter the relaxation dynamics and photochemical behavior of Ru(II) complexes, highlighting the value of gas-phase spectroscopy for isolating intrinsic molecular properties.

Publication 2 This study systematically investigated how electronic substituents on bipyridine (X-series, $[Ru(X_2\text{-bpy})_2(nnp)_2]^{2+}$) and pyridine (Y-series, $[Ru(bpy)_2(py{-}Y)_2]^{2+}$) ligands affect the excited-state dynamics and reactivity of Ru(II) polypyridine complexes. Combining gas-phase UV photodissociation (UVPD), transient photodissociation (τ-PD), solution-phase transient absorption (TA) spectroscopy, and TD-DFT calculations, the work establishes direct correlations between substituent Hammett parameters (σ_p^+) and photophysical behavior.

Gas-phase UVPD spectra revealed that electron-withdrawing substituents on bipyridine ligands (X-series) induce red-shifts in MLCT bands, while similar groups on pyridine ligands (Y-series) cause blue-shifts. TD-DFT calculations accurately reproduced these trends, confirming that σ_p^+ values effectively correlate with MLCT energetics. τ-PD experiments

showed that in the X-series, increasing σ_p^+ leads to prolonged ^{3}MLCT lifetimes and reduced ligand dissociation yields, consistent with stabilization of the MLCT state and a wider MLCT–MC energy gap. In contrast, in the Y-series, increasing σ_p^+ leads to shortened ^{3}MLCT lifetimes and increased ligand dissociation yield, due to a lowering of the MC states and enhanced MLCT–MC coupling.

CID measurements and DFT-derived bond dissociation energies (BDEs) corroborate these observations: in the Y-series, increasing σ_p^+ values (i.e., more electron-withdrawing substituents) lead to lower BDEs and lower CID appearance energies ($E_{com}^{50\%}$), indicating weaker Ru–pyridine bonds and enhanced ligand loss. In the X-series, where substitution occurs on the bipyridine ligand and the dissociating ligand is nnp, the electronic influence was weaker and more indirect, with only a subtle trend in BDEs. Time-resolved photodissociation experiments revealed a strong link between ligand electronics and excited-state dynamics: in the X-series, higher σ_p^+ values lead to prolonged ^{3}MLCT lifetimes and suppressed dissociation, while in the Y-series, the same change in σ_p^+ values leads to shortened excited-state lifetimes and promoted photodissociation due to stabilization of the dissociative ^{3}MC states. These patterns were mirrored in solution-phase transient absorption spectroscopy. The ^{3}MLCT lifetimes in the Y-series increased with electron-donating substituents and correlated with lower ligand dissociation quantum yields. Importantly, both gas-phase and solution-phase data aligned with the kinetic models revealed in Publication 1.

In conclusion, this work demonstrates that the excited-state dynamics and photoreactivity of Ru(II) complexes can be fine-tuned through systematic ligand functionalization guided by the σ_p^+ parameter. The approach enables predictive control of MLCT and MC state energetics and provides a general framework for designing Ru-based complexes for photochemical applications. Moreover, gas-phase studies offer an efficient screening strategy to pre-select promising candidates for solution-phase behavior.

Publication 3 This study explores the photophysical and catalytic properties of heterobimetallic Au(I)/Ru(II) cyclophanyl complexes with systematically varied Ru–Au

distances, achieved through positional isomerism on a [2.2]paracyclophane (**PCP**) bridge. Using UVPD, solution-phase TA spectroscopy, electrochemistry, DFT calculations, and catalytic testing, the work probes how spatial arrangement affects metal-to-metal (M–M) communication. Gas-phase UVPD spectra revealed broad MLCT features, including an additional red-shifted band (~350 nm) in the para-isomer (**pAuRu**), possibly linked to a weak shoulder observed at 320 nm in solution. All AuRu isomers displayed higher extinction coefficients than the monometallic PCP-Ru reference. TD-DFT analysis confirmed MLCT transitions originate from the Ru center to the phenylpyridine and bipyridyl ligands, with the LUMO localized on the bipyridyl and the HOMO on the cyclometalated fragment.

Transient absorption spectroscopy identified three decay components. The two fast ones matched typical Ru(II) polypyridine behavior, while a third ($\tau_3 \approx 68$ ps) was most pronounced in **pAuRu** and attributed to charge separation or internal conversion. Under 312 nm excitation, **pAuRu** exhibited a distinct excited-state absorption (ESA) at 475 nm that intensified after 1 ps, further supporting the presence of an alternative relaxation pathway. Notably, gas-phase photodissociation spectroscopy revealed no direct Ru–Au coupling, suggesting such interactions are stronger in solution.

Electrochemical measurements showed that the Ru(II) → Ru(III) oxidation potential shifted systematically with metal separation. **pAuRu** exhibited the largest shift (+0.09 V), consistent with through-space electronic communication. Catalytic testing in the Meyer–Schuster rearrangement confirmed the functional impact of M–M interactions: **pAuRu** achieved the highest yield (63%), while other isomers (**mAuRu**: 30%, **oAuRu**: 26%, **gAuRu**: 13%) were less active. This trend correlates with metal separation and likely reflects a combination of electronic communication, redox tuning, and steric effects.

In conclusion, this work demonstrates that careful spatial control of metal centers can fine-tune excited-state dynamics and redox behavior, offering a pathway to optimize cooperative effects in bimetallic photocatalysts.

Publication 4 This study investigates how nuclearity, charge, and structural features influence the photophysical behavior of heteroleptic Cu(I) complexes with pyridyl-triazole ligands, including mononuclear species (**CuL**, **CuLH**, **[CuLH]$^+$**) and dinuclear analogues (**Cu_2L'**, **$Cu_2L'H_2$**, **$[Cu_2L'H]^+$**, **$[Cu_2L'H_2]^{2+}$**). They were compared using gas-phase UV photodissociation (UVPD), time-resolved photodissociation (τ-PD), solution-phase transient absorption (TA) spectroscopy, luminescence lifetime measurements, and photoluminescence quantum yield determination, TADF and theoretical calculations. A comprehensive set of spectroscopic and computational methods was employed, including UV/Vis and emission spectroscopy, solution-phase transient absorption (TA), gas-phase UV photodissociation (UVPD), time-resolved photodissociation (τ-PD), photoluminescence quantum yield and lifetime measurements, as well as advanced theoretical calculations.

Time-resolved experiments revealed three characteristic decay components across all systems. Ultrafast sub-picosecond and few-picosecond processes were assigned to structural relaxation and vibrational cooling, followed by slower components (~30–50 ps in solution) attributed to intersystem crossing (ISC) into long-lived ^{3}MLCT states. In the gas phase, these processes were confirmed by τ-PD but extended beyond the picosecond detection window, indicating increased triplet lifetimes in the absence of solvent-mediated nonradiative decay.

Gas-phase UVPD spectra showed broader and red-shifted MLCT bands for dinuclear species compared to mononuclear complexes, reflecting increased electronic delocalization and stronger ligand–metal interactions. TD-DFT and *GW*-BSE calculations reproduced these shifts and showed only minor flattening distortions in the excited-state geometries due to steric constraints, which contribute to enhanced photostability and reduced nonradiative decay. Importantly, no direct Cu–Cu bonding interaction was observed; the differences between mono- and dinuclear systems arise from ligand-mediated effects and structural rigidity. In subsequent experiments, microsecond-resolved gas-phase τ-PD using a ns-pump/fs-probe setup enabled tracking of long-lived excited states. For **[CuLH]$^+$**, lifetimes of τ_1 = 2.8 µs and τ_2 = 22 µs were observed, while **$[Cu_2L'H]^+$** exhibited τ_1 = 37 µs and τ_2 > 270 µs, suggesting enhanced triplet-state stabilization in the dimer. These extended lifetimes are consistent with

TADF-relevant behavior previously inferred from temperature-dependent emission studies of **$[Cu_2L'H_2]^{2+}$**. Oscillatory modulations in the decay traces, especially in the dimer, were attributed to secular ion motion within the RF quadrupole field of the ion trap rather than to intrinsic molecular processes, emphasizing the importance of accounting for instrument effects in long-time gas-phase kinetics.

Overall, this work shows that nuclearity and structural control can modulate excited-state behavior in Cu(I) complexes. Dinuclear systems exhibit notably prolonged triplet lifetimes and features relevant to delayed fluorescence, making them promising platforms for photonic or photocatalytic applications.

Additional Researches The study of **polyoxovanadates (POVs)** investigated the intrinsic photophysical properties, focusing on the $\{V_{10}\}$ cluster, using ion trap UV photodissociation (UVPD) and time-resolved photodissociation (τ-PD) spectroscopy. Electrospray ionization (ESI) of $[V_{10}O_{28}]^{6-}$ resulted in significant fragmentation, reflecting high gas-phase fragility. Adding formic acid reduced the number of fragment ions and enhanced signal intensity for $[H_4V_{10}O_{28}]^{2-}$ and $[(^nBu_4N)H_3V_{10}O_{28}]^{2-}$ enabling spectroscopic measurements. UVPD spectra showed broad, unstructured absorption features, similar to solution-phase spectra of $\{V_{10}\}$ species, and largely unaffected by the presence of the $^nBu_4N^+$ counterion. This suggests that the observed transitions are intrinsic to the vanadate framework. τ-PD experiments were only feasible for $[V_{10}O_{26}]^{2-}$, a thermally stable dehydration product. The transient signal exhibited a fast decay (~250 fs), followed by a slower component >10 ps, likely reflecting internal conversion and vibrational relaxation. Other species lacked sufficient signal stability due to extensive fragmentation and overlapping isotopic distributions. The study highlights both the potential and limitations of ion trap spectroscopy for POVs and points to the need for softer ionization methods (e.g., cold-spray ESI) and higher-resolution mass spectrometry to enable broader and more reliable investigation of these fragile, complex systems.

The study of the **Ru^{II}-phenazine-Rh^{III} dyad** ($[(tbbpy)_2Ru(tpphz)Rh(Cp^*)Cl]^{3+}$, RutpphzRh) explored the gas-phase properties and its reduced species using ion trap CID, ETD, UVPD, and

τ-PD spectroscopy. ETD allowed generation of the dication $[RutpphzRh]^{2+}$ and monocation $[RutpphzRh]^{+}$. Fragmentation pathways shifted with charge state: the trication and dication primarily lost HCl, while the monocation eliminated [RhCp*Cl], indicating increased lability of the Rh–N(tpphz) bond upon reduction. UVPD spectra for the three charge states featured bands in four spectral regions (265–525 nm). While π–π* transitions were assigned with some confidence, the MLCT and charge-transfer bands—particularly in the 415–525 nm range—show red shifts upon reduction. However, the exact electronic nature (e.g., Ru→tpphz vs. Rh→tpphz vs. ligand-centered) remains ambiguous. Preliminary assignments suggest increasing delocalization and stabilization of charge-separated states with reduction, supported by TDDFT comparisons to related systems. τ-PD measurements on $[RutpphzRh]^{3+}$ showed low-amplitude oscillations (~2.5 ps) but no resolvable lifetimes. Signal limitations and anisotropy effects hindered kinetic modeling. Overall, this proof-of-concept highlights the need for further data and theory to unambiguously assign excited states in Ru–Rh complexes.

6. Final Conclusion

This thesis has explored the intrinsic photophysical and photochemical behavior of various transition metal (TM) complexes using gas-phase action spectroscopy in combination with complementary spectroscopic and computational methods. It was demonstrated that the presence or absence of solvation—particularly through hydration shells—significantly influences the nature and dynamics of charge-transfer states. Studies on Ru(II) polypyridine complexes showed that systematic ligand substitution enables precise control over the MLCT–MC equilibria, allowing photophysical properties to be tuned for specific applications. Furthermore, in heterobimetallic Au(I)/Ru(II) complexes, it was shown that the distance between two metal centers—modulated via [2.2]paracyclophane scaffolds—affects electronic communication and excited-state relaxation. Similar structure-property relationships were observed in Cu(I) systems, where changes in nuclearity and charge state strongly influenced MLCT state lifetimes and promoted thermally activated delayed fluorescence (TADF) in dinuclear species. By contrast, polyoxovanadates (POVs) were found to be extremely fragile under gas-phase ESI conditions, highlighting the need for improved ionization techniques to study such species spectroscopically. For the Ru(II)–tpphz–Rh(III) complex, first insights into charge-dependent fragmentation and absorption behavior were obtained, though electronic state assignments remain partially ambiguous due to signal limitations.

Overall, this work demonstrates that gas-phase spectroscopy provides a powerful tool to access intrinsic electronic structures and excited-state dynamics of TM complexes—unobscured by solvent or solid-state effects. Across several structurally and electronically diverse systems, it was shown that the gas phase offers unique mechanistic insight not attainable in condensed phases, and thus establishes a valuable framework for the rational design of photoactive complexes in catalysis, energy conversion, and optoelectronic applications.

7. References

[1] J. K. McCusker, "Electronic structure in the transition metal block and its implications for light harvesting." *Science* **2019**, *363* (6426), 484-488. DOI: 10.1126/science.aav9104

[2] Y. Qin, Q. Peng, "Ruthenium Sensitizers and Their Applications in Dye-Sensitized Solar Cells." *International Journal of Photoenergy* **2012**, *2012*, 1-21. DOI: 10.1155/2012/291579

[3] A. n. Vlček, "The life and times of excited states of organometallic and coordination compounds." *Coordination Chemistry Reviews* **2000**, *200-202*, 933-978. DOI: 10.1016/s0010-8545(00)00308-8

[4] J. K. McCusker, "Photocatalysis. Fuel from photons." *Science* **2001**, *293* (5535), 1599-1601. DOI: 10.1126/science.1064112

[5] A. Dodabalapur, "Organic light emitting diodes." *Solid State Communications* **1997**, *102* (2-3), 259-267. DOI: 10.1016/s0038-1098(96)00714-4

[6] W. R. Browne, A. A. Holder, M. A. Lawrence, J. L. Bullock Jr, L. Lilge, "Ruthenium Complexes." 2018. DOI: 10.1002/9783527695225.

[7] D. W. Thompson, A. Ito, T. J. Meyer, "$[Ru(bpy)_3]^{2+*}$ and other remarkable metal-to-ligand charge transfer (MLCT) excited states." *Pure and Applied Chemistry* **2013**, *85* (7), 1257-1305. DOI: 10.1351/pac-con-13-03-04

[8] A. H. Zewail, "Femtochemistry: Atomic-Scale Dynamics of the Chemical Bond." *The Journal of Physical Chemistry A* **2000**, *104* (24), 5660-5694. DOI: 10.1021/jp001460h

[9] J. L. Knee, L. R. Khundkar, A. H. Zewail, "Picosecond monitoring of a chemical reaction in molecular beams: Photofragmentation of $R–I \rightarrow R^{\ddagger}+I$." *The Journal of Chemical Physics* **1985**, *83* (4), 1996-1998. DOI: 10.1063/1.449339

[10] N. F. Scherer, J. L. Knee, D. D. Smith, A. H. Zewail, "Femtosecond Photofragment Spectroscopy: The Reaction ICN → CN + I." *The Journal of Physical Chemistry* **1985**, *89* (24), 5141-5143. DOI: 10.1021/j100270a001

[11] J. S. Baskin, A. H. Zewail, "Freezing Atoms in Motion: Principles of Femtochemistry and Demonstration by Laser Stroboscopy." *Journal of Chemical Education* **2001**, *78* (6). DOI: 10.1021/ed078p737

[12] A. H. Zewail, "Femtochemistry: Recent Progress in Studies of Dynamics and Control of Reactions and Their Transition States." *The Journal of Physical Chemistry* **1996**, *100* (31), 12701-12724. DOI: 10.1021/jp960658s

[13] R. Berera, R. van Grondelle, J. T. Kennis, "Ultrafast transient absorption spectroscopy: principles and application to photosynthetic systems." *Photosynthesis Research* **2009**, *101* (2-3), 105-118. DOI: 10.1007/s11120-009-9454-y

[14] H. Chosrowjan, S. Taniguchi, F. Tanaka, "Ultrafast fluorescence upconversion technique and its applications to proteins." *The FEBS Journal* **2015**, *282* (16), 3003-3015. DOI: 10.1111/febs.13180

[15] J. Xu, J. R. Knutson, "Ultrafast fluorescence spectroscopy via upconversion applications to biophysics." *Methods Enzymol* **2008**, *450*, 159-183. DOI: 10.1016/S0076-6879(08)03408-3

[16] A. Stolow, A. E. Bragg, D. M. Neumark, "Femtosecond time-resolved photoelectron spectroscopy." *Chemical Reviews* **2004**, *104* (4), 1719-1757. DOI: 10.1021/cr020683w

[17] M. Maiuri, M. Garavelli, G. Cerullo, "Ultrafast Spectroscopy: State of the Art and Open Challenges." *Journal of the American Chemical Society* **2019**, *142* (1), 3-15. DOI: 10.1021/jacs.9b10533

[18] B. M. Garraway, K. A. Suominen, "Wave-packet dynamics: new physics and chemistry in femto-time." *Reports on Progress in Physics* **1995**, *58* (4), 365-419. DOI: 10.1088/0034-4885/58/4/001

[19] M. Gruebele, A. H. Zewail, "Femtosecond wave packet spectroscopy: Coherences, the potential, and structural determination." *The Journal of Chemical Physics* **1993**, *98* (2), 883-902. DOI: 10.1063/1.464253

[20] M. Chergui, "Ultrafast photophysics of transition metal complexes." *Accounts of Chemical Research* **2015**, *48* (3), 801-808. DOI: 10.1021/ar500358q

[21] M. Chergui, "On the interplay between charge, spin and structural dynamics in transition metal complexes." *Dalton Transactions* **2012**, *41* (42), 13022-13029. DOI: 10.1039/c2dt30764b

[22] S. Karmakar, S. Keshavamurthy, "Intramolecular vibrational energy redistribution and the quantum ergodicity transition: a phase space perspective." *Physical Chemistry Chemical Physics* **2020**, *22* (20), 11139-11173. DOI: 10.1039/d0cp01413c

[23] S. E. Braslavsky, "Glossary of terms used in photochemistry, 3rd edition (IUPAC Recommendations 2006)." *Pure and Applied Chemistry* **2007**, *79* (3), 293-465. DOI: 10.1351/pac200779030293

[24] T. J. Penfold, E. Gindensperger, C. Daniel, C. M. Marian, "Spin-Vibronic Mechanism for Intersystem Crossing." *Chemical Reviews* **2018**, *118* (15), 6975-7025. DOI: 10.1021/acs.chemrev.7b00617

[25] R. M. van der Veen, A. Cannizzo, F. van Mourik, A. Vlcek, Jr., M. Chergui, "Vibrational relaxation and intersystem crossing of binuclear metal complexes in solution." *Journal of the American Chemical Society* **2011**, *133* (2), 305-315. DOI: 10.1021/ja106769w

[26] E. Pomarico, P. Pospisil, M. E. F. Bouduban, J. Vestfrid, Z. Gross, S. Zalis, M. Chergui, A. Vlcek, "Photophysical Heavy-Atom Effect in Iodinated Metallocorroles: Spin-Orbit Coupling and Density of States." *The Journal of Physical Chemistry A* **2018**, *122* (37), 7256-7266. DOI: 10.1021/acs.jpca.8b05311

[27] P. Muller, K. Brettel, "$[Ru(bpy)_3]^{2+}$ as a reference in transient absorption spectroscopy: differential absorption coefficients for formation of the long-lived ^{3}MLCT excited state." *Photochemical & Photobiological Sciences* **2012**, *11* (4), 632-636. DOI: 10.1039/c2pp05333k

[28] D. M. A.-R. a. J. K. McCusker, "An Overview of the Physical and Photophysical Properties of $[Ru(bpy)_3]^{2+}$." 2018. DOI: 10.1002/9783527674145.ch1.

[29] J. Twilton, C. Le, P. Zhang, M. H. Shaw, R. W. Evans, D. W. C. MacMillan, "The merger of transition metal and photocatalysis." *Nature Reviews Chemistry* **2017**, *1* (7). DOI: 10.1038/s41570-017-0052

[30] M. Baharfar, A. C. Hillier, G. Mao, "Charge-Transfer Complexes: Fundamentals and Advances in Catalysis, Sensing, and Optoelectronic Applications." *Advanced Materials* **2024**, *36* (42), e2406083. DOI: 10.1002/adma.202406083

[31] X. Long, W. Qiu, Z. Wang, Y. Wang, S. Yang, "Recent advances in transition metal–based catalysts with heterointerfaces for energy conversion and storage." *Materials Today Chemistry* **2019**, *11*, 16-28. DOI: 10.1016/j.mtchem.2018.09.003

[32] A. Pigliucci, G. Duvanel, L. M. Daku, E. Vauthey, "Investigation of the influence of solute-solvent interactions on the vibrational energy relaxation dynamics of large molecules in liquids." *The Journal of Physical Chemistry A* **2007**, *111* (28), 6135-6145. DOI: 10.1021/jp069010y

[33] J. Zanzi, Z. Pastorel, C. Duhayon, E. Lognon, C. Coudret, A. Monari, I. M. Dixon, Y. Canac, M. Smietana, O. Basle, "Counterion Effects in $[Ru(bpy)_3](X)_2$-Photocatalyzed Energy Transfer Reactions." *JACS Au* **2024**, *4* (8), 3049-3057. DOI: 10.1021/jacsau.4c00384

[34] A. M. Khan, S. Khizar, S. A. Khan, S. Ali, A. Shah, M. F. Nazar, F. J. Iftikhar, F. Shah, R. A. Khan, A. R. Khan, "Investigation of counterion effects of transition metal cations (Fe^{3+}, Cu^{2+}, Zn^{2+}) on cetrimonium bromide using cyclic voltammetry." *Journal of Molecular Liquids* **2020**, *313*. DOI: 10.1016/j.molliq.2020.113599

[35] T. Hiraga, N. Kitamura, H. B. Kim, S. Tazuke, N. Mori, "Pressure and temperature effects on the excited state of the tris(2,2'-bipyridine)ruthenium(II) complex." *The Journal of Physical Chemistry* **1989**, *93* (8), 2940-2945. DOI: 10.1021/j100345a019

[36] S. Scheins, J. Overgaard, G. A. Timco, A. Stash, Y. S. Chen, F. K. Larsen, M. Christensen, M. R. Jorgensen, S. R. Madsen, M. S. Schmokel, B. B. Iversen, "Pressure versus temperature effects on intramolecular electron transfer in mixed-valence complexes." *Chemistry* **2013**, *19* (1), 195-205. DOI: 10.1002/chem.201201669

[37] V. E. Bondybey, M. K. Beyer, "Temperature Effects in Transition Metal Ion and Cluster Ion Reactions." *The Journal of Physical Chemistry A* **2001**, *105* (6), 951-960. DOI: 10.1021/jp002746p

[38] T. B. van Driel, K. S. Kjaer, R. W. Hartsock, A. O. Dohn, T. Harlang, M. Chollet, M. Christensen, W. Gawelda, N. E. Henriksen, J. G. Kim, K. Haldrup, K. H. Kim, H. Ihee, J. Kim, H. Lemke, Z. Sun, V. Sundstrom, W. Zhang, D. Zhu, K. B. Moller, M. M. Nielsen, K. J. Gaffney, "Atomistic characterization of the active-site solvation dynamics of a model photocatalyst." *Nature Communications* **2016**, *7*, 13678. DOI: 10.1038/ncomms13678

[39] A. O. Dohn, E. O. Jonsson, K. S. Kjaer, T. B. van Driel, M. M. Nielsen, K. W. Jacobsen, N. E. Henriksen, K. B. Moller, "Direct Dynamics Studies of a Binuclear Metal Complex in Solution: The Interplay Between Vibrational Relaxation, Coherence, and Solvent Effects." *The Journal of Physical Chemistry Letters* **2014**, *5* (14), 2414-2418. DOI: 10.1021/jz500850s

[40] J. Eng, C. Gourlaouen, E. Gindensperger, C. Daniel, "Spin-vibronic quantum dynamics for ultrafast excited-state processes." *Accounts of Chemical Research* **2015**, *48* (3), 809-817. DOI: 10.1021/ar500369r

[41] M. Radon, G. Drabik, M. Hodorowicz, J. Szklarzewicz, "Performance of quantum chemistry methods for a benchmark set of spin-state energetics derived from experimental data of 17 transition metal complexes (SSE17)." *Chemical Science* **2024**, *15* (48), 20189-20204. DOI: 10.1039/d4sc05471g

[42] A. Nandy, C. Duan, M. G. Taylor, F. Liu, A. H. Steeves, H. J. Kulik, "Computational Discovery of Transition-metal Complexes: From High-throughput Screening to Machine Learning." *Chemical Reviews* **2021**, *121* (16), 9927-10000. DOI: 10.1021/acs.chemrev.1c00347

[43] K. D. Vogiatzis, M. V. Polynski, J. K. Kirkland, J. Townsend, A. Hashemi, C. Liu, E. A. Pidko, "Computational Approach to Molecular Catalysis by 3d Transition Metals: Challenges and Opportunities." *Chemical Reviews* **2019**, *119* (4), 2453-2523. DOI: 10.1021/acs.chemrev.8b00361

[44] A. Ghosh, "Transition metal spin state energetics and noninnocent systems: challenges for DFT in the bioinorganic arena." *Journal of Biological Inorganic Chemistry* **2006**, *11* (6), 712-724. DOI: 10.1007/s00775-006-0135-4

[45] K. Egashira, A. Terasaki, "Optical absorption spectrum of the chromium dimer cation: Measurements by photon-trap and photodissociation spectroscopy." *Chemical Physics Letters* **2015**, *635*, 13-15. DOI: 10.1016/j.cplett.2015.06.038

[46] S. K. Stephenson, R. J. Saykally, "Velocity modulation spectroscopy of ions." *Chemical Reviews* **2005**, *105* (9), 3220-3234. DOI: 10.1021/cr040100d

[47] M. Allan, E. Kloster-Jensen, J. P. Maier, "Emission spectra of the radical cations of diacetylene ($\tilde{A}^2\Pi_u \rightarrow \tilde{X}^2\Pi_g$), triacetylene ($\tilde{A}^2\Pi_g \rightarrow \tilde{X}^2\Pi_u$), and tetraacetylene ($\tilde{A}^2\Pi_u \rightarrow \tilde{X}^2\Pi_g, O_0^0$), and the

lifetimes of some vibronic levels of the Ã states." *Chemical Physics* **1976**, *17* (1), 11-18. DOI: 10.1016/0301-0104(76)85002-1

[48] M. Allan, J. P. Maier, O. Marthaler, E. Kloster-Jensen, "Emission spectra of two $C_6H_6^+$ cations in the gas phase: competition of the radiative, $\tilde{A}(\pi^{-1}) \rightarrow \tilde{X}(\pi^{-1})$, and fragmentation decay of the $\tilde{A}(\pi^{-1})$ excited state of 2,4- and 1,3-hexadiyne radical cations." *Chemical Physics* **1978**, *29* (3), 331-337. DOI: 10.1016/0301-0104(78)85083-6

[49] J. P. Maier, "Open-shell organic cations: spectroscopic studies by means of their radiative decay in the gas phase." *Accounts of Chemical Research* **1982**, *15* (1), 18-23. DOI: 10.1021/ar00073a003

[50] J. P. Maier, "Spectroscopic structure of open-shell polyatomic cations." *Chemical Society Reviews* **1988**, *17*. DOI: 10.1039/cs9881700045

[51] J. P. Maier, "Approaches to spectroscopic characterization of cations." *International journal of mass spectrometry and ion processes* **1991**, *104* (1), 1-22. DOI: 10.1016/0168-1176(91)85001-3

[52] D. Imanbaew, Y. Nosenko, C. Kerner, K. Chevalier, F. Rupp, C. Riehn, W. R. Thiel, R. Diller, "Excited-state dynamics of a ruthenium(II) catalyst studied by transient photofragmentation in gas phase and transient absorption in solution." *Chemical Physics* **2014**, *442*, 53-61. DOI: 10.1016/j.chemphys.2014.03.005

[53] J. Martens, G. Berden, C. R. Gebhardt, J. Oomens, "Infrared ion spectroscopy in a modified quadrupole ion trap mass spectrometer at the FELIX free electron laser laboratory." *Review of Scientific Instruments* **2016**, *87* (10), 103108. DOI: 10.1063/1.4964703

[54] H. Kang, C. Jouvet, C. Dedonder-Lardeux, S. Martrenchard, C. Charrière, G. Grégoire, C. Desfrançois, J. P. Schermann, M. Barat, J. A. Fayeton, "Photoinduced processes in protonated tryptamine." *The Journal of Chemical Physics* **2005**, *122* (8), 84307. DOI: 10.1063/1.1851503

[55] M. Yamashita, J. B. Fenn, "Electrospray ion source. Another variation on the free-jet theme." *The Journal of Physical Chemistry* **1984**, *88* (20), 4451-4459. DOI: 10.1021/j150664a002

[56] D. Nolting, T. Schultz, I. V. Hertel, R. Weinkauf, "Excited state dynamics and fragmentation channels of the protonated dipeptide H_2N-Leu-Trp-COOH." *Phys Chem Chem Phys* **2006**, *8* (44), 5247-5254. DOI: 10.1039/b609726j

[57] D. Nolting, R. Weinkauf, I. V. Hertel, T. Schultz, "Excited-state relaxation of protonated adenine." *ChemPhysChem: A European Journal of Chemical Physics and Physical Chemistry* **2007**, *8* (5), 751-755. DOI: 10.1002/cphc.200600727

[58] L. Schüßler, R. G. E. Israil, P. Hütchen, W. R. Thiel, R. Diller, C. Riehn, "Ultrafast spectroscopy of Ru(II) polypyridine complexes in the gas phase and the liquid phase: $[Ru(2,2'\text{-bipyridine})_2(\text{nicotinamide})_2]^{2+}$." *Physical Chemistry Chemical Physics* **2023**, *25* (6), 4899-4914. DOI: 10.1039/d2cp03765c

[59] P. Hütchen, "Rutheniumbipyridylkomplexe und deren photochemische Variation." Doctoral dissertation, Technische Universität Kaiserslautern, Kaiserslautern, Germany, 2021. https://nbn-resolving.org/urn:nbn:de:hbz:386-kluedo-63369.

[60] Y. Zhang, M. Schulz, M. Wächtler, M. Karnahl, B. Dietzek, "Heteroleptic diimine–diphosphine Cu(I) complexes as an alternative towards noble-metal based photosensitizers: Design strategies, photophysical properties and perspective applications." *Coordination Chemistry Reviews* **2018**, *356*, 127-146. DOI: 10.1016/j.ccr.2017.10.016

[61] Y. Zhang, P. Traber, L. Zedler, S. Kupfer, S. Grafe, M. Schulz, W. Frey, M. Karnahl, B. Dietzek, "Cu(i) vs. Ru(ii) photosensitizers: elucidation of electron transfer processes within a series of structurally related complexes containing an extended pi-system." *Physical Chemistry Chemical Physics* **2018**, *20* (38), 24843-24857. DOI: 10.1039/c8cp04595j

[62] C. Zippel, R. Israil, L. Schüßler, Z. Hassan, E. K. Schneider, P. Weis, M. Nieger, C. Bizzarri, M. M. Kappes, C. Riehn, "Metal-to-Metal Distance Modulated Au (I)/Ru (II) Cyclophanyl Complexes: Cooperative Effects in Photoredox Catalysis." *Chemistry–A European Journal* **2021**, *27* (61), 15188-15201. DOI: 10.1002/chem.202102341

[63] M. Grupe, P. Boden, P. Di Martino-Fumo, X. Gui, C. Bruschi, R. Israil, M. Schmitt, M. Nieger, M. Gerhards, W. Klopper, "Time-Resolved Spectroscopy and Electronic Structure of Mono-and Dinuclear Pyridyl-Triazole/DPEPhos-Based Cu (I) Complexes." *Chemistry–A European Journal* **2021**, *27* (61), 15252-15271. DOI: 10.1002/chem.202102760

[64] C. Bizzarri, A. P. Arndt, S. Kohaut, K. Fink, M. Nieger, "Mononuclear and dinuclear heteroleptic Cu(I) complexes based on pyridyl-triazole and DPEPhos with long-lived excited-state lifetimes." *Journal of Organometallic Chemistry* **2018**, *871*, 140-149. DOI: 10.1016/j.jorganchem.2018.07.013

[65] B. Schwarz, C. Streb, "Architectural control of urea in supramolecular 1D strontium vanadium oxide chains." *Dalton Transactions* **2015**, *44* (9), 4195-4199. DOI: 10.1039/c4dt03691c

[66] B. Schwarz, J. Forster, M. K. Goetz, D. Yücel, C. Berger, T. Jacob, C. Streb, "Visible-Light-Driven Water Oxidation by a Molecular Manganese Vanadium Oxide Cluster." *Angewandte Chemie International Edition* **2016**, *55* (21), 6329-6333. DOI: 10.1002/anie.201601799

[67] M. Ernst, D. B. Silva, R. R. Silva, R. Z. Vencio, N. P. Lopes, "Mass spectrometry in plant metabolomics strategies: from analytical platforms to data acquisition and processing." *Natural Product Reports* **2014**, *31* (6), 784-806. DOI: 10.1039/c3np70086k

[68] J. B. Fenn, "Electrospray wings for molecular elephants (Nobel lecture)." *Angewandte Chemie International Edition in English* **2003**, *42* (33), 3871-3894. DOI: 10.1002/anie.200300605

[69] J. B. Fenn, M. Mann, C. K. Meng, S. F. Wong, C. M. Whitehouse, "Electrospray ionization for mass spectrometry of large biomolecules." *Science* **1989**, *246* (4926), 64-71. DOI: 10.1126/science.2675315

[70] J. A. Loo, H. R. Udseth, R. D. Smith, "Peptide and protein analysis by electrospray ionization-mass spectrometry and capillary electrophoresis-mass spectrometry." *Analytical Biochemistry* **1989**, *179* (2), 404-412. DOI: 10.1016/0003-2697(89)90153-x

[71] I. Domínguez, A. Garrido Frenich, R. Romero-González, "Mass spectrometry approaches to ensure food safety." *Analytical Methods* **2020**, *12* (9), 1148-1162. DOI: 10.1039/c9ay02681a

[72] G. R. Asbury, J. Klasmeier, H. H. Hill, Jr., "Analysis of explosives using electrospray ionization/ion mobility spectrometry (ESI/IMS)." *Talanta* **2000**, *50* (6), 1291-1298. DOI: 10.1016/s0039-9140(99)00241-6

[73] Bruker, "Training Document: amaZon Series User Manual Rev. A." 2016. (accessed 05.03.2025).

[74] M. W. Forbes, A. M. Nagy, R. A. Jockusch, "Photofragmentation of and electron photodetachment from a GFP model chromophore in a quadrupole ion trap." *International Journal of Mass Spectrometry* **2011**, *308* (2-3), 155-166. DOI: 10.1016/j.ijms.2011.08.016

[75] J. Zeleny, "Instability of Electrified Liquid Surfaces." *Physical review* **1917**, *10* (1), 1-6. DOI: 10.1103/PhysRev.10.1

[76] M. Dole, L. L. Mack, R. L. Hines, R. C. Mobley, L. D. Ferguson, M. B. Alice, "Molecular Beams of Macroions." *The Journal of Chemical Physics* **1968**, *49* (5), 2240-2249. DOI: 10.1063/1.1670391

[77] M. Yamashita, J. B. Fenn, "Negative ion productlon with the electrospray ion source." *The Journal of Physical Chemistry* **1984**, *88* (20), 4671-4675. DOI: 10.1021/j150664a046

[78] C. M. Whitehouse, R. N. Dreyer, M. Yamashita, J. B. Fenn, "Electrospray interface for liquid chromatographs and mass spectrometers." *Analytical chemistry* **1985**, *57* (3), 675-679. DOI: 10.1021/ac00280a023

[79] Bruker, "Training Document: amaZon series_Compass1.7_intro to ion trap MS."
[80] L. Konermann, E. Ahadi, A. D. Rodriguez, S. Vahidi, "Unraveling the mechanism of electrospray ionization." *Analytical chemistry* **2013**, *85* (1), 2-9. DOI: 10.1021/ac302789c
[81] G. I. Taylor, "Disintegration of water drops in an electric field." *Proceedings of the Royal Society of London. Series A. Mathematical and Physical Sciences* **1997**, *280* (1382), 383-397. DOI: 10.1098/rspa.1964.0151
[82] M. Cloupeau, B. Prunet-Foch, "Electrostatic spraying of liquids in cone-jet mode." *Journal of electrostatics* **1989**, *22* (2), 135-159. DOI: 10.1016/0304-3886(89)90081-8
[83] L. Rayleigh, "XX. On the equilibrium of liquid conducting masses charged with electricity." *The London, Edinburgh, and Dublin Philosophical Magazine and Journal of Science* **1882**, *14* (87), 184-186.
[84] M. Cloupeau, B. Prunet-Foch, "Electrostatic spraying of liquids: Main functioning modes." *Journal of electrostatics* **1990**, *25* (2), 165-184. DOI: 10.1016/0304-3886(90)90025-q
[85] J. V. Iribarne, B. A. Thomson, "On the evaporation of small ions from charged droplets." *The Journal of Chemical Physics* **1976**, *64* (6), 2287-2294. DOI: 10.1063/1.432536
[86] P. Kebarle, "A brief overview of the present status of the mechanisms involved in electrospray mass spectrometry." *Journal of mass spectrometry* **2000**, *35* (7), 804-817. DOI: 10.1002/1096-9888(200007)35:7<804::AID-JMS22>3.0.CO;2-Q
[87] P. Kebarle, M. Peschke, "On the mechanisms by which the charged droplets produced by electrospray lead to gas phase ions." *Analytica Chimica Acta* **2000**, *406* (1), 11-35. DOI: 10.1016/s0003-2670(99)00598-x
[88] M. Wilm, "Principles of electrospray ionization." *Molecular & cellular proteomics* **2011**, *10* (7), M111 009407. DOI: 10.1074/mcp.M111.009407
[89] S. Banerjee, S. Mazumdar, "Electrospray ionization mass spectrometry: a technique to access the information beyond the molecular weight of the analyte." *International journal of analytical chemistry* **2012**, *2012* (1), 282574. DOI: 10.1155/2012/282574
[90] J. F. Parcher, M. Wang, A. G. Chittiboyina, I. A. Khan, "In-source collision-induced dissociation (IS-CID): Applications, issues and structure elucidation with single-stage mass analyzers." *Drug Testing and Analysis* **2018**, *10* (1), 28-36. DOI: 10.1002/dta.2249
[91] W. Paul, H. Steinwedel, "Notizen: Ein neues Massenspektrometer ohne Magnetfeld." *Zeitschrift für Naturforschung A* **1953**, *8* (7), 448-450. DOI: 10.1515/zna-1953-0710
[92] W. Paul, "Electromagnetic Traps for Charged and Neutral Particles (Nobel Lecture)." *Angewandte Chemie International Edition in English* **2003**, *29* (7), 739-748. DOI: 10.1002/anie.199007391
[93] R. I. Thompson, T. J. Harmon, M. G. Ball, "The rotating-saddle trap: a mechanical analogy to RF-electric-quadrupole ion trapping?"; *Canadian Journal of Physics* **2002**, *80* (12), 1433-1448. DOI: 10.1139/p02-110
[94] G. Littich, "Electrostatic control and transport of ions on a planar trap for quantum information processing." Master's Thesis, ETH Zürich and University of California, Berkeley, 2011.
[95] R. E. March, "An Introduction to Quadrupole Ion Trap Mass Spectrometry." *Journal of mass spectrometry* **1997**, *32* (4), 351-369. DOI: 10.1002/(sici)1096-9888(199704)32:4<351::Aid-jms512>3.0.Co;2-y
[96] R. E. March, "Quadrupole ion trap mass spectrometry: theory, simulation, recent developments and applications." *Rapid Communications in Mass Spectrometry* **1998**, *12* (20), 1543-1554. DOI: 10.1002/(sici)1097-0231(19981030)12:20<1543::Aid-rcm343>3.0.Co;2-t
[97] R. E. March, "Quadrupole ion trap mass spectrometry: a view at the turn of the century." *International Journal of Mass Spectrometry* **2000**, *200* (1-3), 285-312. DOI: 10.1016/s1387-3806(00)00345-6

[98] J. F. T. Raymond E. March, "Quadrupole Ion Trap Mass Spectrometry." John Wiley & Sons, 2005.

[99] M. G. Berlin-Udi, "Treatments of a Surface Ion Trap: A Study of Electric-Field Noise near a Contaminated Metal Surface." Doctoral thesis, University of California, Berkeley, 2020. https://escholarship.org/uc/item/8tp4d3x3.

[100] F. M. Arscott, "Theory and Application of Mathieu Functions. By N. W. Mclachlan. Pp. xii, 401. (Dover, New York.)." *The Mathematical Gazette* **1968**, *52* (379), 94-95. DOI: 10.2307/3614519

[101] L. Ruby, "Applications of the Mathieu equation." *American Journal of Physics* **1996**, *64* (1), 39-44. DOI: 10.1119/1.18290

[102] R. N. Jazar, R. N Jazar, "Mathieu equation." In *Approximation Methods in Science and Engineering*, Springer New York, NY, 2020; pp 395-472.

[103] J. N. Louris, J. S. Brodbelt-Lustig, R. Graham Cooks, G. L. Glish, G. J. van Berkel, S. A. McLuckey, "Ion isolation and sequential stages of mass spectrometry in a quadrupole ion trap mass spectrometer." *International journal of mass spectrometry and ion processes* **1990**, *96* (2), 117-137. DOI: 10.1016/0168-1176(90)87025-c

[104] G. Stafford, Jr., "Ion trap mass spectrometry: a personal perspective." *Journal of the American Society for Mass Spectrometry* **2002**, *13* (6), 589-596. DOI: 10.1016/S1044-0305(02)00385-9

[105] K. R. Jennings, "Collision-induced decompositions of aromatic molecular ions." *International Journal of Mass Spectrometry and Ion Physics* **1968**, *1* (3), 227-235. DOI: 10.1016/0020-7381(68)85002-8

[106] A. K. Shukla, J. H. Futrell, "Tandem mass spectrometry: dissociation of ions by collisional activation." *Journal of mass spectrometry* **2000**, *35* (9), 1069-1090.

[107] A. R. Johnson, E. E. Carlson, "Collision-Induced Dissociation Mass Spectrometry: A Powerful Tool for Natural Product Structure Elucidation." *Anal Chem* **2015**, *87* (21), 10668-10678. DOI: 10.1021/acs.analchem.5b01543

[108] J. M. Wells, S. A. McLuckey, "Collision-induced dissociation (CID) of peptides and proteins." *Methods Enzymol* **2005**, *402*, 148-185. DOI: 10.1016/S0076-6879(05)02005-7

[109] E. J. Soderblom, M. B. Goshe, "Collision-induced dissociative chemical cross-linking reagents and methodology: Applications to protein structural characterization using tandem mass spectrometry analysis." *Anal Chem* **2006**, *78* (23), 8059-8068. DOI: 10.1021/ac0613840

[110] K. Levsen, H. Schwarz, "Collisional Activation Mass Spectrometry—A New Probe for Determining the Structure of Ions in the Gas Phase." *Angewandte Chemie International Edition in English* **1976**, *15* (9), 509-519. DOI: 10.1002/anie.197605091

[111] A. K. Shukla, J. H. Futrell, "Tandem mass spectrometry: dissociation of ions by collisional activation." *Journal of mass spectrometry* **2000**, *35* (9), 1069-1090. DOI: 10.1002/1096-9888(200009)35:9<1069::AID-JMS54>3.0.CO;2-C

[112] V. Gabelica, E. De Pauw, "Internal energy and fragmentation of ions produced in electrospray sources." *Mass Spectrometry Reviews* **2005**, *24* (4), 566-587. DOI: 10.1002/mas.20027

[113] J. Roithova, "Characterization of reaction intermediates by ion spectroscopy." *Chemical Society Reviews* **2012**, *41* (2), 547-559. DOI: 10.1039/c1cs15133a

[114] J. Oomens, B. G. Sartakov, G. Meijer, G. von Helden, "Gas-phase infrared multiple photon dissociation spectroscopy of mass-selected molecular ions." *International Journal of Mass Spectrometry* **2006**, *254* (1-2), 1-19. DOI: 10.1016/j.ijms.2006.05.009

[115] R. Hartmer, D. A. Kaplan, C. R. Gebhardt, T. Ledertheil, A. Brekenfeld, "Multiple ion/ion reactions in the 3D ion trap: Selective reagent anion production for ETD and PTR from a single compound." *International Journal of Mass Spectrometry* **2008**, *276* (2-3), 82-90. DOI: 10.1016/j.ijms.2008.05.002

[116] J. E. Syka, J. J. Coon, M. J. Schroeder, J. Shabanowitz, D. F. Hunt, "Peptide and protein sequence analysis by electron transfer dissociation mass spectrometry." *Proceedings of the National Academy of Sciences* **2004**, *101* (26), 9528-9533. DOI: 10.1073/pnas.0402700101

[117] M. S. Kim, A. Pandey, "Electron transfer dissociation mass spectrometry in proteomics." *Proteomics* **2012**, *12* (4-5), 530-542. DOI: 10.1002/pmic.201100517

[118] J. Wiesner, T. Premsler, A. Sickmann, "Application of electron transfer dissociation (ETD) for the analysis of posttranslational modifications." *Proteomics* **2008**, *8* (21), 4466-4483. DOI: 10.1002/pmic.200800329

[119] N. M. Riley, "Advancing Electron Transfer Dissociation Technologies for Characterization of Proteomes and Post-translational Modifications." Doctoral dissertation, University of Wisconsin-Madison, 2018.

[120] Y. Qi, D. A. Volmer, "Electron-based fragmentation methods in mass spectrometry: An overview." *Mass Spectrometry Reviews* **2017**, *36* (1), 4-15. DOI: 10.1002/mas.21482

[121] N. M. Riley, J. J. Coon, "The Role of Electron Transfer Dissociation in Modern Proteomics." *Analytical chemistry* **2018**, *90* (1), 40-64. DOI: 10.1021/acs.analchem.7b04810

[122] S. J. Kregel, G. K. Thurston, E. Garand, "Photoelectron spectroscopy of anthracene and fluoranthene radical anions." *The Journal of Chemical Physics* **2018**, *148* (23), 234306. DOI: 10.1063/1.5036757

[123] W. J. Richter, H. Schwarz, "Chemical Ionization—A Mass-Spectrometric Analytical Procedure of Rapidly Increasing Importance." *Angewandte Chemie International Edition in English* **1978**, *17* (6), 424-439. DOI: 10.1002/anie.197804241

[124] F. H. Field, "Chemical ionization mass spectrometry." *Accounts of Chemical Research* **1968**, *1* (2), 42-49. DOI: 10.1021/ar50002a002

[125] F. H. Field, "Chemical Ionization Mass Spectrometry." In *Ion-Molecule Reactions*, Vol. 1; Springer, 1972; pp 261-313.

[126] D. F. Hunt, F. W. Crow, "Electron capture negative ion chemical ionization mass spectrometry." *Analytical chemistry* **1978**, *50* (13), 1781-1784. DOI: 10.1021/ac50035a017

[127] R. C. Dougherty, "Negative chemical ionization mass spectrometry: applications in environmental analytical chemistry." *Biomed Mass Spectrom* **1981**, *8* (7), 283-292. DOI: 10.1002/bms.1200080702

[128] J. G. Dillard, "Negative ion mass spectrometry." *Chemical Reviews* **1968**, *73* (6), 589-643. DOI: 10.1021/cr60286a002

[129] F. Turecek, R. R. Julian, "Peptide radicals and cation radicals in the gas phase." *Chemical Reviews* **2013**, *113* (8), 6691-6733. DOI: 10.1021/cr400043s

[130] M. U. Munshi, S. M. Craig, G. Berden, J. Martens, A. F. DeBlase, D. J. Foreman, S. A. McLuckey, J. Oomens, M. A. Johnson, "Preparation of Labile Ni^+ (cyclam) Cations in the Gas Phase Using Electron-Transfer Reduction through Ion–Ion Recombination in an Ion Trap and Structural Characterization with Vibrational Spectroscopy." *The Journal of Physical Chemistry Letters* **2017**, *8* (20), 5047-5052. DOI: 10.1021/acs.jpclett.7b02223

[131] R. E. March, J. F. J. Todd, "Practical Aspects of Trapped Ion Mass Spectrometry, Volume IV." CRC press, 2010. DOI: 10.1201/9781420083729.

[132] D. Nolting, T. Schultz, I. Hertel, R. Weinkauf, "Excited state dynamics and fragmentation channels of the protonated dipeptide H 2 N-Leu-Trp-COOH." *Physical Chemistry Chemical Physics* **2006**, *8* (44), 5247-5254.

[133] D. Imanbaew, "Time-resolved pump-probe action spectroscopy on isolated organic dyes and supramolecular photocatalysts." Doctoral dissertation, Technische Universität Kaiserslautern, Kaiserslautern, Germany, 2017. https://nbn-resolving.org/urn:nbn:de:hbz:386-kluedo-46965.

[134] N. R. Daly, "Scintillation Type Mass Spectrometer Ion Detector." *Review of Scientific Instruments* **1960**, *31* (3), 264-267. DOI: 10.1063/1.1716953

[135] G. W. Goodrich, W. C. Wiley, "Continuous Channel Electron Multiplier." *Review of Scientific Instruments* **1962**, *33* (7), 761-762. DOI: 10.1063/1.1717958

[136] J. Ladislas Wiza, "Microchannel plate detectors." *Nuclear Instruments and Methods* **1979**, *162* (1-3), 587-601. DOI: 10.1016/0029-554x(79)90734-1

[137] A. D. Scarbrough, "An Analog-to-Digital Converter." *Transactions of the I.R.E. Professional Group on Electronic Computers* **1953**, *EC-2* (3), 5-7. DOI: 10.1109/irepgelc.1953.5407732

[138] K. Busch, "Space charge in mass spectrometry." *Spectroscopy* **2004**, *19* (6), 35-38.

[139] Q. Bian, M. W. Forbes, F. O. Talbot, R. A. Jockusch, "Gas-phase fluorescence excitation and emission spectroscopy of mass-selected trapped molecular ions." *Physical Chemistry Chemical Physics* **2010**, *12* (11), 2590-2598. DOI: 10.1039/b921076h

[140] T. H. Maiman, "Stimulated Optical Radiation in Ruby." *Nature* **1960**, *187* (4736), 493-494. DOI: 10.1038/187493a0

[141] P. Moulton, "Ti-doped sapphire: tunable solid-state laser." *Optics News* **1982**, *8* (6), 9-9. DOI: 10.1364/on.8.6.000009

[142] W. L. Zhou, Y. Mori, T. Sasaki, S. Nakai, K. Nakano, S. Niikura, B. Craig, "Intracavity frequency doubling of a continuous wave Ti:sapphire laser with over 70% conversion efficiency." *Applied Physics Letters* **1995**, *66* (19), 2463-2465. DOI: 10.1063/1.113996

[143] K. WALL, A. Sanchez, "Titanium sapphire lasers." *The Lincoln laboratory journal* **1990**, *3* (3), 447-462.

[144] R. R. Joyce, P. L. Richards, "Far-Infrared Spectra ofAl2O3Doped with Ti, V, and Cr." *Physical review* **1969**, *179* (2), 375-380. DOI: 10.1103/PhysRev.179.375

[145] M. Seidel, J. Brons, G. Arisholm, K. Fritsch, V. Pervak, O. Pronin, "Efficient High-Power Ultrashort Pulse Compression in Self-Defocusing Bulk Media." *Scientific Reports* **2017**, *7* (1), 1410. DOI: 10.1038/s41598-017-01504-x

[146] S. Backus, C. G. Durfee, M. M. Murnane, H. C. Kapteyn, "High power ultrafast lasers." *Review of Scientific Instruments* **1998**, *69* (3), 1207-1223. DOI: 10.1063/1.1148795

[147] P. F. Moulton, "Spectroscopic and laser characteristics of Ti:Al_2O_3." *Journal of the Optical Society of America B* **1986**, *3* (1). DOI: 10.1364/josab.3.000125

[148] V. Chvykov, "Ti:Sa Crystal Geometry Variation vs. Final Amplifiers of CPA Laser Systems Parameters." *Crystals* **2022**, *12* (8). DOI: 10.3390/cryst12081127

[149] V. Chvykov, "Ti:Sa Crystals in Ultra-High Peak and Average Power Laser Systems." *Crystals* **2021**, *11* (7), 841. DOI: 10.3390/cryst11070841

[150] P. Smith, M. Duguay, E. Ippen, "Mode-locking of lasers." *Progress in Quantum Electronics* **1974**, *3*, 107-229. DOI: 10.1016/0079-6727(74)90002-0

[151] M. Kauf, R. Patel, J. Bovatsek, "High Speed Processing for Microelectronics and Photovoltaics." *Laser Technik Journal* **2009**, *6* (1), 33-37. DOI: 10.1002/latj.200990006

[152] I. V. Ilina, A. V. Ovchinnikov, D. S. Sitnikov, M. M. Rakityanskiy, M. B. Agranat, Y. V. Khramova, M. L. Semenova, "Application of femtosecond laser pulses in biomedical cell technologies." *High Temperature* **2013**, *51* (2), 173-178. DOI: 10.1134/s0018151x13020089

[153] W. Chen, P. Xue, T. Yuan, D. Y. Chen, "Medical application of ultrafast laser." In *Commercial and Biomedical Applications of Ultrafast Lasers II*, 2000; SPIE: Vol. 3934, pp 87-92. DOI: 10.1117/12.386351.

[154] S. H. Chung, E. Mazur, "Surgical applications of femtosecond lasers." *Journal of Biophotonics* **2009**, *2* (10), 557-572. DOI: 10.1002/jbio.200910053

[155] C. H. von Helmolt, U. Kruger, K. Kruger, G. Grosskopf, "A mobile broad-band communication system based on mode-locked lasers." *IEEE transactions on microwave theory and techniques* **1997**, *45* (8), 1424-1430. DOI: 10.1109/22.618446

[156] R. L. Fork, B. I. Greene, C. V. Shank, "Generation of optical pulses shorter than 0.1 psec by colliding pulse mode locking." *Applied Physics Letters* **1981**, *38* (9), 671-672. DOI: 10.1063/1.92500

[157] J.-C. Diels, W. Rudolph, "Ultrashort Laser Pulse Phenomena." Elsevier, 2006. DOI: 10.1016/b978-0-12-215493-5.X5000-9.

[158] F. X. Kurtner, J. A. der Au, U. Keller, "Mode-locking with slow and fast saturable absorbers-what's the difference?"; *IEEE Journal of Selected Topics in Quantum Electronics* **1998**, *4* (2), 159-168. DOI: 10.1109/2944.686719

[159] S. Yefet, A. Pe'er, "A Review of Cavity Design for Kerr Lens Mode-Locked Solid-State Lasers." *Applied Sciences* **2013**, *3* (4), 694-724. DOI: 10.3390/app3040694

[160] D. E. Spence, P. N. Kean, W. Sibbett, "60-fsec pulse generation from a self-mode-locked Ti:sapphire laser." *Optics letters* **1991**, *16* (1), 42-44. DOI: 10.1364/ol.16.000042

[161] J. Kleinbauer, R. Knappe, R. Wallenstein, "Principles of ultrashort pulse generation." *Femtosecond Technology for Technical and Medical Applications* **2004**, *96*, 9-17. DOI: 10.1007/978-3-540-39848-6_2

[162] R. W. Boyd, A. L. Gaeta, E. Giese, "Nonlinear Optics." In *Springer Handbook of Atomic, Molecular, and Optical Physics*, Springer Handbooks, Springer, 2023; pp 1097-1110.

[163] C. Rullière, "Femtosecond Laser Pulses." Springer New York, NY, 2005. DOI: 10.1007/b137908.

[164] D. Strickland, G. Mourou, "Compression of amplified chirped optical pulses." *Optics communications* **1985**, *55* (6), 447-449. DOI: 10.1016/0030-4018(85)90151-8

[165] S. Kruppa, "Photochemistry and Ultrafast Dynamics of Mass-selected Multinuclear Coinage Metal Complexes Studied by Electronic Photodissociation Ion Spectroscopy in an Ion Trap." Doctoral dissertation, Technische Universität Kaiserslautern, Kaiserslautern, Germany, 2021. https://nbn-resolving.org/urn:nbn:de:hbz:386-kluedo-62586.

[166] I. K. Krasyuk, S. G. Lukishova, P. P. Pashinin, A. M. Prokhorov, "Laser system with a regenerative amplifier for generation of trains of pulses of variable amplitude." *Soviet Journal of Quantum Electronics* **1975**, *4* (7), 832-834. DOI: 10.1070/QE1975v004n07ABEH009349

[167] A. V. V. Nampoothiri, T. Kundu, B. P. Singh, "Single pulse selection from a cw mode-locked laser." *Review of Scientific Instruments* **1998**, *69* (3), 1240-1242. DOI: 10.1063/1.1148757

[168] A. E. Siegman, "Lasers." University science books, 1986.

[169] W. Koechner, "Solid-State Laser Engineering." Springer New York, NY, 2006. DOI: 10.1007/0-387-29338-8.

[170] L. Mesa Photonics, "User's Manual: VideoFROGscan - Realtime Ultrafast Pulse Measurement (Vs 003)." 2018. https://www.mesaphotonics.com/wp-content/uploads/manual.pdf (accessed 05.03.2025).

[171] L. Conversion, "User's Manual: "TOPAS-C_Manual-V2-2016-10-03"." 2016.

[172] L. Conversion, "User's Manual: "External Crystal Stages_Manual-2021-02-18"." 2021.

[173] EKSPLA, "Technical Description/User's Manual: "NT242 Series Tunable Diode Pumped Laser System - PGD236_NT242-1k-SHSF"." 2020.

[174] F. O. Talbot, S. V. Sciuto, R. A. Jockusch, "Fluorescence imaging for visualization of the ion cloud in a quadrupole ion trap mass spectrometer." *Journal of the American Society for Mass Spectrometry* **2013**, *24* (12), 1823-1832. DOI: 10.1007/s13361-013-0742-6

[175] Y. Nosenko, F. Menges, C. Riehn, G. Niedner-Schatteburg, "Investigation by two-color IR dissociation spectroscopy of Hoogsteen-type binding in a metalated nucleobase pair mimic." *Physical Chemistry Chemical Physics* **2013**, *15* (21), 8171-8178. DOI: 10.1039/c3cp44283g

[176] C. S. Hansen, S. J. Blanksby, N. Chalyavi, E. J. Bieske, J. R. Reimers, A. J. Trevitt, "Ultraviolet photodissociation action spectroscopy of the N-pyridinium cation." *The Journal of Chemical Physics* **2015**, *142* (1), 014301. DOI: 10.1063/1.4904267

[177] F. Turecek, "UV-vis spectroscopy of gas-phase ions." *Mass Spectrometry Reviews* **2023**, *42* (1), 206-226. DOI: 10.1002/mas.21726

[178] T. Baer, R. C. Dunbar, "Ion spectroscopy: where did it come from; where is it now; and where is it going?"; *Journal of the American Society for Mass Spectrometry* **2010**, *21* (5), 681-693. DOI: 10.1016/j.jasms.2010.01.028

[179] E. D. Lipson, "Action Spectroscopy." In *Biophysics of Photoreceptors and Photomovements in Microorganisms*, Springer, 1991; pp 293-309.

[180] J. Roithová, D. Schröder, "Theory meets experiment: Gas-phase chemistry of coinage metals." *Coordination Chemistry Reviews* **2009**, *253* (5-6), 666-677. DOI: 10.1016/j.ccr.2008.06.007

[181] R. A. O'Hair, N. J. Rijs, "Gas phase studies of the Pesci decarboxylation reaction: synthesis, structure, and unimolecular and bimolecular reactivity of organometallic ions." *Accounts of Chemical Research* **2015**, *48* (2), 329-340. DOI: 10.1021/ar500377u

[182] R. A. J. O'Hair, "Organometallic Gas-Phase Ion Chemistry and Catalysis: Insights into the Use of Metal Catalysts to Promote Selectivity in the Reactions of Carboxylic Acids and Their Derivatives." *Mass Spectrometry Reviews* **2021**, *40* (6), 782-810. DOI: 10.1002/mas.21654

[183] S. A. McLuckey, D. E. Goeringer, "SPECIAL FEATURE:TUTORIAL Slow Heating Methods in Tandem Mass Spectrometry." *Journal of mass spectrometry* **1997**, *32* (5), 461-474. DOI: 10.1002/(sici)1096-9888(199705)32:5<461::Aid-jms515>3.0.Co;2-h

[184] J. R. Eyler, "Infrared multiple photon dissociation spectroscopy of ions in Penning traps." *Mass Spectrometry Reviews* **2009**, *28* (3), 448-467. DOI: 10.1002/mas.20217

[185] J. R. Yates, C. I. Ruse, A. Nakorchevsky, "Proteomics by mass spectrometry: approaches, advances, and applications." *Annual review of biomedical engineering* **2009**, *11* (1), 49-79. DOI: 10.1146/annurev-bioeng-061008-124934

[186] J. C. Marcum, J. M. Weber, "Electronic photodissociation spectra and decay pathways of gas-phase $IrBr_6^{2-}$." *The Journal of Chemical Physics* **2009**, *131* (19), 194309. DOI: 10.1063/1.3265956

[187] W. E. Boxford, C. E. Dessent, "Probing the intrinsic features and environmental stabilization of multiply charged anions." *Physical Chemistry Chemical Physics* **2006**, *8* (44), 5151-5165. DOI: 10.1039/b609123g

[188] R. Cercola, E. Matthews, C. E. H. Dessent, "Photoexcitation of Adenosine 5'-Triphosphate Anions in Vacuo: Probing the Influence of Charge State on the UV Photophysics of Adenine." *The Journal of Physical Chemistry B* **2017**, *121* (22), 5553-5561. DOI: 10.1021/acs.jpcb.7b03435

[189] N. G. K. Wong, J. A. Berenbeim, M. Hawkridge, E. Matthews, C. E. H. Dessent, "Mapping the intrinsic absorption properties and photodegradation pathways of the protonated and deprotonated forms of the sunscreen oxybenzone." *Physical Chemistry Chemical Physics* **2019**, *21* (26), 14311-14321. DOI: 10.1039/c8cp06794e

[190] J. A. Berenbeim, N. G. K. Wong, M. C. R. Cockett, G. Berden, J. Oomens, A. M. Rijs, C. E. H. Dessent, "Unravelling the Keto-Enol Tautomer Dependent Photochemistry and Degradation Pathways of the Protonated UVA Filter Avobenzone." *The Journal of Physical Chemistry A* **2020**, *124* (15), 2919-2930. DOI: 10.1021/acs.jpca.0c01295

[191] R. Bersohn, A. H. Zewail, "Time Dependent Absorption of Fragments During Dissociation." *Berichte der Bunsengesellschaft für physikalische Chemie* **1988**, *92* (3), 373-378. DOI: 10.1002/bbpc.198800076

[192] R. Schinke, "Photodissociation Dynamics." Cambridge University Press, 1995. DOI: 10.1017/cbo9780511586453.

[193] M. Schmitt, "Gas-Phase Ultraviolet Photodissociation of Coinage Metal and Ruthenium(II) Complexes with Femto- and Nanosecond Pulses." Master's thesis, Rheinland-Pfälzische Technische Universität Kaiserslautern (RPTU), Kaiserlautern, Germany, 2020.

[194] I. V. Hertel, W. Radloff, "Ultrafast dynamics in isolated molecules and molecular clusters." *Reports on Progress in Physics* **2006**, *69* (6), 1897-2003. DOI: 10.1088/0034-4885/69/6/r06

[195] R. Antoine, P. Dugourd, "Visible and ultraviolet spectroscopy of gas phase protein ions." *Physical Chemistry Chemical Physics* **2011**, *13* (37), 16494-16509. DOI: 10.1039/c1cp21531k

[196] M. W. Forbes, R. A. Jockusch, "Gas-phase fluorescence excitation and emission spectroscopy of three xanthene dyes (rhodamine 575, rhodamine 590 and rhodamine 6G) in a quadrupole ion trap mass spectrometer." *Journal of the American Society for Mass Spectrometry* **2011**, *22* (1), 93-109. DOI: 10.1007/s13361-010-0017-4

[197] G. Grégoire, B. Lucas, M. Barat, J. A. Fayeton, C. Dedonder-Lardeux, C. Jouvet, "UV photoinduced dynamics in protonated aromatic amino acid." *The European Physical Journal D* **2008**, *51* (1), 109-116. DOI: 10.1140/epjd/e2008-00085-3

[198] D. Nolting, T. Schultz, I. V. Hertel, R. Weinkauf, "Excited state dynamics and fragmentation channels of the protonated dipeptide H_2N-Leu-Trp-COOH." *Physical Chemistry Chemical Physics* **2006**, *8* (44), 5247-5254. DOI: 10.1039/b609726j

[199] L. Radom, P. M. W. Gill, M. W. Wong, "Simple models for describing the fragmentation behavior of multiply charged cations." *International Journal of Quantum Chemistry* **1988**, *34* (S22), 567-573. DOI: 10.1002/qua.560340861

[200] A. H. Zewail, "Femtochemistry: Atomic-Scale Dynamics of the Chemical Bond Using Ultrafast Lasers (Nobel Lecture) Copyright((c)) The Nobel Foundation 2000. We thank the Nobel Foundation, Stockholm, for permission to print this lecture." *Angewandte Chemie International Edition* **2000**, *39* (15), 2586-2631. DOI: 10.1002/1521-3773(20000804)39:15<2586::aid-anie2586>3.0.co;2-o

[201] H. Kang, C. Jouvet, C. Dedonder-Lardeux, S. Martrenchard, C. Charriere, G. Gregoire, C. Desfrancois, J. P. Schermann, M. Barat, J. A. Fayeton, "Photoinduced processes in protonated tryptamine." *J Chem Phys* **2005**, *122* (8), 84307. DOI: 10.1063/1.1851503

[202] H. Kang, C. Dedonder-Lardeux, C. Jouvet, G. Gregoire, C. Desfrancois, J. P. Schermann, M. Barat, J. A. Fayeton, "Control of bond-cleaving reactions of free protonated tryptophan ion by femtosecond laser pulses." *The Journal of Physical Chemistry A* **2005**, *109* (11), 2417-2420. DOI: 10.1021/jp0407167

[203] D. Imanbaew, J. Lang, M. F. Gelin, S. Kaufhold, M. G. Pfeffer, S. Rau, C. Riehn, "Pump-Probe Fragmentation Action Spectroscopy: A Powerful Tool to Unravel Light-Induced Processes in Molecular Photocatalysts." *Angewandte Chemie* **2017**, *129* (20), 5563-5566. DOI: 10.1002/ange.201612302

[204] C. Harthcock, J. Zhang, W. Kong, "Resonantly enhanced multiphoton ionization and zero kinetic energy photoelectron spectroscopy of benzo[e]pyrene." *Chemical Physics Letters* **2013**, *556*, 23-28. DOI: 10.1016/j.cplett.2012.11.036

[205] Y. Zhao, Y. Jin, C. Li, S. Jia, "Two-color resonance enhanced two-photon ionization and mass analyzed threshold ionization spectroscopy of 2-methoxybenzonitrile." *Journal of Molecular Spectroscopy* **2019**, *363*. DOI: 10.1016/j.jms.2019.111182

[206] Y. Zhang, H. Liu, Y. Weng, "Theoretical and Experimental Investigation of the Electronic Propensity Rule: A Linear Relationship between Radiative and Nonradiative Decay Rates of Molecules." *The Journal of Physical Chemistry Letters* **2023**, *14* (18), 4151-4157. DOI: 10.1021/acs.jpclett.3c00697

[207] S. V. Kruppa, M. Schmitt, R. Israil, F. Bäppler, M. Grupe, L. Schüssler, R. Diller, W. Klopper, C. Riehn, "Gold Rush in Dynamics? Time-resolved Ion Spectroscopy Reveals Ultrafast Processes in Isomorphic, Ligated Ag/Au Coinage Metal Dimers." In The 22nd International Conference on Ultrafast Phenomena 2020, 2020.

[208] R. Wu, T. B. McMahon, "An investigation of protonation sites and conformations of protonated amino acids by IRMPD spectroscopy." *A European Journal of Chemical Physics and Physical Chemistry* **2008**, *9* (18), 2826-2835. DOI: 10.1002/cphc.200800543

[209] D. Imanbaew, J. Lang, M. F. Gelin, S. Kaufhold, M. G. Pfeffer, S. Rau, C. Riehn, "Pump-Probe Fragmentation Action Spectroscopy: A Powerful Tool to Unravel Light-Induced Processes in Molecular Photocatalysts." *Angewandte Chemie International Edition in English* **2017**, *56* (20), 5471-5474. DOI: 10.1002/anie.201612302

[210] S. V. Kruppa, F. Bappler, W. Klopper, S. P. Walg, W. R. Thiel, R. Diller, C. Riehn, "Ultrafast excited-state relaxation of a binuclear Ag(i) phosphine complex in gas phase and solution." *Physical Chemistry Chemical Physics* **2017**, *19* (34), 22785-22800. DOI: 10.1039/c7cp04128d

[211] M. E. Tuckerman, "Statistical Mechanics: Theory and Molecular Simulation." Oxford University Press, 2023. DOI: 10.1093/oso/9780198825562.001.0001.

[212] T. Schlick, "Molecular Modeling and Simulation: An Interdisciplinary Guide." Springer New York, NY, 2010. DOI: 10.1007/978-1-4419-6351-2.

[213] V. Grimm, S. F. Railsback, "Individual-based Modeling and Ecology." In *Individual-based modeling and ecology*, Princeton Series in Theoretical and Computational Biology, Princeton University Press, 2013.

[214] R. O. Jones, "Density functional theory: Its origins, rise to prominence, and future." *Reviews of Modern Physics* **2015**, *87* (3), 897-923. DOI: 10.1103/RevModPhys.87.897

[215] "Gaussian 16 Rev. C.01." Wallingford, CT, 2016. (accessed.

[216] A. D. Becke, "Perspective: Fifty years of density-functional theory in chemical physics." *The Journal of Chemical Physics* **2014**, *140* (18), 18A301. DOI: 10.1063/1.4869598

[217] R. M. Dreizler, E. K. U. Gross, "Density Functional Theory: An Approach to the Quantum Many-Body Problem." Springer Berlin, Heidelberg, 1990. DOI: 10.1007/978-3-642-86105-5.

[218] E. Fermi, "Eine statistische Methode zur Bestimmung einiger Eigenschaften des Atoms und ihre Anwendung auf die Theorie des periodischen Systems der Elemente." *Zeitschrift f□r Physik* **1928**, *48* (1-2), 73-79. DOI: 10.1007/bf01351576

[219] L. H. Thomas, "The calculation of atomic fields." In *Mathematical proceedings of the Cambridge philosophical society*, 1927; Cambridge University Press: Vol. 23, pp 542-548. DOI: 10.1017/S0305004100011683.

[220] E. Teller, "On the Stability of Molecules in the Thomas-Fermi Theory." *Reviews of Modern Physics* **1962**, *34* (4), 627. DOI: 10.1103/RevModPhys.34.627

[221] P. A. Dirac, "Note on Exchange Phenomena in the Thomas Atom." In *Mathematical proceedings of the Cambridge philosophical society*, 1930; Cambridge University Press: Vol. 26, pp 376-385. DOI: 10.1017/S0305004100016108.

[222] E. Schrödinger, "An Undulatory Theory of the Mechanics of Atoms and Molecules." *Physical review* **1926**, *28* (6), 1049-1070. DOI: 10.1103/PhysRev.28.1049

[223] P. Hohenberg, W. Kohn, "Inhomogeneous Electron Gas." *Physical review* **1964**, *136* (3B), B864-B871. DOI: 10.1103/PhysRev.136.B864

[224] W. Kohn, L. J. Sham, "Self-Consistent Equations Including Exchange and Correlation Effects." *Physical review* **1965**, *140* (4A), A1133-A1138. DOI: 10.1103/PhysRev.140.A1133

[225] J. Toulouse, "Review of Approximations for the Exchange-Correlation Energy in Density-Functional Theory." In *Density Functional Theory: Modeling, Mathematical Analysis, Computational Methods, and Applications*, Springer, Cham, 2022; pp 1-90.

[226] U. v. Barth, L. Hedin, "A local exchange-correlation potential for the spin polarized case. i." *Journal of Physics C: Solid State Physics* **1972**, *5* (13), 1629-1642. DOI: 10.1088/0022-3719/5/13/012

[227] C. Peng, H. Bernhard Schlegel, "Combining Synchronous Transit and Quasi-Newton Methods to Find Transition States." *Israel Journal of Chemistry* **2013**, *33* (4), 449-454. DOI: 10.1002/ijch.199300051

[228] A. D. Becke, "Density-functional thermochemistry. I. The effect of the exchange-only gradient correction." *The Journal of Chemical Physics* **1992**, *96* (3), 2155-2160. DOI: 10.1063/1.462066

[229] C. Lee, W. Yang, R. G. Parr, "Development of the Colle-Salvetti correlation-energy formula into a functional of the electron density." *Physical review B* **1988**, *37* (2), 785-789. DOI: 10.1103/PhysRevB.37.785

[230] P. J. Stephens, F. J. Devlin, C. F. Chabalowski, M. J. Frisch, "Ab Initio Calculation of Vibrational Absorption and Circular Dichroism Spectra Using Density Functional Force Fields." *The Journal of Physical Chemistry* **1994**, *98* (45), 11623-11627. DOI: 10.1021/j100096a001

[231] F. Devlin, J. Finley, P. Stephens, M. Frisch, "Ab initio calculation of vibrational absorption and circular dichroism spectra using density functional force fields: a comparison of local, nonlocal, and hybrid density functionals." *The Journal of Physical Chemistry* **1995**, *99* (46), 16883-16902.

[232] S. Hirata, M. Head-Gordon, R. J. Bartlett, "Configuration interaction singles, time-dependent Hartree–Fock, and time-dependent density functional theory for the electronic excited states of extended systems." *The Journal of Chemical Physics* **1999**, *111* (24), 10774-10786. DOI: 10.1063/1.480443

[233] A. D. Becke, "A new mixing of Hartree–Fock and local density-functional theories." *The Journal of Chemical Physics* **1993**, *98* (2), 1372-1377. DOI: 10.1063/1.464304

[234] E. Runge, E. K. U. Gross, "Density-Functional Theory for Time-Dependent Systems." *Physical review letters* **1984**, *52* (12), 997-1000. DOI: 10.1103/PhysRevLett.52.997

[235] M. A. Marques, E. K. Gross, "Time-dependent density functional theory." *Annual Review of Physical Chemistry* **2004**, *55* (1), 427-455. DOI: 10.1146/annurev.physchem.55.091602.094449

[236] M. E. Casida, "Time-dependent density-functional theory for molecules and molecular solids." *Journal of Molecular Structure: THEOCHEM* **2009**, *914* (1-3), 3-18. DOI: 10.1016/j.theochem.2009.08.018

[237] C. A. Ullrich, "Time-Dependent Density-Functional Theory." Oxford University Press, 2011. DOI: 10.1093/acprof:oso/9780199563029.001.0001.

[238] M. E. Casida, "Time-Dependent Density Functional Response Theory for Molecules." In *Recent Advances in Density Functional Methods*, Recent Advances in Computational Chemistry, World Scientific, 1995; pp 155-192.

[239] L. Lacombe, N. T. Maitra, "Developing new and understanding old approximations in TDDFT." *Faraday Discussions* **2020**, *224* (0), 382-401. DOI: 10.1039/d0fd00049c

[240] P. Weber, "Ultrafast dynamics and UV/VIS action spectroscopy of mono- and bimetallic complexes in an ion trap, utilizing electron transfer reduction." Master's thesis, Rheinland-Pfälzische Technische Universität Kaiserslautern (RPTU), Kaiserlautern, Germany, 2023.

[241] F. Menges, "Structure and Reactivity of Isolated Mononuclear and Oligonuclear Metal Complexes." Doctoral Dissertation, Technische Universität Kaiserslautern, Kaiserslautern, Germany, 2013. https://nbn-resolving.org/urn:nbn:de:hbz:386-kluedo-35513.

[242] J. D. Bhawalkar, G. S. He, P. N. Prasad, "Nonlinear multiphoton processes in organic and polymeric materials." *Reports on Progress in Physics* **1996**, *59* (9), 1041-1070. DOI: 10.1088/0034-4885/59/9/001

[243] A. K. Rappé, E. R. Bernstein, "Ab Initio Calculation of Nonbonded Interactions: Are We There Yet?"; *The Journal of Physical Chemistry A* **2000**, *104* (26), 6117-6128. DOI: 10.1021/jp0008997

[244] K. A. Peterson, D. Figgen, M. Dolg, H. Stoll, "Energy-consistent relativistic pseudopotentials and correlation consistent basis sets for the 4d elements Y-Pd." *The Journal of Chemical Physics* **2007**, *126* (12), 124101. DOI: 10.1063/1.2647019

[245] D. Figgen, G. Rauhut, M. Dolg, H. Stoll, "Energy-consistent pseudopotentials for group 11 and 12 atoms: adjustment to multi-configuration Dirac–Hartree–Fock data." *Chemical Physics* **2005**, *311* (1-2), 227-244. DOI: 10.1016/j.chemphys.2004.10.005

[246] J. Oomens, G. von Helden, G. Meijer, "Experimental observation of laser-induced coherent ion motion in a quadrupole trap." *International Journal of Mass Spectrometry* **2002**, *221* (2), 163-176. DOI: 10.1016/s1387-3806(02)00988-0

[247] T. S. Neugebauer, "Dynamics of the Collision-Induced Dissociation Process in Quadrupole Ion Traps and its Application." Doctoral dissertation, Friedrich-Alexander-Universität, Erlangen-Nürnberg (Germany), 2019. https://nbn-resolving.org/urn:nbn:de:bvb:29-opus4-125562.

[248] C. Streb, K. Kastner, J. Tucher, "Polyoxometalates in photocatalysis." *Physical Sciences Reviews* **2019**, *4* (6), 20170177. DOI: 10.1515/psr-2017-0177

[249] C. Streb, K. Kastner, J. Tucher, "15. Polyoxometalates in photocatalysis." In *Chemical Photocatalysis*, De Gruyter, 2020; pp 363-378.

[250] Y. Hayashi, "Hetero and lacunary polyoxovanadate chemistry: Synthesis, reactivity and structural aspects." *Coordination Chemistry Reviews* **2011**, *255* (19-20), 2270-2280. DOI: 10.1016/j.ccr.2011.02.013

[251] Y. Ji, L. Huang, J. Hu, C. Streb, Y.-F. Song, "Polyoxometalate-functionalized nanocarbon materials for energy conversion, energy storage and sensor systems." *Energy & Environmental Science* **2015**, *8* (3), 776-789. DOI: 10.1039/c4ee03749a

[252] J. M. Cameron, L. Vila-Nadal, R. S. Winter, F. Iijima, J. C. Murillo, A. Rodriguez-Fortea, H. Oshio, J. M. Poblet, L. Cronin, "Investigating the Transformations of Polyoxoanions Using Mass Spectrometry and Molecular Dynamics." *Journal of the American Chemical Society* **2016**, *138* (28), 8765-8773. DOI: 10.1021/jacs.6b02245

[253] J. Dopta, L. K. Mahnke, W. Bensch, "New pronounced progress in the synthesis of group 5 polyoxometalates." *CrystEngComm* **2020**, *22* (19), 3254-3268. DOI: 10.1039/d0ce00315h

[254] Fabian L. Huber, S. Amthor, B. Schwarz, B. Mizaikoff, C. Streb, S. Rau, "Multi-phase real-time monitoring of oxygen evolution enables in operando water oxidation catalysis studies." *Sustainable Energy & Fuels* **2018**, *2* (9), 1974-1978. DOI: 10.1039/c8se00328a

[255] N. M. Al Hasan, G. E. Johnson, J. Laskin, "Gas-phase synthesis of singly and multiply charged polyoxovanadate anions employing electrospray ionization and collision induced dissociation." *Journal of the American Society for Mass Spectrometry* **2013**, *24* (9), 1385-1395. DOI: 10.1007/s13361-013-0683-0

[256] D. Favre, C. E. Bobst, S. J. Eyles, H. Murakami, D. C. Crans, I. A. Kaltashov, "Solution- and gas-phase behavior of decavanadate: implications for mass spectrometric analysis of redox-active polyoxidometalates." *Inorganic chemistry frontiers* **2022**, *9* (7), 1556-1564. DOI: 10.1039/d1qi01618k

[257] O. W. Howarth, M. Jarrold, "Protonation of the decavanadate(6–) ion: a vanadium-51 nuclear magnetic resonance study." *Journal of the Chemical Society, Dalton Transactions* **1978**, (5), 503-506. DOI: 10.1039/dt9780000503

[258] M. Aureliano, D. C. Crans, "Decavanadate ($V_{10}O_{28}^{6-}$) and oxovanadates: oxometalates with many biological activities." *Journal of Inorganic Biochemistry* **2009**, *103* (4), 536-546. DOI: 10.1016/j.jinorgbio.2008.11.010

[259] D. E. Romonosky, A. Laskin, J. Laskin, S. A. Nizkorodov, "High-resolution mass spectrometry and molecular characterization of aqueous photochemistry products of common types of secondary organic aerosols." *The Journal of Physical Chemistry A* **2015**, *119* (11), 2594-2606. DOI: 10.1021/jp509476r

[260] K. Yamaguchi, "Cold-spray ionization mass spectrometry: principle and applications." *Journal of mass spectrometry* **2003**, *38* (5), 473-490. DOI: 10.1002/jms.488

[261] K. Yamaguchi, "Cold-spray ionization mass spectrometry: applications in structural coordination chemistry." *Mass Spectrometry (Tokyo)* **2013**, *2* (Spec Iss), S0012. DOI: 10.5702/massspectrometry.S0012

[262] T. Waters, X. Huang, X. B. Wang, H. K. Woo, A. O'Hair R, A. G. Wedd, L. S. Wang, "Photoelectron spectroscopy of free multiply charged Keggin anions alpha-$[PM_{12}O_{40}]^{3-}$ (M = Mo, W) in the gas phase." *The Journal of Physical Chemistry A* **2006**, *110* (37), 10737-10741. DOI: 10.1021/jp063594m

[263] N. D. Rodrigues, M. Staniforth, V. G. Stavros, "Photophysics of sunscreen molecules in the gas phase: a stepwise approach towards understanding and developing next-generation sunscreens." *Proceedings of the Royal Society A: Mathematical, Physical and Engineering Sciences* **2016**, *472* (2195), 20160677. DOI: 10.1098/rspa.2016.0677

[264] A. B. Wolk, C. M. Leavitt, E. Garand, M. A. Johnson, "Cryogenic ion chemistry and spectroscopy." *Accounts of Chemical Research* **2014**, *47* (1), 202-210. DOI: 10.1021/ar400125a

[265] V. Artero, M. Chavarot-Kerlidou, M. Fontecave, "Splitting water with cobalt." *Angewandte Chemie International Edition in English* **2011**, *50* (32), 7238-7266. DOI: 10.1002/anie.201007987

[266] K. Kalyanasundaram, "Photophysics, photochemistry and solar energy conversion with tris(bipyridyl)ruthenium(II) and its analogues." *Coordination Chemistry Reviews* **1982**, *46*, 159-244. DOI: 10.1016/0010-8545(82)85003-0

[267] J. J. Concepcion, J. W. Jurss, M. K. Brennaman, P. G. Hoertz, A. O. Patrocinio, N. Y. Murakami Iha, J. L. Templeton, T. J. Meyer, "Making oxygen with ruthenium complexes." *Accounts of Chemical Research* **2009**, *42* (12), 1954-1965. DOI: 10.1021/ar9001526

[268] V. Balzani, A. Credi, M. Venturi, "Photochemical conversion of solar energy." *ChemSusChem* **2008**, *1* (1-2), 26-58. DOI: 10.1002/cssc.200700087

[269] G. S. Bindra, M. Schulz, A. Paul, R. Groarke, S. Soman, J. L. Inglis, W. R. Browne, M. G. Pfeffer, S. Rau, B. J. MacLean, M. T. Pryce, J. G. Vos, "The role of bridging ligand in hydrogen generation by photocatalytic Ru/Pd assemblies." *Dalton Transactions* **2012**, *41* (42), 13050-13059. DOI: 10.1039/c2dt30948c

[270] C. Chiorboli, S. Fracasso, M. Ravaglia, F. Scandola, S. Campagna, K. L. Wouters, R. Konduri, F. M. MacDonnell, "Primary photoinduced processes in bimetallic dyads with extended aromatic bridges. tetraazatetrapyridopentacene complexes of ruthenium(II) and osmium(II)." *Inorganic Chemistry* **2005**, *44* (23), 8368-8378. DOI: 10.1021/ic051062z

[271] Y. Halpin, M. T. Pryce, S. Rau, D. Dini, J. G. Vos, "Recent progress in the development of bimetallic photocatalysts for hydrogen generation." *Dalton Transactions* **2013**, *42* (46), 16243-16254. DOI: 10.1039/c3dt52319e

[272] S. Kaufhold, D. Imanbaew, C. Riehn, S. Rau, "Rational in situ tuning of a supramolecular photocatalyst for hydrogen evolution." *Sustainable Energy & Fuels* **2017**, *1* (10), 2066-2070. DOI: 10.1039/c7se00401j

[273] M. H. Putra, B. Bagemihl, S. Rau, A. Gross, "Prediction of Strong Solvatochromism in a Molecular Photocatalyst." *Chemistry* **2024**, *30* (1), e202302643. DOI: 10.1002/chem.202302643

[274] L. Zedler, A. K. Mengele, K. M. Ziems, Y. Zhang, M. Wachtler, S. Grafe, T. Pascher, S. Rau, S. Kupfer, B. Dietzek, "Unraveling the Light-Activated Reaction Mechanism in a Catalytically Competent Key Intermediate of a Multifunctional Molecular Catalyst for Artificial Photosynthesis." *Angew Chem Int Ed Engl* **2019**, *58* (37), 13140-13148. DOI: 10.1002/anie.201907247

[275] B. E. Gupta, Anil J., "Basic Organometallic Chemistry: Concepts, Syntheses, and Applications of Transition Metals "; Universities Press, 2010.

[276] C. Kuhnt, M. Karnahl, S. Tschierlei, K. Griebenow, M. Schmitt, B. Schafer, S. Krieck, H. Gorls, S. Rau, B. Dietzek, J. Popp, "Substitution-controlled ultrafast excited-state processes in Ru-dppz-derivatives." *Physical Chemistry Chemical Physics* **2010**, *12* (6), 1357-1368. DOI: 10.1039/b915770k

[277] L. Han, C. E. Costello, "Electron transfer dissociation of milk oligosaccharides." *Journal of the American Society for Mass Spectrometry* **2011**, *22* (6), 997-1013. DOI: 10.1007/s13361-011-0117-9

[278] A. Pita-Milleiro, M. G. Alferez, J. J. Moreno, M. F. Espada, C. Maya, J. Campos, "Unveiling the Latent Reactivity of Cp* Ligands ($[C_5Me_5]^-$) toward Carbon Nucleophiles on an Iridium Complex." *Inorganic Chemistry* **2023**, *62* (15), 5961-5971. DOI: 10.1021/acs.inorgchem.2c04381

[279] M. U. Munshi, J. Martens, G. Berden, J. Oomens, "Vibrational Spectra of the Ruthenium-Tris-Bipyridine Dication and Its Reduced Form in Vacuo." *The Journal of Physical Chemistry A* **2020**, *124* (12), 2449-2459. DOI: 10.1021/acs.jpca.0c00888

[280] M. U. Munshi, J. Martens, G. Berden, J. Oomens, "Gas-Phase Infrared Ion Spectroscopy Characterization of Cu(II/I)Cyclam and Cu(II/I)2,2'-Bipyridine Redox Pairs." *The Journal of Physical Chemistry A* **2019**, *123* (19), 4149-4157. DOI: 10.1021/acs.jpca.9b00793

[281] M. E. Huber, A. Ceman, P. Weber, L. Berg, N. R. East, C. Riehn, K. Heinze, J. Meyer, "Gas-Phase Characterization of Redox-Active Manganese Complexes." *Journal of the American Society for Mass Spectrometry* **2024**, *35* (11), 2642-2649. DOI: 10.1021/jasms.4c00113

[282] S. Losse, H. Görls, R. Groarke, J. G. Vos, S. Rau, "One-Step Synthesis of 4,4′-Dicyano-2,2′-bipyridine and Its Bis(4,4′-di-tert-butyl-2,2′-bipyridine)ruthenium(II) Complex." *European Journal of Inorganic Chemistry* **2008**, *2008* (28), 4448-4452. DOI: 10.1002/ejic.200701304

[283] L. Zedler, P. Wintergerst, A. K. Mengele, C. Muller, C. Li, B. Dietzek-Ivansic, S. Rau, "Outpacing conventional nicotinamide hydrogenation catalysis by a strongly communicating heterodinuclear photocatalyst." *Nature Communications* **2022**, *13* (1), 2538. DOI: 10.1038/s41467-022-30147-4

[284] L. Jasikova, J. Roithova, "Infrared Multiphoton Dissociation Spectroscopy with Free-Electron Lasers: On the Road from Small Molecules to Biomolecules." *Chemistry* **2018**, *24* (14), 3374-3390. DOI: 10.1002/chem.201705692

[285] A. Juris, V. Balzani, F. Barigelletti, S. Campagna, P. Belser, A. von Zelewsky, "Ru(II) polypyridine complexes: photophysics, photochemistry, eletrochemistry, and chemiluminescence." *Coordination Chemistry Reviews* **1988**, *84*, 85-277. DOI: 10.1016/0010-8545(88)80032-8

[286] M. Bräutigam, M. Wächtler, S. Rau, J. r. Popp, B. Dietzek, "Photophysical Dynamics of a Ruthenium Polypyridine Dye Controlled by Solvent pH." *The Journal of Physical Chemistry C* **2012**, *116* (1), 1274-1281. DOI: 10.1021/jp209103m

[287] M. Karnahl, S. Tschierlei, C. Kuhnt, B. Dietzek, M. Schmitt, J. Popp, M. Schwalbe, S. Krieck, H. Gorls, F. W. Heinemann, S. Rau, "Synthesis and characterization of regioselective substituted tetrapyridophenazine ligands and their Ru(II) complexes." *Dalton Transactions* **2010**, *39* (9), 2359-2370. DOI: 10.1039/b917484b

[288] I. Ortmans, P. Didier, A. Kirsch-De Mesmaeker, "New Charge Transfer Luminescent Polymetallic Complexes of Rhodium(III), Iridium(III), and Ruthenium(II) with the Bridging Ligand 1,4,5,8,9,12-Hexaazatriphenylene." *Inorganic Chemistry* **1995**, *34* (14), 3695-3704. DOI: 10.1021/ic00118a017

[289] J. Cao, Y. Zhou, "Excited state relaxation processes of H_2-evolving Ru-Pd supramolecular photocatalysts containing a linear or non-linear bridge: a DFT and TDDFT study." *Physical Chemistry Chemical Physics* **2017**, *19* (18), 11529-11539. DOI: 10.1039/c6cp07857e

[290] L. Zedler, C. Muller, P. Wintergerst, A. K. Mengele, S. Rau, B. Dietzek-Ivansic, "Influence of the Linker Chemistry on the Photoinduced Charge-Transfer Dynamics of Hetero-dinuclear Photocatalysts." *Chemistry* **2022**, *28* (35), e202200490. DOI: 10.1002/chem.202200490

Eidesstaatliche Erklärung

Hiermit erkläre ich, M. Sc. Roumany Israil, dass die vorliegende Arbeit gemäß der Promotionsordnung des Fachbereichs Chemie der Rheinland-Pfälzischen Technischen Universität, Standort Kaiserslautern, eigenständig und unter Verwendung der angegebenen Quellen und Hilfsmittel verfasst wurde. Alle verwendeten Literaturquellen sind als solche gekennzeichnet. Diese Arbeit liegt weder in gleicher noch in abgewandelter Form in einem anderen Prüfungsverfahren vor.

Kaiserslautern, den

Roumany G. E. Israil

Academic Résumé

Roumany G. E. Israil

Education

June 2025

Doctor of Natural Sciences (Dr. rer. nat.) – Chemistry (Grade: 1.0)
Rheinland-Pfälzische Technische Universität (RPTU), Kaiserslautern
Dissertation: *Ultrafast Ion Spectroscopy of Transition Metal Complexes in Gas Phase*

2017 – 2019
Master of Science – Chemistry (Grade: 2.0)
Technische Universität Kaiserslautern (now RPTU)
Thesis: *Spectroscopy, Fragmentation and Ultrafast Dynamics on Ru(II) Polypyridyl Complexes in an Ion Trap*

2012 – 2016
Bachelor of Science – Chemistry (Grade: 3.1)
Universität des Saarlandes
Thesis: *Synthese von wasserlöslichen, biaziden Photosäuren auf Basis von Pyrenol*

2009 – 2012
Abitur – Gymnasium am Steinwald, Neunkirchen (Grade: 2.8)
Advanced Courses: Mathematics & German

2006 – 2009
Realschulabschluss – Alex-Deutsch-Schule, Neunkirchen (Grade: 1.5)

Research Experience

2019 – 2023 - Doctoral Researcher & Scientific Assistant, RPTU Kaiserslautern

- Specialization in spectroscopic and mass spectrometric analyses of transition metal complexes
- Quantum chemical calculations in coordination with experimental studies
- Research topics include:
    - Ru(II) polypyridine complexes
    - Mono-/dinuclear pyridyl-triazol/DPEPhos-based Cu(I) complexes
    - Au(I)/Ru(II) cyclophanyl complexes
    - Peroxovanadate systems
    - Ru(II)/Rh(I) photocatalysts
- Presentation of findings at international conferences
- Publication of research in peer-reviewed journals
- Supervision of undergraduate theses and laboratory practicals

Technical & Laboratory Skills

- **Spectroscopy**: Ultrafast laser spectroscopy (fs/ns UVPD, transient absorption), UV-Vis
- **Mass Spectrometry**: ESI-MS, MS/MS, ion trap techniques, GC-MS, HPLC-MS
- **Computational Chemistry**: DFT, TD-DFT, Gaussian
- **Programming & Data Analysis**: Python, R, OriginLab
- **Laboratory Management**: Maintenance of mass spectrometers and laser systems

Conferences & Publications

Peer-Reviewed Publications

- *Physical Chemistry Chemical Physics* (2023): Ultrafast spectroscopy of Ru(II) polypyridine complexes in gas and liquid phases.
- *Chemistry – A European Journal* (2021): Photoredox catalysis in Au(I)/Ru(II) cyclophanyl complexes and Cu(I) complexes using time-resolved spectroscopy.
- Manuscript submitted (2024): Ligand-driven control of electronic state lifetimes in Ru(II) polypyridine complexes.

Conference Proceedings

- *Ultrafast Phenomena 2022*: Ligand dissociation dynamics of Ru(II) complexes in gas and solution phases.
- *Ultrafast Phenomena 2020*: Time-resolved ion spectroscopy of Ag/Au dimers.

Selected Conference Presentations

- *International Conference on Ultrafast Phenomena* (2020, 2022)
- *DPG Spring Meetings* (2021, 2022)
- *Bunsen Conferences* (2020, 2021)
- *3MET PhD Meetings & Collaborative Symposia* (2018–2021)
- *Workshop on Light-Controlled Reactivity of Metal Complexes* (2020)
- *SAMOP DPG Conference* (2021)

Certifications & Additional Training

February – April 2025 Training in GMP, Regulatory Affairs, GCP
2022 Certified Quality Officer (TÜV)
2022 Laser Safety Officer Certification
2020 – 2021 Workshops: Project Management, Scientific Writing, Communication & Leadership

Languages

- **German** (Native)
- **English** (Fluent)
- **Arabic** (Fluent)
- **Italian** (Conversational)
- **French** (Basic)
- **Coptic** (Basic)

Diese Arbeit endet hier – nicht mit einem Punkt, sondern mit einem Semikolon.

Sie steht zwischen dem, was war, und dem, was noch kommt.

Die Türen stehen offen: zum nächsten Labor, zum nächsten Paper, zum nächsten Gedanken.

Was bleibt, ist die Neugier – und die leise Hoffnung, dass jede Erkenntnis zur nächsten (eindeutigen) Frage führt.